Structure of liquid and glassy materials from ambient to extreme conditions: a multiprobe approach

Chirawatkul, Prae

Award date:
2010

Awarding institution:
University of Bath

Structure of liquid and glassy materials from ambient to extreme conditions: a multiprobe approach

Prae Chirawatkul

A thesis submitted for the degree of Doctor of Philosophy

University of Bath
Department of Physics
November 2010

Abstract

The structure of molten $Au_{0.81}Si_{0.19}$, $Au_{0.72}Ge_{0.28}$ and $Ag_{0.74}Ge_{0.26}$ alloys with a composition at or near to the eutectic was investigated by using neutron diffraction (ND). The results suggest that the Au-Au distance in the alloys is similar to that of liquid Au, there is a preference for Au-Si bonds and show that there are pre-peaks in the total structure factors for $Au_{0.72}Ge_{0.28}$ and $Ag_{0.74}Ge_{0.26}$ at 1.3(2) and 1.6(3) $Å^{-1}$, respectively. The asymptotic decay of the pair correlation functions was found to agree both with a theoretical prediction based on simple pair potentials and a fractal model for metallic glasses.

The structure of glassy $(R_2O_3)_{0.2}(Al_2O_3)_{0.2}(SiO_2)_{0.6}$, where R denotes Dy, Ho or a 50:50 mixture of Dy and Ho, was investigated by using the method of isomorphic substitution in ND, x-ray diffraction (XRD) and extended x-ray absorption fine structure (EXAFS) spectroscopy. The network is made from SiO_4 tetrahedral units with a distribution of AlO_4, AlO_5 and AlO_6 units giving an average coordination number of 4.5(1). There is a distribution of RO_5, RO_6, RO_7, RO_8 and RO_9 units with an average coordination number of 7.2(3) and an average R-O distance of 2.33(2) Å. The EXAFS results confirmed that Dy and Ho are isomorphic and were used to refine an RMC model of the structure. R-Al and R-Si nearest neighbour shells with average distances of 3.15(3) and 3.6(1) Å were required to fit the EXAFS results.

The structure of glassy and liquid $ZnCl_2$ was studied by using ND and XRD. The material has a network structure made from $ZnCl_4$ tetrahedra units which is retained in the liquid at temperatures near to the boiling point. An increase of temperature promotes edge sharing connectivity as inferred from a decrease of the Zn-Zn nearest neighbour distance and average Zn-Cl coordination number. An EXAFS study on crystalline $ZnCl_2$ at room temperature shows that Zn remains 4-fold coordinated at pressures less than 1 GPa, is 4+2-fold coordinated at 2-4 GPa, and is 6-fold coordinated above 4 GPa. For liquid $ZnCl_2$, Zn is 4-fold coordinated by Cl at a pressure of about 1 GPa and could be 6-fold coordinated at 2-3 GPa.

Acknowledgements

There are many people who have helped me in many ways during my PhD. Firstly, I would like to thank my supervisor Prof Phil Salmon for his helpful advice, inspiration and encouragement. Lots of thanks to former and present members of our Liquid and Amorphous Materials (LAM) group at the University of Bath, Harry Bone, Prof Takeshi and Yasuyo Usuki, Dr Anita Zeidler, Dr James Drewitt, Dean Whittaker and Kamil Wezka for their friendship and great help. Go Team Bath!

The sample preparation would not be possible without the help from our friendly technicians at the University of Bath. I thank Wendy Lambson and Paul Reddish from the physics department and Phil Jones from the chemistry department. I would also like to thank the staffs at the physics department especially Eva Ashcroft, Alison Humphries, and Adrian Hooper, for their help in many occasions.

I very much appreciate great support during the experiments and helpful discussions concerning the data analysis from the experimental scientists and technicians at the BM29, ID24 and ID27 beamlines at the European Synchrotron Radiation Facility (ESRF) and at the D4c diffractometer at the Institut Laue-Langevin (ILL), especially Dr Giuliana Aquilanti, Dr Angela Trapananti, Dr Wilson Crichton, Olivier Mathon, Dr Henry Fischer and Pierre Palleau. I would also like to thank Dr Adrian Barnes, Dr Silvia Ramos and Pinit Kidkhunthod for useful discussions concerning EXAFS data analysis. I would like to acknowledge our collaborators, Dr Shinji Kohara from the SPring8 for measuring our samples and providing us with x-ray results and Prof Shin'ichi Takeda and Dr Yukinobu Kawakita from Kyushu University for providing us with the alloy samples and the x-ray data.

Lots of loves and thanks to my family and friends in Thailand. Thank you mom and dad for the inspiration and the support. I thank Anan Niyom who listens to all my problems even when it involves receiving a phone call at 2 o'clock in the morning and thank our big family at the Bath University Thai Association especially to Patchara Popaitoon, Mayuree Srikulwong, Vetat and Araya Eakpisankit, Arissara Painmanakul and Merinda Thirakornratch.

Lastly, I would like to thank the Thai government and the Synchrotron Light Research Institute (SLRI) of Thailand for providing financial support for my PhD and the Office of Educational Affairs Royal Thai Embassy for their help during my stay in the UK.

Contents

Chapter 1

Introduction

Many properties of materials are related to their structure. For example, different structural phases of Ge-Sb-Tb alloys, which are used in digital video discs (DVDs), exhibit considerable differences in their optical reflectivity and electrical conductivity [1, 2] and a semiconductor with a quantum dot structure shows enhanced optical properties compared to a conventional semiconductor [3]. Structural information is therefore important to understand the nature of materials as well as their technological applications. The structure of materials found in nature can be roughly categorised as being crystalline or amorphous. For crystals, the concept that a material is made from a repetition of unit cells enables a structure to be identified by using diffraction techniques [4, 5]. In the case of amorphous materials, however, there is no long range order, the concept of a unit cell cannot be applied and it becomes a challenge to obtain the structure. Useful reviews can be found in [6, 7, 8, 9, 10].

Amorphous materials include liquids and glasses. The structure of liquids is complicated as the liquid state is intermediate between a solid and gas such that the thermal and potential energies are equally important [6]. Glasses are, like crystals, solid materials but the structure is disordered and is similar to a liquid. Indeed, as glass is produced by the rapid cooling of a liquid, the structure can be considered to be that of a frozen liquid. Even though glasses are common in everyday objects, a complete theory which describes the nature of glass is still lacking. In fact, glass still poses one of the most complicated problem in solid state physics. As quoted

by the Nobel laureate, P. W. Anderson, 'The deepest and most interesting unsolved problem in solid state theory is probably the theory of the nature of glass and the glass transition' [11].

Although the glass transition is not understood, it is observed that some materials more readily form a glass. Good glass formers include SiO_2, $GeSe_2$ and $ZnCl_2$ which have a network structure in both the glassy and molten states [12, 13, 14]. It is also observed that it is easier to form a glass if there is a small temperature interval between the melting point and the glass transition temperature, which is the temperature where a supercooled liquid transforms into a glass [10, 15]. This is applied in the case of glass formation in eutectic alloys where the composition gives the lowest melting point. The relation between glass forming ability and structure is necessary to understand the nature of glass.

In recent years, due to an interest in geology and other areas of science, and the availability of high pressure experimental setups employing e.g. a Paris-Edinburgh press [16] or diamond anvil cell [17], the properties of amorphous materials under extreme conditions have been widely studied. In crystalline materials under different thermodynamic conditions, first order phase transformations are observed giving rise to polymorphic structures [18]. A well known example of a material exhibiting polymorphism is carbon which exists as e.g. graphite, graphene, fullerene or diamond. In the case of liquids and glasses, many studies show a change in the local coordination environment under high temperature and high pressure conditions [19] and there is a possibility of so called polyamorphism [20, 21], i.e. a first order phase transformation between two liquids with identical compositions but different densities.

Apart from the fundamental aspects of glass formation, much research is motivated by the technological importance of glassy materials [9, 22]. For example, amorphous semiconductors can be used as computer memory storage [15], silicate glasses are used in everyday objects such as windows and are also important in telecommunications technology, chalcogenide glasses are used in many types of optical devices including re-writable DVDs [23] and mid infrared (wavelength of 3-20 μm) waveguides [24, 25], boro-silicate glasses are used to make laboratory ware, and rare-earth

alumino-silicate glasses are important to laser technology [26]. Knowledge about the structure of these glasses could improve their functionality and ultimately lead to the engineering design of new materials.

Experimental Techniques

Although the structure of amorphous materials has always been difficult to study due to the lack of long range ordering which limits the amount of information that can be obtained experimentally, several experimental techniques and computational methods can be employed. The pair correlation functions and average coordination numbers can be obtained directly from measured neutron diffraction (ND) or x-ray diffraction (XRD) patterns [5, 27, 28]. For multi-component systems, diffraction results can be difficult to interpret as the pair correlation functions overlap. Several techniques such as the isotopic or isomorphic substitution method in ND [13, 29] or anomalous XRD [30] have been employed to reduce the complexity associated with a single diffraction pattern. These methods are, however, complicated and rely e.g. on the availability of suitable isotopes or isomorphic elements in the case of ND and suitable absorption edges in the case of XRD. A site specific experimental probe such as x-ray absorption spectroscopy (XAS) [31], which includes x-ray absorption near edge structure (XANES) and extended x-ray absorption fine structure (EXAFS) techniques, can be useful. The information obtained from XAS is the local coordination environment of the absorbing element. For example, the XANES spectrum provides a signature of the electronic structure of an absorbing atom and, in some cases, 3- or 4-body correlation functions can also be determined [32]. The EXAFS method gives the nearest neighbour atomic distances and the corresponding coordination numbers. Although it is necessary to have an initial structural model to interpret the EXAFS spectrum, the technique is very sensitive to the local coordination environment such that small changes can be detected. Indirect structural information can be obtained from other probes such as nuclear magnetic resonance (NMR) [33] or Raman spectroscopy [34]. NMR can be used to determine the coordination environments of specific nuclei in a material along with the fractional abundances of different structural units, see for example [35]. The lo-

cal coordination environment and intermediate range order can also be inferred from the vibrational modes measured by using Raman spectroscopy, see for example [36]. In addition, computational methods such as molecular dynamics (MD) simulation [37, 38], which requires information about the potentials of interaction between the atoms in a system, or Reverse Monte Carlo (RMC) modeling [39], which requires experimental data, can be used to construct a 3-dimensional picture of a system. This gives insight into, for example, the bond angle distributions and ring statistics which are difficult to obtain directly from experiment.

As each experimental technique or computational method has advantages and disadvantages, it is important to choose an appropriate method to study the system of interest. If the system can be studied by using more than one method then more structural information can be gained providing that each method gives complementary information. This aspect is demonstrated in the work presented in this thesis.

Thesis Outline

The present work is organised into nine chapters. In chapters 2, the theory for ND, XRD and EXAFS spectroscopy is briefly described. This description includes the main theory and important equations relevant to the interpretation of the data acquired from each experimental technique. The neutron and x-ray sources, the employed instruments and the data analysis procedures for ND and EXAFS are described in chapter 3.

In chapter 4, ND measurements for three molten alloys at or near their eutectic compositions, namely $Au_{0.81}Si_{0.19}$, $Au_{0.72}Ge_{0.28}$ and $Ag_{0.74}Ge_{0.26}$, are presented and the results are discussed. The measured correlation functions are compared with those previously obtained from XRD [40] and ND [41]. In addition, the asymptotic decay of the pair correlation functions in real space is investigated.

In chapter 5, the structure of $(R_2O_3)_{0.2}(Al_2O_3)_{0.2}(SiO_2)_{0.6}$ glasses, where R denotes Dy, Ho or a 50:50 mixture of Dy and Ho, is investigated. The methods of isomorphic substitution in ND, XRD and EXAFS spectroscopy at the Dy or Ho L_{III}

edge were employed. In addition, MD simulation and RMC modeling were used to obtain additional information. The ND results at both the total structure factor and difference function levels are presented and discussed. The XRD results for the Dy based glass provide complementary information to the ND results and the results obtained from EXAFS spectroscopy give further information on the local coordination environment of the rare-earth ions. The information provided by the MD and RMC models on the local coordination environment of the rare-earth, Al and Si atoms is discussed.

In chapter 6, ND and XRD measurements on glassy $ZnCl_2$ at room temperature and liquid $ZnCl_2$ at several temperatures in the range from 328 to 704 °C (mp = 290 °C and bp = 732 °C [42]) are presented and the results are discussed. In chapters 7 and 8, the structures of glassy, crystalline and liquid $ZnCl_2$ at temperatures ranging from ambient to 750(50) °C and pressures ranging from ambient to 4.7(1) GPa are investigated by using XAS at the Zn K edge. Chapter 7 includes a discussion about a reaction between $ZnCl_2$ and hexagonal BN at high temperature. Chapters 7 and 8 include a discussion of the transformation in the crystalline and liquid states between 4-fold and 6-fold coordinated Zn centred structural motifs.

The key results are concluded in chapter 9 which also includes suggestions for future work.

Chapter 2

Theory

In this chapter, the theory related to the experimental techniques used to acquire the results presented in this thesis is briefly described. The chapter is divided into three main sections to cover neutron diffraction (ND), x-ray diffraction (XRD) and extended x-ray absorption fine structure (EXAFS) spectroscopy. In each section, the main theory and important equations relevant to the interpretation of the data acquired from each experimental technique are given.

2.1 Neutron Diffraction (ND)

2.1.1 Introduction

ND [5, 28] is a powerful technique to study the structure of materials. The technique employs thermal neutrons which have an energy of the order of 10^2 meV. The energy of thermal neutrons corresponds to a de Broglie wavelength of the same order of magnitude as inter-atomic distances. Thus interference phenomena can take place and the atomic structure of materials can be investigated. Moreover, neutrons have zero charge. This means that neutrons are scattered directly by the nuclei of a target material which greatly simplifies the scattering theory. The zero charge also means that neutrons can penetrate deeply into a target material thus enabling the study of bulk structures.

Neutrons can also be used to study other properties of materials. For example, the energy of thermal neutrons is comparable to many excitations in condensed matter. The amount of energy transferred during inelastic scattering is typically a large fraction of the neutron incident energy, therefore making it measurable. Neutrons also have a finite magnetic moment. The interaction between the magnetic moments of neutrons and unpaired electrons in a target material can, therefore, be used to study the density distribution of unpaired electrons.

In this section, the basic theoretical background to ND relating to the study of the structure of disordered materials, is described. The section includes a description of neutron scattering phenomena, introduces the differential scattering cross-section and defines several of the correlation functions used to represent the structure of materials.

2.1.2 Neutron Scattering

Consider a monochromatic neutron beam scattered from a single point-like scattering center located at the origin of coordinates. The incident beam is represented by a simple plane wave:

$$\Psi_{inc} = \psi_{inc} e^{i[\mathbf{k}_0 \cdot \mathbf{r} - \omega_0 t]} \equiv \psi_0 e^{i\mathbf{k}_0 \cdot \mathbf{r}} \tag{2.1}$$

where ψ_{inc} is the amplitude of the incoming wave, $\mathbf{k}_0$ is the incident wavevector, $\mathbf{r}$ is the position vector of the neutron, and $\hbar\omega_0$ is the incident energy.

The wavelength of a thermal neutron is about 4-5 order of magnitudes larger than the range of nuclear forces. The scattering is, therefore, isotropic and the scattered neutron can be represented by a spherical wave. The scattered wave at a distance R from the scattering center can be written as

$$\Psi_{scatt,1} = \frac{-\psi_0 b_i}{R} e^{ik_f R} \tag{2.2}$$

where b_i is a scattering length which is characteristic of the nucleus at the scattering center and k_f is the modulus of the wavevector of the scattered neutron.

If a second scattering center i with scattering length b_i is present at a position $\mathbf{r}_i$ then a phase shift term has to be introduced to the scattered wavefunction. The

phase shift can be determined by considering the path lengths for the different scattering centers as shown in figure 2.1. From the figure, the path difference for the wave scattered by the scattering center at the origin and at the position $\mathbf{r}_i$ is given by

$$\begin{aligned} \text{path difference} &= r_i \cos\alpha - r_i \cos\beta \\ &= \mathbf{r}_i \cdot \hat{\mathbf{k}}_0 - \mathbf{r}_i \cdot \hat{\mathbf{k}}_f \\ &= \mathbf{r}_i \cdot \frac{\mathbf{k}_0}{|\mathbf{k}_0|} - \mathbf{r}_i \cdot \frac{\mathbf{k}_f}{|\mathbf{k}_f|}. \end{aligned}$$

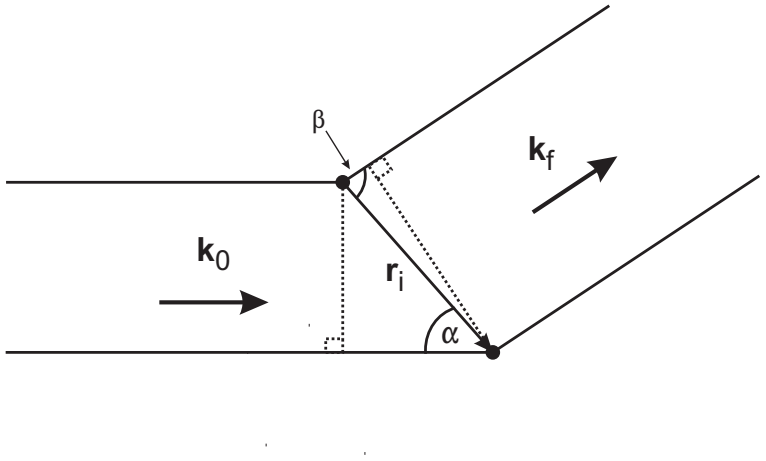

Figure 2.1: The diagram shows the path difference for a neutron scattered by a nucleus located at the origin of coordinates and a nucleus located at a position $\mathbf{r}_i$.

If we assume that the energy transfer in this process is very small compared to the incident energy we have $|\mathbf{k}_0| \approx |\mathbf{k}_f| = \frac{2\pi}{\lambda}$ where λ is the de Broglie wavelength of the incident neutron. The path difference can, therefore, be written as

$$\text{path difference} = \frac{\lambda}{2\pi}\mathbf{r}_i \cdot \mathbf{q},$$

where $\mathbf{q}$ is the scattering vector defined as $\mathbf{q} = \mathbf{k}_0 - \mathbf{k}_f$. Thus, the phase difference is given by

$$\text{phase difference} = \text{path difference} \times \frac{2\pi}{\lambda} = \mathbf{r}_i \cdot \mathbf{q} = \mathbf{q} \cdot \mathbf{r}_i.$$

Hence, the scattered wave can then be written as

$$\Psi_{scatt,2} = \frac{-\psi_0}{R} e^{ik_f R} b_i e^{i\mathbf{q}\cdot\mathbf{r}_i}. \tag{2.3}$$

Consider a monatomic system comprising N point-like scattering centers. Each scattering center is located at a position $\mathbf{r}_i$ and has a scattering length b_i. In this case, the scattered waved is found by summing all of the phase shifted contributions for pairs of scattering centers such that

$$\Psi_{scatt,N} = \frac{-\psi_0}{R} e^{ik_f R} \sum_{i=1}^{N} b_i e^{i\mathbf{q}\cdot\mathbf{r}_i}. \tag{2.4}$$

2.1.3 Differential Scattering Cross-Section

A typical scattering geometry in an ND experiment is shown in figure 2.2. Consider the intensity measured by a detector which covers a small solid angle $d\Omega = \frac{dS}{R^2}$ where dS is the area of the detector. The intensity is related to the differential scattering cross-section which is defined by [5, 28]

$$\frac{d\sigma}{d\Omega} \equiv \frac{\text{number of neutrons scattered per second toward the detector into } d\Omega}{\Phi d\Omega}, \tag{2.5}$$

where Φ is the incident flux i.e. the number of incident neutrons per second per cross-sectional area of the incident beam.

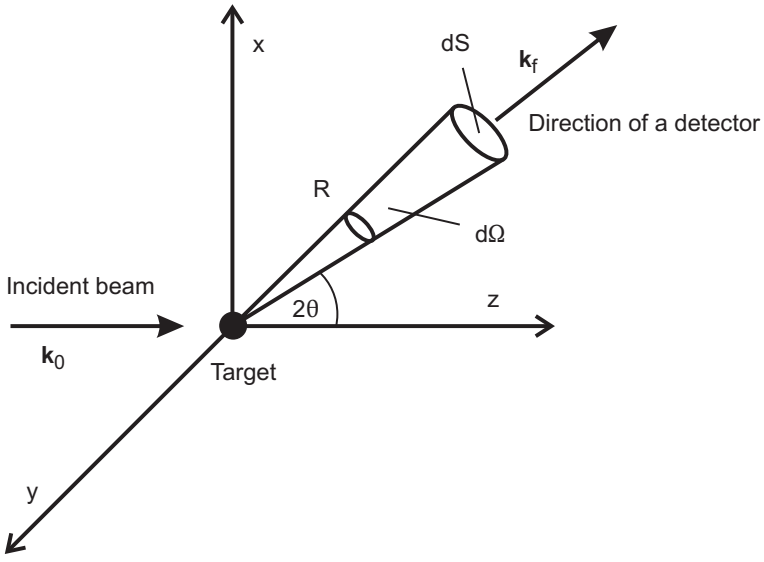

Figure 2.2: A typical scattering geometry in a diffraction experiment.

If we assume that $k_0 = k_f$ and that the detector is located at a large distance R away from the target, the differential scattering cross-section for N scattering

centers, is given by [28]

$$\begin{aligned}\frac{d\sigma}{d\Omega}(\mathbf{q}) &= \frac{|\Psi_{scatt,N}|^2 dS}{|\Psi_{inc}|^2 d\Omega} = \frac{\left|(-\psi_0/R)e^{ik_f R}\sum_i^N b_i e^{i\mathbf{q}\cdot\mathbf{r}_i}\right|^2 (R^2 d\Omega)}{\left|\psi_0 e^{i\mathbf{k}_0\cdot\mathbf{r}}\right|^2 d\Omega} \\ &= \left|\sum_{i=1}^{N} b_i e^{i\mathbf{q}\cdot\mathbf{r}_i}\right|^2 . \end{aligned} \tag{2.6}$$

For a real sample the positions of the scattering centers are not fixed and each scattering center can have a different scattering length. Equation 2.6 is then re-written as

$$\frac{d\sigma}{d\Omega}(\mathbf{q}) = \overline{\left\langle \left|\sum_{i=1}^{N} b_i e^{i\mathbf{q}\cdot\mathbf{r}_i}\right|^2 \right\rangle} = \left\langle \sum_{i,j}^{N} \overline{b_i b_j^*} e^{i\mathbf{q}\cdot\mathbf{r}_{ij}} \right\rangle , \tag{2.7}$$

where $\mathbf{r}_{ij} = \mathbf{r}_i - \mathbf{r}_j$ is the relative position of the scattering centers i and j. The asterisk represents a complex conjugate as b_i can have both a real and an imaginary part, where the latter is related to absorption events. For most nuclei the real part is much greater than the imaginary part so that the imaginary part can be neglected. An exception, however, occurs in the case of diffraction experiments where the incident neutron energy is close to an absorption resonance of the scattering center.

The triangular brackets in equation 2.7 denote a thermal average of the atomic positions and it is introduced by the fact that, in a real sample, the atoms undergo thermal displacement during the course of a measurement. The horizontal bar over the scattering lengths in equation 2.7 represents the need to take into account the variation of the scattering length due to the spin states of the nuclei and the isotopes that are present. Providing there is no correlation between the value of a scattering length and the position of a scattering center, the averaging is made by considering an ensemble of systems of identical structure and isotopic composition where the scattering lengths for each member of the ensemble are distributed differently [28].

As the differential scattering cross-section is written in terms of the scattering vector $\mathbf{q}$, it is useful to relate the scattering vector to the scattering angle. Figure 2.3 shows the scattering triangle which describes a scattering event and, assuming that $|\mathbf{k}_0| = |\mathbf{k}_f|$, the modulus of the scattering vector q can be written in terms of

the scattering angle, 2θ, such that

$$q = \frac{4\pi \sin\theta}{\lambda}, \tag{2.8}$$

where λ is the incident neutron wavelength.

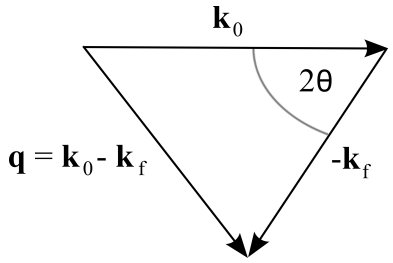

Figure 2.3: The scattering triangle.

2.1.4 Coherent and Incoherent Scattering Lengths

Consider the term $\overline{b_i b_j^*}$ in equation 2.7. If we assume that there is no correlations between the scattering lengths and the position of different scattering centers, then $\overline{b_i b_j^*} = \overline{b^2}$ when $i = j$ and $\overline{b_i b_j^*} = \bar{b}^2$ when $i \neq j$ [5]. Thus equation 2.7 becomes

$$\begin{aligned} \frac{d\sigma}{d\Omega}(\mathbf{q}) &= \bar{b}^2 \left\langle \sum_{i,j\neq i}^{N} e^{i\mathbf{q}\cdot\mathbf{r}_{ij}} \right\rangle + N\overline{b^2} \\ &= \bar{b}^2 \left\langle \sum_{i,j}^{N} e^{i\mathbf{q}\cdot\mathbf{r}_{ij}} \right\rangle + N(\overline{b^2} - \bar{b}^2). \end{aligned} \tag{2.9}$$

The first term on the right hand side of equation 2.9 represents coherent scattering. This term contains information about the relative positions of the scattering centers and the coherent scattering length is defined by $b_{coh} \equiv \bar{b}$. The second term on the right hand side of equation 2.9 represents incoherent scattering. This term comes from the variation of the scattering lengths about their mean value and contains no structural information. The incoherent scattering length is defined by $b_{inc}^2 \equiv \overline{b^2} - \bar{b}^2$. With the definitions for the coherent and incoherent scattering lengths, equation 2.9 can be re-written as

$$\frac{d\sigma}{d\Omega}(\mathbf{q}) = b_{coh}^2 \left\langle \sum_{i,j}^{N} e^{i\mathbf{q}\cdot\mathbf{r}_{ij}} \right\rangle + N b_{incoh}^2. \tag{2.10}$$

The scattering processes involve interactions between neutrons and the nuclei of atoms in the target material. At present, there is no reliable theory for predicting the magnitude of these interactions. Therefore, the coherent and incoherent scattering lengths are obtained empirically [43].

2.1.5 Pair Correlation Functions

A function which describes the pair correlations between the positions of scattering centers is the structure factor $S(\mathbf{q})$ which is defined by

$$S(\mathbf{q}) \equiv \frac{1}{N} \left\langle \sum_{i,j}^{N} e^{i\mathbf{q}\cdot\mathbf{r_{ij}}} \right\rangle, \tag{2.11}$$

such that the relation between $S(\mathbf{q})$ and the differential scattering cross-section of equation 2.10 is given by

$$\frac{1}{N}\left(\frac{d\sigma}{d\Omega}(\mathbf{q})\right) = b_{coh}^2 S(\mathbf{q}) + b_{incoh}^2. \tag{2.12}$$

or

$$\frac{1}{N}\left(\frac{d\sigma}{d\Omega}(\mathbf{q})\right) = b_{coh}^2 [S(\mathbf{q}) - 1] + (b_{coh}^2 + b_{incoh}^2). \tag{2.13}$$

Structural information about a system can be obtained by extracting $S(\mathbf{q})$ from the experimental data and Fourier transforming to give the real space pair distribution function $g(\mathbf{r})$. $g(\mathbf{r})$ is proportional to the probability of finding an atom at a distance r from a central atom at the origin of coordinates and is defined as

$$n_0 g(\mathbf{r}) \equiv \frac{1}{N} \left\langle \sum_{i,j\neq i}^{N} \delta(\mathbf{r} - \mathbf{r_{ij}}) \right\rangle, \tag{2.14}$$

where $n_0 = \frac{N}{V}$ is the atomic number density, V is the volume of the sample and $\delta(\mathbf{r} - \mathbf{r_{ij}})$ is a Dirac delta function. If equation 2.11 is re-written in terms of $\delta(\mathbf{r} - \mathbf{r_{ij}})$ then

$$S(\mathbf{q}) = 1 + \frac{1}{N} \left\langle \int \sum_{i,j\neq i}^{N} \delta(\mathbf{r} - \mathbf{r_{ij}}) e^{i\mathbf{q}\cdot\mathbf{r}} d\mathbf{r} \right\rangle. \tag{2.15}$$

By combining equation 2.15 with the definition of $g(\mathbf{r})$ in equation 2.14, we have

$$S(\mathbf{q}) = 1 + n_0 \int g(\mathbf{r}) e^{i\mathbf{q}\cdot\mathbf{r}} d\mathbf{r} \tag{2.16}$$

or

$$S(\mathbf{q}) - 1 = n_0 \int [g(\mathbf{r}) - 1] e^{i\mathbf{q}\cdot\mathbf{r}} d\mathbf{r} + n_0 \int e^{i\mathbf{q}\cdot\mathbf{r}} d\mathbf{r}. \tag{2.17}$$

The second term on the right hand side of equation 2.17 is given by

$$n_0 \int e^{i\mathbf{q}\cdot\mathbf{r}} d\mathbf{r} = n_0 V \delta_{\mathbf{q},0} = N \delta_{\mathbf{q},0} \tag{2.18}$$

where $\delta_{\mathbf{q},0}$ is the Kronecker delta where $\delta_{\mathbf{q},0} = 1$ when $\mathbf{q} = 0$ and $\delta_{\mathbf{q},0} = 0$ otherwise. As this term only contributes when $\mathbf{q} = 0$, which corresponds to forward scattering, it can be neglected. Hence, the Fourier transform relations between $S(\mathbf{q})$ and $g(\mathbf{r})$ are given by

$$S(\mathbf{q}) - 1 = n_0 \int [g(\mathbf{r}) - 1] e^{i\mathbf{q}\cdot\mathbf{r}} d\mathbf{r} \tag{2.19}$$

and

$$g(\mathbf{r}) - 1 = \frac{1}{n_0 (2\pi)^3} \int [S(\mathbf{q}) - 1] e^{-i\mathbf{q}\cdot\mathbf{r}} d\mathbf{q}. \tag{2.20}$$

Because liquids and glasses are isotropic, equations 2.19 and 2.20 can be simplified by assuming spherical symmetry such that

$$S(q) - 1 = \frac{n_0 4\pi}{q} \int_0^\infty [g(r) - 1] r \sin(qr) dr, \tag{2.21}$$

and

$$g(r) - 1 = \frac{1}{n_0 2\pi^2 r} \int_0^\infty [S(q) - 1] q \sin(qr) dq. \tag{2.22}$$

A representation of $g(r)$ for an isotropic system is given in figure 2.4. The first peak position corresponds to the nearest-neighbours coordination shell and the area under the peak can be used to calculate the coordination number of neighbouring atoms in a given range. The coordination number is given by [28]

$$\bar{n} = 4\pi n_0 \int_{r_1}^{r_2} g(r) r^2 dr, \tag{2.23}$$

where r_1 and r_2 are the minimum and the maximum distances of the selected range.

It should be noted that the derivation of the differential scattering cross-section is for a small sample and only involves single scattering events. In an experiment, however, it is also possible for neutrons to be scattered more than once before hitting the detector. In addition, the finite size of a sample leads to attenuation of the incident and scattered neutron beams due to scattering and absorption. The details of the data correction procedures can be found in chapter 3, section 3.5.

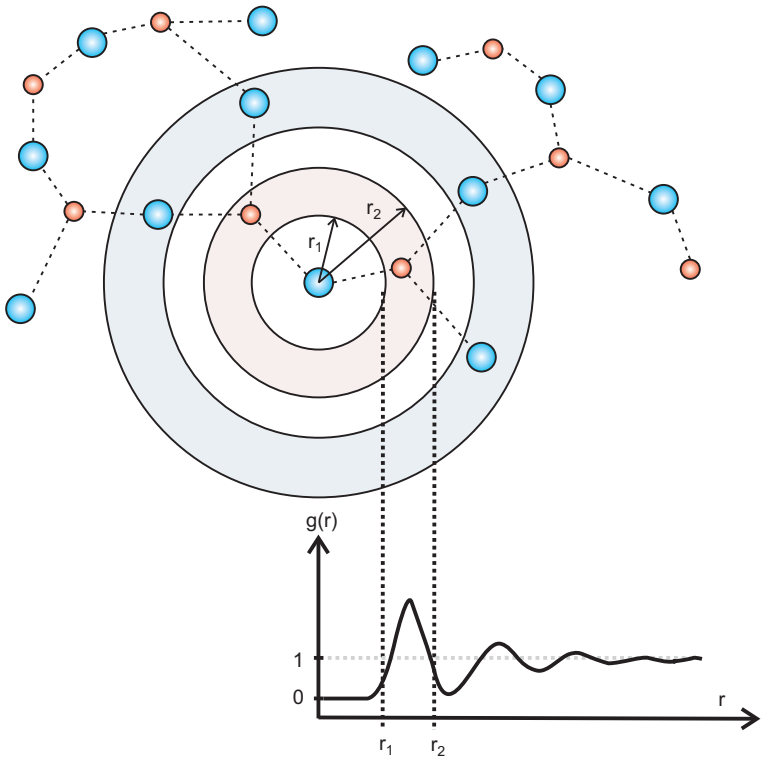

Figure 2.4: An illustration of the pair distribution function $g(r)$.

2.1.6 Polyatomic Systems

For a polyatomic system, the measured intensity depends on a weighted sum of partial pair correlation functions. Each correlation function is weighted by the coherent scattering lengths and atomic fractions of the atomic species involved. Similar to equation 2.13, the differential scattering cross-section for a polyatomic system is given by

$$\frac{1}{N}\left(\frac{d\sigma}{d\Omega}(q)\right) = F(q) + \sum_{\alpha} c_\alpha \left(b^2_{\alpha,coh} + b^2_{\alpha,incoh}\right) \tag{2.24}$$

$$\equiv F(q) + \sum_{\alpha} c_\alpha \overline{b^2_\alpha}, \tag{2.25}$$

where c_α is the atomic fraction while $b_{\alpha,coh}$ and $b_{\alpha,incoh}$ are the coherent and incoherent neutron scattering lengths for an atoms of type α. The term $\sum_\alpha c_\alpha \left(b^2_{\alpha,coh} + b^2_{\alpha,incoh}\right)$ in equation 2.24 is called a self-scattering term as it does not involve correlations between any two atomic species. $F(q)$ is a total structure factor defined by

$$F(q) \equiv \sum_{\alpha,\beta}^{n} c_\alpha c_\beta b_\alpha b_\beta \left[S_{\alpha\beta}(q) - 1\right], \tag{2.26}$$

where $S_{\alpha\beta}(q)$ is a partial structure factor and n denotes the number of different chemical species. This function is a more general version of $S(q)$ for a monatomic system. It contains information about the positions of atoms of type β relative to the positions of atoms of type α.

The Fourier transform of the total structure factor gives the total pair distribution function $G(r)$. Similar to equation 2.26, $G(r)$ is also defined in terms of a weighted sum of partial pair distribution functions $g_{\alpha\beta}(r)$ where

$$G(r) \equiv \sum_{\alpha,\beta}^{n} c_\alpha c_\beta b_\alpha b_\beta \left[g_{\alpha\beta}(r) - 1\right]. \tag{2.27}$$

$g_{\alpha\beta}(r)$ is proportional to the probability of finding an atom of type β at a radial distance r from an atom of type α. The average coordination number of atoms of type β around an atom of type α located at the origin of coordinates can be obtained from $g_{\alpha\beta}(r)$ by the relation

$$\bar{n}_\alpha^\beta = 4\pi n_0 c_\beta \int_{r_1}^{r_2} g_{\alpha\beta}(r) r^2 dr, \tag{2.28}$$

where r_1 and r_2 are the minimum and maximum radii for the region of interest.

The Fourier transform relations between $F(q)$ and $G(r)$ are given by

$$F(q) = \frac{4\pi n_0}{q} \int_0^\infty rG(r)\sin(qr)dr \tag{2.29}$$

and

$$G(r) = \frac{1}{n_0 2\pi^2 r} \int_0^\infty qF(q)\sin(qr)dq. \tag{2.30}$$

2.1.7 The Static Approximation and Placzek Corrections

The derivation so far is based on the assumption that the energy transfer during the scattering process is very small compared to the energy of an incident neutron i.e. $k_0 \approx k_f$. This assumption is called the static approximation. The validity of this approximation can be examined in terms of timescales [28]. If the maximum energy transfer in a scattering event is $\hbar\omega_{max}$, the minimum characteristic time for atomic motion, corresponding to a period of atomic vibration in a solid or a relaxation time in a liquid, is $\tau_{min} \sim \omega_{max}^{-1}$. For an incident neutron of energy $E_0 = \hbar\omega_0$, the characteristic time for diffraction or 'snapshot' time is $\tau_{snapshot} \sim \omega_0^{-1}(a/\lambda_0)$.

This is the time it takes an incident neutron of wavelength λ_0 to travel one atomic distance a. If the static approximation is to be valid then $\tau_{snapshot} \ll \tau_{min}$ such that the structure remains relatively static during the time a neutron passes from one atom to another. For an ND experiment, the incident neutron energy typically corresponds to a snapshot time between 10^{-15} and 10^{-13} s. This is only one or two orders of magnitude smaller than a typical value of τ_{min}. Therefore, a correction for inelastic scattering is necessary.

For a heavy element, the inelasticity correction can be made by using the method introduced by Plazcek [44]. Consider first the coherent term in the differential scattering cross-section given by equation 2.12. In a real ND experiment where there are finite energy transfers this must be re-written in terms of the effective coherent differential scattering cross-section

$$\frac{1}{N}\left(\frac{d\sigma_{coh}}{d\Omega}(q)\right)_{eff} = b_{coh}^2 \int_{-\infty}^{\omega_{max}} \epsilon(k_f)\left(\frac{k_f}{k_0}\right) S(q,\omega)d\omega, \tag{2.31}$$

where $\epsilon(k_f)$ is the efficiency of the detector for neutrons with a final scattering vector $\mathbf{k}_f$. In the static approximation $\hbar\omega \ll E_0$ such that $k_f/k_0 \simeq 1$, $\epsilon(k_f)$ becomes the efficiency for elastically scattered neutron, and the upper limit in equation 2.31 can be extended to infinity. Then

$$\begin{aligned}\frac{1}{N}\left(\frac{d\sigma_{coh}}{d\Omega}(q)\right)_{eff} &= \epsilon(k_0) b_{coh}^2 \int_{-\infty}^{\infty} S(q,\omega)d\omega & (2.32)\\ &= \epsilon(k_0) b_{coh}^2 S(q) & (2.33)\end{aligned}$$

where $S(q) \equiv \int_{-\infty}^{\infty} S(q,\omega)d\omega$ is an integral over the dynamical structure $S(q,\omega)$ at constant q. In a diffraction experiment at a reactor source, the integral of equation 2.31 is made by a detector at constant scattering angle 2θ as opposed to constant q. If the scattering event is truly elastic, these integration paths are the same. However, the inelasticity causes a difference between the two integration paths as shown in figure 2.5.

Yarnell et al. [44] have evaluated equation 2.31, taking into account the different paths of integration and found that the effective coherent differential scattering cross-section can be written as

$$\frac{1}{N}\left(\frac{d\sigma_{coh}}{d\Omega}(q)\right)_{eff} = \epsilon_0 b_{coh}^2 \left[S(q) + P(q)\right], \tag{2.34}$$

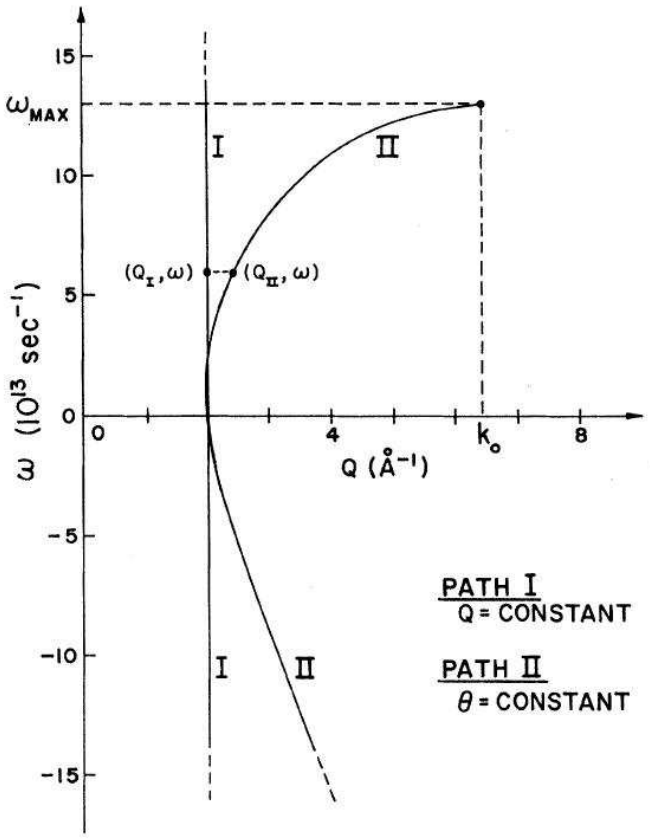

Figure 2.5: Integration paths in $q - \omega$ space [44]. Path I corresponds to an integral where q is constant and leads to the definition of $S(q)$. In a real diffraction measurement, however, the detector makes an integration along path II where the scattering angle 2θ is constant.

where $\epsilon_0 = \epsilon(k_0)$ is the detector efficiency at the energy of the incident beam and $P(q)$ is the Placzek term, representing the effect of inelastic scattering, and is given by

$$P(q) = \frac{m}{2M}\left(\frac{E_{rec}}{E_0} + \frac{k_B T}{E_0}\right) - C_1\frac{E_{rec}}{E_0} + C_2\left(\frac{E_{rec}}{E_0}\right)^2 - C_3\left(\frac{E_{rec}}{E_0}\right)\left(\frac{k_B T}{E_0}\right). \quad (2.35)$$

In equation 2.35, m is the neutron mass, M is the mass of an atom in the target material, E_0 is the incident neutron energy, $E_{rec} = \frac{\hbar^2 q^2}{2M}$ is the recoil energy resulting from the collision between a neutron and a nucleus in the target material, k_B is Boltzmann's constant and C_1, C_2 and C_3 are constants which depend on the detector efficiency $\epsilon(k)$.

On re-arranging equation 2.34 we have

$$\frac{1}{N\epsilon_0}\left(\frac{d\sigma_{coh}}{d\Omega}(q)\right)_{eff} = b_{coh}^2\left[(S(q)-1) + (P(q)+1)\right]. \quad (2.36)$$

Inelasticity corrections also apply to the incoherent term in equation 2.12 so that the total effective differential scattering cross-section can be written as

$$\frac{1}{N\epsilon_0}\left(\frac{d\sigma}{d\Omega}(q)\right)_{eff} = b_{coh}^2(S(q)-1) + [b_{coh}^2 + b_{incoh}^2](P(q)+1), \tag{2.37}$$

where the Placzek correction for the coherent and incoherent scattering terms is assumed to be the same.

For a polyatomic system, the total differential scattering cross-section of equation 2.24 becomes

$$\frac{1}{N\epsilon_0}\left(\frac{d\sigma}{d\Omega}(q)\right)_{eff} = F(q) + \sum c_\alpha(b_{\alpha,coh}^2 + b_{\alpha,inc}^2)(1+P_\alpha(q)). \tag{2.38}$$

Note that in equations 2.37 and 2.38 the Placzek correction is only applied to the self-scattering terms. In principle, an inelasticity correction should also be applied to the interference terms. This correction is, however, generally much smaller than for the self-term because the momentum transfer in the scattering event is not confined to a single atom but is distributed over all the atoms in the coherence volume of the incident neutron [28].

2.1.8 Magnetic Neutron Scattering

As a neutron has a magnetic moment, if the material under investigation has unpaired electrons, the magnetic field created by the unpaired electrons can introduce magnetic neutron scattering. Including the magnetic neutron scattering cross-section, the total differential scattering cross-section can be written as

$$\left(\frac{d\sigma}{d\Omega}(q)\right)_{total} = \left(\frac{d\sigma}{d\Omega}(q)\right)_{nuclear} + \left(\frac{d\sigma}{d\Omega}(q)\right)_{mag}. \tag{2.39}$$

For paramagnetic samples, such as rare-earth compounds, the magnetic differential scattering cross-section [45] is given by

$$\left(\frac{d\sigma}{d\Omega}(q)\right)_{mag} = c_\alpha(\gamma r_e)^2\frac{1}{6}J(J+1)g^2f_{\alpha,m}^2(q), \tag{2.40}$$

where c_α and $f_{\alpha,m}(q)$ are the atomic fraction and magnetic form factor of paramagnetic element α, respectively, $\gamma = 1.913$ is the magnitude of the neutron magnetic moment in units of the nuclear magneton, $r_e = 2.818 \times 10^{-15}$ m is the classical

radius of an electron, J is the total angular momentum quantum number, and g is the Landé splitting factor. The derivation of equation 2.40 assumes unpolarised neutrons and the absence of an external magnetic field.

The magnetic form factor is q dependent because the spatial extent of the electrons is comparable to the incident neutron wavelength. It can be obtained [29] from the expression

$$\begin{aligned} f^2_{\alpha,m}(q) &= \langle j_0(q)\rangle^2 + C_{02}\langle j_0(q)\rangle\langle j_2(q)\rangle + C_{22}\langle j_2(q)\rangle^2 + C_{24}\langle j_2(q)\rangle\langle j_4(q)\rangle \\ &\quad + C_{44}\langle j_4(q)\rangle^2 + C_{46}\langle j_4(q)\rangle\langle j_6(q)\rangle + C_{66}\langle j_6(q)\rangle^2. \end{aligned} \tag{2.41}$$

The radial integrals $\langle j_K(q)\rangle$ for $K = 0$, 2, 4 or 6 are given in [46]. The coefficients C_{ij}, where $i = 0$, 2, 4, or 6 and $j = 2$, 4, or 6, for trivalent rare-earth ions can be found in appendix E3 of reference [45].

2.2 High Energy X-ray Diffraction (XRD)

2.2.1 Introduction

High energy x-rays have an incident energy of the order of 10^2 keV which corresponds to a wavelength of around 0.1 Å. Therefore, XRD is also a very useful technique to study the structure of materials. XRD theory can be described in a similar way to ND, the main difference being that x-rays are scattered by the electron cloud of atoms in the target materials rather than by the nuclei.

There are some advantages in using high energy XRD as a structural probe. Firstly, there is no need for inelasticity corrections. The snapshot time for high energy x-rays is very small, about six orders of magnitude smaller than that of a neutron. Therefore, the static approximation is comfortably satisfied. Secondly, at high energy the absorption cross-section of x-rays is small so that the correction for attenuation is also small. Thirdly, use of a short wavelength gives a high maximum q value. This is important for the study of disordered materials as a wide measurement q range leads to improved resolution in real space. In this section, an outline is given of the theoretical background to XRD.

2.2.2 Differential Scattering Cross-Section

The theory for XRD is more complicated compared with ND. This is mainly because x-rays interact with the electrons in a target material. Many interaction processes can occur and contribute to the total differential cross-section. The main processes that occur in the energy range of diffraction experiments include Compton scattering, fluorescence and resonant-Raman scattering. The total x-ray differential scattering cross-sections can be written as

$$\begin{aligned}\left[\frac{d\sigma}{d\Omega}(\mathbf{q})\right]_X^{total} &= \left[\frac{d\sigma}{d\Omega}(\mathbf{q})\right]_X^{Ray-T} + \left[\frac{d\sigma}{d\Omega}(\mathbf{q})\right]_X^{fluo} + \left[\frac{d\sigma}{d\Omega}(\mathbf{q})\right]_X^{r-Raman} \\ &+ \left[\frac{d\sigma}{d\Omega}(\mathbf{q})\right]_X^{Compton} + \left[\frac{d\sigma}{d\Omega}(\mathbf{q})\right]_X^{other}, \end{aligned} \tag{2.42}$$

where the subscript X indicates x-ray cross-sections. The superscript 'other' represents other processes which are assumed to give only a small contribution to the total cross-section. The superscript 'Ray-T' refers to the Rayleigh-Thomson or x-ray diffraction differential scattering cross-section which, for isotropic systems, can be written in an analogous way to equation 2.25 for ND:

$$\frac{1}{N}\left[\frac{d\sigma}{d\Omega}(q)\right]_X^{Ray-T} = F_X(q) + \overline{f^2(q)}, \tag{2.43}$$

where $F_X(q)$ represents the x-ray total structure factor and $\overline{f^2(q)} = \sum_\alpha c_\alpha f_\alpha^2(q)$ where $f_\alpha(q)$ is the x-ray form factor for an atom of type α.

The cross-sections from processes other than diffraction have to be either calculated and subtracted from the total cross-section or avoided by making a suitable choice of experiment.

2.2.3 X-ray Pair Correlation Functions

Similar to neutrons, the x-ray total structure factor $F_X(q)$ for a polyatomic system is defined by

$$F_X(q) \equiv \sum_{\alpha,\beta}^{n} c_\alpha c_\beta f_\alpha(q) f_\beta^*(q) \left[S_{\alpha\beta}(q) - 1\right], \tag{2.44}$$

where $S_{\alpha\beta}(q)$ is the partial structure factor. It is useful to mention that in many cases the x-ray total structure factor is represented by $S_X(q)$ where

$$S_X(q) = \frac{F_X(q)}{\overline{f(q)}^2} + 1, \tag{2.45}$$

and $\overline{f(q)} = \sum_\alpha c_\alpha f_\alpha(q)$.

Because x-rays are scattered by electron clouds, the scattering centers cannot be treated as point-like. The distribution of electrons around the nucleus causes the x-ray form factor to be q dependent. The x-ray form factor for each atomic species can be calculated [47]. In electron units, a form factor is equal to the number of electron in an atom at $q = 0$ and decreases as q increases. An example of an x-ray form factor is shown in figure 2.6.

The x-ray total pair distribution function $G_X(r)$ is obtained by Fourier transforming $S_X(q)$:

$$G_X(r) - 1 = \frac{1}{n_0 2\pi^2 r} \int_0^\infty [S_X(q) - 1] q \sin(qr) dq. \tag{2.46}$$

$G_X(r)$ can also be written in terms of a weighted sum of partial pair distribution functions $g_{\alpha\beta}(r)$. However, unlike $G(r)$ in equation 2.27, the weighting functions for $g_{\alpha\beta}(r)$ in $G_X(r)$ are r dependent since the x-ray form factors are q dependent [48].

As the x-ray form factor for some elements can be very different from the neutron scattering length, the results from these two experimental techniques can be used to complement each other and more structural information can be obtained on the system under investigation.

2.2.4 Fluorescence and Resonant-Raman Scattering

If the incident x-ray energy is at or above the absorption edge of the atoms in a target material, an electron in the target material can absorb the x-ray and it is excited into a continuum state. This causes an atom to be in an excited state. The atom can subsequently de-excite via the Auger process or by emitting fluorescence. If the incident x-ray energy is slightly below an absorption edge, the x-ray can loose energy via resonant-Raman scattering wherein the x-ray interacts with a virtual

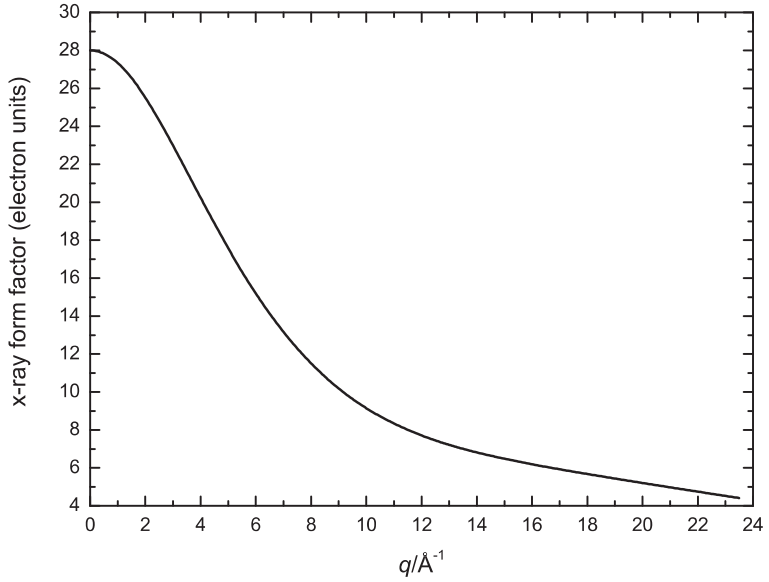

Figure 2.6: The x-ray form factor for Zn^{2+}

electronic state of the atom and is re-emitted at energy less than the incident x-ray energy.

Normally, the x-ray energy for a diffraction experiment is chosen to avoid absorption edges. However, if fluorescence or resonant-Raman scattering is unavoidable, a detector filter can be used. Because the fluorescence spectrum is a characteristic of the absorption edge energy and the energy loss due to resonant-Raman scattering is always constant [28], these energies can be calculated and the filter can be selected accordingly.

2.2.5 Compton Scattering

When the x-ray energy is of the order of keV, which is the energy range for high energy XRD experiments, the interaction between an x-ray and the target material can be dominated by the Compton effect. The Compton effect is analogous to billiard ball scattering of x-rays by the electrons in the target material. An x-ray transfers some of its energy to the electron which results in a wavelength shift of the scattered x-ray which, for a free electron, can be calculated using

$$\Delta\lambda = \lambda_f - \lambda_0 = \frac{h}{m_e c}[1 - \cos(2\theta)] \tag{2.47}$$

where λ_0 and λ_f are the wavelengths of an x-ray before and after the Compton scattering event, m_e is the electron mass, h is the Planck constant, and c is the speed of light. The Compton scattering cross-section for each element can be found in [49].

2.3 Extended X-Ray Absorption Fine Structure (EXAFS) Spectroscopy

2.3.1 Introduction

EXAFS spectroscopy is another powerful technique used to study structure of materials. Although the structural information obtained by using the EXAFS technique is limited to the local environment of an absorbing atom, the technique can be used to complement the information obtained from other methods such as diffraction. There are some advantages to using EXAFS. For example, the experimental setup for an absorption measurement is relatively simple. Moreover, since the technique gives information on a specific atomic species, it can be used to explore multi-component systems which can be difficult to study using diffraction. As long-range order is not required to interpret the EXAFS results, the technique can be applied to both ordered and disordered systems.

The basic theoretical background for the technique has been reviewed extensively in [50] and more recently in [51]. The important aspects of the theory are described in the following sections. This includes an account of the EXAFS phenomenon, the EXAFS equation and consideration of many-body effects, multiple scattering, and the cumulant expansion method for disordered systems.

2.3.2 EXAFS Phenomenon

As an x-ray beam passes through a target material, the beam is absorbed by electrons in the target material. The absorption coefficient for a single isolated atom is a smoothly decaying function with increasing x-ray energy unless the energy of

the x-ray is equal to or greater than the binding energy of a core electron. In this case, an electron can absorb the x-ray and it is excited into a continuum state, thus sharply increasing the absorption. The sharp rise in the absorption coefficient is called an absorption edge and the electron which is knocked out of the atom by the x-ray is called a photoelectron. The energy of the photoelectron is equal to the difference between the energy E of the x-ray and the binding energy E_0 of the electron. The wavevector of a photoelectron can, therefore, be written as

$$k = \sqrt{\frac{2m_e(E - E_0)}{\hbar^2}}, \tag{2.48}$$

where m_e is the electron mass. If the photoelectron is originally from the inner most or $n = 1$ shell, the absorption edge is called the K edge. The L and M edges correspond to a photoelectron from the $n = 2$ and $n = 3$ shells, respectively.

For atoms in a condensed system, there is also a small modification to the absorption coefficient which extends from just above the absorption edge to a few keV from the absorption edge. This modification is a result of interference between the wavefuntions of an outgoing and backscattered photoelectron. When the photoelectron leaves the absorbing atom, it is scattered by the electrons in neighbouring atoms. In the case when the photoelectron is backscattered and returns to the absorbing atom, it either adds to or subtracts from the outgoing photoelectron wavefunction depending on whether the waves are in phase or out of phase. The phase difference changes as a function of the photoelectron energy and causes an oscillation in the absorption coefficient. The phenomenon is illustrated in figure 2.7.

The spectrum beyond an absorption edge, where oscillations due to neighbouring atoms are observed, can be considered to consist of two main regions. The first region is called the X-ray Absorption Near Edge Structure or XANES region and covers x-ray energies within the first 30 or so eV from the absorption edge. The XANES region is where the photoelectron has a small kinetic energy and the interaction between the electrons and the atoms is very strong [52]. The XANES spectra can be used to qualitatively describe the energy state of electrons in the absorbing atoms and act as a signature of the electronic structure of the target material [52]. The second region beyond 30 eV from an absorption edge falls into the Extended

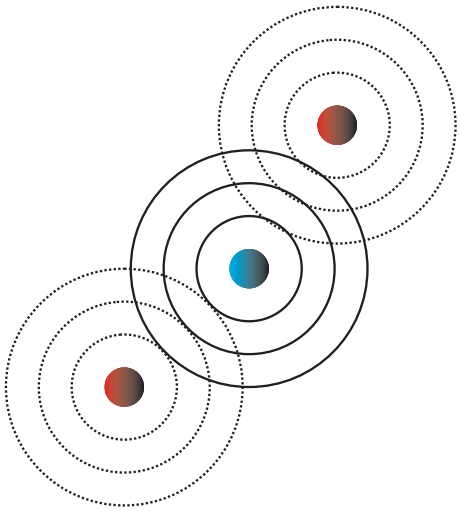

Figure 2.7: The EXAFS phenomenon. The blue sphere and the red spheres are the absorbing atom and nearest neighbour atoms, respectively. The outgoing photoelectron is represented by solid lines and the dotted lines represent the backscattered photoelectron.

X-ray Absorption Fine Structure or EXAFS regime which is the region of interest for this part of the chapter. An example of an absorption spectrum which indicates the boundary dividing the XANES and EXAFS regions is shown in figure 2.8.

The EXAFS signal, $\chi(E)$ or $\chi(k)$, refers only to the oscillatory part of the absorption coefficient in the EXAFS region, as shown in the inset of figure 2.9. It is extracted from the absorption coefficient, $\mu(E)$, by using the equation

$$\chi(E) = \frac{\mu(E) - \mu_0(E)}{\Delta\mu_0}, \tag{2.49}$$

where $\mu_0(E)$ is a smooth function representing the absorption of an isolated atom and $\Delta\mu_0$ is a normalisation factor which is, in practice, equal to the edge step $\Delta\mu_0 = \mu(E_a) - \mu(E_b)$ where E_a and E_b are the energies after and before the absorption edge, respectively. Usually the EXAFS signal is written in terms of the photoelectron wavevector i.e. as $\chi(k)$ with the energy E related to k by equation 2.48.

2.3.3 EXAFS Equation

Consider a system containing one absorbing atom placed at the origin of co-ordinates surrounded by neighbouring atoms, figure 2.10. At an energy above the absorption edge, the outgoing photoelectron at a distance r from the absorbing atom

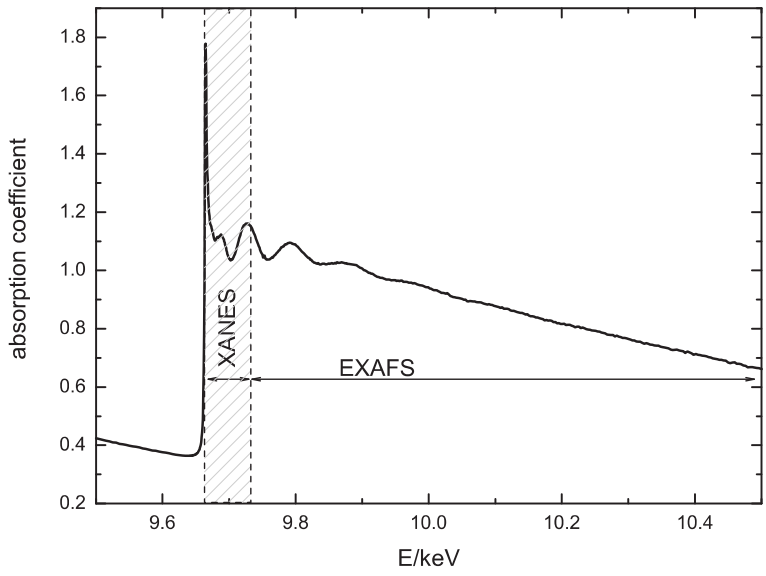

Figure 2.8: An example of the absorption spectrum around an absorption edge showing the XANES and the EXAFS regions.

can be represented by a spherical wavefunction which is proportional to $r^{-1}e^{ikr}$. Let the outgoing photoelectron be backscattered by a neighbouring atom j at position $\mathbf{r}_j$. Then the backscattered wavefunction at position $\mathbf{r}_j$ is proportional to the product of the outgoing photoelectron wavefunction at $\mathbf{r}_j$ and the backward scattering amplitude $T_j(2k)$. If the backscattered photoelectron can also be represented by a spherical wave, then the wavefunction at a distance $|\mathbf{r}-\mathbf{r}_j|$ away from the backscattering atom is given by

$$T_j(2k)\frac{e^{ikr_j}}{r_j}\cdot\frac{e^{ik|\mathbf{r}-\mathbf{r}_j|}}{|\mathbf{r}-\mathbf{r}_j|}. \tag{2.50}$$

At the position of the absorbing atom, $\mathbf{r}=0$, the wavefunction of the backscattering center is therefore proportional to

$$T_j(2k)\frac{e^{i2kr_j}}{r_j^2}. \tag{2.51}$$

In equation 2.51, the phase shift $2kr_j$ is introduced by the photoelectron as it travels with wavevector k for a distance $2r_j$. If we also take into account the spatial variation of the potential of both the absorbing and neighbouring atoms, an additional phase shift of $\delta_j(k)-\pi/2$ has to be added to equation 2.51 [50] which becomes

$$T_j(2k)\frac{e^{i[2kr_j+\delta_j(k)-\pi/2]}}{r_j^2}. \tag{2.52}$$

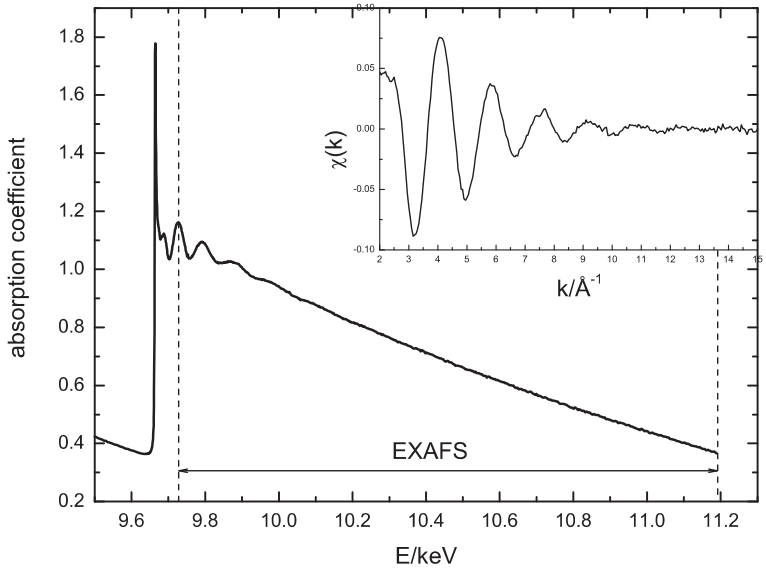

Figure 2.9: An absorption spectrum of glassy $ZnCl_2$. The inset shows the EXAFS oscillations extracted from the absorption spectrum in the EXAFS region.

The measured EXAFS signal is proportional to the real part of equation 2.52 such that

$$\begin{aligned} \chi_j(k) &= K\frac{T_j(2k)}{r_j^2}\cos[2kr_j + \delta_j(k) - \pi/2] \\ &= K\frac{T_j(2k)}{r_j^2}\sin[2kr_j + \delta_j(k)], \end{aligned} \tag{2.53}$$

where K is a constant of proportionality. It is usual to incorporate K and $T_j(2k)$ into a single term by defining the backscattering amplitude $F_j(k) \equiv KT_j(2k)k = \frac{m_e}{2\pi\hbar^2 k}t_j(2k)$, such that equation 2.53 becomes

$$\chi_j(k) = \frac{F_j(k)}{kr_j^2}\sin[2kr_j + \delta_j(k)]. \tag{2.54}$$

The calculation of the terms $t_j(2k)$ and $\delta_j(k)$ are described in [50]. In the single scattering approximation, the total EXAFS signal for all neighbouring atoms is given by

$$\chi(k) = \sum_{j=1}^{\text{all neighbours}} \frac{F_j(k)}{kr_j^2}\sin[2kr_j + \delta_j(k)]. \tag{2.55}$$

Several physical effects have been left out in the derivation of equation 2.55. These include the lifetime of the excited photoelectron state, thermal vibration of the atoms, static disorder, and many-body effects. If we include these contributions

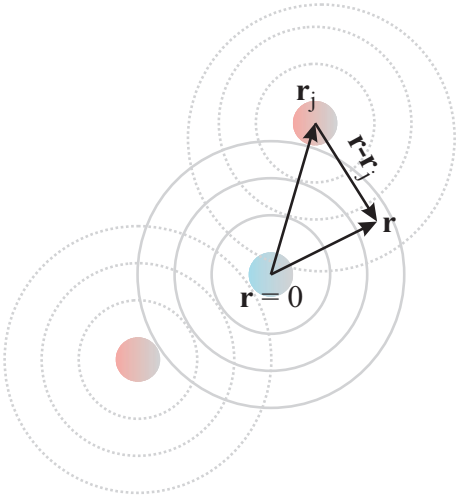

Figure 2.10: A diagram showing the coordination system for an outgoing photoelectron (solid lines) originating from the absorbing atom located at the origin of coordinates $\mathbf{r} = 0$ and the backscattered photoelectron (dotted lines) from a neighbouring atom at position $\mathbf{r}_j$.

then equation 2.55 becomes

$$\chi(k) = \sum_{j=1}^{\text{all neighbours}} S_0^2 \frac{F_j(k)}{kr_j^2} e^{-2(r_j-\Delta)/\lambda} e^{-2k^2\sigma_j^2} \sin[2kr_j + \delta_j(k)]. \tag{2.56}$$

S_0^2 is called the amplitude reduction factor and is a dimensionless parameter representing many-body effects. The term $e^{-2(r_j-\Delta)/\lambda}$, where λ is the photoelectron mean free path and $r_j - \Delta$ is an effective distance, relates to the lifetime of the excited photoelectron and represents the probability that the photoelectron can travel to the backscatterer and return to the absorbing atom without further scattering or its core hole being filled. The term $e^{-2k^2\sigma_j^2}$ represents the structural disorder of the system which is due to thermal vibration of the atoms, static disorder of the atoms or both. The parameter σ_j^2 is called the EXAFS Debye-Waller factor and represents the root mean square (rms) deviation of the position r_j of an atom about its mean distance $\langle r_j \rangle$.

The origin of the $e^{-2k^2\sigma_j^2}$ term can be understood by considering equation 2.55 which can be rewritten as

$$\chi(k) = \text{Im}\left\{ \sum_{j=1}^{\text{all neighbours}} \frac{F_j(k)}{kr_j^2} e^{i(2kr_j+\delta_j(k))} \right\}. \tag{2.57}$$

If thermal vibration and static disorder of the atoms are taken into account, equation

2.57 can be written in terms of a thermal average

$$\chi(k) = \mathrm{Im}\left\{ \left\langle \sum_{j=1}^{\text{all neighbours}} \frac{F_j(k)}{kr_j^2} e^{i(2kr_j+\delta_j(k))} \right\rangle \right\}. \tag{2.58}$$

Assuming that the r_j dependence of the $F_j(k)$ and $\delta_j(k)$ terms is negligible [53], equation 2.58 is simplified to

$$\begin{aligned} \chi(k) &= \mathrm{Im}\left\{ \sum_{j=1}^{\text{all neighbours}} \frac{F_j(k)e^{i\delta_j(k)}}{k} \left\langle \frac{e^{i2kr_j}}{r_j^2} \right\rangle \right\} \\ &\simeq \mathrm{Im}\left\{ \sum_{j=1}^{\text{all neighbours}} \frac{F_j(k)e^{i\delta_j(k)}}{k\langle r_j\rangle^2} \langle e^{i2kr_j} \rangle \right\}. \end{aligned} \tag{2.59}$$

The average $\langle e^{i2kr_j} \rangle$ can be written as

$$\begin{aligned} \langle e^{i2kr_j} \rangle &= \langle e^{i2k\langle r_j\rangle}\, e^{i2k(r_j-\langle r_j\rangle)} \rangle \\ &= e^{i2k\langle r_j\rangle} \langle\, e^{i2k(r_j-\langle r_j\rangle)} \rangle, \end{aligned} \tag{2.60}$$

where

$$\langle e^{i2k(r_j-\langle r_j\rangle)} \rangle = \int P(r_j) e^{i2k(r_j-\langle r_j\rangle)} dr_j \tag{2.61}$$

and $P(r_j)dr_j$ is the probability of finding an atom j in the range r_j to $r_j + dr_j$. If the deviation $(r_j - \langle r_j\rangle)$ is small and has equal chance of being positive or negative or if $P(r_j)$ follows a Gaussian distribution[1] then [27]

$$\begin{aligned} \langle e^{i2k(r_j-\langle r_j\rangle)} \rangle &= e^{-\frac{1}{2}\langle 4k^2(r_j-\langle r_j\rangle)^2\rangle} \\ &\equiv e^{-2k^2\sigma_j^2} \end{aligned} \tag{2.62}$$

where the EXAFS Debye-Waller factor $\sigma_j^2 = \langle (r_j - \langle r_j\rangle)^2 \rangle$.

The summation in equation 2.56 can be made over coordination shells having an average distance $R_{0,j}$ instead of over every individual neighbour distance r_j. Let N_j be defined as the coordination number for the j^{th} coordination shell or the number of degeneracies for the EXAFS signal corresponding to the distance $R_{0,j}$. In this way equation 2.56 can be re-written as

$$\chi(k) = \sum_{j}^{\text{all shells}} S_0^2 N_j \frac{F_j(k)}{kR_{0,j}^2} e^{-2(R_{0,j}-\Delta)/\lambda} e^{-2k^2\sigma_j^2} \sin[2kR_{0,j} + \delta_j(k)]. \tag{2.63}$$

Equation 2.63 is the main equation on which EXAFS data analysis is based.

[1] If x is small and has equal chance of being positive or negative then $\langle e^{ix} \rangle = \langle 1 + ix - x^2/2! + ... \rangle \simeq \langle 1 - x^2/2! \rangle \simeq e^{-\frac{1}{2}\langle x^2\rangle}$ since $\langle x \rangle = 0$ [27].

2.3.4 Many-Body Effects

In an EXAFS experiment the interactions between electrons in a system are important. The interactions, which involve relaxation of passive electrons and multi-electron excitation, lower the amplitude and smear out the EXAFS oscillations [50].

Passive electrons are electrons in an absorbing atom which are not excited by an incident x-ray. After the core electron has been knocked out, the passive electrons are subjected to a new potential similar to the potential of an atom with an atomic number increased by one. This sudden change of potential relaxes the wavefunction of these electrons to a lower energy state. This relaxation of the passive electrons requires a modification of the EXAFS equation which is based on a one electron transition. It is found that the modification can be made by the introduction of an amplitude reduction factor S_0^2 which has a typical value between 0.7 and 1.10 [50, 54].

Although the relaxed passive electrons cause the amplitude of $\chi(k)$ to decrease by the factor S_0^2, the total absorption integrated over all energies must remain the same. In fact, the loss of amplitude is compensated by multi-electron excitations. Due to strong correlations between the electrons in a system, a photoelectron can excite other electrons and introduce shake-up and shake-off processes. In the shake-up process the second electron is excited to a bound state and in the shake-off process the second electron is excited to a continuum state and thus becomes another photoelectron. These processes broaden the EXAFS oscillations as the photoelectrons are left with different energies and in some cases they introduce a step in the background to the $\chi(k)$ signal. Experimental evidence of a double electron excitation in an absorption spectrum has been reported [55]. The results also suggest that the second excited electron can be an electron from the same or different atom as the photoelectron. The value of S_0^2 mainly depends on the atomic species of the absorbing atom with a small variation due to different chemical environments [50]. Estimated values of S_0^2, made from a calculation of the shake-off probability in a photoionization process for elements having an atomic number between 2 and 92, are described in [56].

Apart from the parameter S_0^2, many-body effects also causes variations in the effective distance and photoelectron mean free path. These variations are accounted for in the backscattering amplitude $F_j(k)$ and the $e^{-2(R_{0,j}-\Delta)/\lambda}$ term.

2.3.5 Multiple Scattering

Multiple scattering refers to the situation where a photoelectron is scattered by more than one neighbouring atoms before returning coherently to the absorbing atom and producing a contribution to the EXAFS signal. There can also be an effect from further scattering by the absorbing atom itself. One of the approaches used to treat multiple scattering is to consider the effects path by path [57].

A scattering path is described by the number of legs along which the photoelectron travels. Some examples of possible scattering paths consisting of 2, 3 or 4 legs are shown in figure 2.11. The backscattering amplitude and the phase shift for each scattering path are calculated separately. Thus, the effect of multiple scattering can be included in the EXAFS equation 2.63 by re-writing it in terms of a sum over all possible single and multiple scattering paths with their corresponding degeneracies, that is

$$\chi(k) = \sum_{j=1}^{\text{all paths}} S_0^2 N_j \frac{F_j^{eff}(k)}{kR_{0,j}^2} e^{-2(R_{0,j}-\Delta)/\lambda} e^{-2k^2\sigma_j^2} \sin[2kR_{0,j} + \delta_j^{eff}(k)], \qquad (2.64)$$

where the superscript eff represents the effective scattering amplitude or phase shift when scattering from every atom involved in a multiple or single scattering path j is taken into account and $R_{0,j}$ is the half path length which is equal to the distance between an absorbing and backscattering atom in the case of single scattering events.

Although multiple scattering effects can make an important contribution to an EXAFS signal, the signal is still dominated by single scattering events. The most important multiple scattering paths give a large $F_j^{eff}(k)$ value and correspond to scattering in the forward direction, the so called shadowing or focusing effect [50]. Several of the geometries associated with the focusing effect are highlighted in figure 2.11.

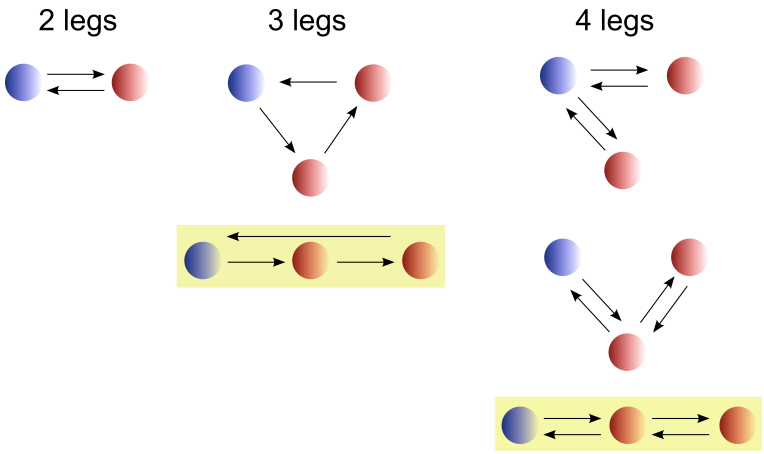

Figure 2.11: Examples of scattering paths consisting of 2, 3 or 4 legs where the arrows mark the individual legs. The blue spheres are absorbing atoms and the red spheres are the neighbouring atoms. The highlighted paths are those involving linear geometries which introduce a focusing effect.

2.3.6 EXAFS Equation for Disordered Systems: Cumulant Expansion

In the case of a highly disordered system, equation 2.55 has to be written in the more general form [58]

$$\chi(k) = \mathrm{Im}\left\{ \sum_{j=1}^{\text{all neighbours}} \frac{S_0^2 F_j(k)}{k} \int \frac{P(r_j,\lambda)}{r_j^2} e^{i(2kr_j+\delta_j(k))} dr_j \right\}, \tag{2.65}$$

where

$$P(r_j,\lambda) = P(r_j) e^{-2r_j/\lambda} \tag{2.66}$$

is an effective distribution function and λ is the photoelectron mean free path. The effect of a non-Gaussian distribution for $P(r_j)$ can be treated by using a cumulant expansion [53]. Consider equation 2.65 for a pair of atoms a distance r apart,

$$\chi(k) = \mathrm{Im}\left\{ \frac{S_0^2 F(k)}{k} \int \frac{P(r,\lambda)}{r^2} e^{i(2kr+\delta(k))} dr \right\}. \tag{2.67}$$

Assuming that the r dependence of $\delta(k)$ is negligible, the main effect of structural disorder is given by the integral

$$\int \frac{P(r,\lambda)}{r^2} e^{i2kr} dr \simeq \frac{1}{R_0^2} \int P(r,\lambda) e^{i2kr} dr \tag{2.68}$$

$$= \frac{1}{R_0^2} \cdot \langle e^{i2kR_0} e^{i2k(r-R_0)} \rangle$$

$$= \frac{1}{R_0^2} \cdot e^{i2kR_0} \cdot e^{-W+i\phi}, \tag{2.69}$$

where $R_0 = \langle r \rangle$ is the average value of r while W and ϕ are defined in terms of n^{th} order cumulants C_n, that is

$$-W + i\phi = \sum_{n=1}^{\infty} \frac{(2ik)^n}{n!} C_n. \tag{2.70}$$

The C_n can be determined from the relation [59, 60],

$$C_n = \left(\frac{d^n K(t)}{dt^n} \right)_{t=0}, \tag{2.71}$$

where $K(t)$ is a cumulant-generating function $K(t) = \sum_{n=1}^{\infty} C_n t^n / n!$ which is related to the moment generating function $M(t)$ by

$$K(t) = \ln M(t), \tag{2.72}$$

where $M(t)$ for a given function X is defined by $M(t) \equiv \sum_{n=0}^{\infty} \langle X^n \rangle t^n / n!$ and $\langle ... \rangle$ is a specified linear average.

For the EXAFS equation, the C_n are related to the moments $\langle r_s^n \rangle$ where $r_s = r - R_0$ [53]. Examples of some cumulants are as follows:-

$$\begin{aligned} C_1 &= \langle r_s \rangle = \Delta R \\ C_2 &= \langle (r_s - \langle r_s \rangle)^2 \rangle = \sigma^2 \\ C_3 &= \langle r_s^3 \rangle - 3\langle r_s^2 \rangle \langle r_s \rangle + 2\langle r_s \rangle^3 \\ C_4 &= \langle r_s^4 \rangle - 3\langle r_s^2 \rangle^2 - 4\langle r_s^3 \rangle \langle r_s \rangle + 12\langle r_s^2 \rangle \langle r_s \rangle^2 - 6\langle r_s \rangle^4. \end{aligned} \tag{2.73}$$

It follows that [58]

$$W = \sigma^2 \frac{(2k)^2}{2!} - C_4 \frac{(2k)^4}{4!} + ... \tag{2.74}$$

and

$$\phi = 2k\Delta R - C_3 \frac{(2k)^3}{3!} + ... \tag{2.75}$$

For most systems, four cumulants are sufficient [58] and equation 2.67 becomes

$$\begin{aligned} \chi(k) = \mathrm{Im} \Bigg\{ & \frac{S_0^2 F(k)}{k R_0^2} \exp\{-2k^2\sigma^2 + \frac{2}{3}k^4 C_4\} \\ & \exp\{i(2k(R_0 + \Delta R) - \frac{4}{3}k^3 C_3 + \delta(k))\} \Bigg\}. \end{aligned} \tag{2.76}$$

It can be seen from equation 2.76 that for highly disordered systems the EXAFS Debye-Waller factor is corrected by the addition of an even cumulant whereas the

phase of $\chi(k)$ is corrected by the addition of an odd cumulant. If the structural disorder is small then $C_3 = C_4 = 0$ and the term representing the thermal and static disorder in equation 2.76 becomes $e^{-2k^2\sigma^2}$ which is the same as in equation 2.56.

The approximation made in equation 2.68 can be improved by adding corrections to the average distance and the first cumumlant [53], such that

$$R_0^2 \rightarrow (R_0 + \Delta R)^2, \tag{2.77}$$

$$\Delta R \rightarrow \Delta R - \frac{2\sigma^2}{R_0}. \tag{2.78}$$

Thus equation 2.76 becomes

$$\begin{aligned} \chi(k) &= \mathrm{Im}\Bigg\{ \frac{S_0^2 F(k)}{k(R_0 + \Delta R)^2} \exp\{-2k^2\sigma^2 + \frac{2}{3}k^4 C_4\} \\ &\qquad \exp\{i(2k(R_0 + \Delta R) - \frac{4k\sigma^2}{R_0} - \frac{4}{3}k^3 C_3 + \delta(k))\} \Bigg\}. \end{aligned} \tag{2.79}$$

By including all nearest neighbours and multiple scattering events (cf. equation 2.64), the EXAFS equation 2.65 for highly disordered systems can be rewritten as

$$\begin{aligned} \chi(k) &= \mathrm{Im}\Bigg\{ \sum_{j=1}^{\text{all paths}} \frac{S_0^2 N_j F_j^{eff}(k)}{k(R_{0,j} + \Delta R_j)^2} \exp\{-2k^2\sigma_j^2 + \frac{2}{3}k^4 C_{4,j}\} \\ &\qquad \exp\{i(2k(R_{0,j} + \Delta R_j) - \frac{4k\sigma_j^2}{R_{0,j}} - \frac{4}{3}k^3 C_{3,j} + \delta_j^{eff}(k))\} \Bigg\}. \end{aligned} \tag{2.80}$$

Equation 2.80 is the version of the EXAFS equation used in the data analysis described in chapter 3.

It should be noted that the method of applying a cumulant expansion for structures with a non-Gaussian distribution of atoms is still quite controversial [61]. The method is, however, employed by ARTEMIS [62] and is used to produce the results presented in this thesis.

Chapter 3

Experimental Method

3.1 Introduction

In this chapter, the neutron and x-ray sources, the instruments and the data analysis procedures for ND and EXAFS are described. For ND, the experiments were performed using the D4c diffractometer [63] at the Institut Laue-Langevin (ILL) in Grenoble, France. For EXAFS, the experiments were performed using the BM29 and ID24 beamlines [64, 65] at the European Synchrotron Radiation Facility (ESRF) also in Grenoble, France. In addition, the chapter includes a description of the instruments used to obtain the high energy XRD results discussed in chapters 5 and 6 , namely the ID15B beamline [66] at the ESRF and the BL04B2 beamline [67, 68] at the SPring-8 in Hyogo, Japan.

3.2 Neutron Reactor Sources

Neutron beams are generally produced in one of two ways, by a fission reaction or by a spallation process [69]. In this study, all the ND experiments were performed at the ILL which is a reactor source. Neutron beams produced by a reactor source have a constant high flux which is suitable for diffractometers using monochromatic beams.

In a reactor source neutron beams are produced by the fission of ^{235}U nuclei.

Neutrons produced in this way are fast neutrons with MeV energies. In order to reduce their energies to a suitable range for diffraction or inelastic scattering experiments, the neutrons need to pass through a moderator where they undergo multiple inelastic collisions with light particles, which have comparable mass to neutrons, such as hydrogen or deuterium until they are in thermal equilibrium. The energy of neutrons after the moderation process is limited mainly by the temperature of the moderator.

Institut Laue-Langevin (ILL)

There are three types of moderator at the ILL [70]. The instruments use neutrons from different moderators depending on the range of neutron energies they require. Thermal neutrons are produced by a heavy water moderator at the temperature of 300 K. The moderator gives a neutron flux having a peak in the Maxwellian distribution at 1.2 Å. Hot and cold neutrons are available from a graphite moderator at 2400 K and a liquid deuterium moderator at 25 K, respectively. The graphite moderator improves the flux of neutrons with wavelengths below 0.8 Å. The liquid deuterium moderator improves the flux of neutrons with wavelengths above 3 Å.

There are about 40 instruments at the ILL [71]. The experimental methods available include inelastic scattering, elastic scattering and experiments in the fields of nuclear and particle physics research.

3.3 Synchrotron Sources

A synchrotron [72, 73] is a machine which can produce intense electromagnetic radiation. It consists of three main parts, an accelerator, a storage ring and beamlines. The schematic of a synchrotron is shown in figure 3.1. An electron beam is normally produced with an electron gun. This beam is then accelerated by using the combination of a linear accelerator (linac) and a booster to the energy of the order of GeV and maintained at a constant energy in a storage ring.

In the storage ring the electron beam is guided by a combination of different kinds of magnet, namely dipole or bending, quadrupole and sextupole magnets.

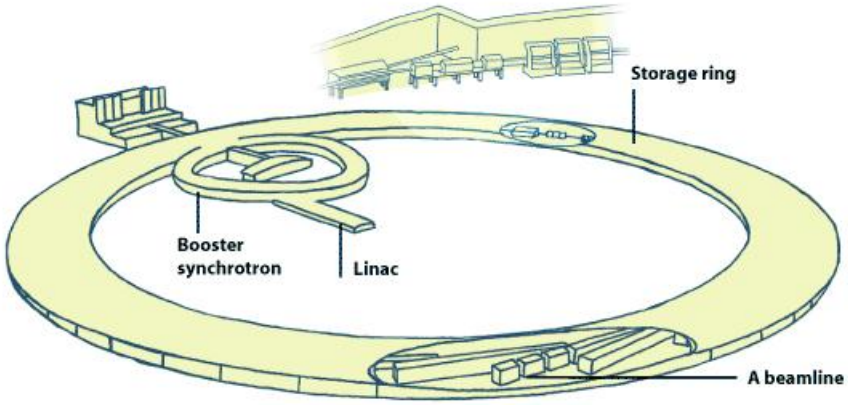

Figure 3.1: A schematic of a synchrotron showing its three main parts, an accelerator (which consists of a linac and a booster), a storage ring and a beamline [74].

Each bending magnet forces the electron beam to move in a curved trajectory. The storage ring is actually not a circle but a polygon with bending magnets at each corner. The quadrupoles and sextupoles are used to focus the beam and reduce the chromatic aberration of the electrons, respectively.

Because the electron is a charged particle, it gives out electromagnetic radiation when it is forced to move in a curved trajectory. A beamline comprises a set of apparatus which uses radiation emitted from the storage ring so called synchrotron radiation. Beamlines are either connected to bending magnets or insertion devices. Insertion devices are essentially sets of dipole magnets which improve the quality of the emitted radiation by forcing the electron beam to move in a sinusoidal trajectory. They are placed in the straight part of the ring between the bending magnets. The energy range of radiation produced from the synchrotron depends on the electron energy in the storage ring. The available energy can range from infrared to hard x-rays or in some synchrotron facilities gamma rays. The radiation profile of each beamline depends on the specifications of insertion devices or bending magnets to which the beamline connects.

The quality of synchrotron radiation is quantified by its brilliance. Brilliance

is defined as

$$\text{Brilliance} = \frac{\text{Number of photons per second}}{(\text{divergence, mrad}^2)(\text{area of source, mm}^2)(0.1\%\ \text{bandwidth})}, \tag{3.1}$$

where bandwidth is a photon energy range. The development of synchrotron has been to improve a radiation brilliance. The radiation brilliance from third generation synchrotron facilities such as the ESRF and SPring-8 is about 10^{12} times greater than radiation produce by using x-ray tubes. Figure 3.2 shows the development in the brilliance of radiation produced by using synchrotron, x-ray tubes and free-electron laser. A synchrotron can support many experimental techniques used in many research fields including physics, materials science, chemistry, biology and medicine. There are over 60 synchrotron facilities worldwide [75].

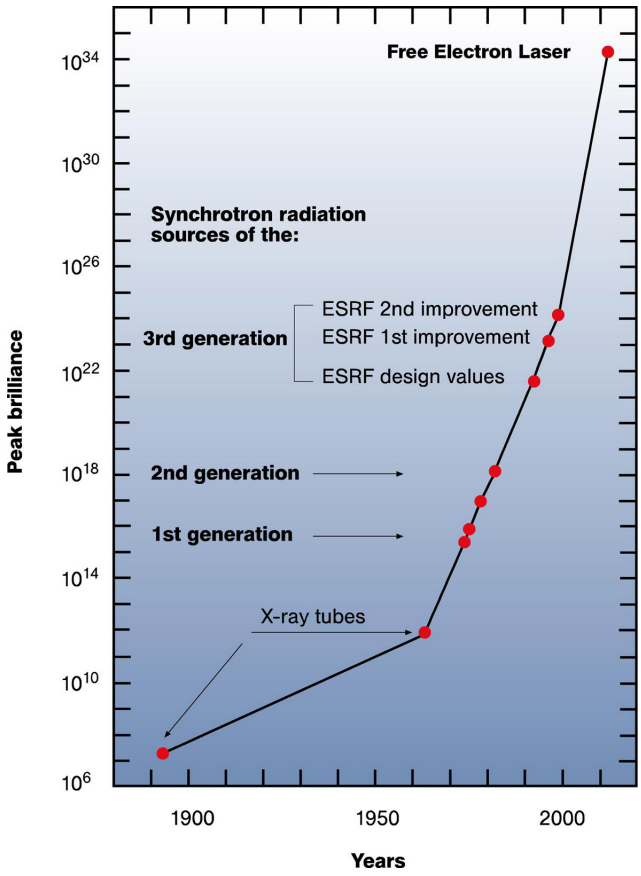

Figure 3.2: A development of x-ray source through time. A third generation synchrotron gives an x-ray brilliance about 10^{12} times greater than an x-ray tube [76].

European Synchrotron Radiation Facility (ESRF)

The ESRF [74] is a third generation synchrotron facility located in Grenoble, France. The storage ring has a 844.4 m circumference which can maintain an electron beam energy of 6 GeV. The facility houses over 40 beamlines which support many different scientific communities. Research areas at the ESRF include structural biology, the structure of materials, electronic structure and magnetism, atomic dynamics and extreme conditions, soft condensed matter and x-ray imaging.

SPring-8

SPring-8 [77] is a third generation synchrotron facility located in Harima Science Park City, Hyogo, Japan. The storage ring has a 1436 m circumference which can maintain an electron beam energy of 8 GeV. The radiation available for experiments includes soft x-rays, hard x-rays and high energy gamma rays. SPring-8 houses over 60 beamlines. The beamlines support scientific research in many fields including materials science, life science/medical applications, environmental science and Earth and planetary science. There is also a large number of beamlines dedicated to research for industrial applications.

3.4 Instruments

3.4.1 D4c Diffractometer

D4c [78] is a two-axis diffractometer at the ILL. The instrument uses the neutron from a hot source and a Cu crystal monochromator. Available incident wavelengths are 0.35 Å, 0.5 Å and 0.7 Å which correspond to Cu(331), Cu(220) and Cu(200) reflections, respectively. The instrument also includes a filter to remove higher order harmonic contaminations. A detector array consists of nine 1-D position sensitive detectors. Each detector contains 64 cells and the detector array cover scattering angles from 1.5° to 140°.

A layout of the D4c and a picture of the instrument are shown in figures 3.3 and

3.4. From the layout, a moderated neutron beam passes through a monochromator, where a single wavelength is selected, then enters an evacuated sample chamber. The direct beam, which passes through the sample without scattering, is blocked by the beamstop and the scattered neutrons are measured by an array of detectors. A diffraction pattern is thereby measured as a function of scattering angle.

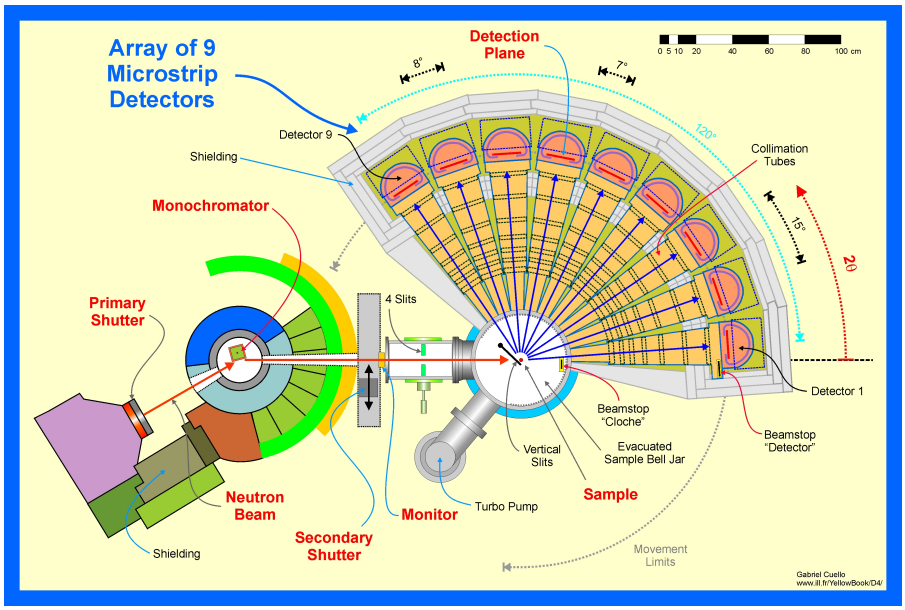

Figure 3.3: Layout of the D4c diffractometer [63].

As shown in figure 3.3, there are gaps of approximate 7° between adjacent detectors. In order to measure the corresponding diffraction signal, the array of detectors needs to be moved during the measurement. Some of the scattering angles are, therefore, measured several times by different detector cells. The whole spectrum is determined by regrouping the individual spectra measured from the different detector array positions using an appropriate efficiency file which contains the relative efficiency of each detector cell. The detector efficiency file is measured regularly to ensure the quality of the regrouped spectrum.

A sample with cylindrical geometry is usually used on D4c. The maximum sample size visible to the detectors corresponding to a 20 mm diameter with a 50 mm height. The sample chamber is a cylindrical bell jar of 55 cm height and 46 cm diameter and has a thin aluminium window. The chamber can be equipped with a cryostat, a furnace, or a user-provided equipment such as a pressure cell.

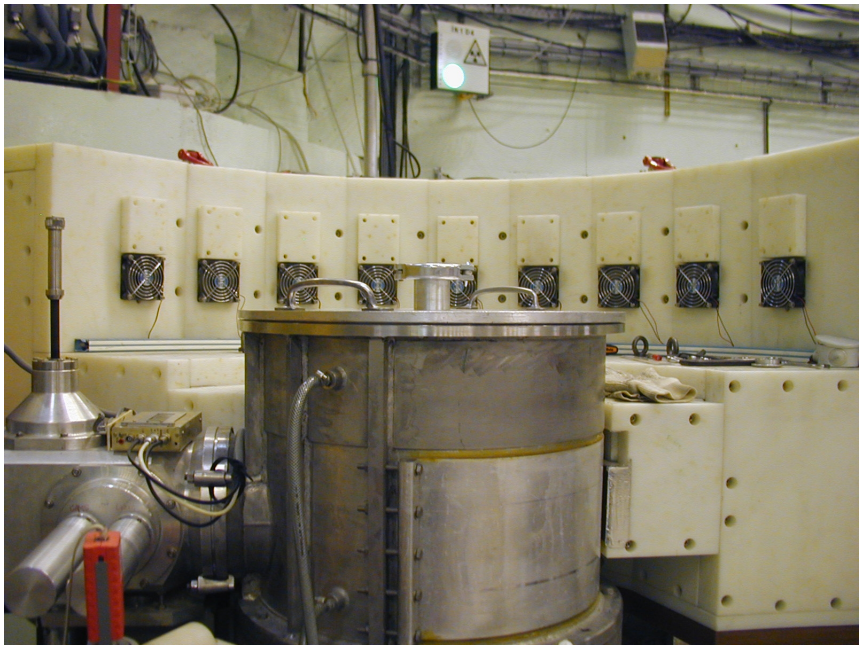

Figure 3.4: A side view of the sample chamber of the D4c diffractometer. The detector array around the sample chamber spans the scattering angle range from 1.5° to 140°.

3.4.2 ID15B X-ray Diffraction Beamline

ID15B [66] is a high energy XRD beamline at the ESRF. The beamline employs a monochromatic incident beam of energy 30, 60 or 90 keV. The diffraction pattern is measured using one of the available 2D-detectors namely charge coupled device (CCD) detectors MAR133 and MAR165, an image plate MAR345, a Pixium detector, or an image intensifier. A typical sample has a slab geometry. It is also possible to mount the sample in, for example, a cryostat or a furnace.

3.4.3 BL04B2 X-ray Diffraction Beamline

BL04B2 [67, 68] is a high energy XRD beamline at the SPring-8. The beamline is equipped with a two-axis x-ray diffractometer. The diffractometer employs a monochromatic incident beam from a Si crystal, the first and the third harmonic Si(111) reflections providing an incident x-ray energy of 37.8 and 113.3 keV, respectively, and the Si(220) reflection providing an incident x-ray energy of 61.7 keV.

The diffraction pattern for a sample can be measured using two different types of detector. The first detector is a Ge detector which is located on the 2θ main arm,

see figure 3.5, and covers a scattering angle range from -10° to 150° with a scan step of 0.001°. The advantage of using this kind of detector is the small background scattering, however, the data acquisition time can take from 2 to 12 hr. The second detector is an x-ray image intensifier which is located on the 2θ sub arm and covers the scattering angle range from -120° to 10° with a scan step of 0.001°. By using this detector, a diffraction pattern can be measured within 30 ms but with a large contribution from the background scattering. An experiment can be performed with either of the detectors or both.

A typical beam size for diffraction experiment is 2.5 mm × 0.5 mm. Samples are typically held in a Pyrex or silica capillary with a 2 mm inner diameter and 0.2 mm wall thickness. The diffractometer is also equipped with a furnace which can heat the sample up to 1100 °C.

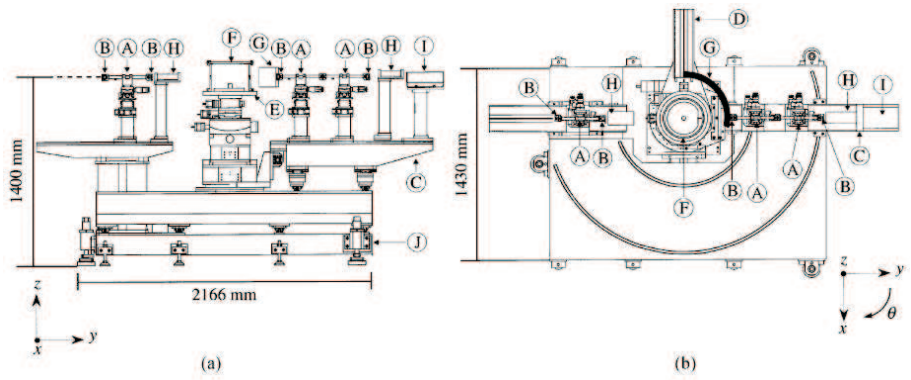

Figure 3.5: Layout of BL04B2 high energy XRD beamline, (a) side view, (b) top view. The main components are denoted as A to J where A are collimators, B are slits, C is a 2θ main arm, D is a 2θ sub arm, E is a θ stage, F is a vacuum chamber, G is a beamstop, H is an ionization chamber, I is a scintillation counter or a solid state detector and J is a table [67].

3.4.4 BM29 XAS Beamline

BM29 is an x-ray absorption spectroscopy (XAS) beamline [64, 79] at the ESRF. The beamline is equipped with a double crystal monochromator. There are three crystal pairs available to used in the monochromator. The crystals are the Si(111) reflection for an energy range from 4.5 to 24 keV, the Si(311) reflection for an energy range from 5 to 50 keV, and the Si(511) reflection for an energy range

from 10 to 74 keV. The choice of crystal pairs depends on the absorption edge of interest. The EXAFS signal can be measured in either transmission or fluorescence mode with beam dimensions of 1.0 mm × 0.2 mm. Various sample environments can be set up by employing, for example, a cryostat, a furnace or a pressure cell.

Experimental Setup for Transmission Mode

In transmission mode, a typical experimental setup is shown in figure 3.6. From the figure, the beam from the x-ray source is monochromated by a double crystal monochromator. The energy of the monochromatic beam is changed by rotating the monochromator crystals relating to the beam. Because the energy scan involves a mechanically moving part, the energy calibration can be shifted during the experiment. A reference sample is usually placed after the sample as an in situ check of the energy calibration. The reference is normally a foil of the same or similar element as the absorbing element in the sample and has a known absorption edge energy. I_0, I_1 and I_2 are ionization chambers.

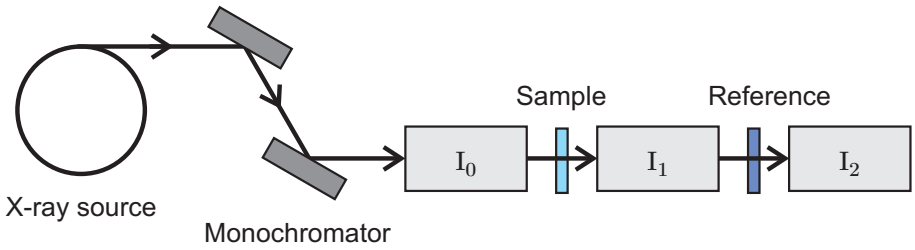

Figure 3.6: An EXAFS experimental setup in transmission mode. I_0, I_1 and I_2 denote ionization chambers.

The ionization chambers are filled with a mixture of Ar or N_2 gas with He gas. Ar and N_2 are ionizing gases and He is used to ensure that the gas mixture exerts suitable pressure to the ionization chambers. The selection of the type of ionizing gas and the ratio between the ionization gas and He depends on the energy range of the experiment and the required efficiency of the ionization chamber. The first ionization chamber measures the intensity I_0 of the incoming x-ray beam. The gas in the first chamber should absorb about 30% of the x-ray beam. The second chamber measures the intensity I_1 of the beam after it has passed through the sample and should absorb about 70% of the x-ray beam. The last chamber measures the

intensity I_2 of the beam after it has passed through the reference sample and should absorb the rest of the x-ray beam. The second chamber should absorb most of the x-ray beam because it measures the absorption of the sample. The other two chambers can have low efficiencies because I_0 should be relatively constant as a function of energy and I_2 is only a measurement of the energy edge position of the reference sample. The ionization chambers I_1 and I_2 for the BM29 beamline are shown in figure 3.7.

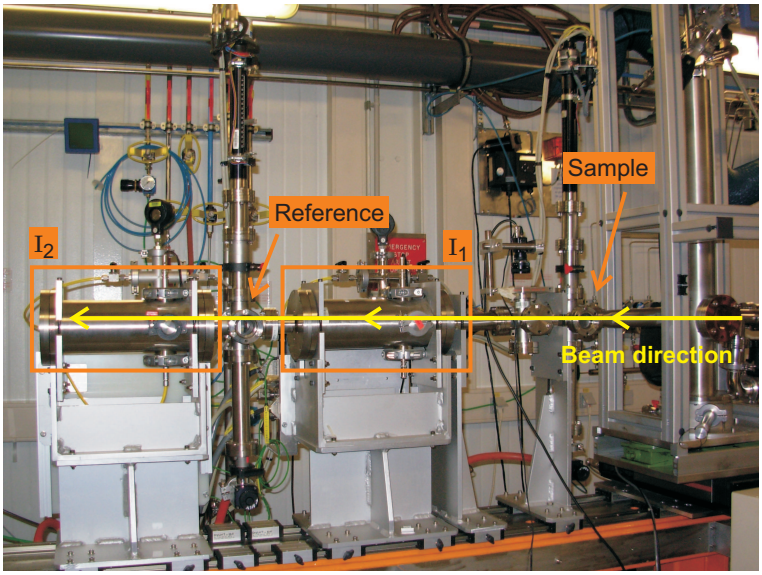

Figure 3.7: A picture showing the ionization chambers I_1 and I_2 together with the reference and sample chambers for the BM29 beamline at the ESRF.

The absorption of the sample and the reference are calculated from the measured intensity by

$$\mu_{sample}(E)x_{sample} = \ln\left(\frac{I_0}{I_1}\right) \tag{3.2}$$

$$\mu_{ref}(E)x_{ref} = \ln\left(\frac{I_1}{I_2}\right), \tag{3.3}$$

where $\mu(E)$ is an absorption coefficient at energy E and x_{sample} and x_{ref} are the thickness of the sample and the reference, respectively.

Sample Requirement

For measurements in transmission mode it is important that a sample has an appropriate thickness as the sample thickness affects the amplitude of $\chi(k)$ signif-

icantly. Theoretically, $\chi(k)$ will contain the least statistical error if $\Delta\mu_0 x = 2.6$, where $\Delta\mu_0$ is the edge step [80]. However, a thickness effect needs to be considered. The thickness effect occurs when some part of the incoming x-ray beam is not attenuated by the sample which could result from an uneven distribution of absorbing particles in the sample or fluorescence photons. It has been found that the thickness effect does not produce great distortion to the $\chi(k)$ if $\Delta\mu_0 x < 1.5$ [81].

Practically, samples are usually prepared with a sample thickness equal to their absorption lengths which is the thickness which introduce a negligible absorption before an absorption edge i.e. $\mu(E_b)x_{abs} = 0$ and for which the intensity ratio I_0/I_1 drops to $1/e$ after the absorption edge i.e. $\mu(E_a)x_{abs} = 1$. Thus the absorption length can be calculated from

$$x_{abs} = \frac{1}{\Delta\mu_0}, \tag{3.4}$$

where $\Delta\mu_0 = \mu(E_a) - \mu(E_b)$, and E_a and E_b are usually taken to be energies at ± 50 eV from the absorption edge. The values of $\mu(E_b)$ and $\mu(E_a)$ can be found in [82].

Powdered samples are usually prepared in the form of pellets to ensure an even thickness. However, the absorption length is normally of the order of μm and it is not possible to make a pellet of this thickness. Therefore, the sample needs to be mixed with a 'matrix' material. The matrix material is usually a material with a small atomic number, a very small absorption coefficient and does not react with the sample. Examples of matrix materials are graphite, cellulose, BN and LiF. The selection of the matrix material depends on the sample and the experimental conditions. By mixing the sample with the matrix material, the thickness of a pellet can be made up to a few mm. It should be noted that the inhomogeneity of the sample can enhance the thickness effect thus the sample needs to be entirely mixed with the matrix material and the grain size of the sample needs to be smaller than the absorption length to ensure a uniform signal.

Data Treatment

The instrumentation can lead to glitches in a measured absorption spectrum and the energy calibration can be shifted slightly during a measurement. The data

obtained from the beamline, therefore, should be treated for these effect before analysis. Glitches in the data are often due to the monochromator and an example is shown in figure 3.8. The double crystal monochromator used on the BM29 beamline scans energy by rotating the two crystals and at the same time keeping them parallel to each other. Sometimes the two crystals can lose their parallelism and result in a glitch in the absorption spectrum at some energy. Glitches can also arise from reflection of the monochromator crystal or defects in the crystal planes.

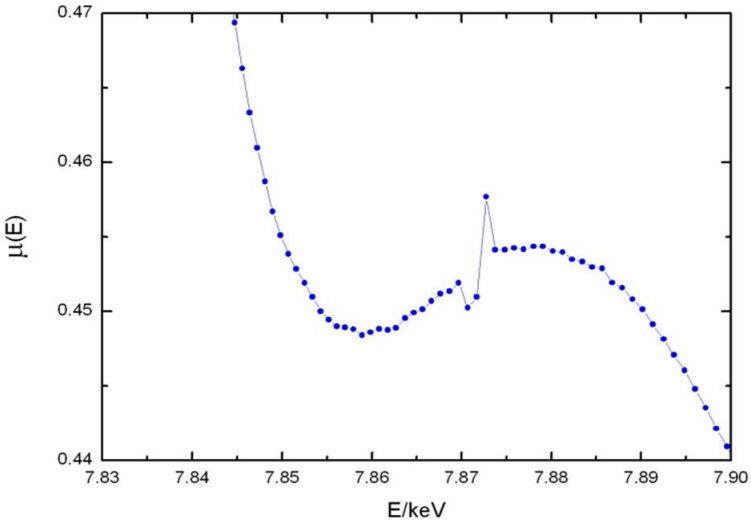

Figure 3.8: A glitch at $E \approx 7.87$ keV in the absorption signal.

The glitches, caused by the monochromator, have to appear in I_0, I_1 and I_2 and most of them should be canceled in the intensity ratio I_0/I_1 due to the linearity of the ionization chambers. However, if some of the glitches remain, they need to be removed from the data as they are not relevant to the structure of the target material. Glitches that cover only a few data points, like the one shown in figure 3.8, can be easily removed by removing those data points. However, it might not be possible to remove big glitches without affecting the shape of the absorption spectrum. In some cases, an interpolation can be made to replace some of the data points.

If necessary, the energy scale can be calibrated by adjusting the scale such that an absorption edge of the reference sample is at the correct energy. As the measurements usually consist of more than one scan to improve the statistics of the

data and the monochromator calibration can be shifted between scans, the data sets need to be aligned before merging. This can be achieved by aligning the absorption spectrum for the reference sample of every scan to that of the first scan which has been calibrated.

3.4.5 ID24 Energy Dispersive XAS Beamline

ID24 is an energy dispersive XAS beamline [65, 83] at the ESRF. The optical scheme of ID24 is very different to that of a conventional EXAFS experimental setup such as that of the BM29 beamline. The optical scheme is shown in figure 3.9.

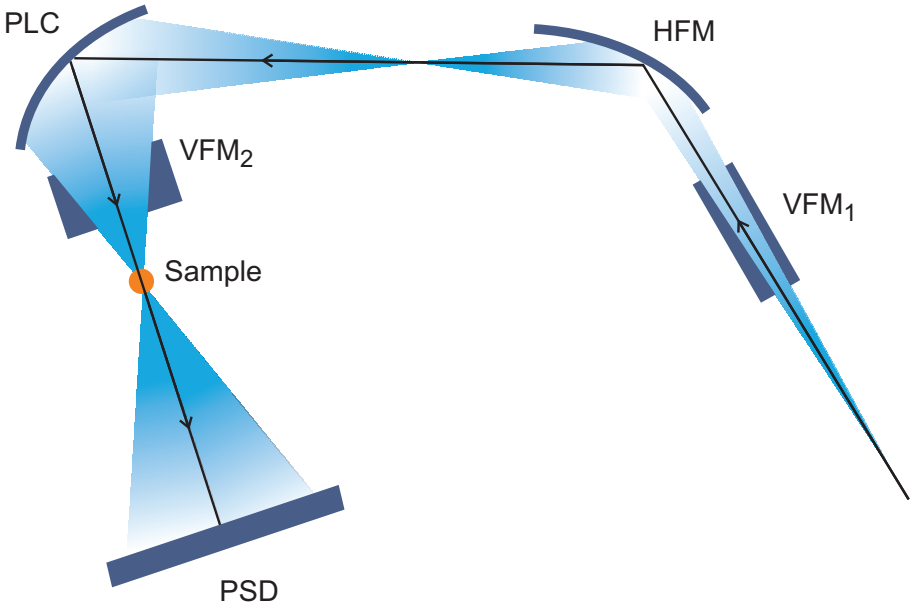

Figure 3.9: The optical scheme for the ID24 beamline [65]. The main components are horizontal and vertical focussing mirrors (HFM and VFM), a polychromator crystal (PLC) and a position sensitive detector (PSD). The sample is placed at the focal plane between the third mirror and the detector.

In figure 3.9, the first two mirrors VFM_1 and HFM reject the third harmonic and focus the beam vertically and horizontally. The polychromator (PLC) is a bent crystal. The white beam from the second mirror is scattered from the polychromator crystal at a different angle depending on the energy of the x-rays. The crystal is bent in order to focus the beam at the sample before the beam diverges again by an angle which is a function of energy. The intensity of the absorption signal at different

energies is then measured by a position sensitive detector (PSD) placed after the sample. The last mirror VFM_2 is used to refocus the beam such that final beam size hitting the sample is of the order of 2 μm $\times$ 1 μm full-width at half-maximum (FWHM).

There are some major advantages of EXAFS measurement using this setup. Because there is no moving part involved during the measurement, the stability of the focal spot and the energy calibration is high. The data acquisition speed is also very high compared with a conventional setup as the whole absorption spectrum is measured simultaneously. In fact, the data acquisition speed is only limited by the readout time of the detector. One spectrum can be measured in 0.1 ms such that it is ideal for tracking rapid changes in the local structure of many systems in the field of biophysics, chemistry or material science. Another advantage is that the setup enables the use of a diamond anvil cell (DAC) for a high pressure experiment. Bragg peaks introduced by a diamond can be removed from the absorption spectrum by tilting the pressure cell such that the x-ray is scattered from a plane which minimises the intensity of the Bragg peak in the direction of the detector. This can be achieved conveniently by using an experimental setup which has a high data acquisition speed.

It is useful to also mention some limitations of this setup. The major one is the short k range. This is in the case when a DAC is used as the x-rays are scattered by the diamond which gives a significant background. According to the EXAFS equation 2.56, $\chi(k)$ is greatly damped at high k values thus the background from the diamond reduces the signal to noise ratio considerably and shortens the usable k range. Another disadvantage of using this setup is the fact that the I_0 and I_1 signals have to be measured separately. This results in more glitches from the polychromator that do not cancel in the intensity ratio I_1/I_0.

The detector for the absorption signal is a fast readout low noise (FReLoN) CCD camera developed by the Instrument Support Group at the ESRF [84]. Also, a MAR345 image plate is positioned after the sample above the plane of the direct beam to measure diffraction patterns, see figure 3.10. For diffraction measurements, an additional slit is placed after the polychromator to select a particular wavelength.

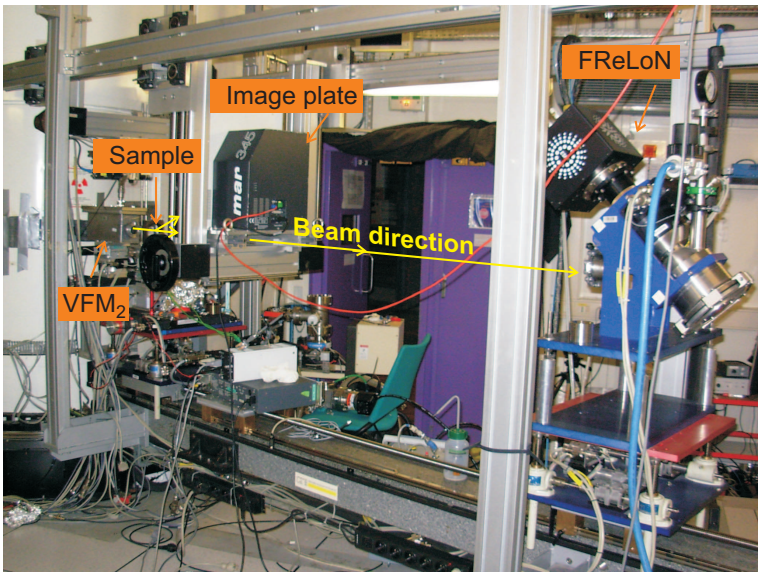

Figure 3.10: A picture of ID24 showing the second focussing mirror (VFM_2), a sample position, a MAR345 image plate detector and a FReLoN camera.

Data Treatment

There can also be glitches in the absorption coefficient measured using ID24. The glitches can arise from defects in the polychromator crystal and, if the DAC is used, from the Bragg peaks of diamond. As the acquisition speed is very high, the severity of the glitch can be reduced by averaging 100 measured spectra. Glitches can also arise from contaminants deposited on the surface of the third mirror. The glitches introduced by the dirty mirror can be removed by averaging 10 spectra measured at random positions on the mirror.

The FReLoN camera records the absorption signal as a function of pixel. The pixel scale can be converted to an energy scale by measuring a material which has a reference absorption spectrum. This material is normally a foil which has well known absorption edges to justify the reference spectrum. Maximum and minimum points of the oscillation as well as the maximum and minimum points of the derivative on the pixel scale are then mapped onto the corresponding points of the reference absorption spectrum which is on the energy scale.

3.5 ND Data Analysis

In the previous chapter, the differential scattering cross-section $d\sigma/d\Omega$ is related to the measured intensity. The equations were derived on the basis that there is only scattering from the sample and the sample itself is small enough that there is no attenuation of the neutron beam by the sample. However, in a real experiment, there is always scattering from the sample environment and background scattering. The measured intensity from the sample is also attenuated by an absorption process and multiple scattering can also occur. These factors, therefore, need to be taken into consideration in the data analysis.

The data analysis procedure described in this section is based on diffraction experiments with a monochromatic incident beam. The process requires attenuation corrections, environment and background corrections and normalisation of the data. At the end of this section, some checks are described which can be used to determine the efficacy of the data analysis.

3.5.1 Attenuation Corrections for Cylindrical Geometry

If there is no sample container or furnace involved, the measured intensity from the sample is described by

$$I_S^E(\theta) = A_{S,S}(\theta)I_S(\theta) + a(\theta)M_S(\theta), \tag{3.5}$$

where $A_{S,S}(\theta)$ is an attenuation coefficient which results from attenuation of the beam by the sample in the presence of the sample, $I_S(\theta) = a(\theta)d\sigma/d\Omega$ is the single scattered intensity from the sample, $M_S(\theta)$ is the multiple scattering cross section of the sample, and $a(\theta)$ is a normalisation factor. It is convenient to write all of the parameters as a function of the scattering angle 2θ since the attenuation corrections are calculated in terms of this variable. Because structure factors are function of q, the variable θ will be later converted to q by using the relation $q = \frac{4\pi \sin\theta}{\lambda}$ in equation 2.8.

For a thin planar sample of thickness t, the attenuation coefficient of the sample

at $2\theta = 0$ can be calculated by using

$$A_{S,S}(\theta = 0) = e^{-\mu_S t}, \tag{3.6}$$

where $\mu_S = \frac{N}{V}\sigma_{total}$ is the attenuation factor of the sample, N is the number of particles in the sample, V is the volume of the sample, and σ_{total} is the total cross-section of the sample measured at the incident wavelength.

To calculate $A_{S,S}(\theta)$ for $\theta > 0$, the path length of the incident and scattered beam in the sample need to be taken into account. For a sample with cylindrical geometry, the attenuation needs to be calculated for the sample geometry and for each scattering angle. If there is a container and furnace involved the attenuation from these materials also needs to be taken into account[85].

The multiple scattering cross-section [86] for a bare sample can be calculated by

$$M_S(\theta) = NA_{S,S}(\theta)(b^2_{coh} + b^2_{incoh})\Delta_S(\theta)(P_\alpha(\theta) + 1), \tag{3.7}$$

where $\Delta_S(\theta)$ is the ratio of multiple to single scattered nucleus and $P_\alpha(\theta)$ is a Placzek correction. Although, from equation 3.7, the multiple scattering cross-section contains no structural information, it significantly affects the level of the signal and needs to be corrected for. The multiple scattering from a container or furnace can be calculated similarly.

3.5.2 Correction for Sample Environment

If the sample is in a container and inside a furnace the measured intensity is given by

$$\begin{aligned} I^E_{S+C+H}(\theta) &= A_{S,SCH}I_S(\theta) + A_{C,SCH}(\theta)I_C(\theta) + A_{H,SCH}(\theta)I_H(\theta) \\ &\quad + a(\theta)M_{S+C+H}(\theta), \end{aligned} \tag{3.8}$$

where $I_S(\theta), I_C(\theta), I_H(\theta)$ are the single scattered intensities for the sample, the container and the furnace, respectively, $M_{S+C+H}(\theta)$ is a multiple scattering cross-section for the sample with the container and the furnace. $A_{S,SCH}(\theta)$ is the attenuation coefficient of the sample in the presence of the sample, container and furnace, $A_{C,SCH}(\theta)$

is the attenuation coefficient for the container in the presence of the sample, container and furnace, and $A_{H,SCH}(\theta)$ is the attenuation coefficient of the furnace in the presence of the sample, container and furnace.

$I_S(\theta)$ can be determined from equation 3.8 by performing additional measurements for an empty container inside the furnace and an empty furnace. Note that the additional measurements have to be performed at the same temperature and wavelength as the measurement for the sample. The measured intensities are

$$I^E_{C+H}(\theta) = A_{C,CH}(\theta)I_C(\theta) + A_{H,CH}(\theta)I_H(\theta) + a(\theta)M_{C+H}(\theta) \tag{3.9}$$

for the empty container inside the furnace and

$$I^E_H(\theta) = A_{H,H}(\theta)I_H(\theta) + a(\theta)M_H(\theta) \tag{3.10}$$

for the empty furnace. By substituting $I_C(\theta)$ and $I_H(\theta)$ from equations 3.9 and 3.10 in equation 3.8, we have

$$\begin{aligned} I_S(\theta) &= \frac{1}{A_{S,SCH}(\theta)}\Bigg[(I^E_{S+C+H}(\theta) - a(\theta)M_{S+C+H}(\theta)) \\ &- \frac{A_{C,SCH}(\theta)}{A_{C,CH}(\theta)}\left\{(I^E_{C+H}(\theta) - a(\theta)M_{C+H}(\theta)) - \frac{A_{H,CH}(\theta)}{A_{H,H}(\theta)}(I^E_H(\theta) - a(\theta)M_H(\theta))\right\} \\ &- \frac{A_{H,SCH}(\theta)}{A_{H,H}(\theta)}(I^E_H(\theta) - a(\theta)M_H(\theta))\Bigg]. \end{aligned} \tag{3.11}$$

In the case where no furnace is used during the measurement $I_H(\theta) = 0$ and equation 3.11 is simplified to

$$\begin{aligned} I_S(\theta) &= \frac{1}{A_{S,SC}(\theta)}\Bigg[(I^E_{S+C}(\theta) - a(\theta)M_{S+C}(\theta)) \\ &- \frac{A_{C,SC}(\theta)}{A_{C,C}(\theta)}(I^E_C(\theta) - a(\theta)M_C(\theta))\Bigg]. \end{aligned} \tag{3.12}$$

The sample container is often made from vanadium. As vanadium has $b_{coh} \approx 0$, the differential scattering cross-section from the container only has an incoherent part and is, therefore, uniform. However, in some high temperature experiments, such as those on molten alloys described in chapter 4 and on molten $ZnCl_2$ described in chapter 6, the samples were held in silica ampoules. The coherent scattering length of silica is not negligible and its scattering pattern shows significant structure. In these cases, the dimensions of the containers need to be measured accurately to ensure that the correct amount of silica is subtracted from the total signal.

3.5.3 Correction for Background

Apart from scattering from the sample, container and furnace, there is also background scattering from the instrument itself. Therefore, an appropriate background intensity has to be subtracted from the intensity measured for the sample, container and furnace such that

$$I^{E}_{S+C+H}(\theta) = I^{E+bkg}_{S+C+H}(\theta) - I^{bkg}_{S+C+H}(\theta) \quad (3.13)$$

$$I^{E}_{C+H}(\theta) = I^{E+bkg}_{C+H}(\theta) - I^{bkg}_{C+H}(\theta) \quad (3.14)$$

$$I^{E}_{H}(\theta) = I^{E+bkg}_{H}(\theta) - I^{bkg}_{H}(\theta) \quad (3.15)$$

where $I^{E}(\theta)$ is a background corrected intensity, $I^{E+bkg}(\theta)$ is a measured intensity which includes a contribution from the background and $I^{bkg}(\theta)$ is a background intensity.

Let $I^{E}_{0}(\theta)$ be the measured intensity for an empty instrument. For high scattering angles, the background intensities can be written as

$$I^{bkg}_{S+C+H}(\theta) \simeq A_{S,SCH}(\theta) I^{E}_{0}(\theta) \quad (3.16)$$

$$I^{bkg}_{C+H}(\theta) \simeq A_{C,CH}(\theta) I^{E}_{0}(\theta) \quad (3.17)$$

$$I^{bkg}_{H}(\theta) \simeq A_{H,H}(\theta) I^{E}_{0}(\theta), \quad (3.18)$$

where $I^{E}_{0}(\theta)$ is assumed to be attenuated by the presence of only the furnace. For low scattering angles, the attenuation by the sample and container needs to be taken into account when calculating the $I^{bkg}_{S+C+H}(\theta)$.

Consider the scattering at low scattering angles. If we divide a sample chamber into three zones as shown in figure 3.11, where α is the region where the neutron beam passes before the sample, β is the region after the beam has passed through the sample, and γ is the rest of the chamber, the intensity measured for the empty chamber can be written as

$$I^{E}_{0}(\theta) = I_{\alpha}(\theta) + I_{\beta}(\theta) + I_{\gamma}(\theta). \quad (3.19)$$

If the sample is highly attenuating, less neutron beam can pass through the sample, thus the scattering from zone β, $I_{\beta}(\theta)$, will become significantly smaller. If there is

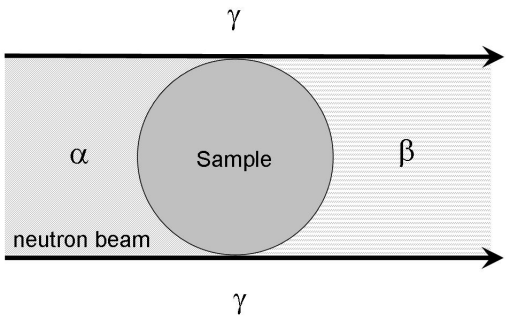

Figure 3.11: An illustration of the different zones in the sample chamber that contribute to the background scattering.

no container or furnace the attenuated background can be written as

$$I_S^{bkg}(\theta) = I_\alpha(\theta) + A_{S,S}(\theta)I_\beta(\theta) + I_\gamma(\theta), \tag{3.20}$$

If we measure the intensity for an absolute absorber placed at the sample position, $^{10}B_4C$ in the case of neutrons of wavelength ≈ 0.5 Å, then

$$I^E_{\mathrm{B_4C}}(\theta) = I_\alpha(\theta) + I_\gamma(\theta). \tag{3.21}$$

By using equations 3.19 to 3.21, the background intensity in the presence of the sample can thus be re-written as

$$I_S^{bkg}(\theta) = I_{B_4C}(\theta) + A_{S,S}(\theta)(I_0^E(\theta) - I^E_{B_4C}(\theta)). \tag{3.22}$$

In the presence of the sample, container and furnace, the background can be written as

$$I^{bkg}_{S+C+H}(\theta) = A_{H,H}(\theta)I_{B_4C}(\theta) + A_{S,SCH}(\theta)(I_0^E(\theta) - I^E_{B_4C}(\theta)), \tag{3.23}$$

where the furnace is assumed to also attenuate the scattering from zone α and γ. The attenuation coefficient $A_{S,SCH}(\theta)$ is used instead of $A_{SCH,SCH}(\theta)$ which is the attenuation coefficient for the sample, container and furnace in the presence of the sample, container and furnace, on the basis that the sample dominates the attenuation of the scattering from zone β.

3.5.4 Normalisation

The normalisation factor, $a(\theta)$, in equation 3.5, is a parameter which converts a cross-section to a measured intensity. It, therefore, takes into account the solid angle subtended by the detectors. The factor can be determined by measuring the intensity scattered by vanadium. Because the scattering cross-section is represented in q space, the normalisation factor is now written as a function of q.

Vanadium has $b_{coh} \approx 0$ so, from equation 2.38, the differential scattering cross-section for vanadium can be written as

$$\frac{1}{N_V}\left(\frac{d\sigma}{d\Omega}(q)\right)_V = b^2_{V,inc}(1 + P_V(q)). \tag{3.24}$$

Following equation 3.5, the measured intensity for vanadium is given by

$$I^E_V(q) = A_{V,V}(q)I_V(q) + a(q)M_V(q) = a(q)\left[A_{V,V}(q)\left(\frac{d\sigma}{d\Omega}(q)\right)_V + M_V(q)\right]. \tag{3.25}$$

By using equations 3.24 and 3.25, the normalisation factor can be calculated from

$$a(q) = \frac{I^E_V(q)}{N_V A_{V,V}(q)\left[b^2_{V,inc}(1 + P_V(q))\right] + M_V(q)}. \tag{3.26}$$

3.5.5 Efficacy of the Data Analysis

To test the quality of the corrected data sets, the following tests are made.

Level Limit

From chapter 2, the $F(q)$ is related to the differential scattering cross-section by equation 2.24,

$$\frac{1}{N}\left(\frac{d\sigma}{d\Omega}(q)\right) = F(q) + \sum_\alpha c_\alpha \overline{b^2_\alpha},$$

where $\overline{b^2_\alpha} = \left(b^2_{\alpha,coh} + b^2_{\alpha,incoh}\right)$. Because a cross-section is a measured quantity, the value is always equal or greater than zero i.e.

$$\frac{1}{N}\left(\frac{d\sigma_{coh}}{d\Omega}\right) = F(q) + \sum_\alpha c_\alpha \overline{b^2_\alpha} \geq 0. \tag{3.27}$$

Therefore, from equation 3.27, we have a level limit for the $F(q)$ function,

$$F(q) \geq -\sum_\alpha c_\alpha \overline{b^2_\alpha}. \tag{3.28}$$

Sum Rule Relation

From equation 2.22, we have

$$g(r) - 1 = \frac{1}{n_0 2\pi^2 r} \int_0^\infty [S(q) - 1] q \sin(qr) dq. \tag{3.29}$$

In the limit as $r \to 0$, $\sin(qr) \to qr$ and $g(r) \to 0$, equation 3.29 gives the sum rule relation

$$-n_0 2\pi^2 = \int_0^\infty [S(q) - 1] q^2 dq. \tag{3.30}$$

For a polyatomic system, it follows that

$$-n_0 2\pi^2 G(0) = \int_0^\infty F(q) q^2 dq \tag{3.31}$$

where

$$G(0) = -\sum_{\alpha,\beta}^{n} c_\alpha c_\beta b_\alpha b_\beta, \tag{3.32}$$

and

$$F(q) = \sum_{\alpha,\beta}^{n} c_\alpha c_\beta b_\alpha b_\beta \left[S_{\alpha\beta}(q) - 1 \right].$$

Back Fourier Transform

Theoretically, $g_{\alpha\beta}(r) = 0$ for r values smaller than the first nearest neighbour distance. This leads to the expression for $G(0)$ given by equation 3.32. However, when obtaining $G(r)$ from the Fourier transform of $F(q)$, there are always oscillations left in the low r region due to e.g. statistical noise on the measured data sets. As the oscillations do not come from the structure of the material, the back Fourier transform of $G(r)$ without the low r oscillation should be identical to the measured $F(q)$. A discrepancy between $F(q)$ and the back transform in the small q region usually indicates the use of an incorrect effective density in the data analysis procedure.

The effective density refers to the actual density of the sample at the time of the experiment. When using a powdered sample or a liquid, it is often lower than the mass density because of the packing of the powder or the presence of bubbles in the case of a liquid. The effective density reflects the real number of particles seen by the neutron beam and it is used in the calculation of the attenuation coefficients and multiple scattering cross-sections.

3.6 EXAFS Data Analysis

The EXAFS data analysis consists of two main parts. The first part involves the method used to extract $\chi(k)$ from the measured absorption spectrum. The second part involves the use of $\chi(k)$ to refine a structural model for the system. The model used in the refinement corresponds to the best guessed structure according to previous knowledge of the sample from the literature and/or other experiments. In many cases it is found that the first few models do not fit the experimental data or that the refined values are not sensible. This can result from an unsuitable model, inappropriate data treatment or an incorrect extraction of $\chi(k)$ from the measured data. Therefore, an iterative procedure needs to be adopted and the process is summarised in figure 3.12.

The EXAFS results presented in this thesis were analyzed using the programs ATHENA and ARTEMIS [62], which employ the theoretical standard from FEFF 6 [57] for the calculation of $\chi(k)$. The data analysis procedure described in this section is that used by ATHENA and ARTEMIS.

3.6.1 Extracting the EXAFS signal $\chi(k)$

After the measured absorption spectrum $\mu(E)$ has been treated for glitches and the energy scale has been calibrated, the EXAFS signal is extracted using equation 2.49,

$$\chi(E) = \frac{\mu(E) - \mu_0(E)}{\Delta\mu_0},$$

and the relation between k and E given by equation 2.48,

$$k = \sqrt{\frac{2m_e(E - E_0)}{\hbar^2}},$$

where m_e is the electron mass and E_0 is the absorption edge energy. Extraction of the $\chi(k)$ function thus requires knowledge of the background $\mu_0(E)$ and the edge step $\Delta\mu_0$ which acts as a normalisation factor. In EXAFS experiments, the background and normalisation factor can only be estimated. The choice of fitting range and fitting parameters used to obtain the background and the normalisation factor has to be made system by system. The process is summarised as follows.

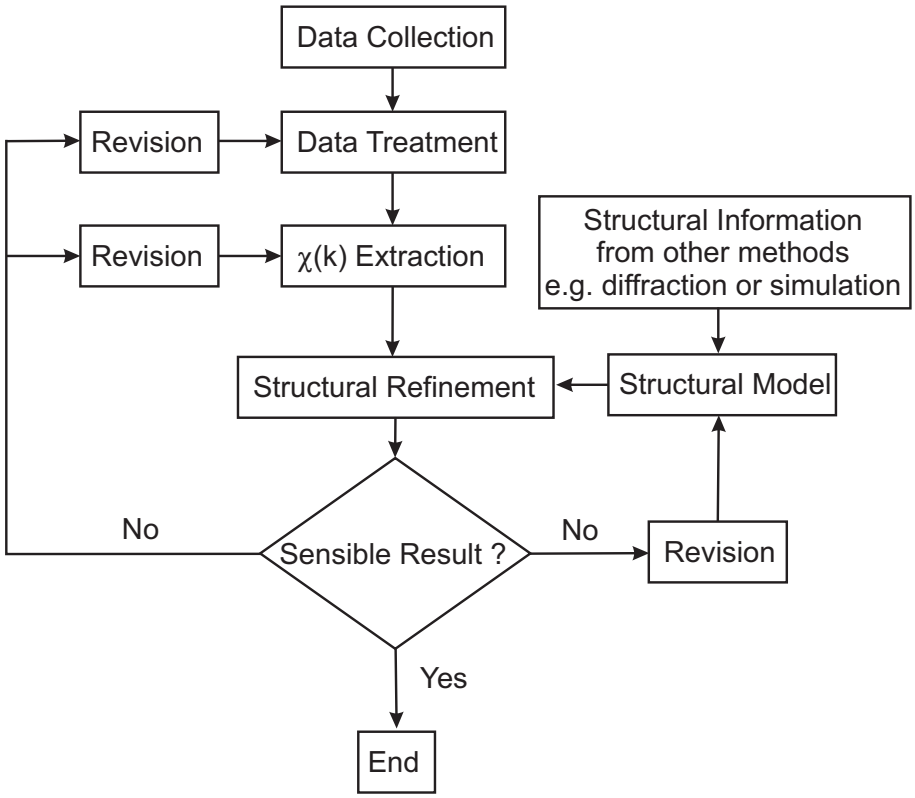

Figure 3.12: A flow chart showing the EXAFS data analysis procedure. The process allows for revisions of the guessed structural model, the data treatment and the $\chi(k)$ extraction process.

Pre-edge Removal and Normalisation

The pre-edge refers to the energy region up to around 20 eV before an absorption edge. An example of a measured absorption spectrum is shown in figure 3.13. From the figure, the absorption spectrum in the pre-edge region does not contain any sharp features. The pre-edge can, therefore, be fitted using a linear function. In the post-edge region, the absorption spectrum usually has a slope and the data in this region are, therefore, fitted with a quadratic polynomial to represent the slope on the spectrum. A diagram showing pre-edge and post-edge fits is given in figure 3.14 .

The pre- and post-edge fits are used to calculate the normalisation factor $\Delta\mu_0$ which is determined from the difference between the pre-edge fit and the fit to the post-edge region at the position of the absorption edge, E_0. The pre-edge fit is also subtracted from the whole absorption spectrum such that the spectrum oscillates around a roughly constant level. A normalised spectrum is shown in figure 3.15.

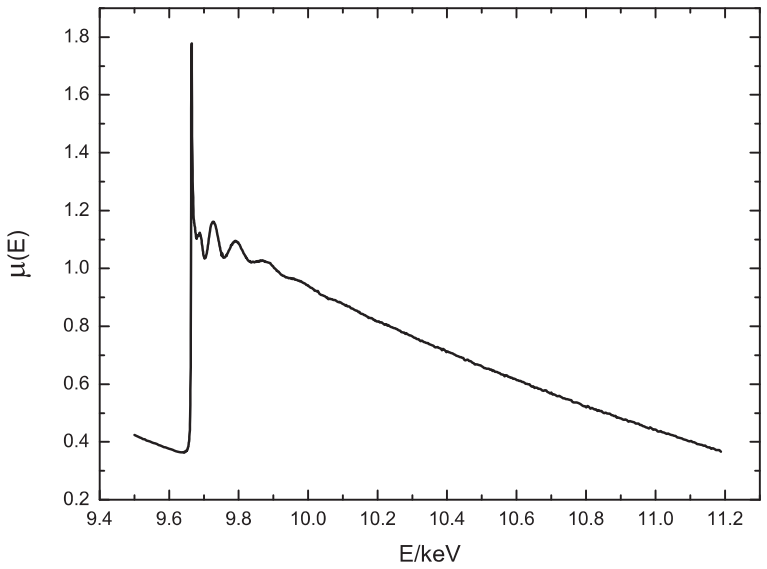

Figure 3.13: An example of an absorption spectrum measured in transmission mode and plotted as a function of the x-ray energy.

Also shown in figure 3.15 is the first derivative of the normalised absorption spectrum. The vertical dotted line marks the first maximum of the first derivative of the spectrum which is used to find an experimental value for E_0 and hence a value for $\Delta\mu_0$.

Background Removal

By definition, the background to the $\chi(k)$ function is the absorption spectrum of an isolated atom $\mu_0(E)$ which, in reality, cannot be measured. Since an isolated atom has no neighbouring atoms to introduce interference effects, $\mu_0(E)$ is represented by a smooth function. In ATHENA, the background is generated from a piecewise fourth degree polynomial spline with the spline knots placed at equal intervals in k. The spline is varied to fit the low frequency part of the measured $\mu(E)$ spectrum using the AUTOBK algorithm [87]. This algorithm uses the Fourier transform of $\chi(k)$, $\tilde{\chi}(R)$, where the tilde denotes a complex function, to guide in the adjustment of the spline fit parameters.

The $\tilde{\chi}(R)$ function is calculated from the $\chi(k)$ function by using the relation [88, 89]

$$\tilde{\chi}(R) = \frac{1}{\sqrt{2\pi}} \int_0^\infty k^\omega \chi(k) W(k) e^{i2kR} dk, \tag{3.33}$$

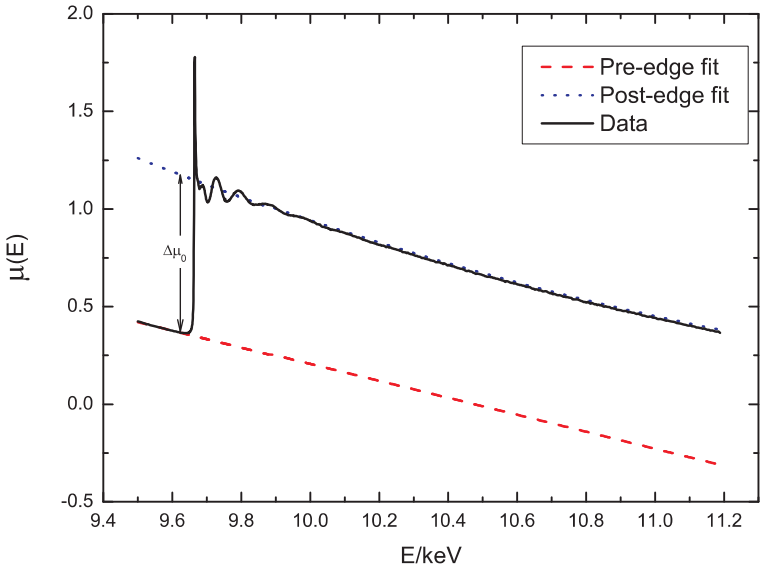

Figure 3.14: An example of pre-edge and post-edge fits to an absorption spectrum. The edge step $\Delta\mu_0$ is the difference between the absorption spectrum for the pre-edge and post-edge fits at the absorption edge energy.

where $\omega = 0$, 1, 2, or 3 determines the k weighting of $\chi(k)$ and $W(k)$ is a window function. $\tilde{\chi}(R)$ is a complex function because FEFF uses both the real and complex parts of the momentum in the $\chi(k)$ calculation, as described in [53, 88]. The Fourier back transform of $\tilde{\chi}(R)$ is given by

$$\tilde{\chi}(k) = \frac{1}{\sqrt{2\pi}} \int_0^\infty \tilde{\chi}(R) W(R) e^{-i2kR} dR, \tag{3.34}$$

where $W(R)$ is a window function in real space.

According to the EXAFS equation 2.64, $\chi(k)$ is damped at high k values. The purpose of the k^ω weighting factor in equation 3.33 is to modify $\chi(k)$ such that the oscillations in the $\chi(k)$ function have a constant amplitude over the measurement range. The choice of ω depends mainly on the atomic number Z of the backscattering elements and the noise level at high k. The $\chi(k)$ spectra for high Z backscatterers have a large amplitude in the high k region such that appropriate weighting factors are typically k^0 or k^1 whereas the $\chi(k)$ spectra for low Z backscatterers have a large amplitude in the low k region such that appropriate weighting factors are typically k^2 or k^3 [89]. However, as the amplitude of a $\chi(k)$ function is small at high k values, the associated signal to noise ratio can be very low such that a lower k weighting is preferred, regardless of the Z value, in order to avoid refining a model with noise.

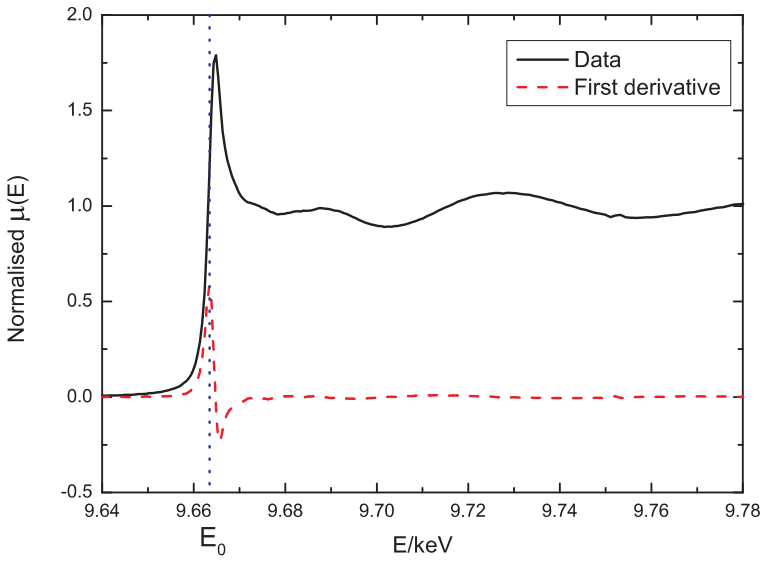

Figure 3.15: Example of an absorption spectrum and its first derivative. The vertical dotted line marks the position of the absorption edge which is the position of the first maximum in the derivative.

The window functions $W(k)$ and $W(R)$ are used to select a suitable range for the data analysis in k- and R-space, respectively. In the case of $W(k)$, the low k limit is usually set to around $k = 2$ Å^{-1} as the absorption spectrum corresponding to lower k values falls into the XANES region where the EXAFS equation cannot be applied. The high k limit of $W(k)$ is usually limited by the noise level. In the case of $W(R)$, the low R limit is usually set to around the beginning of the first peak representing structural information and the high R limit is usually limited by the amount of structural information available.

The magnitude of the $\tilde{\chi}(R)$ function, $|\tilde{\chi}(R)|$, shows similar feature to the pair distribution function obtained from diffraction except that it can also include n-body correlations from the multiple scattering signal. Like the pair distribution function, the peak position in $|\tilde{\chi}(R)|$ relates to an atomic distance. Therefore, features in the low R region of $|\tilde{\chi}(R)|$ before the first peak can be considered to have a non-structural origin. The AUTOBK algorithm is coded to generate a background which, when subtracted from $\mu(E)$, minimises the non-structural features before a certain cutoff value R_{bkg} in $|\tilde{\chi}(R)|$. An example of a normalised absorption spectrum and the background generated by the AUTOBK algorithm is shown in figure 3.16.

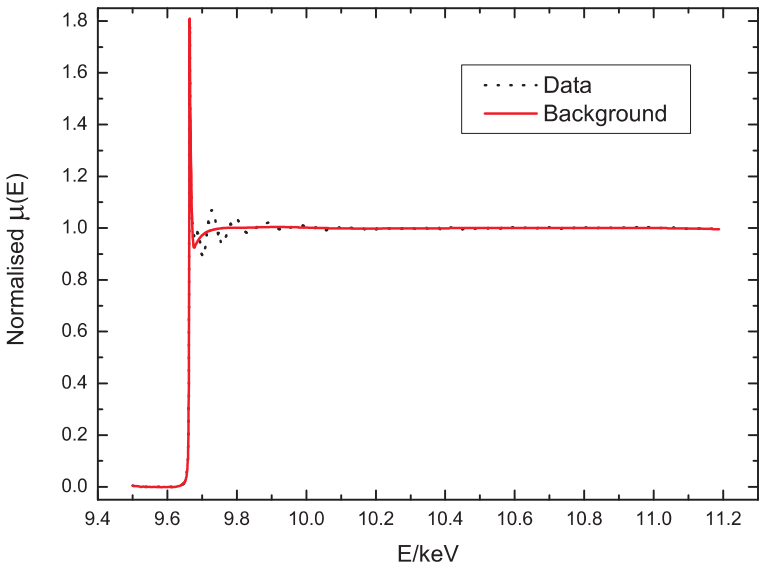

Figure 3.16: An example of a normalised absorption spectrum (dotted curve) and the background generated by the AUTOBK algorithm (solid curve).

3.6.2 Structural Refinement

The expanded EXAFS equation 2.80 is given by

$$\chi(k) = \mathrm{Im}\left\{ \sum_{j=1}^{\text{all paths}} \frac{S_0^2 N_j F_j^{eff}(k)}{k(R_{0,j}+\Delta R_j)^2} \exp\{-2k^2\sigma_j^2 + \frac{2}{3}k^4 C_{4,j}\} \right.$$
$$\left. \exp\{i(2k(R_{0,j}+\Delta R_j) - \frac{4k\sigma_j^2}{R_{0,j}} - \frac{4}{3}k^3 C_{3,j} + \delta_j^{eff}(k))\} \right\}.$$

The FEFF code can be used to calculate $F_j^{eff}(k)$, $\delta_j^{eff}(k)$ and $R_{0,j}$ based on an initial structural model. The $k^\omega\chi(k)$ and corresponding $\tilde{\chi}(R)$ functions can then be determined using initial values for S_0^2 and, for each scattering path, σ_j^2, N_j, ΔR_j, $C_{3,j}$ and $C_{4,j}$. These parameters are subsequently refined by fitting the calculated function to $\tilde{\chi}(R)$ obtained from the measured $k^\omega\chi(k)$. It is also possible to refine the absorption edge energy that was determined experimentally by using the parameter ΔE_0 such that

$$k = \sqrt{\frac{2m_e(E-(E_0+\Delta E_0))}{\hbar^2}}. \tag{3.35}$$

To refine the parameters, the best fit is determined by minimising the statistical parameter χ^2 [88],

$$\chi^2 = \frac{N_{idp}}{N_{data}} \sum_{i=1}^{N_{data}} \left| \frac{\tilde{\chi}(R_i)_{data} - \tilde{\chi}(R_i)_{model}}{\epsilon_i} \right|^2. \tag{3.36}$$

N_{data} is the number of data points in the range defined by $W(R)$. Since both the real and imaginary parts of $\tilde{\chi}(R)$ are fitted, $N_{data} = 2(R_{max} - R_{min})/\delta R$, where R_{max} and R_{min} are the maximum and minimum R values in the $W(R)$ range and δR is the spacing of the data point in R. The parameter ϵ_i represents the measurement uncertainty. Although ϵ_i contains both random fluctuations and systematic errors, only the random fluctuations are used by default in ARTEMIS. The random fluctuations are evaluated from the root mean square deviation of the $|\tilde{\chi}(R)|$ function about its mean value over the range from 15 to 25 Å where the fluctuations are assumed to arise from white noise as the signal to noise ratio is very low beyond $R = 15$ Å [88]. N_{idp} is the number of independent data points in the $W(R)$ range which reflects the amount of information that can be obtained from a fit within the specified range [90]. It is calculated from the equation,

$$N_{idp} = \frac{2\Delta k \Delta R}{\pi} + 2, \tag{3.37}$$

where Δk and ΔR are the widths of the $W(k)$ and $W(R)$ window functions, respectively, determined from the difference between the lower and upper limits of the functions.

3.6.3 Statistical Parameters

Apart from χ^2, the goodness of the fit can also be determined from the reduced chi-squared, χ^2_ν, and $\mathcal{R}$-factor parameters [88]. χ^2_ν is calculated from the equation

$$\chi^2_\nu = \frac{\chi^2}{N_{idp} - N_{var}}, \tag{3.38}$$

where $N_{var} < N_{idp}$ is the number of variables in the fit. χ^2_ν is useful when comparing the quality of fits with different numbers of variables to the same data. If the value of χ^2_ν increases when an additional fitted variable is added to a model, that variable does not improve the fit. For a good fit χ^2_ν should be around 1. A high value of χ^2_ν can arise from a bad model or from a poor estimation of ϵ_i as systematic errors can be introduced by a bad choice of background function.

The $\mathcal{R}$-factor is a statistical parameter which can be used to determine the goodness of fit regardless of the measurement error. The $\mathcal{R}$-factor is calculated by

using the expression

$$\mathcal{R} = \frac{\sum_{i=1}^{N_{data}} |\tilde{\chi}(R_i)_{data} - \tilde{\chi}(R_i)_{model}|^2}{\sum_{i=1}^{N_{data}} |\tilde{\chi}(R_i)_{data}|^2}. \tag{3.39}$$

A value of $\mathcal{R} \leq 2\%$ generally indicates a good fit [88]. If a model gives a good fit according to the value of $\mathcal{R}$ but gives a large χ^2_ν value, it is possible that the model is good but that the measurement error on the data set is dominated by a systematic error.

3.6.4 Structural Parameters

The structural parameters are obtained from the refinement procedure and, because they are determined from a mathematical process, their values need to be checked whether they are physically sensible. One good check concerns the values of ΔR_j, ΔE_0, σ_j^2 and S_0^2. For example, the values for $R_{0,j}$ and E_0 should not change significantly from their initial values so typical values for ΔR_j and ΔE_0 are less than 0.5 Å and 10 eV, respectively. The value of σ_j^2 should always be positive for every scattering path and take a value around 0.003 to 0.02 Å^2 and the value for S_0^2 should take a value around 0.7-1.10 [50, 54]. Stability of the refined values with respect to an increase in the number of fitted parameters is also an indication of a good model.

The errors on the refined values are determined from the fit [53, 88]. Consider two variables x and y and define χ_0^2 as the minimum value of χ^2 which gives the best fit. The errors Δx and Δy obtained from the fit are determined from the points along the contour which give $\chi^2 = \chi_0^2 + 1$, see figure 3.17.

In practice many of the fitted parameters are highly correlated. If two parameters are correlated, it means that a change in one parameter from its best-fit value causes another parameter to change from its best-fit value which makes it difficult to identify whether a refined value is obtained because it improves the model or whether it is obtained in response to a change in another parameter. Figure 3.18 shows the contour of the $\chi^2 = \chi_0^2 + 1$ ellipse which has axes that are not parallel to the x and y axes when parameters x and y are correlated. The correlation is measured by $\cos(\theta_c)$ and is equal to zero if $\theta_c = 90^\circ$ as in figure 3.17. Also shown in

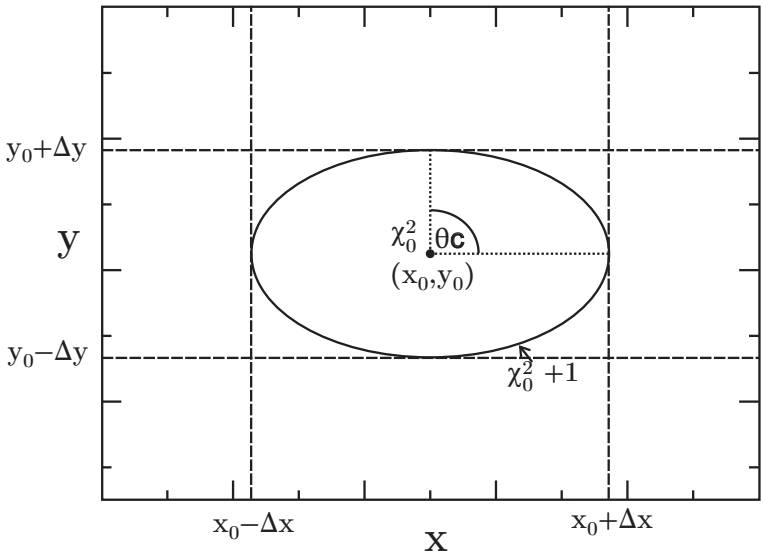

Figure 3.17: A diagram to illustrate how the errors on refined parameters are calculated. The points along the contour of the ellipse give $\chi^2 = \chi_0^2 + 1$ and the correlation between x and y is given by $\cos(\theta_c)$.

figure 3.18 is the effect of correlation which gives the new estimated error $\Delta x'$ and $\Delta y'$.

The EXAFS Debye-Waller factor σ_j^2 and the path degeneracy N_j or the shift in atomic distance ΔR and energy edges ΔE_0 are good examples of pairs of highly correlated parameters [89], especially when $\chi(k)$ is measured over a small k range such that the amount of available information is limited. In these cases, the values obtained from the fit must be interpreted with caution. However if N_j or ΔE_0 can be fixed during the fitting procedure, then the values of σ_j^2 or ΔR_j can be more accurately determined.

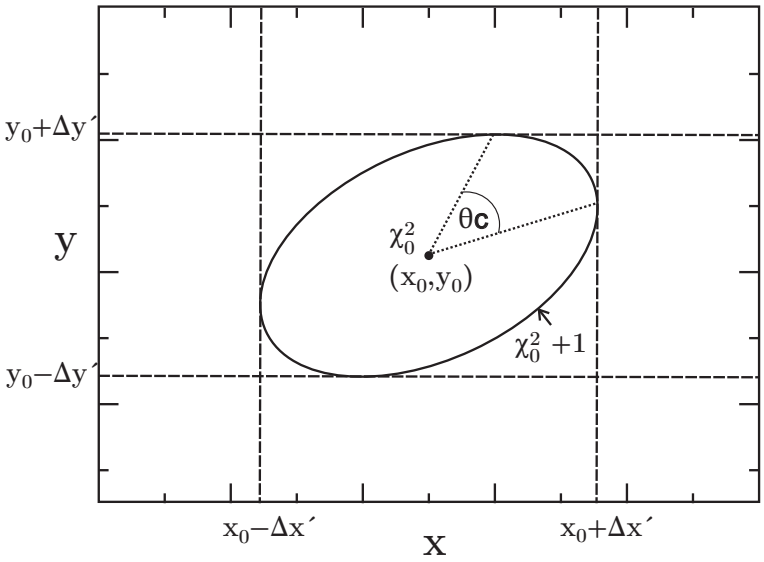

Figure 3.18: The points along the contour of the ellipse give $\chi^2 = \chi_0^2 + 1$ when the correlation relating to $\cos(\theta_c) \neq 0$.

Chapter 4

Molten Glass Forming Alloys and Related Systems

4.1 Introduction

Metallic glasses have received much recent attention as a result of a growing interest in bulk metallic glasses (BMG) and their promising physical and mechanical properties for engineering applications [91, 92]. A BMG is usually an alloy which consists of three or more metal or metalloid elements. The many element combination lowers the quench rate required to make a vitreous material thus enabling the glass to be cast up to cm thicknesses [91]. Despite the success in manufacturing BMGs, much of the literature involving BMGs focuses on those factors which improve the glass forming ability [93, 94, 95] and the atomic arrangements associated with glass formation are still not well known. Sheng et al. [96] have investigated the structures of some binary metallic glasses. The results of this study along with other investigations, such as an EXAFS study on liquid Cu [97] and an ND experiment on some supercooled metallic melts [98], give evidence for icosahedral ordering of the local structure as first proposed by Frank [99]. This local structure is believed to play an important role in the mechanism of glass formation.

In this chapter we present the results of an ND study on the structure of three molten alloys at or near their eutectic compositions, namely $Au_{0.81}Si_{0.19}$, $Au_{0.72}Ge_{0.28}$

and $Ag_{0.74}Ge_{0.26}$. The eutectic point is the composition at which the melting temperature is lowest. The eutectic alloys are important for technological applications as they are often used as soldering materials, especially the Au-Si material as Au and Si are commonly found in electronic devices [100, 101]. Moreover, the eutectic Au-Si alloy is also used as a catalyst for manufacturing Si nanowires [102, 103].

Apart from its technological importance the Au-Si alloy also has a deep eutectic region [104] which is believed to be one of the important indicators of good glass forming ability [105]. In fact, Au-Si was the first alloy to be made into a metallic glass [106]. In addition, the molten Au-Si eutectic alloy has received much recent attention following the discovery of uncommonly thick crystalline layers on the surface of the molten alloy (6-7 well-defined atomic layers) as opposed to a few atomic layers as often found in liquid metals above their melting temperatures [100, 107]. As there is experimental evidence of coupling between the structure of the liquid alloy and the crystalline surface [108, 109], insight into the liquid structure would be very useful.

$Au_{0.72}Ge_{0.28}$ and $Ag_{0.74}Ge_{0.26}$ are, like $Au_{0.81}Si_{0.19}$, also noble metal-semiconductor alloys which have a deep eutectic region [110, 111]. The phase diagrams showing the melting curves of the alloys as a function of composition are presented in figures 4.1 to 4.3. Pershan et al. found that although the Au-Ge system has a deep eutectic region and a similar melting temperature to Au-Si there are no thick surface crystalline layers [112]. Structural information on the molten state of these three alloys and the difference between their atomic arrangements could, therefore, help to identify the structural features which enable thick surface crystallisation and glass formation.

This chapter is divided into seven sections. In section 4.2, the background theory for ND is reviewed and the experimental detail is described in section 4.3. Section 4.4 includes a discussion about the densities, scattering lengths, and some aspects of the data correction procedure that was used. In section 4.5, the ND results in both real and reciprocal space are presented. In section 4.6, the results are compared with those obtained from similar experiments in the literature. The asymptotic behaviour of the total pair distribution functions of the three alloys was also compared with a theoretical prediction [113] and with an empirical equation for

metallic glasses [114]. The work is then concluded in section 4.7.

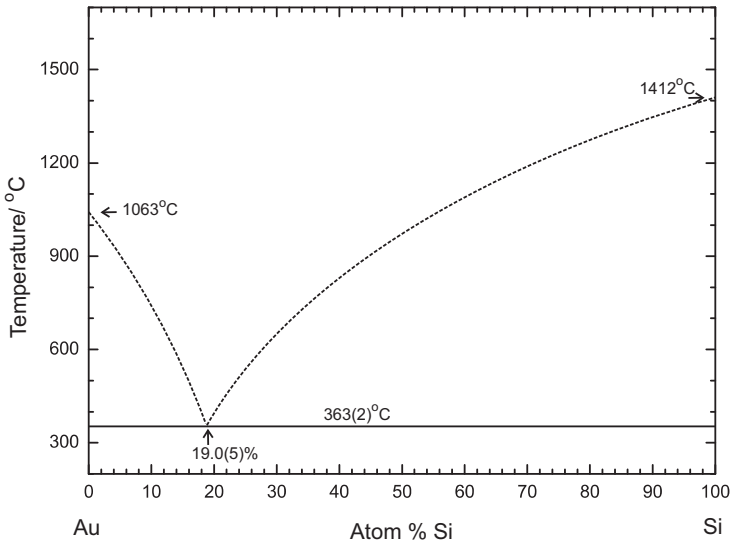

Figure 4.1: Phase diagram of the Au-Si system redrawn from [115] showing the eutectic composition at 19 atomic % Si and the melting curve as a function of concentration.

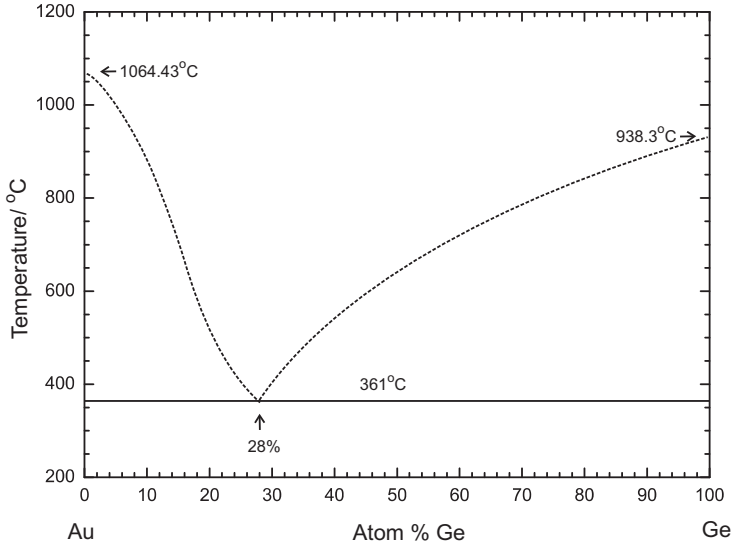

Figure 4.2: Phase diagram of the Au-Ge system redrawn from [110] showing the eutectic composition at 28 atomic % Ge and the melting curve as a function of concentration.

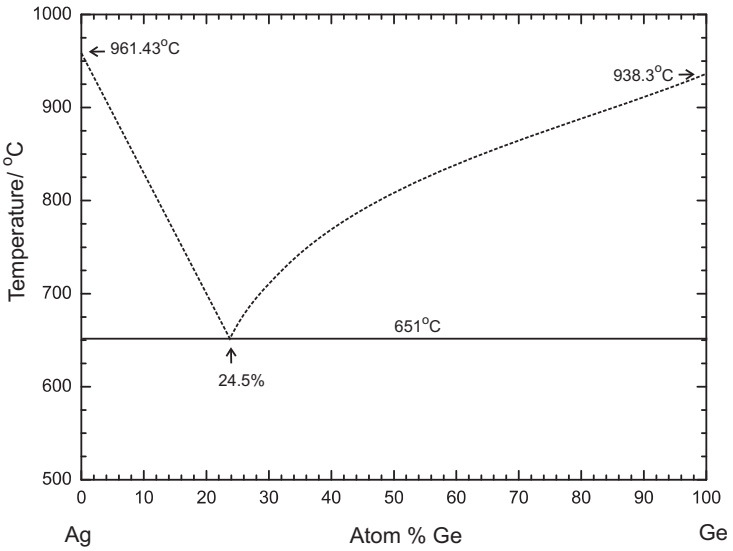

Figure 4.3: Phase diagram of the Ag-Ge system redrawn from [111] showing the eutectic composition at 24.5 atomic % Ge and the melting curve as a function of concentration.

4.2 Background Theory

In this section the main theory required for the ND experiments is summarised. As the molten alloys are isotropic, their structure can be described using the total structure factor and pair distribution function defined in chapter 2. From equation 2.26, the total structure factor $F(q)$ for a two component system can be written as

$$F(q) = c_\alpha^2 b_\alpha^2 \left[S_{\alpha\alpha}(q) - 1\right] + 2c_\alpha c_\beta b_\alpha b_\beta \left[S_{\alpha\beta}(q) - 1\right] + c_\beta^2 b_\beta^2 \left[S_{\beta\beta}(q) - 1\right], \qquad (4.1)$$

where $S_{\alpha\beta}(q)$ is a partial structure factor, and c_α and b_α denote the atomic fraction and coherent neutron scattering length of an atom of type α, respectively.

The total pair distribution function $G(r)$ is obtained from the Fourier transform relation

$$G(r) = \frac{1}{n_0 2\pi^2 r} \int_0^\infty F(q) q \sin(qr) dq \qquad (4.2)$$

where n_0 is the atomic number density such that

$$G(r) = c_\alpha^2 b_\alpha^2 \left[g_{\alpha\alpha}(r) - 1\right] + 2c_\alpha c_\beta b_\alpha b_\beta \left[g_{\alpha\beta}(r) - 1\right] + c_\beta^2 b_\beta^2 \left[g_{\beta\beta}(r) - 1\right]. \qquad (4.3)$$

As $g_{\alpha\beta}(r)$ is proportional to the probability of finding an atom of type β at a radial distance r from an atom of type α, its first peak position represents the nearest neighbour atomic distance between the two types of atom. The average coordination

number for each type of atomic pair can be determined by finding the area under a peak in the relevant $r^2 g_{\alpha\beta}(r)$ function. The average coordination number of atoms of type β around an atom of type α can be calculated using equation 2.28,

$$\bar{n}_{\alpha}^{\beta} = 4\pi n_0 c_\beta \int_{r_1}^{r_2} g_{\alpha\beta}(r) r^2 dr,$$

where r_1 and r_2 are the minimum and maximum radii for the region of interest.

Maximum structural information can be acquired from the results of a diffraction experiment by extracting the full set of $S_{\alpha\beta}(q)$ and $g_{\alpha\beta}(r)$ functions. Hence, if only a single $F(q)$ (or $G(r)$) is measured, limited information about the atomic distances and coordination numbers can be determined.

Because the experimental results from ND in this chapter are compared with XRD data from literature, it is convenient to define $S_N(q)$ and $G_N(r)$ such that they are equivalent to the x-ray $S_X(q)$ and $G_X(r)$ functions;

$$S_N(q) = \frac{F(q)}{\langle b \rangle^2} + 1 \tag{4.4}$$

and

$$G_N(r) = \frac{G(r)}{\langle b \rangle^2} + 1, \tag{4.5}$$

where $\langle b \rangle = c_\alpha b_\alpha + c_\beta b_\beta$ is the average coherent neutron scattering length.

4.3 Experiment

The ND experiments were performed using the D4c diffractometer at the ILL with an incident neutron wavelength of 0.4963(1) Å for the molten $Au_{0.81}Si_{0.19}$ alloy and 0.4967(1) Å for the molten $Au_{0.72}Ge_{0.28}$ and $Ag_{0.74}Ge_{0.26}$ alloys. The neutron wavelength along with the zero angle offset of the detectors were determined by using the diffraction pattern from a powdered Ni sample. The beam heights were chosen to be 2.5 cm for the molten $Au_{0.81}Si_{0.19}$ measurement and 4.2 cm for the molten $Au_{0.72}Ge_{0.28}$ and $Ag_{0.74}Ge_{0.26}$ measurements. The beam heights were smaller than the height of the smallest liquid sample to ensure that the incident beam fully illuminated the samples.

The samples were prepared from Ge and Si of 99.9999% purity, Au of 99.995% purity and Ag of 99.5% purity in Kyushu University, Japan, by the group of Prof Shin'ichi Takeda. The samples were received in the form of billets which were then remelted under vacuum in silica ampoules with an inner diameter of 3 mm. The samples were subsequently placed into silica ampoules with a 4 mm inner diameter and 1 mm wall thickness and sealed under a vacuum of 10^{-5} torr, see figure 4.4.

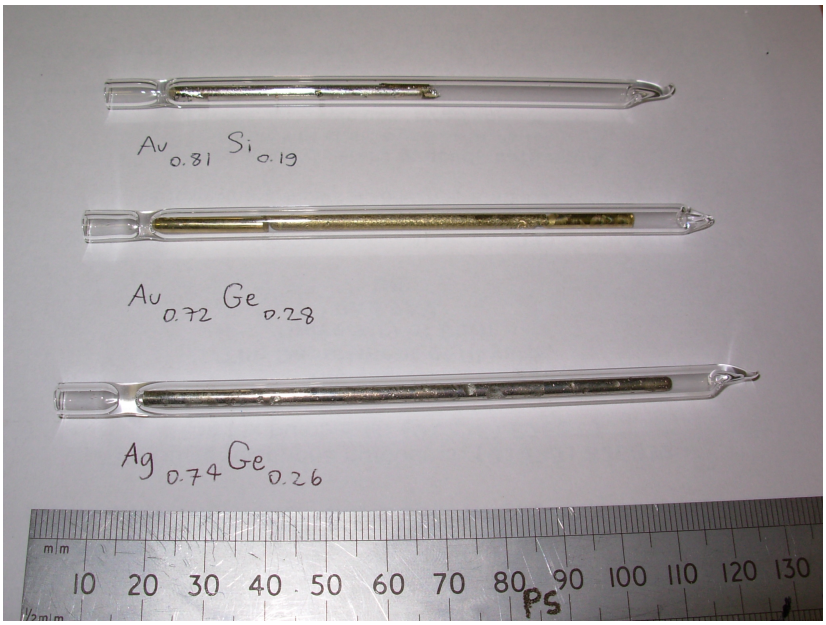

Figure 4.4: $Au_{0.81}Si_{0.19}$, $Au_{0.74}Ge_{0.26}$ and $Ag_{0.76}Ge_{0.24}$ alloys sealed in silica ampoules of 4 mm inner diameter and 1 mm wall thickness prior to the ND experiments.

At the ILL, the ampoules were placed in a vanadium furnace (available temperature range of 50 to 1150 °C [78]) situated inside the evacuated D4c bell jar. The experiments were made on the samples at just above their melting points i.e. at 392(2) °C for $Au_{0.81}Si_{0.19}$ (mp = 363 °C [115]), 393(2) °C for $Au_{0.72}Ge_{0.28}$ (mp = 361 °C [110]), and 703(2) °C for $Ag_{0.74}Ge_{0.26}$ (mp = 651 °C [111]). The measurements were made using a series of 30 minute scans thus enabling a stability check to be made by calculating the ratio between the measured intensities for consecutive scans. If the sample is stable, the ratio is unity. The final signal was obtained by averaging all the scans. The total counting times were 4 hours for the $Au_{0.72}Ge_{0.28}$ and $Ag_{0.74}Ge_{0.26}$ alloys and 8 hours for the $Au_{0.81}Si_{0.19}$ alloy. Diffraction measurements were also made for an empty furnace and an empty silica ampoule in the furnace

at 394(2) °C and 704(2) °C , and for a $^{10}B_4C$ absorber of dimensions comparable to the samples in the furnace at room temperature. In addition, the diffraction pattern for a vanadium rod of 6.37(1) mm diameter was measured inside the furnace at room temperature, along with the empty furnace at room temperature, for data normalisation purposes.

4.4 Data Treatment

The ND data were treated using a standard procedure as described in chapter 3. In this section, some aspects of the data treatment specific for molten $Au_{0.81}Si_{0.19}$, $Au_{0.72}Ge_{0.28}$ and $Ag_{0.74}Ge_{0.26}$ are described. These include an account of the absorption cross-sections near resonance, the difficulty in correcting for the silica container scattering, and an estimation of the alloy densities which leads to an approximation for the sample height.

4.4.1 Absorption Cross-Section

Away from a neutron absorption resonance, the neutron absorption cross-section at a particular wavelength can usually be calculated by using a reference value, that is

$$\sigma_{abs} = \sigma_{abs,ref}\frac{\lambda}{\lambda_{ref}}, \tag{4.6}$$

where σ_{abs} is the absorption cross-section at wavelength λ and $\sigma_{abs,ref}$ is the reference absorption cross-section measured or calculated at wavelength λ_{ref}.

The reference absorption cross-sections used in this analysis were taken from Sears [43] with a reference neutron wavelength of 1.798 Å. The absorption cross-sections were calculated using equation 4.6 except those for Au and Ag which were obtained from the Monte Carlo N-Particle (MCNP) [116] library in the Korea Atomic Energy Research Institute (KAERI) online database [117]. The incident neutron wavelength for the diffraction experiments was about 0.5 Å corresponding to a neutron energy of around 0.3 eV. For Au and Ag, there is an absorption resonance near this energy [118]. Figure 4.5 shows the total and absorption cross-sections of Au

and Ag where the peaks correspond to the absorption resonances at 4.890(2) eV for Au, at 16.30(5) eV for ^{107}Ag and at 5.19(1) eV for ^{109}Ag [118]. These absorption resonances call into question the validity of equation 4.6.

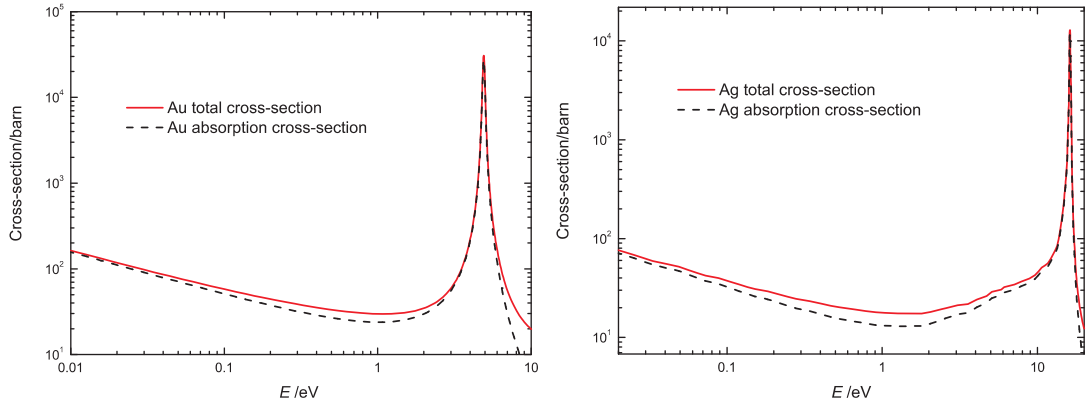

Figure 4.5: The total and absorption cross-sections of Au and Ag. The dashed lines give the absorption cross-section and the solid lines give the total cross-section as a function of energy [117].

Figure 4.6 shows a comparison between the absorption cross-sections as a function of the neutron wavelength for Au and Ag as acquired from the KAERI database [117] and from Sears' tables [43] by using equation 4.6. From the figure, the absorption cross-sections obtained from the KAERI database show a deviation from the linear relation given by equation 4.6. The absorption cross-sections at 0.5 Å are compared in table 4.1. From the table, the absorption cross-sections for Au and Ag obtained from the KAERI database is about 10 and 5%, respectively, higher than those calculated from Sears [43]. Because the alloy samples used in the diffraction experiments are Au and Ag rich, the difference between the absorption cross-section values is significant. The absorption cross-sections and the scattering lengths used in the data analysis are summarised in table 4.2.

Element	Absorption cross-section at 0.5 Å (barn)	
	Sears [43]	KAERI [117]
Au	27.43(3)	30.91
Ag	17.6(1)	18.90

Table 4.1: A comparison between the absorption cross-sections of Au and Ag as calculated according to the values given by Sears [43] and as obtained from the KAERI database [117].

It should be noted here that D4c is the most suitable instrument to study

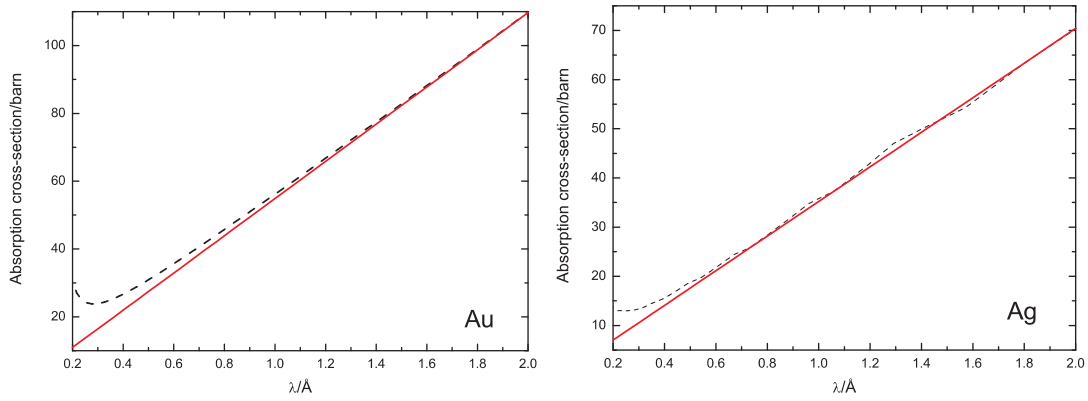

Figure 4.6: The absorption cross-sections of Au and Ag as a function of neutron wavelength. The dashed lines give the absorption cross-section obtained from the KAERI database [117] and the solid lines give the absorption cross-section calculated from equation 4.6 according to the values given by Sears [43].

Element	Coherent scattering length (fm)	Scattering cross-section (barn)	Absorption cross-section (barn) at 0.4963 Å	Absorption cross-section (barn) at 0.4967 Å
Au	7.63(6)	7.75(13)	30.77	30.79
Ag	5.922(7)	4.99(3)	-	18.80
Ge	8.185(20)	8.60(6)	-	0.61(1)
Si	4.1491(10)	2.167(8)	0.047(8)	-

Table 4.2: Coherent scattering lengths, scattering cross-sections, and absorption cross-sections for Au, Ag, Ge and Si as used in the data analysis.

these systems. This is because the absorption resonances of Au and Ag are in the energy range of thermal neutrons. Diffractometers which employ the Time of Flight measurement technique cannot be used to measure usable signals as resonance effects will dominate the results. Diffraction experiments are, therefore, best made using a diffractometer with a constant incident neutron energy and with a wavelength reasonably far from the resonance. For D4c, the available neutron wavelengths are 0.35, 0.5 and 0.7 Å. Although the wavelength of 0.7 Å, corresponding to an energy of 0.167 eV, is further away from the resonance, inspection of figure 4.5 shows that the absorbtion cross-sections of Au and Ag for this energy are also higher than those for 0.5 Å neutrons. For neutrons of wavelength 0.35 Å, the incident flux on D4c is much reduced compared to 0.5 and 0.7 Å. A neutron wavelength of 0.5 Å is, therefore, the most suitable for making diffraction experiments on alloys containing Au or Ag.

4.4.2 Silica Container

In the ND experiments, the samples were held in silica ampoules. Because the diffraction pattern from silica is structured, it is important that the correct amount of scattering from silica is subtracted from the measured sample in container signal. The dimensions of the containers were measured by using vernier calipers. The outer diameters were measured at four points along the length of the ampoule, twice perpendicular to each other at each point. The obtained values showed that the ampoules were uniform along their lengths. The inner diameters were measured after the diffraction experiment when the ampoules were broken open.

The measured outer diameters were 6.00(3), 5.96(3), 5.92(3) and 6.02(3) mm for the $Au_{0.81}Si_{0.19}$, $Au_{0.72}Ge_{0.28}$ and $Ag_{0.74}Ge_{0.26}$ alloys and for the empty container, respectively, and the measured inner diameters were 4.12(3), 4.14(3), 4.12(3) and 4.10(3) mm for the $Au_{0.81}Si_{0.19}$, $Au_{0.72}Ge_{0.28}$ and $Ag_{0.74}Ge_{0.26}$ alloys and for the empty container, respectively. In the data analysis procedure, due to the difference in dimensions between the empty container and the containers used for the samples, the intensity measured for the empty container, i.e. the $I^E_{C+H}(\theta)$ term in equation 3.11, needed to be scaled before subtraction from the sample measurements. The scaling factor was adjusted to ensure that the first silica peak at around 1.6 Å [119] could not be observed in the fully corrected $G(r)$ function. The scaling factors used were 96, 90 and 98% for the $Au_{0.81}Si_{0.19}$, $Au_{0.72}Ge_{0.28}$ and $Ag_{0.74}Ge_{0.26}$ alloys, respectively.

4.4.3 Density

The mass density of the crystalline $Au_{0.81}Si_{0.19}$, $Au_{0.72}Ge_{0.28}$ and $Ag_{0.74}Ge_{0.26}$ alloys was measured using Archimedes principle. The mass of each sample was measured in air and in distilled water and the mass density was calculated from the relation,

$$D_s = D_f \frac{m_a}{m_a - m_f}, \tag{4.7}$$

where $D_f = 0.9979948$ g/cm^3 is the density of distilled water at 21 °C [120], m_a is the mass of a sample in air and m_f is the mass of a sample in distilled water.

The mass density of the molten $Au_{0.81}Si_{0.19}$, $Au_{0.72}Ge_{0.28}$ and $Ag_{0.74}Ge_{0.26}$ alloys was initially estimated by using Vegard's law [121],

$$\rho = \frac{x_1 m_1 + x_2 m_2}{x_1 v_1 + x_2 v_2}, \tag{4.8}$$

where x_i and m_i are the atomic fraction and atomic mass for an atom of type i and v_i is the atomic volume for a pure liquid of type i. The mass densities used for the pure liquids near their melting point are summarised in table 4.3 and the mass densities calculated by using equation 4.8 are compared with the measured mass densities of the crystalline samples in table 4.4.

Element	Density ($g \cdot cm^{-3}$)	Temperature (°C)	Reference
Au	17.34(5)	1085	[122]
Ag	9.14(3)	977	[122]
Si	2.52(1)	1414	[123]
Ge	5.57(1)	938	[123]

Table 4.3: The mass densities of pure liquid Au, Ag, Si, and Ge near or at the melting temperature. These values were used in equation 4.8 to provide an initial estimate of the density of the molten $Au_{0.81}Si_{0.19}$, $Au_{0.72}Ge_{0.28}$ and $Ag_{0.74}Ge_{0.26}$ alloys.

Alloy	Density ($g \cdot cm^{-3}$)		
	crystalline	liquid (Vegard's law)	liquid (XRD)
$Au_{0.81}Si_{0.19}$	15.43(1)	14.57(4)	15.688
$Au_{0.72}Ge_{0.28}$	14.594(6)	13.71(3)	14.944
$Ag_{0.74}Ge_{0.26}$	8.960(4)	8.14(2)	9.097

Table 4.4: The mass densities of crystalline and liquid $Au_{0.81}Si_{0.19}$, $Au_{0.72}Ge_{0.28}$ and $Ag_{0.74}Ge_{0.26}$.

From table 4.4, the mass densities of the liquids determined by using Vegard's law are smaller than the mass densities measured for the crystalline materials which, for the $Au_{0.81}Si_{0.19}$ and $Au_{0.72}Ge_{0.28}$ alloys, disagrees with the results reported by Waghorne et al. who found that upon melting $Au_{0.81}Si_{0.19}$ contracts by about 1-2% and $Au_{0.72}Ge_{0.28}$ by about 5% [124]. Because an XRD experiment was also performed on these samples [40, 125], another estimate of the liquid density could be made [125]. The XRD data was initially analysed using the number density determined from Vegard's law. The number density was then adjusted and the data analysis repeated until the measured $S_X(q)$ function was found to agree with the Fourier back transform of the corresponding $G_X(r)$ function after the small r

oscillations up to the beginning of the first peak were set to the $G_X(0)$ limit. The number densities determined from this method are 0.0573, 0.0555 and 0.0555 $Å^{-3}$ for liquid $Au_{0.81}Si_{0.19}$, $Au_{0.72}Ge_{0.28}$ and $Ag_{0.74}Ge_{0.26}$, respectively. The mass densities calculated from these number densities are presented in table 4.4.

From table 4.4, the mass densities of the liquids determined from the XRD data are about 2% higher than those of the corresponding crystal which better agrees with the results reported by Waghorne et al. [124]. These densities were, therefore, used in the ND data analysis. It should be noted that, for $Au_{0.81}Si_{0.19}$, the number density of the liquid is about 2% higher than the number density of glassy $Au_{0.80}Si_{0.20}$ (0.0564(7) $Å^{-3}$ [126]) and the effect of expansion upon freezing for the $Au_{0.72}Ge_{0.28}$ alloy reported in [124] was observed in the ND experiment. At the end of the diffraction experiment when the sample was cooled down, the $Au_{0.72}Ge_{0.28}$ alloy expanded and broke the ampoule inside the furnace, see figure 4.7.

Because the samples were melted in a vanadium furnace during the diffraction experiment the heights of the samples in the molten state could not be measured directly. The sample heights were, therefore, estimated by using the container dimensions and the densities of the liquid alloys. The estimated values are 2.8, 4.6 and 4.7 cm for molten $Au_{0.81}Si_{0.19}$, $Au_{0.72}Ge_{0.28}$ and $Ag_{0.74}Ge_{0.26}$, respectively, which are well above the beam heights.

Figure 4.7: $Au_{0.74}Ge_{0.26}$ alloy after the diffraction experiment. The alloy broke the ampoule as it expanded when cooled down from the molten state.

4.5 Results

In this section, the corrected $F(q)$ functions from the ND experiment and the corresponding $G(r)$ functions are presented.

4.5.1 Total Structure Factors

The $F(q)$ and the Fourier back transforms for molten $Au_{0.81}Si_{0.19}$, $Au_{0.72}Ge_{0.28}$ and $Ag_{0.74}Ge_{0.26}$ are shown in figure 4.8. As seen in the figure, even though the data have been corrected for attenuation, inelasticity effects and background scattering, there is still a small slope on the data. From Fourier transformation, a slope in reciprocal space corresponds to a peak at very low r in real space. Therefore, the slope in the $F(q)$ functions was removed by using a Fourier transformation method.

First, an $F(q)$ function was Fourier transformed to give $G(r)$. Next the very low r part of this function where there is a peak due to the slope (from $r = 0$ to 0.31 Å) was set to $G(0)$, the dashed line in figure 4.9, and then the modified $G(r)$ was Fourier back transformed to reciprocal space. The Fourier back transforms obtained from this procedure were subsequently treated as the new data sets while the Fourier back transforms used for the consistency checks were obtained by Fourier transforming $G(r)$, which corresponds to the new data sets, after all of the low r part up to the beginning of the first peak were set to the $G(0)$ limit.

The fully corrected data and their Fourier back transforms are shown in figure 4.10. The data and the Fourier back transforms are in good agreement and there is no slope left on the data. Note that the $F(q)$ data sets start from $q = 0.55$ Å^{-1} ($2\theta = 2.46°$). This is due to a large background signal on D4c at low scattering angles which comes from scattering of the direct beam after hitting the shielding located close to the first detector, see the layout of D4c in figure 3.3. The measured intensity for scattering vectors smaller than $q = 0.55$ Å^{-1} was, therefore, disregarded and, instead, the data were extrapolated assuming that $F(q) \propto q^2$ in the low q region [127]. The fitted lines and the low q part of the $F(q)$ functions for each alloy, plotted as a function of q^2, are shown in figure 4.11. From section 3.5.5, an $F(q)$ function must satisfy the inequality relation $F(q) \geq -\sum_\alpha c_\alpha \overline{b_\alpha^2}$. The level limit, -$\sum_\alpha c_\alpha \overline{b_\alpha^2}$,

for the $Au_{0.81}Si_{0.19}$, $Au_{0.72}Ge_{0.28}$ and $Ag_{0.74}Ge_{0.26}$ alloys along with the fitted $F(0)$ values and the fitted ranges are summarised in table 4.5. The data show that within the errors $F(q) \geq -\sum_\alpha c_\alpha \overline{b_\alpha^2}$ for all three alloys.

Alloy	Level limit (barn)	$F(0)$ (barn)	Fitted range (Å^{-2})
$Au_{0.81}Si_{0.19}$	-0.532(8)	-0.520(2)	0.30-0.72
$Au_{0.72}Ge_{0.28}$	-0.635(9)	-0.627(1)	0.30-0.81
$Ag_{0.74}Ge_{0.26}$	-0.47(2)	-0.438(2)	0.36-1.21

Table 4.5: Level limits for the $Au_{0.81}Si_{0.19}$, $Au_{0.72}Ge_{0.28}$ and $Ag_{0.74}Ge_{0.26}$ alloys calculated from equation 3.28 and the $F(0)$ obtained by fitting a straight line to the low q part of $F(q)$ (when plotted as a function of q^2) in the specified range.

4.5.2 Total Pair Distribution Functions

The $G(r)$ for the molten $Au_{0.81}Si_{0.19}$, $Au_{0.72}Ge_{0.28}$ and $Ag_{0.74}Ge_{0.26}$ alloys are shown in figure 4.12 and are Fourier transforms of the spline fitted $F(q)$ functions presented in figure 4.10 with the low q part of the function extrapolated using the method given above. The measured $F(q)$ functions and the spline fits are plotted in figure 4.13.

4.6 Discussion

In this section, the measured correlation functions for the molten $Au_{0.81}Si_{0.19}$, $Au_{0.72}Ge_{0.28}$ and $Ag_{0.74}Ge_{0.26}$ alloys are compared with similar data found in the literature. The effect of the weighting factors for each partial pair correlation function is discussed. Table 4.6 gives the neutron and x-ray weighting factors corresponding to each pair correlation function. Note that, as the x-ray form factors are q dependent, the form factors at $q = 0$, $f_\alpha(0)$, were used to produce the data presented in this table. The asymptotic behaviour of the real space functions is also investigated.

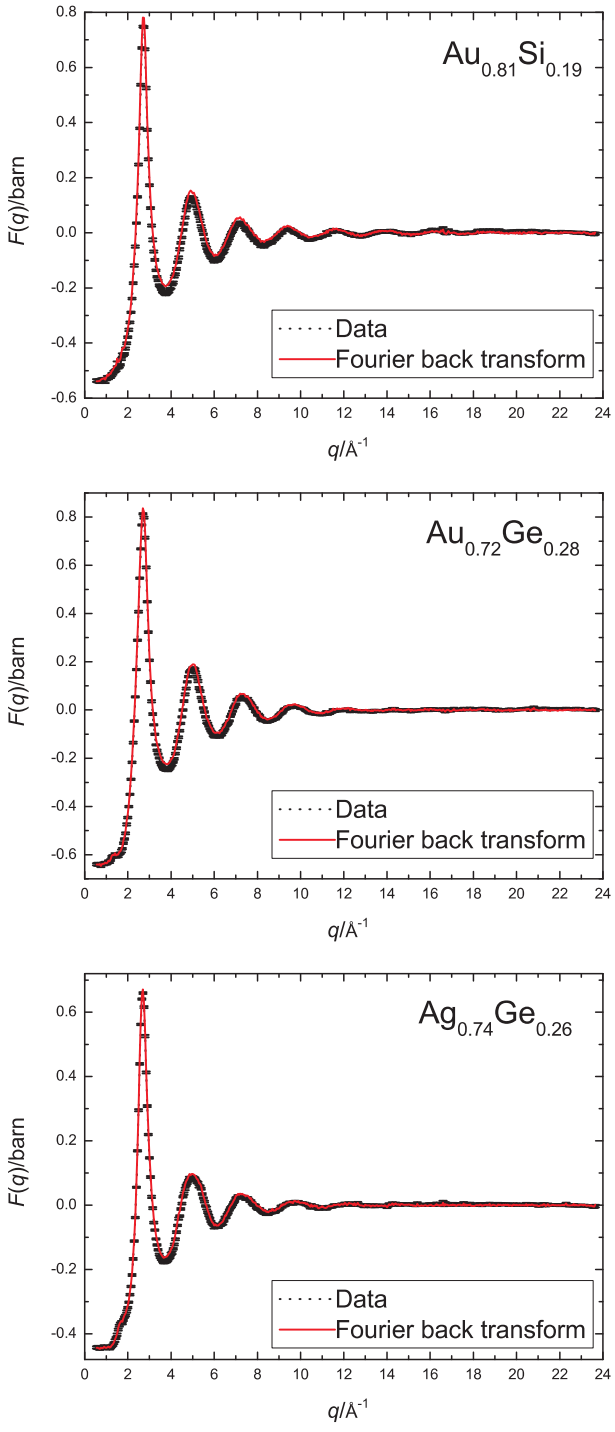

Figure 4.8: The $F(q)$ functions for molten $Au_{0.81}Si_{0.19}$, $Au_{0.72}Ge_{0.28}$ and $Ag_{0.74}Ge_{0.26}$ alloys at 392(2), 393(2) and 703(2) °C, respectively. The dotted lines give the measured $F(q)$ functions (with error bars of the order of $\pm 10^{-3}$ barn) and the solid lines give the Fourier back transforms of the corresponding $G(r)$ functions given by the solid lines in figure 4.9 after the low r part up to the beginning of the first peak is set to the $G(0)$ limit.

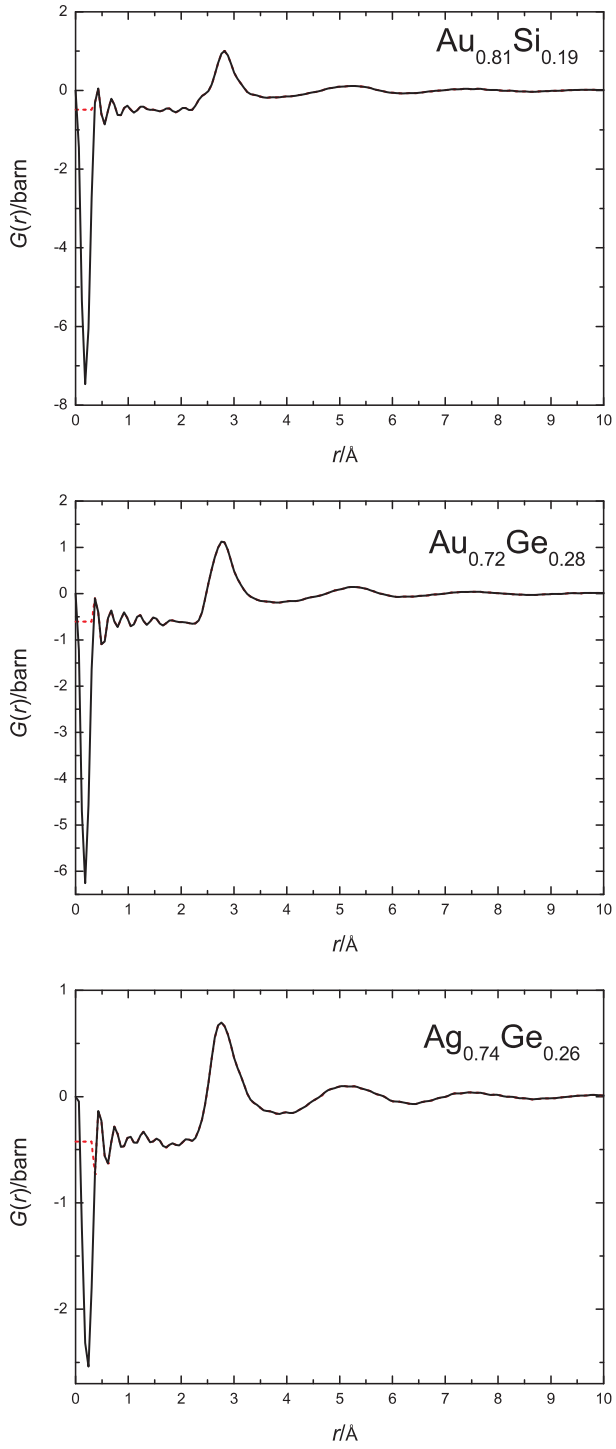

Figure 4.9: The $G(r)$ functions for molten $Au_{0.81}Si_{0.19}$, $Au_{0.72}Ge_{0.28}$ and $Ag_{0.74}Ge_{0.26}$ alloys at 392(2), 393(2) and 703(2) °C, respectively. The dashed lines show the low r part of the modified $G(r)$ where a large peak at low r has been removed.

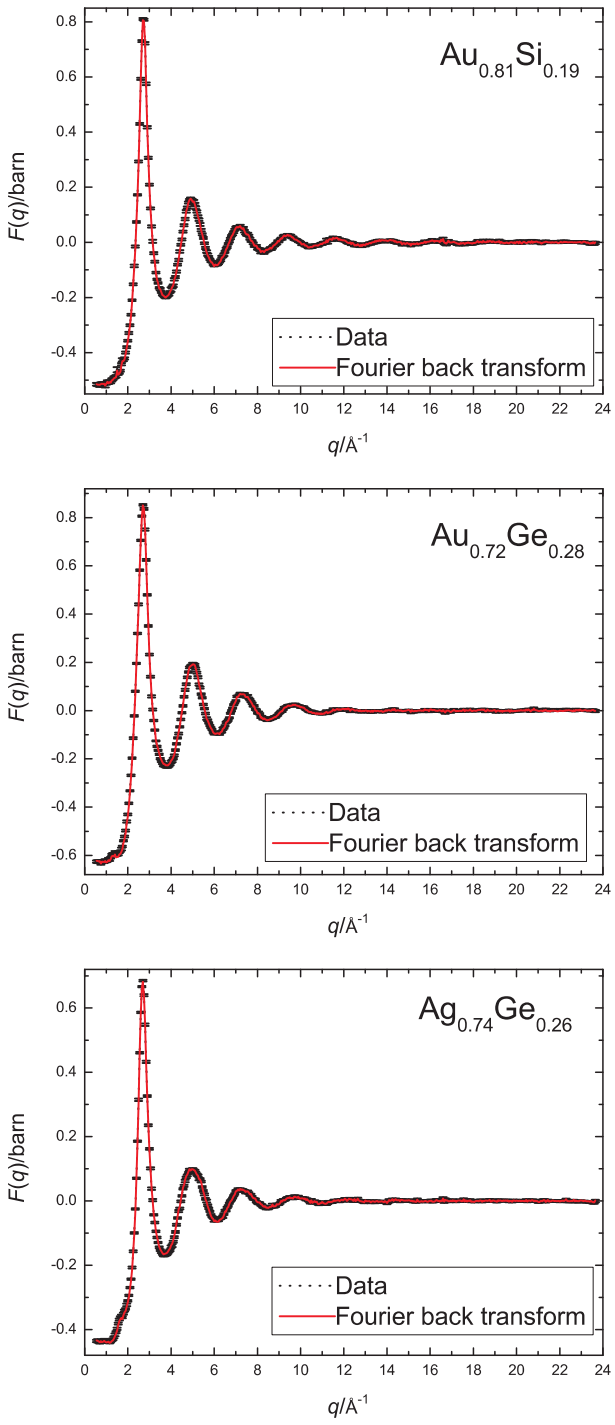

Figure 4.10: The fully corrected $F(q)$ functions for molten molten $Au_{0.81}Si_{0.19}$, $Au_{0.72}Ge_{0.28}$ and $Ag_{0.74}Ge_{0.26}$ alloys at 392(2), 393(2) and 703(2) °C, respectively, with their corresponding error bars. The dotted lines give the $F(q)$ functions as obtained from the Fourier back transforms of the $G(r)$ functions given by the solid lines in figure 4.9 after the data up to $r = 0.31$ Å were set to the $G(0)$ limit. The error bars are of the order of $\pm 10^{-3}$ barn and the solid lines give the Fourier back transforms of the corresponding $G(r)$ functions given by the solid lines in figure 4.12 after the small r oscillations up to the beginning of the first peak are set to the $G(0)$ limit.

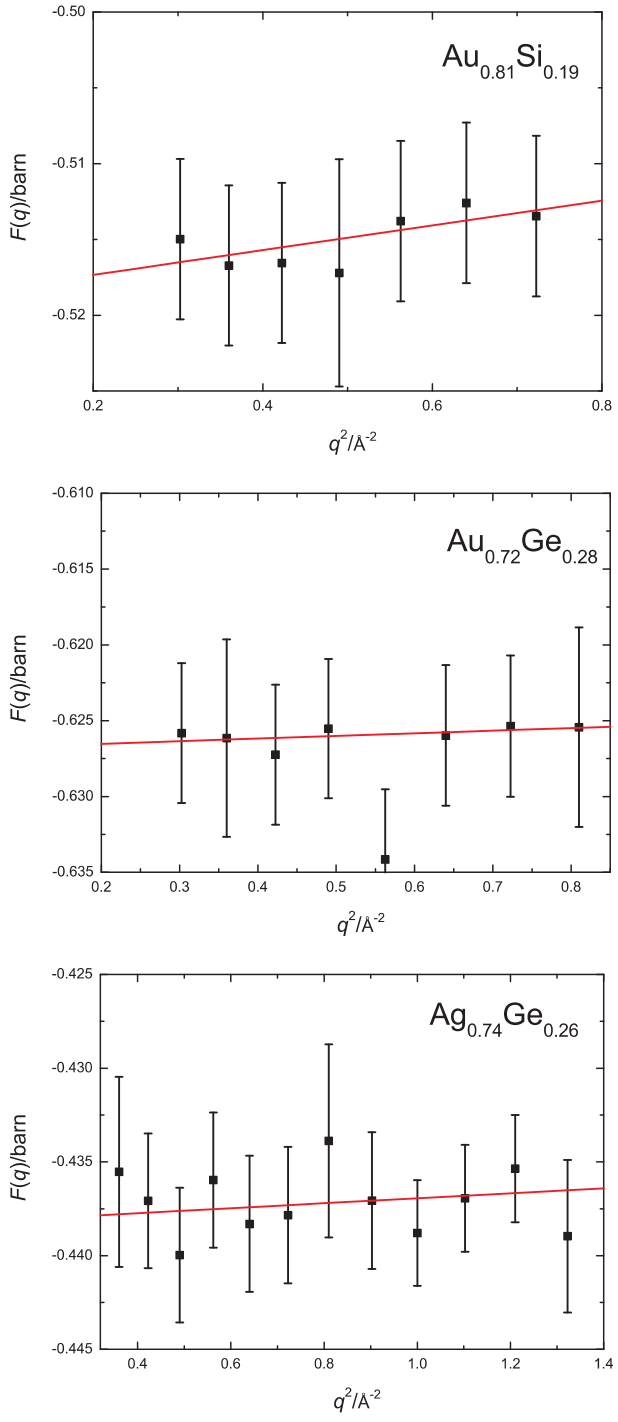

Figure 4.11: The low q part of the $F(q)$ functions for molten $Au_{0.81}Si_{0.19}$, $Au_{0.72}Ge_{0.28}$ and $Ag_{0.74}Ge_{0.26}$ alloys at 392(2), 393(2) and 703(2) °C, respectively, plotted as a function of q^2. The $F(q)$ data are shown as points with error bars. The solid lines give linear fits to the low q part of the data.

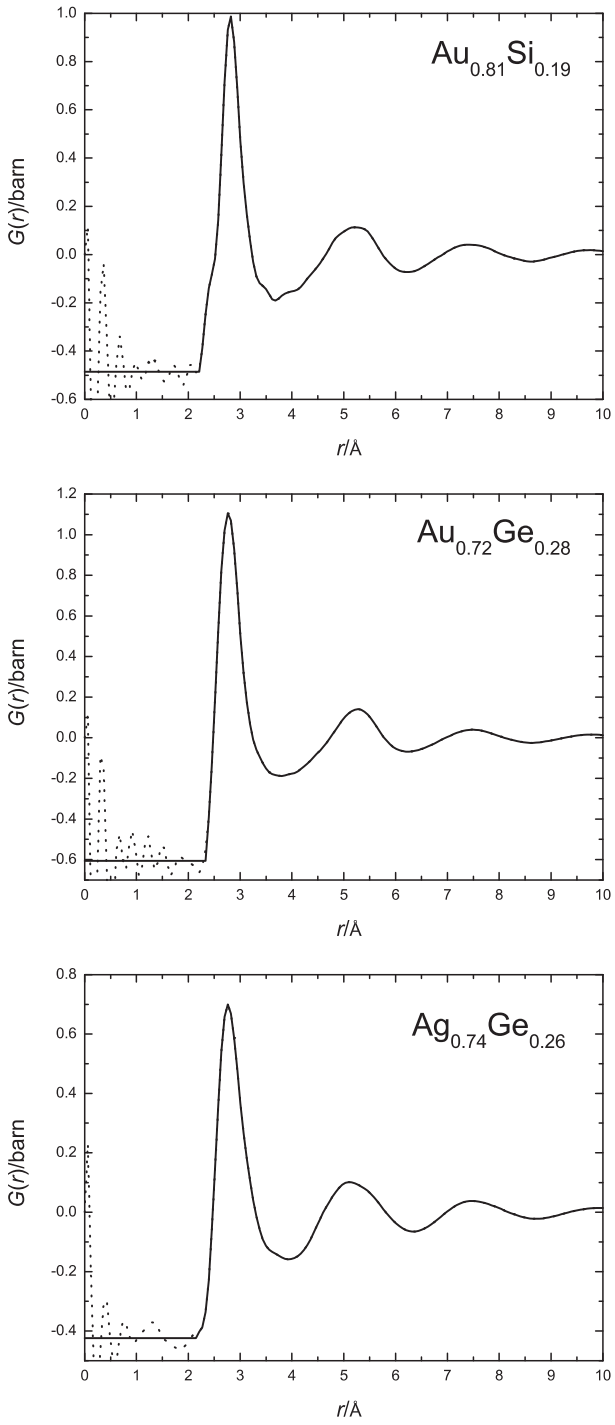

Figure 4.12: The $G(r)$ functions for molten $Au_{0.81}Si_{0.19}$, $Au_{0.72}Ge_{0.28}$ and $Ag_{0.74}Ge_{0.26}$ alloys at 392(2), 393(2) and 703(2) °C, respectively, as obtained by Fourier transforming the spline fitted $F(q)$ functions shown in figure 4.13. The dotted lines at low r show the artifacts obtained from the Fourier transform procedure.

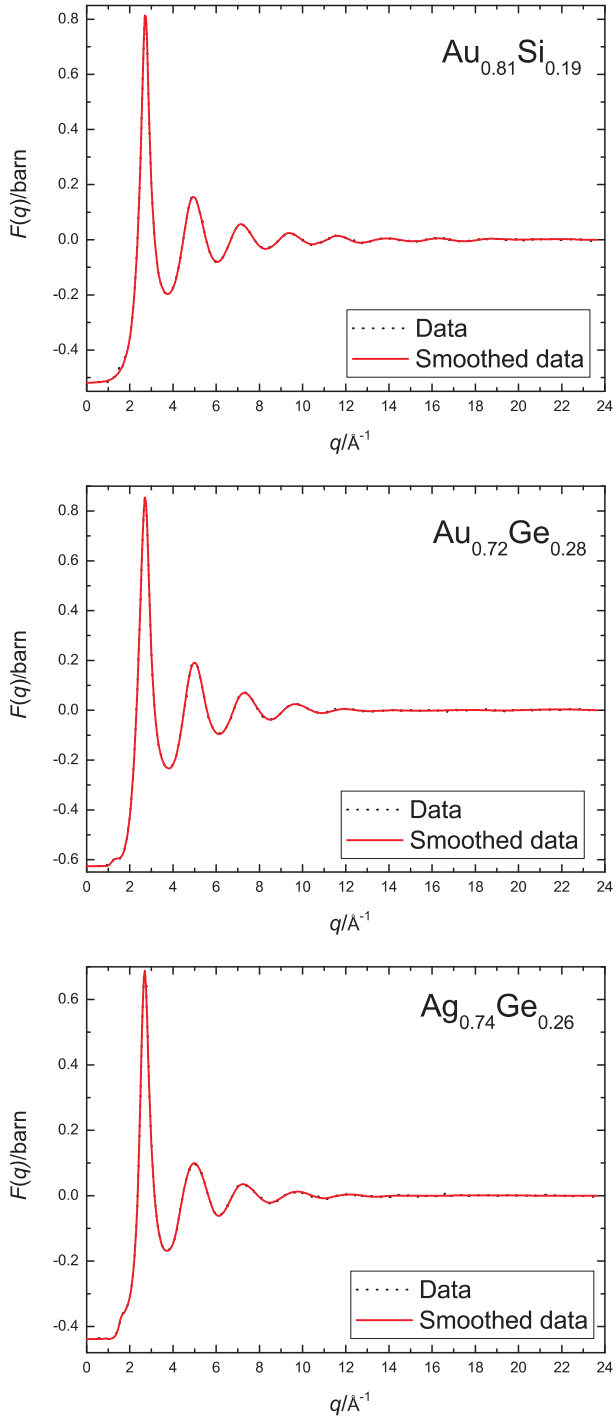

Figure 4.13: The spline fits to the $F(q)$ functions for molten $Au_{0.81}Si_{0.19}$, $Au_{0.72}Ge_{0.28}$ and $Ag_{0.74}Ge_{0.26}$ alloys at 392(2), 393(2) and 703(2) °C, respectively. The dotted lines give the data and the solid lines give the spline fits.

Sample	Pair correlation	Neutron weighting factor		X-ray weighting factor at $q = 0$	
		in barn	in %	in electron units	in %
$Au_{0.81}Si_{0.19}$	Au-Au	0.382(6)	78.6	4091(11)	92.2
	Au-Si	0.0974(8)	20.1	7.075(8)	7.7
	Si-Si	0.006214(3)	1.3	340.3(5)	0.1
$Au_{0.72}Ge_{0.28}$	Au-Au	0.302(5)	49.8	3233(0)	74.6
	Au-Ge	0.251(2)	41.5	1018.4(1)	23.5
	Ge-Ge	0.0525(4)	8.7	80(2)	1.9
$Ag_{0.74}Ge_{0.26}$	Ag-Ag	0.1920(5)	45.3	1210(5)	65.1
	Ag-Ge	0.1865(7)	44.0	578.5(1)	31.2
	Ge-Ge	0.0453(3)	10.7	69(1)	3.7

Table 4.6: Neutron and x-ray weighting factors for all of the partial pair correlation functions present in the $Au_{0.81}Si_{0.19}$, $Au_{0.72}Ge_{0.28}$ and $Ag_{0.74}Ge_{0.26}$ alloys. The weighting factors were calculated by using the definitions given in equations 2.26 and 2.44 with neutron scattering lengths taken from table 4.2 and atomic x-ray form factors taken from [47].

4.6.1 Total Structure Factors

An interesting feature found in the $F(q)$ for the molten $Au_{0.72}Ge_{0.28}$ alloy is a small pre-peak at around 1.3(2) $Å^{-1}$. This pre-peak was observed in an XRD experiment performed by Hoyer and Jödicke [128]. According to these authors, the pre-peak is an indication of intermediate range ordering involving associated regions of Au and Ge atoms. Although the pre-peak was not observed in a more recent XRD experiment performed by Fujii et al.[40], the feature can be seen in the results of this study as shown in figure 4.14. In addition, a pre-peak at around 1.6(3) $Å^{-1}$ can also be seen in the $F(q)$ function for the molten $Ag_{0.74}Ge_{0.26}$ alloy.

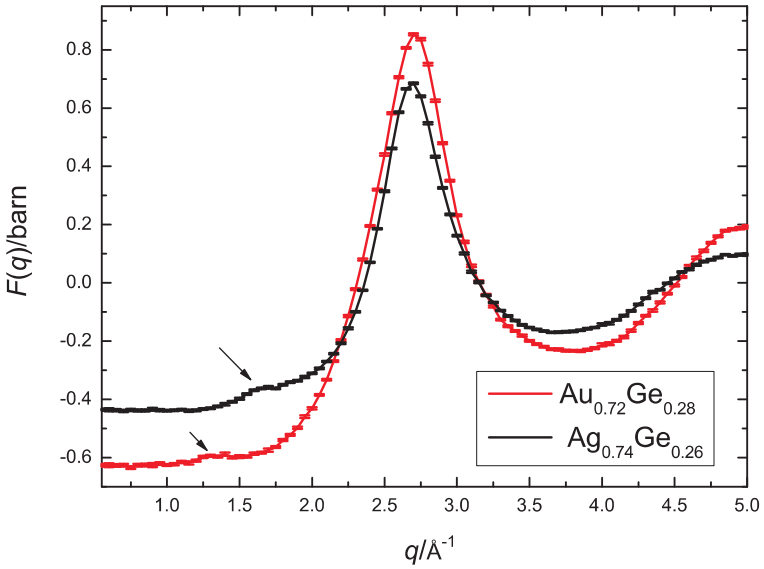

Figure 4.14: Pre-peaks in the $F(q)$ functions for molten $Au_{0.72}Ge_{0.28}$ at 393(2) °C and molten $Ag_{0.74}Ge_{0.26}$ at 703(2) °C.

4.6.2 Total Pair Distribution Functions

$Au_{0.81}Si_{0.19}$

For molten $Au_{0.81}Si_{0.19}$, the position of the first peak in the $G(r)$ function of figure 4.12 is at 2.83(2) Å. This peak could have contributions from more than one pair correlation function but as the sample is 81% Au the main contribution should come from the Au-Au pair correlations, see table 4.6. In fact, the Au-Au distance in liquid Au is 2.8 Å [40, 129] which is very similar to the position of the first peak for the molten $Au_{0.81}Si_{0.19}$ alloy.

The structure of molten $Au_{0.81}Si_{0.19}$ has been measured by using XRD [40] with a maximum q value of 20.025 Å^{-1}. It is useful to compare the data sets in real space. The $G_N(r)$ for the present work was re-calculated by Fourier transforming $F(q)$ truncated at $q = 20.05$ Å^{-1}. Figure 4.15 shows a comparison between the $G_N(r)$ obtained from this work and the $G_X(r)$ obtained from the XRD results [40]. The results from both experiments are very similar except for a shoulder on the low r side of the first peak at around 2.4 Å in the ND data.

An MD simulation for a range of glassy Au_xSi_{1-x} alloys [129] shows that the Si-Si and Au-Au bond distances in the alloy are the same as those in the pure liquid,

i.e. 2.4 Å for Si-Si and 2.8 Å for Au-Au. The Si-Si bond distance from the simulation is similar to the bond distance obtained from XRD studies of molten silicon which give 2.48 Å [130] and 2.45 Å [131]. The simulation suggested that for Au rich Au-Si amorphous alloys, there is a strong interaction between Au and Si atoms such that the Si atoms are more or less evenly distributed and form Si-centred tri-capped trigonal prism Kasper polyhedra with an Au-Si bond distance of around 2.4 Å. An MD simulation for molten $Au_{0.81}Si_{0.19}$ alloy [132] also suggests a preference of Au-Si bonds in the system. According to these information, the low r shoulder on the first peak in the $G(r)$ of the present work is due to a contribution from both the Au-Si and Si-Si correlations.

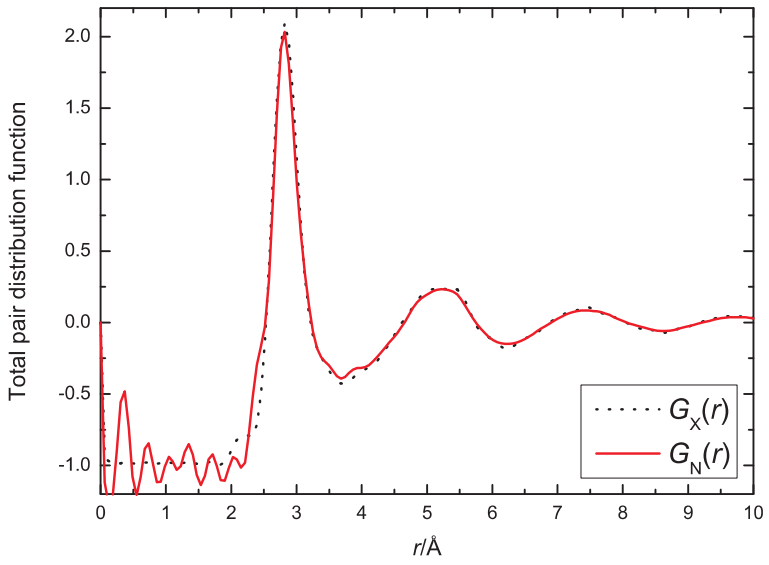

Figure 4.15: The measured total pair distribution functions for molten $Au_{0.81}Si_{0.19}$. The solid line gives the result obtained from ND at 392(2) °C. The dotted line gives the result obtained from high energy XRD at 380 °C [40].

As shown in figure 4.15, the shoulder on the first peak in $G_N(r)$ cannot be seen in the XRD results. This is due to a difference between the x-ray and neutron scattering lengths. Recall the definition of the total structure factors for neutron and x-ray diffraction given in equations 2.26 and 2.44,

$$F(q) \equiv \sum_{\alpha,\beta}^{n} c_\alpha c_\beta b_\alpha b_\beta \left[S_{\alpha\beta}(q) - 1\right]$$

and

$$F_X(q) \equiv \sum_{\alpha,\beta}^{n} c_\alpha c_\beta f_\alpha(q) f_\beta^*(q) \left[S_{\alpha\beta}(q) - 1\right].$$

The corresponding $G_N(r)$ and $G_X(r)$ functions can also be written in terms of a summation over all of the partial pair distribution functions in the system weighted by atomic fractions and scattering length contributions. From table 4.6, the weighting factors for the Au-Si and Si-Si correlations for both neutron and x-ray diffraction are very small compared to the weighting factor for the Au-Au correlations. This is mainly due to the high atomic fraction of Au. For the Au-Si correlations, the weighting factor of about 20% for ND is more than twice the 8% weighting factor for XRD. As there is hardly any contribution from the Si-Si correlations for both neutron and x-ray diffraction, the low r shoulder on the first peak of $G(r)$ at around 2.4 Å in the ND result is attributed to Au-Si correlations which supports the preference of Au-Si bonds as found from the MD simulations [129, 132]. RMC modelling of the XRD data for liquid $Au_{0.81}Si_{0.19}$ at various temperatures [40] found a Au-Si coordination number of around 10 which is similar to the coordination number of 9 for the Si-centred units predicted by the MD simulation of glassy Au_xSi_{1-x} alloys [129].

$\mathbf{Au_{0.72}Ge_{0.28}}$

For molten $Au_{0.72}Ge_{0.28}$, the position of the first peak in the $G(r)$ of figure 4.12 is at 2.76(2) Å which is similar to the Au-Au bond distance of 2.8 Å in liquid Au [40, 129]. An EXAFS measurement on liquid Ge gave a Ge-Ge bond distance of 2.62(2) Å [133]. Diffraction experiments on liquid Ge also gave a similar Ge-Ge bond distance of 2.66(2) Å [134] and 2.64 Å [135]. From table 4.6, the Au-Au and Au-Ge correlations dominate the total correlation function and have comparable weighting factors. As the position of the first peak for the $Au_{0.72}Ge_{0.28}$ alloy is at 2.76(2) Å which is lower than the Au-Au distance found in liquid Au it is possible that Au-Ge correlations also contribute significantly to the first peak in $G(r)$. It should be noted that the nearest neighbour Au-Ge distance in crystalline $Au_{0.8}Ge_{0.2}$ ranges from 2.85 to 2.86 Å [136].

The structure of molten $Au_{0.72}Ge_{0.28}$ has also been measured by using XRD

[40] with a maximum q value of 19.95 Å^{-1}. The $G_N(r)$ for the present work was re-calculated by Fourier transforming $F(q)$ truncated at $q = 19.95$ Å^{-1} and is compared with the $G_X(r)$ in figure 4.16. From the figure, the position of the first peak in $G_X(r)$ is at 2.79(2) Å which is shifted slightly to the high r side compared with $G_N(r)$. This peak shift could be due to a higher contribution from the Au-Au correlations in the XRD pattern, see table 4.6.

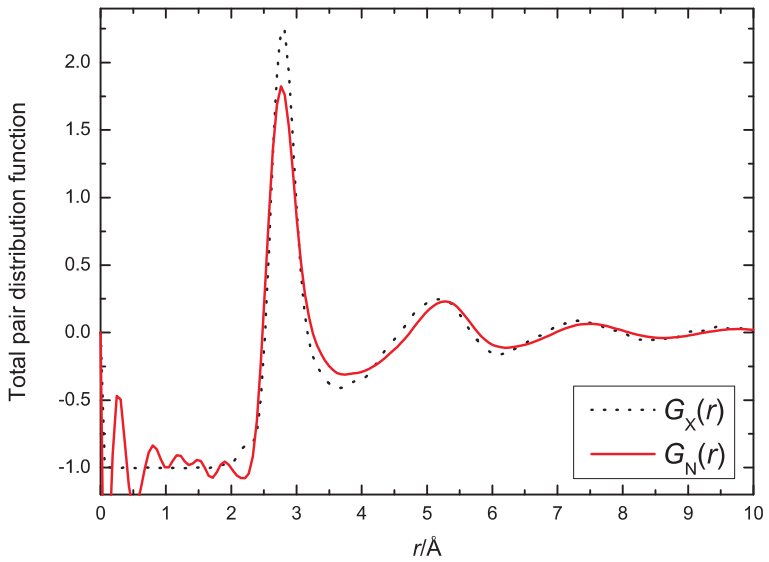

Figure 4.16: The total pair distribution functions for molten $Au_{0.72}Ge_{0.28}$. The solid line gives the result obtained from ND at 393(2) °C. The dotted line gives the result obtained from high energy XRD at 380 °C [40].

$Ag_{0.74}Ge_{0.26}$

For molten $Ag_{0.74}Ge_{0.26}$, the position of the first peak of the $G(r)$ in figure 4.12 is at 2.77(2) Å. The structure of the eutectic composition of Ag-Ge alloys, $Ag_{0.76}Ge_{0.24}$, has been measured by using the method of isotopic substitution in ND using Ag isotopes by Bellissent-Funel et al. [41]. The diffraction experiment was made using the D4 diffractometer (an older version of D4c) at the ILL. Due to the limitations of the instrument at the time, the structure factors were measured only up to a maximum q value of 12 Å^{-1}. The nearest neighbour distances obtained from the results were 2.92 Å for the Ag-Ag correlations, 2.66 Å for the Ag-Ge correlations and 3.12 Å for the Ge-Ge correlations. Because of the limited q range,

the real space resolution was low and the coordination numbers could not be reliably extracted from the partial pair distribution functions.

Since the eutectic composition and the composition studied in this work are very similar, it is useful to compare the results. The $G(r)$ for the Bellissent-Funel et al. [41] experiment was obtained by digitising the three partial pair distribution functions and combining them using equation 2.27. The $G(r)$ for the present work was re-calculated by Fourier transforming $F(q)$ truncated at q=12 Å^{-1}. A comparison between the data sets is shown in figure 4.17. Also shown in this figure are the weighted $g_{\alpha\beta}(r)$ functions corresponding to the Ag-Ag, Ge-Ge and Ag-Ge correlations from [41]. From the figure, the two $G(r)$ functions show similar overall features except for a small shift in the position of the first peak which suggests slightly different structures. It should be noted that the lower intensity and the broader features of the $G(r)$ function from [41] could be a result of the method used to extract the partial structure factors which is outlined in [137].

According to the atomic distances reported in [41], the range of the first peak in $G(r)$ for the $Ag_{0.74}Ge_{0.26}$ alloy from about 2.2 Å to 3.6 Å, see figure 4.17, will include a contribution from all of the pair correlation functions. Although the D4 diffractometer has been improved and the maximum q value is now 23.65 Å^{-1} for 0.5 Å incident neutrons, the nearest neighbour atomic distances for each pair correlation function cannot be distinguish in the measured $G(r)$.

The structure of molten $Ag_{0.74}Ge_{0.26}$ has also been measured by using XRD [125] with a maximum q value of 23.425 Å^{-1}. A comparison between the neutron and x-ray diffraction results is shown in figure 4.18. From the figure, the position of the first peak in $G_X(r)$ is at 2.81(2) Å which is slightly larger than the peak position in $G_N(r)$. In fact, the first three peaks in $G_X(r)$ are slightly shifted to the high r side compared with $G_N(r)$. This could be a result of a higher contribution from the Ag-Ag correlations in the XRD pattern, see table 4.6. From figure 4.17, the positions of the first and second peaks of the $g_{\mathrm{AgAg}}(r)$ function are significantly larger than those of the $g_{\mathrm{AgGe}}(r)$ function.

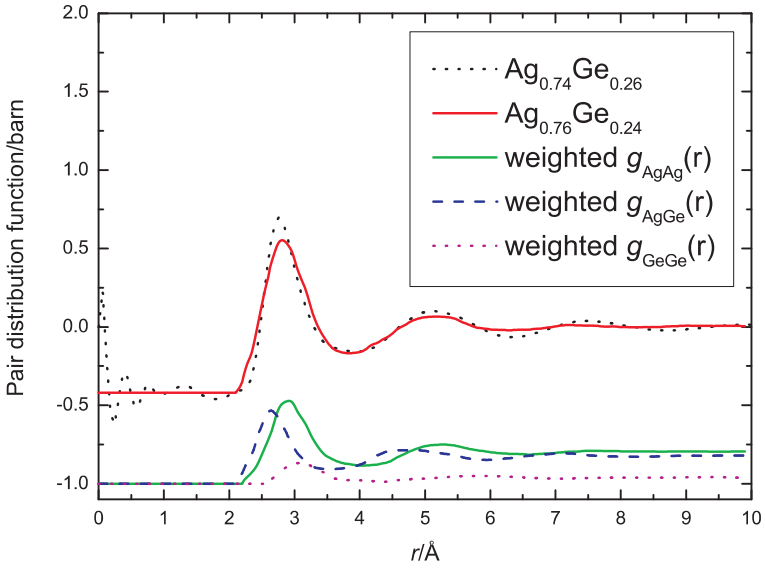

Figure 4.17: A comparison between the $G(r)$ function for molten $Ag_{0.76}Ge_{0.24}$ at 850 °C as obtained by combining the partial pair distribution functions digitised from [41] and the $G(r)$ function for molten $Ag_{0.74}Ge_{0.26}$ at 703(2) °C from the present work. Also shown are the weighted $g_{\alpha\beta}(r)$ functions for molten $Ag_{0.76}Ge_{0.24}$ as measured using the method of isotopic substitution in ND [41], displaced vertically for clarity of presentation.

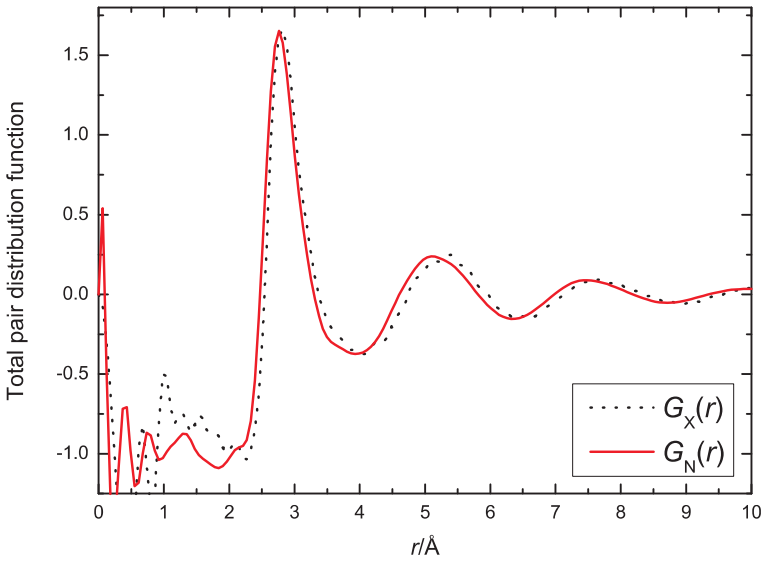

Figure 4.18: The total pair distribution functions for molten $Ag_{0.74}Ge_{0.26}$. The solid line gives the result obtained from ND at 703(2) °C. The dotted line gives the result obtained from high energy XRD at 700 °C [125].

4.6.3 Asymptotic Decay of the Pair Distribution Functions

There are two approaches describing the asymptotic behaviour of $G(r)$. The first one is a theoretical approach based on calculations using short ranged repulsive pair potentials [113] or short ranged repulsive pair potentials and long ranged Coulomb potentials [138]. The second one is a semi-empirical equation derived from the diffraction results for many metallic glasses [114]. According to the first approach, the asymptotic behaviour of $r[g_{ij}(r) - 1]$ is given by an exponentially damped periodic function

$$r[g_{ij}(r) - 1] = A_{ij}e^{-\alpha_0 r}\cos(\alpha_1 r - \theta_{ij}), \tag{4.9}$$

where A_{ij} and θ_{ij} are the amplitude and phase of the $r[g_{ij}(r) - 1]$ function, α_0^{-1} is the decay length, and $2\pi\alpha_1^{-1}$ is the wavelength of the oscillations. Provided all of the $r[g_{ij}(r) - 1]$ functions share a common decay length and a common wavelength of oscillation, $rG(r)$ will also follow an exponentially damped oscillatory function at large r values i.e.

$$rG(r) = Ae^{-\alpha_0 r}\cos(\alpha_1 r - \theta), \tag{4.10}$$

where A and θ are the amplitude and phase. The relation in equation 4.10 has been found to hold for several binary liquids and network glasses [139]. The experimental $rG(r)$ functions from the present study were used to test the validity of equation 4.10 for the molten $Au_{0.81}Si_{0.19}$, $Au_{0.72}Ge_{0.28}$ and $Ag_{0.74}Ge_{0.26}$ alloys.

The values of α_0 and α_1 can be determined directly from the experimental data by fitting to equation 4.10. In addition, α_0 can be found from a linear fit to the maxima of the $\ln|rG(r)|$ function. If we take the natural logarithm of equation 4.10 then

$$\ln|rG(r)| = -\alpha_0 r + \ln|\cos(\alpha_1 r - \theta)| + C, \tag{4.11}$$

where C is a constant. Equation 4.11 is in the form of a linear equation with a negative gradient given by α_0. The second term on the right hand side of equation 4.11 represents the oscillations of the function. For this term, because the maximum value of $|\cos(\alpha_1 r - \theta)|$ is one and $\ln(1)$ is zero, the maxima of the oscillatory function should follow the linear function

$$\ln|rG(r)| = -\alpha_0 r + C \tag{4.12}$$

at large r values. Therefore, α_0 can also be determined from a linear fit to these data points. The $\ln|rG(r)|$ functions for the alloys and the corresponding fits are shown in figure 4.19. Note that the data can only be fitted in a certain range. The minimum side of the range is limited by the fact that equation 4.10 only applies to $rG(r)$ functions at large r and the maximum side of the range is limited by the signal to noise ratio as the amplitude of the oscillations in $rG(r)$ decreases with increasing r. The fitted range for each system is presented in table 4.7.

The $rG(r)$ functions were fitted to equation 4.10 using the Levenberg-Marquardt algorithm for nonlinear least squares fitting. The fitted ranges were chosen to be the same as those used for the linear fit to the $\ln|rG(r)|$ functions. The data and the fits are shown in figure 4.20 and, as can be seen by inspection of the figure, equation 4.10 gives a reasonably good fit for all of the molten alloys. The quality of the fit was examined using the R^2 function defined as

$$R^2 = 1 - \frac{\sum_i (y_i - f_i)^2}{\sum_i (y_i - \overline{y})^2}, \tag{4.13}$$

where y_i represents a data point, f_i is the fitted function, and $\overline{y}$ is the average value of y_i in the fitted range. The R^2 values for these fits are presented in table 4.7.

The values of α_0 and α_1 obtained from the real space fits should be consistent with the q space data. The parameter α_1, which is related to the wavelength of the oscillations in real space, is roughly the position of the principal peak in $F(q)$ while α_0, which describes the decay of the oscillations in real space, should be approximately equal to the half width at half maximum (HWHM) of the principal peak [139]. The values of α_0 and α_1 obtained from the fits and from $F(q)$ are summarised in table 4.9.

Sample	R^2	Fitted range (Å)
$Au_{0.81}Si_{0.19}$	0.99744	6.26-30.56
$Au_{0.72}Ge_{0.28}$	0.99608	6.26-21.23
$Ag_{0.74}Ge_{0.26}$	0.99688	5.22-18.10

Table 4.7: The goodness of fit parameter, R^2, and fitted ranges for fits to the $rG(r)$ functions for molten $Au_{0.81}Si_{0.19}$, $Au_{0.72}Ge_{0.28}$ and $Ag_{0.74}Ge_{0.26}$ using equation 4.10.

Alternatively, the asymptotic behaviour of $G(r)$ has been described by using a relation for fractal structures [114]. For a non-fractal system, it is argued that

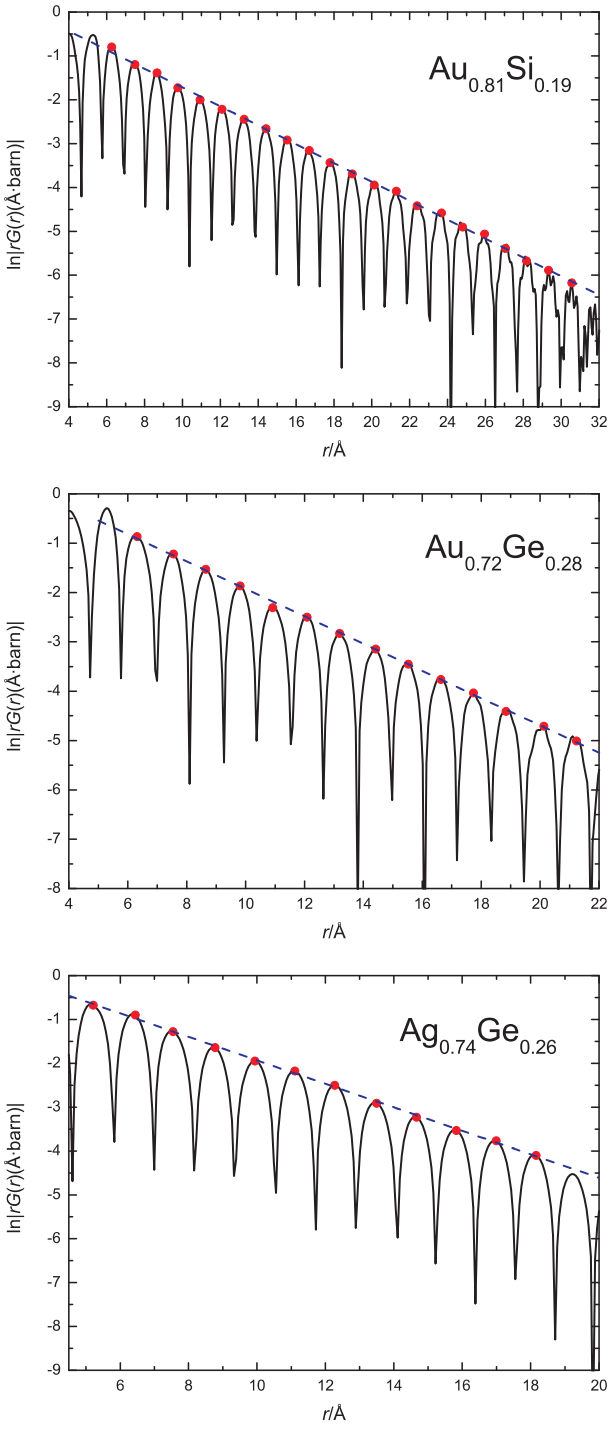

Figure 4.19: The $\ln|rG(r)|$ functions obtained from the data for molten $Au_{0.81}Si_{0.19}$, $Au_{0.72}Ge_{0.28}$ and $Ag_{0.74}Ge_{0.26}$. The dots mark the maximum amplitude of each oscillation in the $\ln|rG(r)|$ functions and the dashed lines give linear fits to these data points.

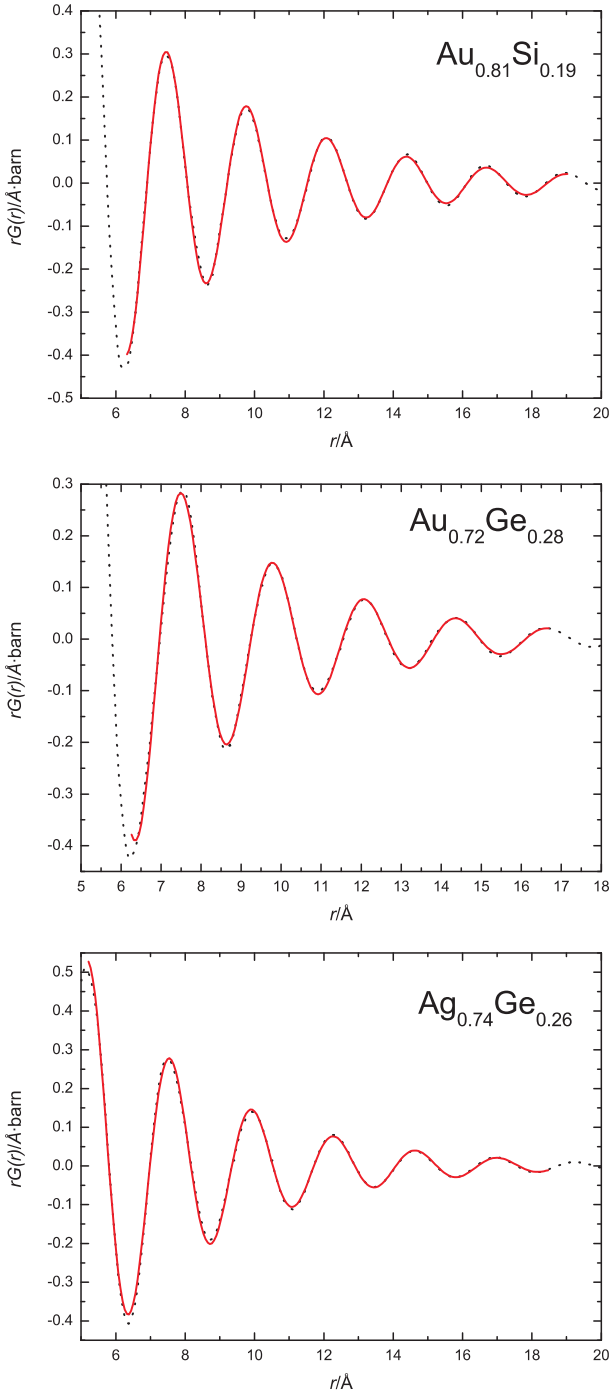

Figure 4.20: The dotted lines give the experimental $rG(r)$ functions for the molten $Au_{0.81}Si_{0.19}$, $Au_{0.72}Ge_{0.28}$ and $Ag_{0.74}Ge_{0.26}$ alloys at 392(2), 393(2) and 703(2) °C, respectively. The solid lines give the fits to the data using the relation given by equation 4.10.

the position of the first (or principal) peak, q_1, in the $F(q)$ function should be proportional to $v_a^{1/D}$ where $D = 3$ for a non-fractal system, $v_a = 1/n_0$ is the atomic volume and n_0 is the atomic number density. Ma et al. [114] have investigated this relation for many metallic glasses. The study found that q_1 for metallic glasses is proportional to $v_a^{0.443(7)}$ which suggests that the structure of metallic glasses is fractal with a fractal dimension $D_f = 1/0.433 = 2.31$.

If a system is fractal, its differential cluster correlation function can be expressed as

$$C(r) = (\frac{A}{r^{D-D_f}})e^{\frac{-r}{\xi}} \sin(q_1 r + \phi), \tag{4.14}$$

where $C(r)$ is equivalent to $G(r)/\langle b\rangle^2$, A and ϕ are the amplitude and phase of the $C(r)$ function and ξ is a cutoff length for the correlation function. To compare with equation 4.10, equation 4.14 can be re-written as

$$r^{D'}G(r) = A'e^{\frac{-r}{\xi}} \sin(q_1 r + \phi), \tag{4.15}$$

where $A' = A \cdot \langle b\rangle^2$ and $D' = D - D_f = 0.69$ for metallic glasses. Similar to equation 4.12, we can take the natural logarithm of equation 4.15 and obtain a relation for the maximum points in the oscillations of the $\ln|r^{0.69}G(r)|$ function as

$$\ln\left|r^{0.69}G(r)\right| = \frac{-r}{\xi} + C', \tag{4.16}$$

where C' is a constant.

Ma et al. [114] determined the fractal dimension for metallic glasses by fitting a straight line to a plot of $\ln(q_1)$ versus $\ln(v_a)$ as shown in figure 4.21. To this figure four more data points have been added corresponding to the molten $Au_{0.81}Si_{0.19}$, $Au_{0.72}Ge_{0.28}$ and $Ag_{0.74}Ge_{0.26}$ alloys from this work and to glassy $Au_{0.80}Si_{0.20}$ from [126].

From figure 4.21, all of the additional data points are in the vicinity of the fitted line suggesting a similar fractal dimension to that of the metallic glasses. Moreover, equation 4.15 is very similar to equation 4.10 which gives good fits to the real space data for these molten alloys. It is, therefore, interesting to investigate the structures of these alloys in terms of a fractal approach.

In Ma et al. [114], the minimum of the fitted range was determined by comparing the real space function obtained by using the full q range of $F(q)$ and the real

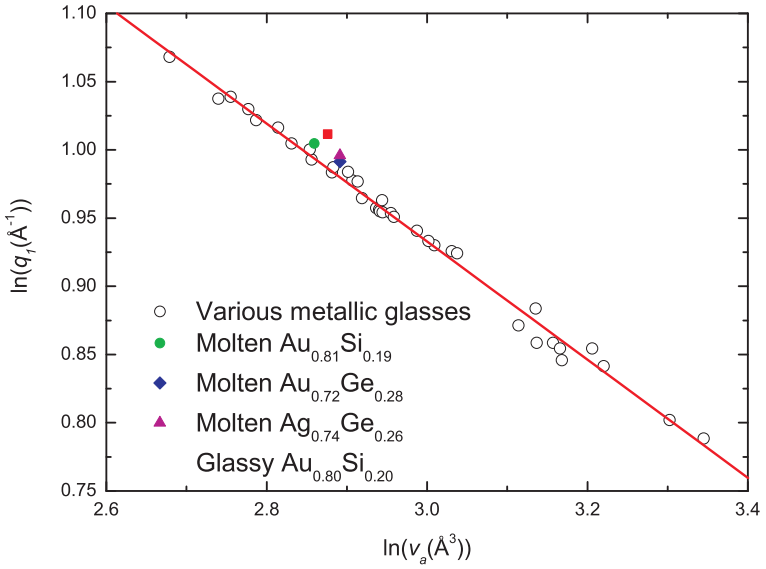

Figure 4.21: $\ln(q_1)$ as a function of $\ln(v_a)$ for various metallic glasses, molten $Au_{0.81}Si_{0.19}$ at 392(2) °C, molten $Au_{0.72}Ge_{0.28}$ at 393(2)(1) °C, molten $Ag_{0.74}Ge_{0.26}$ at 703(2) °C and glassy $Au_{0.80}Si_{0.20}$ from [126]. The data points for the metallic glasses are redrawn from [114] and a linear fit to the metallic glass data gives a gradient of 0.433(7).

space function obtained by truncating $F(q)$ at the high q side of the second peak. For the molten $Au_{0.81}Si_{0.19}$, $Au_{0.72}Ge_{0.28}$ and $Ag_{0.74}Ge_{0.26}$ alloys, this corresponds to q = 6.10, 6.20 and 6.15 Å^{-1} , respectively. These two real space functions will have some discrepancies in the low r region which correspond to the high q part in $F(q)$. The minimum of the fitted range was chosen to be the minimum r value at which the two real-space functions agree. Figure 4.22 shows a comparison between the $G(r)$ functions corresponding to the full q range of $F(q)$ and to the truncated q range of $F(q)$ for molten $Au_{0.81}Si_{0.19}$, $Au_{0.72}Ge_{0.28}$ and $Ag_{0.74}Ge_{0.26}$.

From figure 4.22, the minimum r values at which the two $G(r)$ functions agree are 7.49, 7.37 and 7.41 Å for the $Au_{0.81}Si_{0.19}$, $Au_{0.72}Ge_{0.28}$ and $Ag_{0.74}Ge_{0.26}$ alloys, respectively. As these values are comparable with the values used earlier in the fit to equation 4.10 (see table 4.7), the same fitted ranges were used in order to compare the quality of the fits between the two approaches.

The $r^{0.69}G(r)$ functions and the fits to equation 4.15 for molten $Au_{0.81}Si_{0.19}$, $Au_{0.72}Ge_{0.28}$ and $Ag_{0.74}Ge_{0.26}$ are shown in figure 4.23. The $\ln|r^{0.69}G(r)|$ functions and the linear fits to the maxima of the oscillations are shown in figure 4.24. From

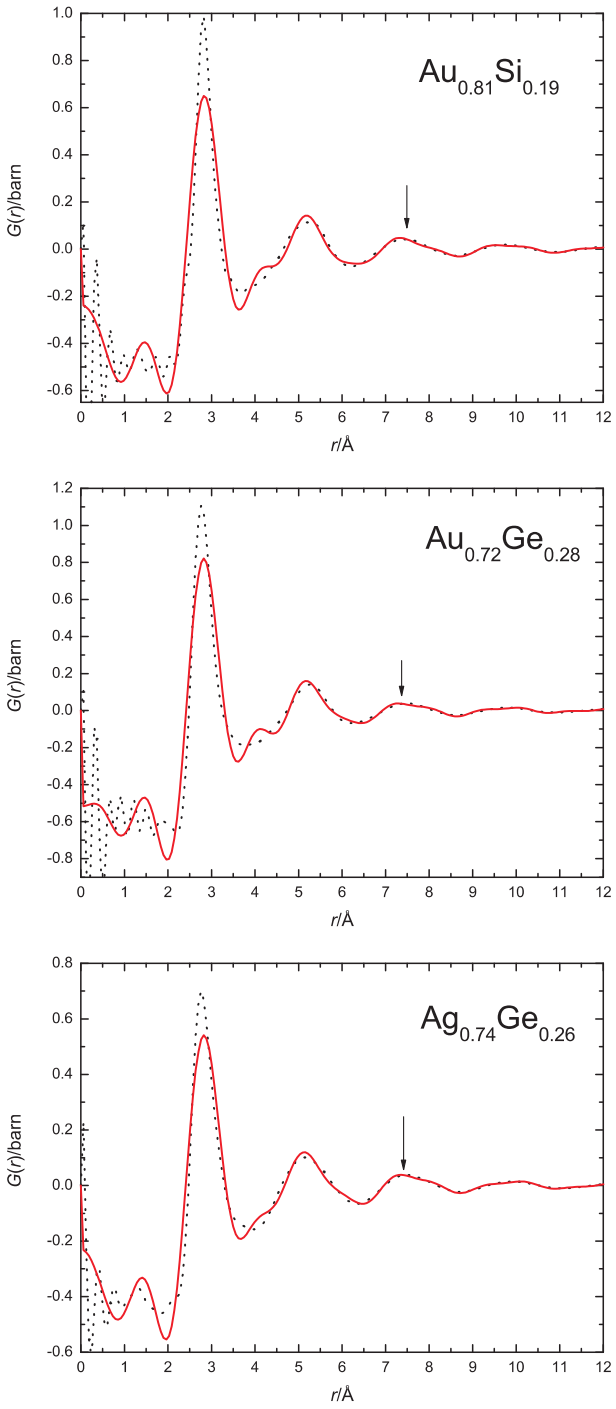

Figure 4.22: The dotted lines give the $G(r)$ functions obtained by Fourier transforming the full $F(q)$ functions and the solid lines give the $G(r)$ functions obtained by Fourier transforming the $F(q)$ functions after truncating at a q value corresponding to the high q side of the second peak. The data correspond to molten $Au_{0.81}Si_{0.19}$, $Au_{0.72}Ge_{0.28}$ and $Ag_{0.74}Ge_{0.26}$ alloys at 392(2), 393(2) and 703(2) °C, respectively. The arrows mark the minimum r value at which the two $G(r)$ functions agree.

figure 4.23, although equation 4.15 gives a reasonably good fit for these molten alloys there is a small shift between the fits and the data sets which arises from the fact that, unlike equation 4.10, equation 4.15 does not allow the wavelength of the oscillations in the $r^{0.69}G(r)$ functions to vary during the fitting procedure but is instead fixed by the value given by q_1, namely 2.72(2), 2.71(2) and 2.69(2) Å^{-1} for $Au_{0.81}Si_{0.19}$, $Au_{0.72}Ge_{0.28}$ and $Ag_{0.74}Ge_{0.26}$, respectively. Figure 4.25 shows the $r^{0.69}G(r)$ functions and the fits to equation 4.15 with q_1 allowed to be a variable in the fitting procedure. The R^2 values for all of the fits are summarised in table 4.8.

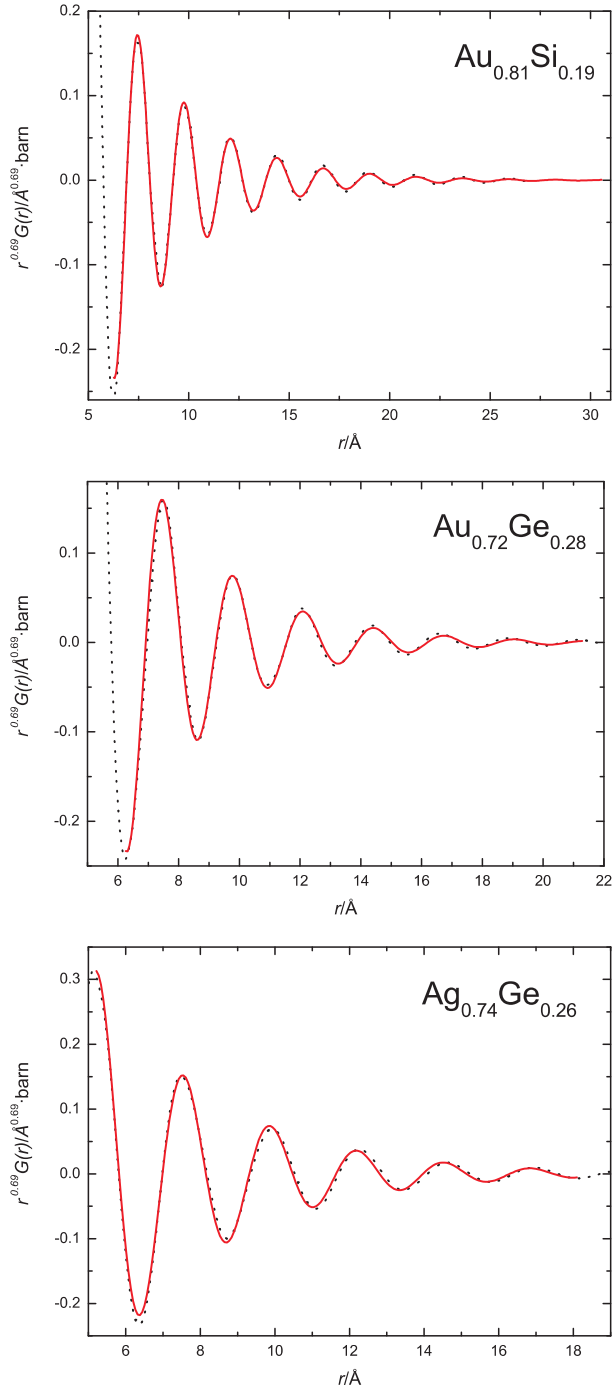

Figure 4.23: The dotted lines give the experimental $r^{0.69}G(r)$ functions for molten $Au_{0.81}Si_{0.19}$, $Au_{0.72}Ge_{0.28}$ and $Ag_{0.74}Ge_{0.26}$ alloys at 392(2), 393(2) and 703(2) °C, respectively. The solid lines give the fits to the data using the relation given by equation 4.15.

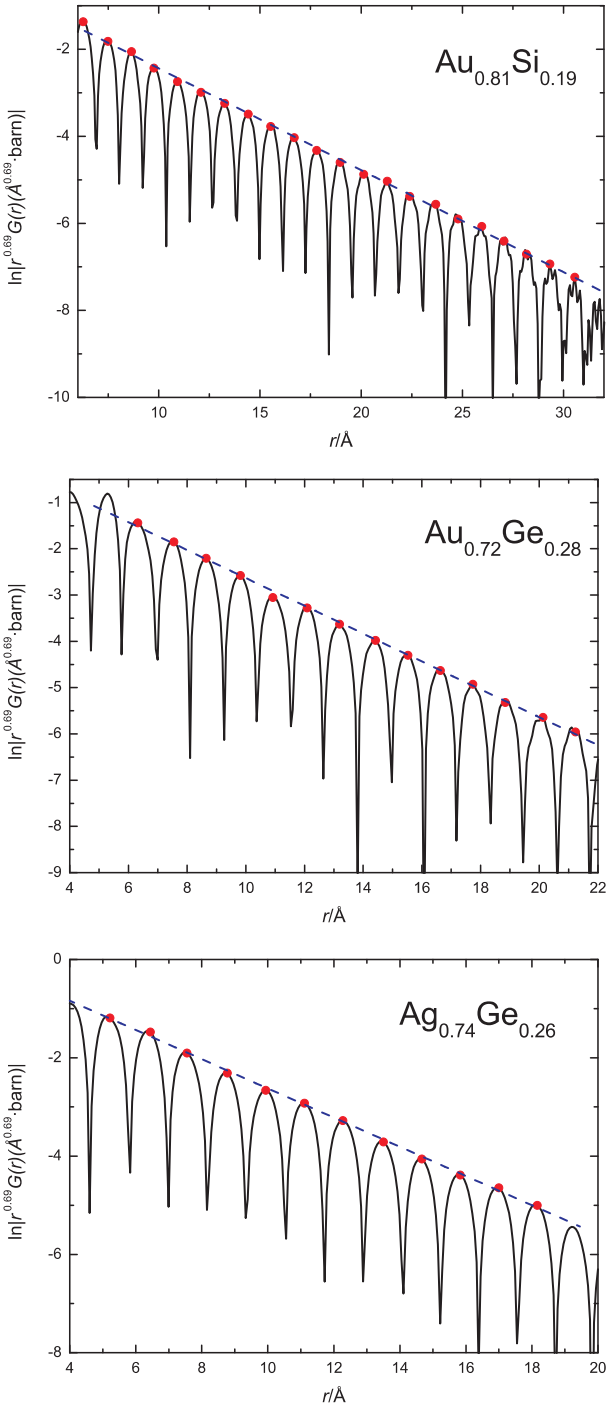

Figure 4.24: The $\ln|r^{0.69}G(r)|$ functions obtained from the data for molten $Au_{0.81}Si_{0.19}$, $Au_{0.72}Ge_{0.28}$ and $Ag_{0.74}Ge_{0.26}$. The dots mark the maximum amplitude of each oscillation in the $\ln|r^{0.69}G(r)|$ functions and the dashed lines give linear fits to these data points.

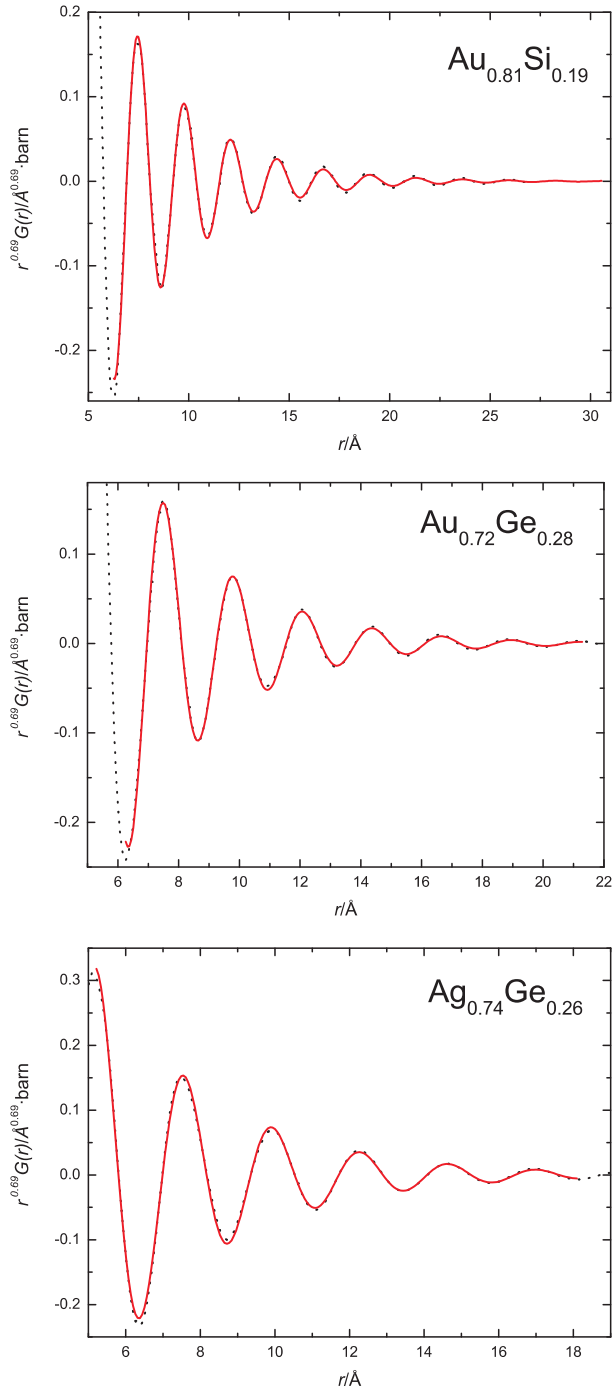

Figure 4.25: The dotted lines give the experimental $r^{0.69}G(r)$ functions for molten $Au_{0.81}Si_{0.19}$, $Au_{0.72}Ge_{0.28}$ and $Ag_{0.74}Ge_{0.26}$ alloys at 392(2), 393(2) and 703(2) °C, respectively. The solid lines give the fits to the data using the relation given by equation 4.15 but with q_1 allowed to be variable in the fitting procedure.

Although equations 4.10 and 4.15 give different interpretations of the asymptotic behaviour of $r^n G(r)$, they have a similar form. Both equations have an exponential term that represents the decay and a sinusoidal term that represents the oscillations. The differences lie in the power of r which multiplies the $G(r)$ function. Comparing equations 4.10 and 4.15, we have $\alpha_0 = \frac{1}{\xi}$ and $\alpha_1 = q_1$. The values of α_0 and α_1 obtained from the principal peak in $F(q)$ and from the fits to equations 4.10, 4.12, 4.15 (with and without varying q_1) and 4.16 are summarised in table 4.9.

Sample	R^2		Fitted range (Å)
	Fit to equation 4.15	Fit to equation 4.15 (vary q_1)	
$Au_{0.81}Si_{0.19}$	0.99590	0.99590	6.26-30.56
$Au_{0.72}Ge_{0.28}$	0.99410	0.99789	6.26-21.23
$Ag_{0.74}Ge_{0.26}$	0.99346	0.99714	5.22-18.10

Table 4.8: The goodness of fit parameter, R^2, and fitted ranges for fits to the $r^{0.69}G(r)$ functions for molten $Au_{0.81}Si_{0.19}$, $Au_{0.72}Ge_{0.28}$ and $Ag_{0.74}Ge_{0.26}$ using equation 4.15.

	$Au_{0.81}Si_{0.19}$		$Au_{0.72}Ge_{0.28}$		$Ag_{0.74}Ge_{0.26}$	
	α_0(Å^{-1})	α_1(Å^{-1})	α_0(Å^{-1})	α_1(Å^{-1})	α_0(Å^{-1})	α_1(Å^{-1})
From the principal peak in $F(q)$	0.25(2)	2.72(2)	0.30(2)	2.71(2)	0.26(2)	2.69(2)
Fit to equation 4.10	0.232(1)	2.722(1)	0.283(2)	2.748(3)	0.273(2)	2.659(2)
Fit to equation 4.12	0.215(2)	-	0.277(3)	-	0.268(3)	-
Fit to equation 4.15	0.270(2)	-	0.329(3)	-	0.310(4)	-
Fit to equation 4.16	0.234(2)	-	0.301(3)	-	0.297(4)	-
Fit to equation 4.15 (vary q_1)	0.270(2)	2.720(2)	0.323(2)	2.745(2)	0.311(2)	2.659(2)

Table 4.9: The values for α_0 and α_1 obtained from the principal peak in $F(q)$ and from fits of the experimental data to equations 4.10, 4.12, 4.15 (with and without varying q_1) and 4.16.

From table 4.9, the α_1 values determined from the fits of $rG(r)$ to equation 4.10 and to the fits of $r^{0.69}G(r)$ to equation 4.15 are the same as the principal peak position in $F(q)$ within the errors for the $Au_{0.81}Si_{0.19}$ alloy. For the $Au_{0.72}Ge_{0.28}$ alloy, the α_1 values from both fits are slightly higher and for the $Ag_{0.74}Ge_{0.26}$ alloy, the α_1 values from both fits are slightly lower. For α_0, the power of r used to multiply the $G(r)$ functions affects the decay length of the function. The α_0 values from the fits to equations 4.10, 4.12 or 4.16 are, within the error, equal to the HWHM of the principal peak in the measured $F(q)$ functions. These values are smaller than

those obtained from the fits to equation 4.15. For the fits to equation 4.15 or 4.16 the decay length $\alpha_0 = 1/\xi$ where ξ is the cut off length. For metallic glasses, ξ was found to be 4.00(8) Å [114]. The values of ξ for molten $Au_{0.81}Si_{0.19}$, $Au_{0.72}Ge_{0.28}$ and $Ag_{0.74}Ge_{0.26}$ obtained from the fits to equation 4.16 in this work are 4.27(3), 3.32(3) and 3.37(4) Å, respectively.

4.7 Conclusions

The structures of three molten alloys, namely $Au_{0.81}Si_{0.19}$, $Au_{0.72}Ge_{0.28}$ and $Ag_{0.74}Ge_{0.26}$, were investigated by using ND. For molten $Au_{0.81}Si_{0.19}$, the peak positions in $G(r)$ agrees with the XRD results [40]. The shoulder on the low r side of the first peak at $\simeq 2.4$ Å can be interpreted, with the aid of MD simulations [129, 132], as corresponding to the nearest neighbour Au-Si correlations. This information, along with the RMC results [40], support an association of Au and Si atoms and the possible existence of Si-centred clusters. The fact that the shoulder cannot be seen with XRD demonstrates that the application of different experimental techniques to the same system can gain more structural information.

For the molten $Au_{0.72}Ge_{0.28}$ and $Ag_{0.74}Ge_{0.26}$ alloys, the comparison between the $G_N(r)$ and $G_X(r)$ functions shows noticeable peak shifts which is attributed to a significant contrast between the neutron and x-ray weighting factors for the involved correlations. For $Ag_{0.74}Ge_{0.26}$, the comparison of $G(r)$ with the eutectic composition $Ag_{0.76}Ge_{0.24}$ [41] suggests that the structure of the molten state for these alloys is very similar.

Small pre-peaks in the $F(q)$ functions for the molten $Au_{0.72}Ge_{0.28}$ and $Ag_{0.74}Ge_{0.26}$ alloys, were found at $q \simeq 1.3(2)$ Å^{-1} and at $q \simeq 1.6(3)$ Å^{-1}, respectively, suggesting some degree of intermediate range ordering. For the molten $Au_{0.72}Ge_{0.28}$ alloy, this result confirms an observation made by Hoyer and Jödicke [128] and disagrees with the results reported by Fujii et al. [40] and Waghorne et al. [124].

The asymptotic behaviour of $rG(r)$ obtained from this study supports a theoretical prediction based on simple pair potentials [113]. This could be due to the fact that $rG(r)$ is dominated by one pair correlation function in the case of the $Au_{0.81}Si_{0.19}$

alloy. It is also possible that the two dominant correlations for the $Au_{0.72}Ge_{0.28}$ and $Ag_{0.74}Ge_{0.26}$ alloys have similar decay lengths and wavelengths of oscillation such that the large r behaviour of $rG(r)$ also follows equation 4.10. The asymptotic behaviour of $r^{0.69}G(r)$ for the three alloys also agrees well with the behaviour predicted using equation 4.15 for a fractal system [114]. The densities and the position of the first peak in q space follow the relation $1/q \propto v_a^{0.433(7)}$ which suggests that these systems have the same fractal dimension as metallic glasses which is 2.31, although the fits to equation 4.15 give different cutoff lengths for the differential cluster correlation function.

For future work, an atomic model of molten $Au_{0.81}Si_{0.19}$, $Au_{0.72}Ge_{0.28}$ and $Ag_{0.74}Ge_{0.26}$ alloys could be constructed from the ND and XRD data by using the RMC method. The significant contrast between the neutron and x-ray weighting factor will greatly improve the accuracy of the existing RMC model for $Au_{0.81}Si_{0.19}$ and $Au_{0.72}Ge_{0.28}$ system [40, 125]. Additional information on the structural units and intermediate range order could then be gained.

Chapter 5

Rare-earth Alumino-silicate Glasses

5.1 Introduction

Miniature rare-earth doped glass devices such as microchip lasers, channel waveguide lasers, lossless splitters and amplifiers are technologically important [26]. However, the low solubility of rare-earth ions in the host glass limits the doping concentration to a few thousand parts per million as rare-earth ions tend to form clusters when the doping concentration increases [140]. It has been suggested that the clustering of rare-earth ions in SiO_2 glasses is caused by Coulombic interaction between associated cation-anion pairs [141] and an interaction between close proximity rare-earth ions introduces a concentration quenching effect which degrades the favourable optical properties of the glass [26].

It is found from the fluorescence spectra measured for Nd_2O_3 doped SiO_2 glass that the effect of concentration quenching can be reduced by codoping the rare-earth oxide with Al_2O_3 or P_2O_3 [142]. An EXAFS experiment has been made at the Nd L_{III} edge for several rare-earth glasses, including SiO_2 doped with 2400 ppm of Nd_2O_3 and $Nd_2Al_2Si_3O_{12}$ [140]. For the Nd_2O_3 doped SiO_2 glass, the results give a Nd-O nearest neighbour distance of 2.35 Å with a coordination number of 7 and a Nd-Nd next nearest neighbour distance of 3.8 Å with a coordination number of

3 which is consistent with a clustering of Nd ions. For the glass which is codoped with Al_2O_3, the results give the Nd-O nearest neighbour distance of 2.64 Å with a coordination number of 8 together with a next nearest neighbour Nd-Al or Nd-Si distance of 3.57 Å with a coordination number of 3 which suggests that the concentration quenching effect is reduced by dispersion of the rare-earth ions. The EXAFS results are consistent with those obtained from a two dimensional (2D) pulsed EPR experiment on SiO_2 glass doped with 1000 ppm of Yb_2O_3 and codoped with Al or P with an atomic ratio Al:Yb of 3:1 or P:Yb of 10:1. The experiment provides evidence that the Yb-O-Yb or Yb-O-Si linkages in the Yb_2O_3 doped SiO_2 glass are replaced by Yb-O-Al/P linkages in the codoped glass [143].

An MD simulation study on the effect of Al in $(Er_2O_3)_{0.01}(Al_2O_3)_{0.07}(SiO_2)_{0.92}$ glasses [144] did not, however, give evidence for the dispersion of rare-earth ions due to codoping. It was found from the simulation that the majority of Al atoms in the codoped glass are located near rare-earth ions and that a reduction of the concentration quenching effect is caused by an increase in diversity of local coordination environments for the rare-earth ions due to Al as opposed to dispersion of the ions. An MD simulation study on $(Y_2O_3)_{0.45-x}(Al_2O_3)_{0.55}(SiO_2)_x$ glasses where $x = 0.5$, 1.0, 1.5 or 2.0 also gave similar results [145].

Diffraction is another experimental technique that can be useful to study the structure of rare-earth alumino-silicate glasses. However, as these glasses contain 4 atomic species, it is difficult to interpret the results obtained from a measured total structure factor as most of the correlations are overlapped. In this chapter, the method of isomorphic substitution in ND, XRD and EXAFS spectroscopy were employed to study the structure of $(R_2O_3)_{0.2}(Al_2O_3)_{0.2}(SiO_2)_{0.6}$ glasses, where R denotes Dy, Ho or a 50:50 mixture of Dy and Ho. The isomorphic substitution method was used in order to reduce the complexity associated with overlapping correlations and the EXAFS technique was used to study the local coordination environment of the rare-earth ions. New information was therefore obtained on the way in which rare-earth are incorporated into rare-earth ion alumino-silicate glasses.

The local coordination environment of Al in $(R_2O_3)_{0.2}(Al_2O_3)_{0.2}(SiO_2)_{0.6}$ glasses where R denotes Y or La has been studied using NMR spectroscopy [35]. ^{27}Al triple-

quantum magic-angle spinning (3QMAS) spectra have been collected at 9.4 Tesla [35] and fits to the isotropic projections, uncorrected for variations in quadrupolar coupling constants among the Al species [146], give the approximate fractions of AlO_4, AlO_5 and AlO_6 units [147]. For R = Y the relative abundances of AlO_4, AlO_5 and AlO_6 are 78(3), 16(3) and 6(3)% respectively, while for R = La the relative abundances of AlO_4, AlO_5 and AlO_6 are 84(3), 13(3) and 3(1)%, respectively. These give a mean Al-O coordination number of 4.3(1) for the Y alumino-silicate glass and 4.2(1) for the La alumino-silicate glasses. In the case of the rare-earth local environment, an EXAFS experiment on the Er L_{III} edge for 0.08-3 mole% Er_2O_3 doped alumino-silicate glasses gives an Er-O nearest neighbour distance of 2.22 Å with a coordination number of 6.4 and a split second shell of Er-Al neighbours with distances of 3.54 and 3.78 Å [148]. The results also suggest that there is no significant change in the local coordination environment of Er as the concentration of the dopant is varied.

The present chapter is divided into ten sections. In section 5.2, the background theory for the method of isomorphic substitution in ND, XRD and EXAFS spectroscopy is given. The MD and RMC methods used in the present work are also outlined. The experimental details are described in section 5.3. Section 5.4 includes a discussion about the densities, scattering lengths and magnetic form factors used for the ND data analysis. In section 5.5, the ND results in both real and reciprocal space are presented. In section 5.6, the XRD results in both real and reciprocal space are shown and compared with the results obtained from ND. In section 5.7, the extracted EXAFS spectra are presented in both k- and R-space. In section 5.8, the MD and RMC models are described and the results are compared with the experimental results given in sections 5.5 - 5.7. In section 5.9, the model constructed from the RMC method is refined using the measured EXAFS spectra. The work is then concluded in section 5.10.

5.2 Background Theory

In this section the main theory required for ND, XRD and EXAFS spectroscopy is summarised. For ND, the isomorphic substitution method is also described. Because the structural model used for the EXAFS data analysis is obtained from modeling, overviews are given of the MD simulation and RMC modeling methods that were used.

5.2.1 ND Theory

As the rare-earth alumino-silicate glasses are isotropic, their structure can be described using the total structure factor and pair distribution function defined in chapter 2. From equation 2.26, the total structure factor $F(q)$ can be written as

$$F(q) = \sum_{\alpha,\beta}^{n} c_\alpha c_\beta b_\alpha b_\beta \left[S_{\alpha\beta}(q) - 1\right], \tag{5.1}$$

where $S_{\alpha\beta}(q)$ is a partial structure factor, and c_α and b_α denote the atomic fraction and coherent neutron scattering length of an atom of type α, respectively.

The total pair distribution function $G(r)$ is obtained from the Fourier transform relation

$$G(r) = \frac{1}{n_0 2\pi^2 r} \int_0^\infty F(q) q \sin(qr) dq \tag{5.2}$$

where n_0 is the atomic number density such that

$$G(r) = \sum_{\alpha,\beta}^{n} c_\alpha c_\beta b_\alpha b_\beta \left[g_{\alpha\beta}(r) - 1\right]. \tag{5.3}$$

As $g_{\alpha\beta}(r)$ is proportional to the probability of finding an atom of type β at a radial distance r from an atom of type α, its first peak position represents the nearest neighbour atomic distance between the two types of atom. The average coordination number for each type of atomic pair can be determined by finding the area under a peak in the relevant $r^2 g_{\alpha\beta}(r)$ function. The average coordination number of atoms of type β around an atom of type α can be calculated using equation 2.28,

$$\bar{n}_\alpha^\beta = 4\pi n_0 c_\beta \int_{r_1}^{r_2} g_{\alpha\beta}(r) r^2 dr, \tag{5.4}$$

where r_1 and r_2 are the minimum and maximum radii for the region of interest.

Because the experimental results from ND in this chapter are compared with XRD data, it is convenient to define $S_N(q)$ and $G_N(r)$ such that they are equivalent to the x-ray $S_X(q)$ and $G_X(r)$ functions;

$$S_N(q) = \frac{F(q)}{\langle b \rangle^2} + 1 \tag{5.5}$$

and

$$G_N(r) = \frac{G(r)}{\langle b \rangle^2} + 1, \tag{5.6}$$

where $\langle b \rangle = \sum_\alpha c_\alpha b_\alpha$ is the average coherent neutron scattering length.

Maximum structural information can be acquired from the results of a diffraction experiment by extracting the full set of $S_{\alpha\beta}(q)$ and $g_{\alpha\beta}(r)$ functions. Hence, if only a single $F(q)$ (or $G(r)$) is measured, limited information about the atomic distances and coordination numbers can be determined.

5.2.2 Method of Isomorphic Substitution in ND

For multi-component systems, the $F(q)$ and $G(r)$ functions involve many overlapping pair correlations which makes it difficult to gain quantitative information. There are, however, several methods that can be used to separate the overlapping correlations, including the methods of isotopic substitution [13] and isomorphic substitution in ND [29]. The limitation of the former method is the availability and price of suitable isotopes. The latter method involves substituting one or more of the elements with its isomorphic pair. In this work the method of isomorphic substitution in ND was applied to study rare-earth alumino-silicate glass.

Isomorphism refers to two or more elements that form the same compound with an identical structure. Because the process of compound formation mainly involves valence electrons, elements which have the same number of valence electrons can be chemically similar. For rare-earth elements, as the atomic number increases the additional electrons are added to the 4f shell and leave the valence shell unchanged. Moreover, adjacent rare-earth elements also have similar sizes and masses which can make them good isomorphic pairs. As seen by equation 5.1, the $F(q)$ functions

representing the same structure are dissimilar if the scattering lengths of one or more of the elements are different. Thus it is necessary to find isomorphic pairs that have different scattering lengths.

In the following subsections, the difference functions for isomorphic substitution of the rare-earth elements are described. The isomorphic elements or combinations of isomorphic elements are represented by R, R' and R'' and the corresponding total structure factors are represented by ${}^{R}F(q)$, ${}^{R'}F(q)$, and ${}^{R''}F(q)$, respectively. The scattering lengths for the isomorphic elements are denoted b_R, $b_{R'}$, and $b_{R''}$ where $b_R > b_{R'} > b_{R''}$. By using two total structure factors, the first order difference (FOD) and total minus weighted difference (TMWD) functions can be determined. The former contains only those pair correlation functions involving the rare-earth element R and the latter contains those pair correlation functions that do not involve R, the so called matrix atom μ correlations, with a small contribution from the $R - R$ correlations. By using three total structure factors, the second order difference (SOD) function, which is identical to the $R - R$ partial structure factor, can be determined.

First Order Difference (FOD) Functions

From equation 5.1, the correlations present in the ${}^{R}F(q)$, ${}^{R'}F(q)$, and ${}^{R''}F(q)$ functions have different weighting factors if they involve R but the same weighting factor if they only involve μ. If we take a difference between any two $F(q)$ functions, the contributions from the μ-μ correlations will thus cancel and only those correlations involving R remain. The FOD functions are defined by [149]

$$\Delta F_R^{(1)}(q) \equiv {}^{R}F(q) - {}^{R''}F(q) \tag{5.7}$$

$$= \Delta F_{R\mu}^{(1)}(q) + c_R^2 \delta_R^{(1)} \varsigma_R^{(1)} \left[S_{RR}(q) - 1 \right], \tag{5.8}$$

$$\Delta F_R^{(2)}(q) \equiv {}^{R}F(q) - {}^{R'}F(q) \tag{5.9}$$

$$= \Delta F_{R\mu}^{(2)}(q) + c_R^2 \delta_R^{(2)} \varsigma_R^{(2)} \left[S_{RR}(q) - 1 \right] \tag{5.10}$$

and

$$\Delta F_R^{(3)}(q) \equiv {}^{R'}F(q) - {}^{R''}F(q) \quad (5.11)$$

$$= \Delta F_{R\mu}^{(3)}(q) + c_R^2 \delta_R^{(3)} \varsigma_R^{(3)} \left[S_{RR}(q) - 1\right] \quad (5.12)$$

where $\delta_R^{(1)} = b_R - b_{R''}$, $\delta_R^{(2)} = b_R - b_{R'}$, $\delta_R^{(3)} = b_{R'} - b_{R''}$, $\varsigma_R^{(1)} = b_R + b_{R''}$, $\varsigma_R^{(2)} = b_R + b_{R'}$, $\varsigma_R^{(3)} = b_{R'} + b_{R''}$,

$$\Delta F_{R\mu}^{(1)}(q) = \sum_\mu 2 c_R c_\mu b_\mu \delta_R^{(1)} \left[S_{R\mu}(q) - 1\right], \quad (5.13)$$

$$\Delta F_{R\mu}^{(2)}(q) = \sum_\mu 2 c_R c_\mu b_\mu \delta_R^{(2)} \left[S_{R\mu}(q) - 1\right] \quad (5.14)$$

and

$$\Delta F_{R\mu}^{(3)}(q) = \sum_\mu 2 c_R c_\mu b_\mu \delta_R^{(3)} \left[S_{R\mu}(q) - 1\right]. \quad (5.15)$$

It can be seen from equations 5.13 to 5.15 that $\Delta F_{R\mu}^{(1)}(q)/\delta_R^{(1)} = \Delta F_{R\mu}^{(2)}(q)/\delta_R^{(2)} = \Delta F_{R\mu}^{(3)}(q)/\delta_R^{(3)}$. The real space functions corresponding to the $\Delta F_R^{(n)}(q)$ (n = 1, 2 or 3) functions are given by the Fourier transform relation

$$\Delta G_R^{(n)}(r) = \frac{1}{n_0 2\pi^2 r} \int_0^\infty \Delta F_R^{(n)}(q) q \sin(qr) dq. \quad (5.16)$$

Total Minus Weighted Difference (TMWD) Functions

If one of the $F(q)$ function is scaled such that the weighting factors for the $R-\mu$ correlations are the same as for another $F(q)$ function, the difference between the two functions is a so called TMWD function which contains no $R-\mu$ correlations. The TMWD functions are defined by

$$\Delta F^{(1)}(q) \equiv \frac{1}{\delta_R^{(1)}} \left[b_R \cdot {}^{R''}F(q) - b_{R''} \cdot {}^{R}F(q)\right] \quad (5.17)$$

$$= \Delta F_{\mu\mu}(q) - c_R^2 b_R b_{R''} \left[S_{RR}(q) - 1\right] \quad (5.18)$$

$$\Delta F^{(2)}(q) \equiv \frac{1}{\delta_R^{(2)}} \left[b_R \cdot {}^{R'}F(q) - b_{R'} \cdot {}^{R}F(q)\right] \quad (5.19)$$

$$= \Delta F_{\mu\mu}(q) - c_R^2 b_R b_{R'} \left[S_{RR}(q) - 1\right] \quad (5.20)$$

and

$$\Delta F^{(3)}(q) \equiv \frac{1}{\delta_R^{(3)}}\left[b_{R'} \cdot {}^{R''}F(q) - b_{R''} \cdot {}^{R'}F(q)\right] \quad (5.21)$$

$$= \Delta F_{\mu\mu}(q) - c_R^2 b_{R'} b_{R''}\left[S_{RR}(q) - 1\right] \quad (5.22)$$

where

$$\Delta F_{\mu\mu}(q) = \sum_{\mu,\mu'} c_\mu c_{\mu'} b_\mu b_{\mu'}\left[S_{\mu\mu'}(q) - 1\right]. \quad (5.23)$$

The real space functions corresponding to the $\Delta F^{(n)}(q)$ ($n = 1$, 2 or 3) functions are given by the Fourier transform relation

$$\Delta G^{(n)}(r) = \frac{1}{n_0 2\pi^2 r}\int_0^\infty \Delta F^{(n)}(q) q \sin(qr) dq. \quad (5.24)$$

Second Order Difference (SOD) Function

The advantage of the FOD and TMWD functions is that they are obtainable from only two $F(q)$ functions. However, with three $F(q)$ functions the SOD function $S_{RR}(q)$ can be determined where

$$S_{RR}(q) - 1 = \frac{1}{c_R^2 \delta_R^{(3)}}\left(\frac{\Delta F_R^{(2)}(q)}{\delta_R^{(2)}} - \frac{\Delta F_R^{(1)}(q)}{\delta_R^{(1)}}\right), \quad (5.25)$$

or, expressed in terms of the three $F(q)$ functions,

$$S_{RR}(q) - 1 = \frac{(1-\gamma) \cdot {}^{R}F(q) - {}^{R'}F(q) + \gamma \cdot {}^{R''}F(q)}{c_R^2 \gamma(1-\gamma)(\delta_R^{(1)})^2} \quad (5.26)$$

where $\gamma = \delta_R^{(2)}/\delta_R^{(1)}$ and $(1-\gamma) = \delta_R^{(3)}/\delta_R^{(1)}$.

The $\Delta F_{R\mu}^{(n)}(q)$ and $\Delta F_{\mu\mu}(q)$ functions can then be determined from

$$\Delta F_{R\mu}^{(1)}(q) = \frac{-(1-\gamma)\varsigma_R^{(3)} \cdot {}^{R}F(q) + \varsigma_R^{(1)} \cdot {}^{R'}F(q) - \gamma\varsigma_R^{(2)} \cdot {}^{R''}F(q)}{\gamma(1-\gamma)\delta_R^{(1)}}, \quad (5.27)$$

$$\Delta F_{R\mu}^{(2)}(q) = \frac{-(1-\gamma)\varsigma_R^{(3)} \cdot {}^{R}F(q) + \varsigma_R^{(1)} \cdot {}^{R'}F(q) - \gamma\varsigma_R^{(2)} \cdot {}^{R''}F(q)}{(1-\gamma)\delta_R^{(1)}}, \quad (5.28)$$

$$\Delta F_{R\mu}^{(3)}(q) = \frac{-(1-\gamma)\varsigma_R^{(3)} \cdot {}^{R}F(q) + \varsigma_R^{(1)} \cdot {}^{R'}F(q) - \gamma\varsigma_R^{(2)} \cdot {}^{R''}F(q)}{\gamma\delta_R^{(1)}} \quad (5.29)$$

and

$$\Delta F_{\mu\mu}(q) = \frac{b_{R'}b_{R''}(1-\gamma)\cdot {}^{R}F(q) - b_R b_{R''}\cdot {}^{R'}F(q) + b_R b_{R'}\gamma\cdot {}^{R''}F(q)}{\gamma(1-\gamma)(\delta_R^{(1)})^2}. \tag{5.30}$$

The real space functions corresponding to the $\Delta F_{R\mu}^{(n)}(q)$ (n = 1, 2 or 3) and $\Delta F_{\mu\mu}(q)$ functions are given by the Fourier transform relations

$$\Delta G_{R\mu}^{(n)}(r) = \frac{1}{n_0 2\pi^2 r}\int_0^\infty \Delta F_{R\mu}^{(n)}(q) q\sin(qr)dq \tag{5.31}$$

and

$$\Delta G_{\mu\mu}(r) = \frac{1}{n_0 2\pi^2 r}\int_0^\infty \Delta F_{\mu\mu}(q) q\sin(qr)dq. \tag{5.32}$$

5.2.3 High Energy XRD Theory

From equation 2.44, the x-ray total structure factor $F_X(q)$ can be written in terms of the Faber-Ziman partial structure factors $S_{\alpha\beta}(q)$ as

$$F_X(q) = \sum_{\alpha,\beta}^{n} c_\alpha c_\beta f_\alpha(q) f_\beta^*(q)\left[S_{\alpha\beta}(q) - 1\right], \tag{5.33}$$

where $f_\alpha(q)$ is the x-ray form factor for an atom of type α. In this chapter, the x-ray total structure factor is represented by $S_X(q)$ where

$$S_X(q) = \frac{F_X(q)}{\overline{f(q)}^2} + 1, \tag{5.34}$$

and $\overline{f(q)} = \sum_\alpha c_\alpha f_\alpha(q)$ is the average form factor. The total pair distribution function $G_X(r)$ is obtained by Fourier transforming $S_X(q)$ where

$$G_X(r) - 1 = \frac{1}{n_0 2\pi^2 r}\int_0^\infty [S_X(q) - 1] q\sin(qr)dq \tag{5.35}$$

and n_0 is the number density.

An average coordination number can be calculated from $g_{\alpha\beta}(r)$ using equation 5.4. For the $G(r)$ and $G_X(r)$ functions, if only one $g_{\alpha\beta}(r)$ function contributes to a peak, the corresponding average coordination number can be found. In the case of ND, the coordination number determination is straight forward since the weighting factors on the $(g_{\alpha\beta}(r) - 1)$ functions are independent of r, see section 5.5.3. In the case of XRD, however, the q dependent form factors in $S_X(q)$ lead to weighting

factors on the $(g_{\alpha\beta}(r) - 1)$ functions that are r dependent. Coordination numbers have, therefore, to be determined from a modified total pair distribution ${}^{mod}G'_X(r)$. An outline of the method is as follows [48, 150].

Consider the relation between $S_{\alpha\beta}(q)$ and $g_{\alpha\beta}(r)$

$$g_{\alpha\beta}(r) - 1 = \frac{1}{n_0 2\pi^2 r} \int_0^\infty [S_{\alpha\beta}(q) - 1] q \sin(qr) dq. \tag{5.36}$$

Let the q dependent weighting factor on $[S_{\alpha\beta}(q) - 1]$ be regarded as a modification function $M_{\alpha\beta}(q)$ and define a modified pair distribution function as

$$h_{\alpha\beta}(r) = \frac{1}{n_0 2\pi^2 r} \int_0^\infty [S_{\alpha\beta}(q) - 1] M_{\alpha\beta}(q) q \sin(qr) dq, \tag{5.37}$$

where the Fourier transform of $M_{\alpha\beta}(q)$ is given by

$$P_{\alpha\beta}(r) = \frac{1}{2\pi} \int_{-\infty}^\infty M_{\alpha\beta}(q) e^{-iqr} dq. \tag{5.38}$$

Define $d_{\alpha\beta}(r)$ and $d'_{\alpha\beta}(r)$ functions by the relations [48]

$$d_{\alpha\beta}(r) = 4\pi n_0 r [g_{\alpha\beta}(r) - 1] \tag{5.39}$$

$$d'_{\alpha\beta}(r) = 4\pi n_0 r [h_{\alpha\beta}(r)]. \tag{5.40}$$

Then

$$\begin{aligned} d'_{\alpha\beta}(r) &= \frac{2}{\pi} \int_0^\infty [S_{\alpha\beta}(q) - 1] M_{\alpha\beta}(q) q \sin(qr) dq \\ &= d(r) \otimes P_{\alpha\beta}(r) \\ &= 4\pi n_0 r [g_{\alpha\beta}(r) - 1] \otimes P_{\alpha\beta}(r) \\ &= 4\pi n_0 \int_{-\infty}^\infty r' g_{\alpha\beta}(r') P_{\alpha\beta}(r - r') dr' - 4\pi n_0 \int_{-\infty}^\infty r' P_{\alpha\beta}(r - r') dr' \\ &= 4\pi n_0 \int_{-\infty}^\infty r' g_{\alpha\beta}(r') P_{\alpha\beta}(r - r') dr' - 4\pi n_0 r M_{\alpha\beta}(q = 0), \end{aligned} \tag{5.41}$$

where the inverse Fourier transform of equation 5.38 is

$$M_{\alpha\beta}(q) = \int_{-\infty}^\infty P_{\alpha\beta}(r) e^{iqr} dr \tag{5.42}$$

which gives $\int_{-\infty}^\infty P_{\alpha\beta}(r) dr = M_{\alpha\beta}(q = 0)$.

For an XRD experiment on a polyatomic system, the measured structure factor

$$S'_X(q) - 1 \equiv \sum_{\alpha,\beta} M_{\alpha\beta}(q) \left[S_{\alpha\beta}(q) - 1 \right], \tag{5.43}$$

where

$$M_{\alpha\beta}(q) = \frac{c_\alpha c_\beta f_\alpha(q) f^*_\beta(q) M_{cut}(q)}{\overline{f(q)}^2} \tag{5.44}$$

and $M_{cut}(q) = 1$ when $0 \leq q \leq q_{\max}$ and $M_{cut}(q) = 0$ when $q > q_{\max}$. For the rare-earth alumino-silicate glasses presented in this chapter, the peak in $G'_X(r)$ corresponding to the R-O correlations is relatively isolated and it is thus useful to determine the R-O coordination number. From equations 5.33 and 5.34, the prefactor on the $S_{RO}(q)$ function can be removed by defining the modified x-ray total structure factor

$$^{mod}S'_X(q) - 1 = \sum_{\alpha,\beta} {}^{mod}M_{\alpha\beta}(q) \left[S_{\alpha\beta}(q) - 1\right], \tag{5.45}$$

where

$$^{mod}M_{\alpha\beta}(q) = \frac{M_{\alpha\beta}(q)\overline{f(q)}^2}{c_{\mathrm{R}} c_{\mathrm{O}}[f^*_{\mathrm{R}}(q) f_{\mathrm{O}}(q) + f_{\mathrm{R}}(q) f^*_{\mathrm{O}}(q)]}. \tag{5.46}$$

The R-O coordination number can then be calculated from

$$\bar{n}^{\mathrm{O}}_{\mathrm{R}} = 4\pi n_0 c_{\mathrm{O}} \int_{r_1}^{r_2} [\,{}^{mod}G'_X(r) - \,{}^{mod}G'_X(0)] r^2 dr, \tag{5.47}$$

where $^{mod}G'_X(r)$ is the Fourier transform of the $^{mod}S'_X(q)$ function, $g_{\mathrm{RO}}(r) = \,^{mod}G'_X(r) - \,^{mod}G'_X(0)$ and the region of the first peak in $g_{\mathrm{RO}}(r)$ is from r_1 to r_2.

To find the $^{mod}G'_X(0)$ value, first consider

$$^{mod}D'_X(r) = \sum_{\alpha,\beta} {}^{mod}d'_{\alpha\beta}(r). \tag{5.48}$$

As $r \to 0$, $g_{\alpha\beta}(r)$ is zero and from equations 5.41 and 5.48 we have that at small r

$$^{mod}D'_X(r) = -4\pi n_0 r \sum_{\alpha,\beta} {}^{mod}M_{\alpha\beta}(q = 0). \tag{5.49}$$

Since $^{mod}D'_X(r) \equiv 4\pi n_0 r[\,^{mod}G'_X(r) - 1]$ it follows that at small r

$$^{mod}G'_X(r) = 1 - \sum_{\alpha,\beta} {}^{mod}M_{\alpha\beta}(q = 0) \tag{5.50}$$

such that at $r = 0$

$$^{mod}G'_X(0) = 1 - \sum_{\alpha,\beta} {}^{mod}M_{\alpha\beta}(q = 0). \tag{5.51}$$

5.2.4 EXAFS Theory

For crystalline systems or glasses with an ordered local structure, the EXAFS signal $\chi(k)$ can be calculated from a given structural model using equation 2.64

$$\chi(k) = \sum_{j=1}^{\text{all paths}} S_0^2 N_j \frac{F_j^{eff}(k)}{kR_{0,j}^2} e^{-2(R_{0,j}-\Delta)/\lambda} e^{-2k^2\sigma_j^2} \sin[2kR_{0,j} + \delta_j^{eff}(k)] \qquad (5.52)$$

where S_0^2 is the amplitude reduction factor, $F_j^{eff}(k)$ is the backscattering amplitude, $R_{0,j}$ is the nominal half path length, $R_{0,j} - \Delta$ is an effective half path length, N_j, σ_j^2 and δ_j^{eff} are the number of degeneracies, the EXAFS Debye-Waller factor and the signal phase shift for scattering path j, respectively, and λ is the photoelectron mean free path.

By taking into account a degree of structural disorder i.e. a non-Gaussian form for the pair distribution functions, equation 5.52 can be re-written after employing a cumulant expansion, as described in section 2.3.6, as

$$\begin{aligned} \chi(k) \;=\; \text{Im}\Bigg\{ & \sum_{j=1}^{\text{all paths}} \frac{S_0^2 N_j F_j^{eff}(k)}{k(R_{0,j}+\Delta R_j)^2} \exp\{-2k^2\sigma_j^2 + \frac{2}{3}k^4 C_{4,j}\} \\ & \exp\{i(2k(R_{0,j}+\Delta R_j) - \frac{4k\sigma_j^2}{R_{0,j}} - \frac{4}{3}k^3 C_{3,j} + \delta_j^{eff}(k))\} \Bigg\} \end{aligned} \qquad (5.53)$$

where ΔR_j is the difference between the actual and nominal half path length, while $C_{3,j}$ and $C_{4,j}$ are the third and forth order cumulants, respectively.

In EXAFS data analysis, the $\tilde{\chi}(R)$ function obtained by Fourier transforming the measured $k^\omega\chi(k)$ function, where $\omega = 0$, 1, 2, or 3 determines the k weighting of $\chi(k)$, is used to refine the $\tilde{\chi}(R)$ function calculated from a model by fitting S_0^2 and the variables σ_j^2, ΔR_j and N_j for each scattering path j. The value of E_0 can also be refined using the parameter ΔE_0 such that k is given by equation 3.35,

$$k = \sqrt{\frac{2m_e(E - (E_0 + \Delta E_0))}{\hbar^2}}.$$

The refinement minimises the statistical parameter χ^2,

$$\chi^2 = \frac{N_{idp}}{N_{data}} \sum_{i=1}^{N_{data}} \left| \frac{\tilde{\chi}(R_i)_{data} - \tilde{\chi}(R_i)_{model}}{\epsilon_i} \right|^2, \qquad (5.54)$$

where N_{data} is the number of data points in the R window range, N_{idp} is the number of independent data points in this range, and ϵ_i is the measurement uncertainty. χ^2_ν was used to compare the goodness of the fits where

$$\chi^2_\nu = \frac{\chi^2}{N_{idp} - N_{var}} \tag{5.55}$$

and $N_{var} < N_{idp}$ is the number of variables in the fit. As χ^2_ν depends on an estimation of the measurement uncertainty ϵ_i, the $\mathcal{R}$-factor was also calculated for each fit where

$$\mathcal{R} = \frac{\sum_{i=1}^{N_{data}} |\tilde{\chi}(R_i)_{data} - \tilde{\chi}(R_i)_{model}|^2}{\sum_{i=1}^{N_{data}} |\tilde{\chi}(R_i)_{data}|^2}. \tag{5.56}$$

5.2.5 Molecular Dynamics (MD) Simulation

The method of MD simulation [37, 38] employs the use of potentials to create a 3D model of a system. The simulation starts from an initial configuration, which could be a random distribution of particles, and then the forces derived from specified potentials are used to move the particles according to Newton's laws of motion. The desired configuration is obtained when the system reaches equilibrium e.g. its energy is minimised and fluctuating about a constant. The potentials used in the simulation presented in this chapter are Buckingham and Coulomb potentials, see section 5.8 for details. The former represents the short ranged 2-body interactions while the latter is applied because the system comprises charged particles and is treated using the Ewald sum technique outlined in [37].

Forces are derived from each potential by taking the first derivative,

$$\mathbf{f}_i = -\frac{\partial}{\partial \mathbf{r}_i}\left[\sum_n \mathcal{U}_n(\mathbf{r}^N)\right], \tag{5.57}$$

where $\mathcal{U}_n(\mathbf{r}^N)$ is a specified potential n and $\mathbf{r}^N = (\mathbf{r}_1, \mathbf{r}_2, ..., \mathbf{r}_N)$ represents the complete set of $3N$ particle coordinates. The trajectories for each particle can then be calculated from Newton's equations of motion,

$$\frac{\partial \mathbf{p}_i}{\partial t} = \mathbf{f}_i \tag{5.58}$$

and

$$\frac{\partial \mathbf{r}_i}{\partial t} = \mathbf{v}_i = \frac{\mathbf{p}_i}{m_i} \tag{5.59}$$

where $\frac{\partial}{\partial t}$ represents the first derivative with respect to time, while m_i, $\mathbf{v}_i$ and $\mathbf{p}_i$ are the mass, velocity and momentum of particle i. There are several integration algorithms that can be used to solve equations 5.58 and 5.59 for a given time step δt. The most common is one form or another of a Verlet algorithm [151]. For the MD results presented in this chapter the Velocity Verlet (VV) algorithm in the MD simulation program DL_POLY [152] was used.

In the VV algorithm, the positions of the particles after one time step δt are calculated in two stages. In the first stage, the velocity of a particle for a half time step is calculated. From equations 5.58 and 5.59,

$$\mathbf{v}_i(t + \frac{1}{2}\delta t) = \mathbf{v}_i(t) + \frac{\mathbf{f}_i(t)}{m_i}\frac{\delta t}{2}. \tag{5.60}$$

The position at the full time step can then be determined from

$$\mathbf{r}_i(t + \delta t) = \mathbf{r}_i(t) + \mathbf{v}_i(t + \frac{1}{2}\delta t)\delta t. \tag{5.61}$$

In the second stage, the new position is used to calculate the force for the next time step $\mathbf{f}_i(t + \delta t)$ and the velocity of the particle in the new position is calculated from

$$\mathbf{v}_i(t + \delta t) = \mathbf{v}_i(t + \frac{1}{2}\delta t) + \frac{\mathbf{f}_i(t + \delta t)}{m_i}\frac{\delta t}{2}. \tag{5.62}$$

From the two stage calculation, the positions, velocities and forces for each particle can be updated for each time step δt.

Because the system of interest in this chapter is glassy, the simulation needs to start from an equilibrium liquid state at high temperature before quenching to room temperature [145]. For this, the NVT (constant number of particles, volume and temperature) ensemble was used and the temperature was controlled by using the Berendsen thermostat. In the simulation, the instantaneous temperature is determined from

$$\mathcal{T} = \frac{\Sigma_{i=1}^{\mathcal{N}} m_i v_i^2(t)}{k_B f}, \tag{5.63}$$

where $\mathcal{N}$ is the number of particles in the system, k_B is Boltzmann's constant and f is the number of degrees of freedom for a particle in the system. The temperature is maintained at the desired temperature T_{ext} by connecting the system to a heat bath such that trajectories in the canonical or pseudo canonical ensembles are generated.

For the Berendsen thermostat, the instantaneous temperature is guided towards the desired temperature by scaling the velocity at each step by the scaling factor

$$\chi(t) = \left[1 + \frac{\delta t}{\tau_T}\left(\frac{T_{ext}}{\mathcal{T}(t)} - 1\right)\right]^{1/2}, \tag{5.64}$$

where τ_T is a specified time constant, normally taking a value between 0.5 and 2 ps.

5.2.6 Reverse Monte Carlo (RMC) Modeling

RMC modeling [39] creates a 3D model of a system from at least one x-ray or neutron total structure factor or pair distribution function. The modeling starts from an initial configuration which could be a random distribution of particles in the simulation box. The particles are moved in such a way that the difference between the measured and calculated pair correlation functions is minimised. The desired configuration is obtained when the difference between the measured and calculated pair correlation functions minimises and becomes constant. An overview of the RMC method is as follows [153].

First, an initial configuration consisting of $\mathcal{N}$ particles and the same density as the real sample is constructed. If a crystal structure for a similar system is known, the program ATOM available from the RMCA package [154] can be used to generate the configuration. If a suitable crystal structure is not known, the initial configuration can be constructed from a hard sphere Monte Carlo simulation where the distance of closest approach for each type of particle is set. The initial configuration can also be a random configuration although the procedure will in general take a longer time. The program calculates a partial pair distribution function from a configuration by using the equation

$$g_{\alpha\beta}^{C_o}(\mathbf{r}) = \frac{n_{\alpha\beta}^{C_o}(\mathbf{r})}{4\pi r^2 \Delta r n_0 c_\beta}, \tag{5.65}$$

where $n_{\alpha\beta}^{C_0}(\mathbf{r})$ is the number of particles of type β around a particle of type α between radial distances of r and $r + \Delta r$ averaged over all particles of type α. Superscript C_o signifies that the value will be re-calculated in later steps. Note that the value of $\mathcal{N}$ has to be large enough such that $g_{\alpha\beta}^{C_o}(\mathbf{r}) = 1$ for $r > L/2$ where L^3 is the volume of a cubic simulation box. The Fourier transform of $g_{\alpha\beta}^{C_o}(\mathbf{r})$ gives the partial structure

factor

$$S^{C_o}_{\alpha\beta}(\mathbf{q}) - 1 = n_0 \int [g^{C_o}_{\alpha\beta}(\mathbf{r}) - 1] e^{i\mathbf{q}\cdot\mathbf{r}} d\mathbf{r}. \tag{5.66}$$

and the total structure factor is calculated from

$$F^{C_o}(\mathbf{q}) = \sum_{\alpha,\beta}^{n} c_\alpha c_\beta b_\alpha b_\beta \left[S^{C_o}_{\alpha\beta}(\mathbf{q}) - 1\right] \tag{5.67}$$

in the case of ND or

$$F^{C_o}(\mathbf{q}) = \sum_{\alpha,\beta}^{n} c_\alpha c_\beta f_\alpha(q) f^*_\beta(q) \left[S^{C_o}_{\alpha\beta}(\mathbf{q}) - 1\right] \tag{5.68}$$

in the case of XRD.

The difference between the calculated structure factor $F^{C_o}(\mathbf{q})$ and the structure factor obtained from the experiment $F^E(\mathbf{q})$ is calculated using the relation

$$\chi^2_o = \sum_{i=1}^{m} \frac{(F^{C_o}(q_i) - F^E(q_i))^2}{\sigma^2(q_i)}, \tag{5.69}$$

where the sum is over all m measured data points i and $\sigma^2(q_i)$ is an experimental error. As systematic errors are usually unknown, a uniform value for $\sigma^2(q_i)$ is usually used. A move for one particle is then generated randomly. When the particle is moved, new partial pair distribution functions $g^{C_n}_{\alpha\beta}(\mathbf{r})$, partial structure factors $S^{C_n}_{\alpha\beta}(\mathbf{q})$ and total structure factor $F^{C_n}(\mathbf{q})$ are evaluated. The difference between $F^E(\mathbf{q})$ and $F^{C_n}(\mathbf{q})$,

$$\chi^2_n = \sum_{i=1}^{m} \frac{(F^{C_n}(q_i) - F^E(q_i))^2}{\sigma^2(q_i)}, \tag{5.70}$$

is then compared with the previously calculated value of χ^2_o. If $\chi^2_n < \chi^2_o$, the new configuration is accepted and the new configuration overwrites the old configuration. If $\chi^2_n > \chi^2_o$ the new configuration is accepted with a probability of $e^{\frac{-(\chi^2_n - \chi^2_o)}{2}}$. The structures are re-calculated by iteration until χ^2_n reduces and reaches an equilibrium value. After the modeling reaches equilibrium, the value of χ^2 will still fluctuate and statistically independent configurations can be collected if they are least $5\mathcal{N}$ accepted moves apart [153].

If there are multiple data sets, χ^2 is taken to be the sum,

$$\chi^2 = \sum_{k=1}^{n} \sum_{i=1}^{m} \frac{(F^{C_n}_k(q_i) - F^E_k(q_i))^2}{\sigma^2_k(q_i)}, \tag{5.71}$$

where n is the number of data sets. Physical constraints such as the distance of closest approach between each type of particle (the so called cutoff distance), the maximum displacement of a particle for each move, the coordination numbers and the bond angle distributions can also be included in the simulations by adding extra terms to χ^2. For example, if f_{req} is the required proportion of particles of type α which have a desired coordination number and f_{RMC} is the proportion of particles of type α which have that desired coordination number in the model, an addition term corresponding to this constraint is given by

$$\chi^{2\,\prime} = \chi^2 + (f_{req} - f_{RMC})/\sigma_c^2, \tag{5.72}$$

where $\chi^{2\,\prime}$ represents the χ^2 term calculated from the data as in equation 5.71 with the imposition of other constraints if they are present, while σ_c^2 is the weighting factor for the constraint. It should be noted that the RMC algorithm does not generate a unique solution. The produced configuration is one possible structure that agrees with a given set of experimental data and the applied physical constraints. There are a few RMC algorithm packages available including RMCA [154] and RMC++ [155, 156].

For the results presented in this chapter, a 3D model of the system was calculated using the MD-RMC method which means that an MD simulation was used to create an initial configuration for the RMC modeling. It was found that when a hard sphere model was used as an initial configuration, the RMC model got trapped in a local minimum as seen by a large value for χ^2. As there are no crystal structures available for the system of interest, the initial configuration was obtained from the MD simulation. The configuration obtained from the MD simulation led to pair correlation functions that resemble the experimental data sufficiently well that the local minimum found during the initial RMC modeling was bypassed.

5.3 Experiment

The $(R_2O_3)_{0.2}(Al_2O_3)_{0.2}(SiO_2)_{0.6}$ glasses where R denotes Dy were measured using ND, XRD and EXAFS spectroscopy. For ND, the glasses with R = Ho or a 50:50 mixture of Dy and Ho were also measured in order to use the method of

isomorphic substitution. For EXAFS, the glass where R = Ho was also measured and the local structure of Ho was compared with that of Dy.

The glass samples were prepared by dry mixing powders of 99.99% purity Dy_2O_3, 99.99% purity Ho_2O_3 and 99.995% purity SiO_2 commercially available from Alfa-Aeser, and 99.998% purity Al_2O_3 commercially available from Sigma-Aldrich in a Pt-Rh crucible with the correct weight percent. The powder mixture was then put inside a furnace and left at 1600 °C for one hour. Because these samples are not hygroscopic they were quenched in air on a liquid N_2 cooled Cu block while dousing with liquid N_2. Pictures of the glasses are shown in figure 5.1 and details for each experiment are described in the following.

(a) (b) (c)

Figure 5.1: (a), (b) and (c) show the as prepared $(R_2O_3)_{0.2}(Al_2O_3)_{0.2}(SiO_2)_{0.6}$ glasses where R denotes (a) Dy, (b) Ho or (c) a 50:50 mixture of Dy and Ho.

5.3.1 ND Experiment

For the ND experiment, the glasses were crushed into small pieces and filled into a cylindrical vanadium can of 4.8 mm inner diameter with a 0.1 mm wall thickness. The vanadium can was placed inside the evacuated bell jar of the D4c diffractometer at the ILL where the measurements were performed at room temperature with an incident neutron wavelength of 0.49751(1) Å. The measurements were made using a series of 2 hour or 30 minute scans thus enabling a stability check to be made by calculating the ratio between the measured intensities for consecutive scans. If the sample is stable, the ratio is unity. The final signal was obtained by averaging all of the scans and the total counting times were 17 hours for each sample.

The neutron wavelength along with the zero angle offset of the detectors were determined by using the diffraction pattern for a powdered Ni sample. The beam

height was chosen to be 5.2 cm, which was less than the sample height, to ensure that the incident beam fully illuminated the samples. In addition, diffraction measurements were made at room temperature for the empty bell jar, the empty vanadium can, a vanadium rod of 6.37 mm diameter and a $^{10}B_4C$ absorber of 5 mm width for data normalisation and background correction purposes.

5.3.2 High Energy XRD Experiment

For the high energy XRD experiment, the glasses were polished into thin pieces of 1 mm thickness. The measurement was made at room temperature with slab geometry on beamline ID15B at the ESRF. The incident x-ray wavelength was 0.1397 Å. The data were treated [157] using a standard data analysis procedure [28] with the Compton scattering correction taken from [158] and the atomic x-ray form factors taken from [159].

5.3.3 EXAFS Experiment

For the EXAFS experiment, the glasses were finely ground, mixed with cellulose powder and pressed into pellets using a 13 mm die. The glasses were ground by either a ball milling machine or a diamond file. Although the former is a much more convenient method, it could induce crystallisation as the glasses are subjected to great forces during the grinding procedure. A second set of samples was therefore prepared by using a diamond file. Although cellulose decomposes at a relatively low temperature it makes a strong pellet suitable for a room temperature experiment. The chosen mass ratio between the glass and cellulose was based on the required quantity of glass which makes up a thickness of one absorption length x_{abs} and the required quantity of cellulose which can stabilise the pellet. The mass of the glass was determined from

$$m_s = \rho \cdot x_{abs} \cdot A, \tag{5.73}$$

where ρ is the mass density of the glass and A is the surface area of the pellet. For a 13 mm diameter pellet, 100 mg of cellulose is usually enough. Thus the desired mass ratio between cellulose and the sample is $100/m_s$ and the required mass of the

mixture in the pellet is $100 + m_s$ mg. The glass:cellulose mass ratio used was 1:11 for $(Dy_2O_3)_{0.2}(Al_2O_3)_{0.2}(SiO_2)_{0.6}$ and 1:10 for $(Ho_2O_3)_{0.2}(Al_2O_3)_{0.2}(SiO_2)_{0.6}$. Figure 5.2 shows a pellet fitted into the sample holder. The absorption lengths used in the

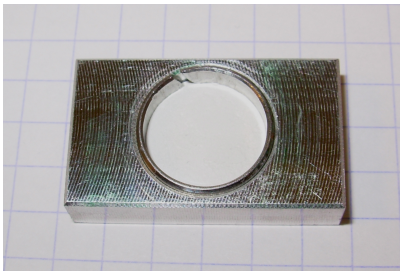

Figure 5.2: A mixture of the $(Dy_2O_3)_{0.2}(Al_2O_3)_{0.2}(SiO_2)_{0.6}$ glass and cellulose pressed into a pellet and placed in the sample holder for the EXAFS measurement.

calculation for this experiment were effective absorption lengths calculated using the program XASAM in the GNXAS package [160]. XASAM determines an effective absorption length by taking into account the effect of attenuation caused by other elements present in the sample. The effective absorption length used was 15.8 μm for $(Dy_2O_3)_{0.2}(Al_2O_3)_{0.2}(SiO_2)_{0.6}$ and 15.9 μm for $(Ho_2O_3)_{0.2}(Al_2O_3)_{0.2}(SiO_2)_{0.6}$.

The EXAFS experiment was performed at room temperature in transmission mode on beamline BM29 at the ESRF. For $(Dy_2O_3)_{0.2}(Al_2O_3)_{0.2}(SiO_2)_{0.6}$, the XAS spectra were collected in the energy range of the Dy L_{III} edge, from 7.602 - 8.651 keV (Dy L_{III} edge = 7.790 keV [161]), and for $(Ho_2O_3)_{0.2}(Al_2O_3)_{0.2}(SiO_2)_{0.6}$ the XAS spectra were collected in the energy range of the Ho L_{III} edge, from 7.879 - 8.929 keV (Ho L_{III} edge = 8.071 keV [161]), using ionization chambers, see section 3.4.4. The ionization chambers I_0, I_1 and I_2 were filled with a mixture of N_2 or Ar and He gas to the operating pressure of the chambers at 2 bar. For I_0, the ionization chamber was filled with 1 bar of N_2 to achieve a 30% efficiency and for I_1 and I_2 the ionization chambers were filled with 0.19 bar of Ar to achieve a 70% efficiency. The reference samples used for an *in situ* check on the energy calibration were Co foil for the measurement in the energy range of the Dy L_{III} edge and Ni foil for the measurement in the energy range of the Ho L_{III} edge as the energies of the K edges for Co and Ni are closest to the energies of the Dy and Ho L_{III} edges, respectively (Co K edge energy = 7.709 keV and Ni K edge energy = 8.333 keV [161]).

5.4 Sample Parameters

The densities of the $(R_2O_3)_{0.2}(Al_2O_3)_{0.2}(SiO_2)_{0.6}$ glasses, where R denotes Dy or Ho, were measured by using Archimedes principle and values of 4.459(5) and 4.557(5) g/cm^3 were obtained, respectively. The number density $n_0 = \rho N_A/M_w$, where $N_A = 6.022 \times 10^{23}$ mol^{-1} is the Avogadro number and M_w is the molecular weight, are 0.078(1) Å^{-3} for both glasses. This number density was also used for the glass where R denotes a 50:50 mixture of Dy and Ho.

For the ND experiment, the coherent scattering lengths, scattering cross-sections and absorption cross-sections for all the elements were taken from [43, 162] except those for Dy since the scattering by the ^{163}Dy and ^{164}Dy isotopes is effected by resonances for an incident neutron wavelength of around 0.5 Å [118, 163]. The coherent scattering lengths, scattering cross-sections and absorption cross-sections for the ^{163}Dy isotope were calculated according to [118] and those for the ^{164}Dy isotope were taken from [163]. Natural Dy contains 7 isotopes. The coherent scattering length, scattering cross-section and absorption cross-section of natural Dy were therefore calculated by weighting the contribution from each isotope by the natural isotopic abundance. The values for natural Dy obtained from reference [43] and those obtained from reference [118, 163] are compared in table 5.1. Several of the parameters used in the data analysis are summarised in table 5.2.

	From reference [43]	From reference [118, 163]
Coherent scattering length (fm)	16.9(2)	15.7(2)
Scattering cross-section (barn)	90.3(9)	76(3)
Absorption cross-section at 0.5 Å (barn)	276(4)	283(13)

Table 5.1: A comparison between the coherent scattering lengths, scattering cross-sections, and absorption cross-sections of Dy obtained from reference [43] and [118, 163].

Both Dy^{3+} and Ho^{3+} are paramagnetic and the magnetic form factors were calculated using equation 2.41. However, as equation 2.41 was derived for an isolated atom, the form factor can be different for an element which is in a compound. For these glasses, the magnetic form factor due to Ho^{3+} was scaled by 95% in order to completely remove a slope in the measured $F(q)$ functions which was due to the magnetic form factors.

Element	Coherent scattering length (fm)	Scattering cross-section (barn)	Absorption cross-section (barn) at 1.798 Å
Dy	15.7(2)	76(3)	1016(13)
Ho	8.44(3)	9.31(7)	64.7(12)
Al	3.449(5)	1.503(4)	0.231(3)
Si	4.1491(10)	2.167(8)	0.171(3)
O	5.803(4)	4.232(6)	0.00019(2)

Table 5.2: Coherent scattering lengths, scattering cross-sections, and absorption cross-sections for Dy, Ho, Al, Si and O as used in the data analysis.

5.5 ND Results

In this section, the results from the ND experiment are presented at both the total structure factor and difference function levels.

5.5.1 Total Structure Factors

The measured $F(q)$ functions and the Fourier back transforms of the corresponding $G(r)$ functions with the low r oscillation set to the $G(0)$ limit for the $(R_2O_3)_{0.2}(Al_2O_3)_{0.2}(SiO_2)_{0.6}$ glasses are shown in figure 5.3. As seen in the figures, even though the data have been corrected for attenuation, magnetic and multiple scattering, inelasticity effects and background scattering, there is still a slope on the data. Although the slopes are small, they become problematic when forming the difference functions as the numerical values of the latter are themselves much smaller. Thus it was necessary to remove the residual slopes. From the properties of Fourier transforms, a gentle slope in reciprocal space corresponds to a peak at very low r in real space. The slope in the $F(q)$ functions was, therefore, removed by using a Fourier transformation method.

First, an $F(q)$ function was Fourier transformed to give $G(r)$. Next, the very low r part of this function where there is a peak due to the slope (from $r = 0$ to 0.80 Å for R = Dy or from $r = 0$ to 0.74 Å for R = Ho or 50:50 mixture) was set to $G(0)$, the solid lines in figure 5.4. Then the modified $G(r)$ was Fourier back transformed to reciprocal space. The Fourier back transforms obtained from this

procedure were subsequently treated as the new data sets while the back transforms used for the consistency checks were obtained by Fourier transforming $G(r)$ after the low r part of this function up to the beginning of the first peak was set to the $G(0)$ limit.

The fully corrected data and their Fourier back transforms are shown in figure 5.5. The data and the Fourier back transforms are in good agreement and there is no slope left on the data. Note that the $F(q)$ data sets start from $q = 0.40$ Å^{-1} ($2\theta = 1.82°$). This is, as mentioned in chapter 4, due to a large background signal at low scattering angles from the direct beam hitting the D4c detector shielding. Figure 5.6 shows a comparison between the $F(q)$ data sets for the three glasses.

As the $F(q)$ functions below $q = 0.40$ Å^{-1} ($2\theta = 1.82°$) could not be measured, the data at low q values for each sample were estimated by fitting a straight line through the low q part of $F(q)$ when it is plotted as a function of q^2 [127]. The fitted lines and the low q part of the $F(q)$ functions for each glass are plotted as a function of q^2 in figure 5.7 and as a function of q in figure 5.8. From section 3.5.5, an $F(q)$ function must satisfy the inequality relation $F(q) \geq -\sum_\alpha c_\alpha \overline{b_\alpha^2}$. The level limit, -$\sum_\alpha c_\alpha \overline{b_\alpha^2}$, for the three glasses along with the fitted $F(0)$ values and the fitted ranges are summarised in table 5.3. The data show that within the errors $F(q) \geq -\sum_\alpha c_\alpha \overline{b_\alpha^2}$ for all three glasses.

$(R_2O_3)_{0.2}(Al_2O_3)_{0.2}(SiO_2)_{0.6}$	Level limit (barn)	$F(0)$ (barn)	Fitted range (Å^{-1})
R = Dy	-0.49(1)	-0.418(1)	0.4-0.9
R = Ho	-0.327(1)	-0.300(1)	0.4-0.9
R = 50:50 mixture	-0.409(6)	-0.354(1)	0.4-0.9

Table 5.3: Level limits calculated from equation 3.27, the $F(0)$ values obtained by fitting a straight line through the low q part of $F(q)$ when plotted as a function of q^2, and the fitted q range for $(R_2O_3)_{0.2}(Al_2O_3)_{0.2}(SiO_2)_{0.6}$ glasses where R denotes Dy, Ho or a 50:50 mixture of Dy and Ho.

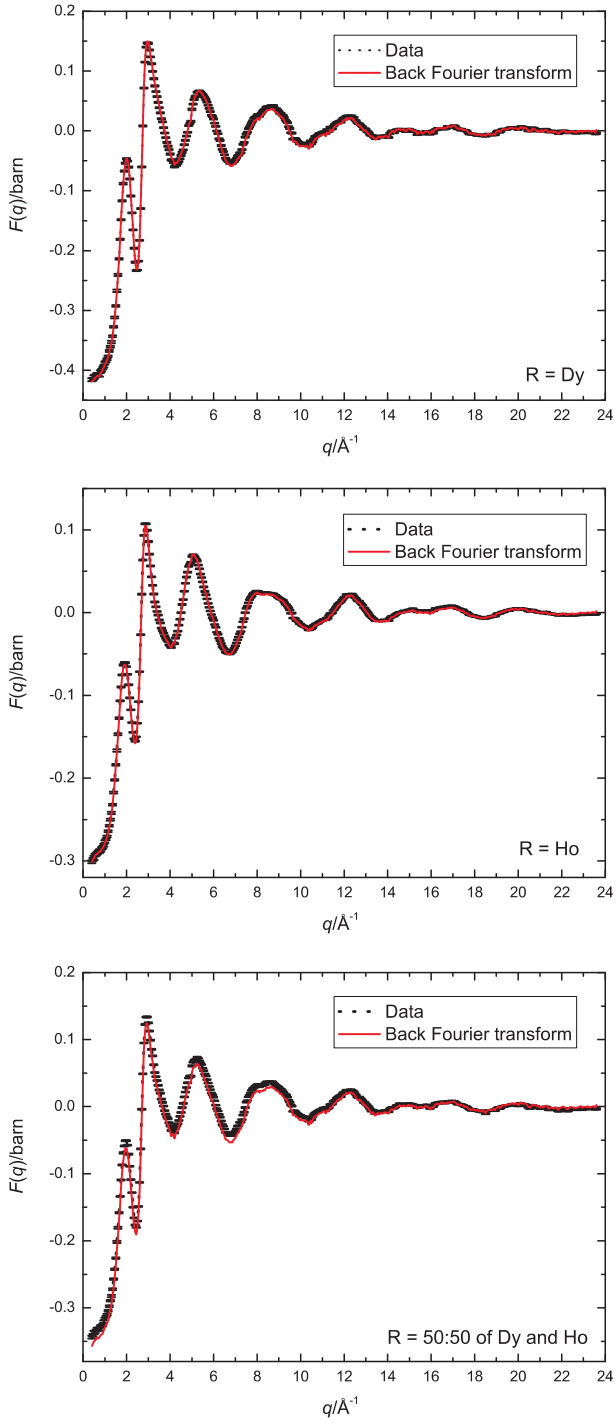

Figure 5.3: The $F(q)$ functions measured at room temperature for the $(R_2O_3)_{0.2}(Al_2O_3)_{0.2}(SiO_2)_{0.6}$ glasses where R denotes Dy, Ho or a 50:50 mixture of Dy and Ho. The dotted lines give the measured $F(q)$ functions (with error bars of the order of $\pm 10^{-3}$ barn) and the solid lines give the Fourier back transforms of the corresponding $G(r)$ functions shown in figure 5.4 after the low r part up to the beginning of the first peak is set to the $G(0)$ limit.

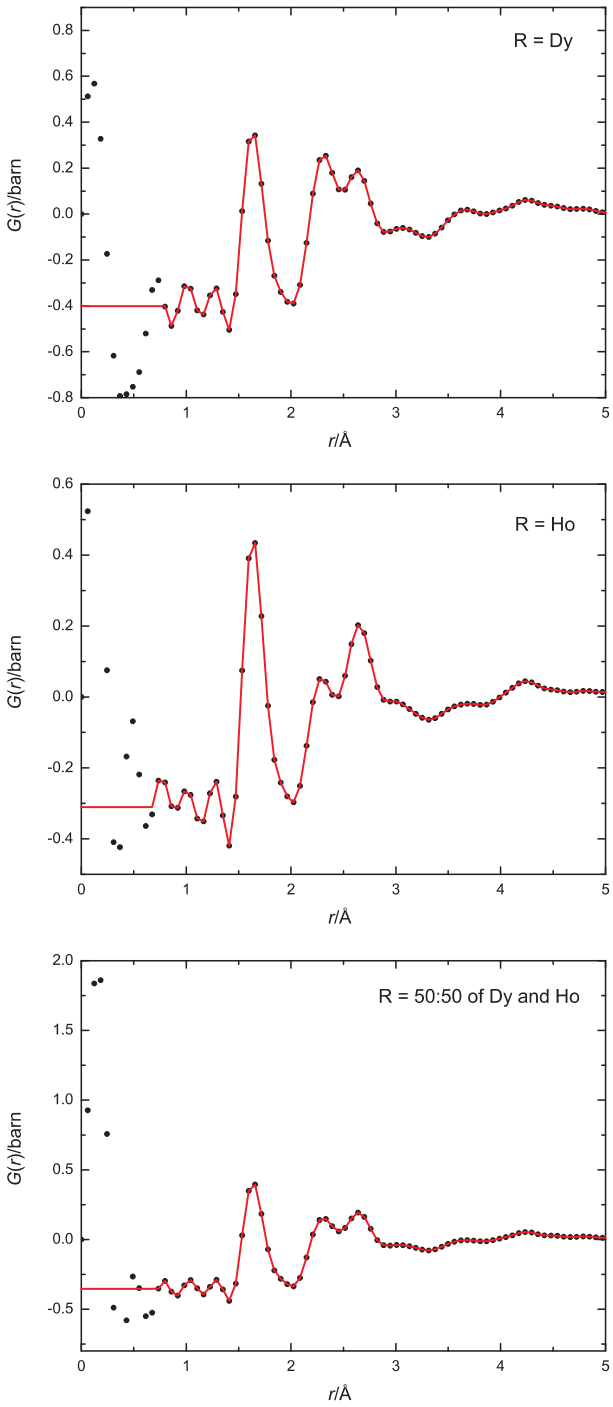

Figure 5.4: The $G(r)$ functions for the $(R_2O_3)_{0.2}(Al_2O_3)_{0.2}(SiO_2)_{0.6}$ glasses at room temperature where R denotes Dy, Ho or a 50:50 mixture of Dy and Ho. The dots give the Fourier transforms of the dotted lines in figure 5.3 and the solid lines give the modified $G(r)$ functions where a large peak at low r has been removed.

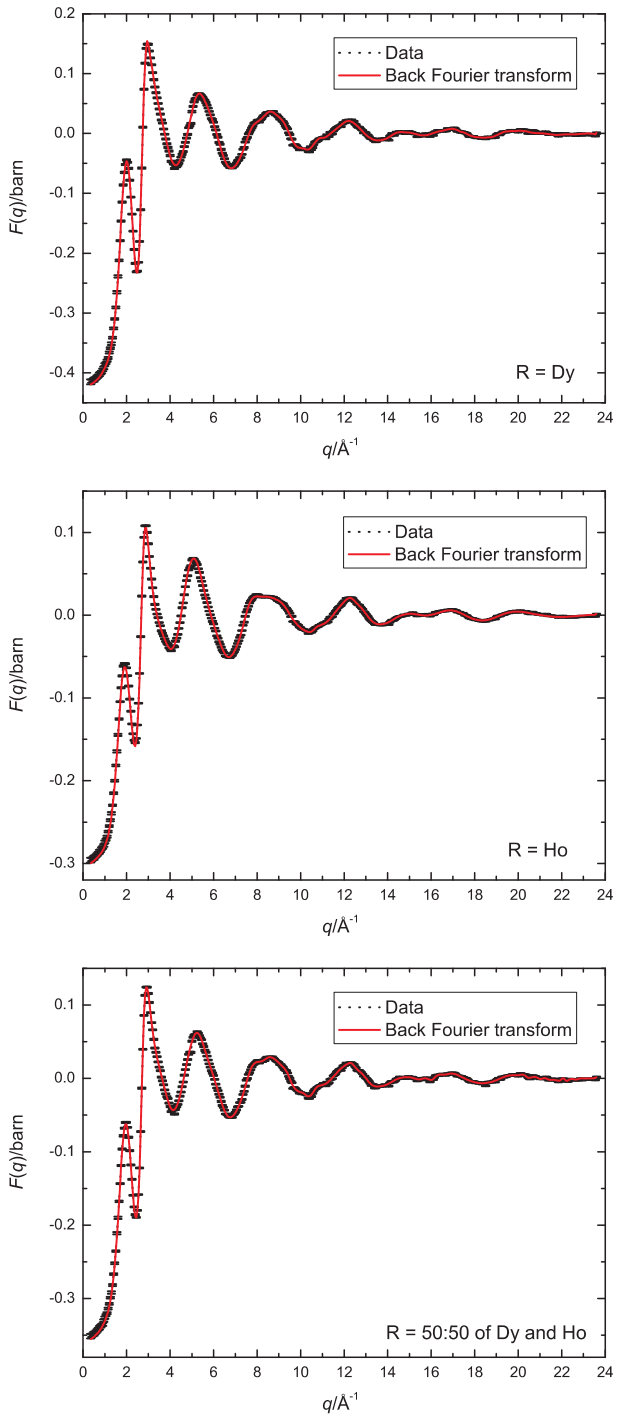

Figure 5.5: The fully corrected $F(q)$ functions for the $(R_2O_3)_{0.2}(Al_2O_3)_{0.2}(SiO_2)_{0.6}$ glasses where R denotes Dy, Ho or a 50:50 mixture of Dy and Ho. The dotted lines give the $F(q)$ functions obtained from the Fourier back transforms of the $G(r)$ functions given by the solid lines in figure 5.4 where a large peak at low r has been set to the $G(0)$ limit. The error bars are of the order of $\pm 10^{-3}$ barn and the solid lines give the Fourier back transforms of the corresponding $G(r)$ functions given by the solid lines in figure 5.9 where the small r oscillations up to the beginning of the first peak are set to the $G(0)$ limit.

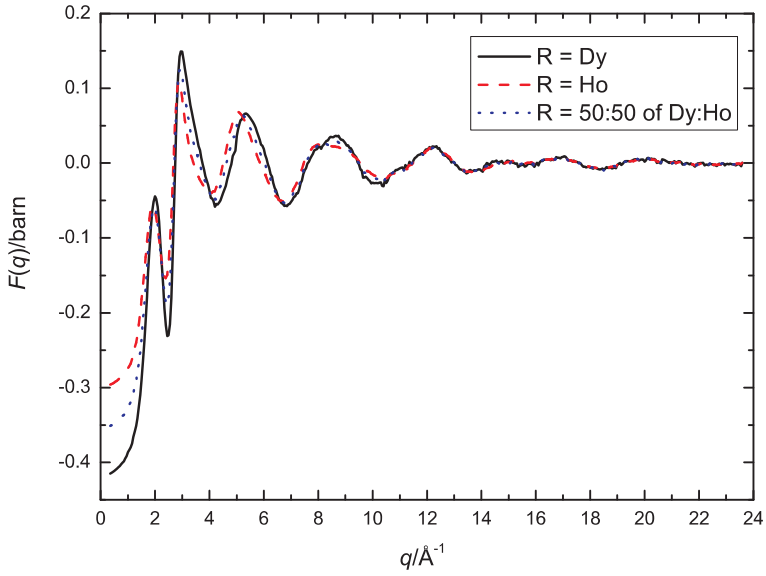

Figure 5.6: The fully corrected $F(q)$ functions for the $(R_2O_3)_{0.2}(Al_2O_3)_{0.2}(SiO_2)_{0.6}$ glasses where R denotes Dy, Ho or a 50:50 mixture of Dy and Ho.

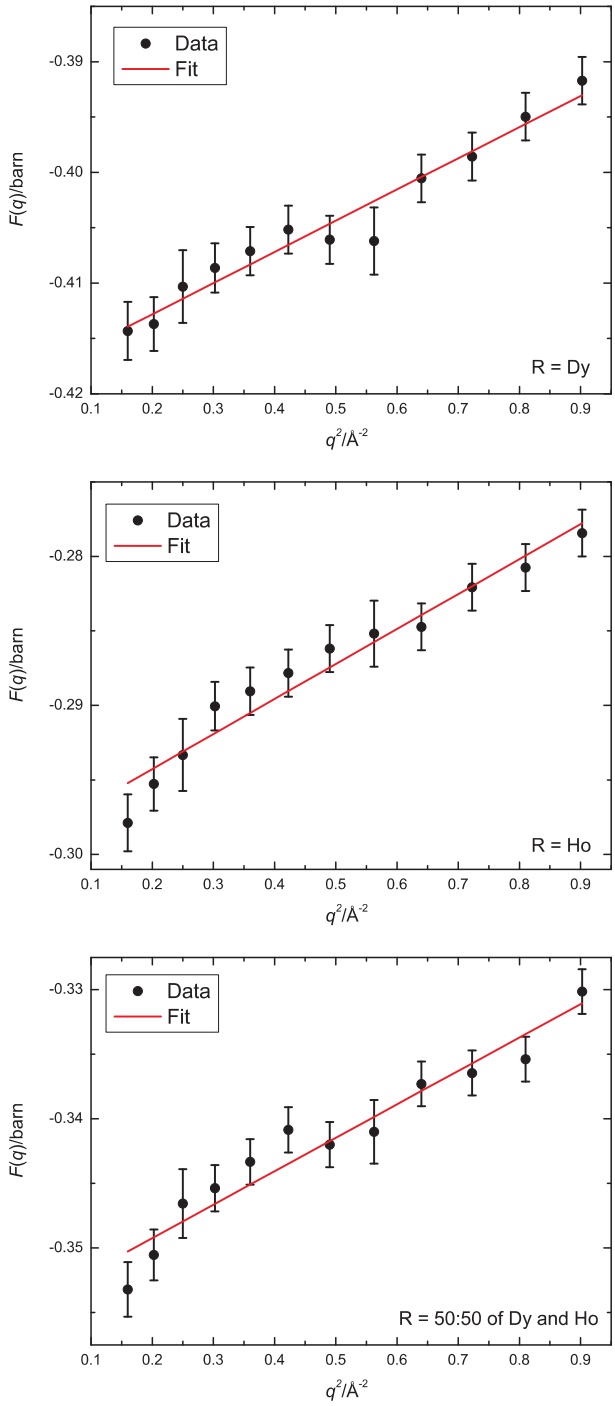

Figure 5.7: The low q part of the $F(q)$ functions for the $(R_2O_3)_{0.2}(Al_2O_3)_{0.2}(SiO_2)_{0.6}$ glasses where R denotes Dy, Ho or a 50:50 mixture of Dy and Ho plotted as function of q^2. The dots with error bars give the data points and the solid lines give linear fits.

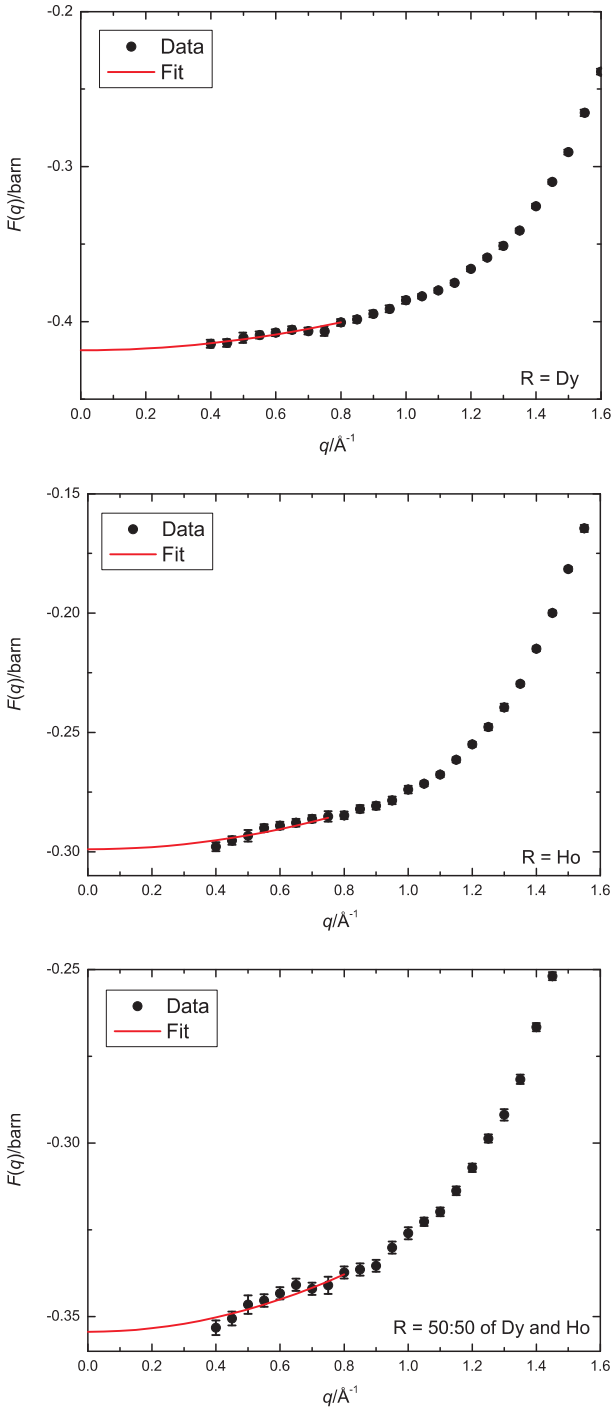

Figure 5.8: The low q part of the $F(q)$ functions for the $(R_2O_3)_{0.2}(Al_2O_3)_{0.2}(SiO_2)_{0.6}$ glasses where R denotes Dy, Ho or a 50:50 mixture of Dy and Ho. The dots with error bars give the data points and the lines give the fits corresponding to figure 5.7.

5.5.2 Total Pair Distribution Functions

The $G(r)$ functions for the $(R_2O_3)_{0.2}(Al_2O_3)_{0.2}(SiO_2)_{0.6}$ glasses are shown in figure 5.9 and are the Fourier transforms of the spline fitted $F(q)$ functions presented in figure 5.5 with the low q part of the function extrapolated using the method given in the previous section and the high q part smoothed by applying a cosine function to the data from $q = 21.0$ Å^{-1} in order to gradually put the last point of $F(q)$ to zero to avoid additional oscillations in $G(r)$ due to Fourier transform artifacts. The measured $F(q)$ functions and the spline fits are plotted in figure 5.10.

If we assume tetrahedral Si-O structural units similar to those found in glassy $La_{0.66}SiAl_{0.55}O_{3.81}$ [164], the Si-O nearest neighbour distance should be similar to 1.60(1) Å as obtained for the SiO_4 units in $Ca_{x/2}Al_xSi_{1-x}O_2$ glasses ($x = 0$, 0.25, 0.5 or 0.67) [119]. An NMR spectroscopy experiment on $(R_2O_3)_{0.2}(Al_2O_3)_{0.2}(SiO_2)_{0.6}$ glasses, where R denotes Y or La, gives a distribution of AlO_4, AlO_5 and AlO_6 units [35, 147]. The Al-O distances corresponding to the AlO_4 and AlO_6 units are 1.75(1) and 1.89(3) Å, respectively, and were obtained from an XRD experiment on $Ca_{x/2}Al_xSi_{1-x}O_2$ glasses ($x = 0$, 0.25, 0.5 or 0.67) and an ND experiment on $RAl_{0.35}P_{3.24}O_{10.12}$ glasses where R denotes La or Ce, respectively, [119, 165]. From figure 5.9, the first peak in the $G(r)$ function for the $(R_2O_3)_{0.2}(Al_2O_3)_{0.2}(SiO_2)_{0.6}$ glasses from $r = 1.5$ to 2 Å should therefore correspond to Si-O and Al-O correlations and the position of the third peak at $r \approx 2.64$ Å should correspond to the O-O correlations associated with the Si and Al centred structural units. As the nearest neighbours for the R atoms are likely to be O, the second peak in $G(r)$ at $r =$ 2.31(3) Å should correspond to the R-O correlations. Because these glasses have four components, most of the 10 pair correlation functions present in the $G(r)$ function are overlapped and only a limited amount of information can be obtained. More structural information can be determined from the difference functions presented in section 5.5.4.

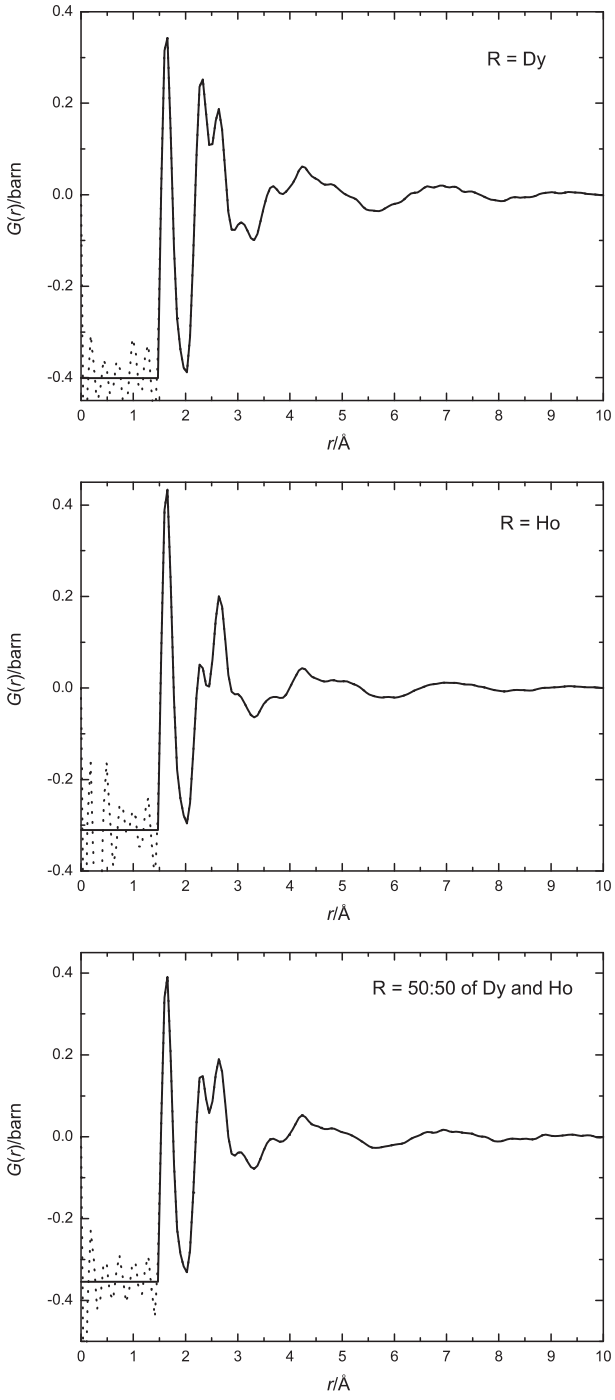

Figure 5.9: The $G(r)$ functions for the $(R_2O_3)_{0.2}(Al_2O_3)_{0.2}(SiO_2)_{0.6}$ glasses where R denotes Dy, Ho or a 50:50 mixture of Dy and Ho as obtained by Fourier transforming the spline fitted $F(q)$ functions shown in figure 5.10. The dotted lines at low r show the artifacts obtained from the Fourier transform procedure.

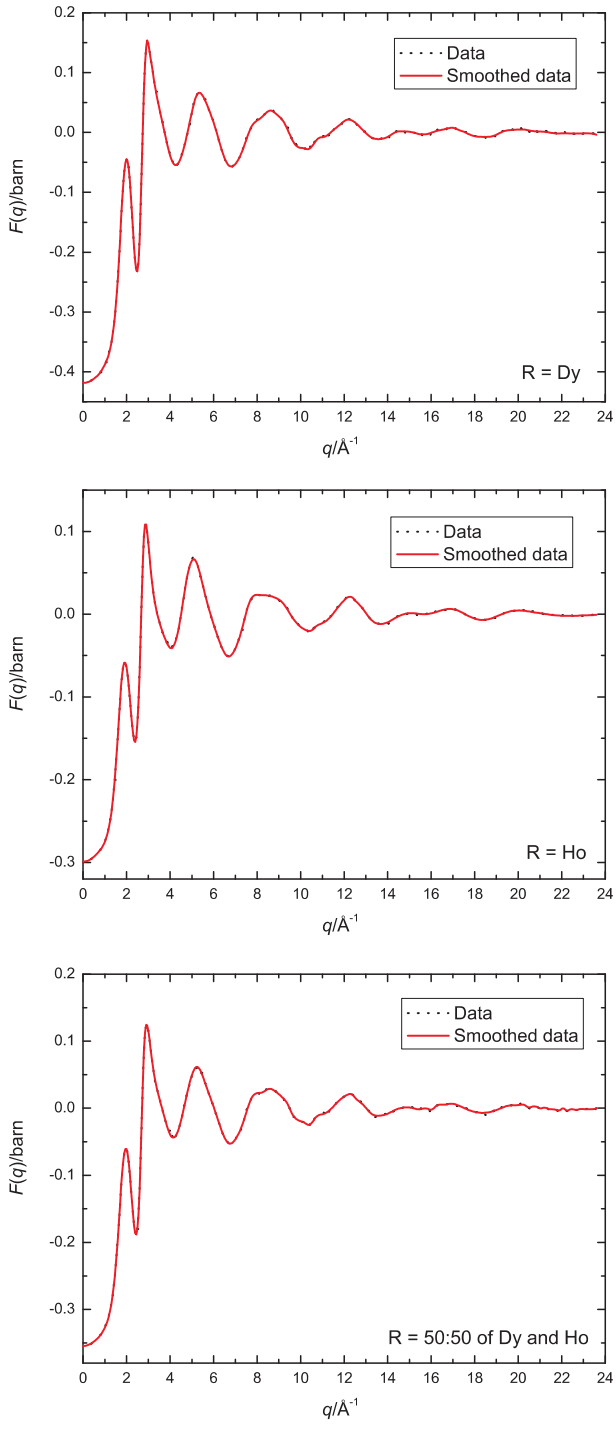

Figure 5.10: Spline fits to the $F(q)$ functions for the $(R_2O_3)_{0.2}(Al_2O_3)_{0.2}(SiO_2)_{0.6}$ glasses where R denotes Dy, Ho or a 50:50 mixture of Dy and Ho. The dotted lines give the data and the solid lines give the spline fits.

5.5.3 Coordination Number

As seen in figure 5.9, the first peak in the $G(r)$ functions for the three glasses is well separated from the rest of the peaks. If we assume that it contains only Al-O and Si-O correlations and the coordination number of O around Si is 4, we can calculate the Al-O average coordination number.

From equation 5.4, the Al-O average coordination number can be determined from

$$\bar{n}^{\mathrm{O}}_{\mathrm{Al}} = 4\pi n_0 c_{\mathrm{O}} \int_{r_1}^{r_2} g_{\mathrm{AlO}}(r) r^2 dr, \tag{5.74}$$

where r_1 and r_2 correspond to the limits for the first peak region. As the first peak corresponds to both Si-O and Al-O correlations, the $G(r) - G(0)$ function in this region can be written as

$$G(r) - G(0) = 2c_{\mathrm{Si}}c_{\mathrm{O}}b_{\mathrm{Si}}b_{\mathrm{O}}g_{\mathrm{SiO}}(r) + 2c_{\mathrm{Al}}c_{\mathrm{O}}b_{\mathrm{Al}}b_{\mathrm{O}}g_{\mathrm{AlO}}(r). \tag{5.75}$$

Hence

$$\begin{aligned} 2\pi n_0 \int_{r_1}^{r_2} [G(r) - G(0)] r^2 dr &= c_{\mathrm{Si}}b_{\mathrm{Si}}b_{\mathrm{O}} \cdot 4\pi n_0 c_{\mathrm{O}} \int_{r_1}^{r_2} g_{\mathrm{SiO}}(r) r^2 dr \\ &\quad + c_{\mathrm{Al}}b_{\mathrm{Al}}b_{\mathrm{O}} \cdot 4\pi n_0 c_{\mathrm{O}} \int_{r_1}^{r_2} g_{\mathrm{AlO}}(r) r^2 dr \\ &= c_{\mathrm{Si}}b_{\mathrm{Si}}b_{\mathrm{O}}\bar{n}^{\mathrm{O}}_{\mathrm{Si}} + c_{\mathrm{Al}}b_{\mathrm{Al}}b_{\mathrm{O}}\bar{n}^{\mathrm{O}}_{\mathrm{Al}}. \end{aligned} \tag{5.76}$$

If we assume that the coordination number of O around Si is 4 i.e. $\bar{n}^{\mathrm{O}}_{\mathrm{Si}} = 4$, which is the value obtained from an NMR study on glassy $La_{0.66}SiAl_{0.55}O_{3.81}$ [164], then

$$\bar{n}^{\mathrm{O}}_{\mathrm{Al}} = \frac{1}{c_{\mathrm{Al}}b_{\mathrm{Al}}} \left(\frac{2\pi n_0}{b_{\mathrm{O}}} \int_{r_1}^{r_2} [G(r) - G(0)] r^2 dr - 4c_{\mathrm{Si}}b_{\mathrm{Si}} \right). \tag{5.77}$$

The $\bar{n}^{\mathrm{O}}_{\mathrm{Al}}$ values calculated using equation 5.77 with the corresponding r ranges are summarised in table 5.4.

As Y, Ho and Dy are isomorphic it is useful to compare the $\bar{n}^{\mathrm{O}}_{\mathrm{Al}}$ values obtained from the NMR experiment on $(Y_2O_3)_{0.2}(Al_2O_3)_{0.2}(SiO_2)_{0.6}$ glass [35, 147]. The NMR results show evidence of 4-, 5- and 6-fold coordinated Al with the main contribution arising from AlO_4 units, 16(3)% from AlO_5 units and 6(3)% from AlO_6 units which gives $\bar{n}^{\mathrm{O}}_{\mathrm{Al}} = 4.3(1)$. This value agrees, within the errors, with the values obtained from the ND work.

Correlation function	Al-O coordination number	Integration range (Å)
${}^{Dy}G(r)$	4.4(1)	1.47 - 2.00
${}^{Mix}G(r)$	4.6(2)	1.47 - 2.04
${}^{Ho}G(r)$	4.4(2)	1.47 - 2.02

Table 5.4: The Al-O average coordination numbers for glassy $(R_2O_3)_{0.2}(Al_2O_3)_{0.2}(SiO_2)_{0.6}$ and corresponding integration ranges. The coordination numbers were determined from the area under the first peak of the $G(r)$ functions obtained from ND.

5.5.4 Difference Functions

The FOD, TWMD and SOD functions presented in this section were calculated by using equations 5.7 to 5.32 with R = Dy, R' = 50:50 mixture of Dy and Ho, and R'' = Ho. The weighting factors for each partial structure factor present in $F(q)$ and the difference functions are summarised in table 5.5.

First Order Difference (FOD) Functions

The FOD functions were calculated from the slope-removed $F(q)$ functions shown in figure 5.5 by using equations 5.7 to 5.11. The calculated $\Delta F_R^{(n)}(q)$ (n = 1, 2 or 3) functions are shown in figure 5.11. The real space $\Delta G_R^{(n)}(r)$ functions in figure 5.12 are Fourier transforms of spline fits to the FOD functions with the high q part smoothed by applying a cosine function from q = 21.0 Å^{-1}. Comparisons between the FOD functions and their spline fits are shown in figure 5.13.

From table 5.5, as the FOD functions contain only those correlations involving R atoms the first peak in $\Delta G_R^{(n)}(r)$ will correspond to the R-O correlations. The position of this peak is 2.33(2), 2.32(2) and 2.33(2) Å for the $\Delta G_R^{(1)}(r)$, $\Delta G_R^{(2)}(r)$, and $\Delta G_R^{(3)}(r)$ functions, respectively. As this peak is well separated from the remaining peaks, the average coordination number of O around R can be calculated using the equation

$$\bar{n}_{\mathrm{R}}^{\mathrm{O}} = 4\pi n_0 c_{\mathrm{O}} \int_{r_1}^{r_2} \left[\frac{\Delta G_R^{(n)}(r) - \Delta G_R^{(n)}(0)}{2 c_{\mathrm{R}} c_{\mathrm{O}} b_{\mathrm{R}} b_{\mathrm{O}}} \right] r^2 dr, \tag{5.78}$$

where $r_1 \leq r \leq r_2$ is the region of the first peak and within this region

$$\frac{\Delta G_R^{(n)}(r) - \Delta G_R^{(n)}(0)}{2 c_{\mathrm{R}} c_{\mathrm{O}} b_{\mathrm{R}} b_{\mathrm{O}}} = g_{\mathrm{RO}}(r). \tag{5.79}$$

	R-R	R-O	R-Al	R-Si	Al-Al	Al-Si	Al-O	Si-Si	Si-O	O-O
${}^{Dy}F(q)$	25.3(2)	116.7(4)	11.56(4)	20.85(7)	1.318(4)	4.757(7)	26.61(4)	4.292(2)	48.02(4)	134.3(2)
${}^{mix}F(q)$	14.8(1)	89.2(4)	8.84(4)	15.95(7)	1.318(4)	4.757(7)	26.61(4)	4.292(2)	48.02(4)	134.3(2)
${}^{Ho}F(q)$	7.1(1)	61.8(6)	6.12(6)	11.0(1)	1.318(4)	4.757(7)	26.61(4)	4.292(2)	48.02(4)	134.3(2)
$\Delta F_R^{(1)}(q)$	18.2(2)	54.9(7)	5.43(7)	9.8(1)	-	-	-	-	-	-
$\Delta F_R^{(2)}(q)$	10.5(2)	27.4(5)	2.72(5)	4.9(6)	-	-	-	-	-	-
$\Delta F_R^{(3)}(q)$	7.7(2)	27.4(7)	2.72(7)	4.9(1)	-	-	-	-	-	-
$\Delta F_{R\mu}^{(1)}(q)$	-	54.9(7)	5.43(7)	9.8(1)	-	-	-	-	-	-
$\Delta F_{R\mu}^{(2)}(q)$	-	27.4(5)	2.72(5)	4.9(6)	-	-	-	-	-	-
$\Delta F_{R\mu}^{(3)}(q)$	-	27.4(7)	2.72(7)	4.9(1)	-	-	-	-	-	-
$\Delta F^{(1)}(q)$	13.4(1)	-	-	-	1.318(4)	4.757(7)	26.61(4)	4.292(2)	48.02(4)	134.3(2)
$\Delta F^{(2)}(q)$	19.3(1)	-	-	-	1.318(4)	4.757(7)	26.61(4)	4.292(2)	48.02(4)	134.3(2)
$\Delta F^{(3)}(q)$	10.2(1)	-	-	-	1.318(4)	4.757(7)	26.61(4)	4.292(2)	48.02(4)	134.3(2)
$\Delta F_{\mu\mu}(q)$	-	-	-	-	1.318(4)	4.757(7)	26.61(4)	4.292(2)	48.02(4)	134.3(2)

Table 5.5: Weighting factors in mbarn for the $S_{\alpha\beta}(q)$ functions present in the $F(q)$, $\Delta F_R^{(n)}(q)$, $\Delta F_{R\mu}^{(n)}(q)$, $\Delta F^{(n)}(q)$ (n = 1, 2 or 3) and $\Delta F_{\mu\mu}(q)$ functions for the $(R_2O_3)_{0.2}(Al_2O_3)_{0.2}(SiO_2)_{0.6}$ glasses where R denotes Ho, Dy or a 50:50 mixture of Dy and Ho. $F(q)$ is defined by equation 5.1 and the definitions of the $\Delta F_R^{(n)}(q)$, $\Delta F_{R\mu}^{(n)}(q)$, $\Delta F^{(n)}(q)$ and $\Delta F_{\mu\mu}(q)$ functions are given in section 5.2.2.

The $\bar{n}_{\mathrm{R}}^{\mathrm{O}}$ values obtained from the FOD functions are summarised in table 5.6.

Correlation function	R-O coordination number	Integration range (Å)
$\Delta G_R^{(1)}(r)$	7.2(1)	2.02 - 2.94
$\Delta G_R^{(2)}(r)$	7.2(1)	2.02 - 2.91
$\Delta G_R^{(3)}(r)$	7.2(3)	2.02 - 2.98

Table 5.6: The R-O average coordination numbers for glassy $(R_2O_3)_{0.2}(Al_2O_3)_{0.2}(SiO_2)_{0.6}$ and corresponding integration ranges. The coordination numbers were determined from the area under the first peak of the $\Delta G_R^{(n)}(r)$ (n = 1, 2 or 3) functions obtained from ND.

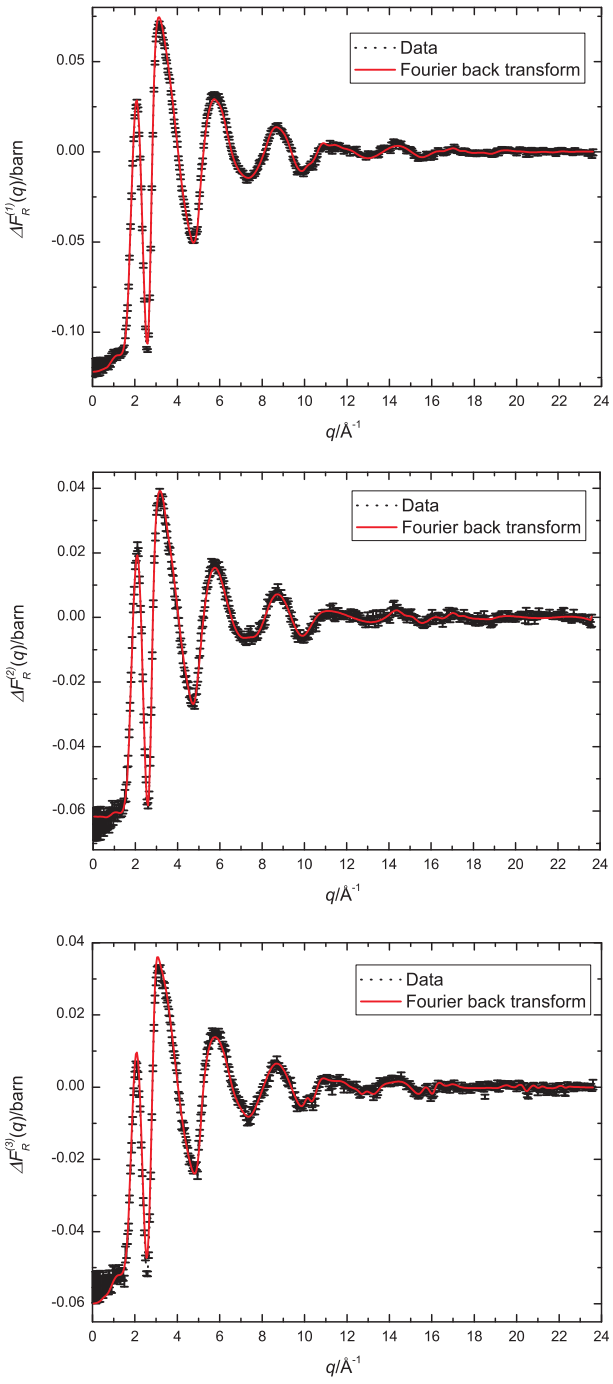

Figure 5.11: The measured $\Delta F_R^{(n)}(q)$ ($n = 1$, 2 or 3) functions for glassy $(R_2O_3)_{0.2}(Al_2O_3)_{0.2}(SiO_2)_{0.6}$. The dotted lines give the $\Delta F_R^{(n)}(q)$ functions (with error bars of the order of $\pm 10^{-3}$ barn) calculated from the $F(q)$ functions by using equations 5.7 to 5.11 and the solid lines give the Fourier back transforms of the corresponding $\Delta G_R^{(n)}(r)$ functions given by the solid lines in figure 5.12 where the low r part up to the beginning of the first peak is set to the $\Delta G_R^{(n)}(0)$ value.

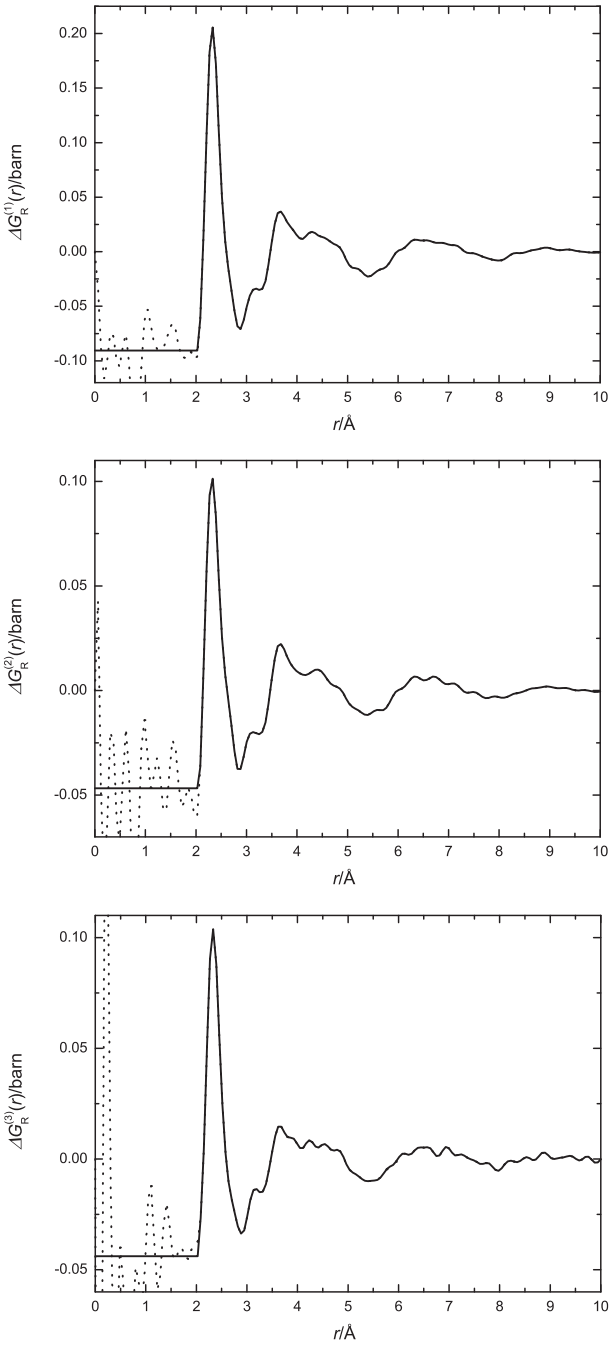

Figure 5.12: The $\Delta G_R^{(n)}(r)$ (n = 1, 2 or 3) functions for glassy $(R_2O_3)_{0.2}(Al_2O_3)_{0.2}(SiO_2)_{0.6}$ as obtained by Fourier transforming the spline fitted $\Delta F_R^{(n)}(q)$ functions shown in figure 5.13. The dotted lines at low r show the artifacts obtained from the Fourier transform procedure.

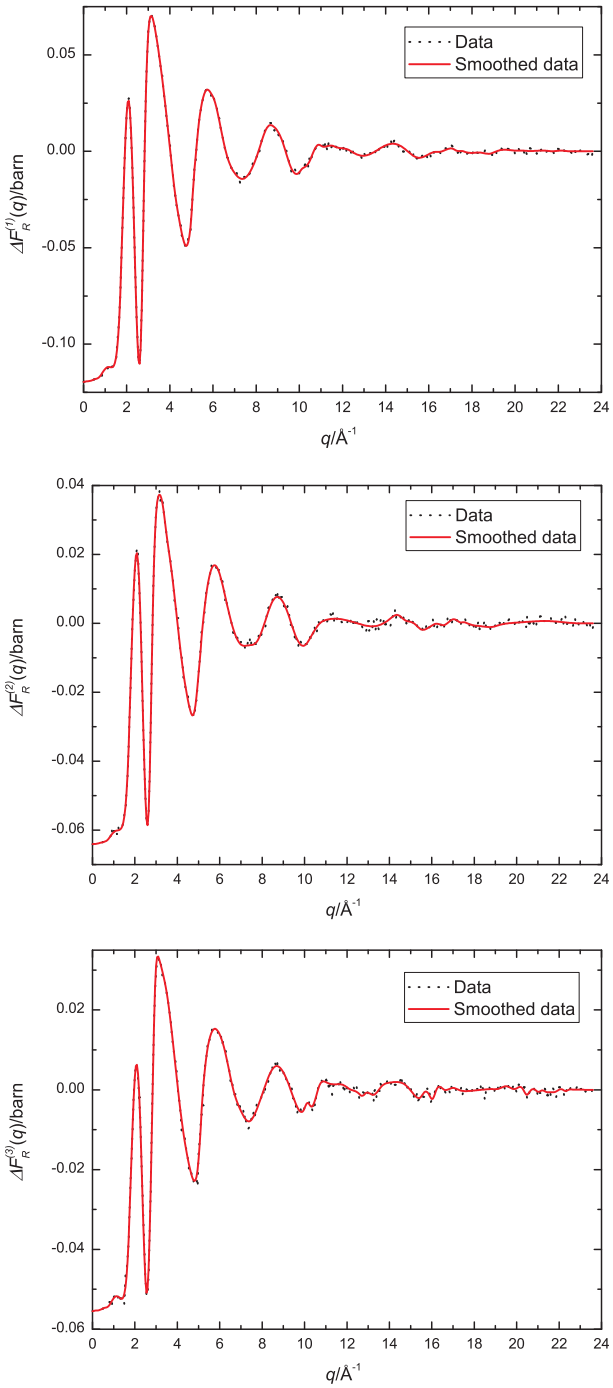

Figure 5.13: Spline fits to the measured $\Delta F_R^{(n)}(q)$ (n = 1, 2 or 3) functions for glassy $(R_2O_3)_{0.2}(Al_2O_3)_{0.2}(SiO_2)_{0.6}$. The dotted lines give the data points and the solid lines give the spline fits.

Total Minus Weighted Difference (TMWD) Functions

The TMWD functions were calculated from the slope-removed $F(q)$ functions shown in figure 5.5 by using equations 5.17 to 5.21. The calculated $\Delta F^{(n)}(q)$ (n = 1, 2 or 3) functions are shown in figure 5.14. The real space $\Delta G^{(n)}(r)$ functions in figure 5.15 are Fourier transforms of spline fits to the TMWD functions with the high q part smoothed by applying a cosine function from $q = 21.0$ Å^{-1}. Comparisons between the TMWD functions and their spline fits are shown in figure 5.16.

From table 5.5, the TMWD functions contain only matrix atom and R-R correlations. In figure 5.15, the first peak in the $\Delta G^{(n)}(r)$ functions is at the same position as the first peak in the $G(r)$ functions in figure 5.9. The $\bar{n}^{\circ}_{\mathrm{Al}}$ coordination number can thus be determined from the area under this peak, using an equation analogous to equation 5.77,

$$\bar{n}^{\circ}_{\mathrm{Al}} = \frac{1}{c_{\mathrm{Al}} b_{\mathrm{Al}}} \left(\frac{2\pi n_0}{b_{\mathrm{O}}} \int_{r_1}^{r_2} [\Delta G^{(n)}(r) - \Delta G^{(n)}(0)] r^2 dr - 4 c_{\mathrm{Si}} b_{\mathrm{Si}} \right), \tag{5.80}$$

and the values are summarised in table 5.7.

Correlation function	Al-O oordination number	Integration range (Å)
$\Delta G^{(1)}(r)$	4.6(2)	1.47 - 2.07
$\Delta G^{(2)}(r)$	4.9(2)	1.47 - 2.13
$\Delta G^{(3)}(r)$	4.2(1)	1.47 - 1.99

Table 5.7: The Al-O average coordination numbers for glassy $(R_2O_3)_{0.2}(Al_2O_3)_{0.2}(SiO_2)_{0.6}$ and corresponding integration ranges. The coordination numbers were determined from the area under the first peak of the $\Delta G^{(n)}(r)$ (n = 1, 2 or 3) functions obtained from ND.

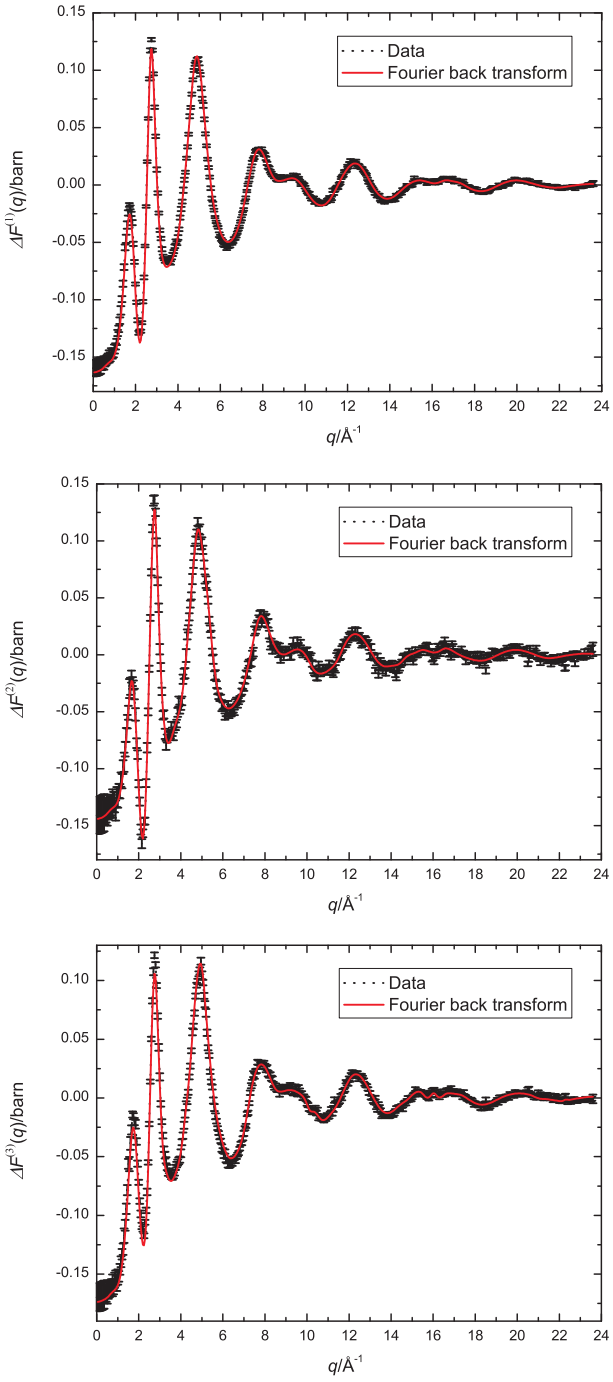

Figure 5.14: The measured $\Delta F^{(n)}(q)$ ($n = 1$, 2 or 3) functions for glassy $(R_2O_3)_{0.2}(Al_2O_3)_{0.2}(SiO_2)_{0.6}$. The dotted lines give the $\Delta F^{(n)}(q)$ functions (with error bars of the order of $\pm 10^{-3}$ barn) calculated from the $F(q)$ functions by using equations 5.17 to 5.21 and the solid lines give the Fourier back transforms of the corresponding $\Delta G^{(n)}(r)$ functions given by the solid lines in figure 5.15 where the low r part up to the beginning of the first peak is set to the $\Delta G^{(n)}(0)$ value.

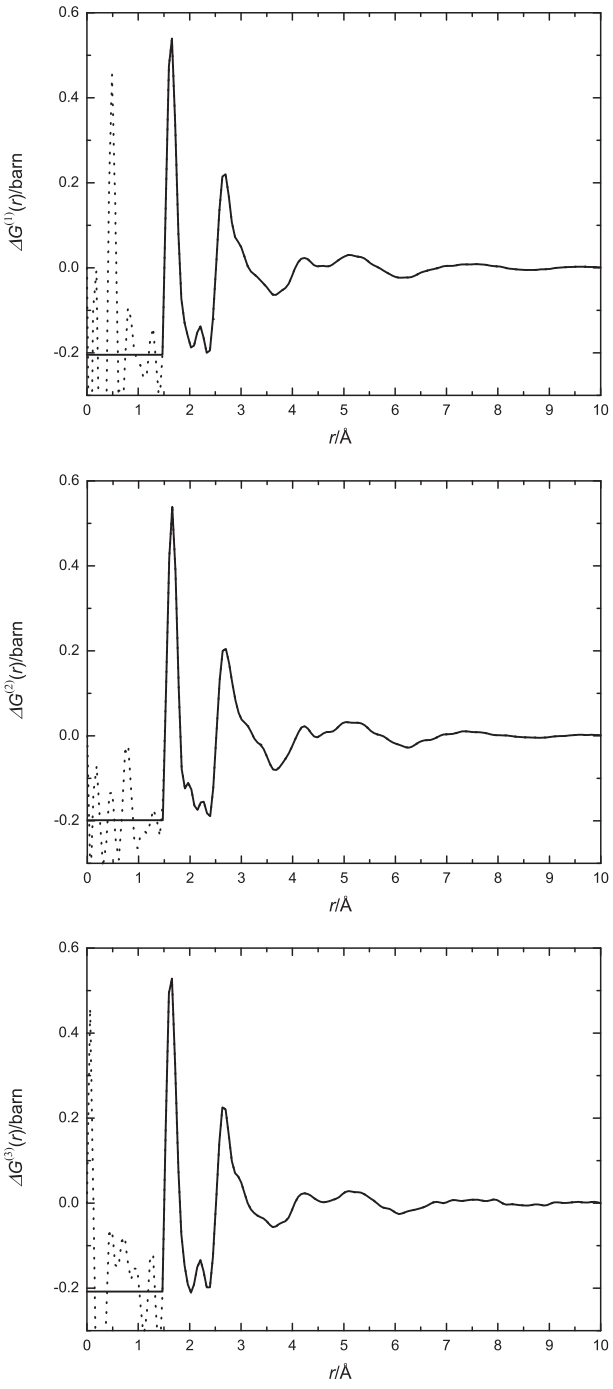

Figure 5.15: The $\Delta G^{(n)}(r)$ (n = 1, 2 or 3) functions for glassy $(R_2O_3)_{0.2}(Al_2O_3)_{0.2}(SiO_2)_{0.6}$ as obtained by Fourier transforming the spline fitted $\Delta F^{(n)}(q)$ functions shown in figure 5.16. The dotted lines at low r show the artifacts obtained from the Fourier transform procedure.

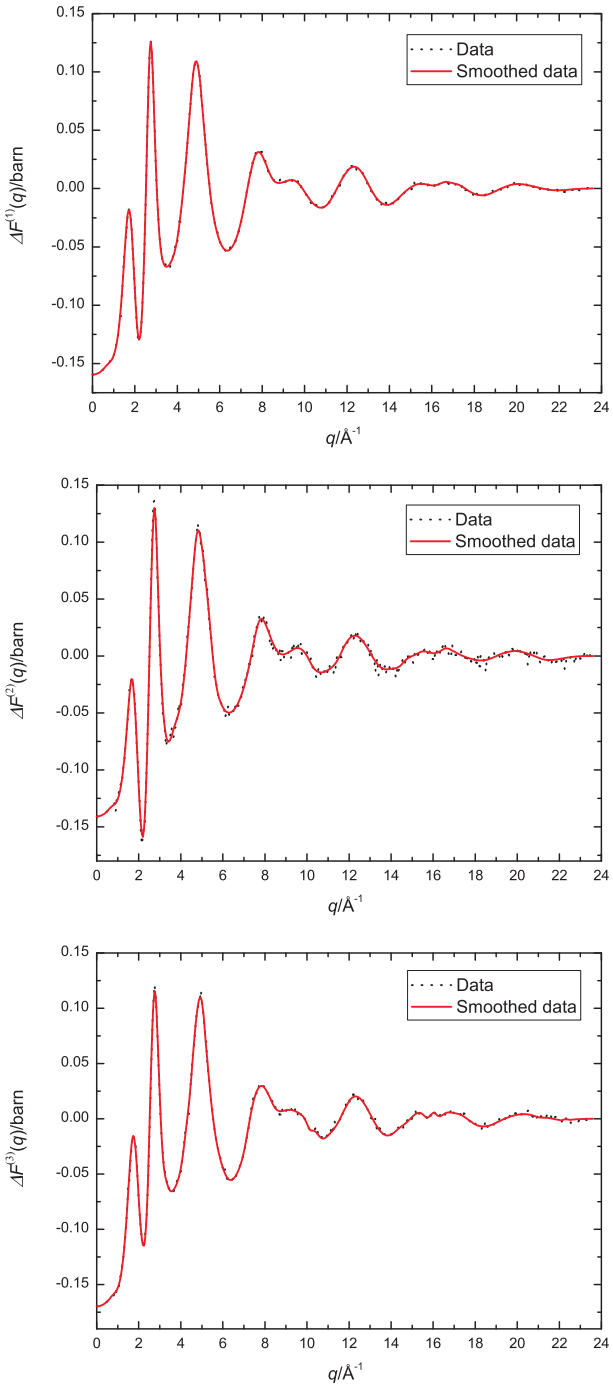

Figure 5.16: Spline fits to the measured $\Delta F_R^{(n)}(q)$ (n = 1, 2 or 3) functions for glassy $(R_2O_3)_{0.2}(Al_2O_3)_{0.2}(SiO_2)_{0.6}$. The dotted lines give the data points and the solid lines give the spline fits.

Second Order Difference (SOD) Functions

The SOD function or $S_{RR}(q)$ was calculated from the slope-removed $F(q)$ functions shown in figure 5.5 by using equation 5.26 and is shown in figure 5.17. The corresponding $g_{\mathrm{RR}}(r)$ function shown in figure 5.18 is the Fourier transform of the smoothed $S_{RR}(q)$ function as obtained by spline fitting the data shown in figure 5.17 and truncating smoothly at $q_{max} = 23.6$ Å^{-1} by using a Lorch function $M(q) = \sin(\pi q/q_{max})/(\pi q/q_{max})$ [166]. The smoothed and un-smoothed data are shown in figure 5.19.

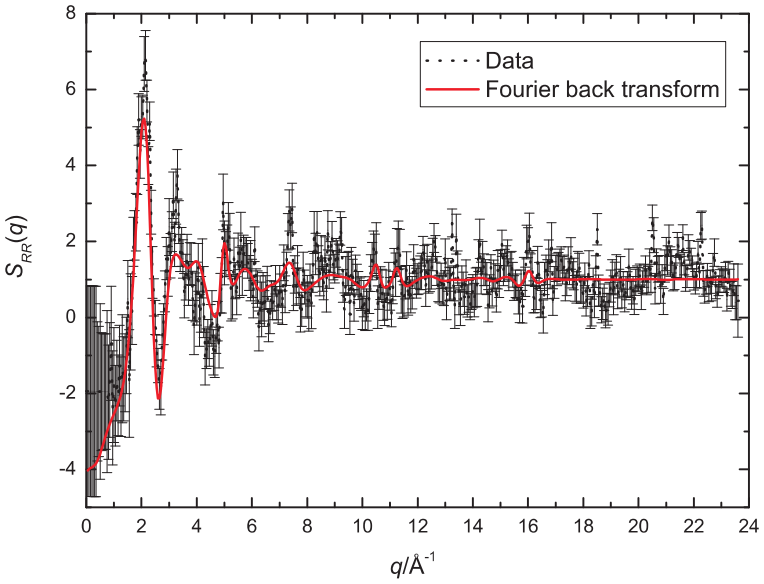

Figure 5.17: The measured $S_{RR}(q)$ function for glassy $(R_2O_3)_{0.2}(Al_2O_3)_{0.2}(SiO_2)_{0.6}$ calculated from the slope-removed $F(q)$ functions shown in figure 5.5 by using equation 5.26. The dotted line gives the $S_{RR}(q)$ function (with error bars of the order of ± 0.1) and the solid line gives the Fourier back transform of $g_{\mathrm{RR}}(r)$ shown by the solid line in figure 5.18 where the low r part up to the beginning of the first peak at 3.68(3) Å is set to the zero.

From figure 5.18, there are two R-R nearest neighbour distances at 3.68(3) and 4.38(5) Å. The first distance also corresponds to a peak in the $\Delta G_R^{(n)}(r)$ and $G_X(r)$ functions shown in figures 5.12 and 5.30, respectively. For the second distance, although there is no clear peak at this position in the $\Delta G_R^{(n)}(r)$ or $G_X(r)$ functions, possibly due to overlapping correlations, the distance is comparable to the R-R distances found in several rare-earth alumino-silicate crystals. The La-La and Eu-Eu nearest neighbour distances in $LaAlSiO_5$ and $Eu_{0.92}Al_{1.76}Si_{2.24}O_8$ are 4.2 and

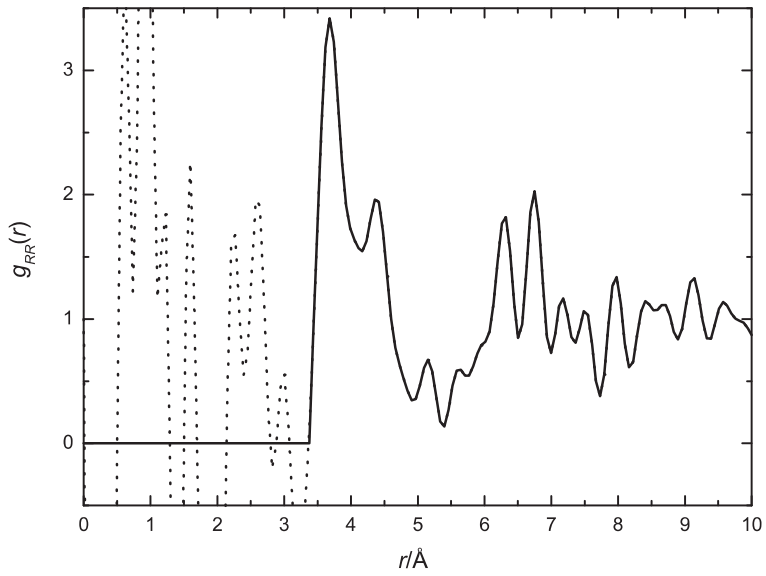

Figure 5.18: The $g_{\mathrm{RR}}(r)$ function for glassy $(R_2O_3)_{0.2}(Al_2O_3)_{0.2}(SiO_2)_{0.6}$ as obtained by Fourier transforming the smoothed $S_{RR}(q)$ function of figure 5.19. The dotted lines at low r show the artifacts obtained from the Fourier transform procedure.

4.1 Å, respectively [167, 168]. In $La_{9.5}(Si_{5.5}Al_{0.5}O_{24})O_2$, $La_{9.71}(Al_{0.19}Si_{0.81}O_4)_6O_2$ and $La_{1.3}Al_4Si_{12}O_{32}$ crystals, the La-La nearest neighbour distances are 2.9-4.0 Å with next nearest neighbour distances of 4.0-4.5 Å [167, 169, 170].

An R-R coordination number of 4.6(1) was determined from the area under the first peak in $g_{\mathrm{RR}}(r)$ by using equation 5.4 with a high r limit for the integration of 5.19 Å. It should be noted that for crystalline $La_{9.5}(Si_{5.5}Al_{0.5}O_{24})O_2$, $La_{9.71}(Al_{0.19}Si_{0.81}O_4)_6O_2$ and $La_{1.3}Al_4Si_{12}O_{32}$ [167, 169, 170], the La-La coordination number corresponding to an r range from 2.9 to 4.5 Å is between 2 and 10.

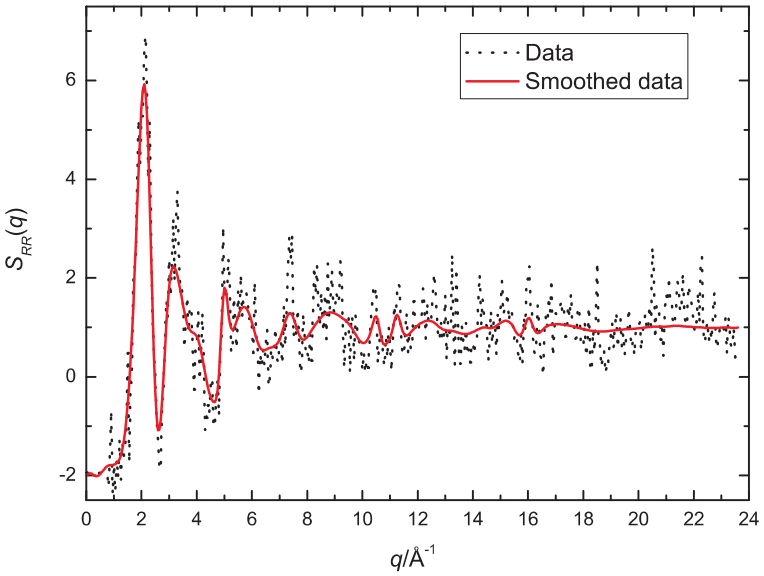

Figure 5.19: The $S_{RR}(q)$ function for glassy $(R_2O_3)_{0.2}(Al_2O_3)_{0.2}(SiO_2)_{0.6}$. The dotted line gives the data as shown in figure 5.17 and the solid line gives the smoothed $S_{RR}(q)$ function.

The $\Delta F_{R\mu}^{(n)}(q)$ (n = 1, 2 or 3) and $\Delta F_{\mu\mu}(q)$ functions were calculated from the slope-removed $F(q)$ functions shown in figure 5.5 by using equations 5.27 to 5.30 and are shown in figures 5.20 and 5.21. It should be noted that the $\Delta F_{\mu\mu}(q)$ function is much smoother than the $\Delta F_{R\mu}^{(n)}(q)$ functions which is consistent with the fact that, as shown in table 5.5, $S_{RR}(q)$ has a larger relative contribution to the FOD as compared to the TMWD functions.

The $\Delta F_{R\mu}^{(n)}(q)$ and $\Delta F_{\mu\mu}(q)$ functions can also be calculated from the $\Delta F_{R}^{(n)}(q)$ and $\Delta F^{(n)}(q)$ functions using equations 5.8 to 5.12 and 5.18 to 5.22. The $\Delta F_{\mu\mu}^{(n)}(q)$ functions calculated from the $\Delta F^{(n)}(q)$ functions should in theory be the same. Similarly, the $\Delta F_{R\mu}^{(n)}(q)/\delta^{(n)}$ functions calculated from the $F_{R}^{(n)}(q)$ functions should also in theory be the same. The differences between the $\Delta F_{R\mu}^{(n)}(q)$ functions and between the $\Delta F_{\mu\mu}(q)$ and the $\Delta F_{\mu\mu}^{(n)}(q)$ functions are shown in figures 5.22 and 5.23. From these figures, the differences are, within the error, negligible.

The $\Delta G_{R\mu}^{(n)}(r)$ and $\Delta G_{\mu\mu}(r)$ in figures 5.24 and 5.25 are Fourier transforms of the smoothed $\Delta F_{R\mu}^{(n)}(q)$ and $\Delta F_{\mu\mu}(q)$ functions. The smoothed $\Delta F_{R\mu}^{(n)}(q)$ functions were obtained by spline fitting the $\Delta F_{R\mu}^{(n)}(q)$ functions shown in figure 5.20 and truncating smoothly at q_{max} = 23.6 Å^{-1} by using a Lorch function [166] while the smoothed $\Delta F_{\mu\mu}(q)$ function was obtained by spline fitting the $\Delta F_{\mu\mu}(q)$ function

shown in figure 5.21 and smoothing the high q part by applying a cosine function from $q = 21.0$ Å^{-1}. The smoothed and un-smoothed data are plotted together in figures 5.26 and 5.27.

As for the $\Delta G_R^{(n)}(r)$ functions, the first peak in $\Delta G_{R\mu}^{(n)}(r)$ is assigned to R-O correlations and the coordination number $\bar{n}_{\mathrm{R}}^{\mathrm{O}}$ was obtained from an equation analogous to equation 5.78. Similarly, as for the $G(r)$ functions, the first peak in $\Delta G_{\mu\mu}(r)$ has a contribution from both Si-O and Al-O correlations and $\bar{n}_{\mathrm{Al}}^{\mathrm{O}}$ was obtained from an equation analogous to equation 5.77 by assuming that $\bar{n}_{\mathrm{Si}}^{\mathrm{O}} = 4$. The $\bar{n}_{\mathrm{R}}^{\mathrm{O}}$ and $\bar{n}_{\mathrm{Al}}^{\mathrm{O}}$ values obtained from the $\Delta G_{R\mu}^{(n)}(r)$ and $\Delta G_{\mu\mu}(r)$ functions along with the $\bar{n}_{\mathrm{Al}}^{\mathrm{O}}$, $\bar{n}_{\mathrm{R}}^{\mathrm{O}}$ and $\bar{n}_{\mathrm{R}}^{\mathrm{R}}$ values obtained from the $G(r)$, $\Delta G_R^{(n)}(r)$, $\Delta G^{(n)}(r)$ and $g_{\mathrm{RR}}(r)$ functions and the corresponding r ranges are presented in table 5.8.

Correlation function	Coordination number			Integration range (Å)
	Al-O	R-O	R-R	
${}^{Dy}G(r)$	4.4(1)	-	-	1.47 - 2.00
${}^{Mix}G(r)$	4.6(2)	-	-	1.47 - 2.04
${}^{Ho}G(r)$	4.4(2)	-	-	1.47 - 2.02
$\Delta G^{(1)}(r)$	4.6(2)	-	-	1.47 - 2.07
$\Delta G^{(2)}(r)$	4.9(2)	-	-	1.47 - 2.13
$\Delta G^{(3)}(r)$	4.2(1)	-	-	1.47 - 1.99
$\Delta G_{\mu\mu}(r)$	4.2(1)	-	-	1.47 - 1.92
$\Delta G_R^{(1)}(r)$	-	7.2(1)	-	2.02 - 2.94
$\Delta G_R^{(2)}(r)$	-	7.2(1)	-	2.02 - 2.91
$\Delta G_R^{(3)}(r)$	-	7.2(3)	-	2.02 - 2.98
$\Delta G_{R\mu}^{(1)}(r)$	-	7.2(2)	-	1.66 - 2.96
$\Delta G_{R\mu}^{(2)}(r)$	-	7.2(2)	-	1.66 - 2.96
$\Delta G_{R\mu}^{(3)}(r)$	-	7.2(2)	-	1.66 - 2.96
$g_{\mathrm{RR}}(r)$	-	-	4.6(1)	3.37 - 5.19

Table 5.8: The Al-O, R-O and R-R average coordination numbers for glassy $(R_2O_3)_{0.2}(Al_2O_3)_{0.2}(SiO_2)_{0.6}$ and corresponding integration ranges. The coordination numbers were determined from the area under the first peak of the specified correlation functions obtained from ND.

From equations 5.8 to 5.12 and 5.13 to 5.15, the difference between the $\Delta F_R^{(n)}(q)$ and $\Delta F_{R\mu}^{(n)}(q)$ functions is the contribution from $S_{RR}(q)$. The $\Delta G_R^{(1)}(r)$ and $\Delta G_{R\mu}^{(1)}(r)$ functions are plotted together in figure 5.28. From the figure, although $\Delta G_{R\mu}^{(1)}(r)$ is

much more noisy, the position of the first peak at around 2.33 Å corresponding to the R-O correlations is the same for both functions and the peak at 3.67(5) Å corresponding to R-R correlations in $\Delta G_R^{(1)}(r)$ is absent in $\Delta G_{R\mu}^{(1)}(r)$. It should be noted that the first peak in $\Delta G_{R\mu}^{(1)}(r)$ is broader and less intense by comparison with the first peak in $\Delta G_R^{(1)}(r)$. This is partly due to the Lorch function used to smooth the data in reciprocal space.

From equations 5.18 to 5.22 and 5.23, the difference between the $\Delta F^{(n)}(q)$ functions and $\Delta F_{\mu\mu}(q)$ is the contribution from $S_{RR}(q)$. The $\Delta G^{(1)}(r)$ and $\Delta G_{\mu\mu}(r)$ functions are plotted together in figure 5.29. From the figure, the position of the first few peaks corresponding to the Si-O, Al-O and O-O correlations is the same for both functions and the small negative peak at around 3.7 Å corresponding to the R-R correlations in $\Delta G^{(1)}(r)$ is absent in $\Delta G_{\mu\mu}(r)$.

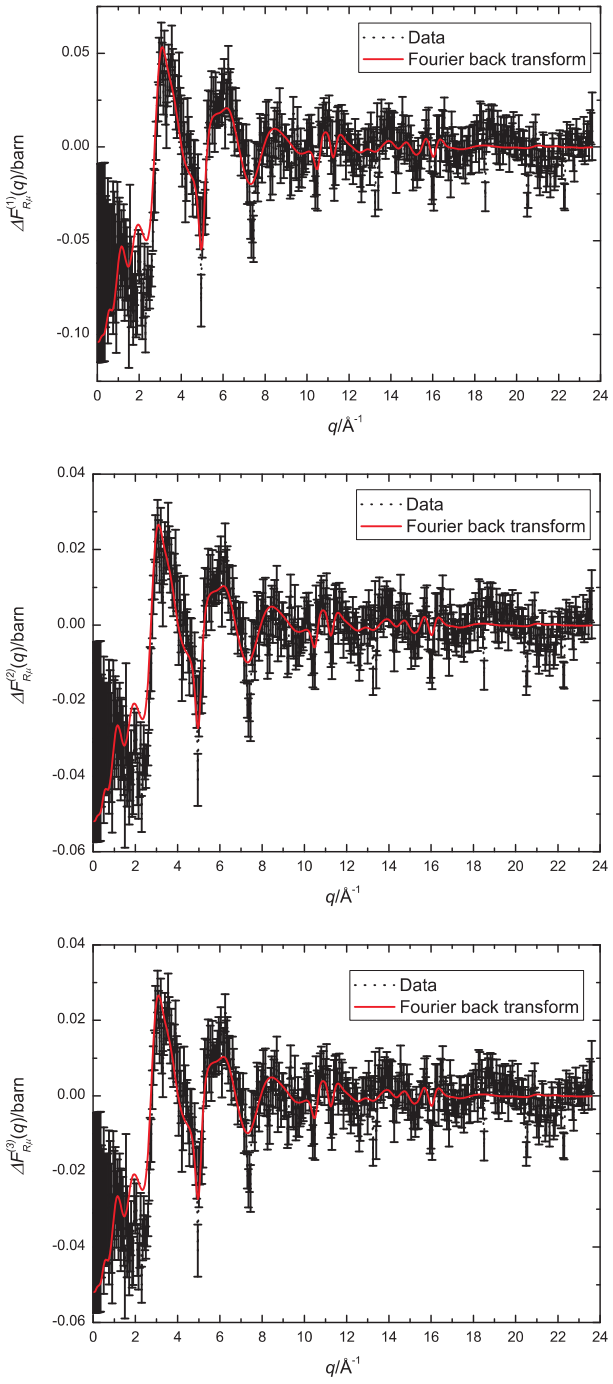

Figure 5.20: The measured $\Delta F^{(n)}_{R\mu}(q)$ ($n = 1$, 2 or 3) functions for glassy $(R_2O_3)_{0.2}(Al_2O_3)_{0.2}(SiO_2)_{0.6}$ calculated from the slope-removed $F(q)$ functions shown in figure 5.5 by using equations 5.27 to 5.29. The dotted lines give the $\Delta F^{(n)}_{R\mu}(q)$ functions (with error bars of the order of ± 0.1 barn) and the solid lines give the Fourier back transforms of the $\Delta G^{(n)}_{R\mu}(r)$ functions given by the solid lines in figure 5.24 where the low r part up to the beginning of the first peak is set to the $\Delta G^{(n)}_{R\mu}(0)$ value.

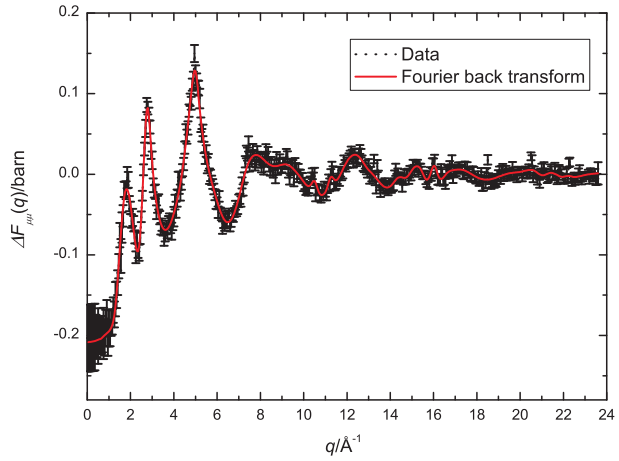

Figure 5.21: The measured $\Delta F_{\mu\mu}(q)$ function for glassy $(R_2O_3)_{0.2}(Al_2O_3)_{0.2}(SiO_2)_{0.6}$ calculated from the slope-removed $F(q)$ functions shown in figure 5.5 by using equation 5.30. The dotted line gives the $\Delta F_{\mu\mu}(q)$ function (with error bars of the order of ± 0.1 barn) and the solid line gives the Fourier back transforms of the $\Delta G_{\mu\mu}(r)$ function given by the solid line in figure 5.25 where the low r part up to the beginning of the first peak is set to the $\Delta G_{\mu\mu}(0)$ value.

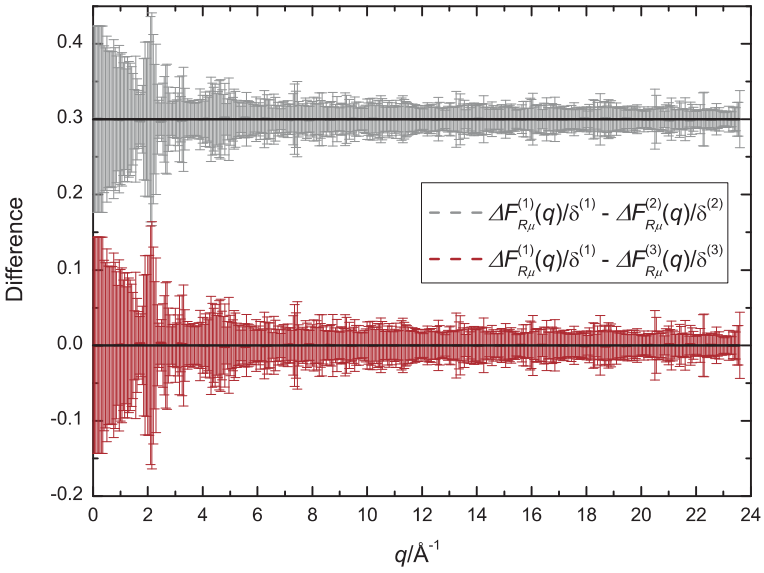

Figure 5.22: The difference between the $\Delta F^{(n)}_{R\mu}(q)/\delta^{(n)}$ (n = 1, 2 or 3) functions for glassy $(R_2O_3)_{0.2}(Al_2O_3)_{0.2}(SiO_2)_{0.6}$ as calculated from the $\Delta F^{(n)}_{R}(q)$ and $S_{RR}(q)$ functions shown in figures 5.11 and 5.17 by using equations 5.8 to 5.12. The functions are displaced vertically for clarity of presentation and the solid horizontal lines mark the level where the difference between functions is zero.

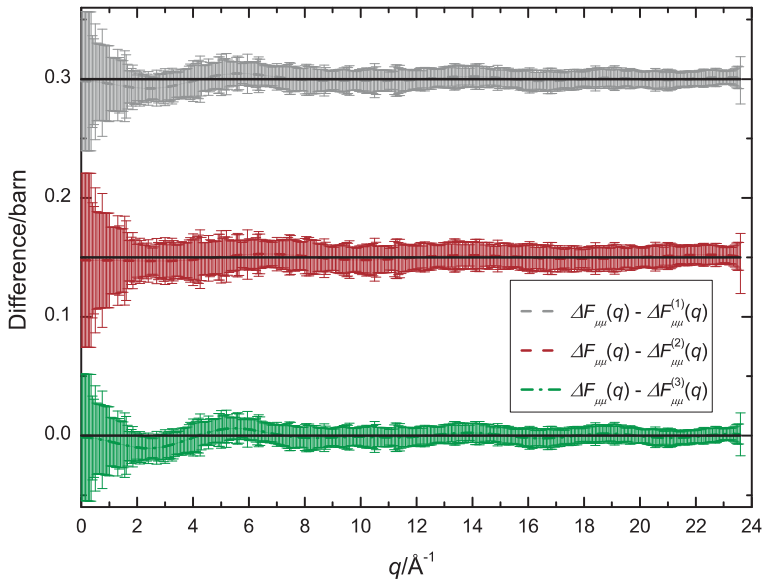

Figure 5.23: The difference between the $\Delta F_{\mu\mu}(q)$ functions, calculated from the slope-removed $F(q)$ functions shown in figure 5.5 using equation 5.30, and the $\Delta F^{(n)}_{\mu\mu}(q)$ functions, calculated from the $\Delta F^{(n)}(q)$ (n = 1, 2 or 3) and $S_{RR}(q)$ functions shown in figures 5.14 and 5.17 by using equations 5.18 to 5.22, for glassy $(R_2O_3)_{0.2}(Al_2O_3)_{0.2}(SiO_2)_{0.6}$. The functions are displaced vertically for clarity of presentation and the solid horizontal lines mark the level where the difference between functions is zero.

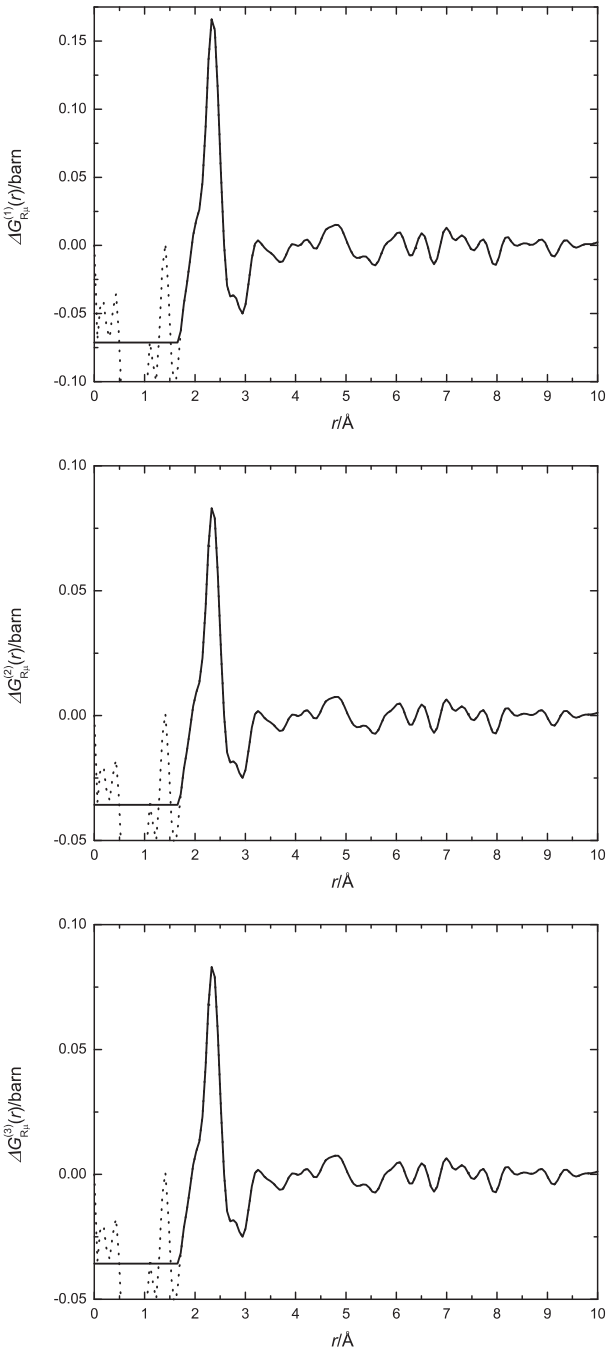

Figure 5.24: The $\Delta G^{(n)}_{R\mu}(r)$ (n = 1, 2 or 3) functions for glassy $(R_2O_3)_{0.2}(Al_2O_3)_{0.2}(SiO_2)_{0.6}$ as obtained by Fourier transforming the smoothed $\Delta F^{(n)}_{R\mu}(q)$ functions shown by the solid lines in figure 5.26. The dotted lines at low r show the artifacts obtained from the Fourier transform procedure.

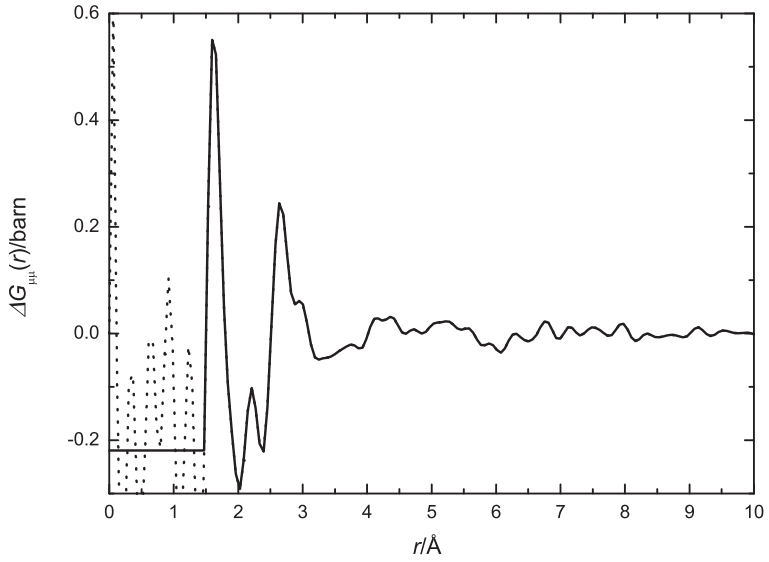

Figure 5.25: The $\Delta G_{\mu\mu}(r)$ function for glassy $(R_2O_3)_{0.2}(Al_2O_3)_{0.2}(SiO_2)_{0.6}$ as obtained by Fourier transforming the smoothed $\Delta F_{\mu\mu}(q)$ function shown by the solid line in figure 5.27. The dotted line at low r shows the artifacts obtained from the Fourier transform procedure.

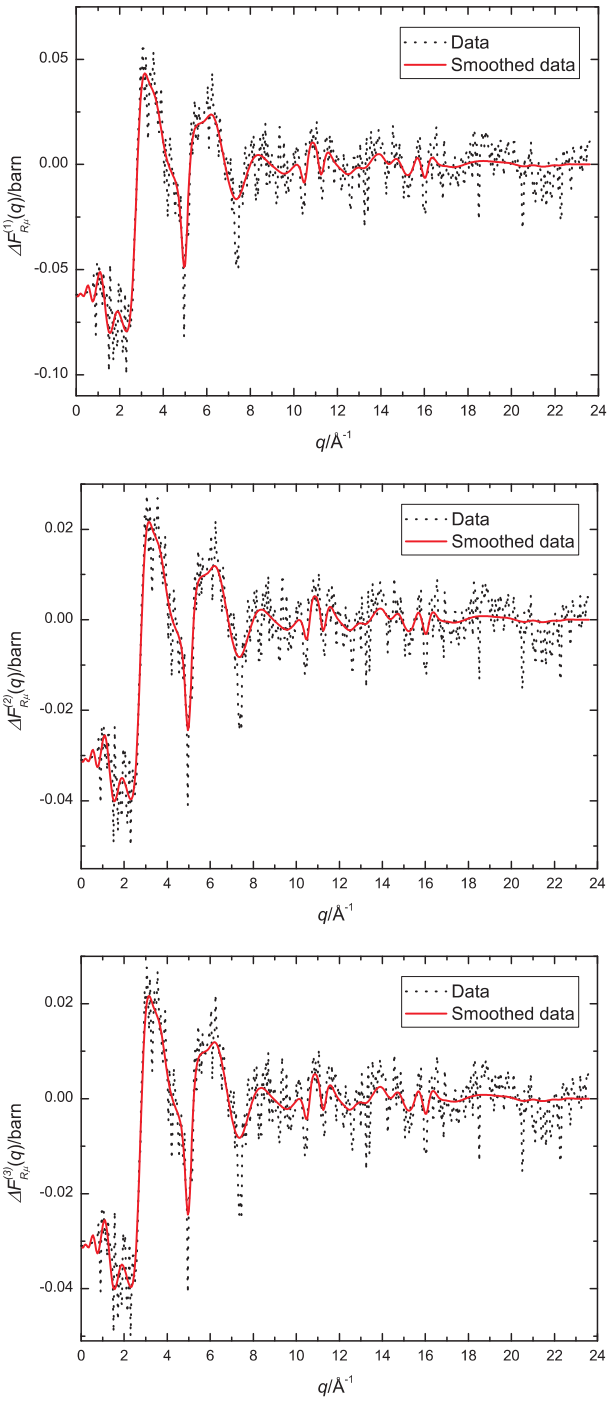

Figure 5.26: The smoothed $\Delta F^{(n)}_{R\mu}(q)$ ($n = 1$, 2 or 3) functions for glassy $(R_2O_3)_{0.2}(Al_2O_3)_{0.2}(SiO_2)_{0.6}$. The dotted lines give the data shown by the dotted lines in figure 5.20 and the solid lines give the smoothed functions.

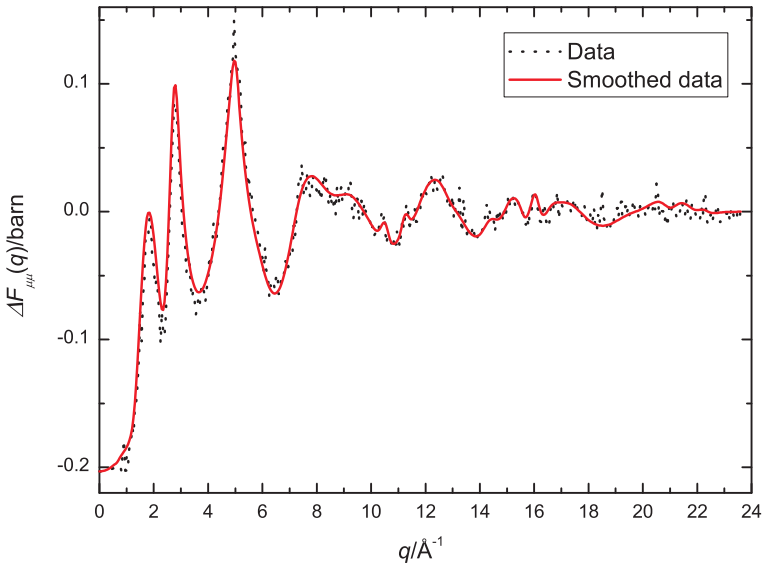

Figure 5.27: The smoothed $\Delta F_{\mu\mu}(q)$ function for glassy $(R_2O_3)_{0.2}(Al_2O_3)_{0.2}(SiO_2)_{0.6}$. The dotted line gives the data shown by the dotted line in figure 5.21 and the solid line gives the smoothed function.

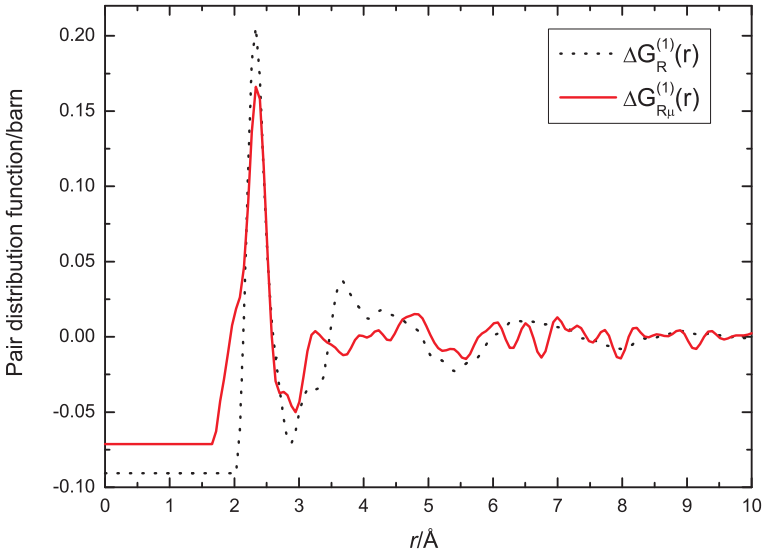

Figure 5.28: A comparison between the $\Delta G_R^{(1)}(r)$ and $\Delta G_{R\mu}^{(1)}(r)$ functions for glassy $(R_2O_3)_{0.2}(Al_2O_3)_{0.2}(SiO_2)_{0.6}$.

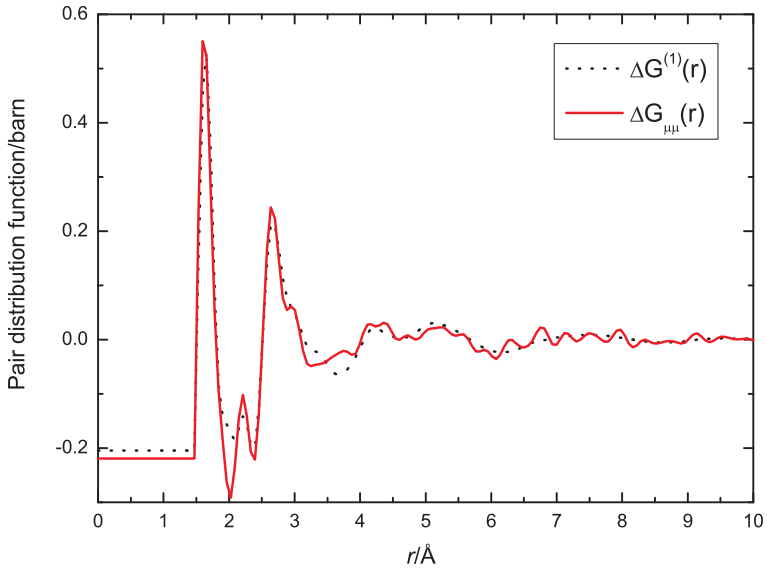

Figure 5.29: A comparison between the $\Delta G^{(1)}(r)$ and $\Delta G_{\mu\mu}(r)$ functions for glassy $(R_2O_3)_{0.2}(Al_2O_3)_{0.2}(SiO_2)_{0.6}$.

5.6 XRD Results

In this section, the $S_X(q)$ and $G_X(r)$ functions obtained from the XRD experiment are presented. Because the same element can have different scattering lengths as seen by neutrons and x-rays, a comparison between the total structure factors and total pair distribution functions obtained from the two techniques can give more structural information about a system. The fully corrected $S_X(q)$ and $G_X(r)$ functions for $(Dy_2O_3)_{0.2}(Al_2O_3)_{0.2}(SiO_2)_{0.6}$ glass are shown in figure 5.30. Also shown in figure 5.30 are the $S_N(q)$ and $G_N(r)$ functions for the same glass. From the figure, there is a significant contrast between the $S_N(q)$ and $S_X(q)$ functions which translates into different relative intensities for the peaks in the corresponding $G_N(r)$ and $G_X(r)$ functions thus making it easier to identify the correlations to which the peaks in the total pair distribution functions correspond.

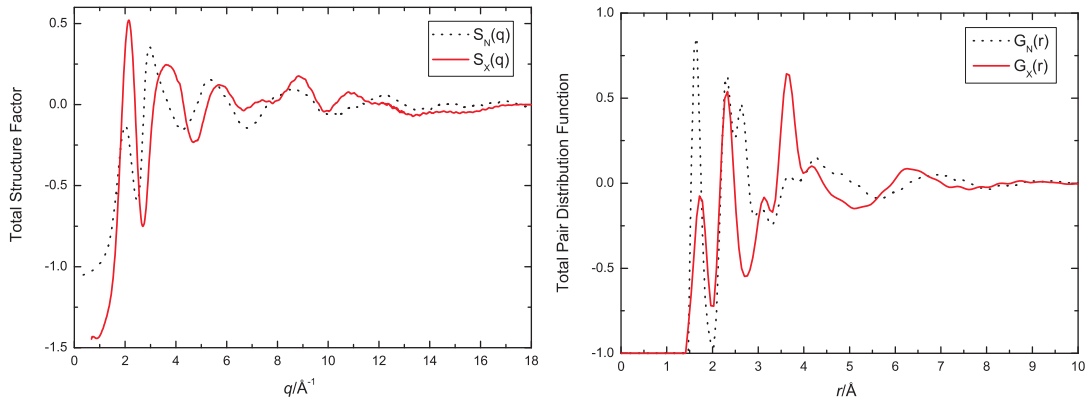

Figure 5.30: A comparison between the total structure factors and the corresponding total pair distribution functions for $(Dy_2O_3)_{0.2}(Al_2O_3)_{0.2}(SiO_2)_{0.6}$ glass as obtained from ND and XRD.

The neutron and x-ray weighting factors for each partial structure factor in $(Dy_2O_3)_{0.2}(Al_2O_3)_{0.2}(SiO_2)_{0.6}$ glass are summarised in table 5.9. From the table, the correlations which have a relatively large contribution are O-O and R-O for the $G_N(r)$ function and R-O and R-R for the $G_X(r)$ function. Thus the peak in both $G_N(r)$ and $G_X(r)$ at $r = 2.31(3)$ Å corresponding to the R-O correlations should have a relatively large intensity (see figure 5.30). The peak at $r = 2.63(5)$ Å has a large intensity in $G_N(r)$ but is almost non-existent in $G_X(r)$ and should correspond to the O-O correlations which have a weighting factor of $\approx 34\%$ for neutrons and $\approx 11\%$ for x-rays. The peak at $r \approx 3.7$ Å has a large intensity in $G_X(r)$ but a

relatively low intensity in $G_N(r)$ and should correspond to the R-R correlations which have a weighting factor of $\approx 6\%$ for neutrons and $\approx 20\%$ for x-rays. The peaks positions corresponding to the identified correlations from the ND and XRD results are summarised in table 5.10.

Pair correlation	ND (%)	XRD ($q = 0$)(%)
R-R	6.408	19.901
R-Al	2.933	8.443
R-Si	5.29	11.756
R-O	29.597	28.938
Al-Al	0.336	0.895
Al-Si	1.211	2.494
Al-O	6.772	6.138
Si-Si	1.092	1.736
Si-O	12.217	8.547
O-O	34.173	10.52

Table 5.9: A comparison between the neutron and x-ray weighting factors for each partial structure factor found in glassy $(R_2O_3)_{0.2}(Al_2O_3)_{0.2}(SiO_2)_{0.6}$ where R = Dy. The weighting factors, which is presented as percentages, were calculated using the definitions of $S_N(q)$ and $S_X(q)$ given by equations 5.1, 5.5, 5.33 and 5.34.

It should be noted that the position of the first peak in $G_N(r)$ and $G_X(r)$ which corresponds to the Al-O and Si-O correlations is at 1.64(2) Å in $G_N(r)$ and at 1.74(3) Å in $G_X(r)$. In $G_N(r)$ the contribution from the Si-O correlations is about 80% higher than the contribution from the Al-O correlations whereas in $G_X(r)$ it is about 40% higher. The difference in the peak position is therefore consistent with an Si-O atomic distance that is smaller relative to the Al-O atomic distance. This agrees with the results obtained from an XRD experiment on $Ca_{x/2}Al_xSi_{1-x}O_2$ glasses ($x = 0$, 0.25, 0.5 or 0.67) and an ND experiment on $RAl_{0.35}P_{3.24}O_{10.12}$ glasses, where R denotes La or Ce [119, 165], which give an Si-O distance of 1.60 Å that is smaller than the Al-O distance of 1.75(1) Å for AlO_4 units or 1.89(3) Å for AlO_6 units.

As seen in figure 5.30, the peak at $r = 2.31(2)$ Å in $G_X(r)$ corresponding to R-O correlations is quite isolated such that $\bar{n}_{\mathrm{R}}^{\mathrm{O}}$ could be estimated from the area under the peak. By using equation 5.47, $\bar{n}_{\mathrm{R}}^{\mathrm{O}} = 8.6(4)$ which is higher than the values

Correlation function	Nearest neighbour distance (Å)			
	Si-O or Al-O	R-O	O-O	R-R
${}^{Dy}G_X(r)$	1.74(3)	2.31(2)	-	3.65(2)
${}^{Dy}G(r)$	1.64(2)	2.31(3)	2.63(5)	3.7(1)
${}^{Mix}G(r)$	1.64(2)	2.31(3)	2.64(5)	3.7(1)
${}^{Ho}G(r)$	1.64(2)	2.31(3)	2.65(5)	3.7(1)
$\Delta G^{(1)}(r)$	1.64(2)	-	2.68(5)	-
$\Delta G^{(2)}(r)$	1.65(2)	-	2.69(5)	-
$\Delta G^{(3)}(r)$	1.64(2)	-	2.67(5)	-
$\Delta G_{\mu\mu}(r)$	1.62(2)	-	2.65(5)	-
$\Delta G_R^{(1)}(r)$	-	2.33(2)	-	3.67(5)
$\Delta G_R^{(2)}(r)$	-	2.32(2)	-	3.68(5)
$\Delta G_R^{(3)}(r)$	-	2.33(2)	-	3.66(5)
$\Delta G_{R\mu}^{(1)}(r)$	-	2.35(3)	-	-
$\Delta G_{R\mu}^{(2)}(r)$	-	2.35(3)	-	-
$\Delta G_{R\mu}^{(3)}(r)$	-	2.35(3)	-	-
$g_{\mathrm{RR}}(r)$	-	-	-	3.68(3), 4.38(5)

Table 5.10: Nearest neighbour distances for Si-O or Al-O, R-O, O-O and R-R correlations for glassy $(R_2O_3)_{0.2}(Al_2O_3)_{0.2}(SiO_2)_{0.6}$ where R denotes Dy, Ho or a 50:50 mixture of Dy and Ho as obtained from ND and XRD experiments.

obtained from ND, see table 5.8. It should be noted that $\bar{n}_{\mathrm{R}}^{\mathrm{O}}$ obtained from XRD is an overestimate because the R-O peak in figure 5.30 is not entirely separated and contributions from other correlations were not taken into account.

5.7 EXAFS Results

XAS measurements for $(R_2O_3)_{0.2}(Al_2O_3)_{0.2}(SiO_2)_{0.6}$ glasses where R denotes Dy or Ho were collected. The data points corresponding to glitches in the absorption spectra were removed and all of the scans were aligned. The $\chi(k)$ functions were extracted from the absorption spectra by using the background functions determined using the AUTOBK algorithm in ATHENA [62], fitted to the data from the energy edge to the last data point with $R_{bkg} = 1$ Å. The absorption spectra and the background functions are shown in figure 5.31. Only one scan was collected for

each sample except for the $(Ho_2O_3)_{0.2}(Al_2O_3)_{0.2}(SiO_2)_{0.6}$ glass prepared by grinding with a diamond file where two scans were measured. The final data set shown in figure 5.31 is the average of both scans.

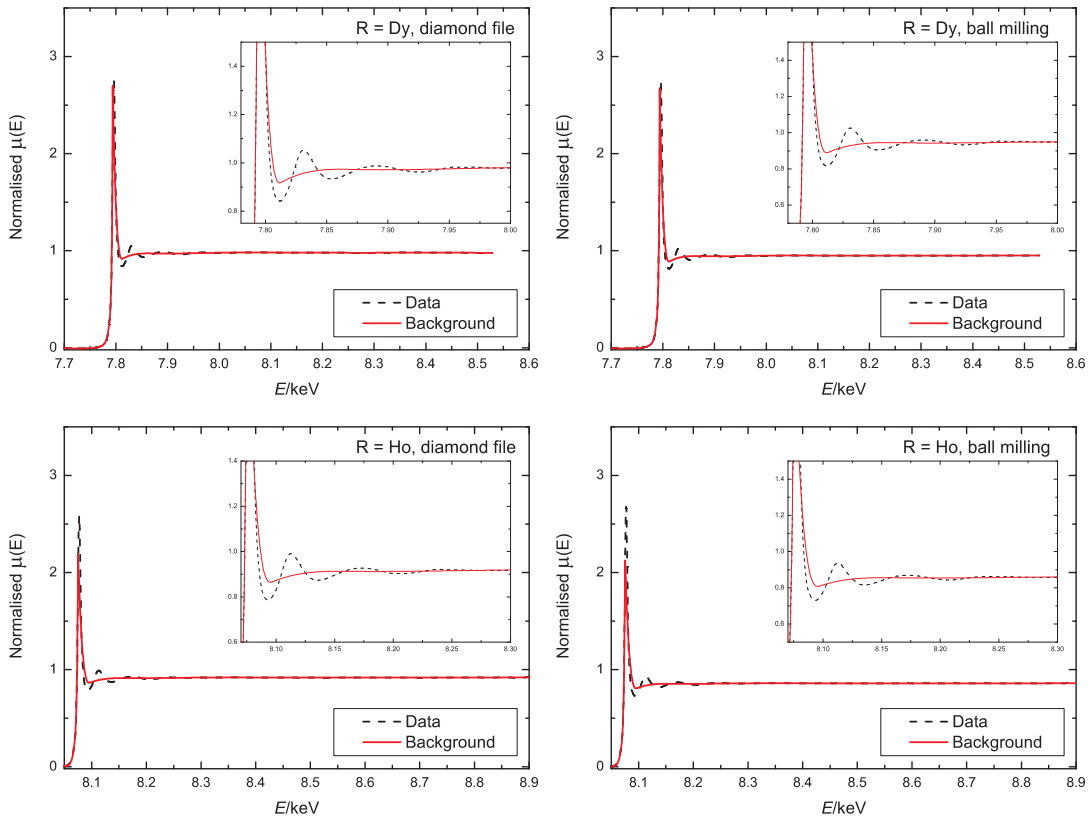

Figure 5.31: Normalised absorption spectra and the fitted background for $(R_2O_3)_{0.2}(Al_2O_3)_{0.2}(SiO_2)_{0.6}$ glass where R denotes Dy or Ho. Each glassy sample was prepared by using two different methods for grinding, namely a ball milling machine or a diamond file. The dashed lines give the measured normalised absorption spectra and the solid lines give the background signal. The insets show the region near the absorption edge energy.

The extracted $\chi(k)$ functions are shown as $k^3\chi(k)$ in figure 5.32. The usable k range for all of the extracted $\chi(k)$ functions is from 2 to 10.66 Å^{-1}. The k range on the high k side was limited mainly by the distortion of the XAS spectra due to scattering from the L_{II} edges which occur at 8.581 keV for Dy and at 8.918 keV for Ho [161]. Apart from the short k range available due to absorption at the L_{II} edge, another disadvantage of performing an experiment on the L_{III} edge includes features in the background caused by double excitations. The energy at which a double excitation should be observed can be estimated by using the rule of Z+1 [171]. For the Dy L_{III} edge the feature corresponds to the energy of the Ho L_{III} edge

($E = 8.071$ keV corresponding to $k = 8.59$ Å^{-1} at the Dy L_{III} edge) and for the Ho L_{III} edge the feature corresponds to the energy of the Er L_{III} edge ($E = 8.358$ keV corresponding to $k = 8.68$ Å^{-1} at the Ho L_{III} edge). The double excitation features for the glasses measured in the present experiment can be seen in figure 5.32. As the glitches cover a large number of data points they are left in the data, although care needs to be taken when refining the data as these features do not contain structural information.

As seen from figure 5.32 there is no significant difference between the samples ground by using the ball milling machine and the diamond file. In fact, all the $k^3\chi(k)$ functions shown in figure 5.32 are very similar which suggests similar local structures for Dy and Ho in these glasses and justifies use of the isomorphic substitution method in ND. The $k^3\chi(k)$ functions for the $(R_2O_3)_{0.2}(Al_2O_3)_{0.2}(SiO_2)_{0.6}$ glasses prepared by using the different methods were therefore merged for better statistics. The merged $k^3\chi(k)$ functions for each glass and corresponding $|\tilde{\chi}(R)|$ functions are shown in figure 5.33.

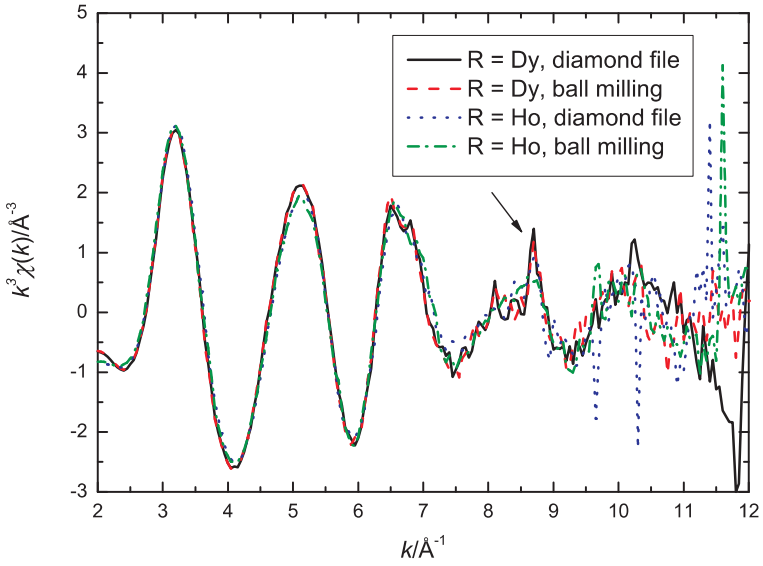

Figure 5.32: The $k^3\chi(k)$ functions extracted from the absorption spectra shown in figure 5.31 for $(R_2O_3)_{0.2}(Al_2O_3)_{0.2}(SiO_2)_{0.6}$ glasses where R denotes Dy or Ho. The arrow marks the feature in the background corresponding to double excitations.

From figure 5.33, both of the $|\tilde{\chi}(R)|$ functions contain two main peaks about 1 Å apart. The first peak at $R \approx 1.8$ Å is most likely due to R-O nearest neighbours. The smaller second peak at $R \approx 2.8$ Å could be due to a distribution of R-O

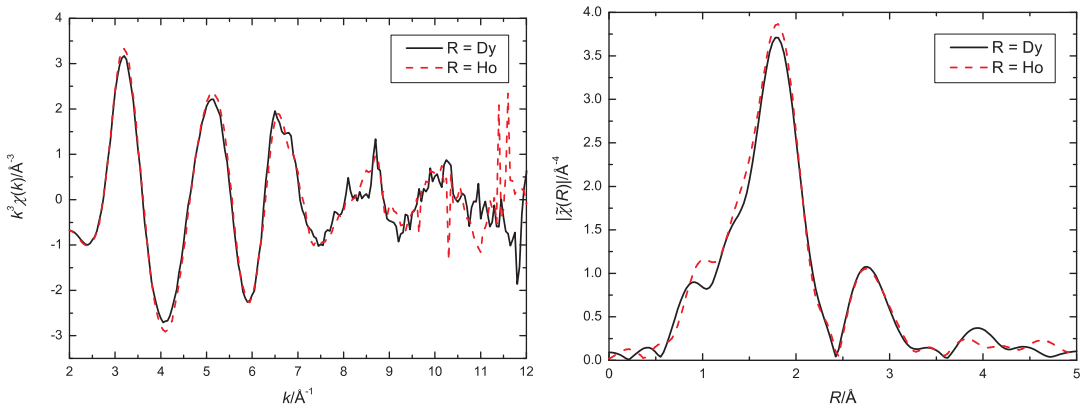

Figure 5.33: The $k^3\chi(k)$ and corresponding $|\tilde{\chi}(R)|$ function for $(R_2O_3)_{0.2}(Al_2O_3)_{0.2}(SiO_2)_{0.6}$ glasses where R denotes Dy or Ho. The $k^3\chi(k)$ functions are averages of the data sets taken for the samples prepared by using a diamond file and a ball milling machine.

distances, multiple scattering from the nearest neighbour O shell, or the Si and/or Al next nearest neighbours as suggested by earlier EXAFS experiment on $Nd_2Al_2Si_3O_{12}$ or 0.08-3 mole% Er_2O_3 doped alumino-silicate glasses [140, 148]. The interpretation of the EXAFS signals will be discussed in sections 5.8.3 and 5.9.

5.8 Modeling

In this section, the details of the MD-RMC method are described. In section 5.8.1, the input parameters are given including the effective charges on the ions for the potentials used in the MD simulation. In section 5.8.2, the results from the MD simulation were used as an initial configuration for the RMC modeling. The input parameters for the RMC model, which include the distances of closest approach and coordination number constraints, are described. The final results from the RMC model were used to generate $\chi(k)$ functions which are compared with the experimental data in section 5.8.3.

5.8.1 MD Model

The MD simulation was made for $(Dy_2O_3)_{0.2}(Al_2O_3)_{0.2}(SiO_2)_{0.6}$ glass by using the program DL_POLY [172, 152]. The model consists of 200 Dy, 200 Al, 300 Si and 1200 O atoms with a number density of 0.078 $Å^{-3}$. The potential used for the

simulation was a combination of Coulomb and Buckingham potentials which can be written as

$$V_{\alpha\beta}(r) = \frac{q_\alpha q_\beta}{4\pi\epsilon_0 r} + A_{\alpha\beta}\exp\{(-r/\rho_{\alpha\beta})\} - C_{\alpha\beta}/r^6, \tag{5.81}$$

where r is a radial distance between atoms of type α and β, q_α is an effective charge on an atom of type α, ϵ_0=8.854×10^{12} C^2/N·m^2 is the permitivity of free space, $A_{\alpha\beta}$, $\rho_{\alpha\beta}$ and $C_{\alpha\beta}$ are Buckingham potential parameters for the atomic pairs α and β. As suggested by Du [145], the potential parameters for several silica and silicate glasses and crystals are transferable. The effective charges and potential parameters for the Si-O, Al-O and O-O pairs were therefore taken from [145] and those for the Dy-O pair were taken from [173]. The values are summarised in table 5.11. As interactions between cation-cation pairs are dominated by the Coulomb potential, the short ranged interactions due to those pairs were not taken into account in the simulation.

α-β	q_α (e)	$A_{\alpha\beta}$ (eV)	$\rho_{\alpha\beta}$ (Å)	$C_{\alpha\beta}$ (eV·Å^{-6})
Dy-O	1.8	79812	0.1947	62.51
Al-O	1.8	12201	0.1956	31.99
Si-O	2.4	13702.905	0.193817	54.681
O-O	-1.2	1844.7458	0.343645	192.58

Table 5.11: Effective charges and parameters for the Buckingham potential used in the MD simulation. The parameters for the Si-O, Al-O and O-O pairs were taken from [145] and those for the Dy-O pair were taken from [173].

As seen by equation 5.81, the $C_{\alpha\beta}/r^6$ term on the right hand side representing attractive dispersion forces can become very large when r is small and can result in atoms being pushed towards each other. The starting configuration for the MD model therefore needs to have appropriate closest approach limits for each atomic pair. Thus a starting configuration for the MD model was generated by making a hard sphere Monte Carlo model using the program RMCA [154] by running with specified cutoff values and without experimental data. The cutoff values were estimated based on the diffraction results presented in sections 5.5 and 5.6 and are presented in table 5.12. It was found, however, that an addition 0.5 Å needed to be added to the original values obtained from the diffraction results in order to prevent the atoms from being pushed too far towards each other.

Pair correlation	Distance of closest approach (Å)
Dy-Dy	3.7
Dy-Al	3.0
Dy-Si	3.0
Dy-O	2.5
Al-Al	3.0
Al-Si	3.0
Al-O	1.9
Si-Si	3.0
Si-O	1.9
O-O	2.5

Table 5.12: The cutoff values used for the hard sphere simulation. The values were estimated based on the diffraction results presented in sections 5.5 and 5.6.

The MD simulation was run using an NVT ensemble (constant number of atoms, volume and temperature), a time step of 2 fs and a Berendsen thermostat for temperature control. The simulation was run in 3 stages. The first stage was a simulation at 4000 K for 80 ps to ensure that the sample was completely molten. After that the simulation was run at 1873 K (the same temperature at which the sample was left in the furnace during the sample preparation) for another 80 ps. The last stage was to instantaneous quench the sample and run the simulation at 300 K for 160 ps to ensure that the system reached equilibrium.

The reciprocal space correlation functions $F(q)$, $\Delta F_{R\mu}^{(n)}(q)$ (n = 1, 2 or 3), $\Delta F_{\mu\mu}(q)$ and $S_{RR}(q)$, and the corresponding real space correlation functions $G(r)$, $\Delta G_{R\mu}^{(n)}(r)$, $\Delta G_{\mu\mu}(r)$ and $g_{\mathrm{RR}}(r)$ reproduced from the simulated $S_{\alpha\beta}(q)$ and $g_{\alpha\beta}(r)$ functions are compared using the ND results in figures 5.34 to 5.36. Also shown is a comparison between the simulated and experimental $S_X(q)$ and $G_X(r)$ where the latter was obtained from $S_X(q)$ by Fourier transformation. From the figures, the correlation functions determined from the MD simulation are similar to the experimental data. All of the main features in the measured reciprocal and real space functions were reproduced, although some discrepancies remain such as the sharpness of the first peak in the case of $F(q)$, $\Delta F_{R\mu}^{(n)}(q)$ and $S_X(q)$ functions or a shift of the first peak position to lower r in the case of $G(r)$, $G_X(r)$, $\Delta G_{\mu\mu}(r)$ and

$g_{\mathrm{RR}}(r)$ functions.

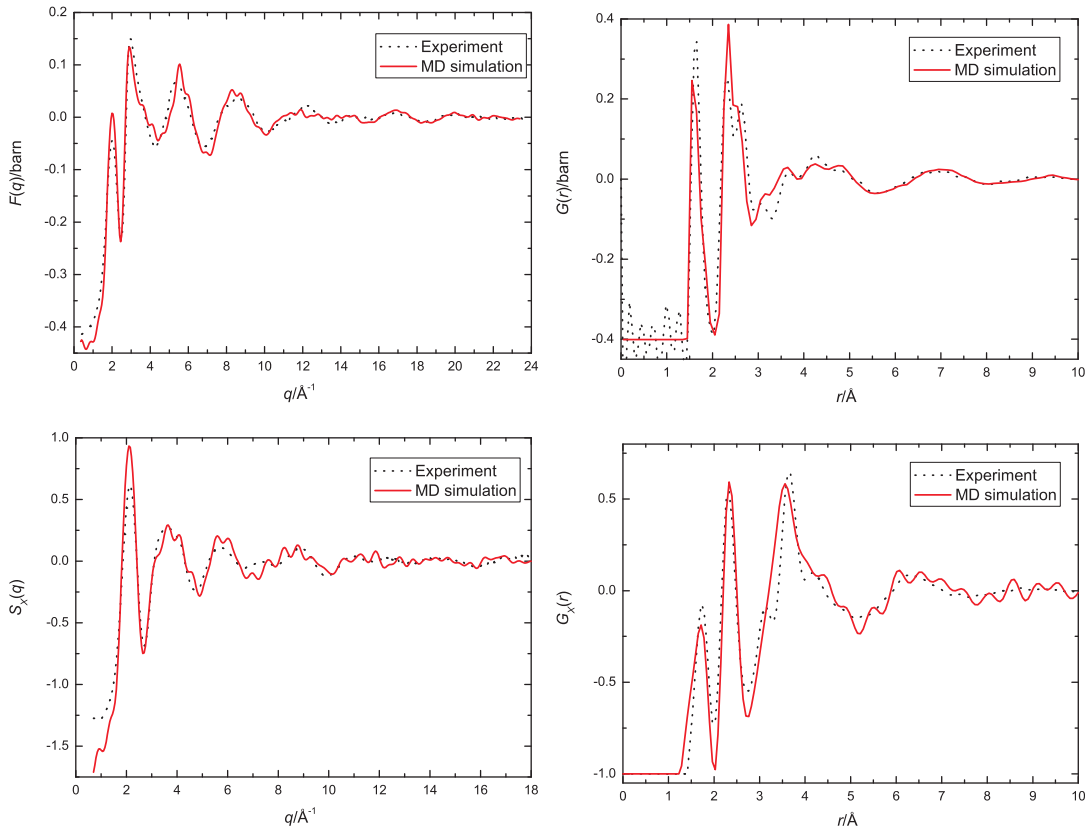

Figure 5.34: A comparison between the $F(q)$, $G(r)$, $S_X(q)$ and $G_X(r)$ functions for $(Dy_2O_3)_{0.2}(Al_2O_3)_{0.2}(SiO_2)_{0.6}$ glass measured using ND and XRD experiments and calculated from the MD simulation. The dotted lines give the experimental data and the solid lines give the simulation results. The experimental error for the $F(q)$ function is of the order of $\pm 10^{-3}$ barn.

The average Dy-Dy, Dy-O, Al-O, Si-O and O-O atomic distances and some coordination numbers obtained from the simulation are presented in table 5.13 and the distribution of coordination numbers are shown in figure 5.37. The Dy-Dy, Dy-O, Al-O and Si-O coordination numbers as well as the distribution of coordination numbers were determined from the simulation results by using the program NextTo in the RMCA package [154] with the high r limits chosen to correspond to the first minimum after the first peak in real space. From figure 5.37, almost all of the Si-O units are 4-fold coordinated. For the Al-O coordination environment, most of the units are 4-fold coordinated and there is about 15 % of 5-fold coordinated units and about 1 % of 6-fold coordinated units. These results are similar to those obtained from NMR spectroscopy for $(Y_2O_3)_{0.2}(Al_2O_3)_{0.2}(SiO_2)_{0.6}$ glass [35, 147] which gives

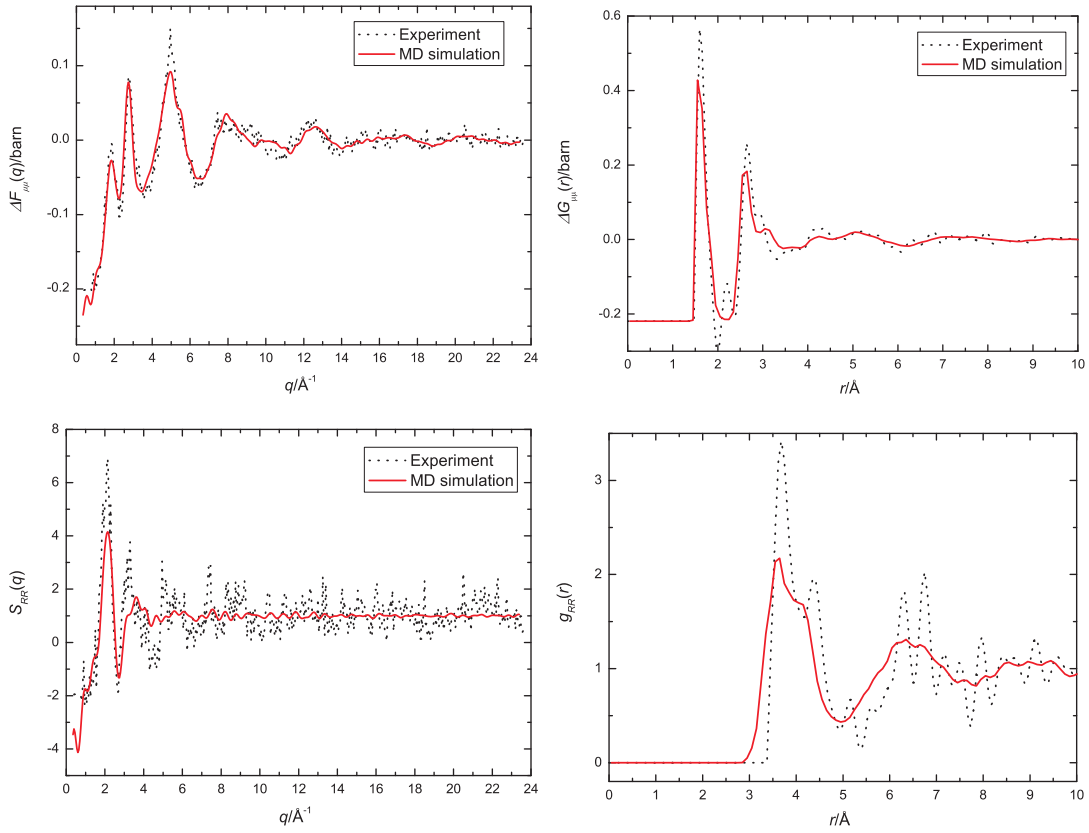

Figure 5.35: A comparison between the $\Delta F_{\mu\mu}(q)$, $S_{RR}(q)$, $\Delta G_{\mu\mu}(r)$ and $g_{\mathrm{RR}}(r)$ functions obtained from the isomorphic substitution method in ND and from MD simulation. The dotted lines give the experimental data and the solid lines give the simulation results. The experimental errors for the $\Delta F_{\mu\mu}(q)$ and $S_{RR}(q)$ functions are of the order of ± 0.1 barn and ± 0.1, respectively.

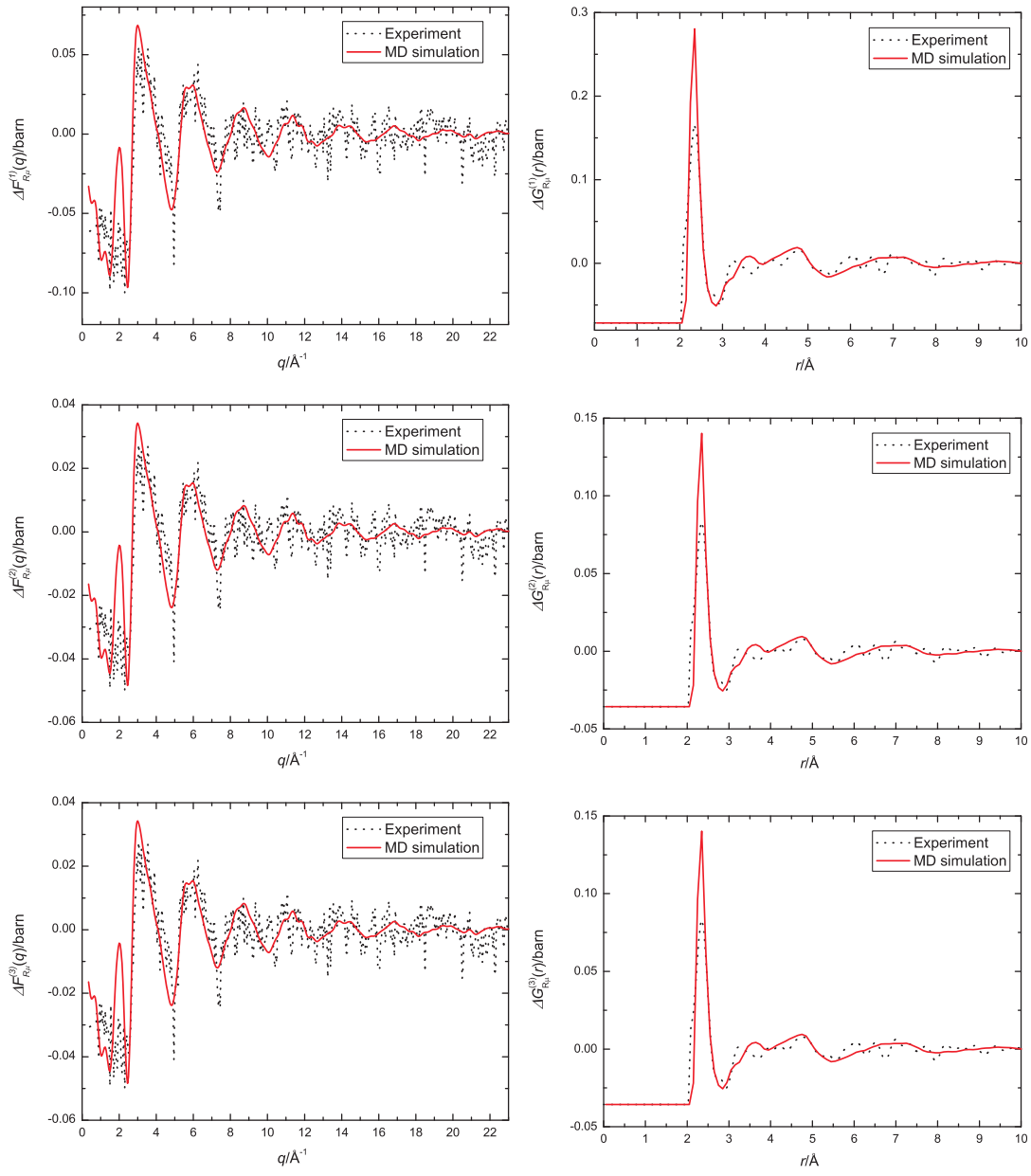

Figure 5.36: A comparison between the $\Delta F^{(n)}_{R\mu}(q)$ and $\Delta G^{(n)}_{R\mu}(r)$ (n = 1, 2 or 3) functions obtained from the isomorphic substitution method in ND and from MD simulation. The dotted lines give the experimental data and the solid lines give the simulation results. The experimental errors for the $\Delta F^{(n)}_{R\mu}(q)$ functions are of the order of $\pm$0.1 barn.

the fractions of 4-, 5- and 6-fold units as 78(3), 16(3) and 6(3) %, respectively. For the Dy-O coordination number, most of the units are 6-fold coordinated with a considerable amount of 5- and 7-fold coordinated units. For the Dy-Dy correlations, the distribution of coordination numbers is very broad with $\bar{n}_{\mathrm{R}}^{\mathrm{R}}$ in the range from zero to 7.

	Nearest neighbour distance (Å)	Coordination number	r range (Å)
Dy-Dy	3.6(1)	3.8	2.85 - 4.95
Dy-O	2.34(2)	6.1	2.05 - 2.75
Al-O	1.77(2)	4.2	1.55 - 2.25
Si-O	1.59(2)	4.0	1.45 - 1.85
O-O	2.61(2)	-	-

Table 5.13: The nearest neighbour distances and coordination numbers for the Dy-Dy, Dy-O, Al-O, Si-O and O-O correlations as obtained from the MD model. The r ranges used to determine the coordination numbers are also given.

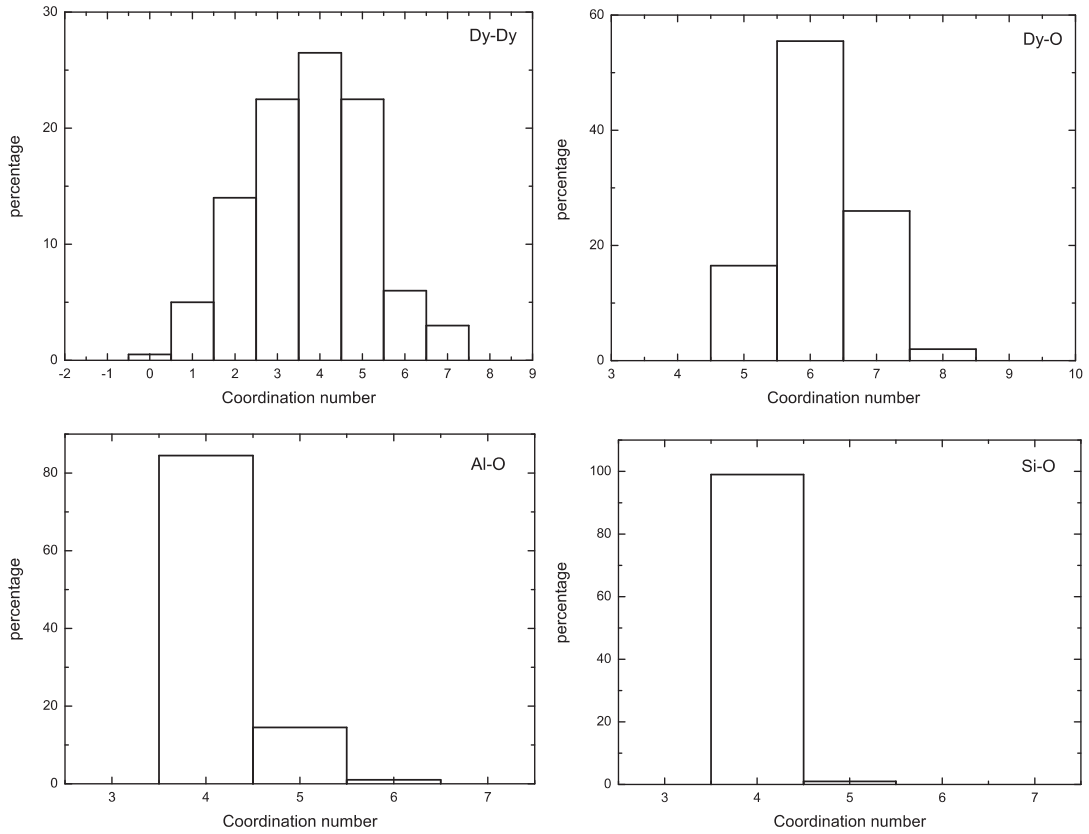

Figure 5.37: The distributions of the Dy-Dy, Dy-O, Al-O and Si-O coordination numbers obtained from the MD simulation of the $(Dy_2O_3)_{0.2}(Al_2O_3)_{0.2}(SiO_2)_{0.6}$ glass.

5.8.2 RMC Model

As there are some discrepancies between the correlation functions obtained from the simulation and experiment, the configuration obtained from the MD model was refined using the experimental data presented in sections 5.5 and 5.6 by using the method of RMC modeling. Because the $S_{RR}(q)$, $\Delta F^{(n)}_{R\mu}(q)$ and $\Delta F_{\mu\mu}(q)$ functions were obtained from three $F(q)$ functions, and thus contain large error bars, they were not used for the refinement. Instead, the MD configuration was refined using i) the $F(q)$ functions from the ND experiment on the $(R_2O_3)_{0.2}(Al_2O_3)_{0.2}(SiO_2)_{0.6}$ glasses, where R denotes Dy, Ho or a 50:50 mixture of Dy and Ho, ii) the $\Delta F^{(n)}_{R}(q)$ and $\Delta F^{(n)}(q)$ functions obtained from the isomorphic substitution method in ND and iii) the $S_X(q)$ function measured in the XRD experiment on the $(Dy_2O_3)_{0.2}(Al_2O_3)_{0.2}(SiO_2)_{0.6}$ glass. The modeling was performed by employing the RMC++ program [155, 174, 156].

Because the Al-O coordination numbers for the $(Y_2O_3)_{0.2}(Al_2O_3)_{0.2}(SiO_2)_{0.6}$ glass have been determined [35, 147] and Y is isomorphic with Dy and Ho, Al-O coordination number constraints were applied according to the NMR results which give 78(3), 16(3) and 6(3) % for the relative fractions of AlO_4, AlO_5 and AlO_6 units, respectively. For the Si-O units, a coordination constraint of 100% 4-fold SiO_4 units was applied. The low r cutoff distances specified for the closest approach distance between each pair of atoms were chosen according to the MD results. It should be noted that in order to satisfy these coordination constraints the simulation needed to initially run without experimental data and the values of σ_c^2 in equation 5.69 for each constraint were set to 10^{-5} and kept at this value when the experimental data were later added to the modeling. During this initial run, only O atoms were allowed to move to ensure that only a small change was made to the configuration obtained from the MD simulation as this configuration already gave pair correlation functions similar to the experimental results, see figures 5.34 to 5.36. By allowing O atoms to move, the local coordination environment of Dy could also change. Therefore, the 16, 56 and 28% fractions of DyO_5, DyO_6 and DyO_7 units obtained from the MD simulation were also used as coordination number constraints in order to maintain the Dy-O coordination number of the MD result. After the initial run the configuration had 99% of SiO_4 units, 77.5% of AlO_4 units, 15.5% of AlO_5 units and 5% of AlO_6 units.

When the experimental data were added to the modeling procedure, the coordination number constraints for the Dy-O units were removed. The initially low r cutoff values were adjusted slightly during the modeling, mainly to remove non-physical spikes at low r in the $g_{\alpha\beta}(r)$ functions. The final cutoff values for each pair of correlation functions are presented in table 5.14. The measured $F(q)$ functions for the three glasses and the $S_X(q)$ function for the $(Dy_2O_3)_{0.2}(Al_2O_3)_{0.2}(SiO_2)_{0.6}$ glass along with the $\Delta F_R^{(n)}(q)$ and $\Delta F^{(n)}(q)$ functions used to refine the model are compared with the results from the RMC procedure in figures 5.38 to 5.41. In these figures, a comparison is also made between the experimental $G_N(r)$, $G_X(r)$, $\Delta G_R^{(n)}(r)$ and $\Delta G^{(n)}(r)$ functions presented in sections 5.5 to 5.6 and those produced from the RMC model. In addition, the $S_{RR}(q)$, $\Delta F_{\mu\mu}(q)$, $\Delta F_{R\mu}^{(n)}(q)$, $g_{\mathrm{RR}}(r)$, $\Delta G_{\mu\mu}(r)$ and $\Delta G_{R\mu}^{(n)}(r)$ functions obtained from the isomorphic substitution method in ND

are compared with those produced from the RMC model in figures 5.42 and 5.43. It should be noted that each correlation function obtained from the RMC method was an average of 50 functions determined from RMC configurations which were collected at $5\mathcal{N}$ accepted moves apart, where $\mathcal{N} = 1900$ is the number of atoms in the model. This gives errors bar in $S_{\alpha\beta}(q)$ of the order of $\pm 10^{-2}$.

Pair correlation	Distance of closest approach (Å)
Dy-Dy	2.73
Dy-Al	2.49
Dy-Si	2.67
Dy-O	2.01
Al-Al	2.49
Al-Si	1.89
Al-O	1.41
Si-Si	2.61
Si-O	1.41
O-O	2.01

Table 5.14: The cutoff values used for the RMC model.

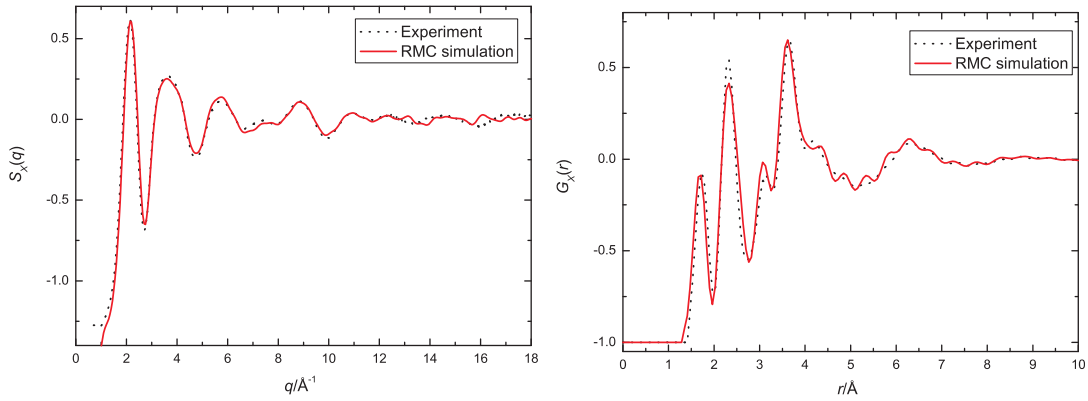

Figure 5.38: A comparison between the $S_X(q)$ and $G_X(r)$ functions for $(Dy_2O_3)_{0.2}(Al_2O_3)_{0.2}(SiO_2)_{0.6}$ glass obtained from the XRD experiment and from the RMC model. The dotted lines give the experimental data and the solid lines give the fits obtained from the model.

From figures 5.38 to 5.43, it can be seen that RMC modeling gives improved fits to the experimental data although some discrepancies such as the sharpness of the first peak in all of the real space functions can be seen. The R-R, R-O, Al-O and Si-O coordination numbers were determined from the simulation results by

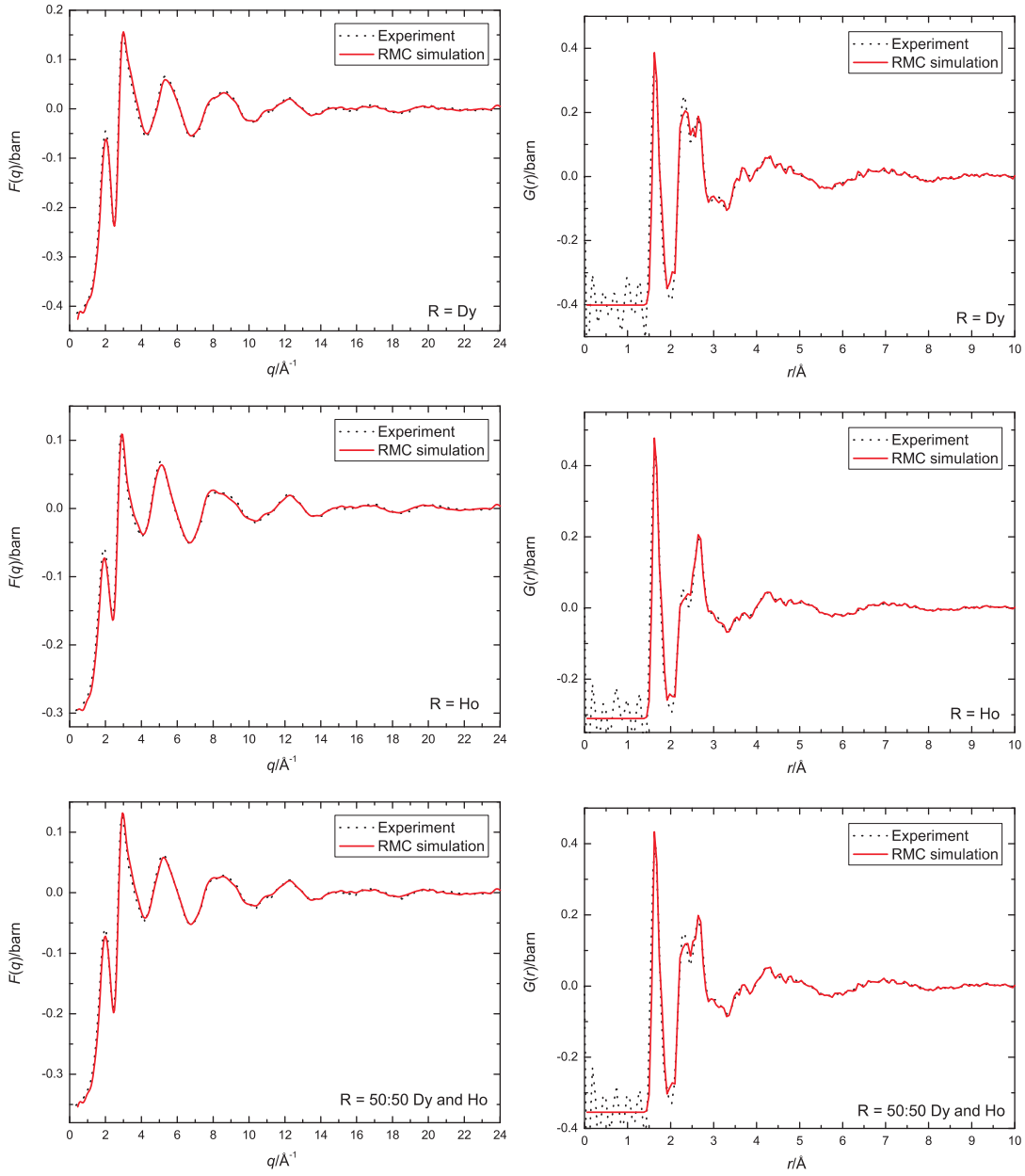

Figure 5.39: A comparison between the $F(q)$ and $G(r)$ functions for $(R_2O_3)_{0.2}(Al_2O_3)_{0.2}(SiO_2)_{0.6}$ glass, where R denotes Dy, Ho or a 50:50 mixture of Dy and Ho, as obtained from the ND experiment and from RMC modeling. The dotted lines give the experimental data and the solid lines give the fits obtained from the model. The experimental error for the $F(q)$ functions is of the order of $\pm 10^{-3}$ barn.

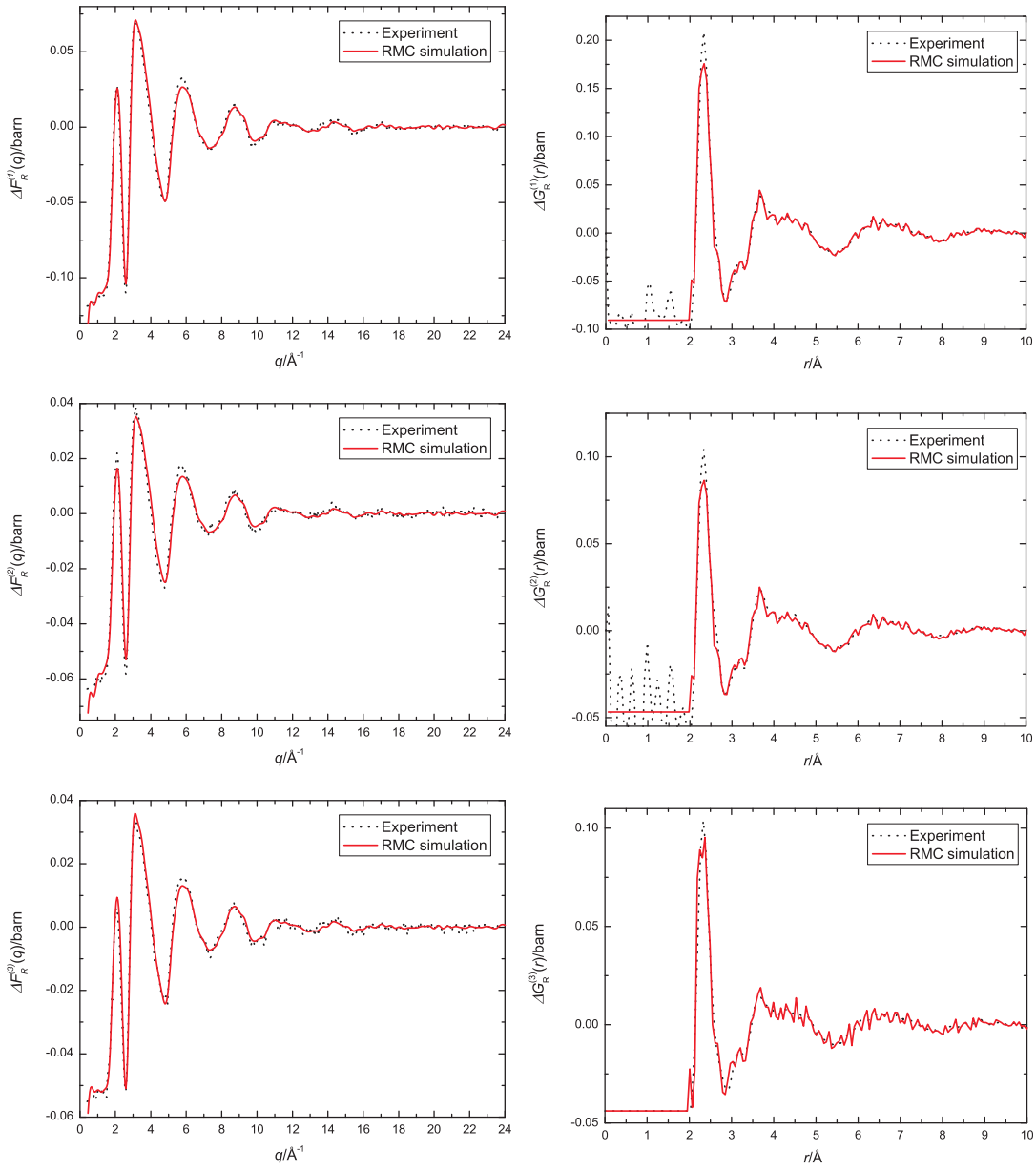

Figure 5.40: A comparison between the $\Delta F_R^{(n)}(q)$ and $\Delta G_R^{(n)}(r)$ functions for glassy $(R_2O_3)_{0.2}(Al_2O_3)_{0.2}(SiO_2)_{0.6}$ as obtained from the isomorphic substitution method in ND and from RMC modeling. The dotted lines give the experimental data and the solid lines give the fits obtained from the model. The experimental error for the $\Delta F_R^{(n)}(q)$ functions is of the order of $\pm 10^{-3}$ barn.

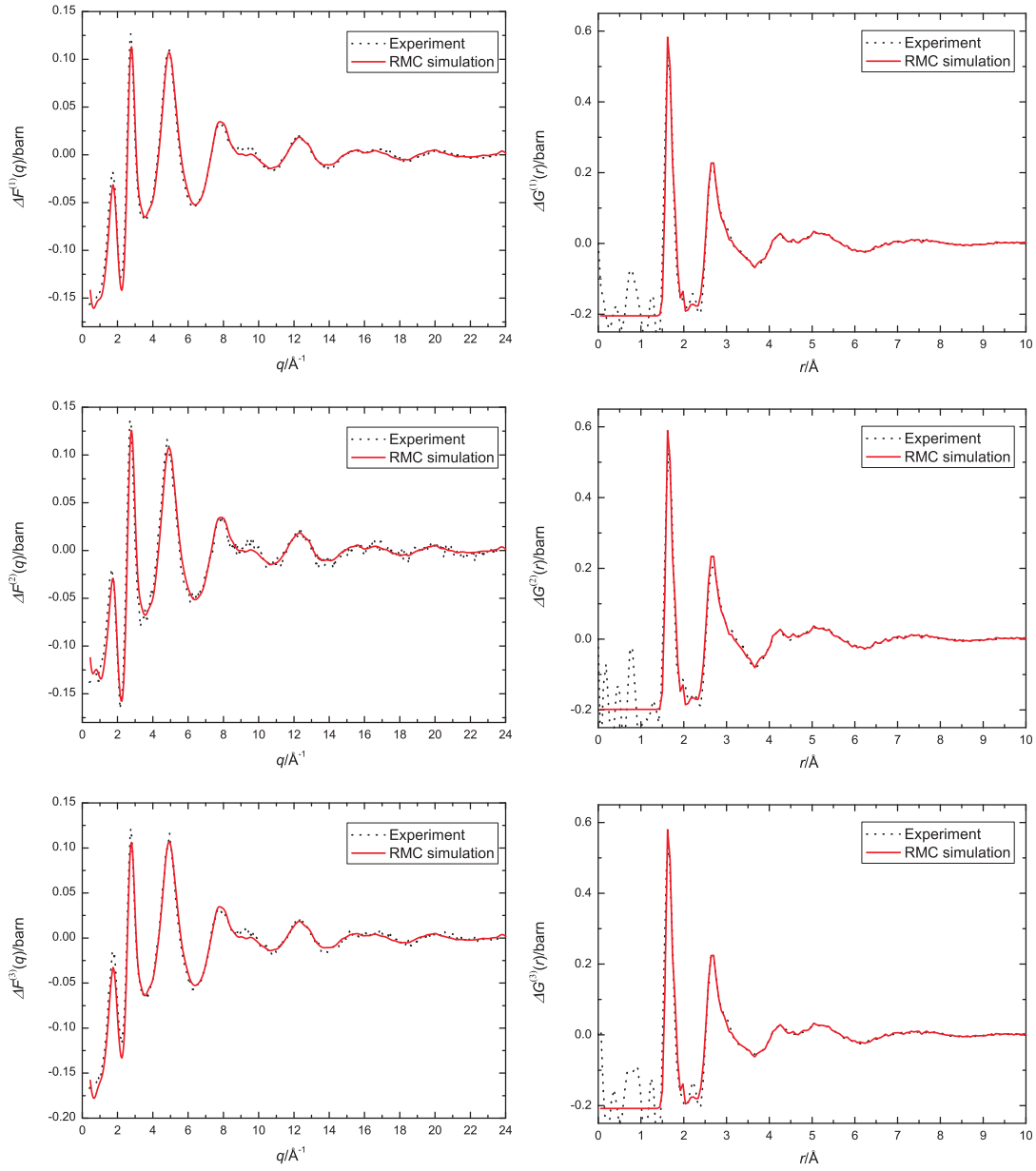

Figure 5.41: A comparison between the $\Delta F^{(n)}(q)$ and $\Delta G^{(n)}(r)$ functions for glassy $(R_2O_3)_{0.2}(Al_2O_3)_{0.2}(SiO_2)_{0.6}$ as obtained from the isomorphic substitution method in ND and from RMC modeling. The dotted lines give the experimental data and the solid lines give the fits obtained from the model. The experimental error for the $\Delta F^{(n)}(q)$ functions is of the order of $\pm 10^{-3}$ barn.

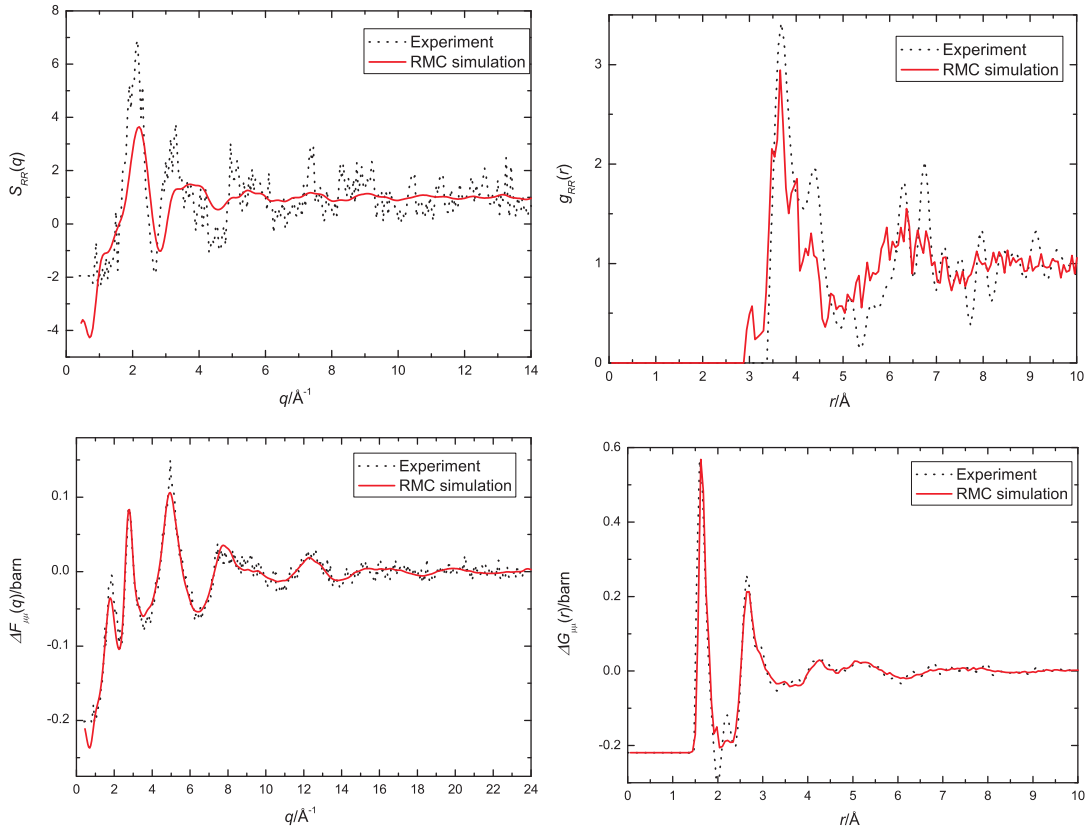

Figure 5.42: A comparison between the $S_{RR}(q)$, $\Delta F_{\mu\mu}(q)$, $g_{\mathrm{RR}}(r)$ and $\Delta G_{\mu\mu}(r)$ functions for glassy $(R_2O_3)_{0.2}(Al_2O_3)_{0.2}(SiO_2)_{0.6}$ as obtained from the isomorphic substitution method in ND and from RMC modeling. The dotted lines give the experimental data and the solid lines give the fits obtained from the model. The experimental errors for the $S_{RR}(q)$ and $\Delta F_{\mu\mu}(q)$ functions are of the order of ± 0.1 and ± 0.1 barn, respectively.

using the program NextTo in the RMCA package [154] with high r limits chosen to correspond to the first minimum after the first peak in real space. The coordination numbers along with the r range and the nearest neighbour distances are presented in table 5.15. The distributions of R-R, R-O, Al-O and Si-O coordination numbers are compared to those obtained from the MD simulation in figure 5.44. From the figure, only the distribution of R-O coordination numbers from the RMC model is significantly different from that given by the MD model as seen e.g. by the lower concentration of RO_6 units and the higher concentration of RO_7 units.

The nearest neighbour distances and coordination numbers for several of the pair correlation functions obtained from the RMC model are compared with those obtained from the MD model and ND and XRD experiments in table 5.16. From the

Correlation	Nearest neighbour distance (Å)	Coordination number	r range (Å)
R-R	3.6(2)	3.54(4)	2.88 - 4.95
R-O	2.32(5)	6.65(1)	1.98 - 2.85
Al-O	1.7(1)	4.2	1.44 - 2.07
Si-O	1.64(2)	4.0	1.44 - 1.89
O-O	2.67(3)	-	-

Table 5.15: The nearest neighbour distances and coordination numbers for the R-R, R-O, Al-O, Si-O and O-O correlations as obtained from the RMC model. The r ranges used to determine the coordination numbers are also given.

table, the first R-R nearest neighbour distance obtained from the experimental data is comparable to that obtained from the models although neither model shows a clear second R-R distance at $r = 4.38(5)$ Å. The R-O, Al-O, Si-O and O-O distances obtained from the models and from the experiments are, within the experimental error, the same.

The R-R coordination numbers obtained from the MD and RMC models are comparable but slightly smaller than the value obtained from experiments. For the R-O coordination number, the MD model gives the smallest value while the RMC model gives a value closer to experiments which, as seen in figure 5.44, is mainly due to a different distribution of the RO_6 and RO_7 units. The mean Al-O coordination numbers obtained from experiment and the MD models are similar to the average value obtained from the NMR experiment on $(Y_2O_3)_{0.2}(Al_2O_3)_{0.2}(SiO_2)_{0.6}$ glass [35, 147] which was used as a coordination number constraint in the RMC modeling. The Si-O coordination number of 4 determined from the MD model is the same as the value obtained from an NMR study on glassy $La_{0.66}SiAl_{0.55}O_{3.81}$ [164] and was used as coordination constraint in the RMC modeling.

Correlation	Nearest neighbour distance (Å)			Coordination number		
	Experiment	MD	RMC	Experiment	MD	RMC
R-R	3.65(2) - 3.7(1), 4.38(5)	3.6(1)	3.6(2)	4.6(1)	3.8	3.54(3)
R-O	2.31(3) - 2.35(3)	2.34(2)	2.32(5)	7.2(3)	6.1	6.65(1)
Al-O	1.62(2) - 1.74(3)	1.77(2)	1.7(1)	4.2(1) - 4.9(2)	4.2	4.3*
Si-O	1.62(2) - 1.74(3)	1.59(2)	1.64(2)	4.0*	4.0	4.0*
O-O	2.63(5) - 2.69(5)	2.61(2)	2.67(3)	-	-	-

Table 5.16: The nearest neighbour distances and coordination numbers for the R-R, R-O, Al-O, Si-O and O-O correlations as obtained from ND and XRD experiments, the MD model and the RMC model. The asterisks mark those parameters that were held fixed in either the analysis of the experimental data or in the model constructed from the RMC procedure.

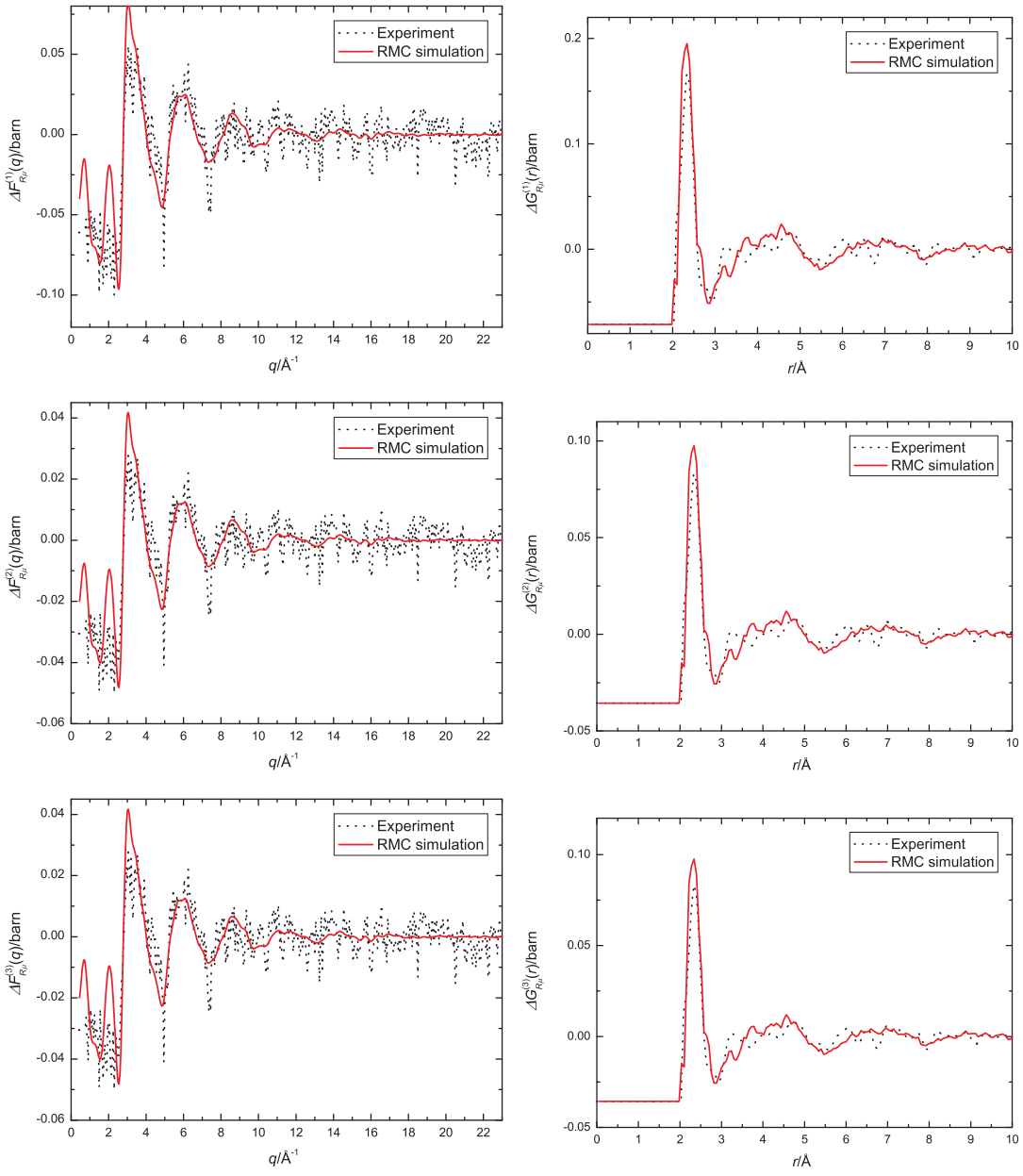

Figure 5.43: A comparison between the $\Delta F^{(n)}_{R\mu}(q)$ and $\Delta G_{R\mu}(r)$ functions for glassy $(R_2O_3)_{0.2}(Al_2O_3)_{0.2}(SiO_2)_{0.6}$ as obtained from the isomorphic substitution method in ND and from the RMC model. The dotted lines give the experimental data and the solid lines give the fits obtained from the model. The experimental error for the $\Delta F^{(n)}_{R\mu}(q)$ functions is of the order of ± 0.1 barn.

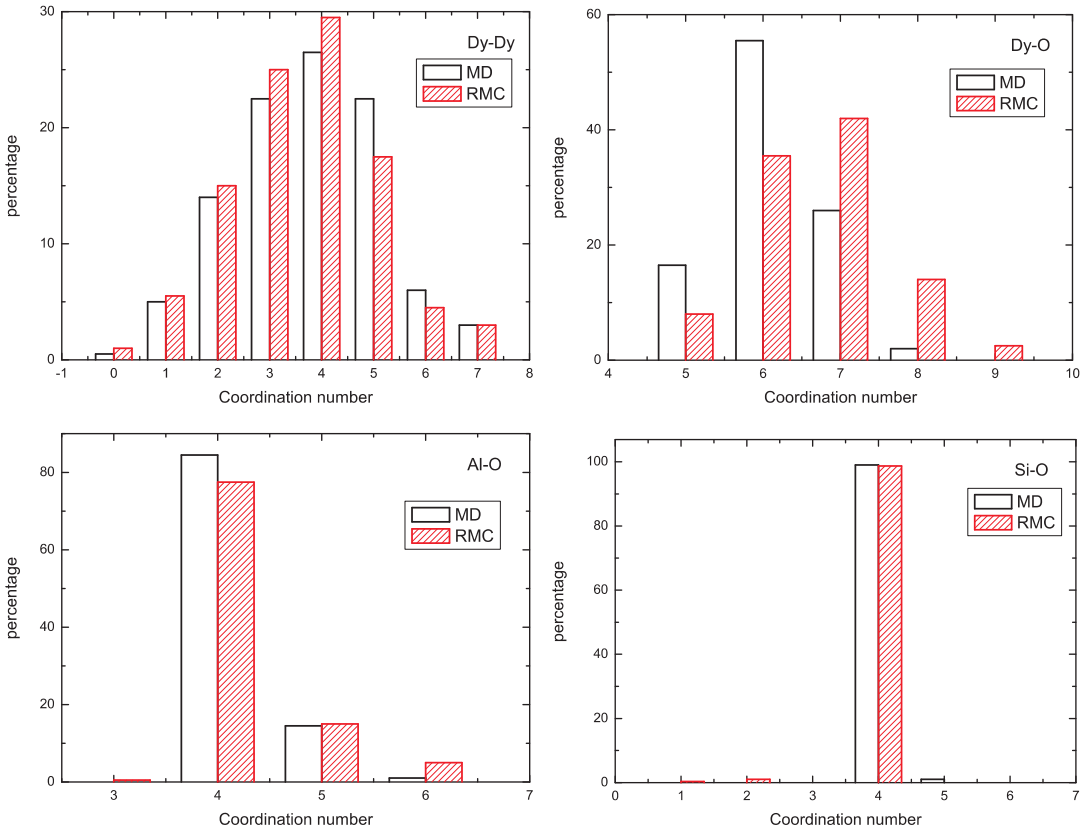

Figure 5.44: The distributions of Dy-Dy, Dy-O, Al-O and Si-O coordination numbers obtained from the RMC model and from the MD simulation of the $(Dy_2O_3)_{0.2}(Al_2O_3)_{0.2}(SiO_2)_{0.6}$ glass.

5.8.3 Comparison between the RMC and EXAFS Results

To examine the local structure of the rare-earth atoms in the glass, the weighted $g_{\alpha\beta}(r)$ functions present in the $\Delta G_R^{(1)}(q)$ function obtained from the RMC model are plotted in figure 5.45. The first coordination environment around the rare-earth atoms is provided by O atoms. The $\chi(k)$ functions corresponding to all the single and multiple scattering paths for all the rare-earth atoms in the RMC model involving R-O neighbouring atoms up to $R = 4$ Å were calculated. The calculations were made at the L_{III} edge of Dy and Ho for each absorbing atom in the RMC model by using the programs FEFF 7 [57] and I.S.A.A.C.S. [175]. The latter was used to identify the positions of the neighbouring atoms which are used by FEFF 7. The values of S_0^2 and the EXAFS Debye-Waller factor $\sigma^2_{\text{R-O}}$ were set at 1 and 0, respectively. The average from all the calculated $\chi(k)$ functions is presented as $k^3\chi(k)$ to provide clarity in the high k region. The $k^3\chi(k)$ and corresponding $|\tilde{\chi}(R)|$ functions are compared with the experimental data in figure 5.46.

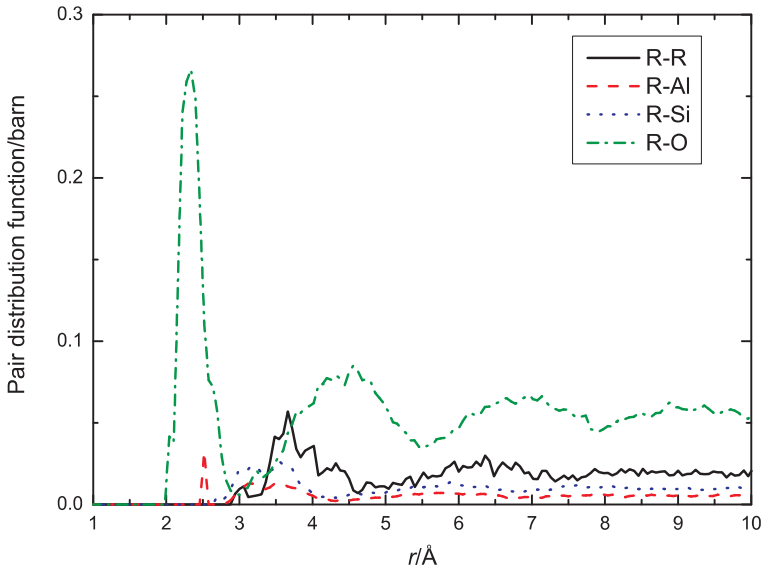

Figure 5.45: The weighted $g_{\alpha\beta}(r) - 1$ functions (see table 5.5) present in the $\Delta G_R^{(1)}(r)$ function for $(R_2O_3)_{0.2}(Al_2O_3)_{0.2}(SiO_2)_{0.6}$ glass, where R denotes Dy or Ho, as obtained from the RMC model.

From figure 5.46, the $k^3\chi(k)$ functions obtained from the RMC model are similar to the experimental data although the intensities of the first few peaks are lower and a shift of the second peak to lower k values can be seen. In real space, the RMC model gives only one peak in the $|\tilde{\chi}(R)|$ functions which suggests that

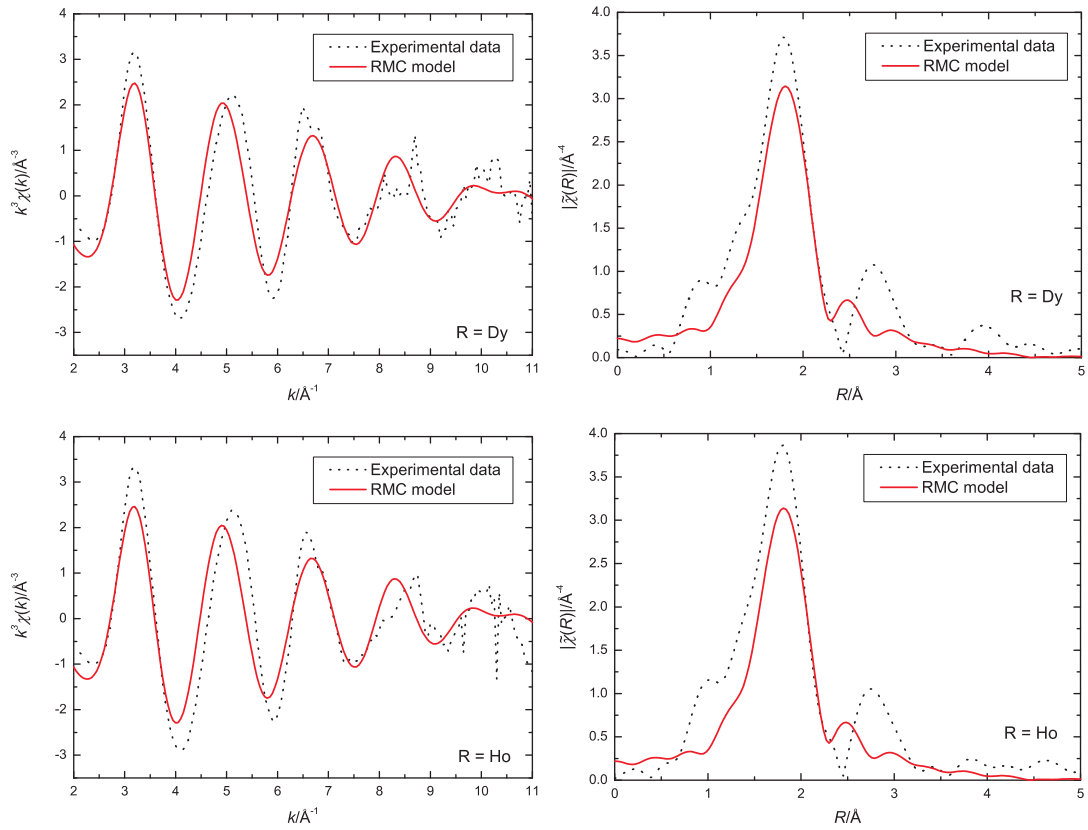

Figure 5.46: The $k^3\chi(k)$ and corresponding $|\tilde{\chi}(R)|$ functions for $(R_2O_3)_{0.2}(Al_2O_3)_{0.2}(SiO_2)_{0.6}$ glass, where R denotes Dy or Ho, as obtained from the EXAFS experiment and from the RMC model using R-O neighbours up to a cutoff distance $R = 4$ Å.

the discrepancy in k-space could result from the lack in the model of a second coordination shell and that the main contribution to the second peak in $|\tilde{\chi}(R)|$ does not come from R-O next nearest neighbours or from multiple scattering involving R-O atoms.

From the weighted ($g_{\alpha\beta}(r)$-1) functions obtained from the RMC model presented in figure 5.45, the second coordination shell can also have contributions from Dy-Al and Dy-Si correlations. Thus O as well as Al and Si neighbours up to $R =$ 4.35 Å (the minimum after the first peak in the $g_{\mathrm{DyAl}}(r)$ and $g_{\mathrm{DySi}}(r)$ functions) were included in the $\chi(k)$ calculation. The calculations were made at the L_{III} edge of Dy and Ho for each absorbing atom in the RMC model using the programs FEFF 7 [57] and I.S.A.A.C.S. [175] with the values of S_0^2 set to 1 and $\sigma^2_{\text{R-O}}$, $\sigma^2_{\text{R-Al}}$ and $\sigma^2_{\text{R-Si}}$ set to 0. The average of all the calculated $\chi(k)$ functions presented as $k^3\chi(k)$ together with their corresponding $|\tilde{\chi}(R)|$ functions, are compared with the experimental data in

figure 5.47.

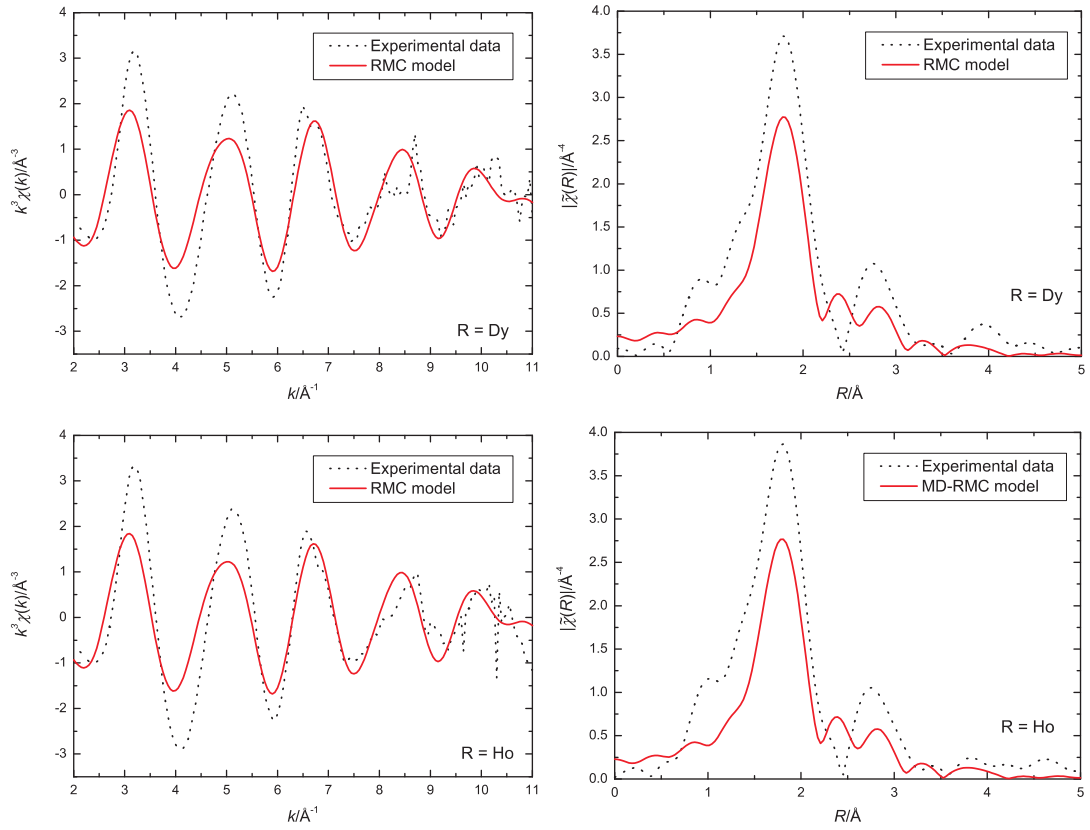

Figure 5.47: The $k^3\chi(k)$ and corresponding $|\tilde{\chi}(R)|$ function for $(R_2O_3)_{0.2}(Al_2O_3)_{0.2}(SiO_2)_{0.6}$ glass, where R denotes Dy or Ho, as obtained from the EXAFS experiment and from the RMC model using R-O, R-Al and R-Si neighbours up to a cutoff distance $R = 4.35$ Å.

From figure 5.47, the inclusion of the R-Al and R-Si neighbours does not remove a discrepancy between the calculated and measured $k^3\chi(k)$ functions. In real space, the features beyond the first peak in the calculated $|\tilde{\chi}(R)|$ function are also different to those in the measured function. Considering that the R-Al and R-Si correlations have a relatively small contribution to the measured $F(q)$ functions, see table 5.5 and figure 5.45, it is difficult to obtain accurate information regarding these correlations from the ND experiments. The RMC model was therefore refined further using the EXAFS data.

5.9 EXAFS Refinement

There is no known crystal structure for the $(R_2O_3)_{0.2}(Al_2O_3)_{0.2}(SiO_2)_{0.6}$ system where R denotes Dy or Ho. Thus the best model for a refinement of the EXAFS data is the model obtained from the RMC method in section 5.8. By using the program I.S.A.A.C.S [175], the R-O coordination environment in the RMC model was identified as comprising 8(1), 35.5(20), 42(2), 14(1) and 0.5(3)% of RO_5, RO_6, RO_7, RO_8 and RO_9 units, respectively. The average R-O atomic distances and the standard deviations about the mean for each type of unit are summarised in table 5.17.

It should be noted that a variety of R-O units is not uncommon for these systems. An MD simulation on $(Y_2O_3)_{0.45-x}(Al_2O_3)_{0.55}(SiO_2)_x$ glass where $x = 0.5$, 1.0, 1.5 or 2.0 also suggests a range of Y-O coordination numbers from 5 to 9 [145]. In crystalline $LaAlSiO_5$, the La-O units comprise three unique local configurations with a coordination number of 7 or 8 [167]. In fact, the asymmetry of the first peak of the $\Delta G_R^{(n)}(r)$ functions in figure 5.12 also gives a good indication that there are various types of R-O units.

R-O unit	$R_{\text{R-O}}$ (Å)	Standard deviation (Å)
5-fold	2.28	0.06
6-fold	2.35	0.06
7-fold	2.40	0.06
8-fold	2.45	0.06
9-fold	2.45	-

Table 5.17: The average R-O atomic distances and the standard deviation about the mean value for the R-O units with coordination numbers of 5, 6, 7 and 8 for $(R_2O_3)_{0.2}(Al_2O_3)_{0.2}(SiO_2)_{0.6}$ glass where R denotes Dy or Ho. As there is only one RO_9 unit in the model, the corresponding standard deviation was not calculated.

The effect on $k^3\chi(k)$ and $|\tilde{\chi}(R)|$ of multiple scattering paths corresponding to the RMC model when R-O neighbours up to a cutoff distance $R = 4$ Å are included is shown in figure 5.48. As seen in this figure, the contributions from multiple scattering paths are small. The local coordination environment of R atoms obtained from the RMC model was therefore used to construct a model comprising five single

scattering paths corresponds to R-O correlations in the RO_5, RO_6, RO_7, RO_8 and RO_9 units with fractional contributions given by the RMC model.

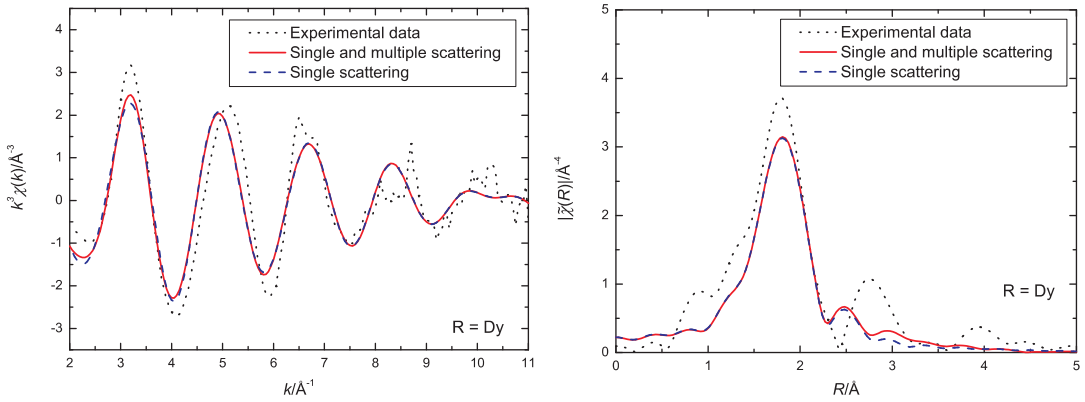

Figure 5.48: The $k^3\chi(k)$ and corresponding $|\tilde{\chi}(R)|$ function for $(Dy_2O_3)_{0.2}(Al_2O_3)_{0.2}(SiO_2)_{0.6}$ glass. The dotted lines give the experimental data. The solid lines give the calculated functions when both single and multiple scattering paths corresponding to the RMC model with R-O neighbours up to a cutoff distance $R = 4$ Å were included and the dashed lines give the calculated functions when only single scattering paths were included.

As can be seen in figure 5.33, $k^3\chi(k)$ becomes considerably distorted beyond $k = 11$ Å^{-1}. The k range used in the refinement was therefore chosen to be from $k = 2$ to 10.66 Å^{-1} and the R range was chosen to be from 1 to 2.5 Å. Due to the small k and R ranges, only 8 independent data points are available. From table 5.17, the standard deviations about the mean R-O distance in different types of units are quite similar suggesting similar degrees of static disorder in these local coordination environments. The R-O scattering paths for these units were therefore refined using the same parameter for $\sigma^2_{\text{R-O}}$. For the R-O atomic distances, the model was refined using the same value for $\Delta R_{\text{R-O}}$ which gives a constant difference between the R-O atomic distances in different units. Thus four parameters, S_0^2, ΔE_0, $\Delta R_{\text{R-O}}$ and $\sigma^2_{\text{R-O}}$, were varied during the fit.

Due to the big glitch in the $k^3\chi(k)$ function at $k = 8.7$ Å^{-1}, as seen in figure 5.33, a lower k-weight such as $k = 1$ or 2 is preferred in order to reduce the importance of the features beyond $k = 7.5$ Å^{-1}. However, it was found that there is no significant difference in the fitted parameters that were obtained using $k = 1$, 2 or 3. The refinement was therefore made using a k-weighting of 3 in order to give a reasonable weighting to the high k part of the functions. The fits to the experimental data

in k- and R-space data are shown in figure 5.49 and the refined parameters are summarised in table 5.18.

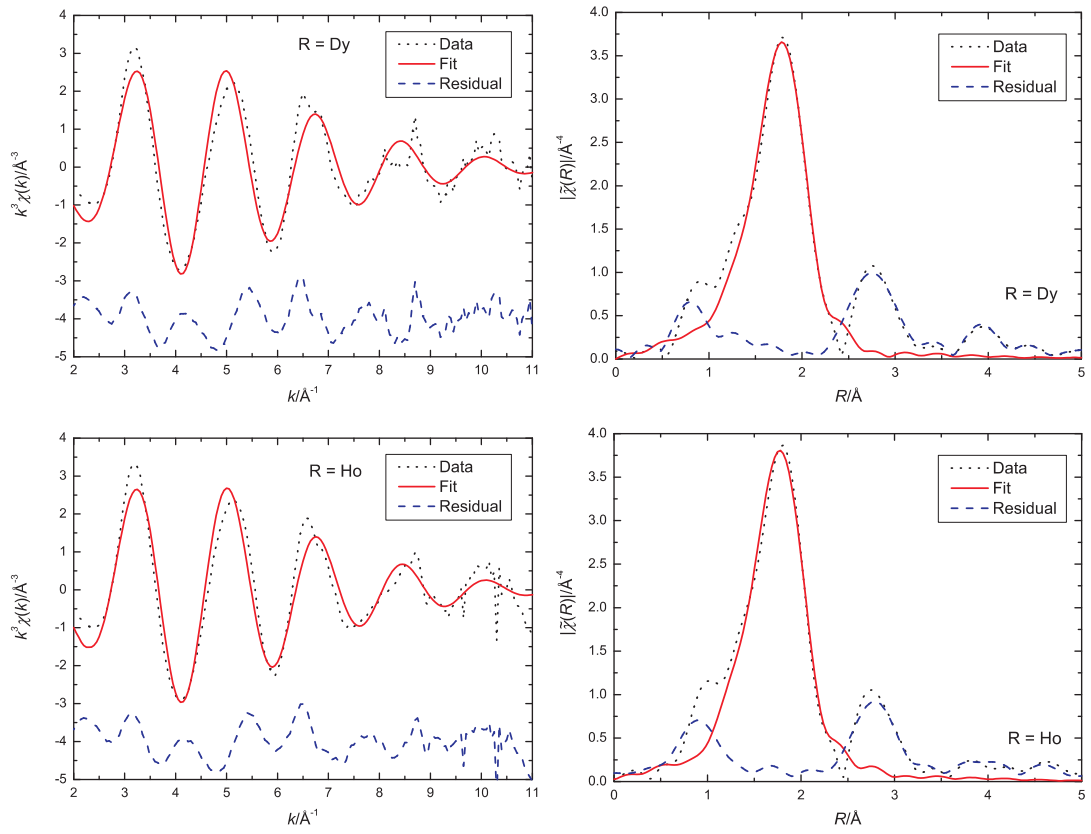

Figure 5.49: The $k^3\chi(k)$ and corresponding $|\tilde{\chi}(R)|$ function for $(R_2O_3)_{0.2}(Al_2O_3)_{0.2}(SiO_2)_{0.6}$ glass, where R denotes Dy or Ho. The dotted lines give the experimental data measured at room temperature at the Dy or Ho L_{III} edge. The solid lines give the fits obtained by refining the R-O local coordination environment using the RMC model and the dashed lines give the residuals.

From figure 5.49, the model gives reasonably good fits to the experimental data and the glitch at about 8.7 Å^{-1} corresponding to the double excitation was not fitted. The discrepancy in the $k^3\chi(k)$ functions, seen as a well defined oscillating residual, is mainly due to omission of a second coordination shell. The weighted averages of the R-O distances presented in table 5.18 are 2.27 and 2.26 Å for R = Dy and Ho, respectively, which are about 0.05 - 0.09 Å smaller than the average values obtained from the experiments or RMC model. For 0.08-3 mole% Er_2O_3 doped alumino-silicate glass [148], the refinement of the EXAFS $k^3\chi(k)$ function measured up to $k \approx 11$ Å^{-1} gives an Er-O distance of 2.22 Å which is similar to the R-O distances obtained from the present study. The $\sigma^2_{\text{Er-O}}$ value obtained

Parameters	R = Dy	R = Ho
$\mathcal{R}$-factor (%)	1.1	1.2
χ^2_ν	83	44
S_0^2	0.75(8)	0.8(1)
ΔE_0 (eV)	-3(1)	-2(1)
$\Delta R_{\text{R-O}}$ (Å)	-0.11(1)	-0.12(1)
$R_{\text{R-O}}$ (Å) for 5-fold units	2.16(1)	2.16(1)
$R_{\text{R-O}}$ (Å) for 6-fold units	2.24(1)	2.23(1)
$R_{\text{R-O}}$ (Å) for 7-fold units	2.29(1)	2.28(1)
$R_{\text{R-O}}$ (Å) for 8-fold units	2.34(1)	2.33(1)
$R_{\text{R-O}}$ (Å) for 9-fold units	2.33(1)	2.32(1)
$\sigma^2_{\text{R-O}}$ (Å^2)	0.013(2)	0.014(2)

Table 5.18: The refined atomic distances for all of the R-O units together with the $\Delta R_{\text{R-O}}$, $\sigma^2_{\text{R-O}}$, $\mathcal{R}$-factor and χ^2_ν values for the fits to the experimental data. The model was obtained from the RMC method and was refined using $\tilde{\chi}(R)$ obtained from the $k^3\chi(k)$ function for glassy $(R_2O_3)_{0.2}(Al_2O_3)_{0.2}(SiO_2)_{0.6}$, where R denotes Dy or Ho, measured at room temperature on the Dy or Ho L_{III} edge.

from reference [148] is 0.031 Å^2. Taking into account that in reference [148] the Er-O coordination shell was fitted using only one local configuration, which gives an average coordination number of 6.4, it is reasonable that the corresponding σ^2 value is large. By comparison, in the present work several different types of RO_n units were included in the model and, while the large distribution of R-O distances between different types of unit is large, the σ^2 value for each individual type of unit is relatively small.

It should be noted that the nearest neighbour distance obtained from EXAFS is expected to be slightly larger than the value obtained from diffraction. This is because the distance obtained from EXAFS includes both the radial and transverse components of the instantaneous relative atomic displacement due to thermal vibration whereas only the radial component is important in the case of diffraction [176, 177]. This discrepancy was found to be of the order of 10^{-2} Å in crystalline AgI [176]. The smaller R-O distance obtained from the EXAFS experiment of the present study, when compared to the values obtained from diffraction, could be due to the effect of disorder which was not accurately represented in the RMC model. A

smaller atomic distance can be obtained from a refinement when an EXAFS spectrum corresponding to a disordered system is fitted to a model based on a symmetric pair distribution function. An error as large as 0.16 Å was obtained from the refinement of liquid zinc fitted using a k range from 3.3 to 11.0 Å^{-1} [58, 178]. Because the effect of disorder is only apparent in the high k region of a measured $\chi(k)$ function, the effect can be undetectable if the k range is too small. In this case, it is nevertheless possible to make a good fit to the data by assuming a model using a symmetrical distribution of nearest neighbour when the high k part of the available data set is dominated by a contribution from the next nearest neighbour shell.

As suggested by reference [148] and the RMC model, the second and third coordination shells correspond to the R-Al and R-Si correlations, respectively. It is useful to try and add this information to the model. The R-Al and R-Si coordination numbers for all rare-earth atoms in the RMC model, up to a cutoff distance of 4.35 Å, range from 1 to 9. Since the second and third coordination shells obtained from the RMC model are not accurate, as seen from figure 5.47, only one average configuration for each coordination shell was added to the model i.e. two single scattering paths were added corresponding to the R-Al and R-Si nearest neighbour correlations. From the RMC model the average R-Al and R-Si distances are 3.50 and 3.51 Å with standard deviations about the mean value of 0.3 and 0.2 Å. The average coordination numbers are 3.1 and 4.4, respectively. It was found that in order to fit the model using the experimental data, the initial $R_{\text{R-Al}}$ distance has to be shifted to 3.3 Å. The refinement was made using a k-weighting of 3, a k range from 2 to 10.66 Å^{-1} and an R range from 1 to 3.6 Å. The fits to the experimental data in k- and R-space are shown in figure 5.50 and the refined parameters are summarised in table 5.19.

From table 5.19, the S_0^2, $\Delta R_{\text{R-O}}$ and $\sigma^2_{\text{R-O}}$ values are, within the experimental errors, the same as for the fits obtained when using the model comprising only an R-O coordination shell, see table 5.18. For the second and third coordination shells, the refined R-Al and R-Si distances of 3.15(3) and 3.6(1) Å are consistent with the ND results, see figure 5.12. However, it should be noted that as this system contains multiple components which have similar atomic numbers a good fit could be made

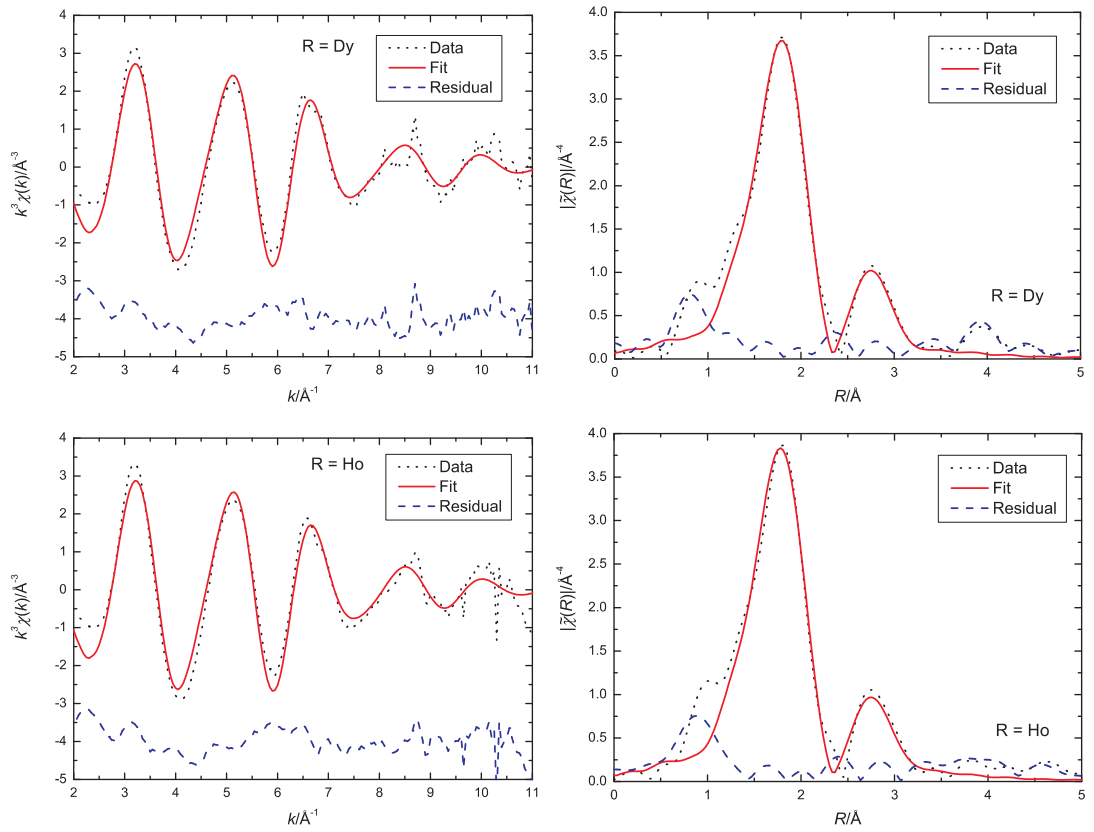

Figure 5.50: The $k^3\chi(k)$ and corresponding $|\tilde{\chi}(R)|$ functions for $(R_2O_3)_{0.2}(Al_2O_3)_{0.2}(SiO_2)_{0.6}$ glass, where R denotes Dy or Ho. The dotted lines give the experimental data measured at room temperature on the Dy or Ho L_{III} edge. The solid lines give the fits obtained by refining the R-O, R-Al and R-Si local coordination environments using the RMC model and the dashed lines give the residuals.

by using a model which contains either R-Si, R-Al or extra R-O neighbours in the second coordination shell. Thus the model used for the fit shown in figure 5.50 is one of several possible models. The absence of a well-defined feature in the residuals shown in figure 5.50 suggests that the contribution from the R-R coordination shell is not important in the fitted range of data points.

Parameters	R = Dy	R = Ho
$\mathcal{R}$-factor (%)	1.3	1.5
χ^2_ν	68	38
S_0^2	0.82(9)	0.9(1)
ΔE_0 (eV)	-0.5(9)	-1(1)
$\Delta R_{\text{R-O}}$ (Å)	-0.10(1)	-0.11(1)
$R_{\text{R-O}}$ (Å) for 5-fold units	2.18(1)	2.17(1)
$R_{\text{R-O}}$ (Å) for 6-fold units	2.25(1)	2.24(1)
$R_{\text{R-O}}$ (Å) for 7-fold units	2.30(1)	2.29(1)
$R_{\text{R-O}}$ (Å) for 8-fold units	2.35(1)	2.34(1)
$R_{\text{R-O}}$ (Å) for 9-fold units	2.35(1)	2.34(1)
$\sigma^2_{\text{R-O}}$ (Å^2)	0.014(2)	0.014(2)
$\Delta R_{\text{R-Al}}$ (Å)	-0.15(2)	-0.15(3)
$R_{\text{R-Al}}$ (Å)	3.15(2)	3.15(3)
$\sigma^2_{\text{R-Al}}$ (Å^2)	0.019(3)	0.021(4)
$\Delta R_{\text{R-Si}}$ (Å)	0.1(1)	0.1(1)
$R_{\text{R-Si}}$ (Å)	3.6(1)	3.6(1)
$\sigma^2_{\text{R-Si}}$ (Å^2)	0.06(3)	0.05(3)

Table 5.19: The refined atomic distances, ΔR and σ^2 values, together with the $\mathcal{R}$-factor and χ^2_ν values for the fits to the experimental data. The model, which comprises three coordination shells, was obtained from the RMC method and was refined using $\tilde{\chi}(R)$ obtained from the $k^3\chi(k)$ function for $(R_2O_3)_{0.2}(Al_2O_3)_{0.2}(SiO_2)_{0.6}$ glass, where R denotes Dy or Ho, measured at room temperature at the Dy or Ho L_{III} edge.

5.10 Conclusions

The structure of $(R_2O_3)_{0.2}(Al_2O_3)_{0.2}(SiO_2)_{0.6}$ glass at room temperature, where R denotes Dy, Ho or a 50:50 mixture of Dy and Ho, was studied by using a combination of the isomorphic substitution method in ND, XRD and EXAFS techniques. The diffraction data were also used to provide a model for the structure via the MD-RMC method such that the local coordination environments of the rare-earth, Al and Si atoms were determined. The comparison between the $G_N(r)$ and $G_X(r)$ functions, figure 5.30, demonstrates that the difference between the neutron and x-ray scattering lengths of an element can be used to help identify the pair correlation functions to which the peaks in a total pair distribution function correspond. The

first peak in the $G_N(r)$ or $G_X(r)$ function at $r = 1.64(2)$ or $1.74(3)$ Å corresponds to Al-O and Si-O correlations, the second peak at $r = 2.31(3)$ Å corresponds to R-O correlations, the peak at $r \approx 2.7$ Å corresponds to O-O correlations and the peak at $r = 3.7(1)$ Å corresponds to R-R correlations.

Regarding the isomorphic substitution method in ND, the $S_{RR}(q)$, $\Delta F^{(n)}_{R\mu}(q)$ and $\Delta F_{\mu\mu}(q)$ functions obtained by using all three $F(q)$ functions were consistent with the $\Delta F^{(n)}_{R}(q)$ and $\Delta F^{(n)}(q)$ functions obtained by using two $F(q)$ functions. The R-R, R-O and Al-O coordination numbers were determined. The $g_{\mathrm{RR}}(r)$ function gives a nearest neighbour R-R coordination number of 4.6(1). The $\Delta G^{(n)}_{R}(r)$ and $\Delta G^{(n)}_{R\mu}(r)$ functions give R-O coordination numbers of 7.2(3). The R-O coordination number obtained from $G_X(r)$ is 8.6(4) but, as seen in figure 5.30, the R-O peak in $G_X(r)$ is not completely isolated i.e. the value obtained can be regarded as an upper limit for the R-O coordination number, in agreement with the ND results. Moreover, if the Si-O coordination number is assumed to be 4, which is the value obtained from an NMR study on glassy $La_{0.66}SiAl_{0.55}O_{3.81}$ [164], the Al-O coordination number can be determined and values of 4.2(1) - 4.9(2) with an average of 4.5(1) were obtained from the $G(r)$, $\Delta G^{(n)}(r)$ and $\Delta G^{(n)}_{\mu\mu}(r)$ functions. These values are consistent with the NMR spectroscopy results for $(Y_2O_3)_{0.2}(Al_2O_3)_{0.2}(SiO_2)_{0.6}$ glass which give an average Al-O coordination number of 4.3(1) [35, 147].

The MD-RMC method was used to create a 3D model for the glasses. The Coulomb and Buckingham potentials were used to drive the MD simulation. For the RMC modeling, the configuration obtained from the MD simulation was used as an initial configuration. The MD configuration was then refined using the $F(q)$ functions measured using ND for the $(R_2O_3)_{0.2}(Al_2O_3)_{0.2}(SiO_2)_{0.6}$ glass, where R denotes Dy, Ho or a 50:50 mixture of Dy and Ho, the $S_X(q)$ function measured using XRD for the $(Dy_2O_3)_{0.2}(Al_2O_3)_{0.2}(SiO_2)_{0.6}$ glass, and all of the FOD and TMWD functions obtained from the isomorphic substitution method in ND that are presented in section 5.5.4. A Si-O coordination number of 4 and the relative fractions of AlO_4, AlO_5 and AlO_6 units obtained from the NMR experiment [35, 147] were used as coordination number constraints. As seen in figures 5.38 to 5.42, the model obtained from the RMC method gives a good fit to the experimental data. From

the model, the R-O local configurations were identified as comprising five types of units, namely RO_5, RO_6, RO_7, RO_8 and RO_9 units, with relative abundances of 8(1), 35.5(20), 42(2), 14(1) and 0.5(3)%, respectively. The average R-O and R-R coordination numbers obtained from the RMC model are 6.65(1) and 3.54(4), respectively, which are about 10% and 15% smaller than the values obtained directly from the isomorphic substitution method.

As shown by figure 5.33, the $k^3\chi(k)$ functions for the $(R_2O_3)_{0.2}(Al_2O_3)_{0.2}(SiO_2)_{0.6}$ glasses, where R denotes Dy or Ho, are very similar, which indicates a similar local structure for the rare-earth atoms in these glasses. Thus justifies use of the isomorphic substitution method. As EXAFS spectroscopy is a local probe, the average distances for the 5-, 6-, 7-, 8- and 9-fold coordinated R-O units from the RMC model were refined using $\tilde{\chi}(R)$ obtained from the measured $k^3\chi(k)$ function. From the refinement, the average R-O distances are 2.21(1) Å for the Dy based glass and 2.20(1) Å for the Ho based glass and $\sigma^2_{\text{R-O}}$ values of 0.013(2) Å^2 and 0.014(2) Å^2 were obtained for the Dy and Ho glasses, respectively. As suggested by the RMC model, R-Al and R-Si correlations were used as the second and third coordination shells and the refined R-Al and R-Si distances are 3.15(3) and 3.6(1) Å, respectively, which are consistent with the ND results. The $\sigma^2_{\text{R-Al}}$ and $\sigma^2_{\text{R-Si}}$ values are 0.019(3) and 0.06(3) Å^2, respectively, for the Dy based glass and 0.021(4) and 0.05(3) Å^2, respectively, for the Ho based glass.

In respect of the R-R correlations, the EXAFS results are consistent with the structure obtained from the RMC model in that the second and third nearest neighbours of these rare-earth atoms are Al and Si and that the contribution from R-R correlations is not important up to a distance of 3.6 Å. The ND and XRD results give an R-R nearest neighbour distance of 3.7(1) Å which agrees with the EXAFS results. It would be interesting to test whether the concentration of Al_2O_3 in R_2O_3-Al_2O_3-SiO_2 glasses reduces the concentration quenching effect observed in rare-earth doped SiO_2 glasses. By studying a range of compositions, the relation between the structure and corresponding change in the fluorescence lifetime could be investigated.

Chapter 6

Liquid $ZnCl_2$ at High Temperature

6.1 Introduction

The structure of liquid and glassy $ZnCl_2$ has been studied using many experimental techniques such as ND [179, 14, 180, 181], XRD [182], Raman spectroscopy [36] and EXAFS spectroscopy [183, 184]. One reason which makes this system attractive for study is the fact that it is one of the few purely ionic systems that can readily form a glass due to its unusually high viscosity of the melt and low melting point temperature [185]. Moreover, the network structure of the glassy state is retained in the melt which is more common for covalently bonded materials. The network structure of glassy and liquid $ZnCl_2$ is formed mainly from corner-sharing tetrahedral units similar to more technologically important materials such as SiO_2 but with a much lower melting point which makes the material more accessible to experiment. In addition, Cl has two stable isotopes with a large coherent neutron scattering length contrast which means that the method of isotopic substitution in ND can be applied to $ZnCl_2$ to measure the partial structure factors.

The structure of disordered network systems like glassy and liquid $ZnCl_2$ can be described in terms of the nature of the local structural motifs and the connectivity of these motifs on an intermediate length scale. It has been shown that the networks can also show ordering on an extended length scale up to ≈ 62 Å which is associated with the principal peak in the $F(q)$ function [180]. The local structural motifs in

glassy and liquid $ZnCl_2$ are believed to be well defined Zn-centred tetrahedral units as observed by using various experimental techniques such as ND, XRD and EXAFS spectroscopy, see references [179] - [184].

A signature of network structure is the appearance of a peak in an $F(q)$ function at around 1 $Å^{-1}$, the so called first sharp diffraction peak (FSDP), which represents intermediate range ordering [186]. The partial structure factors of liquid $ZnCl_2$ were measured for the first time by Biggin and Enderby [14] using the method of isotopic substitution in ND. Biggin and Enderby found that for liquid $ZnCl_2$ the FSDP corresponds to the Zn-Zn correlations. This finding agrees with the results obtained from Reverse Monte Carlo (RMC) modelling [187] of the glass and from studies of the structure of molten $ZnCl_2$ mixed with various alkaline halides [184, 188, 189, 190] which suggests that the FSDP originates from density fluctuations associated with the Zn^{2+} ions. This idea, however, was challenged by Neuefeind who combined x-ray and neutron diffraction data and proposed that the FSDP is dominated by the Zn-Cl correlations [191]. A recent molecular dynamics (MD) simulation on liquid $ZnCl_2$ found that the FSDP has contributions from both the Zn-Zn and Zn-Cl correlations [192]. The simulation also showed that there is a combination of edge-sharing and corner-sharing tetrahedra in the liquid phase.

The temperature dependence of the structure of liquid $ZnCl_2$ has been studied using ND and Raman spectroscopy. From the ND results performed at 300 and 600 °C [181], it was found that the height of the FSDP is not diminished as the temperature increases but that its position is shifted slightly towards lower q values which suggests that the network structure remains at high temperature. However, the Zn-Cl coordination number decreased from 3.93(6) to 3.67(7). The results from a Raman spectroscopy experiment performed on glassy $ZnCl_2$ at room temperature and liquid $ZnCl_2$ up to 800 °C [36] suggested that the lower Zn-Cl coordination number at high temperatures gives evidence for the promotion of an edge-sharing tetrahedral network. Figure 6.1 shows possible forms of structural units at the ends of each edge-sharing cluster proposed in [36]. From the figure, the average Zn-Cl coordination number for the terminal Zn atoms is three.

In this chapter we present a study of the structure of glassy $ZnCl_2$ at room

temperature and liquid $ZnCl_2$ at several temperatures in the range from 328(1) to 704(2) °C (mp = 290 °C and bp = 732 °C [42]) by using ND and XRD. The chapter consists of seven sections. In section 6.2, the background theory for ND and XRD is reviewed and includes an account of the Bhatia-Thornton formalism. The sample preparation and experimental details for both the ND and XRD experiments are described in section 6.3. In section 6.4 some aspects of the data treatment applied to the ND results are described. In section 6.5, the ND and XRD results in real and reciprocal space are presented. Section 6.6 includes an interpretation of the results obtained from both experimental techniques. Conclusions are drawn in section 6.7.

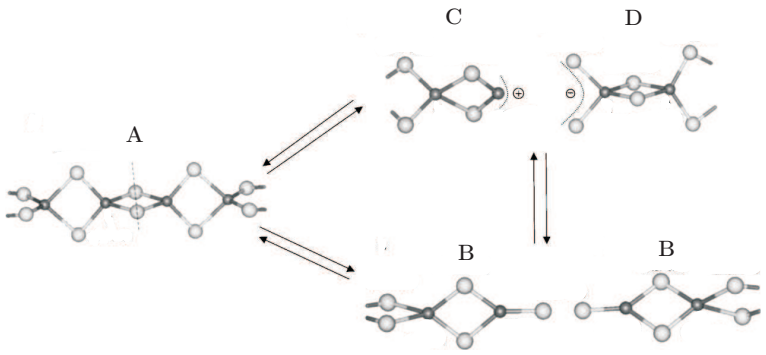

Figure 6.1: Possible terminal units for edge-sharing tetrahedral clusters [36]. Unit A is part of an edge-sharing tetrahedral cluster. If unit A is separated at the dashed line the possible products are two units of type B or a combination of units of types C and D. In both cases, the average Zn-Cl coordination number of the terminal Zn atoms is three.

6.2 Background Theory

In this section the main theory required for the ND and XRD experiments on $ZnCl_2$ is summarised. The Faber-Ziman partial structure factors for disordered materials were defined in chapter 2. The Bhatia-Thornton partial structure factors [193, 194], which are more closely related to the thermodynamic properties of a binary system, are also described.

6.2.1 ND Theory

From equation 2.26, the total structure factor $F(q)$ for $ZnCl_2$ can be written as

$$F(q) = c_{\mathrm{Zn}}^2 b_{\mathrm{Zn}}^2 \left[S_{\mathrm{ZnZn}}(q) - 1\right] + 2c_{\mathrm{Zn}}c_{\mathrm{Cl}}b_{\mathrm{Zn}}b_{\mathrm{Cl}} \left[S_{\mathrm{ZnCl}}(q) - 1\right] + c_{\mathrm{Cl}}^2 b_{\mathrm{Cl}}^2 \left[S_{\mathrm{ClCl}}(q) - 1\right], \quad (6.1)$$

where $S_{\alpha\beta}(q)$ is a Faber-Ziman partial structure factor, and c_α, b_α are the atomic fraction and coherent neutron scattering length of an atom of type α, respectively.

The total pair distribution function $G(r)$ is obtained from the Fourier transform relation

$$G(r) = \frac{1}{n_0 2\pi^2 r} \int_0^\infty F(q) q \sin(qr) dq \quad (6.2)$$

where n_0 is the atomic number density such that

$$G(r) = c_{\mathrm{Zn}}^2 b_{\mathrm{Zn}}^2 \left[g_{\mathrm{ZnZn}}(r) - 1\right] + 2c_{\mathrm{Zn}}c_{\mathrm{Cl}}b_{\mathrm{Zn}}b_{\mathrm{Cl}} \left[g_{\mathrm{ZnCl}}(r) - 1\right] + c_{\mathrm{Cl}}^2 b_{\mathrm{Cl}}^2 \left[g_{\mathrm{ClCl}}(r) - 1\right]. \quad (6.3)$$

As $g_{\alpha\beta}(r)$ is proportional to the probability of finding an atom of type β at a radial distance r from an atom of type α, its first peak position represents the nearest neighbour atomic distance between the two types of atom. The average coordination number for each type of atomic pair can be determined by finding the area under a peak in the relevant $r^2 g_{\alpha\beta}(r)$ function. The average coordination number of atoms of type β around an atom of type α can be calculated using equation 2.28,

$$\bar{n}_\alpha^\beta = 4\pi n_0 c_\beta \int_{r_1}^{r_2} g_{\alpha\beta}(r) r^2 dr,$$

where r_1 and r_2 are the minimum and maximum radii for the region of interest.

In this chapter, because the experimental results from ND and XRD are compared, it is convenient to define $S_N(q)$ and $G_N(r)$ such that they are equivalent to the x-ray $S_X(q)$ and $G_X(r)$ functions;

$$S_N(q) = \frac{F(q)}{\langle b \rangle^2} + 1 \quad (6.4)$$

and

$$G_N(r) = \frac{G(r)}{\langle b \rangle^2} + 1, \quad (6.5)$$

where $\langle b \rangle = c_{\mathrm{Zn}} b_{\mathrm{Zn}} + c_{\mathrm{Cl}} b_{\mathrm{Cl}}$ is the average coherent neutron scattering length.

Maximum structural information can be acquired from the results of a diffraction experiment by extracting the full set of $S_{\alpha\beta}(q)$ and $g_{\alpha\beta}(r)$ functions. Hence, if only a single $F(q)$ (or $G(r)$) is measured, limited information about the atomic distances and coordination numbers can be determined. For $ZnCl_2$, information about the Zn-Cl structural unit can be obtained from $G(r)$. As the first peak in $G(r)$ is well separated from other peaks and corresponds only to the Zn-Cl correlations, the position of the first peak gives the Zn-Cl bond distance and the coordination number of Cl around Zn can be determined by using the equation

$$\bar{n}_{\mathrm{Zn}}^{\mathrm{Cl}} = 4\pi n_0 c_{\mathrm{Cl}} \int_{r_1}^{r_2} \left[\frac{G(r) - G(0)}{2c_{\mathrm{Zn}} c_{\mathrm{Cl}} b_{\mathrm{Zn}} b_{\mathrm{Cl}}} \right] r^2 dr, \tag{6.6}$$

where the region of the first peak is from r_1 to r_2 and within this region

$$g_{\mathrm{ZnCl}}(r) = \frac{G(r) - G(0)}{2c_{\mathrm{Zn}} c_{\mathrm{Cl}} b_{\mathrm{Zn}} b_{\mathrm{Cl}}}. \tag{6.7}$$

$F(q)$ for a two component system can also be written by using the Bhatia-Thornton formalism [193, 194] where

$$\begin{aligned} F(q) &= \langle b \rangle^2 S_{NN}(q) + (b_{\mathrm{Zn}} - b_{\mathrm{Cl}})^2 S_{CC}(q) \\ &+ 2\langle b \rangle (b_{\mathrm{Zn}} - b_{\mathrm{Cl}}) S_{NC}(q) - (c_{\mathrm{Zn}} b_{\mathrm{Zn}}^2 + c_{\mathrm{Cl}} b_{\mathrm{Cl}}^2). \end{aligned} \tag{6.8}$$

In this equation, $S_{NN}(q)$, $S_{CC}(q)$ and $S_{NC}(q)$ are the number-number, concentration-concentration and number-concentration partial structure factors, respectively. $S_{NN}(q)$ gives information about the relative positions of the atomic sites regardless of the chemical species associated with those sites. If a system comprises one chemical species, or if $b_\alpha = b_\beta$, then the weighting factors of $S_{CC}(q)$ and $S_{NC}(q)$ are zero such that $F(q)$ gives $S_{NN}(q)$ directly. $S_{CC}(q)$ gives information about the chemical ordering on the sites described by $S_{NN}(q)$. If the two species present in a system have comparable size and can substitute for one another without causing an energy penalty then $S_{CC}(q)$ is a constant independent of q. $S_{NC}(q)$ represents the correlation between sites and the atomic species occupying those sites.

One of the advantages of using the Bhatia-Thornton formalism is that the partial structure factors at $q = 0$ are directly linked to the thermodynamic properties

of the system [195, 127] i.e.

$$S_{NN}(0) = n_0 k_B T \chi_T + \delta^2 S_{CC}(0) \tag{6.9}$$

$$S_{CC}(0) = k_B T \left(\frac{\partial^2 G}{\partial c_\alpha^2} \right)_{T,P,N} \tag{6.10}$$

$$S_{NC}(0) = -\delta S_{CC}(0) \tag{6.11}$$

where k_B, T, P, N are the Boltzmann constant, absolute temperature, pressure, and total number of particles, respectively, χ_T is the isothermal compressibility, δ is a dilatation factor, and G is the Gibbs free energy per particle. For an ionic system, according to the zeroth moment condition described by Stillinger and Lovett [196], $S_{CC}(0) = 0$ such that $S_{NC}(0) = 0$. Thus from equations 6.8 - 6.11, the isothermal compressibility for $ZnCl_2$ can be expressed in terms of $F(0)$ as

$$\chi_T = \frac{1}{n_0 k_B T} \left[\frac{F(0) + (c_{\text{Zn}} b_{\text{Zn}}^2 + c_{\text{Cl}} b_{\text{Cl}}^2)}{\langle b \rangle^2} \right]. \tag{6.12}$$

6.2.2 High Energy XRD Theory

From equation 2.44, for $ZnCl_2$ the x-ray total structure factor $F_X(q)$ can be written in terms of the Faber-Ziman partial structure factors $S_{\alpha\beta}(q)$ as

$$\begin{aligned} F_X(q) = {} & c_{\text{Zn}}^2 f_{\text{Zn}}^2(q) \left[S_{\text{ZnZn}}(q) - 1 \right] + 2 c_{\text{Zn}} c_{\text{Cl}} f_{\text{Zn}}(q) f_{\text{Cl}}(q) \left[S_{\text{ZnCl}}(q) - 1 \right] \\ & + c_{\text{Cl}}^2 f_{\text{Cl}}^2(q) \left[S_{\text{ClCl}}(q) - 1 \right], \end{aligned} \tag{6.13}$$

where $f_\alpha(q)$ is the x-ray form factor for an atom of type α. In this chapter, the x-ray total structure factor is represented by $S_X(q)$ where

$$S_X(q) = \frac{F_X(q)}{\overline{f(q)}^2} + 1, \tag{6.14}$$

and $\overline{f(q)} = \sum_\alpha c_\alpha f_\alpha(q)$ is the average form factor. The total pair distribution function $G_X(r)$ is obtained by Fourier transforming $S_X(q)$ where

$$G_X(r) - 1 = \frac{1}{n_0 2\pi^2 r} \int_0^\infty [S_X(q) - 1] q \sin(qr) dq. \tag{6.15}$$

$G_X(r)$ can be written in terms of a weighted sum of each partial pair distribution function $g_{\alpha\beta}(r)$.

The average Zn-Cl coordination number can also be calculated from $G_X(r)$, as described in section 5.2.3. For $ZnCl_2$,

$$\bar{n}_{\mathrm{Zn}}^{\mathrm{Cl}} = 4\pi n_0 c_{\mathrm{Cl}} \int_{r_1}^{r_2} [\,{}^{mod}G'_X(r) - {}^{mod}G'_X(0)] r^2 dr, \tag{6.16}$$

where the region of the first peak is from r_1 to r_2, $G'_X(r)$ is defined as the Fourier transform of $S'_X(q)$, where

$$\begin{aligned} {}^{mod}S'_X(q) - 1 &= [S_{\mathrm{ZnCl}}(q) - 1] + \left(\frac{c_{\mathrm{Zn}}^2 f_{\mathrm{Zn}}^2(q)}{2c_{\mathrm{Zn}} c_{\mathrm{Cl}} f_{\mathrm{Zn}}(q) f_{\mathrm{Cl}}(q)} \right) [S_{\mathrm{ZnZn}}(q) - 1] \\ &\quad + \left(\frac{c_{\mathrm{Cl}}^2 f_{\mathrm{Cl}}^2(q)}{2c_{\mathrm{Zn}} c_{\mathrm{Cl}} f_{\mathrm{Zn}}(q) f_{\mathrm{Cl}}(q)} \right) [S_{\mathrm{ClCl}}(q) - 1], \end{aligned} \tag{6.17}$$

and

$${}^{mod}G'_X(0) - 1 = -\left(1 + \frac{c_{\mathrm{Zn}}^2 f_{\mathrm{Zn}}^2(0)}{2c_{\mathrm{Zn}} c_{\mathrm{Cl}} f_{\mathrm{Zn}}(0) f_{\mathrm{Cl}}(0)} + \frac{c_{\mathrm{Cl}}^2 f_{\mathrm{Cl}}^2(0)}{2c_{\mathrm{Zn}} c_{\mathrm{Cl}} f_{\mathrm{Zn}}(0) f_{\mathrm{Cl}}(0)} \right). \tag{6.18}$$

6.3 Experiment

The samples were made from anhydrous beads of 99.999% purity $ZnCl_2$ commercially available from Sigma-Aldrich. Because $ZnCl_2$ is very hygroscopic the samples were handled and prepared in a high purity Argon filled glove box. The diffraction experiments were performed using both high energy x-rays and neutrons. The details of the sample preparation for the diffraction experiments are as follows.

6.3.1 Modulated Differential Scanning Calorimetry (MDSC) Measurement

A small amount of sample (10.76 mg) was powdered and characterised using MDSC (TA Instruments' DSC Q100). The sample was filled in an aluminium pan and the measurement was made from 35 to 195 °C with a ramp rate of 3 °C/min and a modulation of ±1 °C every 60 s. Nitrogen gas was used to purge the sample with a flow rate of 25 ml/min. The measured total heat capacity and its contributions from the reversible heat capacity and non-reversible heat capacity are shown in figure 6.2. Also shown in the figure is the glass transition temperature $T_g = 104(2)$ °C determined from the reversible heat capacity measurement [197, 15], which agrees

with $T_g = 102(5)\,^{\circ}\mathrm{C}$ for $ZnCl_2$ quoted in the literature [198]. It should be noted that T_g determined from the total heat capacity is $84(2)\,^{\circ}\mathrm{C}$. This value is not accurate as the total heat capacity includes an endothermic relaxation due to the release of internal molecular stresses near T_g which is not in the reversible part of the heat capacity [199].

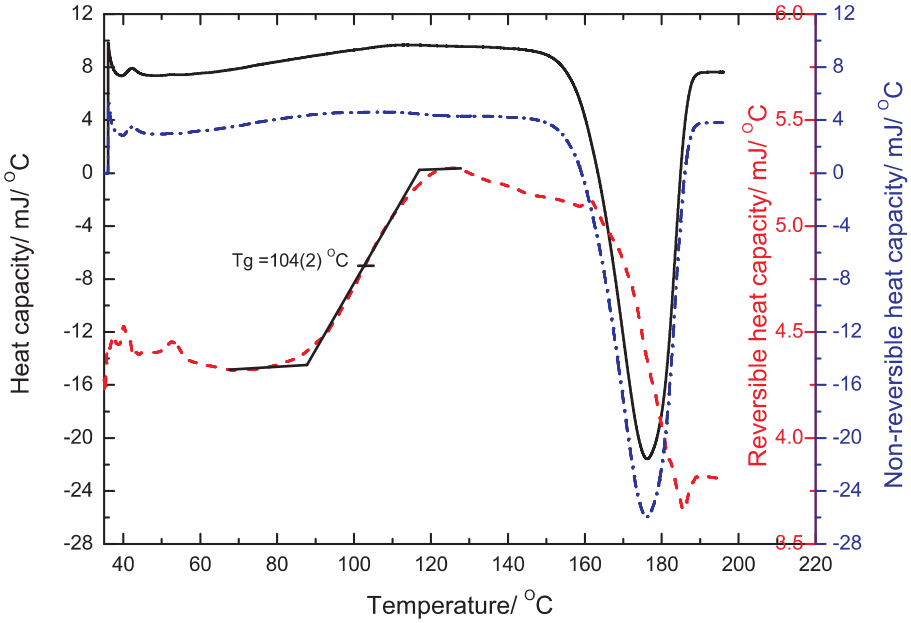

Figure 6.2: Total heat capacity, reversible heat capacity and non-reversible heat capacity of anhydrous beads of 99.999% purity $ZnCl_2$ as measured from 35 to 195 °C using modulated differential scanning calorimetry.

6.3.2 ND Experiment

For the ND experiment, the sample was filled into a silica ampoule of 4 mm inner diameter and 1 mm wall thickness in a glove box with an O_2 level of 123 ppm and an H_2O level of 15 ppm. The ampoule was then sealed under a vacuum of 2.6×10^{-5} torr, see figure 6.3.

The ND experiment was performed using the D4c diffractometer at the ILL. The sample was placed in a vanadium furnace (available temperatures 50 to 1150 °C [78]) situated inside the evacuated D4c bell jar. An incident neutron wavelength of 0.4967(1) Å was used. The incident neutron wavelength as well as the zero

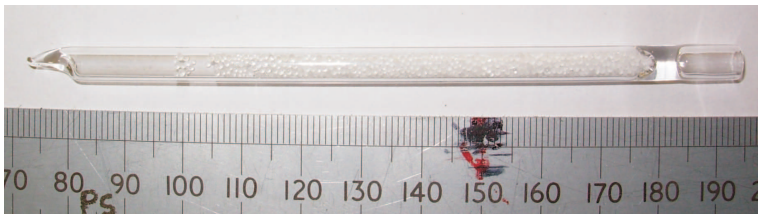

Figure 6.3: The sample for the ND experiment consisting of anhydrous beads of $ZnCl_2$ with 99.999% purity sealed under vacuum in a silica ampoule.

angle offset of the detectors were determined by using the diffraction pattern for a powdered Ni sample. The beam height was chosen to be 4.2 cm.

The sample was measured at four temperatures ranging from slightly above the melting point to near the boiling point, namely 435(2), 535(2), 633(2) and 704(2) °C (mp = 290 °C and bp = 732 °C [42]). The measurements were made using a series of 30 minute and 1 hour scans thus enabling stability checks to be made by calculating the ratio between the measured intensity for consecutive scans. If the sample is stable, the ratio is unity. The final signal was obtained by averaging all the scans.

During the measurements made at 535(2) and 704(2) °C, the ratios between some of the scans varied as a function of scattering angle. This is an indication of density fluctuations due to the formation of bubbles. For the measurements made at 535(2) °C, unstable scans were excluded from the data analysis procedure. For the measurements made at 704(2) °C, many of the scans showed density fluctuations. The final signal at this temperature was, therefore, determined by averaging only those scans which, when combined, cancel the steps in the data caused by density fluctuations. The detail of this method is described in the next section. It should be noted that a measurement was also made at 725(2) °C but the sample was too unstable such that none of the scans were usable.

The total counting times for each temperature were 4.5 hours at 435(2) °C, 2.5 hours at 535(2) °C, 3.5 hours at 633(2) °C and 1.5 hours at 704(2) °C. Measurements of an empty furnace and an empty silica ampoule in the furnace at 434(2), 533(2), 626(2) and 704(2) °C were also performed for the data correction procedure. In addition, the diffraction pattern of a vanadium rod of 6.37 mm diameter was measured inside the furnace at room temperature, along with the empty furnace at

room temperature, for normalisation purposes.

6.3.3 High Energy XRD Experiment

For the high energy XRD experiment, the sample was filled into a silica capillary of 1 mm inner diameter and 1 mm wall thickness by evaporation. First, the $ZnCl_2$ beads were filled into a silica tube attached to a capillary, see figure 6.4, in a glove box with an O_2 level of 0.128 % and an H_2O level of 3 ppm. The cell was then evacuated and sealed under a vacuum of 5.5×10^{-5} torr. The sealed cell was arranged in a furnace in such a way that the tube containing the sample was inside the furnace and the tip of the capillary was outside the furnace. This arrangement, when the cell was heated to around 800 °C, gave a temperature gradient between the tube and the capillary such that the sample evaporated from the tube and condensed in the capillary. The capillary was then sealed with the sample inside.

A glassy sample was made by heating the capillary to around 450 °C and then quenching it quickly by placing the capillary in iced cold water. Glassy and crystalline $ZnCl_2$ can be distinguished by inspection as the glass is clear while the crystalline material is cloudy.

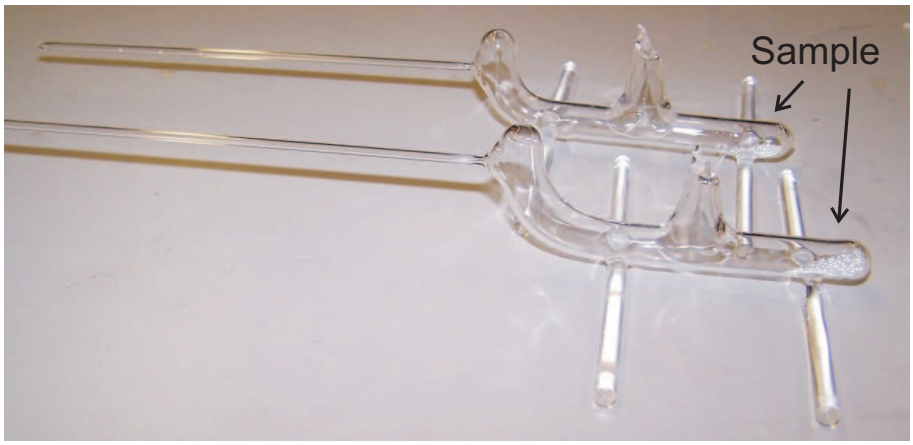

Figure 6.4: Cells used to transport the sample, which consists of anhydrous beads of $ZnCl_2$ with 99.999% purity, into capillaries by evaporation. The cells were made from silica and the evaporation was performed by heating the cell to around 800 °C.

The sample was sent to the SPring-8 synchrotron facility in Hyogo, Japan. The high energy XRD experiment was performed by Dr Shinji Kohara and Prof Takeshi

Usuki using beamline BL04B2 [200]. The incident x-ray energy used was 61.7 keV. The measurements were made in four steps employing a Ge detector. The beam size and scattering angles for each step are summarised in table 6.1. The sample was placed in an evacuated sample chamber, denoted by F in figure 3.5, 790 mm away from an incident slit. There were two receiving slits the first one of width 0.80 mm located at 650 mm from the sample position and the second one of width 0.65 mm located at 850 mm from the sample position.

The sample was measured at room temperature and at 328(1), 340(1), 430(1), 530(1) and 630(1) °C. In addition, an empty capillary was also measured at the same temperatures as the sample for the data correction procedure. The data were treated [201] using a standard data analysis procedure [68] with the Compton scattering correction taken from [158] and the ionic x-ray form factors taken from [159].

Step	Beam size H×W (mm^2)	Scattering angle 2θ (degree)
1	2.5×0.9	0.30-10.0
2	2.5×1.8	9.0-20.0
3	2.5×4.0	19.0-30.0
4	2.5×4.0	29.0-48.0

Table 6.1: Beam sizes (where H and W denote the height and width, respectively) and scattering angles corresponding to each measurement step for the $ZnCl_2$ high energy XRD experiment.

6.4 Data Treatment for ND Experiment

In this section some aspects of the ND data treatment are described. The data were treated using a standard procedure described in chapter 3. The scattering lengths were taken from Sears [43] and the absorption cross-sections were calculated from equation 4.6 using reference values from [43]. The values used are summarised in table 6.2.

The mass density of the sample at different temperatures was calculated using the empirical equation [202]

$$\rho = a + bT + cT^2, \tag{6.19}$$

Element	Zn	Cl
Concentration	0.3333	0.6667
Coherent scattering length (fm)	5.680(5)	9.5770(8)
Scattering cross-section (barn)	4.131(10)	16.8(5)
Absorption cross-section (barn) at 0.4967 Å	3.07(5)	92.5(8)

Table 6.2: Concentration, coherent scattering length, scattering cross-section and absorption cross-section for Zn and Cl used in the data analysis.

where $a = 3.0183$ g/cm^3, $b = -1.0536 \times 10^{-3}$ g/cm^{3}K, $c = 3.7641 \times 10^{-7}$ g/cm^{3}K^2 and ρ, T are in g/cm^3 and K, respectively. The calculated densities and their corresponding atomic number densities are summarised in table 6.3.

Temperature (°C)	Density (g/cm^3)	Number density (Å^{-3})
435(2)	2.4612(1)	0.032624(2)
535(2)	2.4128(1)	0.031982(2)
633(2)	2.3725(1)	0.031448(2)
704(2)	2.3483(1)	0.031127(2)

Table 6.3: Densities of liquid $ZnCl_2$ calculated from equation 6.19 and their corresponding number densities.

In the ND experiment, the sample was held in a silica ampoule. As mentioned in chapter 4, the scattering signal from silica is structured and the difference in dimensions between the container used for the sample and the empty container has to be taken into account in the data correction procedure. The dimensions of the ampoules were measured by using vernier calipers. The outer diameter was measured at four points along the length of an ampoule, twice perpendicular to each other at each point. The inner diameter of the empty container was measured at the open end of the ampoule and the inner diameter of the sample container was estimated from the inner diameter measured from both ends of the tubing used to make the ampoules. The measurements of the outer diameter showed that the ampoules are uniform. The precise outer diameters were 5.98(1) and 6.02(2) mm for the sample container and the empty container, respectively. The inner diameter for both containers was 4.12(1) mm. These values were used in the data correction procedure.

The difference of 0.04 mm between the outer diameter of the sample ampoule and the empty container gives a difference in the illuminated container volume of around 2%. The error was accounted for in the data analysis procedure by applying a scaling factor to the empty container measurement denoted by $I^E_{C+H}(\theta)$ in equation 3.11. The suitability of the scaling factor was assessed by monitoring the first silica peak in $G(r)$ while varying the scaling factor. For the liquid $ZnCl_2$ system, the empty container signal was scaled by 97%.

During the measurement made at 704(2) °C, the sample became unstable and severe density fluctuations were observed as discontinuities in the measured diffraction patterns, see figure 6.5. From figure 6.5, only two scans show no discontinuities in the measured pattern i.e. scans 4 and 5. However, the ratio between these two scans showed structural features which suggested a density fluctuation between the measurement of these scans (see the black line in figure 6.6) and an average of the scans will, therefore, contain steps. It was found that the steps in the final result disappear when combining scans 4, 5 and 8. As shown in figure 6.6 the features in the ratio between scans 4 and 5 are in a different direction compared to the features in the ratio between scans 4 and 8. This dissimilarity arises from the fact that during scan 5 the detector array was moving from high scattering angles to low scattering angles whereas during scan 8 the detector array was moving from low scattering angles to high scattering angles. Because the features in the two ratios are in different directions, the steps cancel when the three scans are combined.

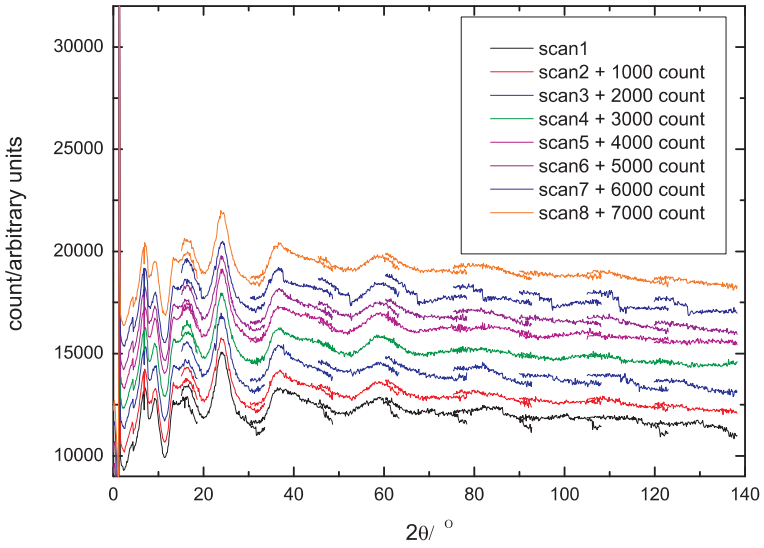

Figure 6.5: Eight diffraction pattern scans for liquid $ZnCl_2$ measured in a silica ampoule inside a furnace at 704(2)°C.

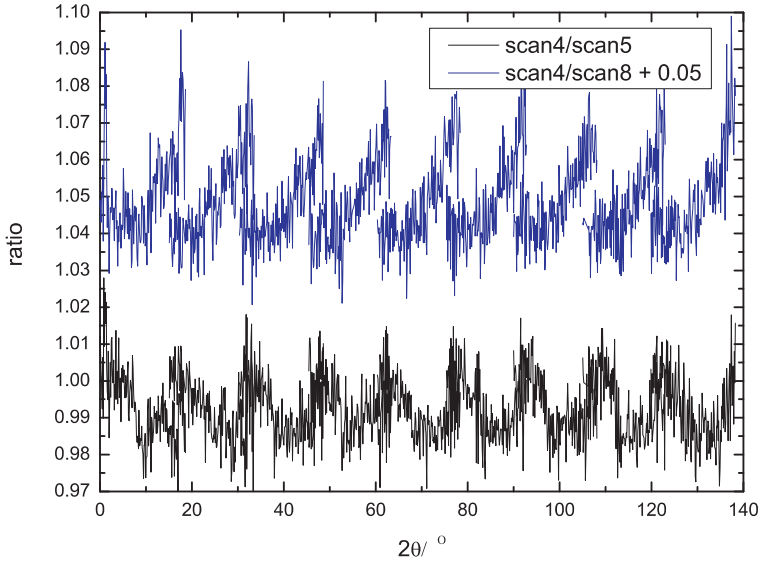

Figure 6.6: Ratio of the diffraction patterns for scans 4 and 5, and for scans 4 and 8 as measured for liquid $ZnCl_2$ in a silica ampoule inside a furnace at 704(2) °C.

6.5 Results

In this section, the total structure factors and corresponding total pair distribution functions obtained from the ND and XRD experiments are presented.

6.5.1 Total Structure Factors

For the ND experiment, the $F(q)$ and the Fourier back transforms for liquid $ZnCl_2$ at 435(2), 535(2), 633(2) and 704(2) °C are shown in figure 6.7. As seen in the figure, even though the data have been corrected for attenuation, inelasticity effects and background scattering, there is still a small slope on the data. From Fourier transformation, a slope in reciprocal space corresponds to a peak at very low r in real space. Therefore, the slope in the $F(q)$ functions was removed by using a Fourier transformation method.

First, an $F(q)$ function was Fourier transformed to give $G(r)$. Next the very low r part of this function where there is a peak due to the slope (from $r = 0$ to 0.31 Å for the measurements made at 435(2) and 633(2) °C and from $r = 0$ to 0.25 Å for the measurements made at 535(2) and 704(2) °C) was set to $G(0)$, the dashed line in figure 6.8, and then the modified $G(r)$ was Fourier back transformed to reciprocal space. The Fourier back transforms obtained from this procedure were subsequently treated as the new data sets while the Fourier back transforms used for the consistency checks were obtained by Fourier transforming $G(r)$, which corresponds to the new data sets, after all of the low r part up to the beginning of the first peak is set to the $G(0)$ limit.

The fully corrected data and their Fourier back transforms are shown in figure 6.9. The data and the Fourier back transforms are in good agreement and there is no slope left on the data. Note that the $F(q)$ data sets start from $q = 0.55$ Å^{-1} ($2\theta = 2.46°$). This is, as mentioned earlier, due to a large background scattering signal at low angles from the direct beam hitting the D4c detector shielding.

From figure 6.9, the $F(q)$ function at 704(2) °C shows residual small steps at $q = 18.95$, 21.05 and 22.65 Å^{-1}. The positions of these steps correspond to $2\theta \approx$

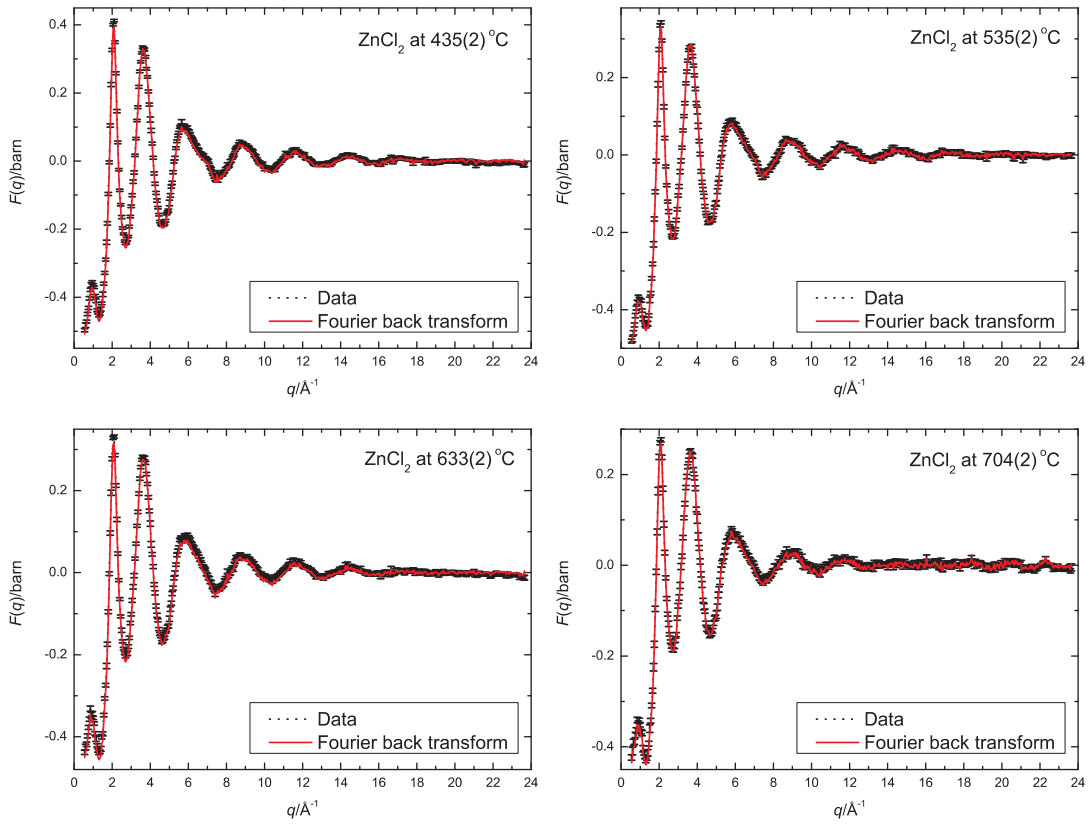

Figure 6.7: The $F(q)$ functions for liquid $ZnCl_2$ at 435(2), 535(2), 633(2) and 704(2) °C as obtained from ND. The dotted lines give the measured $F(q)$ functions (with error bars of the order of $\pm 10^{-3}$ barn) and the solid lines give the Fourier back transforms of the corresponding $G(r)$ functions given by the solid lines in figure 6.8 after the low r part up to the beginning of the first peak is set to the $G(0)$ limit.

97.3, 112.5 and 126.6 degrees in the measured intensity where the steps due to the density fluctuations were observed, see figure 6.5. These non-physical features were removed by applying a cosine window function from $q = 15$ to 19 Å^{-1} and by setting $F(q) = 0$ beyond $q = 19$ Å^{-1}. The effect of the applied cosine window is shown in figure 6.10.

As the $F(q)$ at scattering angles lower than $q = 0.55$ Å^{-1} ($2\theta = 2.46°$) could not be measured, the data at low q values for each temperature needed to be estimated. One method is to fit a straight line through the low q part of $F(q)$ when it is plotted as a function of q^2 [127]. However, figure 6.11 shows that the available low q parts of the $F(q)$ functions when plotted as a function of q^2 are not straight lines, i.e. extrapolation from these points will not give a correct estimate of the function.

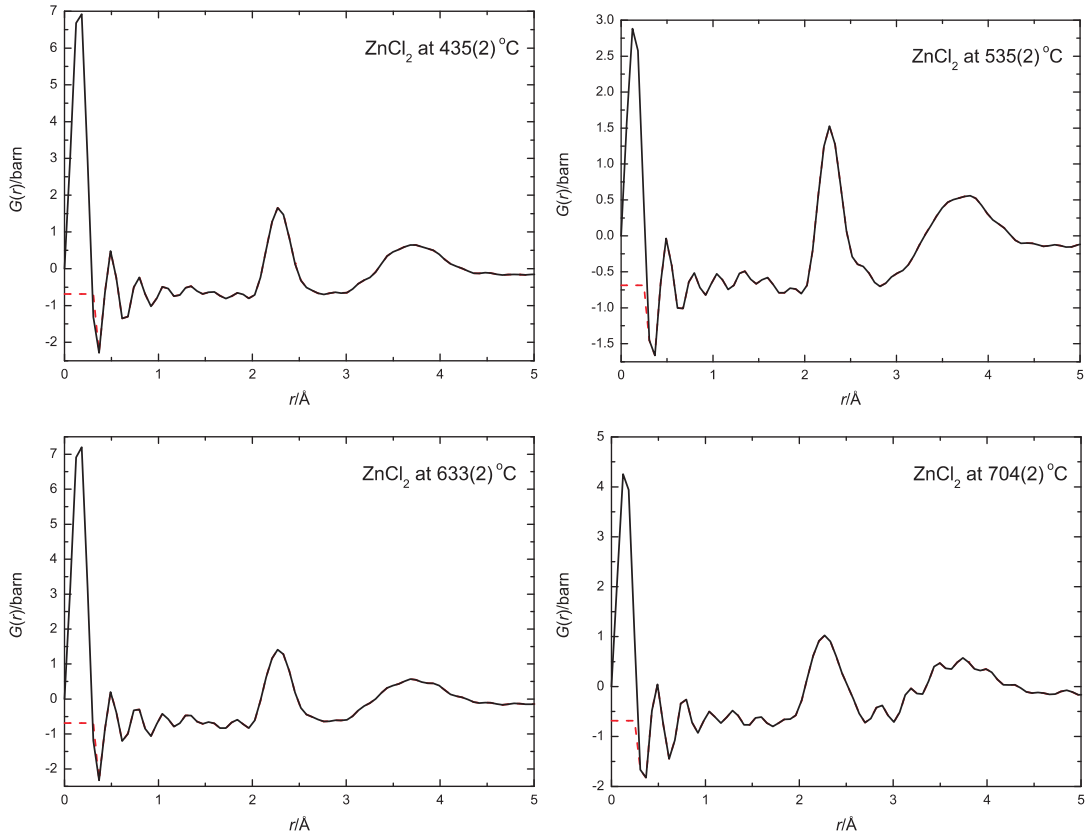

Figure 6.8: The $G(r)$ functions for liquid $ZnCl_2$ at 435(2), 535(2), 633(2) and 704(2) °C. The dashed lines show the low r part of the modified $G(r)$ where a large peak at low r has been removed.

From equation 6.12, the value of $F(0)$ is linked to the isothermal compressibility, χ_T, of the system. The latter can, therefore, be used to estimate the missing part of the $F(q)$ functions.

An empirical equation for the adiabatic compressibility obtained from sound velocity measurements on liquid $ZnCl_2$ at various temperature has been reported by Bockris et al. [203] i.e.

$$\beta_s = 33.2 \times 10^{-11} + 1.30 \times 10^{-13} \cdot t + 3.701 \times 10^{-16} \cdot t^2, \qquad (6.20)$$

where β_s is in m^2/N, t is the temperature in °C and the error on β_s is expected to be $\pm 1\%$. This equation is valid in the temperature range of 410-705 °C and the β_s values at lower temperatures are 3.63×10^{-10} m^2/N at 319 °C, 3.85×10^{-10} m^2/N at 329 °C, 3.99×10^{-10} m^2/N at 342.5 °C and 4.19×10^{-10} m^2/N at 365.9 °C. The isothermal compressibility χ_T is related to β_s by the relation (see for example chapter 5 in

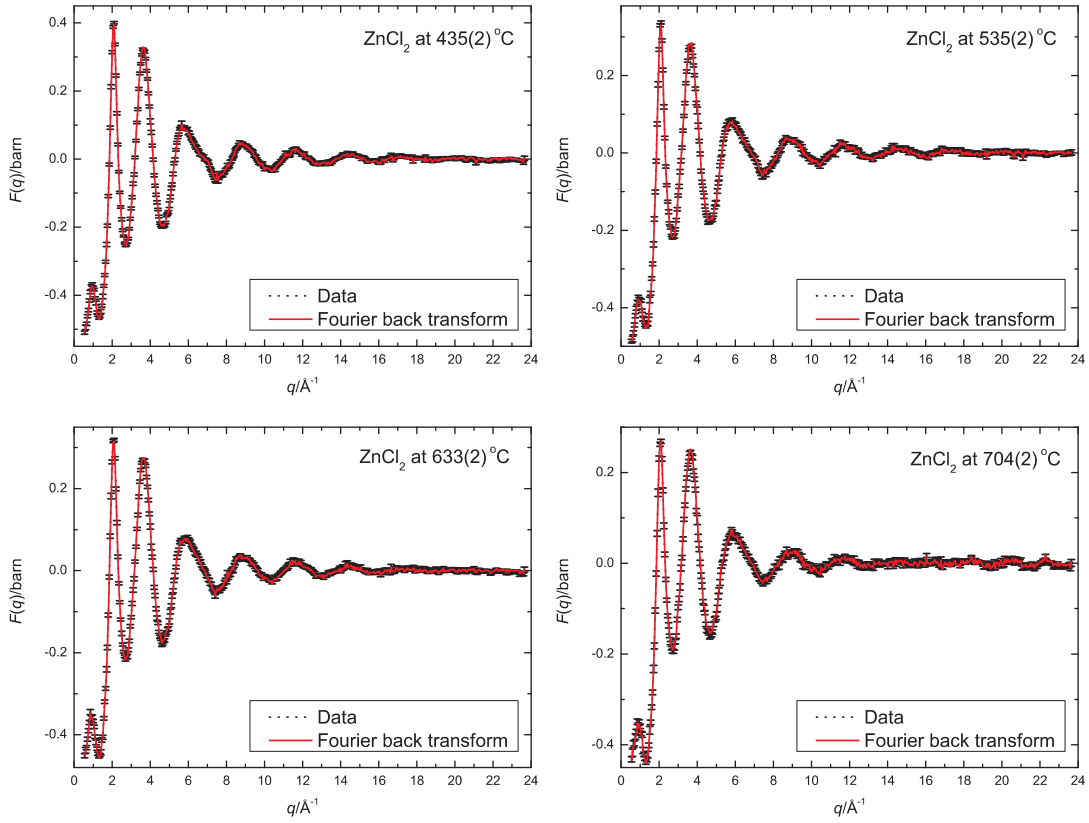

Figure 6.9: The fully corrected $F(q)$ functions for liquid $ZnCl_2$ at 435(2), 535(2), 633(2) and 704(2) °C with their corresponding error bars. The dotted lines give the $F(q)$ functions as obtained from the Fourier back transforms of the $G(r)$ functions given by the solid lines in figure 6.8 after the data up to $r = 0.31$ Å (435(2) and 633(2) °C) or $r = 0.25$ Å (535(2) and 704(2) °C) were set to the $G(0)$ limit. The error bars are of the order of $\pm 10^{-3}$ barn and the solid lines give the Fourier back transforms of the corresponding $G(r)$ functions given by the solid lines in figure 6.15 after the small r oscillations up to the beginning of the first peak are set to the $G(0)$ limit.

[204]),

$$\chi_T = \gamma \cdot \beta_s, \tag{6.21}$$

where $\gamma = C_p/C_v$ is the ratio between the heat capacity at constant pressure C_p and the heat capacity at constant volume C_v. For liquid $ZnCl_2$ at 400, 500 and 600 °C, $\gamma = 1.04$ and at 700 °C $\gamma = 1.05$ [203]. The χ_T determined according to this reference with $\gamma = 1.04$ for the calculations at 328, 332, 340, 435, 535 and 633 °C and $\gamma = 1.05$ for the calculation at 704 °C are presented in table 6.4 along with the compressibilities obtained from other ND experiments on liquid $ZnCl_2$ at 332(5) °C and glassy $ZnCl_2$ at room temperature [205].

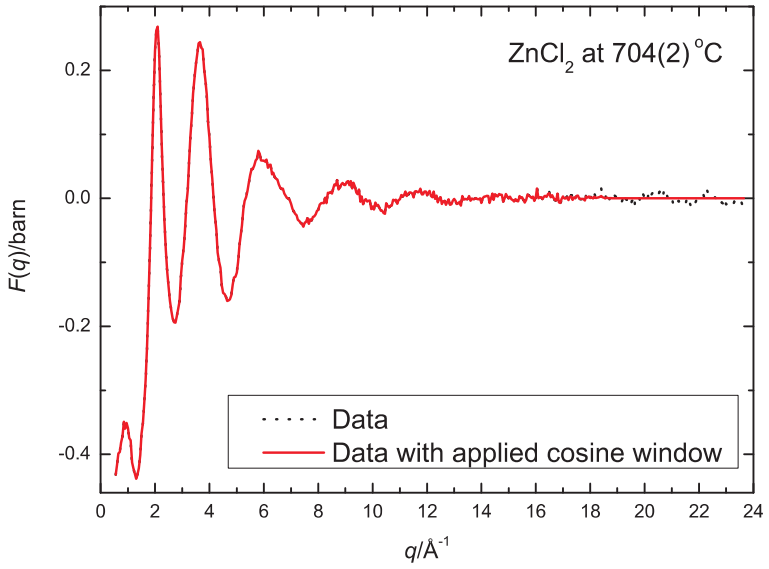

Figure 6.10: The $F(q)$ functions for liquid $ZnCl_2$ at 704(2) °C. The dotted line gives the data as shown in figure 6.9 (the dotted line) and the solid line gives the function with the applied cosine window.

From equation 6.12, $F(0)$ can be calculated from χ_T by using

$$F(0) = n_0 k_B T \langle b \rangle^2 \chi_T - (c_{\mathrm{Zn}} b_{\mathrm{Zn}}^2 + c_{\mathrm{Cl}} b_{\mathrm{Cl}}^2). \tag{6.22}$$

As described in section 3.5.5, $F(q)$ must also satisfy the inequality $F(q) \geq -\sum_\alpha c_\alpha \overline{b_\alpha^2}$ where -$\sum_\alpha c_\alpha \overline{b_\alpha^2}$ = -1.0(2) barn for $ZnCl_2$. The $F(0)$ values determined from the compressibility using equation 6.22 are -0.615(1), -0.590(1), -0.561(2) and -0.536(2) barn for the measurements made at 435(2), 535(2), 633(2) and 704(2) °C, respectively, which all satisfy the inequality relation. The low q extrapolations were made by fitting a straight line through the calculated $F(0)$ and some of the data points in the low q region. The low q part of the $F(q)$ functions plotted versus q^2 and the fitted lines are shown in figure 6.12. Figure 6.13 shows the low q part of the spline fitted $F(q)$ including the extrapolated part for all temperatures.

For the high energy XRD experiment, the $S_X(q)$ for glassy $ZnCl_2$ at room temperature and for liquid $ZnCl_2$ at 328(1), 340(1), 430(1), 530(1) and 630(1) °C are shown in figure 6.14. Although the measured $S_X(q)$ functions do not start from q = 0 $Å^{-1}$, the low q part of the functions could not be extrapolated in the same way as for the neutron $F(q)$. In the Bhatia-Thornton formalism equation 6.8 for XRD

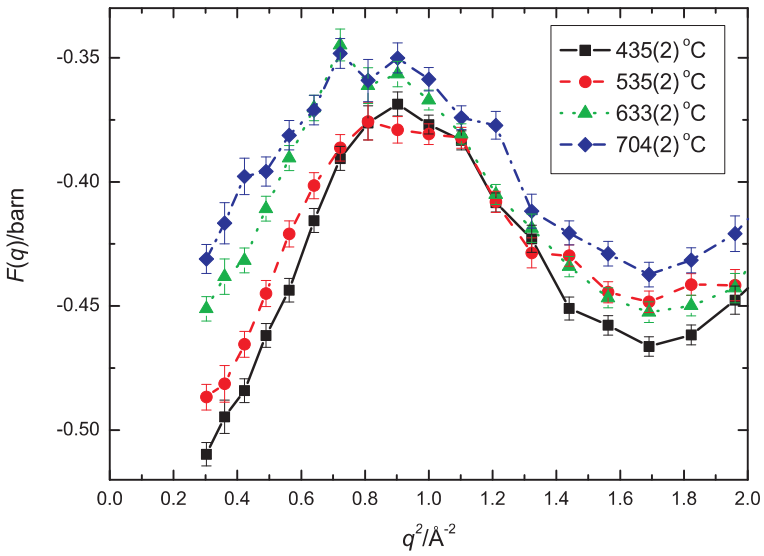

Figure 6.11: The low q part of the $F(q)$ functions plotted as a function of q^2 for liquid $ZnCl_2$ at 435(2), 535(2), 633(2) and 704(2) °C.

becomes

$$\begin{aligned} F_X(q) &= \overline{f(q)}^2 S_{NN}(q) + (f_{\mathrm{Zn}}(q) - f_{\mathrm{Cl}}(q))^2 S_{CC}(q) \\ &+ 2\overline{f(q)}(f_{\mathrm{Zn}}(q) - f_{\mathrm{Cl}}(q)) S_{NC}(q) - (c_{\mathrm{Zn}} f_{\mathrm{Zn}}(q)^2 + c_{\mathrm{Cl}} f_{\mathrm{Cl}}(q)^2). \end{aligned} \quad (6.23)$$

From equation 6.23, although the $S_{NN}(q)$, $S_{CC}(q)$ and $S_{NC}(q)$ functions are proportional to q^2 [127], the x-ray form factors are also q dependent. Thus $F_X(q)$ is not in general proportioned to q^2 at small q values. The $S_X(q)$ values for $q < 0.2$ Å^{-1} were, therefore, set to the $S_X(q = 0.2$ Å$^{-1})$ value.

Temperature (°C)	χ_T ($10^{-10} \cdot \frac{1}{N \cdot m^2}$)	
	reference [205]	reference [203]
RT (glassy)	3.1(7)	-
328	-	4.00(4)
332	4.6(3)	4.00(4)
340	-	4.15(4)
435	-	4.77(5)
535	-	5.28(5)
633	-	5.85(6)
704	-	6.37(6)

Table 6.4: Values of χ_T for glassy $ZnCl_2$ at room temperature and for liquid $ZnCl_2$ at 328, 332, 340, 435, 535, 633 and 704 °C as obtained from the literature. The values in reference [205] were obtained from ND experiments and the values in reference [203] were obtained from sound velocity measurements.

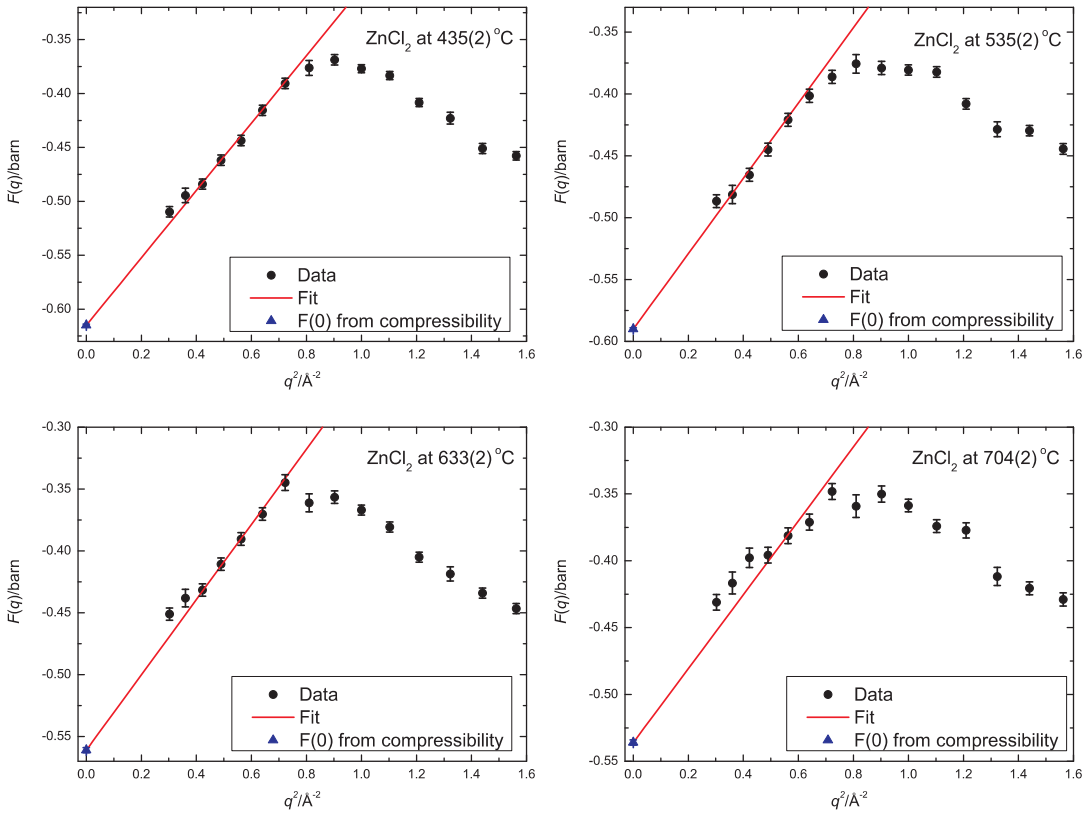

Figure 6.12: The dots with vertical error bars give the low q part of the $F(q)$ functions plotted as a function of q^2 for liquid $ZnCl_2$ at 435(2), 535(2), 633(2) and 704(2) °C. The lines give the fits to the low q region of the $F(q)$ functions and the $F(0)$ data point (a triangle) as calculated from the compressibilities reported in [203].

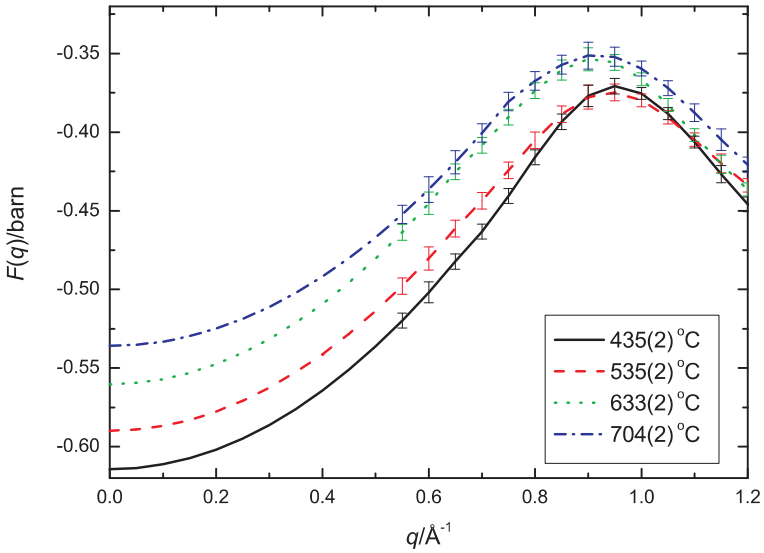

Figure 6.13: The spline fitted $F(q)$ functions including the low q part extrapolated using the χ_T values reported in [203], for liquid $ZnCl_2$ at 435(2), 535(2), 633(2) and 704(2) °C.

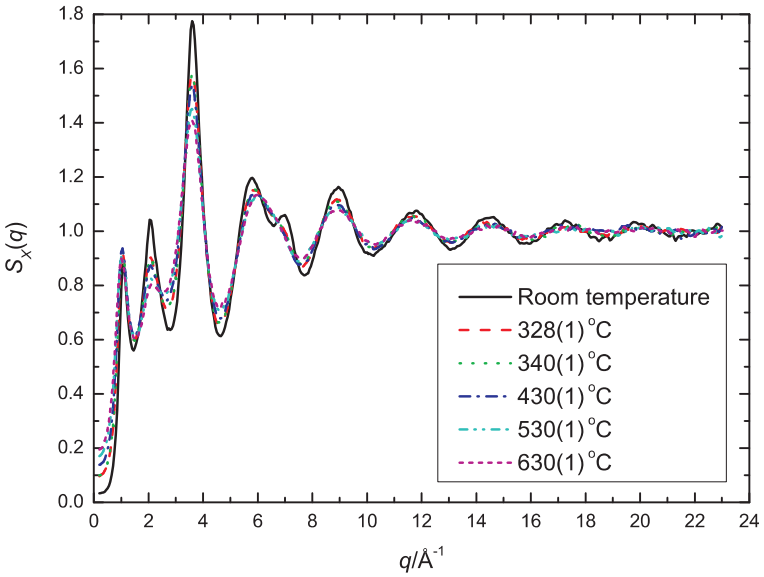

Figure 6.14: The $S_X(q)$ functions for glassy $ZnCl_2$ at room temperature and for liquid $ZnCl_2$ at 328(1), 340(1), 430(1), 530(1) and 630(1) °C as measured by using XRD.

6.5.2 Total Pair Distribution Functions

The $G(r)$ functions for liquid $ZnCl_2$ at 435(2), 535(2), 633(2) and 704(2) °C as measured by using ND are shown in figure 6.15. The functions are the Fourier transforms of the spline fitted $F(q)$ functions presented in figures 6.9 and 6.10. The $F(q)$ and the spline fits are plotted in figure 6.16. For the measurement made at 704(2) °C, the effect in real space of the cosine window applied in reciprocal space is shown in figure 6.17.

The $G_X(r)$ functions for glassy $ZnCl_2$ at room temperature and liquid $ZnCl_2$ at 328(1), 340(1), 430(1), 530(1) and 630(1) °C are shown in figure 6.18. The functions are the Fourier transforms of the $S_X(q)$ shown in figure 6.14 after the functions where $q < 0.2$ Å^{-1} were set to the $S_X(q = 0.2$ Å$^{-1})$ value.

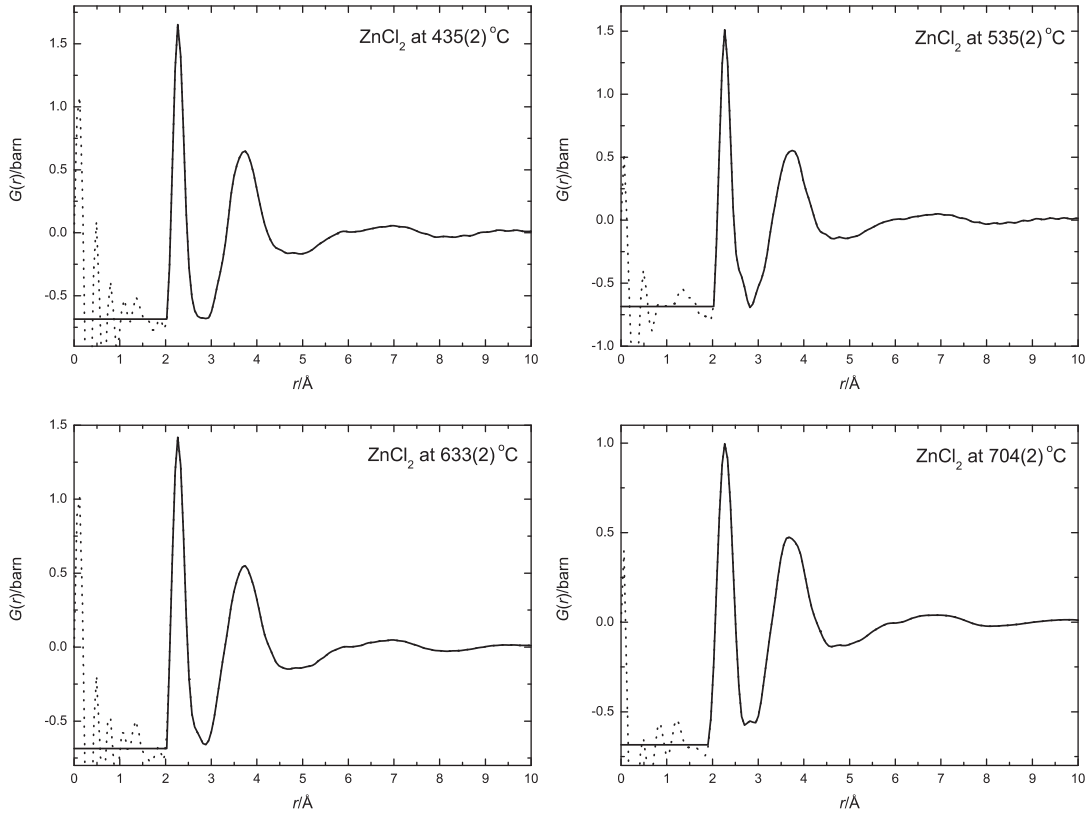

Figure 6.15: The $G(r)$ functions for liquid $ZnCl_2$ at 435(2), 535(2), 633(2) and 704(2) °C as obtained by Fourier transforming the spline fitted $F(q)$ functions shown in figure 6.16. The dotted lines at low r show the artifacts obtained from the Fourier transformation procedure.

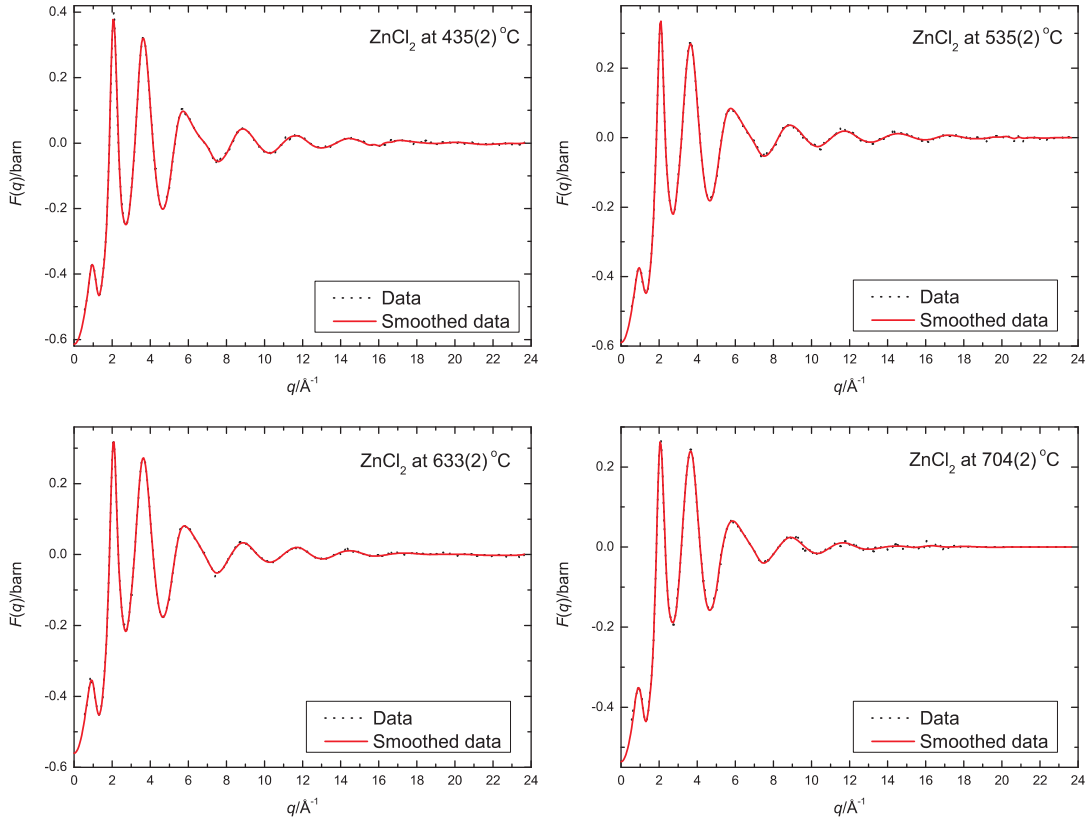

Figure 6.16: Spline fits to the $F(q)$ functions for liquid $ZnCl_2$ at 435(2), 535(2), 633(2) and 704(2) °C. The dotted lines give the data and the solid lines give the spline fits.

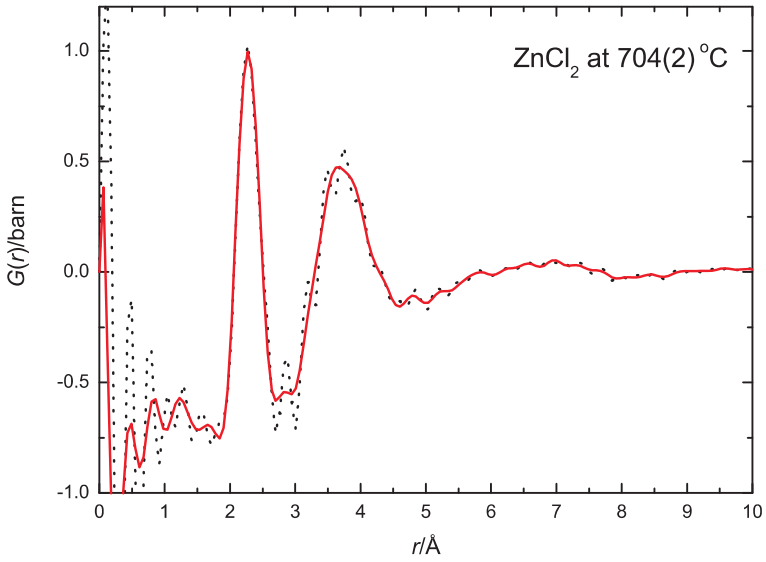

Figure 6.17: The $G(r)$ functions for liquid $ZnCl_2$ at 704(2) °C. The dotted line gives the Fourier transform of the $F(q)$ function shown by the dotted line in figure 6.10 and the solid line gives the Fourier transform of the $F(q)$ function with the applied cosine window as shown by the solid line in figure 6.10.

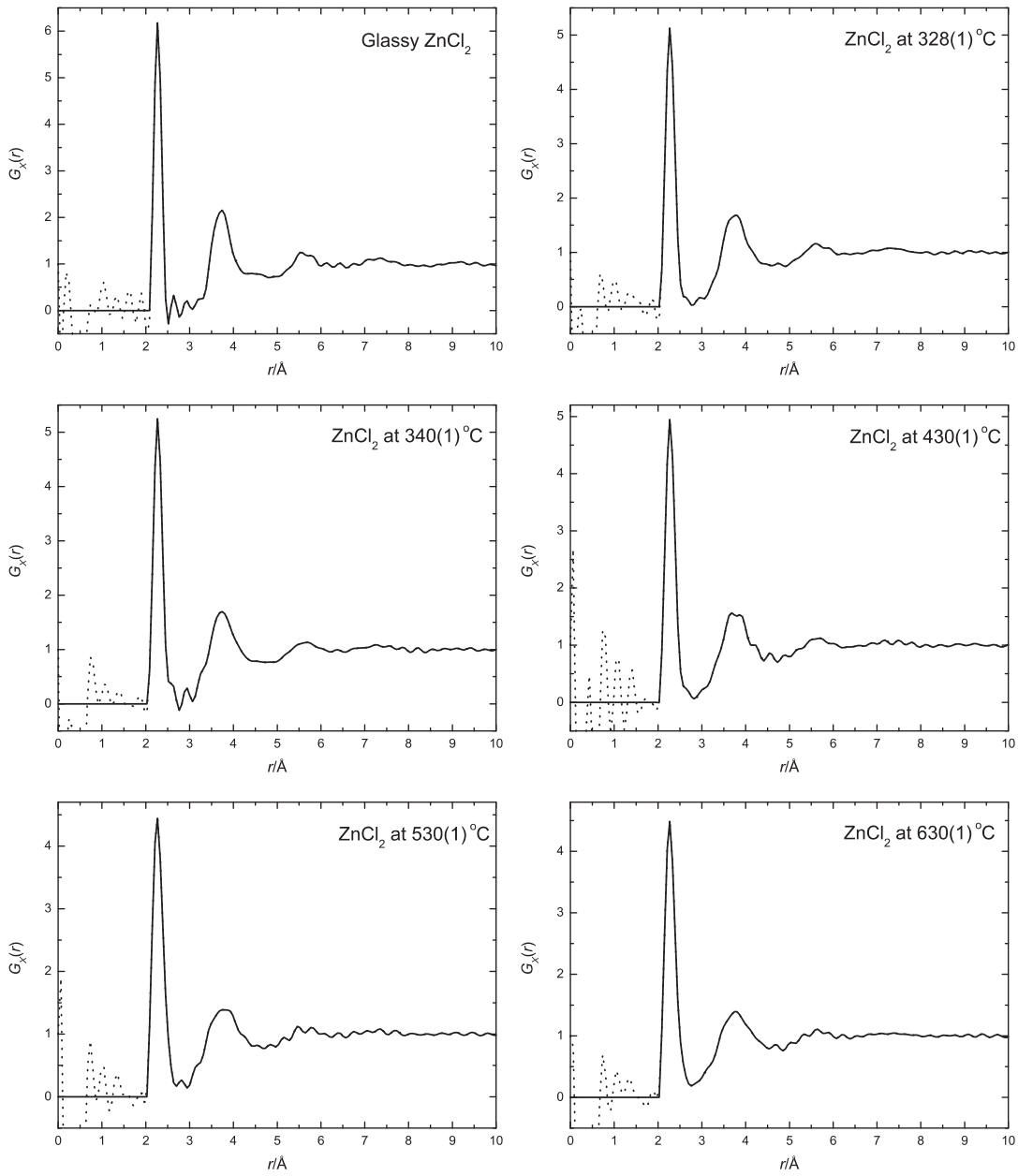

Figure 6.18: The $G_X(r)$ functions for glassy $ZnCl_2$ at room temperature and for liquid $ZnCl_2$ at 328(1), 340(1), 430(1), 530(1) and 630(1) °C as measured by using high energy XRD. The dotted lines at low r show the artifacts obtained from the Fourier transformation procedure.

6.6 Discussion

In this section, a discussion of the results is given including the temperature dependent behaviour of the pair correlation functions. For the total structure factors, the temperature dependence of the FSDP is also investigated.

6.6.1 Total Structure Factors

The temperature dependent behaviour of the $F(q)$ functions for liquid $ZnCl_2$ as measured by using ND is shown in figure 6.19. From the figure, there is a decrease in the intensity of every peak except for the FSDP with increasing temperature. A small broadening of the peaks in $F(q)$ as the temperature increases is expected as the influence of thermal motion becomes stronger at high temperatures. Figure 6.13 shows the FSDP for the $F(q)$ at each temperature. From the figure, the FSDP becomes slightly broader and shifts towards lower q values as the temperature increases. The positions and full width at half maximum (FWHM) of the FSDP are summarised in table 6.5. The persistence of a network structure in liquid $ZnCl_2$ has been observed up to a temperature of 600 °C [181]. The existence of an FSDP in the $F(q)$ measured at 704(2) °C in this study indicates that the network structure in liquid $ZnCl_2$ exists even when the temperature is close to the boiling point.

For the high energy XRD results, shown in figure 6.14, $S_X(q)$ for the glassy sample has sharper peaks than for the liquid but has very similar overall features. The temperature dependent behaviour of the $S_X(q)$ functions for liquid $ZnCl_2$ is similar to the results obtained from ND i.e. a broadening is observed for each peak due to thermal motion. The FSDP obtained from XRD also shifts towards smaller q values as the temperature increases, see figure 6.20. The positions and FWHM of the FSDP are summarised in table 6.5.

As mention earlier, the FSDP is a signature of intermediate range order in a network structure. The periodicity of the network is given by $2\pi/q_{_{FSDP}}$ where $q_{_{FSDP}}$ is the position of the FSDP [180], and the measured values for each temperature are summarised in table 6.5. From the table, there is a difference in the values of the periodicity as obtained from the neutron and x-ray data. This can be attributed

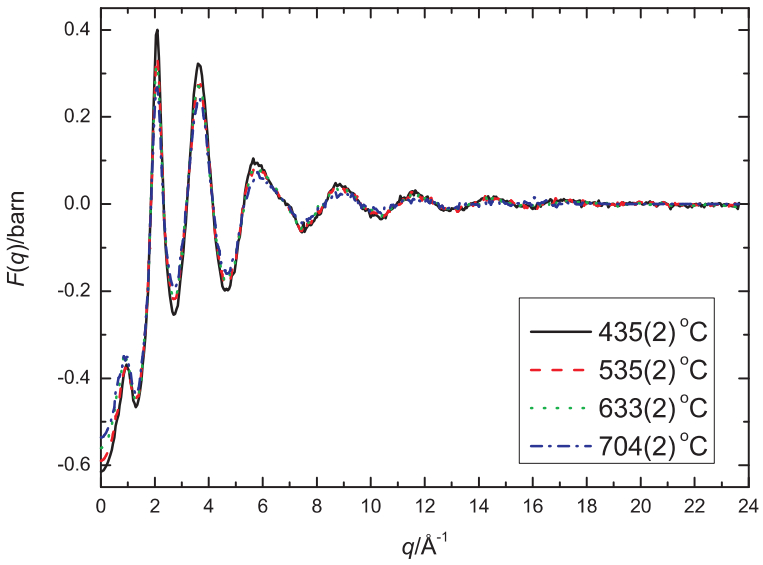

Figure 6.19: The $F(q)$ functions including the low q extrapolation for liquid $ZnCl_2$ at 435(2), 535(2), 633(2) and 704(2) °C as obtained by ND.

to the difference in the neutron and x-ray weighting factors. From figures 6.21 and 6.22, and as discussed below, the FSDP from the neutron data has contributions from all the correlations whereas the FSDP from the x-ray data is dominated by the Zn-Zn correlations.

Temperature (°C)	Peak position ($Å^{-1}$)		FWHM ($Å^{-1}$)		Network periodicity (Å)	
	neutron	x-ray	neutron	x-ray	neutron	x-ray
RT (glassy)	1.09(3) [180]	1.07(1)	-	0.38(2)	5.8(2) [180]	5.87(5)
328(1)	-	1.05(1)	-	0.42(2)	-	5.98(6)
340(1)	-	1.05(1)	-	0.42(2)	-	5.98(6)
$\simeq$ 430	0.96(1)	1.04(1)	0.42(2)	0.43(2)	6.54(7)	6.04(6)
$\simeq$ 530	0.92(1)	1.02(1)	0.50(2)	0.46(2)	6.83(7)	6.16(6)
$\simeq$ 630	0.92(1)	1.01(1)	0.50(2)	0.48(2)	6.83(7)	6.22(6)
704(2)	0.91(1)	-	0.49(2)	-	6.90(8)	-

Table 6.5: Peak positions and FWHM of the FSDP for glassy $ZnCl_2$ at room temperature and for liquid $ZnCl_2$ at 328(1), 340(1), $\simeq$ 430, $\simeq$ 530, $\simeq$ 630 and 704(2) °C as obtained by ND and XRD.

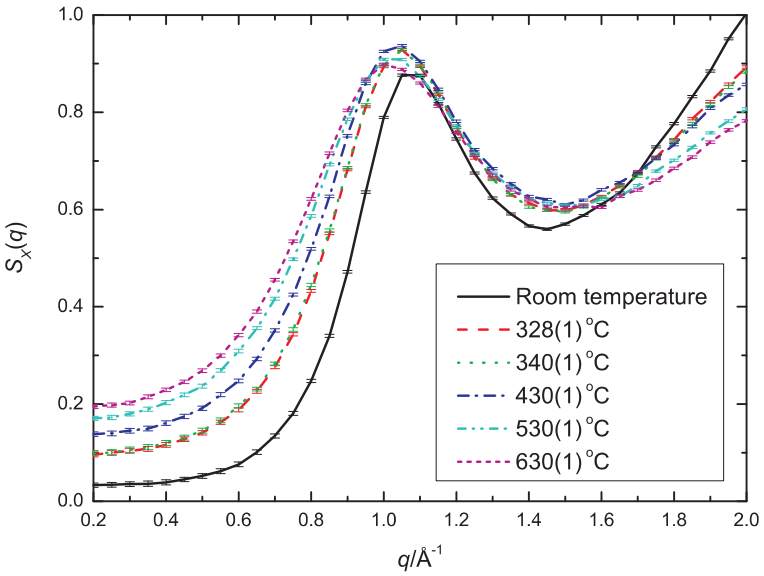

Figure 6.20: The low q part of the $S_X(q)$ functions showing the FSDP for glassy $ZnCl_2$ at room temperature and for liquid $ZnCl_2$ at 328(1), 340(1), 430(1), 530(1) and 630(1) °C.

The full set of partial structure factors for glassy $ZnCl_2$ at room temperature and for liquid $ZnCl_2$ at 332(5) °C have been measured by using the method of isotopic substitution in ND [205]. A comparison between the $S_N(q)$ for liquid $ZnCl_2$ at 332(5) °C as measured in the isotopic substitution experiment [205] and the $S_N(q)$ for liquid $ZnCl_2$ at 435(2) °C as measured in this work is shown in figure 6.21. Also shown are the $S_{\alpha\beta}(q)$ from [205] weighted by the factors presented in table 6.6. The $S_X(q)$ functions for glassy $ZnCl_2$ at room temperature and liquid $ZnCl_2$ at 332(5) °C reproduced from the measured partial structure factors [205] are compared with the $S_X(q)$ functions obtained from this work in figure 6.22. Also shown are the $S_{\alpha\beta}(q)$ from [205] weighted by the factors given in equations 6.13 and 6.14 with the x-ray form factors taken from [159].

Although the lowest temperature at which the $S_N(q)$ for liquid $ZnCl_2$ measured in this work is about 100 °C higher than used in the isotopic substitution experiment, it is useful to make a comparison as we know from figure 6.19 that the structure factor of liquid $ZnCl_2$ varies slowly with increasing temperature. As shown in figure 6.21, the $S_N(q)$ functions from the two experiments agree well within the error bars. The weighted $S_{\alpha\beta}(q)$ functions shown in this figure reveal that the FSDP has contributions from all three partial structure factors.

Pair correlation	Neutron weighting factor		X-ray weighting factor at $q = 0$	
	for $F(q)$ (barn)	for $S_N(q)$	for $F_X(q)$ (electron units)	for $S_X(q)$
Zn-Zn	0.03585(6)	0.05231(9)	87.109(6)	0.19148(9)
Zn-Cl	0.2418(2)	0.3528(3)	223.92(9)	0.4922(3)
Cl-Cl	0.40764(7)	0.5948(2)	143.907(6)	0.3163(2)

Table 6.6: Neutron and x-ray weighting factors for each partial pair correlation function in the $ZnCl_2$ system. The weighting factors were calculated by using the definitions given in equations 6.1, 6.4, 6.13 and 6.14 with neutron scattering lengths taken from [43] and ionic x-ray form factors taken from [159].

The comparison in figure 6.22 shows that the $S_X(q)$ functions from the two experiments agree reasonably well except in the region of the FSDP. This is most likely due to a difference in the neutron and x-ray diffractometer resolution functions which depends on the experimental setup and on the incident x-ray or neutron wavelength. The difference in resolution functions has been shown to effect the intensity and shape of $F(q)$ at small q [206]. The isotopic substitution experiments of reference [205] and the ND experiments in this work were performed using the same instrument and similar incident neutron wavelengths and, therefore, correspond to similar resolution functions. The weighted $S_{\alpha\beta}(q)$ in figure 6.22 show that the FSDP for the $S_X(q)$ function has its main contribution from the Zn-Zn correlations. The high intensity of the FSDP in $S_X(q)$ compared to $S_N(q)$ is, therefore, due to the high weighting factor for the Zn-Zn correlations, see table 6.6.

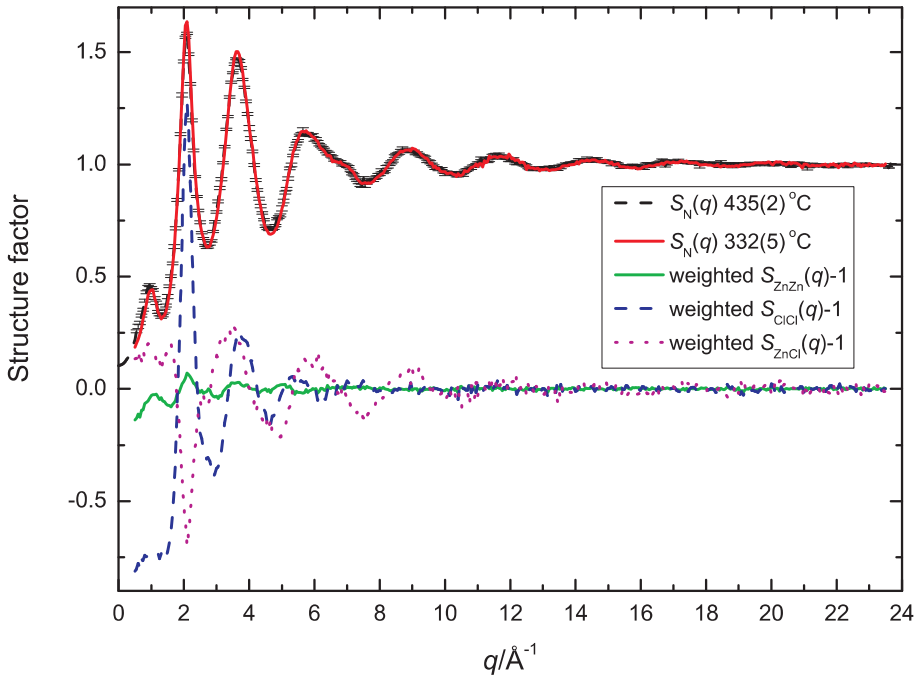

Figure 6.21: The $S_N(q)$ function for liquid $ZnCl_2$ at 332(5) °C reproduced from the measured partial structure factors [205] and the measured $S_N(q)$ function for liquid $ZnCl_2$ at 435(2) °C obtained from this work. The weighted $S_{\alpha\beta}(q)$ show the contributions of each $S_{\alpha\beta}(q)$ to the $S_N(q)$ function.

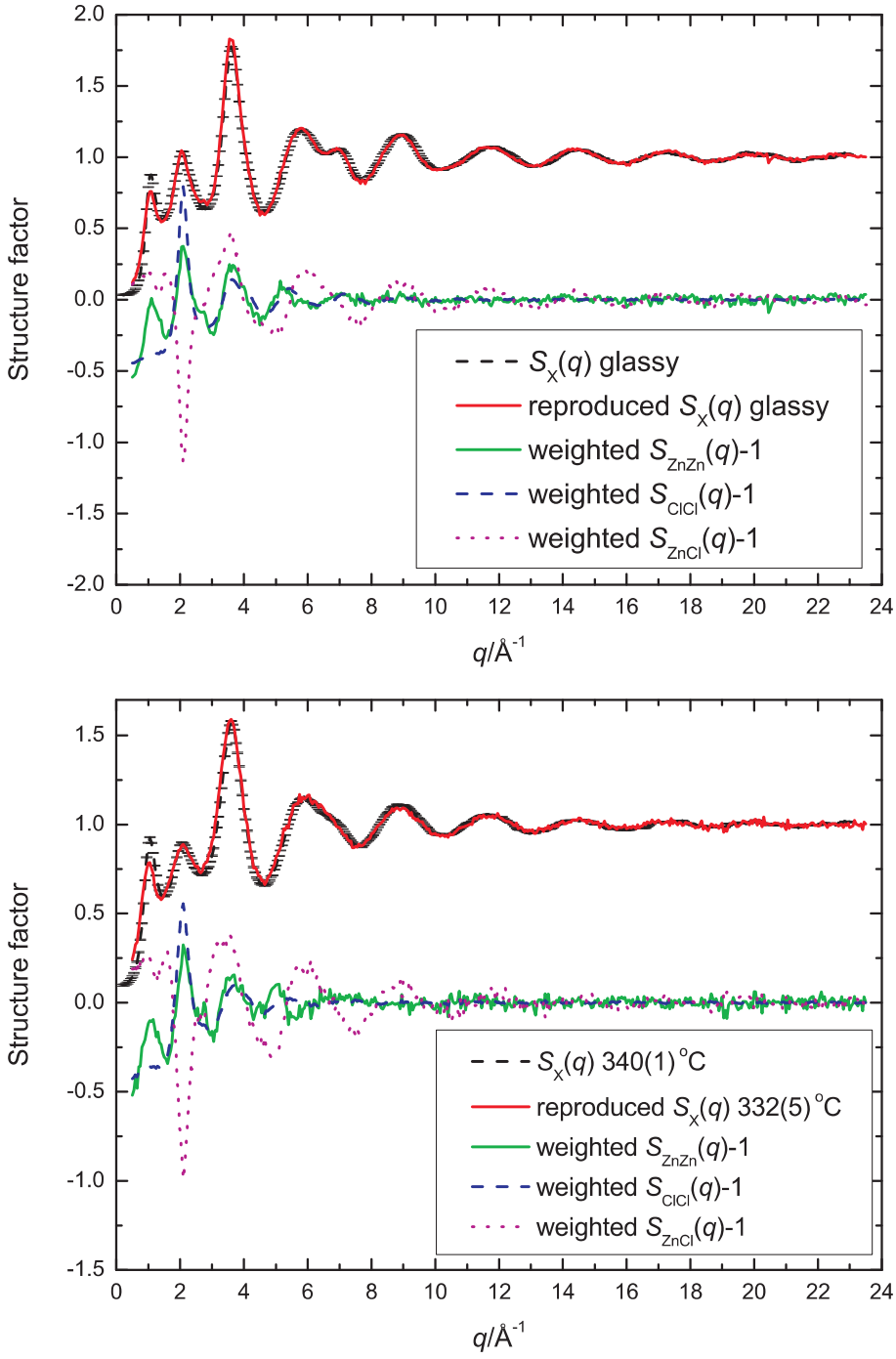

Figure 6.22: The $S_X(q)$ functions for glassy $ZnCl_2$ at room temperature and liquid $ZnCl_2$ at 332(5) °C reproduced from the measured partial structure factors [205] are compared with the measured $S_X(q)$ functions for glassy $ZnCl_2$ at room temperature and liquid $ZnCl_2$ at 340(1) °C from this work. The weighted $S_{\alpha\beta}(q)$ show the contributions of each $S_{\alpha\beta}(q)$ to the $S_X(q)$ function.

6.6.2 Total Pair Distribution Functions

The maximum q values for the ND and XRD measurements in this work are 23.65 and 23.0 $Å^{-1}$, respectively, which are comparable to the maximum q value for the isotopic substitution experiment which is 23.5 $Å^{-1}$. It is, therefore, useful to compare the data sets in real space. In figure 6.23, the $G_N(r)$ function for liquid $ZnCl_2$ from the measurement at 435(2) °C obtained in this work is compared with the $G_N(r)$ function for liquid $ZnCl_2$ at 332(5) °C from the isotopic substitution experiment [205]. Also shown are the $g_{\alpha\beta}(r)$ functions from [205] weighted by the factors presented in table 6.6. From the figure, the two $G_N(r)$ functions agree well. The weighted $g_{\alpha\beta}(r)$ functions show that the Zn-Zn correlations have only a very small contribution to $G_N(r)$.

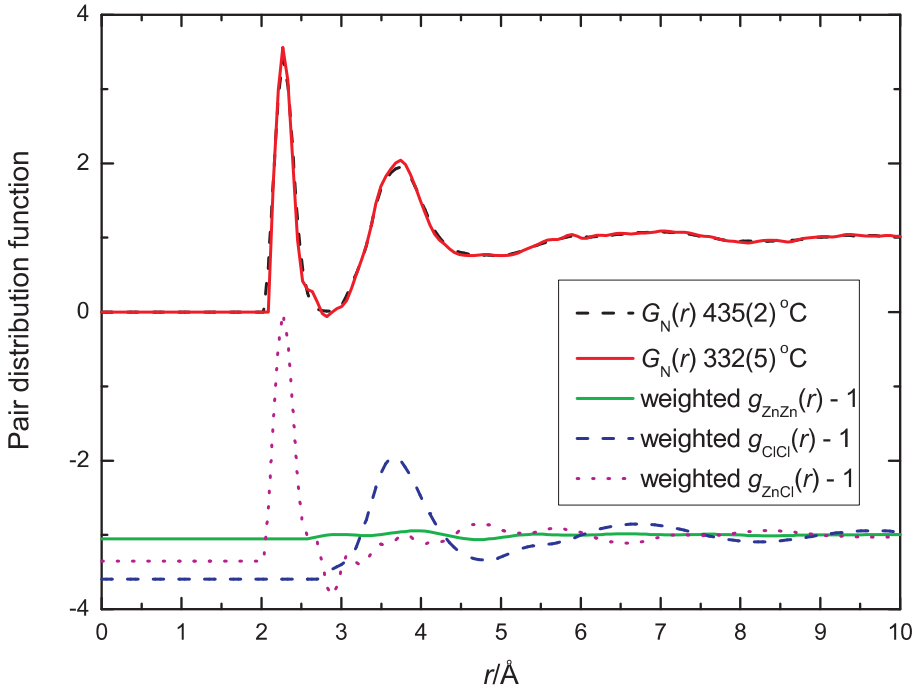

Figure 6.23: The $G_N(r)$ function for liquid $ZnCl_2$ at 332(5) °C from reference [205] and the $G_N(r)$ function for liquid $ZnCl_2$ at 435(2) °C obtained from this work. The weighted $g_{\alpha\beta}(r)$ show the contributions of each $g_{\alpha\beta}(r)$ to the $G_N(r)$ function and are displaced vertically for clarity of presentation.

Figure 6.24 shows a comparison between the $G_X(r)$ functions for glassy $ZnCl_2$ at room temperature and liquid $ZnCl_2$ at 340(1) °C obtained in this work and the $G_X(r)$ functions for glassy $ZnCl_2$ at room temperature and liquid $ZnCl_2$ at 332(5) °C

determined from the Fourier transforms of the reproduced $S_X(q)$ functions shown in figure 6.22. Also shown in this figure are the weighted $g_{\alpha\beta}(r)$ corresponding to the Zn-Zn, Cl-Cl and Zn-Cl correlations. From the figure, the $G_X(r)$ functions for glassy and liquid $ZnCl_2$ obtained from both experiments agree reasonably well which is expected since the only discrepancy between the $S_X(q)$ functions shown in figure 6.22 is in the low q region which corresponds to the high r part of the $G_X(r)$ functions.

The position of the first peak in the $G_N(r)$ or $G_X(r)$ functions shown in figures 6.23 and 6.24, corresponds to the shortest atomic distance which in this case is the Zn-Cl nearest neighbour distance because Zn^{2+} and Cl^- have opposite charges so there is less repulsive force between them. This is confirmed by the $g_{\alpha\beta}(r)$ functions which show that the first peak in $G_N(r)$ and $G_X(r)$ only has a contribution from the Zn-Cl correlations. From the $g_{\alpha\beta}(r)$ functions, the second peak in $G_N(r)$ and $G_X(r)$ has contributions from both the Zn-Zn and Cl-Cl correlations. It should be noted that the Zn-Zn and Cl-Cl nearest neighbour distance are comparable which, as shown by Molecular Dynamics (MD) simulations [207], results from the polarisability of the Cl^- ions i.e. dipoles on the polarisable Cl^- ions shield the repulsive Coulomb interaction between the positively charged Zn^{2+} ions thus shortening the Zn-Zn distance.

Comparisons between the $G_N(r)$ and $G_X(r)$ functions for liquid $ZnCl_2$ at $\simeq$ 430, $\simeq$ 530 and $\simeq$ 630°C are shown in figure 6.25. From this figure, the positions of the first and second peaks in these two functions are the same but there is a difference in the peak intensities which is due to the difference in the neutron and x-ray weighting factors for the partial pair distribution functions. As seen from the weighted $g_{\alpha\beta}(r)$ functions shown in figure 6.23, the second peak in $G_N(r)$ is dominated by the Cl-Cl correlations so the position of the peak at 3.73(3) Å gives a good approximation of the Cl-Cl nearest neighbour distance. For $G_X(r)$, although the second peak has a larger contribution from the Zn-Zn correlations, the Zn-Zn and Cl-Cl nearest neighbour distances are very similar so no difference in the second peak position for the $G_N(r)$ and $G_X(r)$ functions is observed.

Because the first peak in $G_N(r)$ and $G_X(r)$ at 2.27(1) Å has contributions only

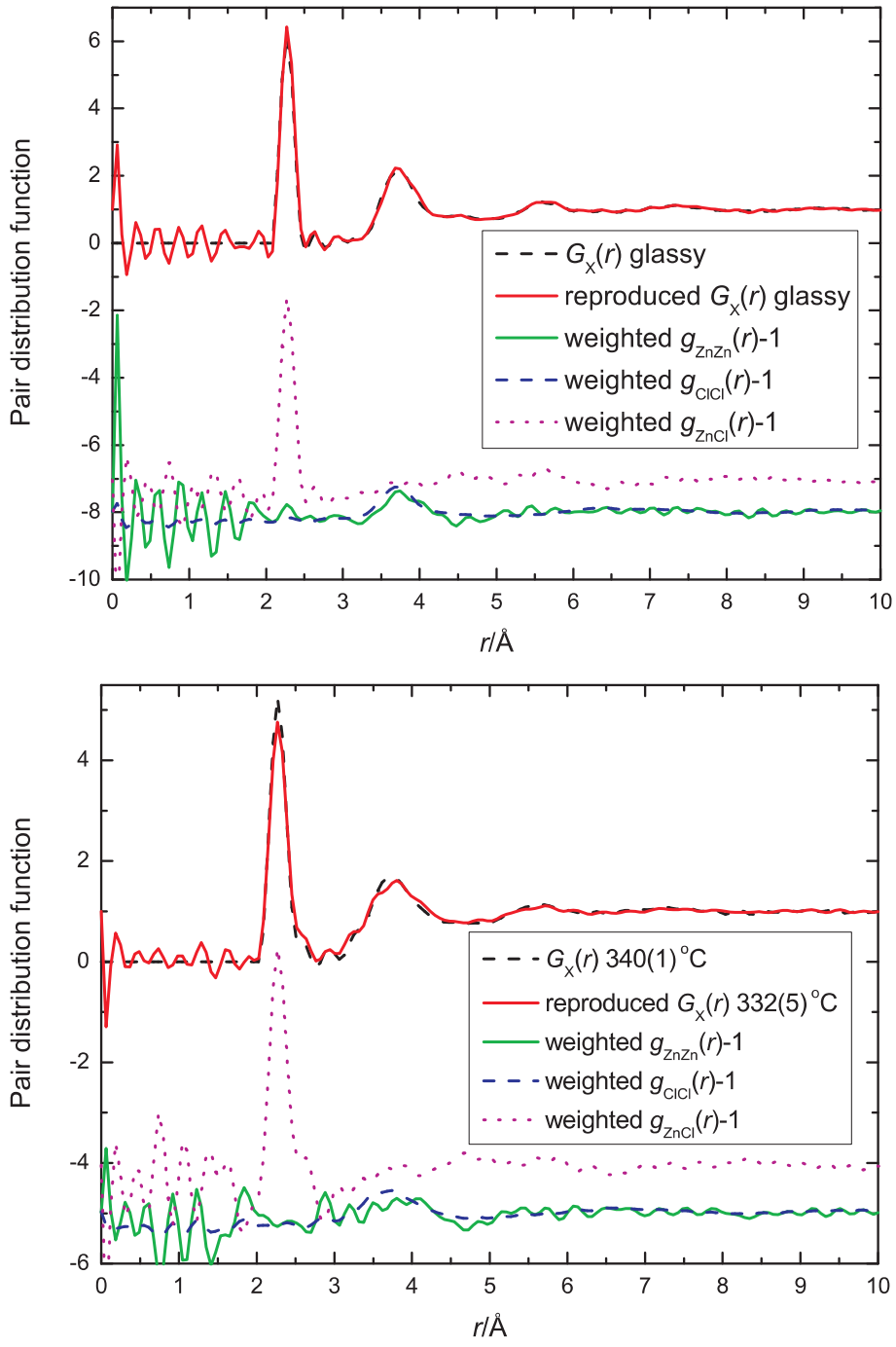

Figure 6.24: The $G_X(r)$ for glassy $ZnCl_2$ at room temperature and liquid $ZnCl_2$ at 332(5) °C as obtained by Fourier transforming the reproduced $S_X(q)$ (maximum q = 23.5 Å^{-1}) taken from reference [205] and the $G_X(r)$ functions for glassy $ZnCl_2$ at room temperature and liquid $ZnCl_2$ at 340(1) °C as obtained from this work (maximum q = 23.0 Å^{-1}). Also shown are the weighted $g_{\alpha\beta}(r)$ for glassy $ZnCl_2$ at room temperature and liquid $ZnCl_2$ at 332(5) °C as obtained by Fourier transforming the weighted $S_{\alpha\beta}(q)$ shown in figure 6.22. The latter are displaced vertically for clarity of presentation.

from the Zn-Cl correlations, the average Zn-Cl coordination number can be calculated from the area under the first peak, using equation 6.6 for $G_N(r)$ or equation 6.16 for $G_X(r)$. The coordination numbers and integration ranges are summarised in table 6.7.

Temperature (°C)	Zn-Cl coordination number		integration range (Å)	
	neutron	x-ray	neutron	x-ray
RT (glassy)	-	3.95(5)	-	2.09-2.45
328(1)	-	3.97(1)	-	2.02-2.76
340(1)	-	3.96(2)	-	2.02-2.67
$\simeq$ 430	4.05(3)	3.98(2)	2.02-2.76	1.96-2.82
$\simeq$ 530	4.01(4)	3.86(5)	2.02-2.76	2.02-2.67
$\simeq$ 630	4.01(5)	3.86(5)	2.02-2.76	2.02-2.76
704(2)	3.9(1)	-	1.90-2.76	-

Table 6.7: Average Zn-Cl coordination numbers determined from $G_N(r)$ and $G_X(r)$ and the corresponding integration ranges for glassy $ZnCl_2$ at room temperature and for liquid $ZnCl_2$ at 328(1), 340(1), $\simeq$ 430, $\simeq$ 530, $\simeq$ 630 and 704(2) °C.

The $G_N(r)$ and $G_X(r)$ functions for liquid $ZnCl_2$ at every measured temperature are shown in figure 6.26. From the figure, the positions of the first and second peaks at 2.27(1) and 3.73(3) Å, respectively, are the same at all temperatures which gives a constant ratio between the peak positions of 1.64(2). For a perfect tetrahedron the ratio between the Zn-Cl and the Cl-Cl atomic distances would be $\sqrt{8/3} = 1.63$. From table 6.7, the average Zn-Cl coordination numbers are around four and the values determined from the $G_N(r)$ and $G_X(r)$ functions are comparable. The ratio of 1.64(2), along with the average Zn-Cl coordination numbers, therefore indicates that the basic structural motif in liquid $ZnCl_2$ is the $ZnCl_4$ tetrahedron. This structural unit is also found in glassy $ZnCl_2$ where the average Zn-Cl coordination number is 3.9(1) and the ratio of the nearest neighbour Zn-Cl and Cl-Cl atomic distances is 1.62(1) [180].

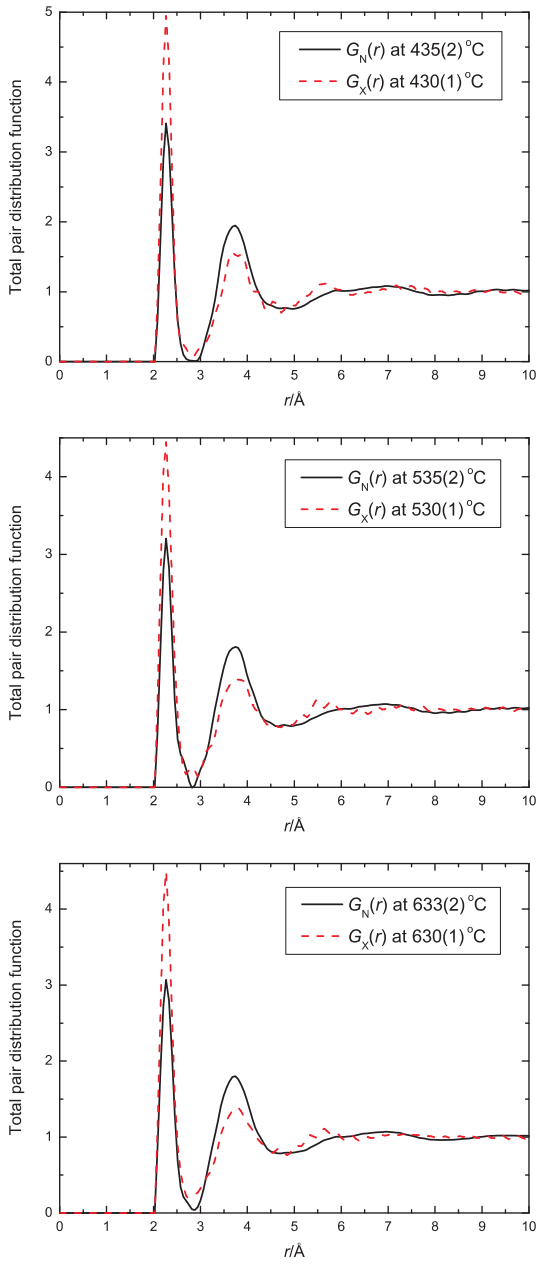

Figure 6.25: The $G_N(r)$ and $G_X(r)$ functions for liquid $ZnCl_2$ at $\simeq$ 430, $\simeq$ 530 and $\simeq$ 630 °C. The solid lines give the $G_N(r)$ as obtained by using ND and the dashed lines give the $G_X(r)$ as obtained by using XRD.

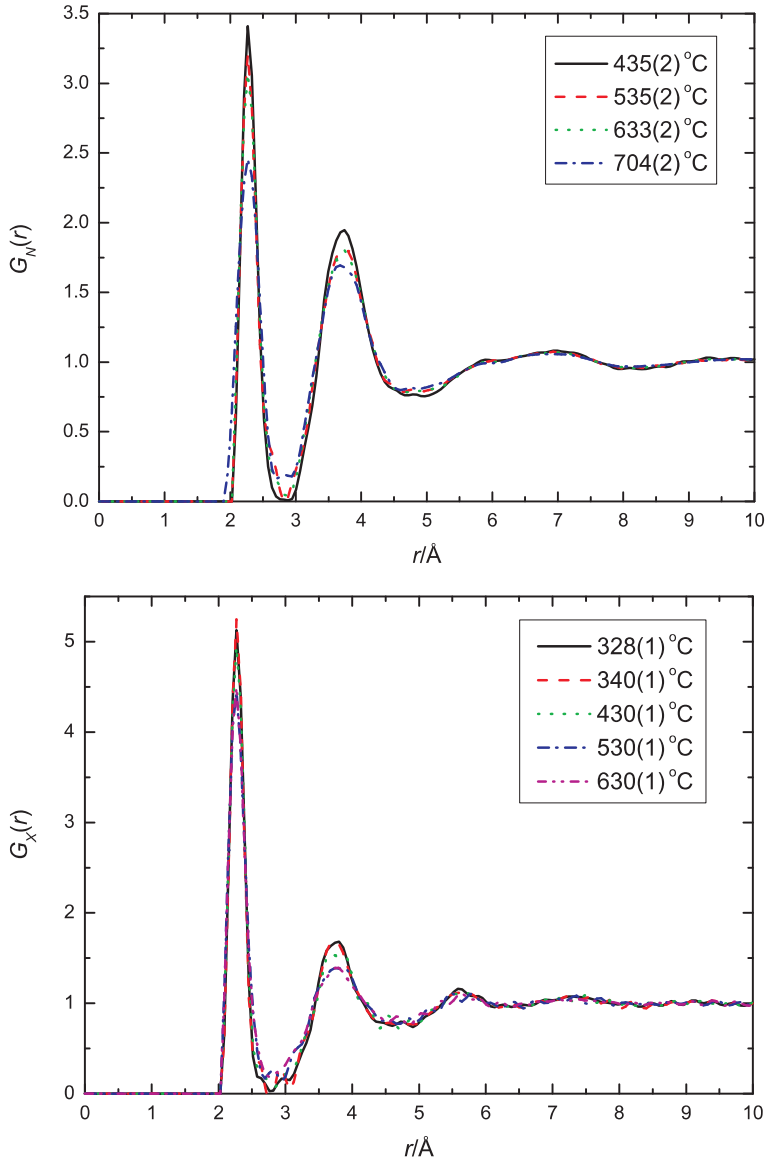

Figure 6.26: The $G_N(r)$ functions for liquid $ZnCl_2$ at 435(2), 535(2), 633(2) and 704(2) °C, and the $G_X(r)$ functions for liquid $ZnCl_2$ at 328(1), 340(1), 430(1), 530(1) and 630(1) °C.

It is interesting that the Zn-Cl coordination numbers obtained from neutron and x-ray diffraction decrease as the temperature increases which agrees with the ND results obtained by [181] and with the model proposed by Yannopoulos et al. [36] based on Raman spectroscopy. According to the model in reference [36], high temperatures promote edge-sharing connectivity between the $ZnCl_4$ tetrahedra which lowers the average Zn-Cl coordination number as the structural units at the ends of each edge-sharing clusters have an average Zn-Cl coordination number of three, see figure 6.1.

If the connectivity between the tetrahedra changes from corner-sharing to edge-sharing the Zn-Zn nearest neighbour distance should become smaller. In fact, if we assume that the tetrahedral unit is regular the maximum Zn-Zn nearest neighbour distance for edge-sharing connectivity is 2.59 Å which is equal to twice the length h shown in figure 6.27. From figure 6.26, the increased thermal motion with increasing temperature reduces the intensity and broadens every peak in the $G_N(r)$ and $G_X(r)$ functions. The effect from thermal motion is similar for the neutron and x-ray results except for a small change in the low r cutoff for the second peak. For $G_N(r)$ the cutoff value is approximately the same for all measured temperatures whereas the cutoff value for $G_X(r)$ changes from $\approx$ 3.19(6) Å for the measurements made at 328(1), 340(1) and 430(1) °C to $\approx$ 2.95(6) Å for the measurements at made 530(1) and 630(1) °C. The fact that the change in the cutoff value can only be observed in $G_X(r)$ suggests that this change is due to the Zn-Zn correlations since these give only a very small contribution to $G_N(r)$ (see figure 6.23) but a much larger contribution to $G_X(r)$ (see figure 6.24).

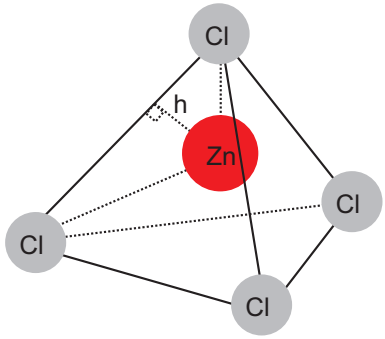

Figure 6.27: $ZnCl_4$ tetrahedral unit.

Although the change in the low r cutoff value in the second peak of $G_X(r)$ implies a promotion of smaller Zn-Zn distances, the cutoff value of around 2.95(6) Å is larger than the maximum value of 2.59 Å expected for regular edge-sharing tetrahedra. Therefore, if the change in the low r cutoff value gives evidence for edge-sharing connectivity a distortion of the $ZnCl_4$ tetrahedral units is required. It should be noted that there is no observed change in the average Zn-Cl and Cl-Cl distances. However, it is possible that small changes occur which cannot be observed within the resolution of the employed instruments.

6.7 Conclusions

The structure of glassy and liquid $ZnCl_2$ was investigated by using ND and XRD. The experiments were performed at room temperature, 328(1), 340(1), $\simeq$ 430, $\simeq$ 530, $\simeq$ 630 and 704(2) °C. From the results, the ratio between the Zn-Cl and Cl-Cl bond distances of 1.64(2) and the average Zn-Cl coordination number of around 4 suggest that the local structural motif in the glass and in the liquid at every measured temperature comprises well defined $ZnCl_4$ tetrahedra.

With regards to the temperature dependent behaviour of the total structure factors, both $F(q)$ and $S_X(q)$ are broadened as the temperature increases as a result of increased thermal motion. The FSDP remains intact with increasing temperature up to near the boiling point and only a small shift of the FSDP towards lower q can be observed. The existence of the FSDP throughout this temperature range indicates the persistence of a network structure and the peak shift suggests a longer periodicity associated with the intermediate range order. This behaviour is different from covalently bonded network liquids such as $GeSe_2$ [208] where the network structure collapses at high temperature. The persistence of a network structure in liquid $ZnCl_2$ could be due to the ionic nature of the melt.

Small changes in the total pair distribution functions as a function of temperature were observed. Both $G_N(r)$ and $G_X(r)$ show a decrease in the sharpness and intensity of the first and second peaks as the temperature increases as shown in figure 6.26. The coordination number also decreases as the temperature increases

which supports the model proposed by Yannopoulos et al. [36] which states that an increase of temperature promotes edge sharing connections between $ZnCl_4$ tetrahedral units and results in a decrease of the average Zn-Cl coordination number. The smaller low r cutoff value for the second peak of the $G_X(r)$ function with increasing temperature could be used as evidence for edge-sharing connectivity provided that the $ZnCl_4$ tetrahedral units are distorted.

Future work on the $ZnCl_2$ system includes the construction of a suitable model for the network structure. By combining ND and XRD results using the method of RMC modelling [39], additional structural information could be extracted, such as whether the connectivity between the $ZnCl_4$ tetrahedral units changes as a function of temperature and the corresponding difference in the intermediate range order of the glass and liquid.

Chapter 7

$ZnCl_2$ under Extreme Conditions: Part I

7.1 Introduction

Liquid state polyamorphism [20, 21] refers to the existence of two or more liquid phases, differentiated by density and entropy, with a first order liquid-liquid (L-L) phase transition between them. Computer simulations predict the existence of polyamorphism in many liquids such as silicon, carbon, silica and water [209, 210, 211, 212, 213]. Also, there is some indirect experimental evidence in support of a first order transition, such as an abrupt change in the electrical conductivity at different pressures for liquid S and Se, which might be associated with an abrupt change in the density [20]. Direct evidence for polyamorphism has also been reported for liquid P and $(Y_2O_3)_{0.2}(Al_2O_3)_{0.8}$ [214, 215], although later experiments suggest that the transition in liquid P is more likely to be a fluid-liquid transition [216] and in the case of liquid $(Y_2O_3)_{0.2}(Al_2O_3)_{0.8}$ the transition could not be reproduced [217]. Despite the absence of indisputable direct experimental evidence for a first order L-L phase transition, some materials are promising candidates [20] and among them is liquid $ZnCl_2$.

There is evidence of low density and high density phases of liquid $ZnCl_2$ from XRD experiments [182]. The low density phase corresponds to a tetrahedral network

in the pressure range below 1.8 GPa, the shaded area in figure 7.1, and the high density phase above 3 GPa has, as its signature, the absence of an FSDP in the x-ray total structure factor. Moreover, the melting curve of $ZnCl_2$, shown by the solid line in figure 7.1, shows a smaller gradient beyond 3 GPa, marked by a vertical arrow. Following the Clapeyron equation,

$$\frac{dP}{dT} = \frac{\Delta H}{T\Delta V}, \tag{7.1}$$

where dP/dT is the slope of the coexistence curve between two phases and ΔH and ΔV are the change in enthalpy and volume due to phase transformation, respectively [204]. The observed decrease in the slope dT/dP in figure 7.1, could therefore result from a lower ΔV value corresponding to a rapid densification of the melt [182]. In the region between 1.8 and 3 GPa there is a triple point between the crystalline phases where Zn is either 4-fold or 6-fold coordinated and the liquid [182, 218], shown by the open circle in figure 7.1. It is possible that a L-L phase transition could be observed in this region mimicking the change in the crystalline phases. An MD simulation also predicts a coexistence line between low density (4-fold coordinated Zn) and high density (6-fold coordinated Zn) glassy $ZnCl_2$ between 0 and 1 GPa under the melting temperature [192] which could suggest the same behaviour for the liquid state.

The purpose of the experiments presented in this and the next chapter is to observe a L-L phase transition in $ZnCl_2$ by attempting to melt crystalline $ZnCl_2$ phases in which Zn is either 4-fold or 6-fold coordinated by Cl. If the liquids correspond to 4-fold and 6-fold coordinated Zn then there will be a transition in the liquid between these coordination environments. The EXAFS method at the Zn K edge is used since the results should be sensitive to the nearest neighbour coordination environment of Zn in the melts. The coordination number is reflected in the Zn-Cl nearest neighbour distance which can be accurately probed using EXAFS.

At ambient pressure, earlier EXAFS experiments at the Zn K edge of $ZnCl_2$ reported the nearest neighbour Zn-Cl atomic distance for the 4-fold coordinated structure to be 2.332 [219] or 2.299(4) Å [183] for the glass and 2.31(1) [184] or 2.298(4) Å [183] for the liquid at 340 °C and 387(10) °C, respectively (mp = 290 °C [42]). The pressure dependent structural behaviour of crystalline $ZnCl_2$ at room

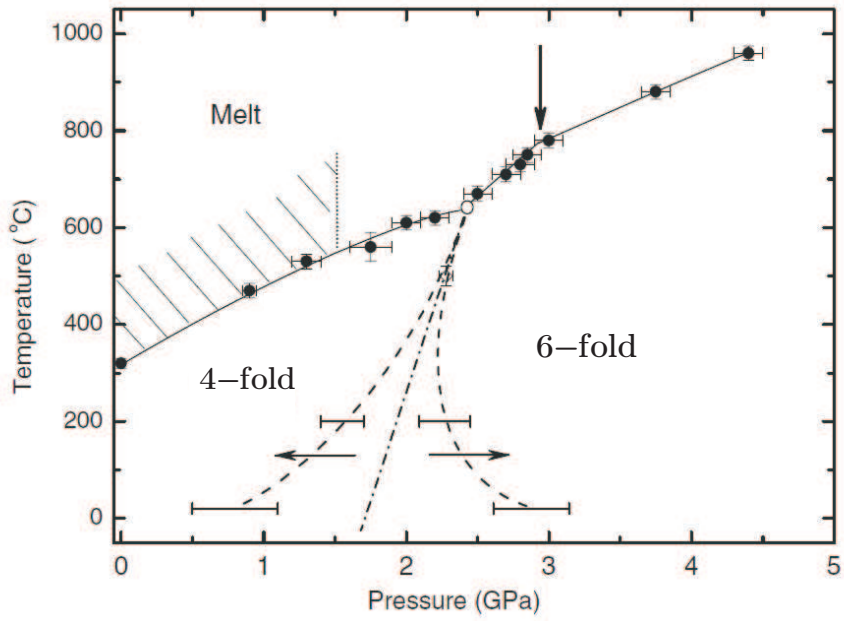

Figure 7.1: Phase diagram for $ZnCl_2$ [182]. The solid line and closed circles give the melting curve measured as a function of pressure. The dashed lines are the kinetic lines for direct and reverse transitions between the 4- and 6-fold crystalline phases with the horizontal bars corresponding to experimental intervals for the transitions. The dash-dotted line gives an estimate of the boundary between the 4- and 6-fold crystalline phases. The open circle gives a triple point between the 4- and 6-fold crystalline phases and the liquid. The shaded area corresponds to a low density liquid phase. The vertical arrow marks the starting pressure for the high density liquid phase.

temperature has also been investigated by using EXAFS spectroscopy [183, 220]. It was found that at low pressures Zn is 4-fold coordinated with a nearest neighbour Zn-Cl distance of 2.300(3) Å. As the pressure is increased, the Zn-Cl distance first decreased up to a pressure of 2.0(1)-3.6(1) GPa where a 4-fold to 6-fold phase transition was observed. At 4 GPa, after the phase transition, Zn was 6-fold coordinated with a Zn-Cl distance of 2.446(4) Å.

In this chapter we present a study of the structure of glassy and crystalline $ZnCl_2$ at room temperature and several pressures in the range from ambient to 4.7(1) GPa by using EXAFS spectroscopy at the Zn K edge. A study of the liquid structure will be presented in the next chapter. This chapter consists of seven sections. In section 7.2, the background theory for x-ray absorption spectroscopy is reviewed and in section 7.3 the experimental detail is described. In section 7.4, the cross calibration method used to determine the temperature and pressure conditions

is described along with the method used to extract the EXAFS signals from the measured spectra. In section 7.5, the XANES spectra measured under different thermodynamic conditions are presented in order to investigate a reaction between the sample and BN which was used as a matrix material. EXAFS spectra for those measurements which were unaffected by the reaction are also presented. In section 7.6, the structural models used in the EXAFS data analysis are described and the results from the refinement procedure are discussed. The work is then concluded in section 7.7.

7.2 Background Theory

In this section the main theory required for analysing x-ray absorption spectroscopy (XAS) data is summarised. The spectrum measured near the absorption edge of a target element can be divided into two main parts, the XANES and the EXAFS regions. The XANES spectra are sensitive to the electronic structure of the target element and can be used to fingerprint that structure [52]. The EXAFS spectra $\chi(k)$ can be analysed quantitatively and structural information, such as atomic distances and coordination numbers, can be obtained [50].

For crystalline systems or glasses with an ordered local structure, $\chi(k)$ can be calculated from a model using equation 2.64

$$\chi(k) = \sum_{j=1}^{\text{all paths}} S_0^2 N_j \frac{F_j^{eff}(k)}{kR_{0,j}^2} e^{-2(R_{0,j}-\Delta)/\lambda} e^{-2k^2\sigma_j^2} \sin[2kR_{0,j} + \delta_j^{eff}(k)] \qquad (7.2)$$

where S_0^2 is the amplitude reduction factor, $F_j^{eff}(k)$ is the backscattering amplitude, $R_{0,j}$ is the nominal half path length, $R_{0,j} - \Delta$ is an effective half path length, N_j, σ_j^2 and δ_j^{eff} are the number of degeneracies, the EXAFS Debye-Waller factor and the signal phase shift for scattering path j, respectively, and λ is the photoelectron mean free path.

By taking into account some degree of structural disorder i.e. a non-Gaussian form for the pair distribution functions, equation 7.2 can be re-written after employ-

ing a cumulant expansion, as described in section 2.3.6,

$$\chi(k) = \mathrm{Im}\left\{ \sum_{j=1}^{\text{all paths}} \frac{S_0^2 N_j F_j^{eff}(k)}{k(R_{0,j}+\Delta R_j)^2} \exp\{-2k^2\sigma_j^2 + \frac{2}{3}k^4 C_{4,j}\} \right. \\ \left. \exp\{i(2k(R_{0,j}+\Delta R_j) - \frac{4k\sigma_j^2}{R_{0,j}} - \frac{4}{3}k^3 C_{3,j} + \delta_j^{eff}(k))\} \right\} \quad (7.3)$$

where ΔR_j is the difference between the actual and nominal half path length, while $C_{3,j}$ and $C_{4,j}$ are the third and forth order cumulants, respectively.

In EXAFS data analysis, the $\tilde{\chi}(R)$ function obtained by Fourier transforming the measured $k^\omega\chi(k)$ function, where $\omega = 0$, 1, 2, or 3 determines the k weighting of $\chi(k)$, is used to refine the $\tilde{\chi}(R)$ function calculated from a model by fitting S_0^2 and the variables σ_j^2, ΔR_j and N_j for each scattering path j. The value of E_0 can also be refined using the parameter ΔE_0 such that k is given by equation 3.35,

$$k = \sqrt{\frac{2m_e(E-(E_0+\Delta E_0))}{\hbar^2}}.$$

The refinement minimises the statistical parameter χ^2,

$$\chi^2 = \frac{N_{idp}}{N_{data}} \sum_{i=1}^{N_{data}} \left| \frac{\tilde{\chi}(R_i)_{data} - \tilde{\chi}(R_i)_{model}}{\epsilon_i} \right|^2, \quad (7.4)$$

where N_{data} is the number of data points in the R window range, N_{idp} is the number of independent data points in this range, and ϵ_i is the measurement uncertainty. In this chapter, the same experimental data were used to refine several models which have different numbers of variables. χ_ν^2 was, therefore, used to compare the goodness of the fits where

$$\chi_\nu^2 = \frac{\chi^2}{N_{idp} - N_{var}} \quad (7.5)$$

and $N_{var} < N_{idp}$ is the number of variables in the fit. As χ_ν^2 depends on an estimation of the measurement uncertainty ϵ_i, the $\mathcal{R}$-factor was also calculated for each fit where

$$\mathcal{R} = \frac{\sum_{i=1}^{N_{data}} |\tilde{\chi}(R_i)_{data} - \tilde{\chi}(R_i)_{model}|^2}{\sum_{i=1}^{N_{data}} |\tilde{\chi}(R_i)_{data}|^2}. \quad (7.6)$$

7.3 Experiment

The XAS spectra were measured in transmission mode on beamline BM29 [64, 79] at the ESRF. The spectra in the energy range of the Zn K edge, from 9.559 -

11.185 keV (Zn K edge = 9.659 keV [161]), were collected using ionization chambers, see section 3.4.4. The ionization chambers I_0, I_1 and I_2 were filled with a mixture of Ar and He gas to the operating pressure of the chambers of 2 bar with 0.1, 0.32 and 0.62 bar of Ar to achieve a 30%, 70% and 90% efficiency, respectively. In addition, XRD data for the sample were measured for an incident wavelength of 1.283 Å by using a MAR345 image plate detector placed near to the sample position, see figure 7.2.

The sample consisted of a mixture of finely ground anhydrous glassy beads of 99.999% purity $ZnCl_2$ commercially available from Sigma-Aldrich and BN powder. Due to the hygroscopic nature of $ZnCl_2$ the samples were prepared in a high purity Ar-filled glove box at the ESRF. A Paris-Edinburgh press [16] was employed to apply pressures up to about 5 GPa to the sample. The sample was held in a 7 mm diameter boron-epoxy gasket. A cylindrical piece of graphite and graphite disks were placed inside the gasket to be used as a furnace which could heat the sample up to $\approx 800\,^{\circ}$C. Mo disks and stainless steel rings were used as electrodes for applying current to the furnace. MgO powder pressed into a disk was used as an insulating infill. All of the components inside the gasket are shown in figure 7.3.

As shown in figure 7.3, a Au foil was placed between the furnace and the gasket. Au and BN were used as the temperature and pressure markers. The diffraction patterns of Au and BN were measured at a wavelength of 0.827 Å for the same thermodynamic conditions as the XAS spectra. The thermodynamic conditions during the XAS measurements were then estimated from the diffraction patterns of Au and BN by using the cross calibration method described in section 7.4.

The sample diameter was 1.5 mm which is much greater than the absorption length of $ZnCl_2$ which is 28 μm, calculated using equation 3.4. Therefore, the sample comprised a mixture of $ZnCl_2$ and BN. The mass ratio between $ZnCl_2$ and BN can be calculated by first considering the mixture to comprise two layers, a BN layer with a thickness of t_{BN} and a $ZnCl_2$ layer with a thickness of $t_{\mathrm{ZnCl_2}}$ such that the thickness of a sample $t_{\mathrm{sample}} = t_{\mathrm{BN}} + t_{\mathrm{ZnCl_2}}$. If M, ρ and A denote the mass, mass density and the surface area of the sample, respectively, then the mass ratio can be

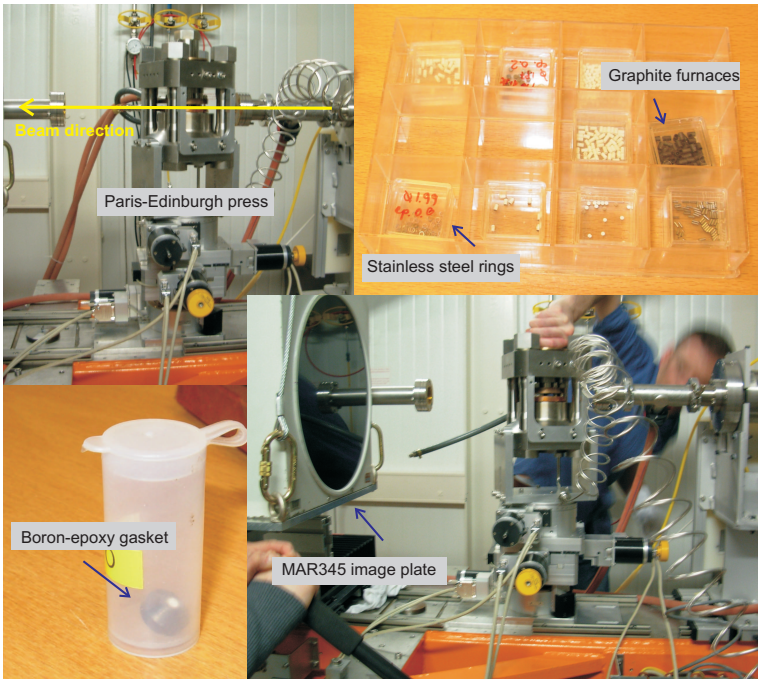

Figure 7.2: Clockwise from top left, the Paris-Edinburgh press mounted on the BM29 beamline, stainless steel rings and graphite furnaces used in the pressure cell, the MAR345 image plate detector mounted near to the sample position and a boron-epoxy gasket.

determined from

$$\begin{aligned} \frac{M_{\mathrm{BN}}}{M_{\mathrm{ZnCl_2}}} &= \frac{\rho_{\mathrm{BN}} A t_{\mathrm{BN}}}{\rho_{\mathrm{ZnCl_2}} A t_{\mathrm{ZnCl_2}}} \\ &= \frac{\rho_{\mathrm{BN}}}{\rho_{\mathrm{ZnCl_2}}} \left(\frac{t_{\mathrm{sample}} - t_{\mathrm{ZnCl_2}}}{t_{\mathrm{ZnCl_2}}} \right) \\ &= \frac{\rho_{\mathrm{BN}}}{\rho_{\mathrm{ZnCl_2}}} \left(\frac{t_{\mathrm{sample}}}{t_{\mathrm{ZnCl}}} - 1 \right), \end{aligned} \tag{7.7}$$

where t_{ZnCl} is taken to be the absorbtion length of $ZnCl_2$. The $ZnCl_2$:BN mass ratio calculated from equation 7.7 is 1:40.

The first sample (sample A) was prepared by mixing ground $ZnCl_2$ and BN powder with a $ZnCl_2$:BN mass ratio of 1:40. The sample was made into a pellet and put inside the boron-epoxy gasket along with the graphite furnace, Mo disks, MgO disks and Au foil as shown in figure 7.3. An initial analysis of the data taken for sample A indicated that crystallisation of $ZnCl_2$ takes place when pressure is applied to press the sample into a pellet and that a reaction occurs between $ZnCl_2$ and BN at high temperature.

In order to test the initial results, five additional samples were prepared and

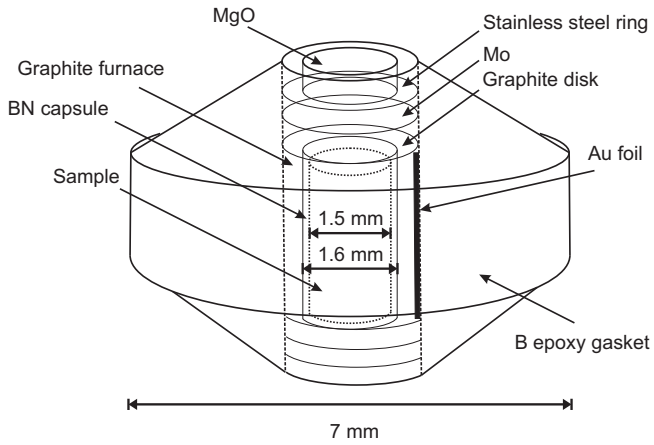

Figure 7.3: The furnace assembly used to hold the sample. All of the components are fitted in the cylindrical hole inside the boron-epoxy gasket as shown.

were labeled as B - F, with compositions given in table 7.1. Samples B and C were ground powders but were not pressed into pellets while sample D was pressed into a pellet. Samples B - D were each placed into a glass capillary for the XAS measurements which were made with temperature increasing from ambient to about the melting point. These samples were heated using a heat gun and the temperature of the samples were read from a thermometer placed next to the glass capillary with an expected uncertainty of $\pm$ 20°C. After heating, the samples were recovered to room temperature and this cycle was repeated several times. Samples E and F were each made into a pellet and were placed into a pressure cell. The measurements for these samples were made under high temperature and high pressure conditions.

The edge step $\Delta\mu_0$ for sample A was about 0.5 instead of the expected value of 1 which could be due to non-uniformity of the mixed powder [81] or due to the particle size of the sample [221]. Samples B, D, E and F were, therefore, prepared with a $ZnCl_2$:BN mass ratio of 1:15 which gave an edge step of ≈ 1. The $ZnCl_2$:BN mass ratio for all of the samples and the type of container used for the XAS measurements are summarised in table 7.1. The thermodynamic histories for the high temperature and high pressure measurements are shown in figure 7.4.

Sample	$ZnCl_2$:BN ratio	Press-pelleted	Container
A	1:40	✓	boron-epoxy gasket
B	1:15	×	glass capillary
C	1:0	×	glass capillary
D	1:15	✓	glass capillary
E	1:15	✓	boron-epoxy gasket
F	1:15	✓	boron-epoxy gasket

Table 7.1: The $ZnCl_2$ to BN mass ratio for each sample and the container used for the XAS measurements.

7.4 Data Treatment

The temperature and pressure conditions of the samples placed in pressure cells were determined from the measured diffraction patterns for Au and BN. The lattice constants found from the diffraction patterns were used to calculate the unit cell volume, namely $V = a^3$ for Au (a cubic structure) and $V = a^2 c \sin 60^\circ$ for BN (an hexagonal structure), where a and c are lattice constants. The temperature and pressure points corresponding to each volume were calculated using a P-V-T equation of state (EOS). For solids a P-V-T EOS is in general written as

$$P(V,T) = P(V,0) + P_{th}(V,T), \tag{7.8}$$

where $P(V,T)$ is the pressure at volume V and absolute temperature T, $P(V,0)$ is the pressure at $T = 0$ K and $P_{th}(V,T)$ is the thermal pressure [222]. The pressure at high temperature and pressure conditions is related to the pressure at ambient conditions by the relation

$$P(V,T) = P(V_a,300) + \Delta P(V_a \rightarrow V,300) + P_{th}(V,300 \rightarrow T), \tag{7.9}$$

where V_a is the volume under ambient conditions, $\Delta P(V_a \rightarrow V,300)$ is the change in pressure when the volume changes from V_a to V at 300 K and $P_{th}(V,300 \rightarrow T)$ is the pressure change when the temperature increases from 300 K to T at constant volume.

For Au, the term $\Delta P(V_a \rightarrow V,300)$ can be described using the third order

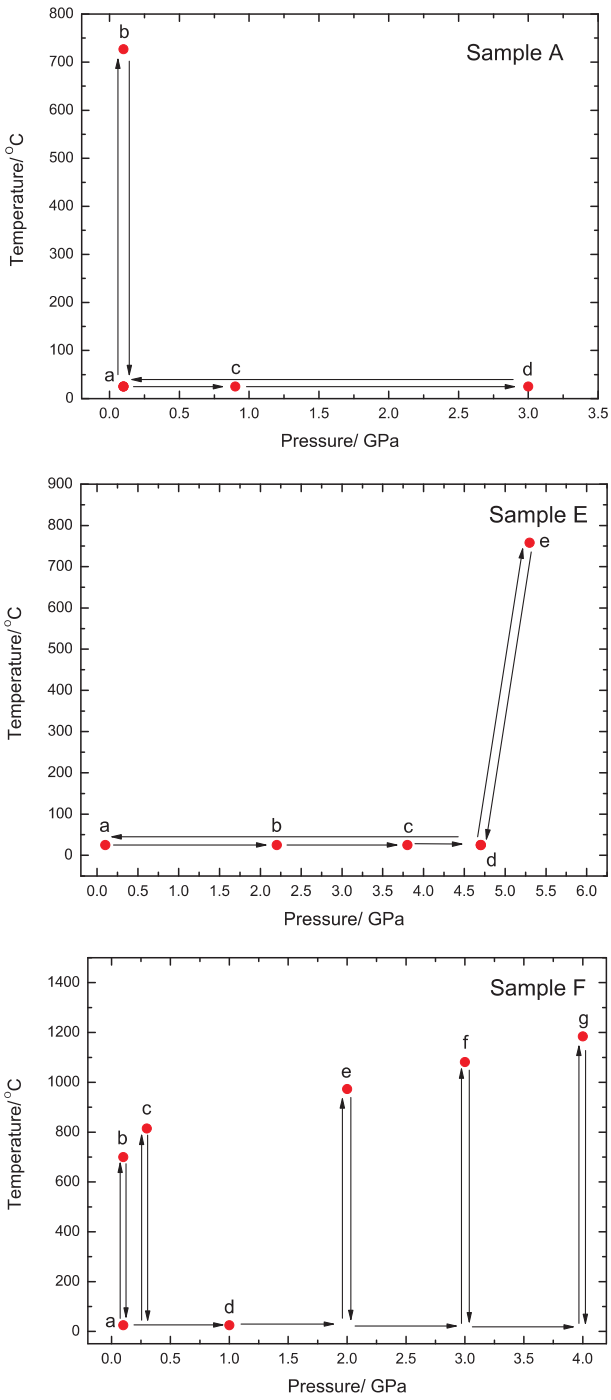

Figure 7.4: Thermodynamic histories for samples A, E and F. The measurements were made in the order from a to d, a to e and a to g for samples A, E and F, respectively. The temperature and pressure conditions of the EXAFS measurements, shown by solid circles, were determined from the cross calibration method using the diffraction patterns for Au and BN, except for the measurements made at room temperature where the pressure was obtained from the diffraction pattern of BN alone.

Birch-Murnaghan equation [223],

$$\Delta P(V_a \rightarrow V, 300) = \frac{3}{2} K_{Ta} \left[\left(\frac{V_a}{V} \right)^{\frac{7}{3}} - \left(\frac{V_a}{V} \right)^{\frac{5}{3}} \right] \left\{ 1 + \frac{3}{4}(K'_{Ta} - 4) \left[\left(\frac{V_a}{V} \right)^{\frac{2}{3}} - 1 \right] \right\}, \tag{7.10}$$

where $K_{Ta} = 167(11)$ GPa is the isothermal bulk modulus under ambient conditions and $K'_{Ta} = \left(\frac{\partial K_{Ta}}{\partial P}\right)_T = 5.5(8)$ [224]. For the $P_{th}(V, 300 \rightarrow T)$ term, if the temperature is higher than the Debye temperature which is 165 K for Au [225], it has been shown that $P_{th}(V, 300 \rightarrow T)$ follows the relation

$$P_{th}(V, 300 \rightarrow T) = \left[\alpha K_T(V_a, T) + \left(\frac{\partial K_T}{\partial T} \right)_V \ln \left(\frac{V_a}{V} \right) \right] (T - 300), \tag{7.11}$$

where $\alpha = \frac{1}{V}\left(\frac{\partial V}{\partial T}\right)_P$ is the volume thermal expansion coefficient, $\alpha K_T(V_a, T) = 7.14 \times 10^{-3}$ GPa/K, $\left(\frac{\partial K_T}{\partial T}\right)_V = -11.5 \times 10^{-3}$ GPa/K and $V_a = 67.85$ Å^3 [223, 224].

For BN, the EOS is described using the modified Birch-Murnaghan equation [226],

$$P(f, T) = 3K_{Ta} f (1 + 2f)^{\frac{5}{2}} \left[1 - \frac{3}{2}(4 - K'_{Ta}) f \right], \tag{7.12}$$

where

$$f = \frac{1}{2} \left[\left(\frac{V_0(T)}{V} \right)^{\frac{2}{3}} - 1 \right], \tag{7.13}$$

$V_0(T) = V_a e^{\int_{T_0}^{T} \alpha_0(T) dT}$, $\alpha_0(T) = 35.259 \times 10^{-6} + 0.2095 \times 10^{-8} T + 1.236 \times 10^{-11} T^2 - 7.1994 \times 10^{-15} T^3$ K^{-1} is the thermal expansion coefficient at zero pressure, $K_{Ta} = 27.6 - 0.81 \times 10^{-2}(T - T_0)$ GPa, $K'_{Ta} = 10.5 + 0.16 \times 10^{-2}(T - T_0)$, $T_0 = 298$ K and $V_a = 36.16$ Å^3 .

From equations 7.9 to 7.13, a series of temperature and pressure points corresponding to a given volume can be calculated for Au and BN. The temperature and pressure condition of a measurement is then determined from the intersection between the lines corresponding to the EOS for Au and BN. An example of this cross-calibration method is shown in figure 7.5. The errors on the temperature and pressure obtained from this method are mainly due to the uncertainty in measurement of the lattice constants and are expected to be less than ±50 K [214] and ±0.1 GPa [226] for temperature and pressure, respectively. For the measurements made at room temperature, the pressure was determined from the EOS of BN. It should be noted that in some cases where the diffraction patterns of Au or BN could

not be measured, the temperature and pressure were estimated from the electric current supplied to the furnace and the oil pressure applied to the press, respectively.

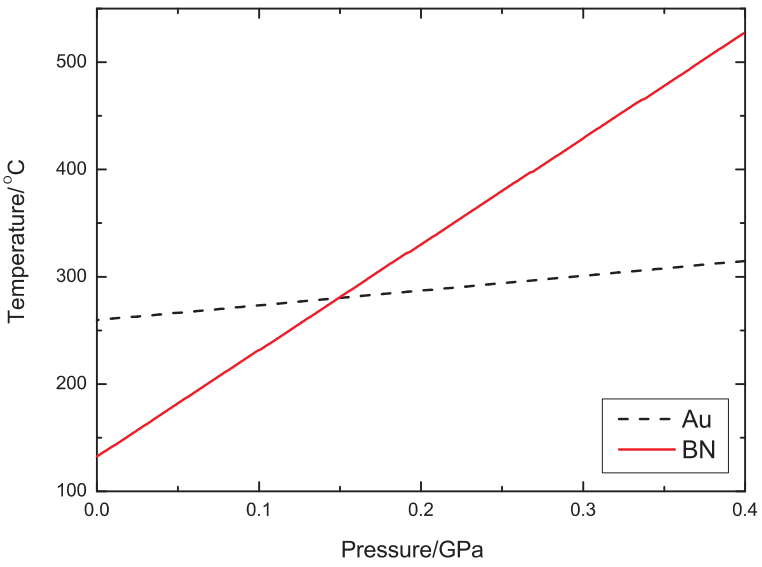

Figure 7.5: The dashed line gives the P-T relation for Au corresponding to a measured unit cell volume of 68.56 Å^3. The solid line gives the P-T relation for BN corresponding to a measured unit cell volume of 36.30 Å^3. The temperature and pressure condition of the sample is given by the intersection between the two lines.

The data points corresponding to glitches in the absorption spectra were removed and all of the scans were aligned. Due to a reaction between $ZnCl_2$ and BN at high temperature, see section 7.5.1 for detail, the only $\chi(k)$ functions that were analysed were extracted from the spectra measured under i) ambient conditions for sample A which contained crystalline $ZnCl_2$ where crystallisation resulted from the pressure applied when the sample was pressed into a pellet, ii) ambient conditions for sample C which contained only glassy $ZnCl_2$ and iii) room temperature for sample E which contained crystalline $ZnCl_2$ at pressures of 2.2(1), 3.8(1) and 4.7(1) GPa. The final absorption spectra used in the data analysis were the averages of 8 scans for sample A, 1 scan for sample C, or 1, 2 and 5 scans for sample E measured at pressures of 2.2(1), 3.8(1) and 4.7(1) GPa, respectively.

The $\chi(k)$ were extracted from the absorption spectra by using equation 2.49. The background functions were determined using the AUTOBK algorithm in ATHENA [62], fitted to the data from the energy edge to the last data point with R_{bkg} =

1.0 Å for glassy sample C, R_{bkg} = 1.1 Å for crystalline samples A and E measured at ambient pressure and at 2.2(1) GPa, respectively, and R_{bkg} = 1.2 Å for crystalline sample E measured at 3.8(1) and 4.7(1) GPa. The absorption spectra and the background fits are shown in figure 7.6. The usable k range of the extracted $\chi(k)$ functions for glassy sample C, which was held in a glass capillary, was 2.4 to 13 $Å^{-1}$ and for crystalline samples A and E, which were held in the pressure cells, it was 2.4 to 11 $Å^{-1}$.

The k range on the high k side of the absorption edge for samples which were held in the high pressure cell was limited by contamination due to the presence of tungsten in the cell. Tungsten is an element found in the drill used to make the cylindrical hole in the boron-epoxy gasket. The energy of the tungsten L_{III} edge is 10.207 keV [161] which corresponds to $k \approx 12$ $Å^{-1}$ for measurements made at the Zn K edge. Figure 7.7 shows a small bump in the absorption spectrum corresponding to absorption by the tungsten L_{III} edge which transforms into a big glitch in k-space.

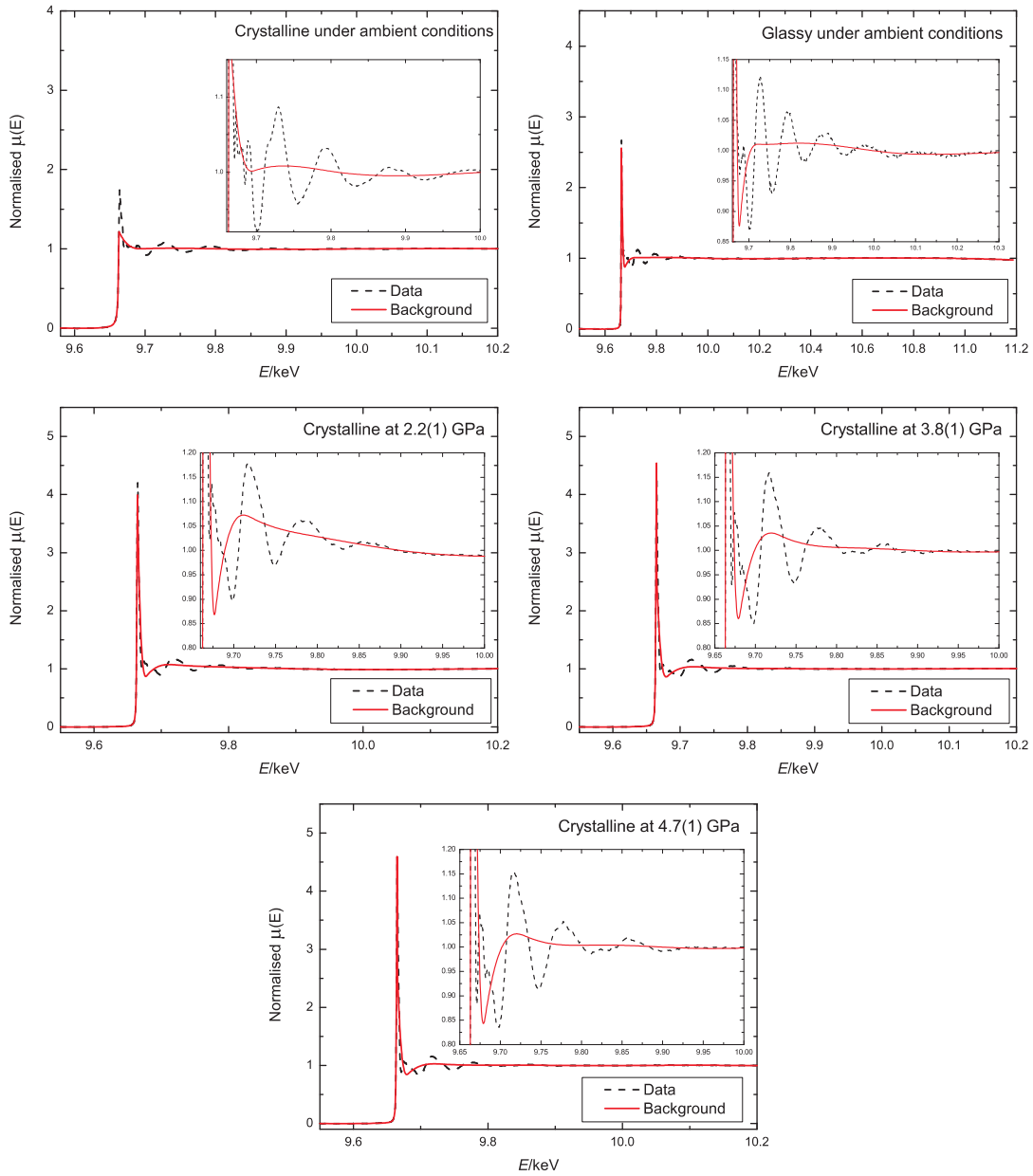

Figure 7.6: Normalised absorption spectra and the fitted background functions $\mu_0(E)$ for crystalline and glassy $ZnCl_2$ samples A and C measured under ambient conditions and for crystalline $ZnCl_2$ sample E measured at room temperature and 2.2(1), 3.8(1) or 4.7(1) GPa. The dashed lines show the measured normalised absorption spectra and the solid lines show the background functions. The insets show the region near the absorption edge energy.

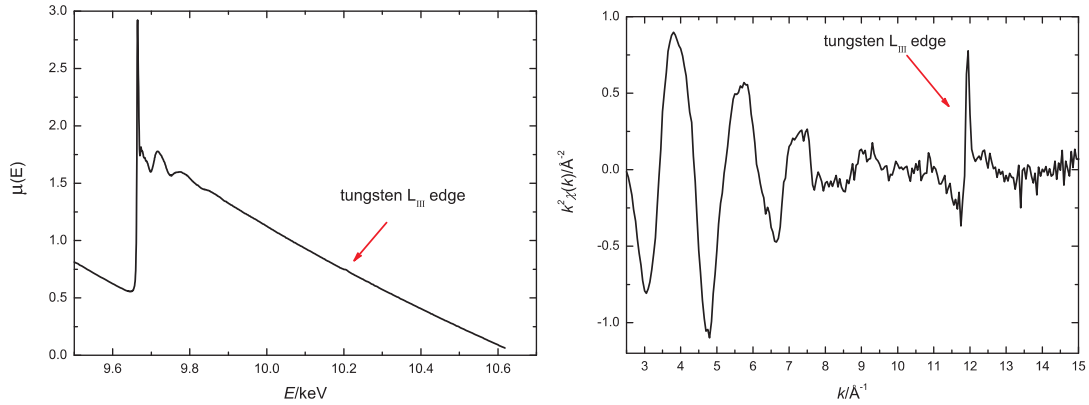

Figure 7.7: An absorption spectrum and the corresponding $k^2\chi(k)$ function for sample E measured at room temperature and 2.2(1) GPa. Arrows mark a small bump in the absorption spectrum and a glitch in the $k^2\chi(k)$ function due to absorption at the tungsten L_{III} edge.

7.5 Results

In this section, the XANES and EXAFS spectra as well as the observed melting temperature as a function of pressure were used to identify a reaction between $ZnCl_2$ and BN at high temperature. In addition, the extracted EXAFS spectra for the measurements made at room temperature, for samples in which no reaction took place, are presented both in k- and R-space.

7.5.1 Reaction between $ZnCl_2$ and BN at high temperature

Because the experiments were performed at high temperatures and pressures, the choice of matrix material is limited. BN is made from small Z elements, has a high melting point (≈3000 °C [42]) and, in general, it is chemically inert [226]. BN is, therefore, a suitable matrix material and it has previously been used as a matrix material in an EXAFS experiment on $ZnCl_2$ at high temperatures [184]. In that experiment, a reaction between BN and $ZnCl_2$ was tested by leaving a mixture of BN and $ZnCl_2$ in the molten state for one hour before recovering to room temperature and comparing the XRD patterns of the sample before and after heating. The test showed no significant difference between the two signals. However, in the present experiment, the measured XANES spectra suggested a reaction.

There are two indications that a reaction between $ZnCl_2$ and BN occurred

at high temperature. The first indication is that the initial XAS spectrum taken under ambient conditions could not be recovered. For sample A, the material was first melted and recovered to room temperature. It was then pressurised at room temperature to 3.0(1) GPa and recovered to ambient pressure. The XANES and EXAFS spectra for the starting material and the recovered samples are shown in figures 7.8 and 7.9. From figure 7.8, the XANES spectra of the recovered samples show similar features but are significantly different from the spectrum of the starting material. Similarly, in figure 7.9, the oscillations of the $k^2\chi(k)$ function and the position of the first peak in the corresponding $|\tilde{\chi}(R)|$ function for both of the recovered samples are shifted significantly from those of the starting material. Due to the relatively large amount of BN in the mixture, the $ZnCl_2$ crystal structure could not be identified by XRD. Further XANES measurements on samples C and D confirmed that only those samples made from a mixture of $ZnCl_2$ and BN have this problem. The XANES spectra for sample C, which consists only of ground $ZnCl_2$, showed identical features after several temperature cycles. As seen in figure 7.10, the XANES spectrum of the starting material was recovered when the sample was quenched after the second melting and the XANES spectrum of the crystalline sample recovered from the first melting was recovered after the third melting. For sample D, as seen in figure 7.11, the starting spectrum could not be recovered after several melting and cooling cycles.

It should be noted that although the starting material used for each sample is glassy $ZnCl_2$, the pressure applied to make pellets induces crystallisation. Samples B and D were made from the same mixture of $ZnCl_2$ and BN except that sample D was made into a pellet. The XANES spectra for both samples under ambient conditions are shown in figure 7.12. From the figure, the XANES spectrum for sample B is smooth which is characteristic of an amorphous structure whereas the XANES spectrum for sample D shows more features from 9.67 to 9.70 keV suggesting a crystalline structure. These data sets are similar to the spectra for glassy and crystalline γ-$ZnCl_2$ [227] measured at the Zn K edge in [183], see figure 7.13.

The second indication of a reaction between $ZnCl_2$ and BN is the change observed in the melting temperature when samples A and F were put into the

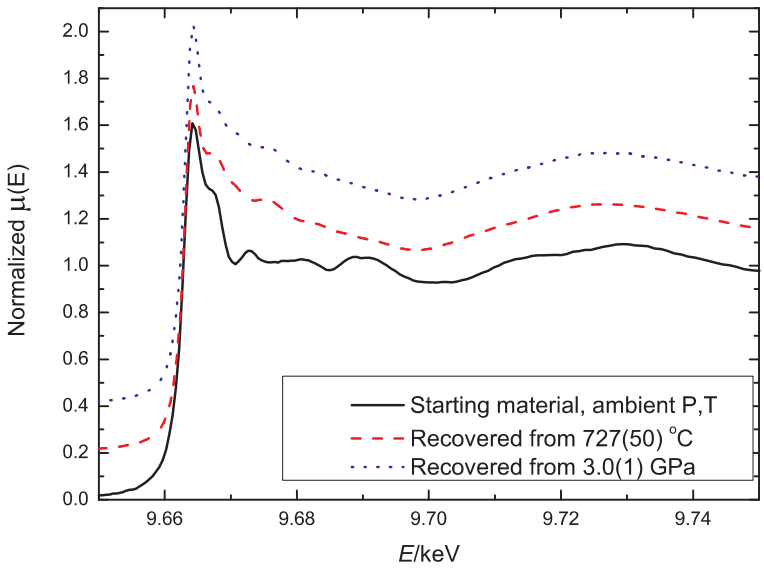

Figure 7.8: The XANES spectra of sample A taken under ambient conditions, shifted vertically for clarity of presentation. The features in the XANES spectrum of the starting material from 9.67-9.70 keV could not be recovered after the sample was melted at 727(50) °C at ambient pressure and recovered to ambient conditions or subsequently pressurised at room temperature to 3.0(1) GPa and recovered to ambient conditions.

pressure cell. When the temperature was increased at ambient pressure, the XANES spectrum of sample A did not show a signature of the molten state, similar to the liquid spectrum in figure 7.13, until the temperature was raised to ≈ 727°C (mp = 290°C [42]). For sample F, the temperature and pressure were increased and decreased to track the melting point as a function of pressure. It was found that the acquired melting temperatures were different to the values reported by Brazhkin et al. [182]. The melting point as a function of pressure from the current work and from reference [182] is shown in figure 7.14. It should be noted that in reference [182] the sample was a pellet made from pure $ZnCl_2$ fine powder and BN was only used as the sample container, such that a reaction between $ZnCl_2$ and BN was not detected.

$ZnCl_2$ has been known to intercalate into the layered structure of graphite through heating [228] or electrochemical process [229]. In the first case the reaction was observed at 400°C, which is within the temperature range of the measurements made in the current study, although the method requires $ZnCl_2$ and graphite to be heated in an atmosphere of Cl. In the present study, the hexagonal phase of

BN which has a graphite-like structure was used as a matrix material. Although the experiment was made in an atmosphere of Ar, the reaction observed at high temperature between $ZnCl_2$ and BN could be due to a small amount of intercalation.

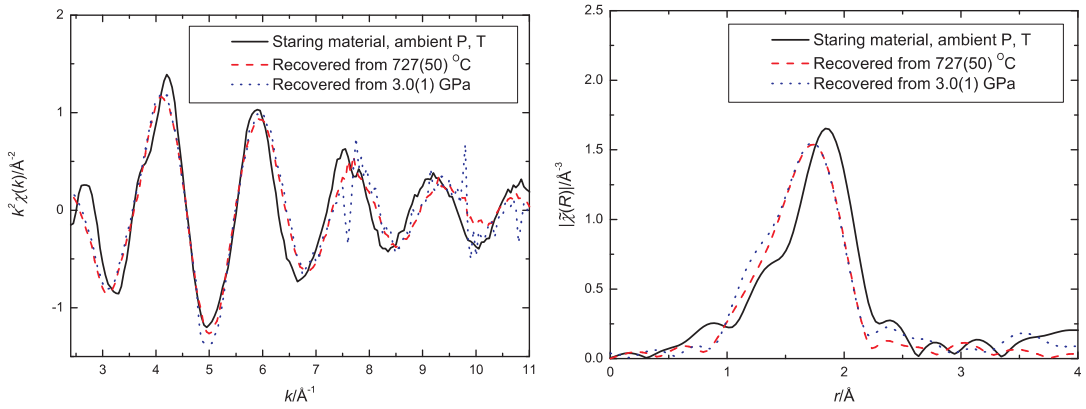

Figure 7.9: The EXAFS spectra of sample A taken under ambient conditions. The third and fourth peaks of the $k^2\chi(k)$ function and the position of the first peak in the $|\tilde{\chi}(R)|$ function of the starting material are shifted after the sample was melted at 727(50) °C at ambient pressure and recovered to ambient conditions or subsequently pressurised at room temperature to 3.0(1) GPa and recovered to ambient conditions.

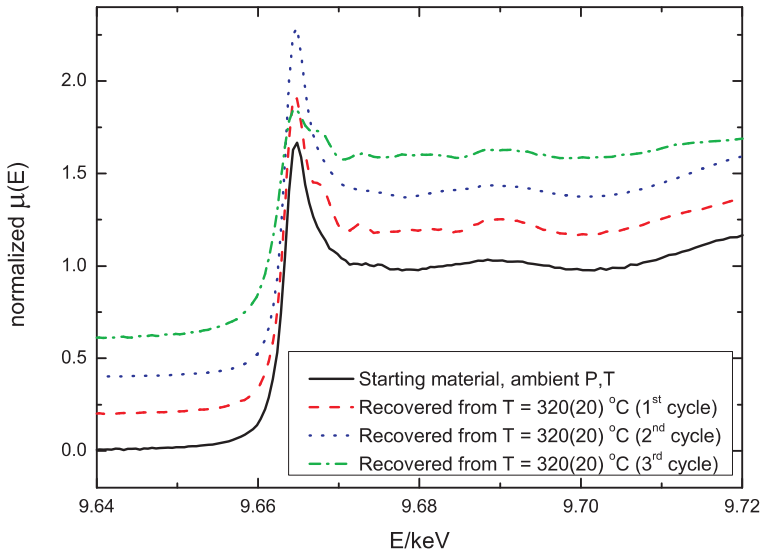

Figure 7.10: The XANES spectra for sample C taken under ambient conditions, shifted vertically for clarity of presentation. The XANES spectrum of the starting material was recovered when the sample was quenched after the second melting and the XANES spectrum of the crystalline sample recovered from the first melting was recovered after the third melting.

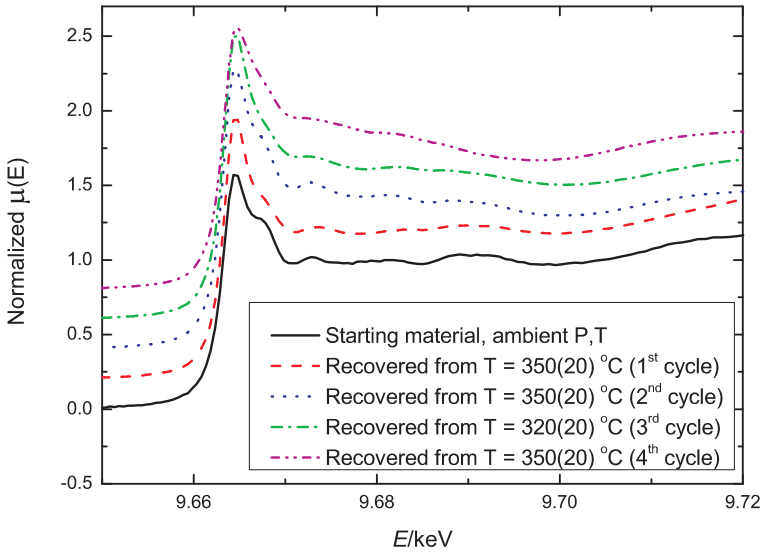

Figure 7.11: The XANES spectra for sample D taken under ambient conditions, shifted vertically for clarity of presentation. The XANES spectrum of the starting material could not be recovered after the sample was melted and cooled for several cycles.

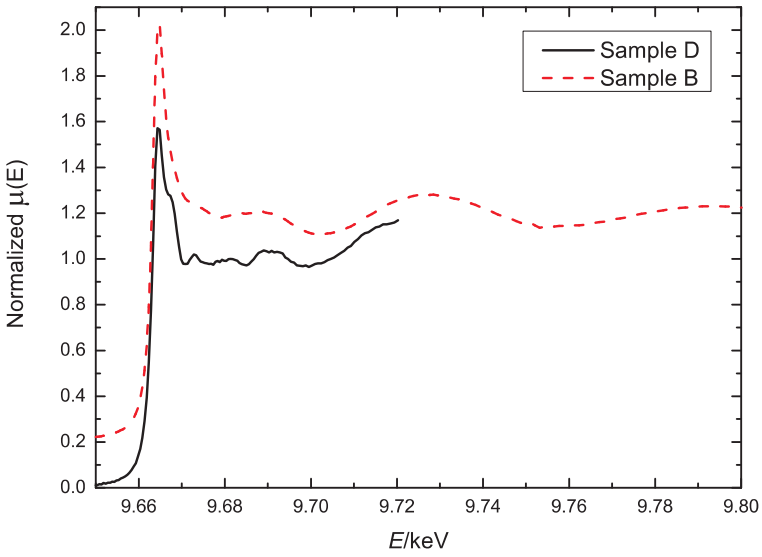

Figure 7.12: The XANES spectra for samples B and D, shifted vertically for clarity of presentation. Both samples consisted of a 1:15 mixture of $ZnCl_2$ and BN. Sample B was in the form of a fine powder contained in a glass capillary whereas sample C was in the form of a pellet and was held in a glass capillary. The features from 9.67 to 9.70 keV in the spectrum for sample D suggest that the sample is crystalline.

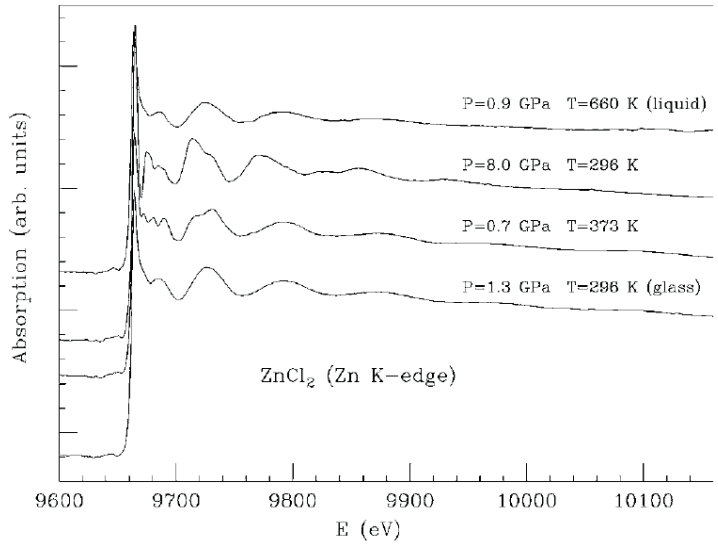

Figure 7.13: The absorption spectra for liquid and glassy $ZnCl_2$, crystalline γ-$ZnCl_2$ [227] (P = 0.7 GPa, T = 373 K) and crystalline $ZnCl_2$ with the $CdCl_2$ type structure (P = 8.0 GPa, T = 296 K) measured at the Zn K edge. The liquid and glassy phases can be distinguished from the two crystalline phases by the XANES features from 9650 to 9750 eV. The graph is taken from [183].

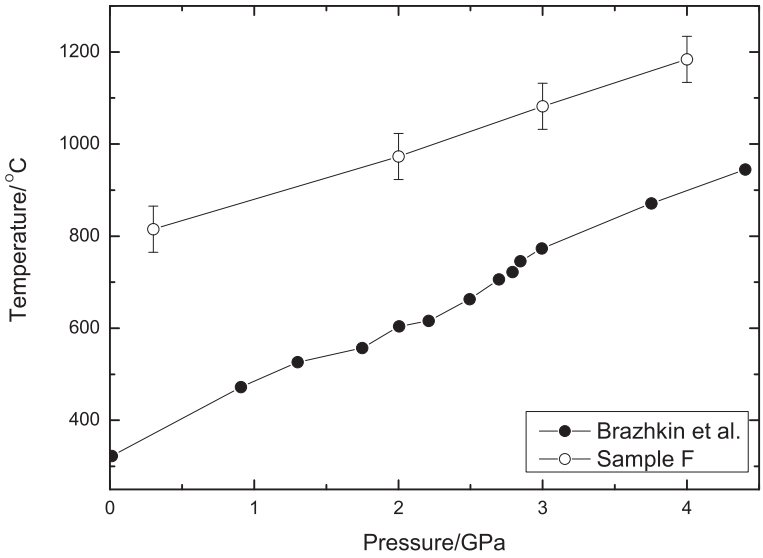

Figure 7.14: The melting curve of $ZnCl_2$ as a function of pressure obtained from the present work for sample F (open circles) compared with that reported in [182] (closed circles).

7.5.2 EXAFS signals for measurements made at room temperature

The EXAFS $k^2\chi(k)$ and corresponding $|\tilde{\chi}(R)|$ functions measured for sample A under ambient conditions and for sample E at room temperature and 2.2(1), 3.8(1) or 4.7(1) GPa are shown in figures 7.15 and 7.16. From figure 7.15, the $k^2\chi(k)$ functions for glassy and crystalline $ZnCl_2$ measured under ambient conditions have the same main oscillation frequency suggesting a similar local coordination environment for Zn. From figure 7.16, the $k^2\chi(k)$ oscillation frequency is modified as the pressure increases which reflects a change in the local coordination environment of Zn.

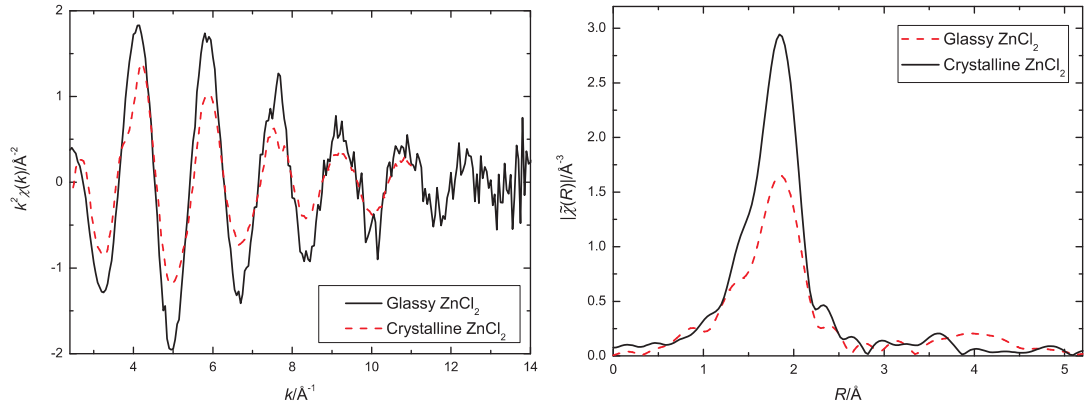

Figure 7.15: The $k^2\chi(k)$ and corresponding $|\tilde{\chi}(R)|$ function measured for glassy $ZnCl_2$ (sample C) and crystalline $ZnCl_2$ (sample A) under ambient conditions.

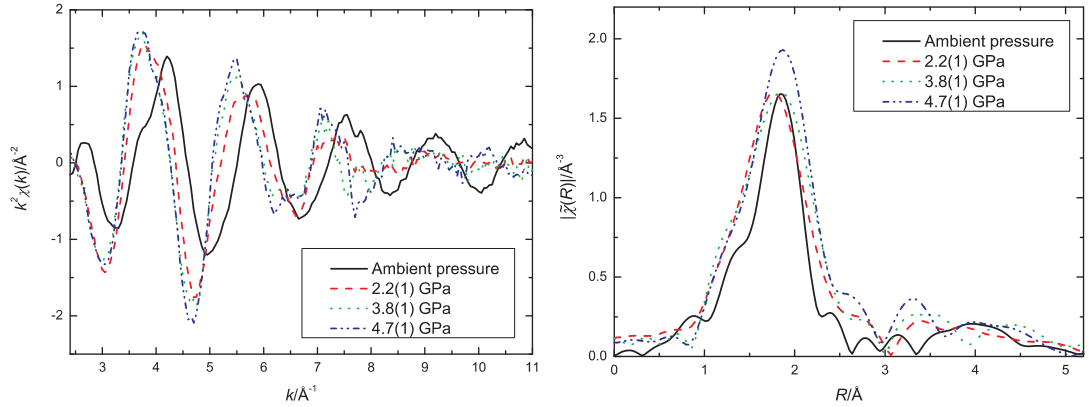

Figure 7.16: The $k^2\chi(k)$ and corresponding $|\tilde{\chi}(R)|$ function measured for crystalline $ZnCl_2$ under ambient conditions (sample A) or at room temperature and either 2.2(1), 3.8(1) or 4.7(1) GPa (sample E).

7.6 Discussion

In this section, the structural models for glassy and crystalline $ZnCl_2$ under several thermodynamic conditions are described and are refined using the experimental $|\tilde{\chi}(R)|$ obtained from $k^2\chi(k)$ functions. The details of the models and the results obtained from the refinement are presented and discussed.

7.6.1 Structural Models

The models for crystalline $ZnCl_2$ were constructed using the results from an XRD experiment performed in the temperature range from ambient to 1000 °C and in the pressure range from ambient to 4 GPa [218, 230]. From the diffraction results, below the melting temperature and 1 GPa, three crystalline phases are identified, namely tetragonal γ-$ZnCl_2$ [227], monoclinic β-$ZnCl_2$ [227, 231] and orthorhombic δ-$ZnCl_2$ [232, 233], all of which comprise 4-fold coordinated Zn. The δ-$ZnCl_2$ phase, which is the stable form of dry $ZnCl_2$ under ambient conditions, and the β-$ZnCl_2$ phase are found at relatively low pressures with δ-$ZnCl_2$ being observed at room temperature and β-$ZnCl_2$ being observed at higher temperature. Both phases transform to the γ-$ZnCl_2$ phase when the pressure is increased.

When the pressure is increased up to 3-4 GPa, crystalline phases comprising 6-fold coordinated Zn are observed, corresponding to the CdI_2-2H, CdI_2-4H and $CdCl_2$(3R) type structures. At room temperature, the structure is identified as a mixed $CdI_2/CdCl_2$ phase but the nature of the structure becomes clearer when the temperature is increased. At 405 °C and 3.46 GPa, the structure is identified as CdI_2-2H which was proposed earlier by Wilson [234]. When the temperature is increased further, CdI_2-2H transforms to the CdI_2-4H type structure and at 737 °C and 3.21 GPa it transforms again to the $CdCl_2$(3R) type structure.

At pressures around 2.5 GPa, structures intermediate between those in which Zn is 4-fold or 6-fold coordinated are observed and the structures are of the $AuTe_2$ or $CrBr_2$ type. As both structures belong to the same space group and have the same local coordination environment for Zn, namely a distorted Zn centred octahedron

consisting of 4 Cl nearest neighbours in the same plane and 2 Cl next nearest neighbours, they are indistinguishable when using EXAFS spectroscopy. In the present study only a model constructed from the $AuTe_2$ structure was refined. The lattice parameters measured for each model are summarised in table 7.2.

Structures	Space group	Lattice parameters					
		a (Å)	b (Å)	c (Å)	α (°)	β (°)	γ (°)
β-$ZnCl_2$	14	6.5131	11.2763	12.1135	90	90.1069	90
γ-$ZnCl_2$	137	3.6792	3.6792	10.2482	90	90	90
δ-$ZnCl_2$	33	6.4818	7.7381	6.1513	90	90	90
CdI_2-2H	164	3.51	3.51	5.489	90	90	120
CdI_2-4H	186	3.5368	3.5368	11.0473	90	90	120
$CdCl_2$(3R)	166	3.556	3.556	16.6440	90	90	120
$AuTe_2$	12	6.0967	3.5046	5.5078	90	90.101	90
$CrBr_2$	12	6.05	3.54	5.622	90	90	90

Table 7.2: Lattice parameters for possible crystal structures of $ZnCl_2$ under various thermodynamic conditions as obtained from XRD [218].

The structural model for glassy $ZnCl_2$ under ambient conditions was obtained from an ND experiment which describes the structure of glassy $ZnCl_2$ as a network consisting mainly of corner sharing tetrahedra with Zn-Cl and Zn-Zn nearest neighbour distances of 2.28(1) Å and 3.75(1) Å, respectively [180]. From this information a single scattering path corresponding to the first Zn-Cl coordination shell was used to construct a model. Additionally, it was found that a model comprising three coordination shells, namely a first Zn-Cl shell, a second Zn-Cl shell and a third Zn-Zn shell similar to the δ-$ZnCl_2$ [232, 233] structure, is also consistent with the experimental data, see detail in the following section.

7.6.2 Refinement

The $\chi(k)$ functions for the different models were calculated using the program ARTEMIS [62] and the data in real space were fitted by varying several parameters namely S_0^2, ΔE_0 and, for each scattering path, σ_j^2 and ΔR_j. As can be seen in figures 7.15 and 7.16, the $k^2\chi(k)$ functions beyond $k = 6$ Å^{-1} show well-defined oscillations. Fits were therefore made to the $\tilde{\chi}(R)$ function obtained from $k^2\chi(k)$ in order to give

a reasonable weighting to the $\chi(k)$ signal beyond $k = 6$ Å^{-1}. The cumulants C_3 and C_4 were set to zero for both the glassy and crystalline models. For the glassy model, this is because the first coordination shell which gives the main contribution to the $\chi(k)$ function is well defined [180]. In fact the first peak in the $G_X(r)$ function for glassy $ZnCl_2$ under ambient conditions, which corresponds to the Zn-Cl correlations, is quite symmetric, see figure 6.18. A value for S_0^2 of 1.2 was obtained from the fit to the glassy data and was subsequently used as a fixed parameter for all of the crystalline data sets.

Glassy $ZnCl_2$

Model 1 for glassy $ZnCl_2$ comprised one Zn-Cl coordination shell with a Zn-Cl atomic distance of 2.28(1) Å as obtained from the ND results. The model was refined using $\tilde{\chi}(R)$, with $1 \leq R(\text{Å}) \leq 4.4$, as obtained by Fourier transforming the measured $k^2\chi(k)$ function with a k range from 2.4 to 13 Å^{-1}. The fits in k- and R-space are shown in figure 7.17. From the figure, the residual for the fit in k-space shows a well-defined oscillation which suggests that the fit could be improved by adding extra scattering paths to the model. The same $\tilde{\chi}(R)$ function with the same R range was used to refine models based on crystalline γ-, β- and δ-$ZnCl_2$ in which Zn is 4-fold coordinated, to search for important extra single or multiple scattering paths. It was found that the added second and third coordination shells for the δ-$ZnCl_2$ model, which correspond to the Zn-Zn (Zn-Zn atomic distance of 3.78 Å and coordination number of 4) and the Zn-Cl (Zn-Cl atomic distance of 3.84 Å and coordination number of 1) correlations improved the fit to the data. The fits using model 2, which contains the first three coordination shells for the crystalline δ-$ZnCl_2$ structure, are shown in figure 7.17 in both k- and R-space. All of the refined parameters for each coordination shell for models 1 and 2 are summarised in table 7.3 together with the $\mathcal{R}$-factor and χ_ν^2 values obtained from each fit.

From table 7.3, the refined values for S_0^2, ΔE_0 and the parameters corresponding to the first coordination shell for both models are the same within the experimental error which suggests a reliable model for the first coordination shell. The $\mathcal{R}$-factor and χ_ν^2 values obtained from the fit using model 2 are about 47 and 31%

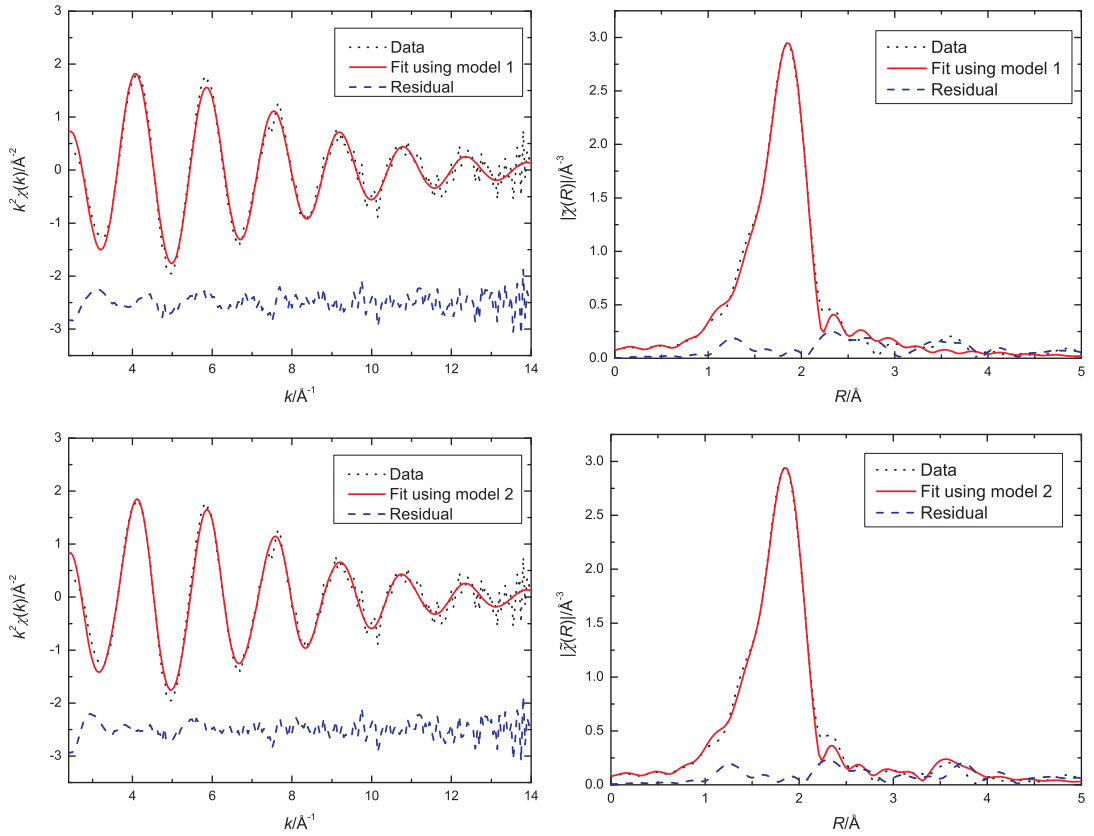

Figure 7.17: The $k^2\chi(k)$ and corresponding $|\tilde{\chi}(R)|$ function measured for glassy $ZnCl_2$ under ambient conditions (sample C). The dotted lines give the data, the solid lines give the fits using model 1, which comprises one Zn-Cl coordination shell, or model 2, which comprises three coordination shells similar to the δ-$ZnCl_2$ crystalline structure. The dashed lines give the residuals.

smaller that those obtained using model 1, respectively, which suggests that the first three coordination shells of Zn in glassy $ZnCl_2$ might be similar to those found in crystalline δ-$ZnCl_2$. However, as seen in figure 7.17, oscillations in the residuals still occur.

From table 7.3, the Zn-Cl nearest neighbour distance of 2.285(5) Å obtained from the refinement is smaller than the value of 2.332 Å obtained from the EXAFS measurement made at 30 °C by Wong and Lytle [219] which also gave a Zn-Cl coordination number of 5.18. It is difficult to identify the reason for the difference in the Zn-Cl distance between the present study and reference [219] but it may arise from the choice of background function. Figure 7.18 shows a comparison between the $k\chi(k)$ and corresponding $|\tilde{\chi}(R)|$ functions obtained from reference [219] and from the present study. From the figure, there is a slight shift in the oscillations of $k\chi(k)$

Parameter	Model 1	Model 2
$\mathcal{R}$-factor (%)	1.5	0.8
χ^2_ν	13	9
S_0^2	1.18(6)	1.24(5)
ΔE_0 (eV)	1.8(6)	2.2(5)
$R_{\text{Zn-Cl}}$ (Å)/degeneracy	2.285(5)/4	2.285(4)/4
$\sigma^2_{\text{Zn-Cl}}$ (Å^2)	0.0054(6)	0.0057(5)
$R_{\text{Zn-Cl}}$ (Å)/degeneracy	-	3.55(4)/1
$\sigma^2_{\text{Zn-Cl}}$ (Å^2)	-	0.006(5)
$R_{\text{Zn-Zn}}$ (Å)/degeneracy	-	3.66(3)/4
$\sigma^2_{\text{Zn-Zn}}$ (Å^2)	-	0.017(4)

Table 7.3: The refined atomic distances and σ^2 values for each scattering path together with the $\mathcal{R}$-factor and χ^2_ν values for the fits to the experimental data. Model 1 comprises one Zn-Cl coordination shell whereas model 2 comprises three coordination shells obtained from the δ-$ZnCl_2$ crystal structure. The refinements were made using $\tilde{\chi}(R)$ obtained from the $k^2\chi(k)$ function for glassy $ZnCl_2$ as measured at room temperature at the Zn K edge.

which leads to a shift in position of the first peak in the $|\tilde{\chi}(R)|$ function from reference [219] to a higher R value. Unlike the work in [219], the present EXAFS results are in accord with the ND data of [180] which give a Zn-Cl distance of 2.28(1) Å.

The refined Zn-Cl next nearest neighbour distance of 3.55(4) Å, presented in table 7.3, is much smaller than the initial value of 3.85 Å obtained from the crystalline δ-$ZnCl_2$ structure but is not un-physical. In fact the $g_{\text{ZnCl}}(r)$ function obtained from an isotopic substitution experiment in ND [205] shows a non-zero contribution in this region, see figure 6.24. The Zn-Zn nearest neighbour distance of 3.66(3) Å obtained from the refinement is not dissimilar to the value of 3.75(1) Å obtained from the ND results [180] given the fact that the contribution of the second and third coordination shells to the $k^2\chi(k)$ function is relatively small.

A model for glassy $ZnCl_2$ has been constructed from ND and XRD results using the RMC method [235]. This model gives a distribution of Zn-Cl structural units, summarised in table 7.4, with an average Zn-Cl nearest neighbour distance of 2.291 Å and an average Zn-Cl coordination number of 3.85. The $k^2\chi(k)$ function corresponding to the single scattering paths involving the first coordination shell of Zn was calculated from the RMC model by using the programs FEFF 7 [57] and

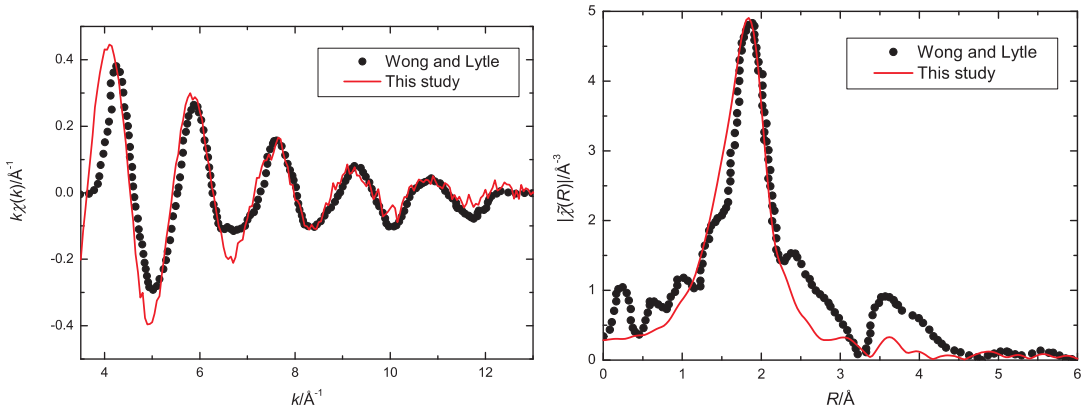

Figure 7.18: The $k\chi(k)$ and corresponding $|\tilde{\chi}(R)|$ function measured for glassy $ZnCl_2$ under ambient conditions in the present study and at 30 °C and ambient pressure in the work of Wong and Lytle [219]. The dots give the data points digitised from reference [219] and the solid lines give the data from the present study.

I.S.A.A.C.S. [175]. The latter was used to identify the positions of the neighbouring atoms which are used by FEFF 7. In this calculation, values for S_0^2 and ΔE_0 of 1.2 and 2 eV were used, respectively, and were obtained from the refined parameters presented in table 7.3. The measured $k^2\chi(k)$ function and that calculated from the RMC model are shown in figure 7.19.

From figure 7.19, the two functions are very similar. In fact, Zn is predominantly 4-fold coordinated in the RMC model with an average Zn-Cl nearest neighbour distance which is, within the experimental error, the same as the value of 2.285(5) Å obtained from the refinement using models 1 or 2. It should be noted that a discrepancy in the intensity of the first few peaks can be seen in figure 7.19. When the single and multiple scattering paths corresponding to atoms up to 4 Å away from an absorbing atom are included in the calculation only a small change is observed, see figure 7.20. This could imply that, in the RMC model, only those single scattering paths involving atoms in the first coordination shell are important.

Another structural model for the first coordination shell of Zn was obtained using the RMC model as a starting point. Four single scattering paths were used, corresponding to the $ZnCl_2$, $ZnCl_3$, $ZnCl_4$ and $ZnCl_5$ units, with different average Zn-Cl nearest neighbour distances. The relative contribution to the model from each structural unit was chosen to be the same as the abundance given in table 7.4. As

Coordination number	Abundance (%)	$R_{\text{Zn-Cl}}$ (Å)	Standard deviation (Å)
2	0.5	2.28(10)	0.08
3	14.3	2.28(10)	0.04
4	84.7	2.29(15)	0.04
5	0.5	2.37(5)	0.03

Table 7.4: The abundance of Zn-Cl structural units with coordination numbers of 2, 3, 4 and 5 in the RMC model for glassy $ZnCl_2$ [235].

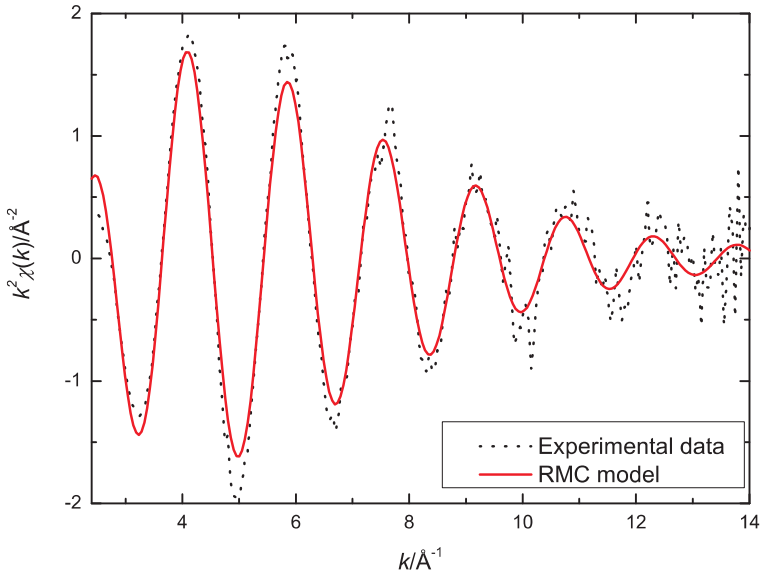

Figure 7.19: The $k^2\chi(k)$ function for glassy $ZnCl_2$. The dotted line gives the experimental data measured under ambient conditions at the Zn K edge. The solid line gives the function, calculated from the RMC model [235], in which the single scattering paths involving nearest neighbour atoms in the first Zn-Cl coordination shell were used together with values for S_0^2 and ΔE_0 of 1.2 and 2 eV, respectively.

the four scattering paths correspond to the same coordination shell and have similar values of $R_{\text{Zn-Cl}}$, they were refined using the same ΔR and $\sigma^2_{\text{Zn-Cl}}$ parameters. The fits in k- and R-space are shown in figure 7.21 and all of the refined parameters together with the $\mathcal{R}$-factor and χ^2_ν values are presented in table 7.5. From figure 7.21, the model gives a reasonably good fit to the experimental data. As seen in table 7.5, the S_0^2 and ΔE_0 values obtained from the refinement are, within the error, the same as those presented in table 7.3.

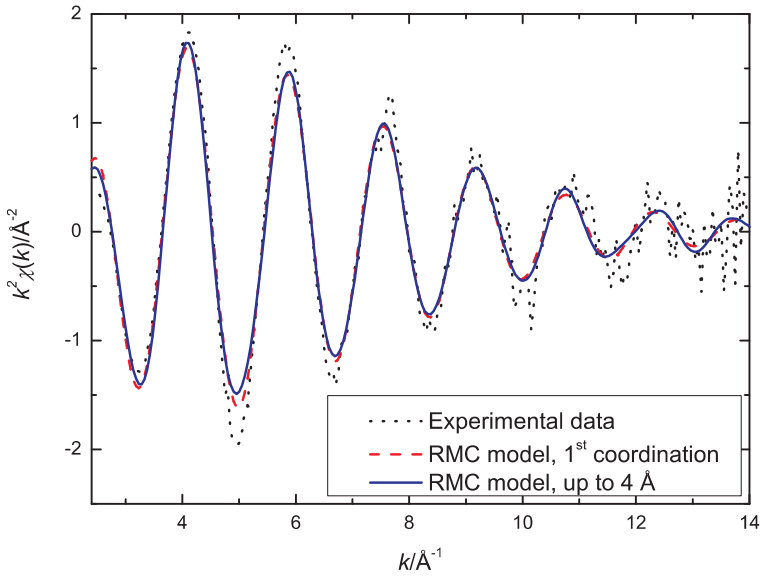

Figure 7.20: The $k^2\chi(k)$ function for glassy $ZnCl_2$. The dotted line gives the experimental data measured under ambient conditions at the Zn K edge. The dashed line gives the function calculated from the RMC model [235] using single scattering paths involving neighbour atoms in the first Zn-Cl coordination shell. The solid line gives the function calculated from the RMC model [235] using both single and multiple scattering paths involving neighbour atoms up to a distance of 4 Å away from a Zn atom. Both calculations used values for S_0^2 and ΔE_0 of 1.2 and 2 eV, respectively.

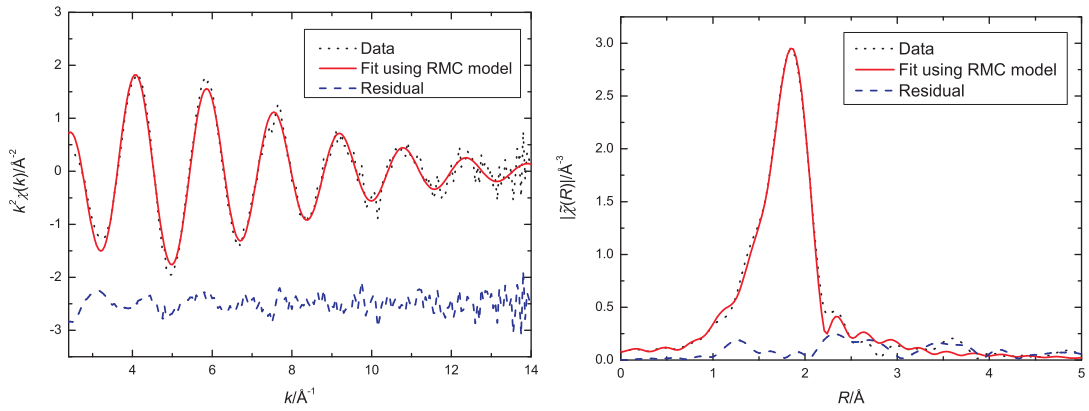

Figure 7.21: The $k^2\chi(k)$ and corresponding $|\tilde{\chi}(R)|$ function measured for glassy $ZnCl_2$ under ambient conditions (sample C). The dotted lines give the data, the solid lines give the fits using the RMC model for the first coordination shell of Zn and the dashed lines give the residuals.

Parameter	
$\mathcal{R}$-factor (%)	1.5
χ^2_ν	15
S_0^2	1.22(7)
ΔE_0 (eV)	1.7(5)
$R_{\text{Zn-Cl}}$ (Å)/degeneracy	2.275(5)/2
	2.271(5)/3
	2.286(5)/4
	2.359(5)/5
$\sigma^2_{\text{Zn-Cl}}$ (Å^2)	0.0053(6)

Table 7.5: The refined atomic distances and σ^2 values together with the $\mathcal{R}$-factor and χ^2_ν values for a fit using the RMC model for the first coordination shell of Zn. The refinement was made using $\tilde{\chi}(R)$ obtained from the $k^2\chi(k)$ function for glassy $ZnCl_2$ measured at room temperature at the Zn K edge.

Crystalline $ZnCl_2$

The β-, γ- and δ-$ZnCl_2$ models were fitted to $\tilde{\chi}(R)$ obtained from the $k^2\chi(k)$ function measured for crystalline $ZnCl_2$ under ambient conditions with S_0^2 fixed at 1.2. For the β- and δ-$ZnCl_2$ models, no multiple scattering paths are important and those single scattering paths up to $R_{0,j} = 4.4$ Å which make a significant contribution to the $k^2\chi(k)$ function were included in the fits. It should be noted that the scattering paths included in the fits were grouped into coordination shells such that paths in the same coordination shell were refined using the same variables. For example, the first coordination shell of β-$ZnCl_2$ consists of 4 slightly different Zn-Cl distances but the model was refined using the same values of σ^2 and ΔR for each of the 4 scattering paths. For the γ-$ZnCl_2$ model, those single scattering paths up to $R_{0,j} = 4.4$ Å which make a significant contribution to the $k^2\chi(k)$ function were included in the fits together with the multiple scattering paths with $R_{0,j} \approx 5$ Å.

The fits in k- and R-space are shown in figure 7.22. The refined parameters for each coordination shell are summarised in table 7.6, together with the $\mathcal{R}$-factor and χ_ν^2 values for each fit. From figure 7.22, all of the models produce reasonably good fits to the data. This is because all three models correspond to corner sharing Zn centred $ZnCl_4$ tetrahedral units. However, as seen in table 7.6, the fit using the γ-$ZnCl_2$ model gives the lowest $\mathcal{R}$-factor and χ_ν^2 values which suggests that the structure of the sample is likely to be γ-$ZnCl_2$. Since the sample was a pellet, it is possible that the pressure applied to press the sample into a pellet is enough to crystallise the sample into a γ-$ZnCl_2$ structure which, according to the XRD results [218, 230], is the structure found at higher pressure compared to the β- and δ-$ZnCl_2$ structure.

Parameter	β-$ZnCl_2$	γ-$ZnCl_2$	δ-$ZnCl_2$
$\mathcal{R}$-factor (%)	2.3	1.5	2.0
χ^2_ν	173	114	128
E_0 (eV)	3.6(6)	3.6(6)	3.2(6)
$R_{\text{Zn-Cl}}$ (Å)/degeneracy	2.294(6)/4	2.292(6)/4	2.292(6)/4
$\sigma^2_{\text{Zn-Cl}}$ (Å^2)	0.0080(6)	0.0079(5)	0.0076(5)
$R_{\text{Zn-Cl}}$ (Å)/degeneracy	-	-	3.70(4)/1
$\sigma^2_{\text{Zn-Cl}}$ (Å^2)	-	-	0.029(7)
$R_{\text{Zn-Zn}}$ (Å)/degeneracy	3.83(8)/4	3.79(8)/4	3.77(5)/4
$\sigma^2_{\text{Zn-Zn}}$	0.02(1)	0.03(1)	0.022(7)
$R_{\text{Zn-Cl}}$ (Å)/degeneracy	4.14(7)/2	-	-
$\sigma^2_{\text{Zn-Cl}}$ (Å^2)	0.01(1)	-	-
$R_{\text{Zn-Cl}}$ (Å)/degeneracy	4.40(4)/12	4.33(4)/12	4.31(4)/9
$\sigma^2_{\text{Zn-Cl}}$ (Å^2)	0.024(8)	0.031(9)	0.029(7)

Table 7.6: The average of refined atomic distances and refined σ^2 values for the single scattering paths in each coordination shell together with the $\mathcal{R}$-factor and χ^2_ν values for crystalline models containing 4-fold coordinated Zn. The models were refined using $\tilde{\chi}(R)$ obtained from the $k^2\chi(k)$ function for crystalline $ZnCl_2$ measured under ambient conditions with S_0^2 fixed at 1.2 during the fitting process.

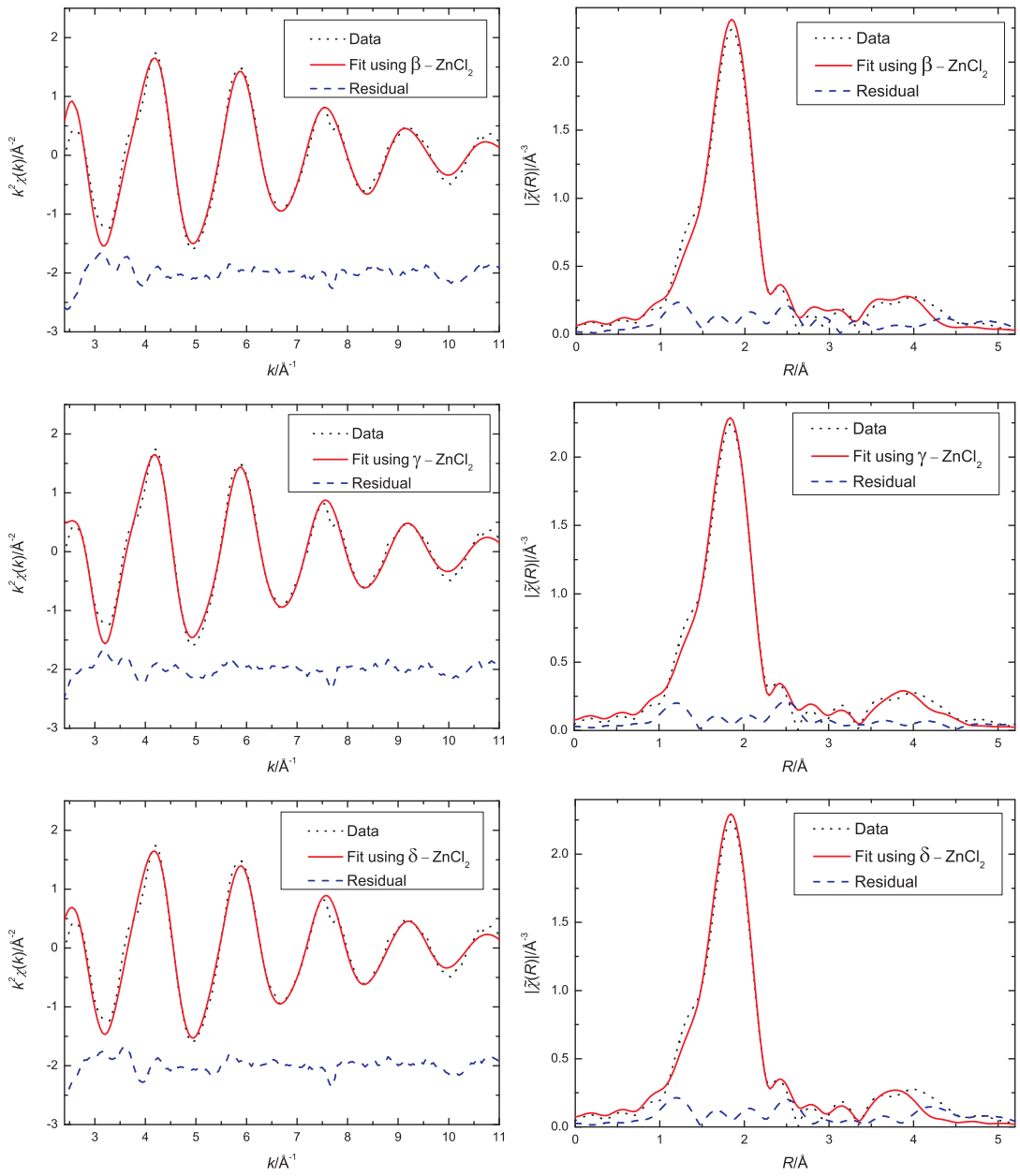

Figure 7.22: The $k^2\chi(k)$ and corresponding $|\tilde{\chi}(R)|$ function measured for crystalline $ZnCl_2$ under ambient conditions. The dotted lines give the data, the solid lines give fits using the β-$ZnCl_2$, γ-$ZnCl_2$ or δ-$ZnCl_2$ models and the dashed lines give the residuals.

From XRD results [218], the structure of $ZnCl_2$ at room temperature and pressures beyond 3 GPa corresponds to 6-fold coordinated Zn. Models for the octahedral phases of $ZnCl_2$ obtained from XRD [218], namely CdI_2-2H, CdI_2-4H and $CdCl_2$, were fitted to the data measured for crystalline $ZnCl_2$ at room temperature and 4.7(1) GPa. For these models, several multiple scattering paths have a significant contribution to the EXAFS signal. Those single and multiple scattering paths up to $R_{0,j} = 7.2$ Å which have a significant contribution to the $k^2\chi(k)$ function were grouped into different coordination shells j and included in the fitting procedure. The measured EXAFS signals and the fits in k- and R-space are shown in figure 7.23. The refined parameters for each coordination shell together with the $\mathcal{R}$-factor and χ^2_ν values for each fit are summarised in table 7.7. From figure 7.23, all of the models produced equally good fits to the data as seen by the absence of any significant feature in the residuals. This confirms that Zn is 6-fold coordinated at this pressure although it is not possible to identify whether the structure is the $CdCl_2$ phase as obtained from Raman spectroscopy and XRD results [236, 237] or a mixed $CdI_2/CdCl_2$ phase as obtained from recent XRD results [218].

Parameter	CdI_2-2H	CdI_2-4H	$CdCl_2$(3R)
$\mathcal{R}$-factor (%)	1.1	1.2	1.1
χ^2_ν	12	14	12
E_0 (eV)	0.6(4)	-0.1(5)	0.2(5)
$R_{\text{Zn-Cl}}$ (Å)/degeneracy	2.391(5)/6	2.387(5)/6	2.389(5)/6
$\sigma^2_{\text{Zn-Cl}}$ (Å^2)	0.0144(4)	0.0143(4)	0.0144(1)
$R_{\text{Zn-Zn}}$ (Å)/degeneracy	3.48(1)/6	3.48(1)/6	3.48(1)/6
$\sigma^2_{\text{Zn-Zn}}$ (Å^2)	0.019(2)	0.019(2)	0.019(2)
$R_{\text{Zn-Cl}}$ (Å)/degeneracy	4.06(9)/6	4.20(4)/6	4.24(7)/6
$\sigma^2_{\text{Zn-Cl}}$ (Å^2)	0.06(2)	0.03(1)	0.02(2)
$R_{\text{Zn-Cl}}$ (Å)/degeneracy	4.99(1)/6	-	-
$\sigma^2_{\text{Zn-Cl}}$ (Å^2)	0.02(1)	-	-
$R_{\text{Zn-Zn}}$ (Å)/degeneracy	7.00(3)/6	7.00(4)/6	7.00(3)/6
$\sigma^2_{\text{Zn-Zn}}$ (Å^2)	0.018(4)	0.018(4)	0.018(4)

Table 7.7: The average of refined atomic distances and refined σ^2 values for the single scattering paths in each coordination shell together with the $\mathcal{R}$-factor and χ^2_ν values for crystalline models containing 6-fold coordinated Zn. The models were refined using $\tilde{\chi}(R)$ obtained from the $k^2\chi(k)$ function for crystalline $ZnCl_2$ measured at room temperature and 4.7(1) GPa with S_0^2 fixed at 1.2 during the fitting process.

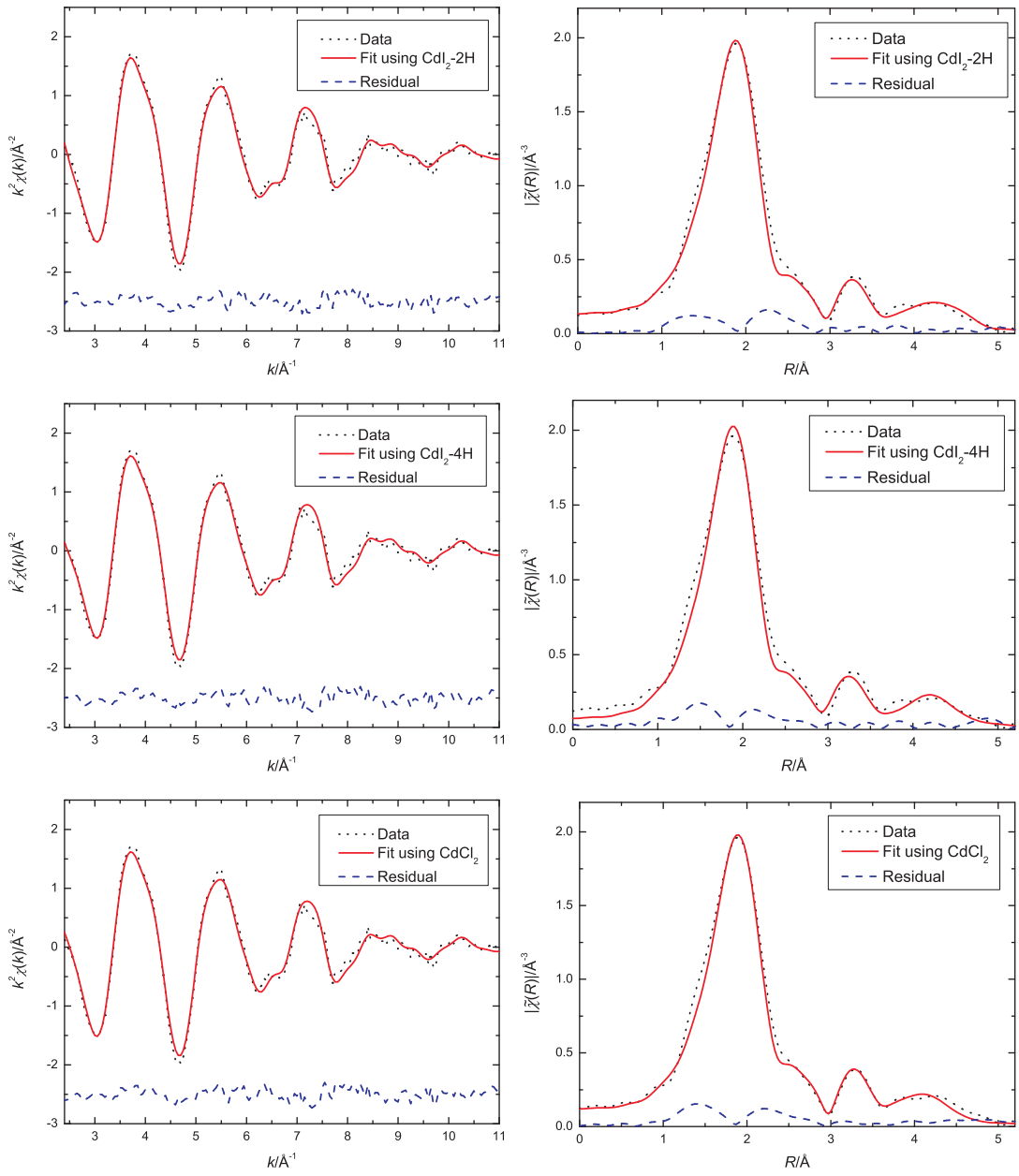

Figure 7.23: The $k^2\chi(k)$ and corresponding $|\tilde{\chi}(R)|$ function measured for crystalline $ZnCl_2$ at room temperature and 4.7(1) GPa. The dotted lines give the data, the solid lines give fits using the CdI_2-2H, CdI_2-4H or $CdCl_2$(3R) models and the dashed lines give the residuals.

From Raman spectroscopy [236, 237], the change in crystal structure from 4-fold to 6-fold coordinated Zn occurs around 2.1 - 2.3 GPa. From figure 7.16, the oscillation frequency and features beyond k = 7 Å^{-1} in the $k^2\chi(k)$ function measured at 2.2(1) GPa are notably different to the $k^2\chi(k)$ functions measured at ambient or 4.7 GPa which suggests a different local coordination environment for Zn at this pressure. The CdI_2-2H model, which is the lowest temperature structure in which Zn is octahedrally coordinated [230], and a distorted octahedral $AuTe_2$ model were refined using $\tilde{\chi}(R)$ obtained from the $k^2\chi(k)$ function for the measurement made at 2.2(1) GPa by including those single and multiple scattering paths up to $R_{0,j} \approx 5$ Å which give a significant contribution to the $k^2\chi(k)$ function. The measured EXAFS signals and the fits in k- and R-space are shown in figure 7.24. The refined parameters for each coordination shell together with the $\mathcal{R}$-factor and χ^2_ν values for each fit are summarised in table 7.8. As seen in figure 7.24 and the results in table 7.8, the $AuTe_2$ model gives a better fit to the data which indicates that the local coordination environment for Zn at this pressure is more consistent with a distorted octahedral model.

For the EXAFS data measured at room temperature and 3.8(1) GPa, Raman spectroscopy and XRD results [218, 236, 237] suggest that the material should contain 6-fold coordinated Zn and the features in the $k^2\chi(k)$ function beyond k = 7 Å^{-1} for the measurement made at 3.8(1) GPa are similar to those found in the $k^2\chi(k)$ function measured at 4.7(1) GPa, see figure 7.16. The octahedral CdI_2-2H and distorted octahedral $AuTe_2$ models were refined using $\tilde{\chi}(R)$ obtained from the $k^2\chi(k)$ function by including those single and multiple scattering paths up to $R_{0,j} \approx 5$ Å which give a significant contribution to the $k^2\chi(k)$ function. The measured EXAFS signals and the fits in k- and R-space are shown in figure 7.25. The refined parameters for each coordination shell together with the $\mathcal{R}$-factor and χ^2_ν values for each fit are summarised in table 7.9. By comparing figures 7.24 and 7.25, it can be seen that the fit to the measurement made at 3.8(1) GPa using the $AuTe_2$ model is not as good as the fit to the measurement made at 2.2(1) GPa. It is possible that at 3.8(1) GPa the sample is in a mixed phase. As seen in table 7.9, the χ^2_ν value for the fit using the CdI_2-2H model is slightly higher than the fit using the $AuTe_2$ model which indicates that the majority of the units should still be distorted

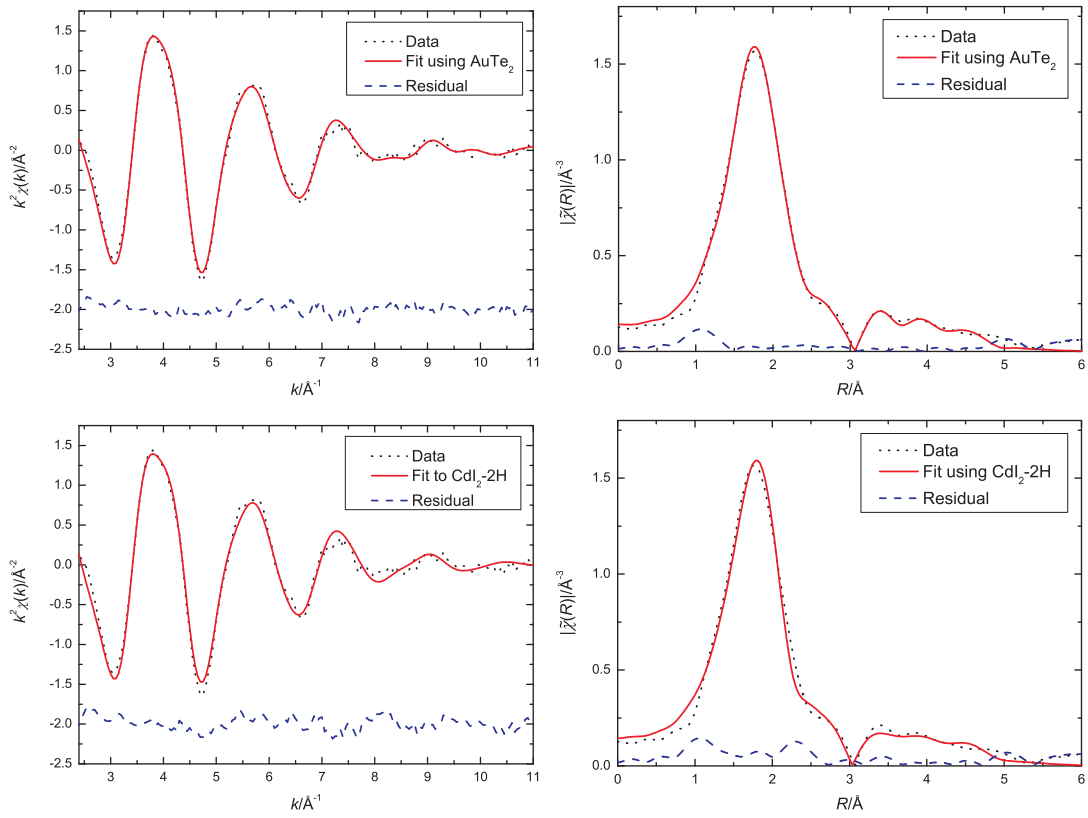

Figure 7.24: The $k^2\chi(k)$ and corresponding $|\tilde{\chi}(R)|$ function measured for crystalline $ZnCl_2$ at room temperature and 2.2(1) GPa. The dotted lines give the data, the solid lines give fits using the $AuTe_2$ or CdI_2-2H models and the dashed lines give the residuals.

Parameter	$AuTe_2$	CdI_2-2H
$\mathcal{R}$-factor (%)	0.32	0.91
χ^2_ν	29	51
E_0 (eV)	-1.6(8)	-1.8(7)
$R_{\text{Zn-Cl}}$ (Å)/degeneracy	2.280(9)/4	2.331(8)/6
$\sigma^2_{\text{Zn-Cl}}$ (Å^2)	0.012(1)	0.0186(6)
$R_{\text{Zn-Cl}}$ (Å)/degeneracy	2.45(2)/2	-
$\sigma^2_{\text{Zn-Cl}}$ (Å^2)	0.009(2)	-
$R_{\text{Zn-Zn}}$ (Å)/degeneracy	3.9(2)/6	3.50(4)/6
$\sigma^2_{\text{Zn-Zn}}$ (Å^2)	0.02(1)	0.028(5)
$R_{\text{Zn-Cl}}$ (Å)/degeneracy	3.67(6)/2	-
$\sigma^2_{\text{Zn-Cl}}$ (Å^2)	0.014(8)	-
$R_{\text{Zn-Cl}}$ (Å)/degeneracy	3.97(2)/4	4.0(1)/6
$\sigma^2_{\text{Zn-Cl}}$ (Å^2)	0.05(5)	0.06(2)
$R_{\text{Zn-Cl}}$ (Å)/degeneracy	4.98(4)/6	5.01(6)/6
$\sigma^2_{\text{Zn-Cl}}$ (Å^2)	0.020(6)	0.02(1)

Table 7.8: The average of refined atomic distances and refined σ^2 values for the single scattering paths in each coordination shell together with the $\mathcal{R}$-factor and χ^2_ν values for the $AuTe_2$ and CdI_2-2H models as refined using $\tilde{\chi}(R)$ obtained from the $k^2\chi(k)$ function measured for crystalline $ZnCl_2$ at room temperature and 2.2(1) GPa with S_0^2 fixed at 1.2 during the fitting process.

octahedra corresponding to the $AuTe_2$ model.

For the crystalline structures, the EXAFS results are consistent with those obtained by using XRD [218] and with the phase diagram reported by Brazhkin et al. [182], see figure 7.1, which indicates crystalline structures with 4-fold coordinated Zn at low pressure, 6-fold coordinated Zn at high pressure and an intermediate phase at the pressures around 2.5 GPa at room temperature. Since an EXAFS experiment has been made by Fillaux et al. [183, 220] on crystalline $ZnCl_2$ under similar thermodynamic conditions, it is useful to compare their results for the evolution of the Zn-Cl nearest neighbour distance as a function of pressure with the results obtained from the present study.

References [183, 220] give a Zn-Cl distance of 2.300(3) Å for 4-fold coordinated Zn measured under ambient conditions and found that the transition from a 4-fold to 6-fold structure occurred around 2.3(1) GPa. During this transition the Zn-Cl

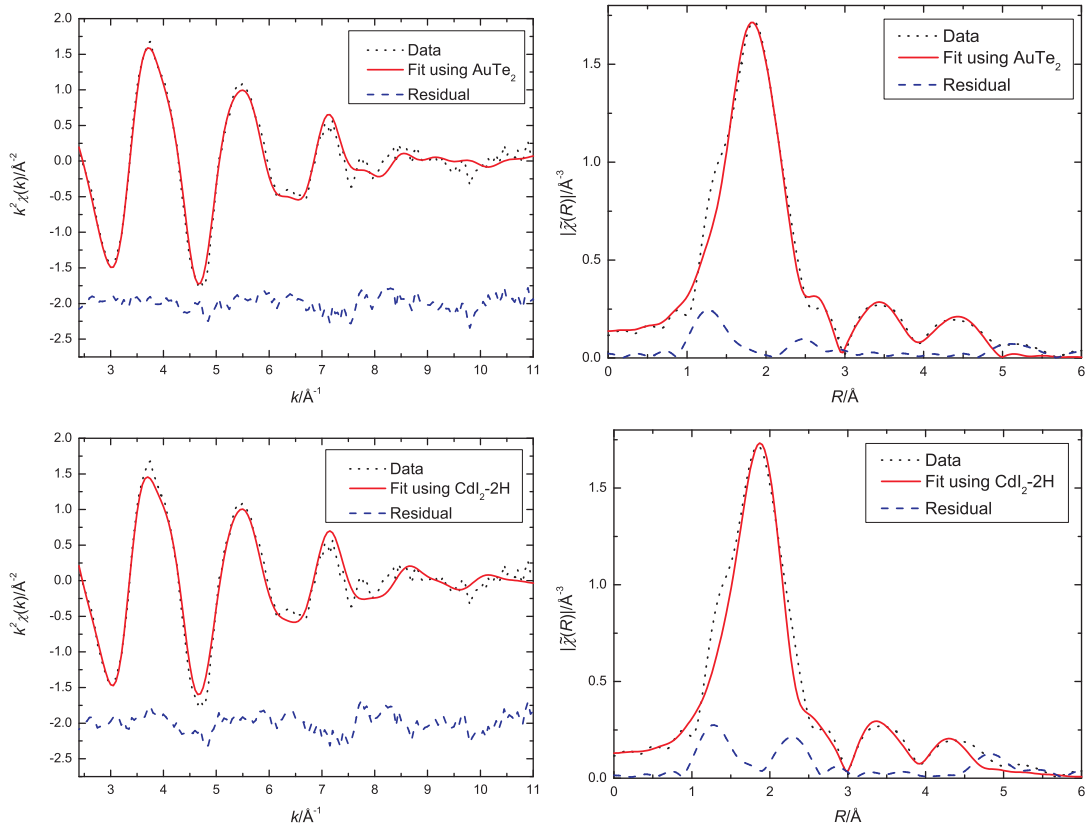

Figure 7.25: The $k^2\chi(k)$ and corresponding $|\tilde{\chi}(R)|$ function measured for crystalline $ZnCl_2$ at room temperature and 3.8(1) GPa. The dotted lines give the data, the solid lines give fits using the $AuTe_2$ or CdI_2-2H models and the dashed lines give the residuals.

Parameter	$AuTe_2$	CdI_2-2H
$\mathcal{R}$-factor (%)	1.3	2.6
χ^2_ν	43	50
E_0 (eV)	0.3(12)	0.3(10)
$R_{\text{Zn-Cl}}$ (Å)/degeneracy	2.33(2)/4	2.39(1)/6
$\sigma^2_{\text{Zn-Cl}}$ (Å^2)	0.010(2)	0.017(1)
$R_{\text{Zn-Cl}}$ (Å)/degeneracy	2.50(2)/2	-
$\sigma^2_{\text{Zn-Cl}}$ (Å^2)	0.006(2)	-
$R_{\text{Zn-Zn}}$ (Å)/degeneracy	3.49(8)/6	3.52(6)/6
$\sigma^2_{\text{Zn-Zn}}$ (Å^2)	0.03(1)	0.027(8)
$R_{\text{Zn-Cl}}$ (Å)/degeneracy	3.8(1)/2	-
$\sigma^2_{\text{Zn-Cl}}$ (Å^2)	0.02(2)	-
$R_{\text{Zn-Cl}}$ (Å)/degeneracy	4.2(1)/4	4.2(1)/6
$\sigma^2_{\text{Zn-Cl}}$ (Å^2)	0.02(1)	0.03(3)
$R_{\text{Zn-Cl}}$ (Å)/degeneracy	4.96(4)/6	4.77(2)/6
$\sigma^2_{\text{Zn-Cl}}$ (Å^2)	0.012(6)	0.02(7)

Table 7.9: The average of refined atomic distances and refined σ^2 values for the single scattering paths in each coordination shell together with the $\mathcal{R}$-factor and χ^2_ν values for the $AuTe_2$ and CdI_2-2H models as refined using $\tilde{\chi}(R)$ obtained from the $k^2\chi(k)$ function measured for crystalline $ZnCl_2$ at room temperature and 3.8(1) GPa with S_0^2 fixed at 1.2 during the fitting process.

distance first increases with increasing pressure at room temperature up to a maximum of 2.446(4) Å at 4.0(1) GPa where Zn is fully 6-fold coordinated. The Zn-Cl distance then decreases with increasing pressure reaching a value of 2.391(3) Å at 11.8(1) GPa. The Zn-Cl distances for the measurements made at ambient pressure and 4.7(1) GPa in the present study were obtained from refinements to the same models as used in references [183, 220], namely the γ-$ZnCl_2$ model for the measurement made at ambient pressure and the $CdCl_2$ model for the measurement made at high pressure. The results presented in tables 7.6 and 7.7, are plotted with the Zn-Cl distances reported in references [183, 220] in figure 7.26. Also in the figure are the data points corresponding to the weighted average of the Zn-Cl nearest and next nearest neighbour distances for the measurements made at 2.2 and 3.8 GPa presented in tables 7.8 and 7.9.

From figure 7.26, the evolution with pressure of the Zn-Cl nearest neighbour

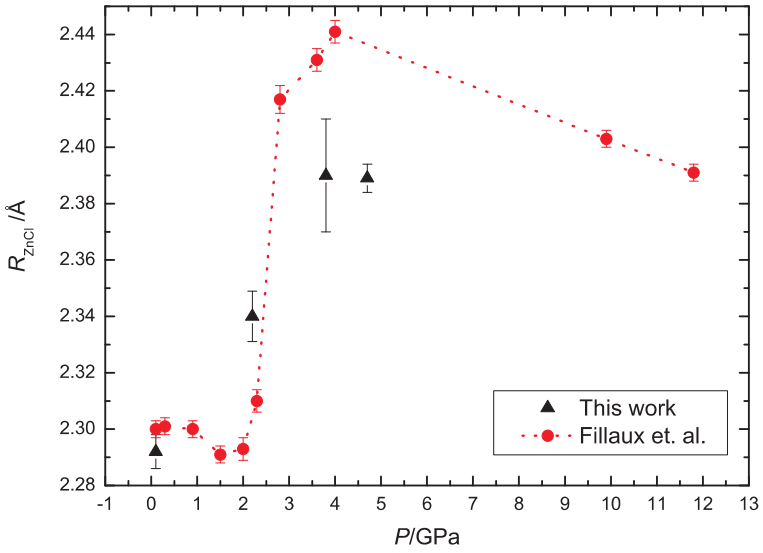

Figure 7.26: The Zn-Cl nearest neighbour distance as a function of pressure for crystalline $ZnCl_2$ as obtained from the EXAFS experiments described in the present work and in the work by Fillaux et al. [183, 220]. The data points corresponding to the measurements made at 2.2 and 3.8 GPa in the present work are the weighted average of the nearest and next nearest neighbour distances presented in tables 7.8 and 7.9.

distance or, in the case of the intermediate phase, the weighted average of the nearest neighbour and next nearest neighbour distances, follows the same trend as in reference [183, 220]. The present results do, however, indicate a slower increase of the Zn-Cl distance with increasing pressure, although only four data points were measured such that the transition could not be fully mapped. In addition, Fillaux et al. found the value of σ^2 for the first coordination shell of the 6-fold structure to be 0.0045(6) Å^2 greater than that for the first coordination shell of the 4-fold structure [183]. From the present study, this difference is greater at 0.0065(5) Å^2.

7.7 Conclusion

The XANES and EXAFS results indicate a reaction between $ZnCl_2$ and BN at high temperature which could be due to intercalation of $ZnCl_2$ into the layered structure of hexagonal BN. As described in section 7.5.1, when a mixture of $ZnCl_2$ and BN was heated and cooled in cycles the starting material could not be recovered. Furthermore, when the mixture was held in a pressure cell the melting temperature

at several pressures was much higher than quoted in references [182, 218]. It should be noted that the XANES spectra of the starting materials show that glassy $ZnCl_2$ can be crystalised when it is subjected to the pressure applied during preparation of a pellet.

The results obtained from a refinement of different structural models to the measured EXAFS spectra agree with those obtained from ND and XRD [180, 182, 218]. For glassy $ZnCl_2$, a model comprising one Zn-Cl coordination shell with a Zn-Cl coordination number of 4 is consistent with the experimental $k^2\chi(k)$ function and a refined Zn-Cl nearest neighbour distance and σ^2 value are 2.285(5) Å and 0.0054(6) Å^2, respectively. The measured $k^2\chi(k)$ function for glassy $ZnCl_2$ could also be fitted using a model comprising the first three coordination shells of the crystalline δ-$ZnCl_2$ structure. This second model gave the same refined parameters for the first Zn-Cl coordination shell as the first model with a next nearest neighbour Zn-Cl distance of 3.57(7) Å (coordination number of 1) and a Zn-Zn distance of 3.69(4) Å (coordination number of 4). The measured EXAFS signal is also consistent with the first coordination environment of Zn as found in an RMC model constructed using ND and XRD results [235]. The refined parameters for the first coordination shell of Zn obtained from the RMC model are, within the experimental error, the same as those obtained from the first and second models.

For crystalline $ZnCl_2$, the EXAFS results agree with those obtained for XRD [182, 230] which show 4-fold coordinated Zn at ambient pressure, 4+2-fold coordinated Zn at intermediate pressure and 6-fold coordinated Zn at high pressure. From the present study, a press pelleted sample of $ZnCl_2$ under ambient conditions has a γ-$ZnCl_2$ structure in which Zn is 4-fold coordinated by Cl atoms. At the intermediate pressures of 2.2(1) or 3.8(1) GPa, the local environment of Zn corresponds to a distorted octahedron as in the $AuTe_2$ type structure. At 4.7(1) GPa, the local environment of Zn corresponds to a structure in which Zn is octahedrally coordinated as in the CdI_2-2H, CdI_2-4H or $CdCl_2$(3R) type structures. Regarding the Zn-Cl distance, the evolution with pressure of the Zn-Cl nearest neighbour distance or, in the case of the intermediate phase, the weighted average of the nearest neighbour and next nearest neighbour distances, follows the same trend as in reference

[183, 220], although a slower change is observed. However, as only four data points were measured in the present work the transition could not be fully mapped.

It is shown that a change in the Zn-Cl coordination number can be inferred from a change in the Zn-Cl nearest neighbour distance. As there was a reaction between $ZnCl_2$ and BN at high temperature, the structure of the melt could not be measured. The experiment on $ZnCl_2$ was, therefore, remade using a different experimental setup, the details of which are presented in the next chapter.

Chapter 8

$ZnCl_2$ under Extreme Conditions: Part II

8.1 Introduction

A second EXAFS experiment was performed in an attempt to observe a liquid-liquid phase transition in molten $ZnCl_2$. Two major aspects of the experimental setup were changed from the first experiment described in chapter 7. The first is a change of beamline from BM29 which employs a conventional EXAFS experimental setup to ID24 [65, 83] at the ESRF which is an energy dispersive EXAFS beamline. The energy dispersive beamline, as mention in section 3.4, has the advantage of high stability of the focal spot and energy calibration. The second change from the first experiment is the use of a diamond anvil cell (DAC) [17] to apply pressure to the sample which allows the sample thickness to be of the order of 1 μm such that a matrix material is not required.

This chapter consists of six sections. The experimental detail is described in section 8.2. In section 8.3, the EOS of Re, which was used to find the temperature and pressure via a cross calibration method, is described along with the extraction of EXAFS signals from the measured absorption spectra. In section 8.4, the XANES and EXAFS spectra are presented and compared with the spectra measured under similar thermodynamic conditions in the BM29 experiment described in chapter 7.

In section 8.5, the structural models used in the EXAFS data analysis for liquid $ZnCl_2$ are described and the results from the refinement are discussed. The work is then concluded in section 8.6.

8.2 Experiment

The experiment was performed in transmission mode on beamline ID24 [65, 83] at the ESRF. ID24 is an energy dispersive beamline and the absorption spectrum in the energy range of the Zn K edge, from 9.590 to 10.099 keV (Zn K edge = 9.659 keV), was collected simultaneously using a fast readout low noise (FReLoN) charge-coupled device (CCD) camera [84].

The sample consisted of finely ground glassy anhydrous beads of 99.999% purity $ZnCl_2$ commercially available from Sigma-Aldrich and was from the same batch as used for the BM29 experiment described in chapter 7. The sample was prepared in a high purity Ar-filled glove box at the ESRF. A diamond anvil cell (DAC) [17] was employed to apply pressure to the sample up to about 5 GPa. A thickness of the order of 1 μm can be used in a DAC so no matrix material was required. The samples prepared for this experiment were 30 μm thick which is close to the calculated absorption length of $ZnCl_2$ which is 28 μm.

During the experiment, the sample was held in a gasket made from Re metal. The sample was filled into a hole at the center of the gasket. The hole in the gasket of 200 μm diameter, which was in the middle of the indentation made by pressing the Re plate between the diamond anvils, was made by using a laser, see figure 8.1. For the first sample (sample A) a ring of BN powder, which was used as one of the temperature and pressure markers, was placed around the sample such that the sample diameter was 150 μm. For the second sample (sample B), the BN ring was removed to avoid any chemical reaction, and the sample diameter was increased to 200 μm.

In the DAC, pressure is applied to the diamonds by a gas filled membrane, see figure 8.2. The deformation of the membrane due to gas pressure reduces the gap between the diamond anvils thus applying pressure to the sample situated between

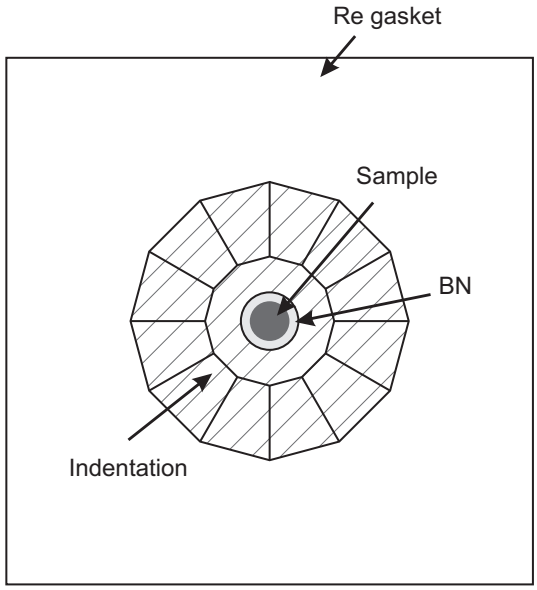

Figure 8.1: Re gasket. For sample A, the $ZnCl_2$ was surrounded by a ring of BN powder which were filled into a hole at the center of the indentation made by diamond anvils in a Re gasket.

them. An oven was made from a tungsten coil placed near the sample which could raise the temperature up to 800-1000 °C. Figure 8.3 shows the oven and the sample gasket placed inside the DAC. During the measurement, the DAC was placed inside a vacuum chamber made from stainless steel equipped with a Mylar window on the side near the detector and a Kapton window on the side near the x-ray source. Although Mylar is more absorbing than Kapton, it is more transparent to the fluorescence spectrum of ruby which is used as a temperature and pressure marker for most experiments performed on the ID24 beamline. The pressure in the vacuum chamber was always kept below 10^{-5} mbar to avoid oxidation of the diamonds and oven.

In the present experiment, for every XAS measurement the diffraction patterns for the sample and for the BN (if present) and Re temperature and pressure markers were measured using x-rays of wavelength 1.289 Å with a MAR345 image plate detector placed near the sample position, see figure 3.10. The diffraction pattern of the sample was used to i) identify the crystal structure and ii) confirm a molten state for the sample via an absence of Bragg peaks. The crystal structure is very useful in helping to construct models for the EXAFS data analysis.

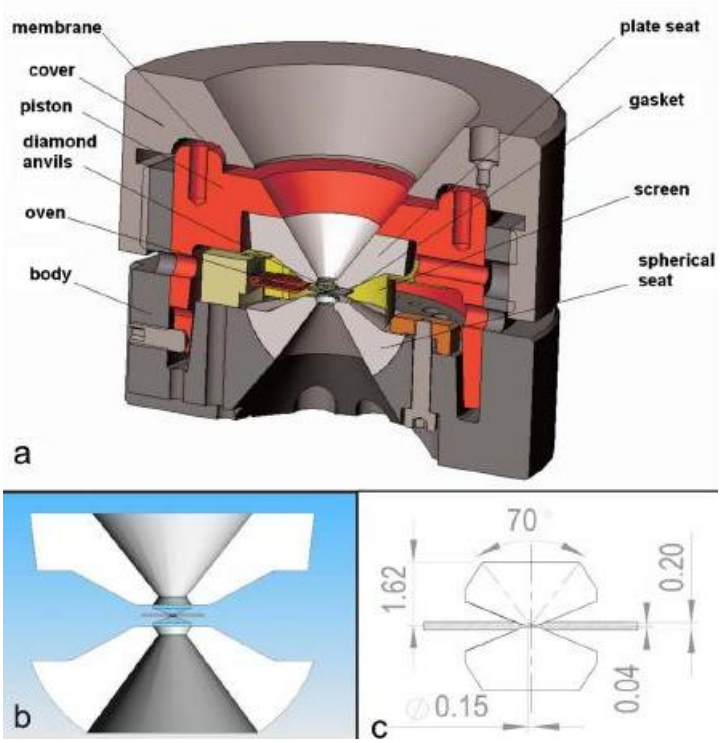

Figure 8.2: Schematic of the DAC [17]. (a) A cross-section of the DAC and its components, (b) a cross-section of the anvil seats, the diamond anvils and the gasket, and (c) a cross-section of the diamond anvils and gasket.

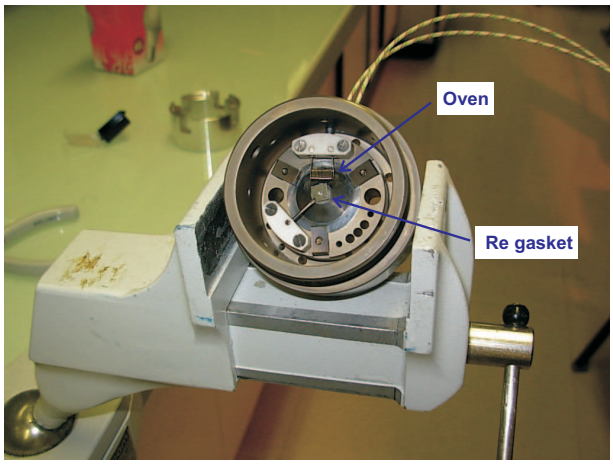

Figure 8.3: The sample gasket and oven inside the DAC.

As for the previous experiment on beamline BM29, the thermodynamic conditions for each XAS measurement were determined by using a cross calibration method, see section 7.4, and the errors on the temperature and pressure are expected to be less than ±50 K [214] and ±0.1 GPa [226], respectively. For sample A, the temperature and pressure conditions were determined using the EOS for BN and Re [222, 226]. Although we know from the BM29 experiment that BN reacts with $ZnCl_2$ at high temperatures, in this case the BN was placed around the sample so there should be no reaction at the center of the sample where the x-ray measurements were made. The temperature values determined from the cross calibration method for sample A were different to those read from a thermocouple placed at the back of the diamonds by about 25 °C which is within the error of the cross calibration method. Sample B was prepared without the BN ring and the pressure was determined from the EOS of Re with the temperature values read from the thermocouple.

8.3 Data Treatment

The EOS of BN is described in section 7.4. For Re, the EOS can be described using equations 7.9 to 7.11 that is

$$\begin{aligned} P(V,T) &= P(V_a,300) + \frac{3}{2}K_{Ta}\left[\left(\frac{V_a}{V}\right)^{\frac{7}{3}} - \left(\frac{V_a}{V}\right)^{\frac{5}{3}}\right]\left\{1 + \frac{3}{4}(K'_{Ta}-4)\left[\left(\frac{V_a}{V}\right)^{\frac{2}{3}} - 1\right]\right\} \\ &\quad + \left[\alpha K_T(V_a,T) + \left(\frac{\partial K_T}{\partial T}\right)_V \ln\left(\frac{V_a}{V}\right)\right](T-300), \end{aligned} \tag{8.1}$$

where $K_{Ta} = 360$ GPa, $K'_{Ta} = \left(\frac{\partial K_{Ta}}{\partial P}\right)_T = 4.5$, $\alpha K_T(V_a,T) = 0.00776$ GPa/K, $\left(\frac{\partial K_T}{\partial T}\right)_V = -0.00815$ GPa/K and $V_a = 29.4087$ Å^3 [222].

The thermodynamic conditions for the EXAFS measurements on samples A and B are shown in figure 8.4. It can be seen that it was not possible to make many measurements, especially in the liquid phase. This is because the oven broke at about 800 °C when sample A was measured and at about 500 °C when sample B was measured. In the case of sample A, an EXAFS measurement of the liquid at high pressure was measured but the oven broke before the diffraction pattern of Re or BN could be measured. The dotted circle in figure 8.4 marks the thermodynamic

condition estimated from the gas pressure applied to the DAC and the temperature read from the thermocouple placed at the back of the diamond anvils.

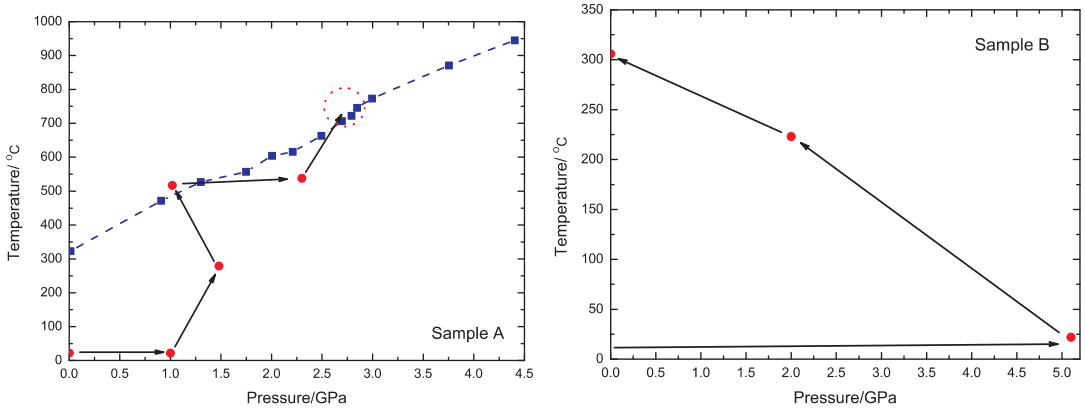

Figure 8.4: The thermodynamic conditions for the measurements made on samples A and B. The temperature and pressure conditions for the EXAFS measurements, shown by dots, were determined from i) the cross calibration method using the EOS of BN and Re for sample A and ii) from the temperature read from the thermocouple attached to the back of a diamond in the DAC and the EOS of Re for sample B. The dotted circle marks the EXAFS measurement where the thermodynamic condition was estimated from the gas pressure applied to the DAC and the temperature read from the thermocouple at the back of the anvils. The squares and dashed line give the melting curve digitised from the $ZnCl_2$ phase diagram [182].

For the crystalline phases, only one absorption spectrum was measured for each thermodynamic condition. For the liquid phase, the final absorption spectra used in the data analysis were the average of 9 spectra in the case of sample A and 10 spectra in the case of sample B. The $\chi(k)$ functions were extracted from the absorption spectra by the method described in chapter 3. The background functions were determined using the AUTOBK algorithm in ATHENA [62], fitted to the data from the absorption edge energy to the last data point with $R_{bkg} = 1$ Å for all spectra. The normalised absorption spectra and the background functions for all of the measurements made for samples A and B are shown in figures 8.5 and 8.6. It should be mentioned that the DAC introduced lots of glitches in the measured spectra and many of them were large and could not be removed without losing the desired signal in the XAS spectra. Thus the usable k ranges were 2.4 to 6.3 Å^{-1} for sample A and 2.4 to 7.9 Å^{-1} for sample B.

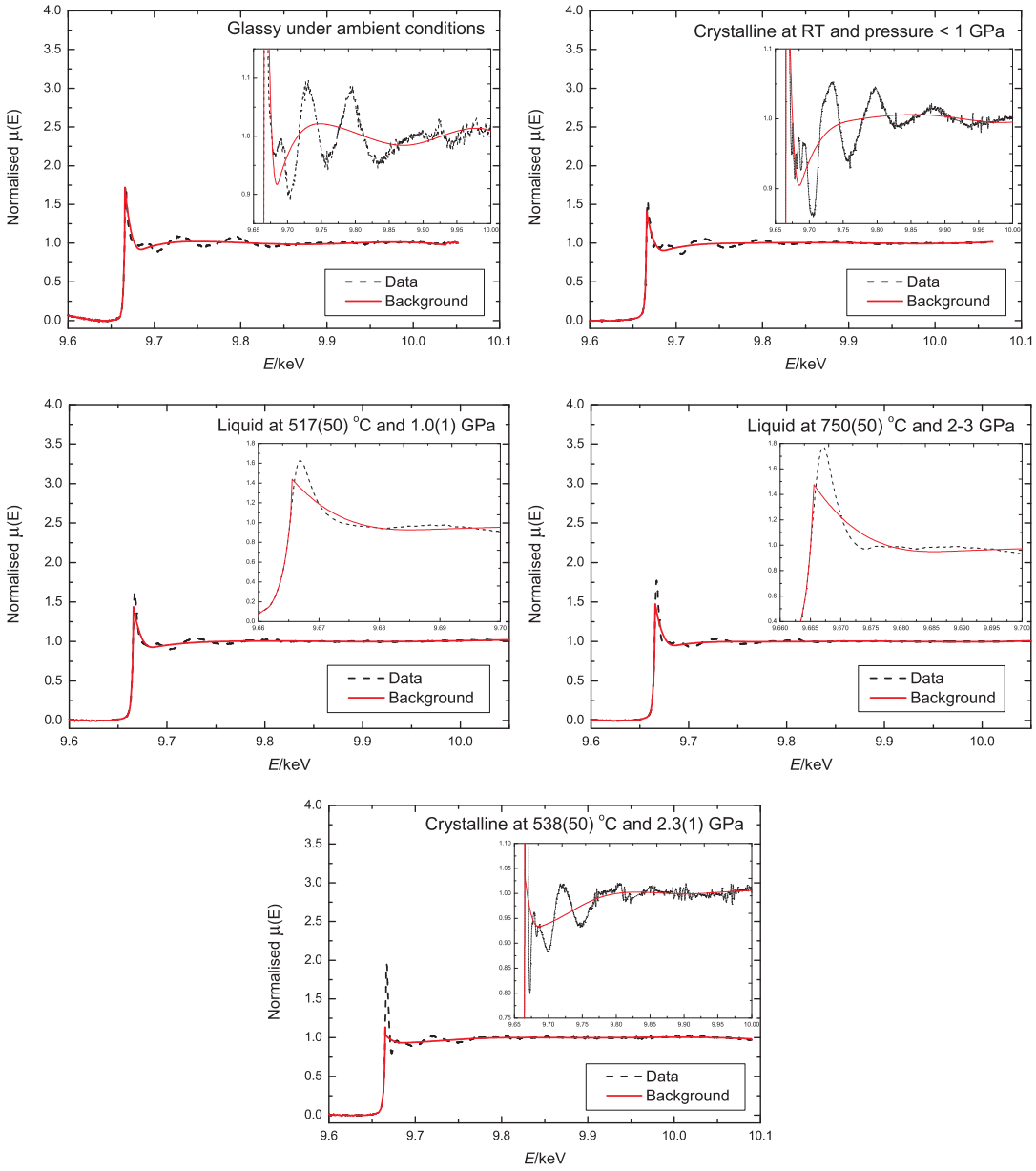

Figure 8.5: The normalised absorption spectra and the fitted background functions for measurements on glassy, crystalline and liquid $ZnCl_2$ for sample A. The glassy state was measured under ambient conditions, the crystalline state was measured at i) room temperature and pressure less than 1 GPa or ii) 538(50) °C and 2.3(1) GPa, and the liquid state was measured at i) 517(50) °C and 1.0(1) GPa or ii) 750(50) °C and 2-3 GPa. The dashed lines give the measured normalised absorption spectra and the solid lines give the background functions. The insets show the region near the absorption edge energy.

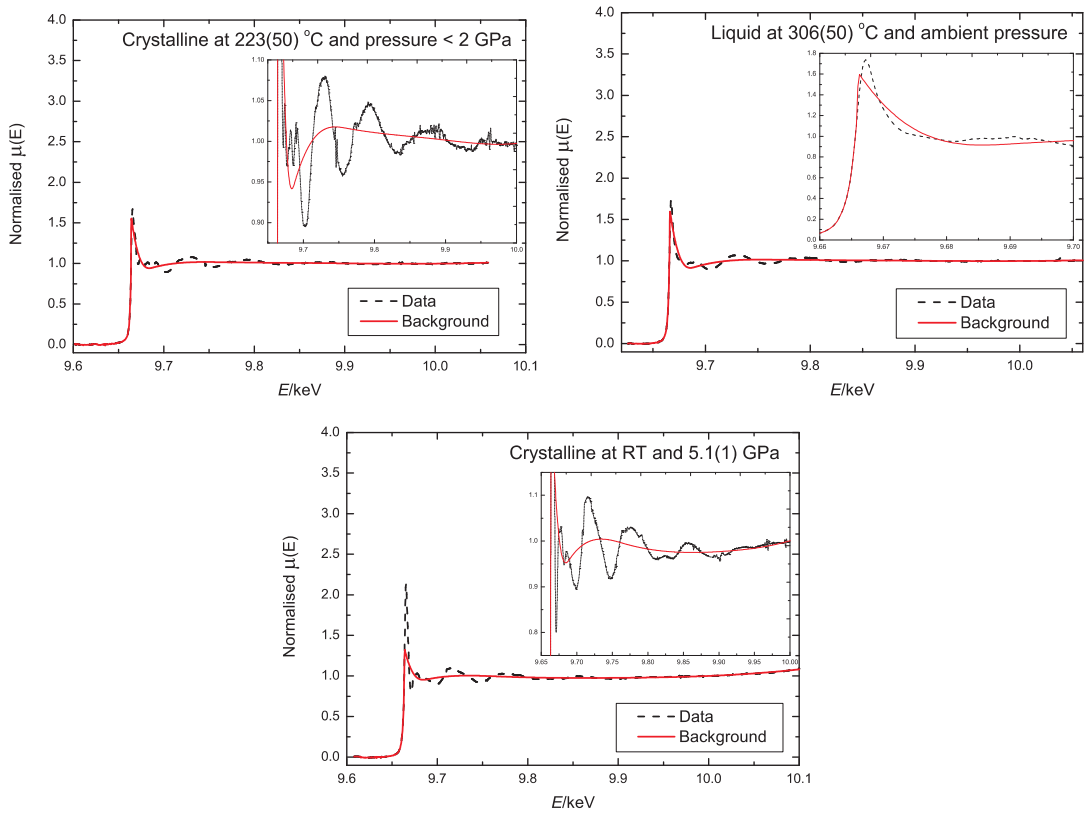

Figure 8.6: The normalised absorption spectra and the fitted background functions for measurements on crystalline and liquid $ZnCl_2$ for sample B. The crystalline state was measured at i) 223(50) °C and pressure less than 2 GPa or ii) room temperature and 5.1(1) GPa. The liquid state was measured at 306(50) °C and ambient pressure. The dashed lines give the measured normalised absorption spectra and the solid lines give the background functions. The insets show the region near the absorption edge energy.

8.4 Results

In this section, the XANES and EXAFS spectra for glassy and crystalline $ZnCl_2$ measured on ID24 are compared with those discussed in chapter 7. The XANES spectra and the $k^2\chi(k)$ functions for glassy $ZnCl_2$ under ambient conditions measured on ID24 for sample A and on BM29 are plotted together in figure 8.7. From the figure, the XANES signature and the EXAFS oscillations are similar for both experiments.

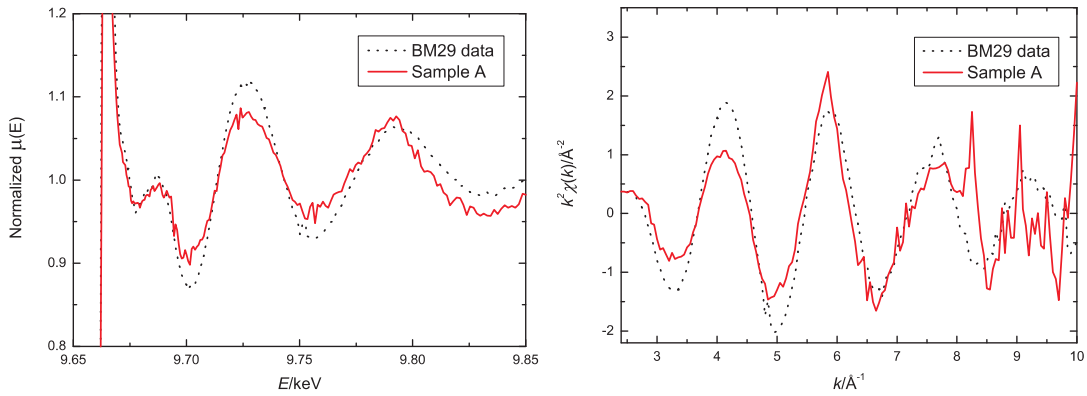

Figure 8.7: The XANES spectra and the $k^2\chi(k)$ functions for glassy $ZnCl_2$ measured under ambient conditions. The solid lines give the data obtained from the current experiment on ID24 and the dotted lines give the data obtained from the BM29 experiment presented in chapter 7.

In figures 8.8 and 8.9, the XANES and EXAFS spectra for sample A measured at room temperature and pressure less than 1 GPa and for sample B measured at 223(50) °C and pressure less than 2 GPa are compared with the spectra measured for crystalline $ZnCl_2$ under ambient conditions from the BM29 experiment. For both of the ID24 measurements, the XRD results measured under the same thermodynamic conditions suggest that the structure is the γ-$ZnCl_2$ phase [238] which is the same crystalline phase as the structure measured from the BM29 experiment, see chapter 7. The XANES and EXAFS spectra for all three measurements show similar features. The three peaks observed in the XANES spectra in the energy range from 9.67 to 9.70 keV may be a signature of $ZnCl_2$ crystal structures in which Zn is 4-fold coordinated. The XANES spectrum corresponding to the γ-$ZnCl_2$ structure in reference [183], see figure 7.13, also shows similar structure. In fact, as seen in the right hand panel of figure 8.8, similar features near the absorption edge could be

reproduced by calculating the XANES spectra for the β-, δ- and γ-$ZnCl_2$ crystalline phases by using the program FEFF 7 [57] with the lattice parameters given in table 7.2.

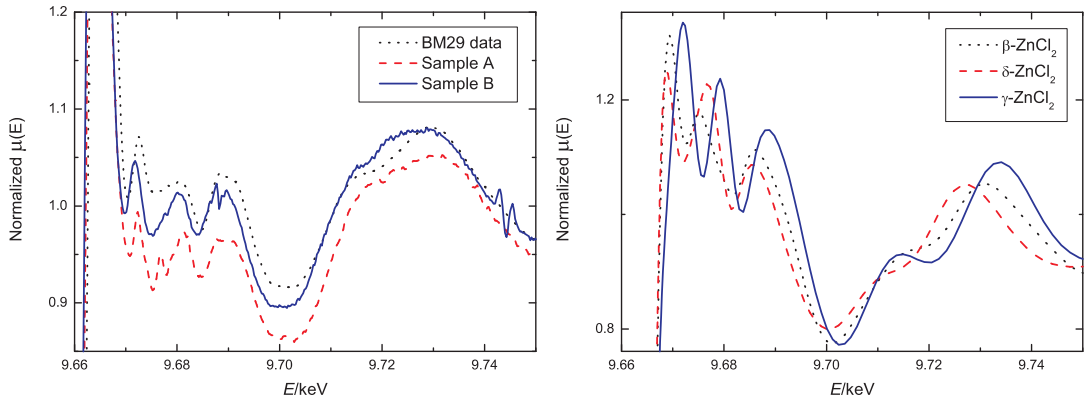

Figure 8.8: The XANES spectra for crystalline $ZnCl_2$. In the left hand panel, the dotted lines give the data obtained from the BM29 experiment presented in chapter 7 as measured under ambient conditions, the dashed line gives the data for sample A measured at room temperature and pressure less than 1 GPa, and the solid line gives the data for sample B measured at 223(50) °C and pressure less than 2 GPa. The right hand panel presents the XANES spectra calculated for the β-, δ- and γ-$ZnCl_2$ crystalline phases using the program FEFF 7 [57] with the lattice parameters given in table 7.2.

In figure 8.10, the XANES spectra for sample A measured at 538(50) °C and 2.3(1) GPa and for sample B measured at room temperature and 5.1(1) GPa are compared with the XANES spectra measured for crystalline $ZnCl_2$ at room temperature and 4.7(1) GPa in the BM29 experiment. According to XRD [218, 238], the crystal structure of $ZnCl_2$ in this temperature and pressure range should correspond to an octahedral or distorted octahedral coordination environment for Zn. The XANES spectra for all three measurements show a big dip at $E \approx 9.67$ keV which could be a signature of $ZnCl_2$ crystal structures with 6-fold coordinated Zn. The XANES spectrum corresponding to the $CdCl_2$ type structure in reference [183], see figure 7.13, also has this feature. In fact, as seen in the right hand panel of figure 8.10, similar features near the absorption edge could be reproduced by calculating the XANES spectra for the $CdCl_2$ and CdI_2-4H type structures with the lattice parameters given in table 7.2 by using the program FEFF 7 [57]. As all of the 6-fold coordinated Zn crystals have similar local structure, the $k^2\chi(k)$ functions corresponding to the measurements shown in the left hand panel of figure 8.10 are

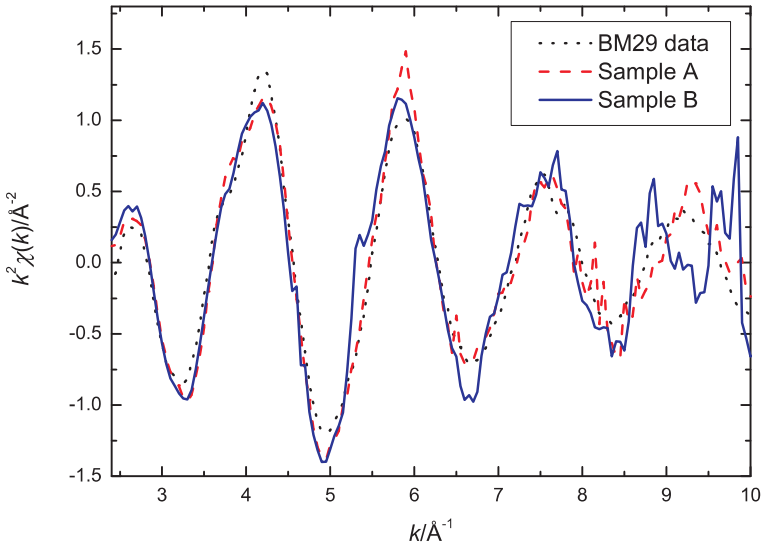

Figure 8.9: The EXAFS spectra for crystalline $ZnCl_2$. The dotted line gives the data obtained from the BM29 experiment presented in chapter 7 as measured under ambient conditions, the dashed line gives the data for sample A measured at room temperature and pressure less than 1 GPa, and the solid line gives the data for sample B measured at 223(50) °C and pressure less than 2 GPa.

similar, see figure 8.11, although for sample A the function is very noisy and features beyond $k = 6$ Å^{-1} are not clear.

For the liquid phase, sample A was measured at 517(50) °C and 1.0(1) GPa and at 750(50) °C and 2-3 GPa, whereas sample B was measured at 306(50) °C and ambient pressure. The XANES spectra and $k^2\chi(k)$ functions for the three liquids are compared in figure 8.12. From the figure, the XANES signatures in the energy range from 9.67 to 9.7 keV for the liquid at ambient pressure and at 1.0(1) GPa are very similar but are different to those for the liquid at 2-3 GPa. The $k^2\chi(k)$ spectra for the three measurements show, however, a similar oscillation frequency although the signals for sample A are heavily damped beyond $k = 6$ Å^{-1}. The physical implications of these results will be discussed in the following section where a refinement to different structural models is made.

It is interesting to compare the XANES spectra together with the $k^2\chi(k)$ and $|\tilde{\chi}(R)|$ functions for crystalline and glassy $ZnCl_2$ measured under ambient conditions from the BM29 experiment and for liquid $ZnCl_2$ measured at 306(50) °C and ambient pressure from the ID24 experiment on sample B since, according to x-ray and neutron diffraction, all of the these structures should correspond to 4-fold coordinated Zn, see

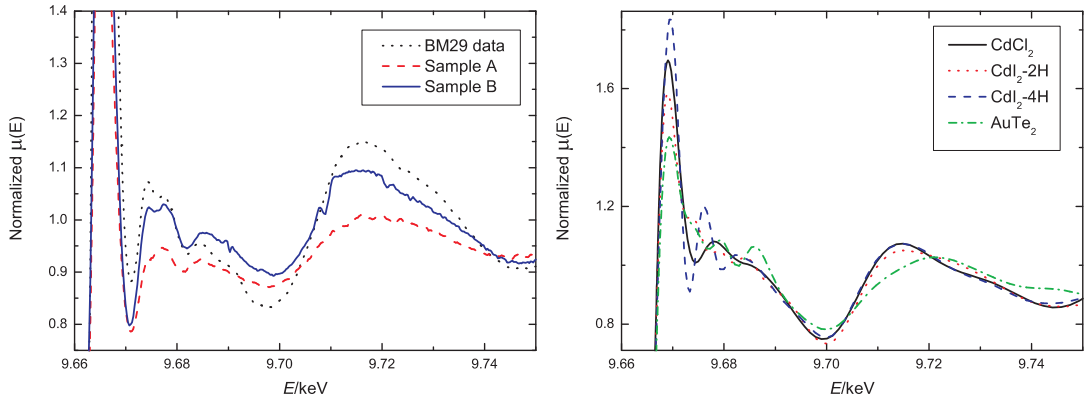

Figure 8.10: The XANES spectra for crystalline $ZnCl_2$. In the left hand panel, the dotted line gives the data obtained from the BM29 experiment presented in chapter 7 at room temperature and 4.7(1) GPa, the dashed line gives the data for sample A measured at 538(50) °C and 2.3(1) GPa, and the solid line gives the data for sample B measured at room temperature and 5.1(1) GPa. The right hand panel presents the XANES spectra calculated for the $CdCl_2$, CdI_2-2H, CdI_2-4H and $AuTe_2$ crystalline phases using the program FEFF 7 [57] with the lattice parameters given in table 7.2.

chapter 6 and references [180, 218]. A comparison of the XANES and the EXAFS spectra in k- and R-space is made in figures 8.13 and 8.14. From figure 8.13, the XANES signature of crystalline $ZnCl_2$ is different to that of the liquid and glass as seen by the appearance of three peaks in the range from 9.67 to 9.70 keV. The frequency of the oscillations in the $k^2\chi(k)$ functions is, however, very similar which is likely to result from the 4-fold coordination environment of Zn in all of the samples. In figure 8.14, the position of the first peak in the $|\tilde{\chi}(R)|$ functions is comparable. Small differences are, however, seen in the range from 3 to 5 Å which corresponds to atomic ordering beyond the nearest neighbours.

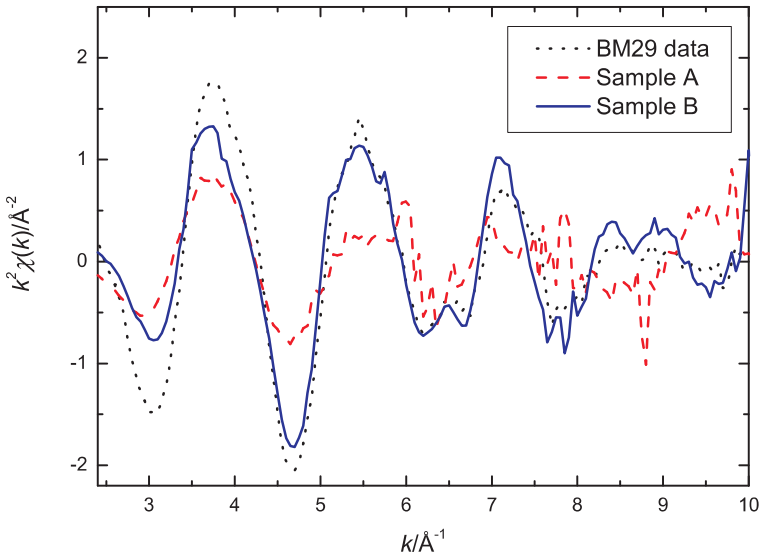

Figure 8.11: The EXAFS spectra for crystalline $ZnCl_2$. The dotted line gives the data obtained from the BM29 experiment presented in chapter 7 at room temperature and 4.7(1) GPa, the dashed line gives the data for sample A measured at 538(50) °C and 2.3(1) GPa and the solid line gives the data for sample B measured at room temperature and 5.1(1) GPa.

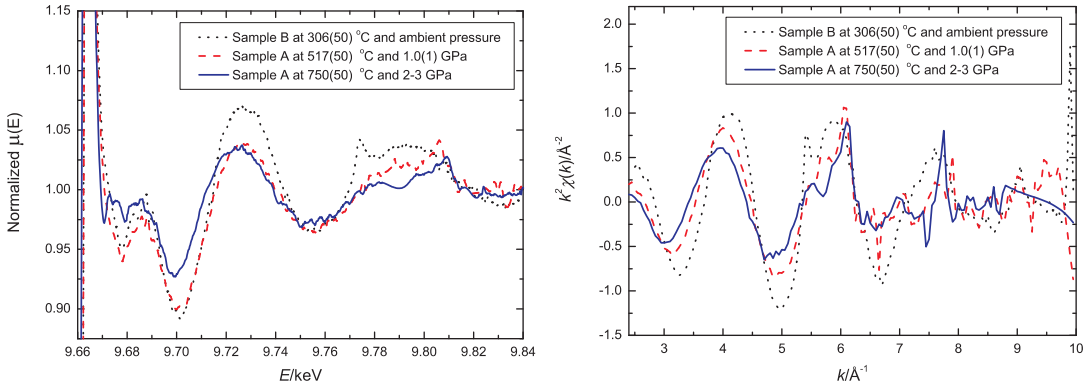

Figure 8.12: The XANES spectra and the $k^2\chi(k)$ functions for liquid $ZnCl_2$. The dotted lines give the data measured for sample B at 306(50) °C and ambient pressure, while the dashed and solid lines give the data measured for sample A at 517(50) °C and 1.0(1) GPa or at 750(50) °C and 2-3 GPa, respectively.

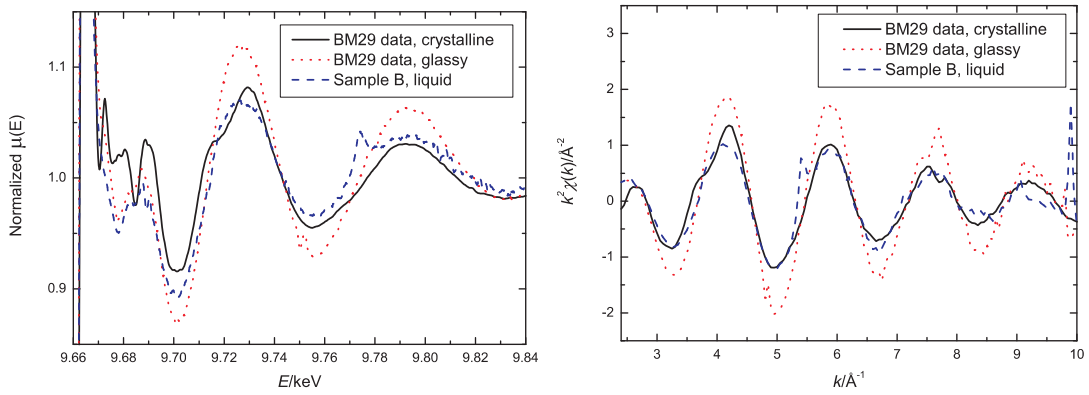

Figure 8.13: The XANES spectra and the $k^2\chi(k)$ functions for crystalline, glassy and liquid $ZnCl_2$. The solid and dotted lines give the data taken for crystalline and glassy $ZnCl_2$ measured under ambient conditions using BM29 (see chapter 7), respectively, while the dashed lines give the data taken for liquid $ZnCl_2$ at 306(50) °C and ambient pressure using ID24.

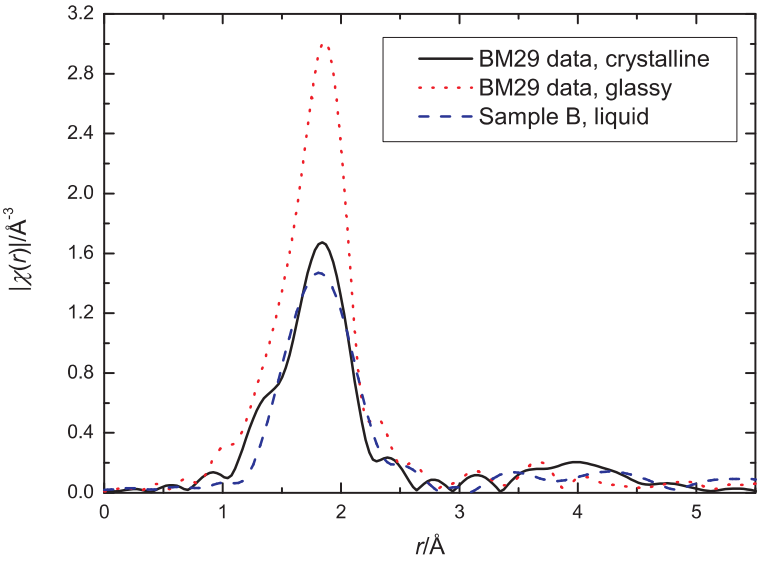

Figure 8.14: The $|\tilde{\chi}(R)|$ spectra for crystalline, glassy and liquid $ZnCl_2$. The solid and dotted lines give the data taken for crystalline and glassy $ZnCl_2$ measured under ambient conditions using BM29 (see chapter 7), respectively, while the dashed line gives the data taken for liquid $ZnCl_2$ at 306(50) °C and ambient pressure using ID24.

8.5 EXAFS Refinement

In this section, the structural models for liquid $ZnCl_2$ are described. The models were refined using $\tilde{\chi}(R)$ obtained from the measured $k^2\chi(k)$ function for sample B at 306(50) °C and ambient pressure and for sample A at either 517(50) °C and 1.0(1) GPa or at 750(50) °C and 2-3 GPa. The parameters obtained from the refinement procedure are discussed.

The first structural model (model 1) for liquid $ZnCl_2$ at ambient pressure was obtained from an ND experiment, see chapter 6. The model comprises one Zn-Cl single scattering path with a Zn-Cl nearest neighbour distance of 2.27(1) Å and a Zn-Cl coordination number of 4. The second model (model 2) was obtained from the RMC method and was constructed by using ND results for liquid $ZnCl_2$ [235]. For this model, the local coordination environment of Zn was identified by using the program I.S.A.A.C.S [175] and the parameters are summarised in table 8.1. Five single scattering paths were included in the model, corresponding to $ZnCl_2$, $ZnCl_3$, $ZnCl_4$, $ZnCl_5$ and $ZnCl_6$ units, with different average Zn-Cl nearest neighbour distances. The relative contribution to the model from each structural unit was chosen to be the same as the abundance given in table 8.1. The same values for ΔR and σ^2 were used for each scattering path.

As suggested by the variety of local coordination environments for Zn in the RMC model, it is sensible to add the cumulants C_3 and C_4 as variables to model 1. However, the local structure of Zn is quite well defined as shown by the symmetrical first peak in the $G_N(r)$ and $G_X(r)$ functions measured at several temperatures and ambient pressure using ND and XRD, see figure 6.26. It was found that incorporation of the third cumulant is enough to improve the fit using model 1 and that if both C_3 and C_4 are allowed to vary the fit becomes unstable and gives a negative σ^2 value. To investigate the effect of C_3 on the refined parameters, two sets of variables were used. In model 1-i, the variables were S_0^2, ΔE_0, ΔR and σ^2, and in model 1-ii, the variables were S_0^2, ΔE_0, ΔR, σ^2 and C_3. As C_3, ΔR and ΔE_0 are highly correlated, the data were also fitted using another set of variables (model 1-iii), namely ΔR, σ^2 and C_3 with the values for S_0^2 and ΔE_0 fixed at 0.7 and 4 eV, respectively, which are the values obtained from the fit using model 2.

Coordination number	Abundance (%)	$R_{\text{Zn-Cl}}$ (Å)	Standard deviation (Å)
2	0.2	2.30(5)	0.06
3	14.5	2.27(17)	0.06
4	74.2	2.30(16)	0.05
5	10.4	2.39(14)	0.04
6	0.7	2.46(4)	0.03

Table 8.1: Coordination numbers, abundance and average atomic distances for the different types of Zn-Cl structural units present in liquid $ZnCl_2$ at ambient pressure as obtained from an RMC model [235].

The models were fitted to $\tilde{\chi}(R)$ obtained from the $k^2\chi(k)$ function measured for sample B at 306(50) °C and ambient pressure with a k range from 2.4 to 7.9 Å^{-1} and an R range from 1 to 3 Å. The fits in k- and R-space are shown in figure 8.15. The refined parameters, $\mathcal{R}$-factor and χ^2_ν values for each fit are summarised in table 8.2.

Variable	Model 1-i	Model 1-ii	Model 1-iii	Model 2
$\mathcal{R}$-factor (%)	1.7	0.7	1.5	1.6
χ^2_ν	69	47	46	67
S_0^2	0.7(1)	0.8(2)	0.7*	0.7(1)
E_0 (eV)	4(2)	7(2)	4*	4(1)
$R_{\text{Zn-Cl}}$ (Å)/degeneracy	2.31(2)/4	2.38(5)/4	2.32(2)/4	2.30(2)/2
				2.27(2)/3
				2.30(2)/4
				2.39(2)/5
				2.46(2)/6
$\sigma^2_{\text{Zn-Cl}}$ (Å^2)	0.006(3)	0.006(3)	0.005(1)	0.005(3)
C_3	-	0.002(1)	0.005(7)	-

Table 8.2: The refined atomic distances and values for σ^2, S_0^2 and ΔE_0 together with the $\mathcal{R}$-factor and χ^2_ν values obtained from fits to $\tilde{\chi}(R)$ obtained from the $k^2\chi(k)$ function measured for liquid $ZnCl_2$ at 306(50) °C and ambient pressure (sample B). The asterisks mark those parameters that were fixed during a fit.

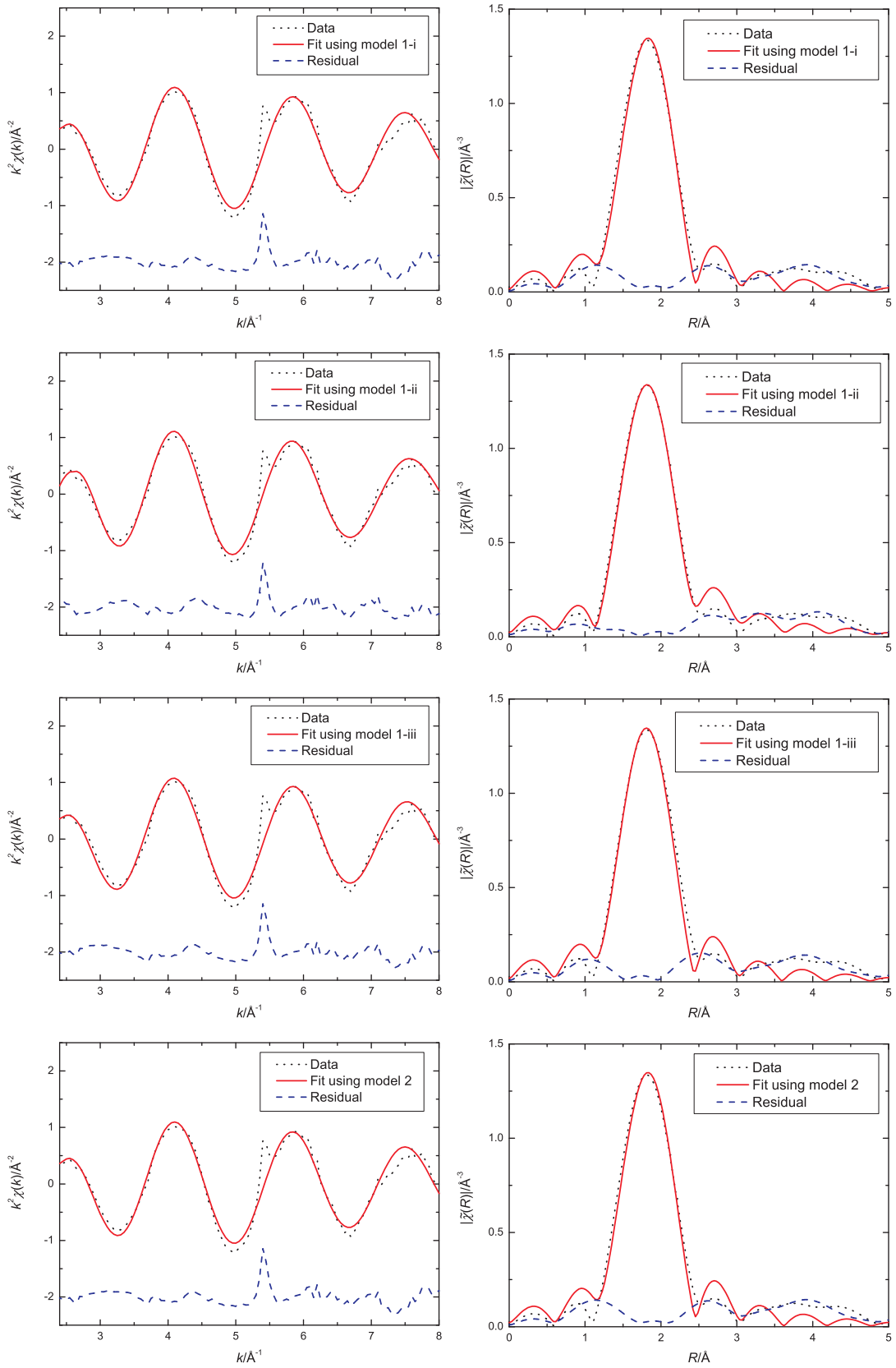

Figure 8.15: The $k^2\chi(k)$ and corresponding $|\tilde{\chi}(R)|$ functions for liquid $ZnCl_2$ at 306(50) °C and ambient pressure as measured for sample B using ID24. The dotted lines give the data, the solid lines give the fits and the dashed lines give the residuals.

As shown in figure 8.15, all model gives reasonably good fits. From table 8.2, the refined Zn-Cl distance from model 1-i and the average Zn-Cl distance of 2.31(2) Å obtained from model 2 are the same, within the error. The distance is comparable to the ND result (chapter 6) but different to the value obtained from the fit using model 1-ii. As ΔR, ΔE_0 and C_3 were allowed to vary during the fit using model 1-ii, the shift of the refined Zn-Cl value could result from a correlation between these three parameters. In fact, both the refined Zn-Cl distance and ΔE_0 value obtained from the fit using model 1-ii are significantly different to the values obtained using models 1-i and 2. In ARTEMIS, the degree of correlation between variables ranges from 0 for no correlation to ± 1 for complete correlation. For the fit using model 1-ii, the pairs of variables ΔR-ΔE_0, ΔR-C_3 and ΔE_0-C_3 have degrees of correlation of 0.9, 1.0 and 0.9, respectively. Although there is a correlation between ΔR-C_3 in the fit using model 1-iii, the fits using models 1-i and 1-iii give a similar refined Zn-Cl distance which suggests that a sensible value for ΔR can still be obtained when C_3 is varied provided ΔE_0 is fixed.

The $\mathcal{R}$-factor and χ^2_ν values corresponding to the fit using model 1-iii are better than those corresponding to model 1-i which suggests that C_3 is important to the fit i.e. that the local structure of the liquid is significantly more disordered than glassy $ZnCl_2$ (chapter 7). Model 2, based on an RMC analysis of the ND data [235], is also consistent with the EXAFS data measured at 306(50) °C.

If we assume that, like crystalline $ZnCl_2$ (chapter 7), Zn remains 4-fold coordinated at pressures below 1 GPa, models 1 and 2 can also be refined using the data measured for sample A at 517(50) °C and 1.0(1) GPa. Models 1-i, 1-ii, 1-iii and 2 were therefore refined using $\tilde{\chi}(R)$ obtained from the $k^2\chi(k)$ function measured for sample A at 517(50) °C and 1.0(1) GPa with a k range from 2.4 to 6.3 Å^{-1} and an R range from 1 to 3 Å. The fits in k- and R-space are shown in figure 8.16. The refined parameters, $\mathcal{R}$-factor and χ^2_ν values for each fit are summarised in table 8.3.

As shown in figure 8.16, all models give reasonably good fits. From table 8.3, the fit using model 1-ii gives a refined Zn-Cl distance that is different to the other models due to a correlation between ΔR, ΔE_0 and C_3. For models 1-i, 1-iii and 2, the refined Zn-Cl distances are about 0.03 Å smaller than those for the measurement

Variable	Model 1-i	Model 1-ii	Model 1-iii	Model 2
$\mathcal{R}$-factor (%)	1.2	0.41	0.93	0.87
χ^2_ν	107	75	56	210
S_0^2	0.5(1)	0.5(1)	0.5*	0.5(2)
E_0 (eV)	2(2)	6(3)	2*	2(3)
$R_{\text{Zn-Cl}}$ (Å)/degeneracy	2.27(2)/4	2.39(8)/4	2.29(2)/4	2.26(2)/2
				2.23(2)/3
				2.26(2)/4
				2.35(2)/5
				2.42(2)/6
$\sigma^2_{\text{Zn-Cl}}$ (Å^2)	0.004(5)	0.005(4)	0.004(1)	0.003(7)
C_3	-	0.005(3)	0.001(1)	-

Table 8.3: The refined atomic distances and values for σ^2, S_0^2 and ΔE_0 together with the $\mathcal{R}$-factor and χ^2_ν values obtained from fits to $\tilde{\chi}(R)$ obtained from the $k^2\chi(k)$ function measured for liquid $ZnCl_2$ at 517(50) °C and 1.0(1) GPa (sample A). The asterisks mark those parameters that were fixed during a fit.

made at 306(50) °C and ambient pressure which could be due to compression of the structural motif at elevated pressure. Similar behaviour is observed in crystalline $ZnCl_2$ under pressure where the Zn-Cl distance decreases by ≈0.01 Å when the pressure is increased at room temperature from ambient to 2.2(1) GPa (see chapter 7).

As shown in table 8.3, the refined S_0^2 values are much smaller than typical values of around 0.7-1.10 [50, 54]. As both S_0^2 and the Zn-Cl coordination number N make a significant contribution to the amplitude of the $\chi(k)$ function, the unusually low value for S_0^2 could indicate an improper value for N. However, when S_0^2 was set to 0.7 (the value obtained from the measurement of sample B made at ambient pressure, table 8.2) in model 1-i, the refined N value is 2.8(7) which is an unlikely coordination number given the elevated pressure. Therefore, the low value of S_0^2 observed from the refinement is most likely due to the integrity of sample A during the measurement e.g. loss of the sample to the vacuum.

For the measurement of sample A made at 750(50) °C and 2-3 GPa, models 1-i, 1-iii and 2 were fitted to the data. Models 1-i and 2 gave bad fits to the data, with $\mathcal{R}$-factors of 4.6 and 3.0 %, respectively. As the energy calibration for

the ID24 beamline should be stable during the measurements owing to the energy dispersive setup, the value of ΔE_0 for this measurement should be the same as for the measurement on sample A made at 517(50) °C and 1.0(1) GPa. Also, as both measurements were performed on the same sample the values for S_0^2 should also be the same. The measured EXAFS signals and the fits in k- and R-space to model 1-iii are shown in figure 8.17. The refined parameters, $\mathcal{R}$-factor and χ_ν^2 values for the fit are summarised in table 8.4.

Variable	
$\mathcal{R}$-factor (%)	1.9
χ_ν^2	48
$R_{\text{Zn-Cl}}$ (Å)/degeneracy	2.46(3)/4
$\sigma^2_{\text{Zn-Cl}}$ (Å^2)	0.009(2)
C_3	0.008(2)

Table 8.4: The refined atomic distance and σ^2 value together with the $\mathcal{R}$-factor and χ_ν^2 values obtained from a fit to $\tilde{\chi}(R)$ obtained from the $k^2\chi(k)$ function measured for liquid $ZnCl_2$ at 750(50) °C and 2-3 GPa (sample A). The S_0^2 and ΔE_0 parameters were fixed at 0.5 and 2 eV during the fit.

From table 8.4, the refined Zn-Cl nearest neighbour distance of 2.46(3) Å is much higher than the values obtained from the measurements made at lower pressures. The increase in the nearest neighbour distance due to increasing pressure could indicate a change in the Zn coordination environment from 4- to 6-fold as observed in crystalline $ZnCl_2$ (chapter 7). It should be mentioned that the refined Zn-Cl distance was, within the error, unchanged when the data were fitted using model 1-iii in which the Zn-Cl coordination number had been changed from 4 to 6. In this fit, however, the $\sigma^2_{\text{Zn-Cl}}$ value became 0.018(3) Å^2 and the $\mathcal{R}$-factor increased to 2.6%. As S_0^2, σ^2 and coordination have strong contributions to the amplitude of the $k^2\chi(k)$ or $\tilde{\chi}(R)$ function, as seen from the EXAFS equation 2.64, the change in coordination number would affect the S_0^2 and σ^2 values. If in this fit the S_0^2 parameter was allowed to vary, values for S_0^2 and $\sigma^2_{\text{Zn-Cl}}$ of 0.3(1) and 0.010(7) Å^2 were obtained, respectively, the $\mathcal{R}$-factor improved to 1.1%, and the Zn-Cl distance was still unchanged. As mentioned earlier, the unusually low S_0^2 value obtained from the refinement of sample A could be due to loss of the sample to the vacuum. It is

therefore difficult to extract the coordination number directly from the data.

As seen in figure 8.12, the XANES spectrum corresponding to the measurement of sample A made at 750(50) °C and 2-3 GPa does not contain a signature of 4-fold or 6-fold coordinated Zn in a crystalline $ZnCl_2$ phase. Three peaks in the range from $E = 9.67$ to 9.70 keV are not observed nor the big dip at $E \approx 9.67$ keV as shown in figures 8.8 and 8.10, respectively. It is, therefore, likely that the sample was in a molten state. However, as no diffraction data were taken at this temperature and pressure, the molten state could not be confirmed. It is therefore possible that the sample was partially molten such that the measured Zn-Cl nearest neighbour distance corresponds to crystalline $ZnCl_2$ which would have an octahedral or distorted octahedral Zn coordination environment in this pressure range.

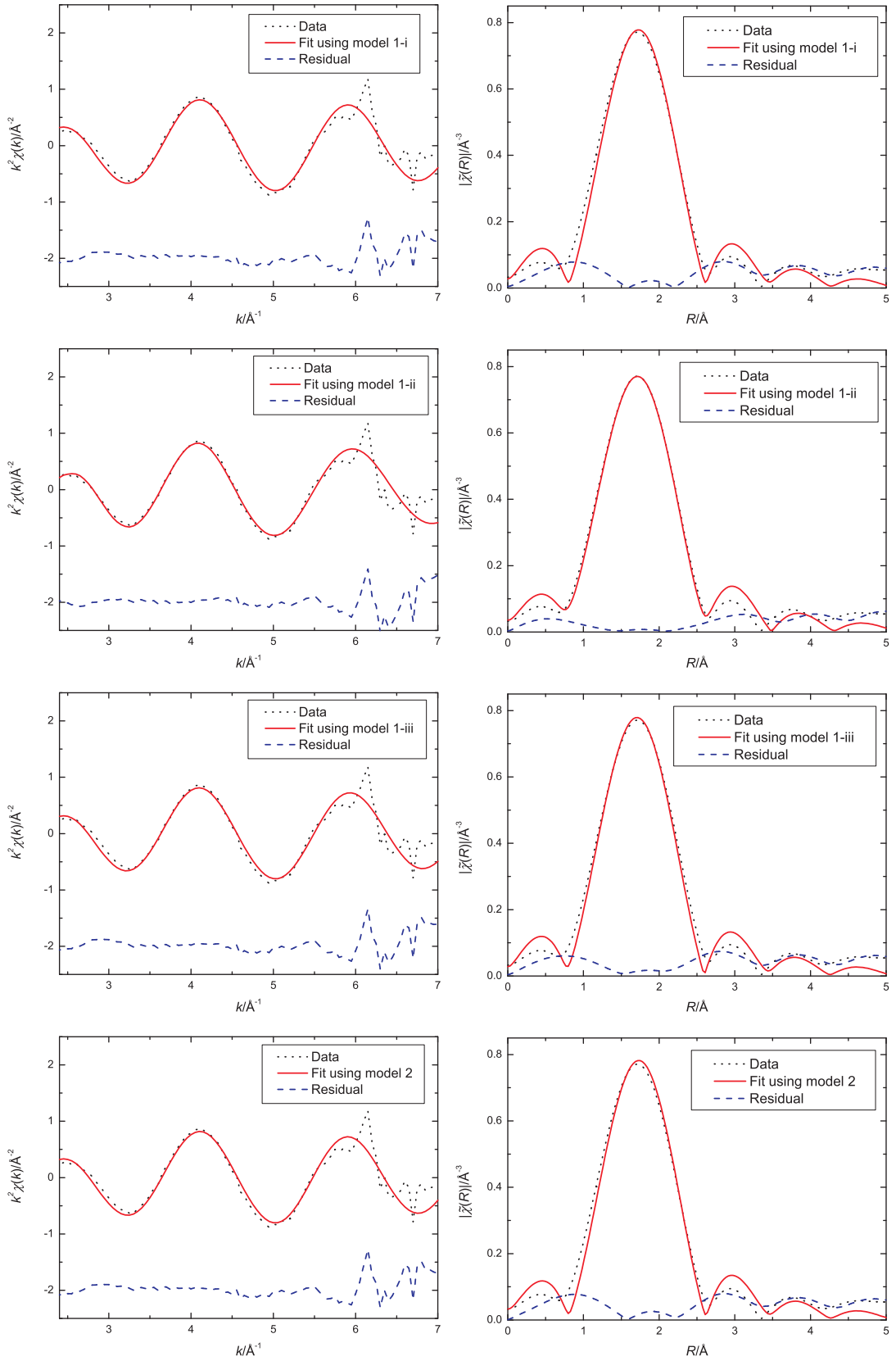

Figure 8.16: The $k^2\chi(k)$ and corresponding $|\tilde{\chi}(R)|$ function for liquid $ZnCl_2$ at 517(50) °C and 1.0(1) GPa as measured for sample A using ID24. The dotted lines give the data, the solid lines give the fits and the dashed lines give the residuals.

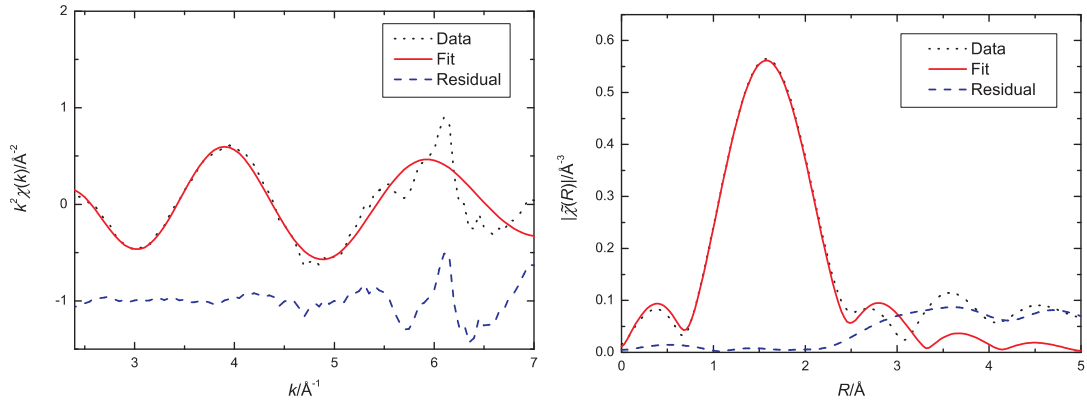

Figure 8.17: The $k^2\chi(k)$ and corresponding $|\tilde{\chi}(R)|$ functions for liquid $ZnCl_2$ at 750(50) °C and 2-3 GPa as measured for sample A using ID24. The dotted lines give the data, the solid lines give the fits and the dashed lines give the residuals.

8.6 Conclusion

The agreement between the XAS measurements for $ZnCl_2$ taken at room temperature and several pressure conditions using BM29 (chapter 7) and similar thermodynamic conditions using ID24 suggests that no reaction took place between the sample and BN or between the sample and Re during the ID24 experiment. The experimental $k^2\chi(k)$ functions for the measurements made at 306(50) °C and ambient pressure or at 517(50) °C and 1.0(1) GPa are consistent with a model in which Zn has a first coordination shell of 4 Cl atom as found from the ND results described in chapter 6 and from the model obtained from the RMC method [235].

The refined Zn-Cl nearest neighbour distance for liquid $ZnCl_2$ at 306(50) °C and ambient pressure is 2.32(2) Å for the model comprising one coordination shell or 2.31(2) Å for the RMC model. These are comparable to a value of 2.27(1) Å obtained from the ND and XRD results described in chapter 6 which were obtained at several temperatures and ambient pressure. As the pressure increases from ambient to 1 GPa, the Zn-Cl nearest neighbour distance decreases by about 0.03 Å. For the measurement made at 750(50) °C and 2-3 GPa, the measured data could not be fitted using the RMC model which suggests a considerably different local coordination environment for Zn. From the model comprising only a first coordination shell, the refinement gives a Zn-Cl nearest neighbour distance of 2.46(3) Å which is much larger than the value obtained at 517(50) °C and 1.0(1) GPa, suggesting that Zn is 6-fold coordinated at this thermodynamic state point. As the XANES spectrum corresponding to this measurement does not contain a signature of 4-fold or 6-fold coordinated Zn in a crystalline $ZnCl_2$ phase. Three peaks in the range from $E =$ 9.67 to 9.70 keV are not observed nor the big dip at $E \approx 9.67$ keV as shown in figures 8.8 and 8.10, respectively. It is, therefore, likely that the sample was in a molten state. However, as no diffraction patterns for the sample or for the temperature and pressure markers were measured, additional experiments are required to confirm a phase transformation to the liquid state. It should be noted that an energy dispersive setup with the DAC is suitable for this system as the sample size is small such that no matrix material is required. However, alternative options for heating the sample such as the use of different heating elements, the use of a whole-cell heater [239] or

the use of induction coils to indirectly heat the sample by heating the Re gasket and diamond seats [240], should be considered.

Chapter 9

Overall Conclusions

In this thesis structural information on several amorphous systems was obtained from ND, high energy XRD and EXAFS spectroscopy experiments. MD simulation and RMC modeling were also used to extract additional structural information. In this chapter, the key results and conclusions are summarised and some suggestions are given for future work.

In chapter 4 the structures of three molten alloys at or near their eutectic compositions, namely $Au_{0.81}Si_{0.19}$, $Au_{0.72}Ge_{0.28}$ and $Ag_{0.74}Ge_{0.26}$, were investigated by using ND. The results show that the Au-Au and Au-Si nearest neighbour distances in molten $Au_{0.81}Si_{0.19}$ are 2.83(2) and $\approx$ 2.4 Å, respectively. The former is similar to the Au-Au nearest neighbour distance found in liquid Au [40, 129] and the latter agrees with the results obtained from MD simulations [129, 132] which suggest association of Au and Si atoms and the possible existence of Si-centred clusters. The structure of molten $Ag_{0.74}Ge_{0.26}$ was found to be similar to the structure of the eutectic composition $Ag_{0.76}Ge_{0.24}$ [41]. Small pre-peaks in the $F(q)$ functions at 1.3(2) and 1.6(3) $Å^{-1}$ were observed for the molten $Au_{0.72}Ge_{0.28}$ and $Ag_{0.74}Ge_{0.26}$ alloys, respectively, which suggests some degree of intermediate range ordering.

For these alloys, the large r behaviour of the $rG(r)$ and $r^{0.69}G(r)$ functions agrees with a theoretical prediction based on simple pair potentials [113] and with a fractal model for metallic glasses [114], respectively. For the prediction based on pair potentials, the agreement could be due to the fact that $rG(r)$ is dominated

by one pair correlation function in the case of the $Au_{0.81}Si_{0.19}$ alloy and that the two dominant correlations for the $Au_{0.72}Ge_{0.28}$ and $Ag_{0.74}Ge_{0.26}$ alloys have similar decay lengths and wavelengths of oscillation. For the prediction based on a fractal model, the agreement could be due to the structural similarity between the molten alloys and the metallic glasses of which the prediction was derived from i.e. both systems give the same fractal dimension of 2.31 as obtained from a relation between the measured densities and the position of the first peak in the measured $F(q)$ functions.

In chapter 5 the structure of $(R_2O_3)_{0.2}(Al_2O_3)_{0.2}(SiO_2)_{0.6}$ glasses at room temperature, where R denotes Dy, Ho or a 50:50 mixture of Dy and Ho, was investigated by using a combination of the isomorphic substitution method in ND, XRD and EXAFS spectroscopy. The correlation functions in real space obtained from ND and XRD give R-R, R-O and O-O nearest neighbour distances of 3.65(2) - 3.7(1), 2.31(3) - 2.35(3) and 2.63(5) - 2.69(5) Å, respectively. The Al-O and Si-O nearest neighbours distances correspond to a combined peak position at 1.62(2) - 1.64(2) Å in the ND results and 1.74(3) Å in the XRD results. The difference functions obtained from the isomorphic substitution method in ND give R-R and R-O coordination numbers of 4.6(1) and 7.2(3), respectively. If the Si-O coordination number is assumed to be 4, which is the value obtained from an NMR study on glassy $La_{0.66}SiAl_{0.55}O_{3.81}$ [164], an Al-O coordination number in the range 4.2(1) - 4.9(2) with an average value of 4.5(1) is obtained. The latter is, within the experimental error, the same as the average Al-O coordination number of 4.3(1) obtained from an NMR spectroscopy study of glassy $(Y_2O_3)_{0.2}(Al_2O_3)_{0.2}(SiO_2)_{0.6}$ [35, 147]. The EXAFS results indicate similarity between the local environments of Dy and Ho in the glass and justify use of the isomorphic substitution method.

A 3D model for the glasses was constructed by using the MD-RMC method. The MD simulation was driven by using Coulomb and Buckingham potentials with the potential parameters obtained from previous MD simulations [145, 173]. The $F(q)$ functions measured using ND for the $(R_2O_3)_{0.2}(Al_2O_3)_{0.2}(SiO_2)_{0.6}$ glass, where R denotes Dy, Ho or a 50:50 mixture of Dy and Ho, the $S_X(q)$ function measured using XRD for the $(Dy_2O_3)_{0.2}(Al_2O_3)_{0.2}(SiO_2)_{0.6}$ glass and all of the first order dif-

ference (FOD) and total minus weighted difference (TMWD) functions obtained from the isomorphic substitution method in ND were used to constrain the RMC model which used the MD model as a starting configuration. A Si-O coordination number of 4 and a relative fractions of AlO_4, AlO_5 and AlO_6 units obtained from the NMR experiment [35, 147] were used as coordination constraints. The R-O local configurations obtained from the RMC model correspond to 8(1), 35.5(20), 42(2), 14(1) and 0.5(3)% of RO_5, RO_6, RO_7, RO_8 and RO_9 units, respectively. A fit to the EXAFS $\tilde{\chi}(R)$ function, obtained from the measured $k^3\chi(k)$ function, using the RMC model gives an average R-O distance of 2.27(1) Å for the Dy based glass and 2.26(1) Å for the Ho based glass. $\sigma^2_{\text{R-O}}$ values of 0.013(2) Å^2 and 0.014(2) Å^2 were also obtained for the Dy and Ho glasses, respectively. The EXAFS signal is consistent with the presence of second and third coordination shells of R-Al and R-Si correlations, respectively. The refined R-Al and R-Si distances are 3.15(3) and 3.6(1) Å, respectively, which are consistent with the ND results. The $\sigma^2_{\text{R-Al}}$ and $\sigma^2_{\text{R-Si}}$ values are 0.019(3) and 0.06(3) Å^2, respectively, for the Dy based glass and 0.021(4) and 0.05(3) Å^2, respectively, for the Ho based glass.

In chapter 6 the structure of glassy and liquid $ZnCl_2$ was investigated by using ND and XRD experiments which were performed at room temperature, 328(1), 340(1), $\simeq$ 430, $\simeq$ 530, $\simeq$ 630 and 704(2)°C (mp = 290°C and bp = 732°C [42]). At every measured temperature, the structural unit of $ZnCl_2$ is a well defined $ZnCl_4$ tetrahedon. The FSDP at $\approx$ 1 Å^{-1} in the $F(q)$ function measured at room temperature remains intact with increasing temperature and only a small shift towards lower q can be observed. The existence of an FSDP at high temperatures indicates the persistence of a network structure which could be due to the ionic nature of the melt. The shift in the position of the FSDP suggests a longer periodicity associated with the intermediate range order. The results also show a decrease of the average Zn-Cl coordination number and indicate a smaller Zn-Zn distance as the temperature increases. This supports the promotion of edge sharing connections between $ZnCl_4$ tetrahedra as suggested by Raman spectroscopy results [36].

In chapter 7 the structure of glassy and crystalline $ZnCl_2$ under several thermodynamics conditions was investigated by using XAS. The XANES spectra of the

starting materials show that glassy $ZnCl_2$ can be crystalised when it is subjected to the pressure applied during preparation of a pellet. Intercalation of $ZnCl_2$ into the layered structure of hexagonal BN, which was used as a matrix material, was observed. The XANES or EXAFS spectra of the starting material could not be recovered when a mixture of $ZnCl_2$ and BN was heated and cooled in cycles. When the mixture was held in a pressure cell, the melting temperature at several pressures was much higher than quoted in reference [182].

The refinement of $\tilde{\chi}(R)$ obtained from the measured $k^2\chi(k)$ function for glassy $ZnCl_2$ using i) a model comprising one Zn-Cl coordination shell with a Zn-Cl coordination number of 4 or ii) a model comprising the first three coordination shells of the crystalline δ-$ZnCl_2$ structure both give a Zn-Cl nearest neighbour distance of 2.285(5) Å, which agrees with the ND results [180], and a $\sigma^2_{\text{Zn-Cl}}$ value of 0.0054(7) Å^2. The measured EXAFS signal is also consistent with the first coordination shell of Zn found in an RMC model for glassy $ZnCl_2$. The model was constructed using ND and XRD results [235] and Zn is predominantly 4-fold coordinated. For crystalline $ZnCl_2$, a press pelleted sample of $ZnCl_2$ under ambient conditions has the γ-$ZnCl_2$ structure in which Zn is 4-fold coordinated by Cl atoms. At intermediate pressures of 2.2(1) and 3.8(1) GPa, the local environment of Zn corresponds to a distorted octahedron as in the $AuTe_2$ type structure. At 4.7(1) GPa, Zn is octahedrally coordinated as in the CdI_2-2H, CdI_2-4H or $CdCl_2$(3R) type structures. Regarding the Zn-Cl distance, the evolution with pressure of the Zn-Cl nearest neighbour distance or, in the case of the intermediate phase, the weighted average of the nearest neighbour and next nearest neighbour distances, follows the same trend as in reference [183, 220], although a slower change is observed.

In chapter 8 the structure of liquid $ZnCl_2$ measured at 306(50) °C and ambient pressure, at 517(50) °C and 1.0(1) GPa or at 750(50) °C and 2-3 GPa was investigated by using EXAFS spectroscopy. A refinement of the $\tilde{\chi}(R)$ functions obtained from the measured $k^2\chi(k)$ functions for the measurements made at i) 306(50) °C and ambient pressure and ii) 517(50) °C and 1.0(1) GPa using a model in which Zn has a first coordination shell of 4 Cl atoms gives Zn-Cl nearest neighbour distances of 2.32(2) and 2.29(2) Å, respectively. The RMC model obtained using the ND

results for liquid $ZnCl_2$ measured at ambient pressure, which comprises 0.2, 14.5, 74.2, 10.4 and 0.7% of $ZnCl_3$, $ZnCl_4$, $ZnCl_5$ and $ZnCl_6$ units, respectively, [235] acts as a suitable starting point for refinement of the measurements made at 306(50) °C and ambient pressure and at 517(50) °C and 1.0(1) GPa. For the measurement made at 750(50) °C and 2-3 GPa, the refined Zn-Cl nearest neighbour distance is 2.46(3) Å which is much larger than the value obtained at lower pressures. This suggests that Zn is 6-fold coordinated at this thermodynamic state point. As the XANES spectrum corresponding to this measurement does not contain a signature of 4-fold or 6-fold coordinated Zn in a crystalline $ZnCl_2$ phase, it is likely that the sample was in a molten state. However, as no diffraction patterns for the sample or for the temperature and pressure markers were measured, a phase transformation to the liquid state could not be confirmed.

Additional experiments and modeling would improve our understanding about the systems of interest. As both ND and XRD data for molten $Au_{0.81}Si_{0.19}$, $Au_{0.72}Ge_{0.28}$, $Ag_{0.74}Ge_{0.26}$ and $ZnCl_2$ at several temperatures and ambient pressure are available, RMC models could be made or improved. In this way, additional information such as the structural differences between the glass former $Au_{0.81}Si_{0.19}$ and the non glass formers $Au_{0.72}Ge_{0.28}$, $Ag_{0.74}Ge_{0.26}$ could be studied. For $ZnCl_2$, the change in the connectivity between the $ZnCl_4$ tetrahedral units as a function of temperature could be investigated. Fluorescence lifetime measurements could be useful for the rare-earth alumino-silicate glasses. It would be interesting to test whether the concentration of Al_2O_3 in R_2O_3-Al_2O_3-SiO_2 glasses reduces the concentration quenching effect observed in rare-earth doped SiO_2 glasses. By studying a range of compositions, the relation between the structure and corresponding change in the fluorescence lifetime could be investigated. Another EXAFS measurements on liquid $ZnCl_2$ under extreme conditions could be made to confirm whether 6-fold coordinated Zn exists at high pressures. An energy dispersive setup with the DAC is suitable for this system as the sample size is small such that no matrix material is required. However, alternative options for heating the sample such as the use of different heating elements, the use of a whole-cell heater [239] or the use of induction coils to indirectly heat the sample by heating the Re gasket and diamond seats [240], should be considered.

Bibliography

[1] B. S. Lee and J. R. Abelson, Journal of Applied Physics **97**, 093509 (2005).

[2] N. Yamada et al., Journal of Applied Physics **69**, 2849-2856 (1991).

[3] V. I. Klimov et al., Science **290**, 314-317 (2000).

[4] B. D. Cullity and S. R. Stock, *Elements of X-ray Diffraction*, Prentice Hall, Upper Saddle River, 2001.

[5] G. L. Squires, *Introduction to the Theory of Thermal Neutron Scattering*, Cambridge University Press, Cambridge, 1978.

[6] P. A. Egelstaff, *An introduction to the liquid state*, Oxford University Press, Oxford, 1994.

[7] N. E. Cusack, *The physics of structurally disordered matter: an introduction*, IOP Publishing Ltd, Bristol, 1987.

[8] S. R. Elliott, *Physics of amorphous materials*, Longman Scientific & Technical, New York, 1990.

[9] R. Zallen, *The Physics of amorphous solids*, John Wiley & Sons Ltd, New York, 1983.

[10] P. M. Ossi, *Disordered Materials, An Introduction*, Springer, Leipzig, 2008.

[11] P. W. Anderson, Science **267**, 1609-1618 (1995).

[12] A. G. Kalampounias, S. N. Yannopoulos and G. N. Papatheodorou, The Journal of Chemical Physics **124**, 014504 (2006).

[13] P. S. Salmon and I. Petri, Journal of Physics Condensed Matter **15**, S1509-S1528 (2003).

[14] S. Biggin and J. E. Enderby, Journal of Physics C: Solid State Physics **14**, 3129 (1981).

[15] R. Simone and M. Wuttig, *Phase Change Materials: Science and Application*, Springer, New York, 2008.

[16] Y. Le Godec et al., Journal of Synchrotron Radiation **16**, 513-523 (2009).

[17] S. Pasternak et al., Review of Scientific Instruments **33**, 2635-2639 (1962).

[18] L. H. V. Vlack, *Elements of Material Science and Engineering*, *Addison-Wesley series in metallurgy and materials*, chapter 3: Crystals (Atomic Order), page 78, Addison-Wesley Publishing Company, Reading, 1975.

[19] V. V. Brazhkin and A. G. Lyapin, Journal of Physics: Condensed Matter **15**, 6059-6084 (2003).

[20] M. Wilding, M. Wilson and P. F. McMillan, Chemical Society Reviews **35**, 964-986 (2006).

[21] P. H. Poole et al., Science **275**, 322-323 (1997).

[22] G. N. Greaves and S. Sen, Advances in Physics **56**, 1-166 (2007).

[23] B. Bureau et al., Solid State Science **10**, 427-433 (2008).

[24] V. G. Ta'eed et al., Optics Express **15**, 9205 (2007).

[25] C. Tsay et al., Optics Letters **35**, 3324-3326 (2010).

[26] P. M. Peters and S. N. Houde-Walter, Journal of Non-Crystalline Solids **239**, 162-169 (1998).

[27] B. E. Warren, *X-ray Diffraction*, Dover Publications, New York, 1990.

[28] H. E. Fischer, A. C. Barnes and P. S. Salmon, Reports on Progress in Physics **69**, 233-299 (2006).

[29] J. C. Wasse and P. S. Salmon, Journal of Physics Condensed Matter **11**, 1381-1396 (1999).

[30] Y. Waseda, *Novel application of anomalous (resonance) X-ray scattering for structural characterization of disordered materials*, Springer, Berlin, 1984.

[31] D. C. Koningsberger and R. Prins, *X-Ray Absorption: Principles, Applications, Techniques of EXAFS, SEXAFS, and XANES*, A Wiley-Interscience, Toronto, 1988.

[32] M. Benfatto and S. Della Longa, Journal of Synchrotron Radiation **8**, 1087-1094 (2001).

[33] P. J. Hore, *Nuclear magnetic resonance*, Oxford University Press, Oxford, 1995.

[34] E. Smith and G. Dent, *Modern Raman spectroscopy: a practical approach*, John Wiley & Sons Ltd, Chichester, 2005.

[35] T. Schaller and J. F. Stebbins, Journal of Chemical Physics **102**, 10690-10697 (1998).

[36] S. N. Yannopoulos et al., Physical Review A **7**, 2130-2144 (1973).

[37] *The DL_POLY_2 User Manual*, W. Smith, T. R. Forester and I. T. Todorov, STFC Daresbury Laboratory, Warrington, January, 2009.

[38] M. P. Allen, *Computational Soft Matter: From Synthetic Polymers to Proteins*, volume 23 of *John von Neumann Institut für Computing Series*, edited by N. Attig et al., page 1-28, Gustav-Stresemann-Institut, Bonn, 2004.

[39] R. L. McGreevy, Journal of Physics Condensed Matter **13**, R887-R913 (2001).

[40] H. Fujii et al., Journal of Non-Crystalline Solids **353**, 2094-2098 (2007).

[41] M. C. Bellissent-Funel et al., Journal of Physics F: Metal Physics **7**, 2485-2494 (1977).

[42] http://www.webelements.com, June, 2008.

[43] V. F. Sears, Neutron News **3**, 26-29 (1992).

[44] J. L. Yarnell et al., Physical Review A **7**, 2130-2144 (1973).

[45] E. Balcar and S. W. Lovesey, *Theory of Magnetic Neutron and Photon Scattering*, Oxford University Press, New York, 1989.

[46] A. J. Freeman and J. P. Desclaux, Journal of Magnetism and Magnetic Materials **12**, 11-21 (1979).

[47] D. Waasmaier and A. Kirfel, Acta Crystallographica Section A **51**, 416-431 (1995).

[48] A. Zeidler et al., Journal of Physics Condensed Matter **21**, 474217 (2009).

[49] D. T. Cromer, Journal of Chemical Physics **50**, 4857-4859 (1969).

[50] E. A. Stern, *X-Ray Absorption: Principles, Applications, Techniques of EXAFS, SEXAFS, and XANES*, volume 92 of *Chemical Analysis: A Series of Monographs on Analytical Chemistry and Its Applications*, edited by D. C. Koningsberger and R. Prins, chapter 1: Theory of EXAFS, page 3, A Wiley-Interscience, Toronto, 1988.

[51] J. J. Rehr and R. C. Albers, Reviews of Modern Physics **72**, 621-653 (2000).

[52] P. J. Durham, *X-Ray Absorption: Principles, Applications, Techniques of EXAFS, SEXAFS, and XANES*, volume 92 of *Chemical Analysis: A Series of Monographs on Analytical Chemistry and Its Applications*, edited by D. C. Koningsberger and R. Prins, chapter 2: Theory of XANES, page 53, A Wiley-Interscience, Toronto, 1988.

[53] M. G. Newville, *Local Thermodynamic Measurements of Dilute Binary Alloys Using XAFS*, PhD thesis Unversity of Washington, 1995.

[54] S. D. Kelly, http://xafs.org/Workshops/APS2009, July, 2010.

[55] A. Filipponi et al., Physical Review B **53**, 15571-15576 (1996).

[56] T. A. Carlson, C. W. Nestor Jr and T. C. Tucker, Physical Review **169**, 27-36 (1968).

[57] J. J. Rehr et al., Journal of the American Chemical Society **113**, 5135-5140 (1991).

[58] E. D. Crozier, J. J. Rehr and R. Ingalls, *X-Ray Absorption: Principles, Applications, Techniques of EXAFS, SEXAFS, and XANES*, volume 92 of *Chemical Analysis: A Series of Monographs on Analytical Chemistry and Its Applications*,

edited by D. C. Koningsberger and R. Prins, chapter 9: Amorphous and Liquid Systems, page 373, A Wiley-Interscience, Toronto, 1988.

[59] J. W. Halley, *Statistical Mechanics: From First Principles to Macroscopic Phenomena*, chapter 6 Imperfect Gases, page 96, Cambridge University Press, New York, 2007.

[60] A. C. Davison, *Statistical Model*, *Cambridge Series in Statistical and Probabilistic Mathematics*, chapter 2 Variation, page 44, Cambridge University Press, New York, 2003.

[61] A. Filipponi, Journal of Physics Condensed Matter **13**, R23-R60 (2001).

[62] B. Ravel and M. Newville, Journal of Sychrotron Radiation **12**, 537-541 (2005).

[63] H. E. Fischer et al., Applied Physics A Materials Science & Processing **74**, S160-S162 (2002).

[64] A. Filipponi et al., Review of Scientific Instruments **71**, 2422-2432 (2000).

[65] S. Pascarelli et al., Journal of Synchrotron Radiation **13**, 351-358 (2006).

[66] http://www.esrf.eu/UsersAndScience/Experiments/StructMaterials/ID15, July, 2009.

[67] S. Kohara et al., Nuclear Instruments and Methods in Physics Research Section A: Accelerators, Spectrometers, Detectors and Associated Equipment **467-468**, 1030-1033 (2001).

[68] S. Kohara et al., Journal of Physics Condensed Matter **19**, 506101 (2007).

[69] A. C. Hannon, S. M. Bennington and S. Langridge, ISIS Neutron Training Course Booklet, Didcot, November, 2006.

[70] *The High Flux Reactor*, http://www.ill.eu/fileadmin/users_files/Other_Sites/YellowBook2008CDRom/page/pg.htm?rub=1_2, September, 2009.

[71] http://www.ill.eu/, September, 2009.

[72] P. J. Duke, *Synchrotron Radiation Production and Properties*, volume 3, Oxford University Press, Oxford, 2000.

[73] J. Als-Nielsen and D. McMorrow, *Elements of Modern X-ray Physics*, John Wiley & Sons Ltd, Chichester, 2000.

[74] http://www.esrf.eu/AboutUs/GuidedTour, June, 2009.

[75] http://www.lightsources.org/cms/?pid=1000098, July, 2009.

[76] http://www.xfel.eu/en/how-does-it-work/, September, 2009.

[77] http://www.spring8.or.jp/en/, July, 2009.

[78] http://www.ill.eu/instruments-support/instruments-groups/instruments/d4/characteristics/, June, 2009.

[79] A. Filipponi et al., Review of Scientific Instruments **74**, 2654-2663 (2003).

[80] S. M. Heald, *X-Ray Absorption: Principles, Applications, Techniques of EXAFS, SEXAFS, and XANES*, volume 92 of *Chemical Analysis: A Series of Monographs on Analytical Chemistry and Its Applications*, edited by D. C. Koningsberger and R. Prins, chapter 3: Design of an EXAFS experiment, page 87, A Wiley-Interscience, Toronto, 1988.

[81] E. A. Stern and K. Kim, Physical Review B **23**, 3781-3787 (1981).

[82] C. T. Chantler et al., *X-Ray Form Factor, Attenuation and Scattering Tables(version 2.1)[Online]*, Available: http://physics.nist.gov/ffast, October, 2008.

[83] http://www.esrf.eu/UsersAndScience/Experiments/ElectStructMagn/ID24/, June, 2009.

[84] J. C. Labiche et al., Review of Scientific Instruments **78**, 091301 (2007).

[85] H. H. Paalman and C. J. Pings, Journal of Applied Physics **33**, 2635-2639 (1962).

[86] A. K. Soper and P. A. Egelstaff, Nuclear Instruments and Methods **178**, 415-425 (1980).

[87] M. Newville et al., Physical Review B **47**, 14126-14131 (1993).

[88] *FEFFIT: Using FEFF to model XAFS data*, M. Newville, University of Chicago, Chicago, July, 1998.

[89] D. E. Sayers and B. A. Bunker, *X-Ray Absorption: Principles, Applications, Techniques of EXAFS, SEXAFS, and XANES*, volume 92 of *Chemical Analysis: A Series of Monographs on Analytical Chemistry and Its Applications*, edited by D. C. Koningsberger and R. Prins, chapter 6: Data Analysis, page 211, A Wiley-Interscience, Toronto, 1988.

[90] E. A. Stern, Physical Review B **48**, 9825-9827 (1993).

[91] J. F. Löffler, Intermetallics **11**, 529 (2003).

[92] J. Zhang and Y. Zhao, Nature **430**, 332-335 (2004).

[93] A. Inoue, Materials Transactions JIM **36**, 866-875 (1995).

[94] A. Inoue, T. Zhang and T. Masumoto, Journal of Non-Crystalline Solids **156**, 473-480 (1993).

[95] Y. Waseda et al., Science and Technology of Advance Materials **9**, 023003 (2008).

[96] H. W. Sheng et al., Nature **439**, 419-425 (2009).

[97] A. Di Cicco, A. Trapananti and S. Faggioni, Physical Review Letters **91**, 135505 (2003).

[98] T. Schenk et al., Physical Review Letters **89**, 075507 (2002).

[99] F. C. Frank, Proceedings of the Royal Society of London Series A, Mathematical and Physical Sciences **215**, 43-46 (1952).

[100] O. G. Shpyrko et al., Physical Review B **76**, 245436 (2007).

[101] Y. T. Cheng, L. Lin and K. Najafi, Journal of Microelectromechanical Systems **9**, 3-8 (2000).

[102] A. L. Pinardi et al., Physical Review B **79**, 045416 (2009).

[103] S. Kodambaka et al., Science **316**, 729-732 (2007).

[104] R. P. Anantatmula et al., Journal of Electronic Materials **4**, 445-463 (1975).

[105] J. Cheney and K. Vecchio, Journal of Alloys and Compounds **471**, 222-240 (2009).

[106] M. Klement, R. H. Willens and P. Duwez, Nature **187**, 869-870 (1960).

[107] O. G. Shpyrko et al., Science **313**, 77-80 (2006).

[108] T. U. Schülli et al., Nature **464**, 1174-1177 (2010).

[109] A. L. Greer, Nature **464**, 1137-1138 (2010).

[110] H. Okamoto and T. B. Massalski, Bulletin of Alloy Phase Diagrams **5**, 601-610 (1984).

[111] R. W. Olesinski and G. J. Abbaschian, Bulletin of Alloy Phase Diagrams **9**, 58-64 (1988).

[112] P. S. Pershan et al., Physical Review B **80**, 125414 (2009).

[113] R. Evans et al., Journal of Chemical Physics **100**, 591-603 (1994).

[114] D. Ma, A. D. Stoica and X. L. Wang, Nature Materials **8**, 30-34 (2009).

[115] W. G. Moffatt, *The handbook of binary phase diagrams*, Genium Pub. Corp., New York, 1976.

[116] Relavant references can be found in http://mcnp-green.lanl.gov/index.html, August, 2009.

[117] http://atom.kaeri.re.kr./cgi-bin/endfplot.pl, July, 2008.

[118] S. F. Mughabghab, *Atlas of neutron resonances : resonance parameters and thermal cross sections Z=1-100*, Elsevier, Amsterdam, 2006.

[119] V. Petkov et al., Physical Review Letters **85**, 3436-3439 (2000).

[120] *CRC handbook of chemistry and physics : a ready-reference book of chemical and physical data*, edited by D. R. Lide, chapter 6: Fluid Properties, page 6-5, CRC Press, Boca Raton, 2009.

[121] A. Bruson and M. Gerl, Journal of Applied Physics **53**, 3616-3619 (1982).

[122] J. Brillo, I. Egry and I. Ho, International Journal of Thermophysics **27**, 494-506 (2006).

[123] S. M. Chathoth et al., Applied Physics Letters **93**, 071902 (2008).

[124] R. M. Waghorne, V. G. Rivlin and G. I. Williams, Journal of Physics F: Metal Physics **6**, 147-156 (1976).

[125] S. Takeda, private communication, October, 2009.

[126] Ph. Mangin et al., Physical Review B **21**, 3047-3056 (1980).

[127] P. S. Salmon, Journal of Physics Condensed Matter **17**, S3537-S3542 (2005).

[128] W. Hoyer and R. Jödicke, Journal of Non-Crystalline Solids **192&193**, 102-105 (1995).

[129] S. H. Lee and G. S. Hwang, The Journal of Chemical Physics **127**, 224710 (2007).

[130] M. Watanabe et al., Journal of Crystal Growth **294**, 16-21 (2006).

[131] H. Kiumra et al., Applied Physics Letters **78**, 604-606 (2001).

[132] A. Pasturel et al., Physical Review B **81**, 140202 (2010).

[133] A. Filipponi and A. Di Cicco, Physical Review B **51**, 12322-12336 (1995).

[134] P. S. Salmon, Journal of Physics F: Metal Physics **18**, 2345-2352 (1988).

[135] S. Gruner, J. Marczinke and W. Hoyer, Journal of Non-Crystalline Solids **355**, 880-884 (2009).

[136] Y. Fujinaga et al., Journal of the Less Common Metals **170**, 277-286 (1991).

[137] F. G. Edwards et al., Journal of Physics C-Solid State Physics **8**, 3483-3490 (1975).

[138] R. J. F. Leote de Carvalho and R. Evans, Molecular Physics **83**, 619-654 (1994).

[139] P. S. Salmon, Journal of Physics Condensed Matter **18**, 11443-11469 (2006).

[140] S. Sen, Journal of Non-Crystalline Solids **261**, 226-236 (2000).

[141] V. McGahay and M. Tomozawa, Journal of Non-Crystalline Solids **159**, 246-252 (1993).

[142] K. Arai et al., Journal of Applied Physics **59**, 3430-3436 (1986).

[143] S. Sen et al., Physical Review B **74**, 100201 (2006).

[144] A. Monteil et al., Journal of Non-Crystalline Solids **348**, 44-50 (2004).

[145] J. Du, Journal of the American Ceramic Society **92**, 87-85 (2009).

[146] P. Florian et al., The Journal of Physical Chemistry B **111**, 9747-9757 (2007).

[147] J. F. Stebbins, private communication, May, 2009.

[148] P. M. Peters and S. N. Houde-Walter, Applied Physics Letters **70**, 541-543 (1997).

[149] P. S. Salmon and S. Xin, Physical Review B **58**, 6115-6123 (1998).

[150] P. S. Salmon, private communication, July, 2008.

[151] M. P. Allen and D. J. Tildesley, *Computer Simulation of Liquids*, Clarendon Press, Oxford, 1989.

[152] W. Smith and I. T. Todorov, Molecular Simulation **32**, 935-943 (2006).

[153] *RMCA version 3.14 Manual*, June, 2005.

[154] http://www.isis.rl.ac.uk/RMC/downloads/rmca.htm, 2009.

[155] G. Evrard and L. Pusztai, Journal of Physics: Condensed Matter **17**, S1-S13 (2005).

[156] http://www.szfki.hu/ nphys/rmc++/downloads.html, 2009.

[157] J. W. E. Drewitt, private communication, March, 2009.

[158] D. T. Cromer and J. B. Mann, The Journal of Chemical Physics **47**, 1892-1893 (1967).

[159] *International Tables for Crystallography*, volume C: Mathematical, Physical and Chemical Tables, edited by A. J. C. Wilson and E. Prince, Kluwer Academic Publisher, Dordrecht, 1999.

[160] *GNXAS package documentation*, A. Filipponi et al., University of Camerino, Camerino, 1992.

[161] A. C. Thompson et al., *X-Ray Data Booklet(second edition)[Online]*, Available: http://xdb.lbl.gov/xdb.pdf, June, 2009.

[162] *Bound coherent neutron scattering lengths from periodic table switchboard*, http://www.ati.ac.at/∼neutropt/scattering/ScatteringLengthsAdvTable.pdf, Setember, 2009.

[163] J. E. Lynn and P. A. Seeger, Atomic Data and Nuclear Data Tables **44**, 191-207 (1990).

[164] E. Leonova et al., Journal of Non-Crystalline Solids **354**, 49-60 (2008).

[165] R. A. Martin et al., Physical Review B **68**, 054203 (2003).

[166] E. Lorch, Journal of Physics C: Solid State Physics **2**, 229-237 (1969).

[167] V. Kahlenberg and H. Krüger, Solid State Sciences **6**, 553-560 (2004).

[168] M. Kitayama, Mineralogical Magazine **52**, 257-265 (1988).

[169] L. León-Reina et al., Solid State Ionics **177**, 1307-1315 (2006).

[170] J. M. Bennett, J. V. Smith and C. L. Angell, Materials Research Bulletin **4**, 77-86 (1969).

[171] A. I. Frenkel et al., Physical Review B **48**, 12449-12458 (1993).

[172] W. Smith, C. W. Yong and P. M. Rodger, Molecular Simulation **28**, 385-471 (2002).

[173] R. A. Martin, G. Mountjoy and R. J. Newport, Journal of Physics Condensed Matter **21**, 075102 (2009).

[174] O. Gereben et al., Journal of Optoelectronics and Advanced Materials **9**, 3021-3027 (2007).

[175] S. Le Roux and V. Petkov, Journal of Applied Crystallography **43**, 181-185 (2010).

[176] G. Dalba et al., Physical Review B **52**, 149-157 (1995).

[177] P. Fornasini et al., Physica Status Solidi (c) **1**, 3085-3088 (2004).

[178] E. D. Crozier and A. J. Seary, Canadian Journal of Physics **58**, 1388-1399 (1980).

[179] J. A. E. Desa et al., Journal of Non-Crystalline Solids **51**, 57-86 (1982).

[180] P. S. Salmon et al., Nature **435**, 75-78 (2005).

[181] D. A. Allen et al., Journal of Chemical Physics **94**, 5071-5076 (1991).

[182] V. V. Brazhkin et al., Journal of Physics Condensed Matter **19**, 246104 (2007).

[183] C. Fillaux et al., Physica Scripta **T115**, 339-341 (2005).

[184] L. Hefeng et al., Journal of Physics: Condensed Matter **6**, 3629-3640 (1994).

[185] R. Ruberto, G. Pastore and M. P. Tosi, Physics Letters A **373**, 1083-1088 (2009).

[186] S. R. Elliott, Physical Review Letters **67**, 711-71 (1991).

[187] L. Pusztai and R. L. McGreevy, Journal of Non-Crystalline Solids **117-118**, 627-630 (1990).

[188] D. A. Allen et al., Journal of Physics: Condensed Matter **4**, 1407-1418 (1992).

[189] Y. S. Badyal and R. A. Howe, Journal of Physics: Condensed Matter **5**, 7189-7202 (1993).

[190] Y. S. Badyal and R. A. Howe, Journal of Physics: Condensed Matter **8**, 3733-3754 (1996).

[191] J. Neuefeind, Physical Chemistry Chemical Physics **3**, 3987-3993 (2001).

[192] B. K. Sharma and M. Wilson, Journal of Physics Condensed Matter **20**, 244123 (2008).

[193] P. S. Salmon, Proceedings of the Royal Society: Mathematical and Physical Sciences **437**, 591-606 (1992).

[194] P. S. Salmon, Journal of Physics Condensed Matter **19**, 455208 (2007).

[195] A. B. Bhatia and D. E. Thornton, Physical Review B **2**, 3004-3012 (1970).

[196] F. H. Stillinger Jr and R. Lovett, Journal of Chemical Physics **49**, 1991-1994 (1968).

[197] *Modulated DSC paper #5: Measurement of Glass Transitions and Enthalpic Recovery*, T. C. Leonard, TA Instruments, Delaware, 2005.

[198] E. Kartini et al., Physica B **241-243**, 909-911 (1998).

[199] P. S. Gill, S. R. Sauerbrunn and M. Reading, Journal of Thermal Analysis **40**, 931-939 (1993).

[200] M. Isshiki et al., Nuclear Instruments and Methods in Physics Research A **467-468**, 663-666 (2001).

[201] T. Usuki, private communication, October, 2009.

[202] G. J. Janz et al., Journal of Physical and Chemical Reference Data **4**, 871 (1975).

[203] J. O'M. Bockris, A. Pilla and J. L. Barton, Revista de Chimie, Academie de la Republique Populair Roumaine **2**, 59-77 (1962).

[204] D. R. Gaskell, *Introduction to the Thermodynamics of Materials*, Taylor & Francis Ltd., London, 2003.

[205] A. Zeidler, *Ordering in Amorphous Binary Systems*, PhD thesis Unversity of Bath, 2009.

[206] P. S. Salmon et al., Journal of Physics Condensed Matter **16**, 195 (2004).

[207] M. Wilson and P. A. Madden, Journal of Physics Condensed Matter **5**, 6833 (1993).

[208] I. Petri, P. S. Salmon and W. S. Howells, Journal of Physics Condensed Matter **11**, 10219 (1999).

[209] S. Sastry and C. A. Angell, Nature **2**, 739-743 (2003).

[210] G. Franzese et al., Nature **409**, 692-695 (2001).

[211] O. Mishima and H. E. Stanley, Nature **396**, 329-335 (1998).

[212] J. N. Glosli and F. H. Ree, Physical Review Letters **82**, 4659-4662 (1999).

[213] I. Saika-Voivod, F. Sciortina and P. H. Poole, Physical Review E **63**, 011202 (2001).

[214] Y. Katayama et al., Nature **403**, 170-173 (2000).

[215] G. N. Greaves et al., Science **332**, 566-570 (2008).

[216] G. Monaco et al., Physical Review Letters **90**, 255701 (2003).

[217] A. C. Barnes et al., Physical Review Letters **103**, 225702 (2009).

[218] W. A. Crichton, Intermediate range-order in $ZnCl_2$, Technical Report HD-146, European Synchrotron Radiation Facility, 2007.

[219] J. Wong and F. W. Lytle, Journal of Non-Crystalline Solids **37**, 273-284 (1980).

[220] C. Fillaux, *Étude structurale et vibrationnelle du chlorure de zinc à hautes pressions et hautes températures*, PhD thesis Unversité Paris 6, 2004.

[221] K. Q. Lu and E. A. Stern, Nuclear Instruments & Methods in Physics Research **212**, 475-478 (1983).

[222] C. S. Zha, W. A. Bassett and S. H. Shim, Review of Scientific Instruments **75**, 2409-2418 (2004).

[223] O. L. Anderson, D. G. Isaak and S. Yamamoto, Journal of Applied Physics **65**, 1534-1543 (1989).

[224] D. L. Heinz and R. Jeanloz, Journal of Applied Physics **55**, 885-893 (1984).

[225] C. Kittel, *Introduction to solid state physics*, John Wiley & Sons Inc., New York, 1996.

[226] Y. Le Godec et al., Equation of State and Order Parameter in Graphite-Like h-BN under High temperature and pressure, in *Science and Technology of High Pressure*, edited by M. H. Manghnani, W. J. Nellis and M. F. Nicol, volume 2, pages 925-928, Hyderabad, India, 2000, International Association for the Advancement of High Pressure Science and Technology (AIRPT), Universities Press (India) Limited.

[227] B. Brehler, Zeitschrift für Kristallographie **115**, 373-402 (1961).

[228] E. Stumpp and F. Werner, Carbon **4**, 538 (1966).

[229] F. Kang, Y. Leng and T. Y. Zhang, Carbon **34**, 889-894 (1996).

[230] W. A. Crichton, private communication, June, 2010.

[231] H. Winkler and B. Brehler, Naturwissenschaften **46**, 553-554 (1959).

[232] J. Brynestad and H. L. Yakel, Inorganic Chemistry **17**, 1376-1377 (1978).

[233] H. L. Yakel and J. Brynestad, Inorganic Chemistry **17**, 3294-3296 (1978).

[234] M. Wilson, Journal of Chemical Physics **118**, 9838-9853 (2003).

[235] T. Usuki, private communication, July, 2010.

[236] C. H. Polsky et al., Physical Review B **61**, 5934-5938 (2000).

[237] M. Sakai, N. Kuroda and Y. Nishina, Journal of the Physical Society of Japan **54**, 4081-4084 (1985).

[238] W. A. Crichton, private communication, June, 2009.

[239] N. Dubrovinskaia and L. Dubrovinsky, Review of Scientific Instruments **74**, 3433-3437 (2003).

[240] K. Shinoda and N. Noguchi, Review of Scientific Instruments **79**, 015101 (2008).